

**Biotemplating Arrays of Nanomagnets Using the
Biomineralisation Protein Mms6**

Johanna Marie Galloway

Submitted in accordance with the requirements for the degree of
Doctorate of Philosophy

The University of Leeds

School of Physics and Astronomy

August, 2012

Intellectual Property and Publication Statement

The candidate confirms that the work submitted is her own, except where work which has formed part of jointly-authored publications has been included. The contribution of the candidate and the other authors to this work has been explicitly indicated below. The candidate confirms that appropriate credit has been given within the thesis where reference has been made to the work of others.

Jointly authored publications are listed in the bibliography (page III), and contributions from others to this work are as follows:

Chapter 3: Optimisation of protein expression and purification in collaboration with A. Rawlings, S. Baldwin & J. Ingram. Iron binding data courtesy of S. Corbett. Quark model of Mms6 courtesy of J. Bramble. Tryptophan fluorescence and CD in collaboration with A. Rawlings. Fabrication of samples and data analysis for QCM-D, XPS, AFM, & fluorescent microscopy was contributed by the candidate.

Chapter 4: Synthesis, TEM imaging & VSM of POFH MNPs, and all ICP-AES & XRD in this chapter courtesy of S. Staniland. Grainsize analysis of POFH and RTCP MNPs in collaboration with S. Staniland. TEM images, EELS maps, EDX spectra were recorded in collaboration with M. Ward, and VSM of RTCP MNPs was contributed by the candidate.

In Chapters 5 & 6, the synthesis, characterisation and analysis of the biotemplated magnetic arrays were contributed by the candidate, except rendering of the 3D MFM plots in 'R' by J. Bramble. SAED recorded in collaboration with M. Ward and A. Walton. XRD recorded and analysed in collaboration with L. Neve.

This copy has been supplied on the understanding that it is copyright material and that no quotation from the thesis may be published without proper acknowledgement.

The right of Johanna Marie Galloway to be identified as Author of this work has been asserted by her in accordance with the Copyright, Designs and Patents Act 1988.

© 2012 The University of Leeds and Johanna Marie Galloway

Bibliography

Galloway & Staniland (2012):

Galloway, J.M. & Staniland, S.S. (2012). Protein and peptide biotemplated metal and metal oxide nanoparticles and their patterning onto surfaces. *J. Mater. Chem.* **22**, pp 12423-12434.

Galloway et al. (2012a):

Galloway, J.M., Bramble, J.P., Rawlings, A.E., Burnell, G., Evans, S.D. & Staniland, S.S. (2012). Nanomagnetic arrays formed with the biomineralization protein Mms6. *J. Nano Res.* **17**, pp 127-146.

Galloway et al. (2012b):

Galloway, J.M., Bramble, J.P., Rawlings, A.E., Burnell, G., Evans, S.D. & Staniland, S.S. (2012). Biotemplated magnetic nanoparticle arrays. *Small* **8**, pp 204-208.

Galloway et al. (2011):

Galloway, J.M., Arakaki, A., Masuda, F., Tanaka, T., Matsunaga, T. & Staniland, S.S. (2011). Magnetic bacterial protein Mms6 controls morphology, crystallinity and magnetism of cobalt-doped magnetite nanoparticles in vitro. *J. Mater. Chem.* **21**, pp 15244-15254.

Acknowledgements

This work was supported by my PhD studentship from the Engineering and Physical Sciences Research Council, and some of the protein work was assisted by funding from the Biotechnology and Biological Sciences Research Council. Any specific contributions of others to the results presented in this work are detailed in the intellectual and property and publications statement on page II.

Firstly, I must thank Tom Hartquist for insisting that I meet with Sarah Staniland to discuss this project in December 2008, and for his encouragement during both the application and research processes. As my main supervisor, Sarah has provided outstandingly enthusiastic support, invaluable guidance and great insight during the many stages of development and execution of this work. I think that her energy and positive attitude were essential in creating many of the links with others that were essential to the completion of this multidisciplinary study. As support supervisors, I would like to thank Gavin Burnell, especially for his patience and eloquence when explaining many fundamental principles of physics, and Steve Evans for sharing his wealth of experience in the surface science arena. Their support was invaluable when Owen came along, and they helped to keep this research moving forward.

I would like to thank all of those in the Molecular and Nanoscale Physics group that have supported me, many are fantastic friends and all are great colleagues. Special thanks goes to Jonathan Bramble for being incredibly helpful, and for sharing his expertise in patterning surfaces and SAM formation processes. I am also grateful to Masayoshi Tanaka for teaching me an awful lot about magnetic bacteria. I would also like to thank Alex Walton for his help with the XPS, SEM and TEM, and Simone Stuart-Cole for her assistance in fitting and interpreting XPS data. I am also grateful to Łukasz Krzemiński for his support when collecting and fitting QCM-D data, Simon Connell for the excellent training in using AFM and MFM to analyse the biotemplated arrays, and Jason Morgan in interpreting the MFM plots. I would also like to thank those that have given up their time to read through parts of this thesis: Sarah, Jonathan, Andrea & Gavin, as well as Jenny Bain, Johannes Roth and James Towey, you are all legendary.

In Biology, Helena Norberczak, Jean Ingram, Andrea Rawlings and Steve Baldwin were fantastic, especially when training me to express and purify proteins. Andrea has also produced a lot of Mms6 protein, and done much to optimise its manufacture, without which this research would not have progressed as far as it has. I would like to thank all of those in the Condensed Matter group in Physics, especially Chris Marrows and Brian Hickey for allowing me to attend their undergraduate lectures as a Ph.D student. Also, Oscar Céspedes and Mannan Ali for their assistance with the VSM. In Earth & Environment, I am grateful to Lesley Neve for running the XRD samples and helping to fit the spectra. Those in Engineering I would like to thank are Mike Ward for his help with TEM, SAED, EDX and EELS, and John Harrington and Richard Walshaw for their guidance when using SEM and EDX mapping.

I would like to offer my thanks to the friends that have helped me to maintain some semblance of sanity by providing welcome distractions to this work. I am especially grateful to Jim, mainly for being lovely, but also for listening, laughing and smiling. I would also like to acknowledge my mum, dad and brother, as they have offered me so much in the way of support and encouragement, and have even tried to take an interest in this subject because I do.

For Bill, Eric, Aileen and Ivy

Abstract

High quality magnetic nanoparticles (MNPs) are used in applications such as electronic data storage. Current methods for synthesising the consistent MNPs required use high temperatures, harsh chemicals and bespoke equipment. As this is energy intensive, expensive and not very environmentally friendly, cheaper and 'greener' alternatives are being sought. Mms6 is a biomineralisation protein from a magnetic bacterium (*Magnetospirillum magneticum* AMB-1), which is able to biotemplate the formation of uniform cubo-octahedral magnetite nanoparticles *in vitro* under mild reaction conditions. The *N*-terminal section is hydrophobic, and may cause the protein to self-assemble in aqueous solution. This self-assembly may facilitate the biotemplating ability of the protein, but it is the acidic *C*-terminal section of the protein that is the most important for binding iron and templating uniform MNPs.

Attachment of Mms6 via the *N*-terminus to a micro-contact printed (μ CP) patterned self-assembled monolayer (SAM) allows the protein to biotemplate uniform, ferrimagnetic magnetite MNPs *in situ*. These biotemplated MNPs were investigated with magnetic force microscopy (MFM), which found that they form multi-particle zones of attraction and repulsion. This is likely to be due to exchange-coupling of MNPs on the surface, with the long-axis of these magnetic features running parallel to the long axis of the assembly of patterned nanoparticles. As magnetite is magnetically soft, the system was doped with cobalt to increase the coercivity of the MNPs, both when templated onto a surface and in a bulk solution. To create biotemplated MNPs for use in data storage, a high coercivity is necessary to ensure that the magnetic orientation, and therefore the data recorded, is retained. The work presented here demonstrates that biotemplating can be used to produce high quality magnetic materials under far milder conditions than required in current industrial synthesis techniques, which should allow the development of more environmentally friendly bioinspired devices in the future.

Table of Contents

Title Page	I
Intellectual Property and Publication Statement	II
Bibliography	III
Acknowledgements	IV
Dedication	VI
Abstract	VII
Table of Contents	VIII
List of Tables	XV
List of Figures	XVII
Abbreviations and Definitions	XXIV
Part I – Introduction and Methods	1
1 Introduction	2
1.1 Context	2
1.2 Aims and Objectives	4
1.3 Magnetic Materials.....	5
1.3.1 Magnetism.....	5
1.3.1.1 Magnetic Domains	8
1.3.1.2 Magnetic Hysteresis.....	9
1.3.1.3 Magnetic Ferrites	12
1.3.2 Nanoparticles (NPs)	14
1.3.3 Magnetic Nanoparticles (MNPs)	14
1.3.4 Formation of Magnetic Nanoparticles	17
1.3.4.1 Thermal Decomposition	18
1.3.4.2 Room Temperature Co-precipitation (RTCP)	19
1.3.4.3 Partial Oxidation of Ferrous Hydroxide (POFH).....	19
1.4 Proteins and Biomineralisation.....	20
1.4.1 Biomineralisation.....	20
1.4.2 Magnetic Bacteria.....	21
1.4.3 Magnetosome Formation.....	25

1.4.4	Biom mineralisation Protein Mms6.....	27
1.4.5	Recombinant Protein Synthesis and Purification.....	29
1.5	Self-Assembled Monolayers (SAMs)	32
1.5.1	Types of SAMs	33
1.5.2	Functionalising SAMs	36
1.5.3	Attachment of Proteins to Surfaces.....	36
1.5.3.1	Affinity Tag Immobilisation.....	37
1.5.3.2	EDC/NHS Activated Ester Linkage	39
1.5.4	Patterning SAMs.....	40
1.5.4.1	Photolithography.....	40
1.5.4.2	Electron Beam (e-beam) and Focussed Ion Beam (FIB) Lithography	41
1.5.4.3	E-beam Chemical Lithography (eBCL)	41
1.5.4.4	Soft UV Photolithography	41
1.5.4.5	Probe Patterning Methods	42
1.5.4.6	Micro-Contact Printing (μ CP).....	42
1.5.4.7	Patterning SAMs for Biotemplated MNP Array Formation.....	43
1.6	Summary of Chapters.....	44
1.7	References.....	44
2	Methods	59
2.1	Protein Synthesis and Purification	59
2.1.1	His ₆ -MBP-Mms6 Production by Auto Induction	59
2.1.2	His ₆ -Mms6 Production by IPTG Induction	61
2.1.3	Immobilised Metal-ion Affinity Chromatography (IMAC)	63
2.1.4	Affinity Tag Cleavage Using the Tobacco Etch Virus (TEV) Protease	63
2.1.5	Sodium Dodecyl Sulfate-Polyacrylamide Gel Electrophoresis (SDS-PAGE) with Tricine.....	64
2.1.5.1	Coomassie Stain	65
2.1.5.2	Western Blot for Hexahistidine.....	65
2.2	Protein Activity and Stability	66
2.2.1	Modelling Mms6 Structure	66
2.2.2	Iron Binding by Mms6	67
2.2.2.1	Chemical Detection of Iron Bound by Mms6.....	67
2.2.2.2	Tryptophan Fluorescence	68
2.2.2.3	Circular Dichroism (CD).....	69

2.2.3	Accessibility of the His-tag on Pre-formed MNPs.....	70
2.3	SAMs of Alkanethiols on Gold.....	71
2.3.1	Gold Substrate Preparation	71
2.3.2	Preparation of Uniform and Mixed SAMs.....	71
2.3.3	Micro-Contact Printing (μ CP).....	72
2.3.4	Characterisation of SAMs.....	73
2.3.4.1	Ellipsometry	73
2.3.4.2	Water Contact Angle	75
2.3.4.3	X-ray Photoelectron Spectroscopy (XPS).....	75
2.4	Protein Attachment to Surfaces.....	77
2.4.1	Methods for Protein Attachment	77
2.4.1.1	Histidine to Ni^{2+} -NTA Terminated SAM	77
2.4.1.2	EDC/NHS onto Carboxyl Terminated SAM	78
2.4.2	Monitoring Protein Attachment	79
2.4.2.1	Quartz Crystal Microbalance with Dissipation (QCM-D).....	79
2.4.2.2	Fluorescence Microscopy	81
2.5	Magnetic Nanoparticle Synthesis	82
2.5.1	Room Temperature Co-precipitation (RTCP).....	82
2.5.2	Partial Oxidation of Ferrous Hydroxide with Potassium Hydroxide (POFHK)	83
2.5.3	POFHK on a Patterned Surface	84
2.5.4	Partial Oxidation of Ferrous Hydroxide with Ammonia and Hydrazine (POFHN)	85
2.5.5	POFHN on a Patterned Surface	86
2.6	Characterisation of Magnetic Nanoparticles	87
2.6.1	Transmission Electron Microscopy (TEM)	87
2.6.2	Scanning Electron Microscopy (SEM)	89
2.6.3	Particle Size Analysis of Electron Microscope Images.....	91
2.6.4	Inductively Coupled Plasma-Atomic Emission Spectroscopy (ICP-AES)	92
2.6.5	Powder X-ray Diffraction (XRD).....	92
2.6.6	Vibrating Sample Magnetometry (VSM)	93
2.6.7	Atomic/Magnetic Force Microscopy (AFM/MFM)	94
2.7	References	96

Part II – Results and Discussion	101
3 Mms6 and Patterning onto Surfaces	102
3.1 Protein Expression and Purification	102
3.1.1 Mms6.....	103
3.1.2 His ₆ -Mms6	104
3.2 Protein Structure and Activity.....	107
3.2.1 Model Structure of Mms6.....	107
3.2.2 Aqueous Iron Binding to Mms6	109
3.2.2.1 Chemical Detection of Iron Bound by Mms6	109
3.2.2.2 Tryptophan Fluorescence of Mms6.....	111
3.2.2.3 Circular Dichroism of Mms6.....	113
3.2.2.4 The Structure and Function of Mms6.....	115
3.2.3 Accessibility of His ₆ -tag on Pre-formed MNPs.....	117
3.3 Protein Attachment to Self-Assembled Monolayers	117
3.3.1 EDC/NHS binding of Protein to a SAM.....	118
3.3.1.1 Monitoring Protein Attachment to SAMs using QCM-D.....	118
3.3.1.2 XPS of PEG SAMs	124
3.3.1.3 Aqueous Heat Stability of SAMs	126
3.3.2 Functionalising SAMs with Nitrilo-triacetic Acid (NTA).....	129
3.3.3 Imaging Protein Attachment.....	134
3.3.3.1 AFM of Protein Patterns	134
3.3.3.2 Fluorescent Microscopy.....	135
3.4 References	138
4 Magnetic Particles Formed from a Bulk Solution	143
4.1 Effect of Cobalt Doping on Non-biotemplated MNPs	144
4.1.1 VSM of POFHK MNPs	144
4.1.2 VSM of POFHN MNPs.....	145
4.1.3 ICP-AES of POFH MNPs.....	146
4.1.4 XRD of POFH MNPs.....	147
4.2 Cobalt Doping and Mms6 in the POFH System.....	149
4.2.1 POFHK TEM and Grainsize Analysis	150
4.2.2 POFHN TEM and Grainsize Analysis.....	151
4.2.3 Quality of POFH MNPs	153
4.3 Cobalt Doping, Mms6 and the RTCP System	154
4.3.1 TEM and Grainsize Analysis of RTCP MNPs	155

4.3.2	Elemental Analysis of RTCP MNPs	157
4.3.2.1	ICP-AES of RTCP MNPs	157
4.3.2.2	EELS and EDX of RTCP MNPs	157
4.3.3	Crystallinity of RTCP MNPs.....	160
4.3.4	VSM of RTCP MNPs	162
4.3.4.1	Magnetisation with Temperature	162
4.3.4.2	Magnetic Hysteresis.....	164
4.3.5	RTCP, 6% Co, Mms6 and His ₆ -Mms6	168
4.4	References	169
5	Optimisation of Magnetic Array Synthesis	172
5.1	Attachment of Preformed Biotemplated MNPs	173
5.2	RTCP Mineralisation of Immobilised Mms6.....	176
5.3	POFHK Mineralisation of Immobilised Mms6	178
5.3.1	Effect of Varying Counter Ions on POFHK.....	178
5.3.2	Effect of Incubation Time and Temperature on POFHK.....	179
5.3.3	Reactant Ratios for POFHK	181
5.3.4	Nanopatterns Mineralised Using POFHK	183
5.3.5	Total Concentration of Reactants for POFHK.....	184
5.4	POFHN After Mms6 Immobilisation.....	186
5.4.1	Effect of Varying Counter Ions on POFHN	186
5.4.2	Effect of Incubation Time and Temperature on POFHN.....	188
5.4.3	Reactant Ratios for POFHN	190
5.4.4	Total Concentration of Reactants for POFHN.....	191
5.5	Summary of Magnetite Formation by POFH.....	191
5.6	Cobalt Doping of POFH Biomineralised Patterns	193
5.6.1	POFHN and 6% Cobalt Doping of Immobilised Mms6 Patterns.....	193
5.6.2	POFHK and 6% Cobalt Doping of Immobilised Mms6 Patterns.....	195
5.6.3	POFHK and 33% Cobalt Ferrite Mineralisation of Immobilised Mms6 Patterns	196
5.7	References	198

6	Characterisation of Biotemplated Magnetic Arrays	199
6.1	Magnetite Templated by Immobilised Mms6	199
6.1.1	Grainsize Analysis from SEM and TEM	200
6.1.2	EDX Elemental Mapping of Biotemplated Magnetite Arrays	204
6.1.3	Crystallinity of Biotemplated Magnetite Arrays	206
6.1.3.1	Selected Area Electron Diffraction (SAED)	206
6.1.3.2	Powder X-ray Diffraction (XRD)	208
6.1.4	VSM of Biotemplated Magnetite Arrays	211
6.1.4.1	Magnetisation with Temperature	211
6.1.4.2	Magnetic Hysteresis	213
6.1.5	MFM of Biotemplated Magnetite Arrays	215
6.2	6% Cobalt Doped Magnetite Templated by Immobilised Mms6	219
6.2.1	Grainsize Analysis from SEM and TEM	219
6.2.2	EDX Elemental Mapping of Biotemplated 6% Cobalt Doped Magnetite Arrays	222
6.2.3	Crystallinity of Biotemplated 6% Cobalt Doped Magnetite Arrays from XRD	223
6.2.4	VSM of Biotemplated 6% Cobalt Doped Magnetite Arrays	225
6.2.5	MFM of 6% Cobalt Doped Magnetite Arrays	227
6.3	Cobalt Ferrite Templated by Immobilised Mms6	230
6.3.1	EDX Elemental Mapping of Biotemplated Cobalt Ferrite Arrays	231
6.3.2	MFM of Biotemplated Cobalt Ferrite Arrays	232
6.4	References	234

Part III – Conclusions and Future Work.....	234
7 Conclusions and Future Work	237
7.1 The Mms6 Protein.....	237
7.1.1 Expression and Purification of Mms6.....	237
7.1.2 Protein and Particle Attachment to SAMs.....	239
7.1.3 Self-assembly of Mms6 in Aqueous Solution.....	240
7.1.4 Mms6 and Iron Binding	242
7.1.5 Interaction of Mms6 with Specific Crystallographic Planes of Magnetite When in an Aqueous Solution.....	244
7.1.6 Mms6 Templating Magnetite MNPs When Immobilised on a Patterned Surface	245
7.2 Biotemplated MNPs Synthesised From a Bulk Solution	248
7.2.1 POFHN and POFHK	248
7.2.2 RTCP	249
7.3 Patterning Mms6 Biotemplated MNPs.....	251
7.3.1 RTCP and Surface Patterning	251
7.3.2 Biotemplated Magnetite Formation on a Surface.....	252
7.3.3 Biotemplated 6% Co Doped Magnetite Formation on a Surface.....	254
7.3.4 Biotemplated Cobalt Ferrite Formation on a Surface	254
7.4 Properties of Mms6 Biotemplated Arrays of MNPs.....	255
7.4.1 Biotemplated Arrays of Magnetite.....	255
7.4.2 Biotemplated Arrays of 6% Cobalt Doped Magnetite	257
7.4.3 Biotemplated Arrays of Cobalt Ferrite.....	258
7.5 Future Directions for Biotemplated Arrays.....	259
7.5.1 Patterning Pre-formed High Anisotropy Biotemplated MNPs	261
7.5.2 Biotemplating Thin-films of High Anisotropy Magnetic Materials	264
7.5.3 Magnetic Recording onto Biotemplated Magnetic Surfaces.....	265
7.5.4 Multi-material Biotemplated Devices.....	267
7.6 References	268

List of Tables

Table 1.1. Table of advantages and disadvantages for each SAM system, based on in text references.	36
Table 1.2. Summary of techniques for patterning self-assembled monolayers to functionalise substrates.	43
Table 2.1. Ratio of stock solutions used to prepare POFHK MNPs.	83
Table 2.2. Ratio of stock solutions used to prepare POFHN MNPs.	85
Table 2.3. Details of spectra used from EVA software to fit XRD patterns.	93
Table 3.1. Summary of Mms6 protein structure based on fitting CD spectra using DichroWeb.	114
Table 3.2. Modelling fits to data from QCM-D shown in Figure 3.10.	120
Table 3.3. Modelling fits to data from QCM-D shown in Figure 3.12.	123
Table 3.4. Details of fitted peaks and relative atomic percentages for PEG-OH and PE-COOH mixed SAMs.	124
Table 3.5. Summary of reaction conditions for <i>L</i> -NTA coupling to carboxylic acid SAMs and subsequent metal ion functionalisation, based on literature cited in table.	130
Table 3.6. Summary of range of reaction conditions used to try and couple <i>L</i> -NTA to carboxylic acid SAMs for transition metal functionalisation based on Table 3.5.	131
Table 4.1. Summary of magnetic properties of non-biotemplated MNPs from both POFH methods.	146
Table 4.2. ICP-AES results for relative abundance of cobalt as a ratio of the total metal ions in the MNPs, from Galloway <i>et al.</i> (2011).	147
Table 4.4. Summary of grainsize analysis data for POFH MNPs, averages, errors and detail of fitted peaks, from Galloway <i>et al.</i> (2011).	150
Table 4.5. Summary of grainsize analysis data for RTCP MNPs, averages, errors and detail of fitted peaks, from Galloway <i>et al.</i> (2011).	155
Table 4.6. Analysis of RTCP XRD peaks and grainsize, from Galloway <i>et al.</i> (2011).	161
Table 4.7. Summary of magnetic properties of RTCP MNPs from VSM hysteresis loops.	166

Table 6.1. Summary of grainsize data comparing different methods of biomineralising magnetite onto patterned Mms6 arrays shown in Figure 6.1, from Galloway <i>et al.</i> (2012a).....	200
Table 6.2. Summary of SAED data from Figure 6.4 with comparison to magnetite & maghemite peaks from EVA software (see Table 2.3), and goethite peaks from Cornell & Schwertmann (2003).....	206
Table 6.3. Table of peak positions for magnetite and maghemite (based on spectra from EVA software, see Table 2.3) and peak positions from samples shown in Figure 6.5, measured in Å.	210
Table 6.4. Summary of grainsize data presented in Figure 6.10, comparing undoped and 6% Co doped MNPs both templated by Mms6 on a surface, and formed with no protein from the bulk solution.	221
Table 6.5. Table of peak positions for magnetite and cobalt ferrite (based on spectra from EVA software, see Table 2.3) and peak positions from samples shown in Figure 6.12, measured in Å.	224

List of Figures

Figure 1.1. Schematic diagram to show the formation of biomineralised arrays of magnetic nanoparticles.	4
Figure 1.2. Schematic to show different types of bulk magnetic ordering.	7
Figure 1.3. Illustration of the magnetic field in and around a material, from Blundell (2001).	8
Figure 1.4. Schematic of domain growth and rotation of magnetisation from Newey & Weaver (1990).	9
Figure 1.5. A diagram of a magnetic hysteresis loop.	10
Figure 1.6. Diagram to show examples of hysteresis loops of materials used for different applications.	12
Figure 1.7. Diagram of the inverse spinel structure of magnetite from Sorescu (1998).	13
Figure 1.8. Schematic illustration of longitudinal and perpendicular granular recording for magnetic data storage, based on PIRAMANAYAGAM (2007).	16
Figure 1.9. Phase diagram of iron oxides and oxyhydroxides formed under variable pE + pH and activity of iron, after Cornell & Schwertmann (2003).	18
Figure 1.10. TEM images of magnetic bacteria from Faivre & Schüler (2008).	22
Figure 1.11. TEM image of magnetic bacterium <i>M. magneticum</i> AMB-1 from Matsunaga <i>et al.</i> (2005).	23
Figure 1.12. Sequence in time (left) and depth (right) of redox dependent chemical gradients in stratified sediments, redrawn from Reddy & DeLaune (2008) and Charman (2002).	24
Figure 1.13. Schematic illustration of bacterial MNP formation in AMB-1, adapted from Arakaki <i>et al.</i> (2008).	25
Figure 1.14. Phase stability (Eh-pH) Pourbaix diagram for the iron-water system likely to exist within the magnetosome (total concentration Fe=10 µM) from Faivre & Schüler (2008).	27
Figure 1.15. High resolution transmission electron microscopy (HRTEM) images of magnetite crystals from Amemiya <i>et al.</i> (2007).	28
Figure 1.16. Schematic summary of Mms6 manufacture, based on Singleton (2004) & Pruden <i>et al.</i> (2002).	30
Figure 1.17. Diagram to show His _x -tag interaction with Ni ²⁺ -NTA during IMAC after Ludden <i>et al.</i> (2008), Abad <i>et al.</i> (2005) and Mrksich & Whitesides (1995).	31

Figure 1.18. Illustration of formation of a SAM from a dilute solution, after Ulman (1996).....	33
Figure 1.19. Stick and ball diagram to show polysiloxane structure at the monolayer-substrate surface after Ulman (1991).....	34
Figure 1.20. Stick and ball diagrams to show some organosulfur compounds that form SAMs on gold surfaces, from Ulman (1996).	34
Figure 1.21. Reaction scheme for protein immobilisation onto a carboxylic acid surface using EDC/NHS, based on the Thermo Scientific website.	39
Figure 2.1. Vector diagram of pBPTNHOMT- <i>mms6</i> plasmid, arrows indicate read direction.....	60
Figure 2.2. Vector diagram for pET28b- <i>mms6</i> plasmid, arrows indicate read direction.....	62
Figure 2.3. Schematic of tricine minigel for SDS-PAGE.....	65
Figure 2.4. Circular dichroic effect and signal detected after transmission, after Kelly <i>et al.</i> (2005).	69
Figure 2.5. Diagram to show stages of micro-contact printing, based on Mrksich & Whitesides (1995).	72
Figure 2.6. Schematic of an ellipsometer, from Ulman (1991).	74
Figure 2.7. Schematic of a water contact angle on a hydrophobic surface, after Ulman (1996).....	75
Figure 2.8. Schematic of photoelectron emission during XPS from Watts & Wolstenholme (2002).	76
Figure 2.9. Structures of molecules used to form SAM and functionalise SAM with NTA for protein attachment.	78
Figure 2.10. Schematic of Voight viscoelastic model, redrawn from the QSense website.	81
Figure 2.11. Diagram of the reaction vessel for mineralisation of a protein patterned surface after Galloway <i>et al.</i> (2012a).	84
Figure 2.12. Schematic of TEM showing ray path, adapted from Reimer & Kohl (2010).....	88
Figure 2.13. Schematic showing interaction of electrons with a substrate during SEM, based on Reimer (1998) and Goldstein <i>et al.</i> (2003).....	90
Figure 2.14. Schematic of imaging with AFM/MFM, based on the Multimode™ SPM Instruction Manual.....	94

Figure 3.1. Stick diagram of an amino acid and the primary amino acid sequence of Mms6.....	102
Figure 3.2. Tricine SDS-PAGE analysis of Mms6 expression and purification, from Galloway <i>et al.</i> (2012a).	104
Figure 3.3. Western blot (upper image) and Coomassie stained SDS-PAGE (lower image) analysis of His ₆ -Mms6 purification.	105
Figure 3.4. Cartoon and surface of model based on the Mms6 primary amino acid sequence.....	108
Figure 3.5. Luminescence due iron bound by His ₆ -SUMO-Mms6 for different concentrations of iron added to the protein.	109
Figure 3.6. Plot of concentration of ferric iron citrate against the luminescence due to the reaction of luminol with iron.	110
Figure 3.7. Cartoon of Mms6 model to show the position of the tryptophan residue.....	112
Figure 3.8. Circular dichroic spectra for His ₈ -Mms6 (green) and His ₈ -Mms6 with iron citrate (blue).....	113
Figure 3.9. Cartoon of Mms6 model to show the position of the 'KSR' motif.k ¹¹ an.....	116
Figure 3.10. Frequency shift during non-specific binding of proteins to SAMs, monitored with QCM-D, only 9 th overtone shown for clarity.	119
Figure 3.11. Cartoons of the protein crystal structure of TEV (pdb file 1q31).....	121
Figure 3.12. QCM-D data for Mms6 attachment to PEG-OH SAM (dotted lines) and mixed SAM of 10% PE-COOH/90% PEG-OH (solid lines).	122
Figure 3.13. XPS spectra and relative abundances of elements in mixed PEG-OH and PE-COOH SAMs.	125
Figure 3.14. (a) Ellipsometric thickness and (b) water contact angle of SAMs before and after heating in water to 90°C for 4 hours.	127
Figure 3.15. QCM-D trace from protein attachment to SAMs treated with aqueous EDC (1 mL, 0.2 mM) and NHS (5 mL, 0.2 mM) for 30 minutes before immersing in L-NTA (0.5 mM in buffer) overnight.	132
Figure 3.16. Detailed XPS spectra of Ni ²⁺ -NTA SAM peaks.	133
Figure 3.17. Tapping mode AFM images of patterned SAM after protein attachment by EDC/NHS.....	135
Figure 3.18. Cartoon of the structure of eGFP, and fluorescent microscopy images of patterned eGFP and mCherry fluorescent proteins.	136
Figure 3.19. Schematic illustration of micro-contact printing and fluorescent protein attachment to SAMs.	137

Figure 4.1. Hysteresis loops of POFHK MNPs, recorded at 10 K, H applied between ± 10 kOe, redrawn from Galloway <i>et al.</i> (2011).	145
Figure 4.2. Hysteresis loops from VSM of POFHN MNPs, recorded at 10 K, H applied between ± 10 kOe, redrawn from Galloway <i>et al.</i> (2011).	146
Figure 4.3. Powder XRD of magnetite MNPs synthesised by POFHN (black) and POFHK (green), after Galloway <i>et al.</i> (2011).	148
Figure 4.4. TEM images and grainsize analysis of POFHK MNPs, from Galloway <i>et al.</i> (2011).	151
Figure 4.5. TEM images and grainsize analysis of POFHN MNPs, from Galloway <i>et al.</i> (2011).	152
Figure 4.6. TEM and grainsize analysis of RTCP MNPs, from Galloway <i>et al.</i> (2011).	156
Figure 4.7. TEM images, EELS maps and EDX analysis of $\text{Co}_{\text{His6-Mms6}}$ and $\text{Co}_{\text{no protein}}$ MNPs, from Galloway <i>et al.</i> (2011).	158
Figure 4.8. Powder XRD diffraction patterns for RTCP MNPs, from Galloway <i>et al.</i> (2011).	161
Figure 4.9. VSM of ZFC (lower trace) and FC (upper trace) measurements for RTCP MNPs, from Galloway <i>et al.</i> (2011).	163
Figure 4.10. Summary of data used to estimate upper size limit of SD and SP particles for different levels of cobalt doping into magnetite, from Galloway <i>et al.</i> (2011).	165
Figure 4.11. Hysteresis loops recorded using VSM of dried MNPs formed by RTCP, from Galloway <i>et al.</i> (2011).	166

Figure 5.1. SEM images of patterned surfaces after incubation with preformed RTCP MNPs.	175
Figure 5.2. SEM images of RTCP and Mms6 protein patterned surfaces, from Galloway <i>et al.</i> (2012a).	177
Figure 5.3. SEM images of Mms6 patterned substrates after POFHK with varying salt counter ions.....	179
Figure 5.4. SEM images of patterned surfaces mineralised using POFHK and under varying mineralisation incubation times and temperatures, adapted from Galloway <i>et al.</i> (2012a).....	180
Figure 5.5. SEM images of substrates with varied ratios of reactants for POFHK and Mms6 patterned surfaces, redrawn from Galloway <i>et al.</i> (2012a).	182
Figure 5.6. SEM of microscale and nanoscale patterned lines of magnetite formed by POFHK onto immobilised Mms6 (25 mM FeSO ₄ , 55 mM KOH, 250 mM KNO ₃).	184
Figure 5.7. SEM image of micro-patterned line of magnetite on immobilised Mms6 using optimum conditions for POFHK method, and schematic of mineral phases produced under varying reactant ratios.	185
Figure 5.8. SEM images of Mms6 micropatterned surfaces after mineralisation with a range of iron salts using POFHN, redrawn from Galloway <i>et al.</i> (2012a).	187
Figure 5.9. SEM images of POFHN mineralised substrates with varying reaction conditions, total 10 mL reaction volume, redrawn from Galloway <i>et al.</i> (2012a & b).	189
Figure 5.10. SEM images of MNPs mineralised using POFHN, total 10 mL reaction volume, from Galloway <i>et al.</i> (2012a & b).	190
Figure 5.11. SEM image of micro-patterned chessboard of magnetite on immobilised Mms6 using optimum conditions for POFHN method, and schematic of varying mineral phases produced under different reactant ratios.....	191
Figure 5.12. SEM images of Mms6 patterned surfaces mineralised using POFHN with (a-b) 6% cobalt doped magnetite and (c-d) cobalt ferrite on micro-patterned Mms6.	194
Figure 5.13. SEM images of Mms6 patterned surfaces mineralised using POFHK with 6% Co doping onto micro-patterned Mms6.	196
Figure 5.14. SEM images of Mms6 patterned surfaces mineralised using POFHK with 33% Co doping (i.e. to form cobalt ferrite, CoFe ₂ O ₄) onto patterned Mms6.	197

Figure 6.1. SEM (left column), TEM (centre column) and grainsize analysis (right column and bottom) of MNPs formed on an Mms6 patterned array, redrawn from Galloway <i>et al.</i> (2012a).....	201
Figure 6.2. (a-b) TEM and (c-f) SEM images of POFHN MNPs, redrawn from Galloway <i>et al.</i> (2012b).....	203
Figure 6.3. EDX spectra and elemental maps from SEM of micro-patterned biomineralised magnetite surface.	205
Figure 6.4. TEM images and SAED patterns for POFHN _{Fe} controls, redrawn from Galloway <i>et al.</i> (2012b).....	207
Figure 6.5. Powder XRD of biomineralised micro-patterned arrays of magnetite and controls, from Galloway <i>et al.</i> (2012a & b).....	210
Figure 6.6. Schematic of a biomineralised sample in the VSM, and temperature versus moment for ZFC (red) and FC (blue) VSM measurements with an applied field of 200 Oe, from Galloway <i>et al.</i> (2012b).....	212
Figure 6.7. Magnetic hysteresis loops from biomineralised samples and controls from Galloway <i>et al.</i> (2012a & b).	214
Figure 6.8. Composite of tapping mode AFM topography and non-contact 200 nm lift height MFM plots, and representative SEM images of biotemplated magnetite patterns, from Galloway <i>et al.</i> (2012a & b).	216
Figure 6.9. Composite of tapping mode AFM topography and non-contact 50 nm lift height MFM plots, and representative SEM image of POFHN _{Fe_Mms6_surface} , from Galloway <i>et al.</i> (2012a & b).....	217
Figure 6.10. (a-b) SEM and (c-d) TEM images of POFHN _{Fe} (reactant conditions as in Figure 5.11) and POFHK _{6%Co} MNPs (reactant conditions as in Figure 5.13).....	220
Figure 6.11. EDX spectra and elemental maps of micro-patterned biomineralised 6% Co doped magnetite on a surface.	222
Figure 6.12. XRD of biomineralised micro-patterned arrays of magnetite, cobalt doped magnetite and controls.	224
Figure 6.13. Magnetic hysteresis loops for 6% cobalt doped and undoped magnetite samples.	225
Figure 6.14. Composites of tapping mode AFM topography and non-contact 200 nm lift height MFM plots, and a representative SEM image of 6% Co doped magnetite patterns.	228
Figure 6.15. Composite of tapping mode AFM topography and non-contact mode 100 nm lift height MFM plots, and representative SEM image of micro-patterned biotemplated 6% Co doped magnetite.	230
Figure 6.16. EDX spectra and elemental maps of nanolines of biomineralised cobalt ferrite, recorded at 20 keV.....	232
Figure 6.17. Composite MFM plots of cobalt ferrite biotemplated by Mms6 onto nanolines.	233

Figure 7.1. Illustration of self-assembly of Mms6 in an aqueous solution, not to scale.	242
Figure 7.2. Illustration of Mms6 biotemplating magnetite cubes when immobilised onto a surface, not to scale.....	246
Figure 7.3. Schematic illustration of Mms6 biomineralisation of magnetite onto a patterned surface, not to scale.	247
Figure 7.4. Illustration of Fe _{His6-Mms6} templated magnetite nanoparticle functionalised with drug molecules.....	250
Figure 7.5. (a) AFM of ferritin attached to a patterned SAM from Martinez <i>et al.</i> (2011) and (b) TEM of a sputtered thin-film of Fe _{0.45} Pt _{0.45} Ag _{0.10} on a MgO seed layer from Zhang <i>et al.</i> (2011).....	262
Figure 7.6. AFM image of biotemplated gold films on a patterned surface from Matmor & Ashkenasy (2011) and an illustration of a dual functional peptide which is biotemplating a metal thin-film onto a surface.	264
Figure 7.7. 2-D magnetic read-back images (left) and read-back waveforms (right) for magnetic tracks written by a drag tester, from Leong <i>et al.</i> (2011).	266

Abbreviations and Definitions

A pull out summary table of commonly used abbreviations is available at the back of this document.

Å	Ångström ($\times 10^{-10}$ m)
α -Fe ₂ O ₃	haematite
α -Fe ₃ O ₄	magnetite
α -Fe ₃ S ₄	greigite
α -FeOOH	goethite
β -FeOOH	akaganéite
γ	surface free energy
γ -Fe ₂ O ₃	maghemite
γ -FeOOH	lepidocrocite
$\Delta_f G^0$	standard Gibbs free energy of formation
λ	wavelength
μ CP	micro-contact printing
μ m	micrometres ($\times 10^{-6}$ m)
μ_r	relative permeability
σ	standard deviation
ω -group	functional group presented at the SAM surface
AEBSF	4-(2-aminoethyl) benzenesulfonyl fluoride hydrochloride
AFM	atomic force microscopy
AF ₀ M	antiferromagnetic
AMB-1	<i>Magnetospirillum magneticum</i> strain AMB-1, a magnetic bacterium
APS	ammonium persulfate
BCC	body centred cubic
BPM	bit patterned media
BSA	bovine serum albumin
C12	dodecane thiol
C18	octadecane thiol
CCD	charge coupled device
CD	circular dichroism
CoFe ₂ O ₄	cobalt ferrite
Co _{His6} -Mms6	6% cobalt doped magnetite MNPs synthesised with His ₆ -Mms6
Co _{Mms6}	6% cobalt doped magnetite MNPs synthesised with Mms6
Co _{no protein}	6% cobalt doped magnetite MNPs synthesised in the absence of protein
C-terminus	carboxyl terminus of a peptide or protein
Cys	cysteine – an amino acid
DCM	dichloromethane
DFP	dual functional peptide
DLS	dynamic light scattering

DM	diamagnetic
DNA	deoxyribose nucleic acid
DTT	dithiothreitol
e ⁻	an electron
eBCL	e-beam chemical lithography
e-beam	electron beam
EDC	ethyl(dimethylaminopropyl) carbodiimide
EDTA	ethylenediaminetetraacetic acid
EDX	energy dispersive X-ray
EELS	electron energy loss spectroscopy
eGFP	enhanced green fluorescent protein
em	fluorescence emission wavelength
emu	electromagnetic units – cgs unit of sample magnetisation
eV	electron volt – non-SI unit of energy
ex	fluorescence excitation wavelength
FC	field cooled
Fe ²⁺	ferrous iron
Fe ³⁺	ferric iron
FEG	field emission gun
Fe _{His6-Mms6}	magnetite MNPs synthesised with His ₆ -Mms6
Fe _{Mms6}	magnetite MNPs synthesised with Mms6
Fe _{no protein}	magnetite MNPs synthesised in the absence of protein
FIB	focussed ion beam
F _i M	ferrimagnetic
FLAG tag	an affinity tag, sequence DYKDDDDK
F _o M	ferromagnetic
FWHM	full width at half maximum
Ga	billion (x10 ⁹) years ago
GST	affinity tag, glutathione-s-transferase, 26 kDa
H	applied magnetic field
H _c	coercivity
HCP	hexagonal close packed crystal structure
HEPES	4-(2-hydroxyethyl)-1-piperazineethanesulfonic acid, a buffer
His ₆ -Mms6	hexahistidine tagged Mms6
His ₈ -TEV	octahistidine tagged tobacco mosaic virus protease
His _x	x histidine repeats, used to create affinity tags
HRP	horseradish peroxidase
HRTEM	high resolution TEM
Hz	Hertz – SI unit of frequency
ICP-AES	inductively coupled plasma - atomic emission spectroscopy
IMAC	immobilised metal-ion affinity chromatography
IPTG	isopropyl-β-D-thiogalactopyranoside
K	Kelvin – SI unit of temperature
kDa	kilo (x10 ³) Dalton, non-SI unit of molecular mass
LB	Luria-Bertani bacterial growth medium
LMR	longitudinal magnetic recording for data storage
L-NTA	N _α ,N _α -bis(carboxymethyl)-L-lysine
M	magnetic flux
Ma	million (x10 ⁶) years ago
MAI	magnetosome island, section of DNA containing genes necessary for magnetosome formation in magnetic bacteria

MBP	maltose binding protein, a solubility enhancing affinity tag, 42.5 kDa
mCherry	a red fluorescent protein
MD	multi-domain
MFM	magnetic force microscopy
MHA	16-mercaptohexadecanoic acid
MH _{max}	magnetic hardness
mixed SAM	SAM made from solution containing 10% PE-COOH/90% PEG-OH
mM	milli molar ($\times 10^{-3}$)
Mms6	magnetosome membrane specific protein of 6 kDa mass, a biomineralisation protein
<i>mms6</i>	gene encoding the Mms6 protein
MNP	magnetic nanoparticle
M _r	remanent magnetisation
MRI	magnetic resonance imaging
M _s	saturation magnetisation
MUA	11-mercaptoundecanoic acid
MU-OH	11-mercaptoundecanol
NHS	<i>N</i> -hydroxy succinimide
nm	nanometres ($\times 10^{-9}$ m)
NP	nanoparticle
NTA	<i>N</i> -nitriolo-triacetic acid
<i>N</i> -terminus	amino terminus of a peptide or protein
Oe	Oersted – cgs unit of applied magnetic field strength
Pa	Pascal – SI unit of pressure
PBS	phosphate buffered saline, a buffer
PCR	polymerase chain reaction
PDMS	poly(dimethyl)siloxane
pE	electron activity, a theoretical measure of redox potential
PE-COOH	carboxyl terminated polyethylene spaced alkanethiol
PEG	polyethylene glycol
PEG-OH	PEG terminated alkanethiol
PFDT	1H,1H,2H,2H perfluorodecane thiol
pI	isoelectric point, pH at which a protein has no net charge
PM	paramagnetic
pM	pico mole ($\times 10^{-12}$)
PMR	perpendicular magnetic recording for data storage
POFH	partial oxidation of ferrous hydroxide
POFHK	POFH with potassium hydroxide
POFHN	POFH with ammonia and hydrazine
ppb	parts per billion ($\times 10^{-9}$)
QCM-D	quartz crystal microbalance with dissipation
rpm	revolutions per minute
RTCP	room temperature co-precipitation
SAED	selected area electron diffraction
SAM	self-assembled monolayer
SD	single domain
SDS	sodium dodecyl sulfate
SDS-PAGE	SDS polymer gel electrophoresis
SEM	scanning electron microscopy
SNOM	scanning near-field optical microscopy
SP	superparamagnetic
SQUID	superconducting quantum interference device

Strep II tag	an affinity tag, sequence WSHPQFEK
SUMO	small ubiquitin-like modifier, a solubility enhancing protein, 12 kDa
T	Tesla – derived SI unit of magnetic flux density
T _B	blocking temperature
TBS	tris buffered saline, a buffer
TBST	TBS with Tween-20 surfactant
TEM	transmission electron microscope
TEMED	tetramethylethylenediamine
TEV	tobacco etch virus protease
T _V	Verwey transition temperature
VDW	Van der Waals forces
VSM	vibrating sample magnetometry
WD	working distance
xFe ₂ O ₃ ·yH ₂ O	ferrihydrite
XPS	X-ray photoelectron spectroscopy
XRD	powder X-ray diffraction
ZFC	zero field cooled

Part I
Introduction
and
Methods

Chapter 1

Introduction

1.1 Context

Applications for magnets, such as use in compasses to navigate the Earth's magnetic field, were discovered long before the mechanism of the phenomenon was understood. Magnetic materials have many uses today, such as for use in transformers, electrical motors, electronic data storage, as well as numerous medical applications.¹⁻³ The size, shape, structure and composition of a magnetic material determines its magnetic behaviour, and therefore the application it is suited to be used for (Section 1.3.1). Magnetic nanoparticles (MNPs) are usually ten to a few hundred nanometers in diameter, and have numerous existing and potential future applications (Section 1.3.3). For most purposes, a uniform size and shape distribution is essential to ensure the magnetic behaviour of the MNPs is consistent. However, uniform MNP synthesis often involves the use of high temperatures, high pressures, toxic chemicals and very carefully controlled reaction and maturation conditions.⁴⁻⁶ Magnetic bacteria are able to form precise magnetic particles with a narrow size distribution under ambient conditions, and without highly toxic chemicals. Therefore, the study of magnetic bacteria and their biomineralisation proteins offers a more environmentally friendly route towards fabricating of high quality, monodispersed MNPs.

Life on Earth is thought to have evolved at about 3.5 Ga as simple prokaryotic bacteria.⁷ About 2.0 Ga, more complicated eukaryotic bacteria emerge in the fossil record.⁷ Eukaryotes have internal compartments, called organelles, which are designed to perform specific tasks (Section 1.4.1). Later, some organisms evolved mechanisms to control the formation of minerals. This biomineralisation is essential to many life functions, and different minerals help to form the tissues essential for: predation (teeth), protection (shells, spines), locomotion and support (bones, exoskeletons), or sensing (small bones in the ear).

Magnetic bacteria biomineralise magnetite ($\alpha\text{-Fe}_3\text{O}_4$) or greigite (Fe_3S_4)⁸ magnetic nanoparticles within lipid and protein bounded organelles called magnetosomes (see Section 1.4.2).⁹ There are a wide range magnetosome MNP morphologies,¹⁰ but within an individual bacterial strain the MNPs are of an extremely consistent size and shape, and they are often arranged into chains.¹¹ This maximises the magnetic moment of the bacterium,¹² and allows it to passively align with an external magnetic field. In nature, this may allow the magnetic bacteria to align with the Earth's magnetic field, and help them to seek their optimal living conditions within varying chemical gradients.¹³ The magnetic bacteria are thought to control the location and formation of MNPs within the cell using genetically encoded proteins.¹⁴⁻¹⁶ A range of proteins work in concert to biomineralise consistent MNPs under mild reaction conditions.⁹ The proposed roles of these proteins include: the transport and accumulation of iron, assembly of crystallite precursors, templating of crystal morphology during nucleation and growth and the arrangement of MNPs into chains.¹⁷⁻¹⁹

Magnetic bacteria are easily separated from sediment or water samples, as many move in response to an applied magnetic field.²⁰ However, they have proven difficult to culture in the lab, possibly due to the narrow ranges in chemical and redox gradients they occupy in nature.²¹ Cultivation of some species has allowed workers to identify and study many key proteins involved in nanomagnet formation in these bacteria.^{15,17-19,22} Mms6 is one such magnetic bacterial biomineralisation protein (Section 1.4.4) that consistently templates uniformly sized cubo-octahedral magnetite MNPs both *in vivo*²³ and *in vitro*.^{22,24} For this study, recombinant Mms6 is used to template the formation of the nanomagnets on to patterned arrays. The Mms6 is dual functional as it is used to both template the formation of uniform, crystalline magnetic particles and to anchor them onto the patterned surface.

In this study, the expression, purification, patterning, immobilisation and structure of Mms6 have been investigated (Chapter 3). Then, Mms6 templated MNPs of magnetite and cobalt doped magnetite formed from an aqueous bulk solution were synthesised and characterised (Chapter 4). The chemistry of iron is complex, and there are many different iron containing minerals that can be formed by slightly adjusting the reaction conditions. Therefore, a range of reaction conditions were trialled to ensure that the mineralisation of the biotemplated magnetic arrays was optimised towards the formation of magnetite and cobalt doped magnetite (Chapter 5). By immobilising the biomineralised MNPs onto arrays (before or after MNP mineralisation) the materials properties and magnetic behaviour of the MNPs on the 2D arrays has also been investigated (Chapter 6). Finally, in Chapter 7 the

conclusions that can be drawn from these results are put into the context of current and potential future work.

1.2 Aims and Objectives

This project is designed to synthesise and characterise protein templated magnetic nanoparticles on a patterned surface, see Figure 1.1. The Mms6 biomineralisation protein (Section 1.4.4), which helps to form uniform magnetite MNPs, is attached selectively to a patterned surface, either before or after MNP formation (see Chapter 5). The advantage of using bioinspired methods to template MNP formation over current industrial techniques is that high quality materials can be synthesised under far milder reaction conditions. This means that biotemplated minerals are often more environmentally friendly to produce than the materials synthesised by current methods. This is because many conventional techniques often require toxic chemicals and high temperatures to fabricate high quality materials (e.g. see Section 1.3.4.1). Biomineralisation may help to develop less harsh, cheaper bio-inspired industrial materials synthesis techniques for the future. As there is an ever expanding diversity of biomineralisation proteins and peptides, some of the methods used here may be suitable for adaptation to biotemplate other desired materials.

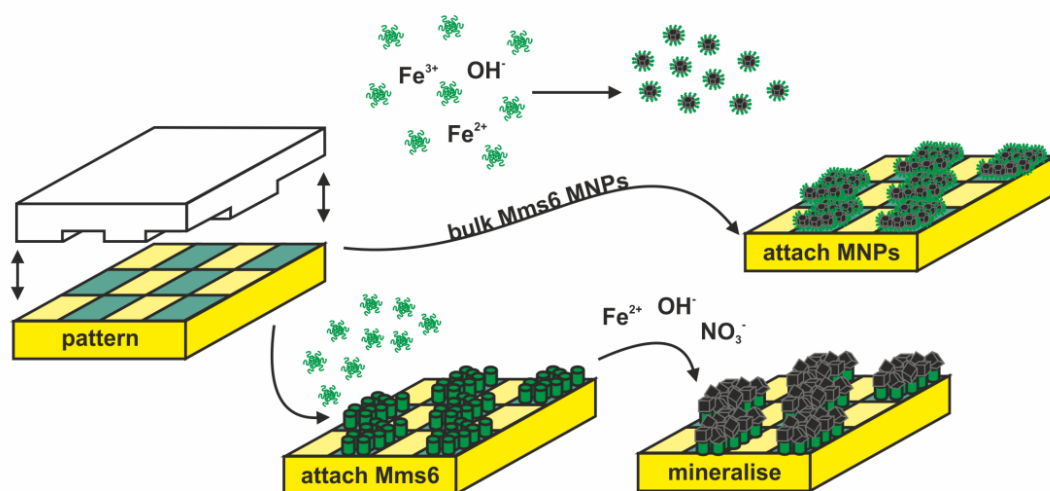


Figure 1.1. Schematic diagram to show the formation of biomineralised arrays of magnetic nanoparticles. Firstly, the substrate is patterned to promote or resist Mms6 protein binding. If the particles are synthesised prior to patterning (top route) functionalising the surface with this pattern should resist or promote protein binding, and therefore MNPs are immobilised, where desired. However, if the Mms6 is attached before MNP mineralisation occurs (lower route), this same pattern of functionalities should resist or promote Mms6 attachment, and thus form areas that promote or resist MNP biomineralisation.

Patterning the particles on a surface allows the magnetic interactions of individual nanomagnets to be probed on the 2D arrays. The main application that utilises 2D magnetic materials on surfaces (either as thin-films or monolayers of MNPs) is magnetic data storage. The magnetic materials used for contemporary data storage have different magnetic properties to the biotemplated magnetite formed by the Mms6 protein in nature. Here, controlled doping of cobalt into the biomineralised magnetite is also investigated. This allows the magnetic properties of the MNPs to be tuned between that of magnetite (high saturation magnetisation/low coercivity) and cobalt ferrite (low saturation magnetisation/high coercivity). It is only by investigating the magnetic interactions of the MNPs on a 2D surface that any possible suitability for data storage can be assessed. Therefore, the aims of this study are to:

- Study the Mms6 protein and the binding of Mms6 with aqueous iron and/or magnetite particles.
- Synthesise and characterise biotemplated magnetite and cobalt doped magnetite MNPs formed from an aqueous bulk solution.
- Selectively pattern Mms6 onto a surface.
- Optimise MNP attachment/formation onto micro-patterned arrays.
- Characterise the biotemplated MNPs on the micro-patterned arrays.

1.3 Magnetic Materials

In this section, magnetism is described for bulk materials and magnetic nanoparticles. There are also some details on different methods of synthesising magnetic nanoparticles. Much of the information on magnetism as described in this section is from Braithwaite & Weaver (1990),¹ Crowell (2001),² Blundell (2001)²⁵ & Newey & Weaver (1990).²⁶

1.3.1 Magnetism

The response of a magnetic material to an external magnetic field is determined by its structure. This structuring occurs on different scales; from the sub-atomic fields created by electrons, the arrangement of atoms into a crystalline structure and the ordering of unit cells to form macroscopic crystals. On the atomic level, magnetic fields are generated by the orbital angular momentum and spin of electrons as they orbit the nucleus of an atom.¹ There is no net magnetic moment on a diamagnetic (DM) atom in the absence of an applied field, because the orbitals are filled with paired electrons. As the electron pairs balance opposing spins, there is no net motion of the electrons, and therefore no net magnetic moment.¹ When an atom is

subjected to an applied magnetic field, the orbits of electrons around an atom are changed. This increases the antiparallel alignment of the magnetic moment on the atom, and creates a slight magnetic repulsion to the applied field.²⁵ Paramagnetic (PM) atoms have unpaired electron spins, which give the atom a randomly orientated magnetic moment in the absence of an applied field.¹ The field caused by the unpaired spins is much greater than the diamagnetic response of the atom, so paramagnetic behaviour dominates in PM atoms.² In isotropic paramagnetic atoms, such as Fe^{3+} , the unpaired electron spins are distributed evenly in the atomic orbitals. Atomic level magnetic anisotropy occurs when the atomic moments on an atom are aligned in preferential directions, such as for Co^{2+} ions.²⁷

Materials that exhibit bulk diamagnetism are composed of diamagnetic atoms that are able to align antiparallel to an applied field, which creates magnetic repulsion in the bulk material. A material that consists of PM atoms can show bulk paramagnetism if the randomly orientated moments on the atoms are only able to align in the presence of an applied field. This means that bulk PMs are attracted to, and bulk DMs repelled by, an externally applied magnetic field.¹ In bulk DM and PM materials, the material needs to be subjected to an applied field to show their magnetic behaviour, as there is no net magnetic moment on these materials when there is no field applied. Other materials are able to exhibit a magnetic moment in the absence of an applied field, which is due to the alignment of atomic paramagnetic moments within the crystal lattice.

If it is energetically favourable, a material will order atomic PM moments to form pairs (or layers), in which each atomic moment is aligned antiparallel with another.²⁵ This means that atomic PM moments within the material are precisely oppositely balanced, so there is no net magnetic moment on the material. This occurs in the presence or absence of an applied field, and is called antiferromagnetism (AF_0M). When all the atomic paramagnetic moments in a material are aligned parallel to each other, the material is ferromagnetic (F_0M), see Figure 1.2.²⁵ However, if the majority of the atomic magnetic moments are aligned within a material, with a minority aligning in a different direction (usually antiparallel) to this, the material is ferrimagnetic (F_iM) rather than ferromagnetic. This is because not all atomic moments are positively contributing to the bulk magnetic moment of the material.²⁸ In both F_0M and F_iM materials, the material will also have a magnetic moment in the absence of an applied field.²⁵ The ordering of atomic PM moments within a material are disrupted by with increasing temperature by thermal energy. When there is enough thermal energy, any magnetic ordering is destroyed, and the material becomes paramagnetic. The temperature at which this occurs is known as the

blocking temperature (T_B) for that material. T_B is also called the Curie temperature for F_iMs and F_oMs , or the Néel temperature for AF_oMs .¹

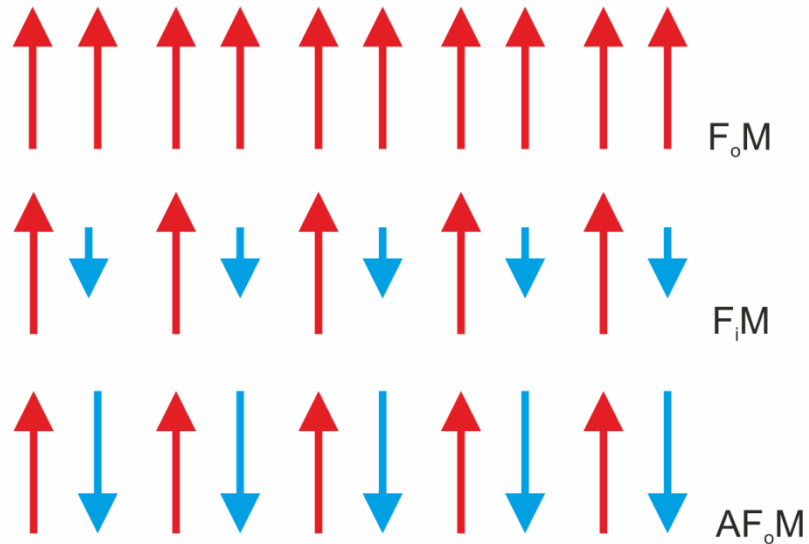


Figure 1.2. Schematic to show different types of bulk magnetic ordering. Arrow direction represents the direction of magnetisation on the atoms, arrow size represents magnitude of magnetisation on the atoms.

The crystal structure of a magnetic material can affect how the electron spins interact, which can make it easier to align the magnetism of a material in certain directions. This magnetocrystalline anisotropy is responsible for creating easy axes of magnetisation in the bulk material, as some axes within the crystal structure require lower energy to align the magnetisation than others, so are preferred.²⁶ Some crystals, such as hexagonal close packed (HCP) cobalt, have one easy axis of magnetisation.²⁵ Other materials have more than one easy axis, for example, body centred cubic (BCC) iron has three easy axes of magnetisation along the cube edges.²⁶ Magnetostriction is another consequence of magnetic anisotropy, whereby compression of a crystal lattice can alter the exchange interaction between adjacent atoms, and thus the easy axes of magnetisation.¹ Equally, magnetisation of a material in particular direction can strain the crystal lattice, which is not favoured as this requires energy. The overall shape of a material can also alter the energy required to align the magnetisation in different directions, and is referred to as shape anisotropy.²⁵

1.3.1.1 Magnetic Domains

Weiss proposed that individual crystals of magnetic materials can be divided into magnetic zones, called domains.²⁹ Magnetic domains were imaged by Bitter approximately 25 years later.³⁰ For bulk magnetic materials, the demagnetisation energy can become extremely large. When a magnetic field encounters the edge of a magnetic material, it diverges, which produces a demagnetising field and costs demagnetisation energy.²⁵ Figure 1.3 shows a schematic of a magnetic material and its field lines to illustrate these competing energies. Many magnetic materials split up into magnetic domains, because this reduces the demagnetisation energy as less of the magnetic field is outside the magnetic material.¹ However, energy is required to create the walls between domains, as the direction of magnetisation within the wall zones is not often able to align with an easy axis of magnetisation.

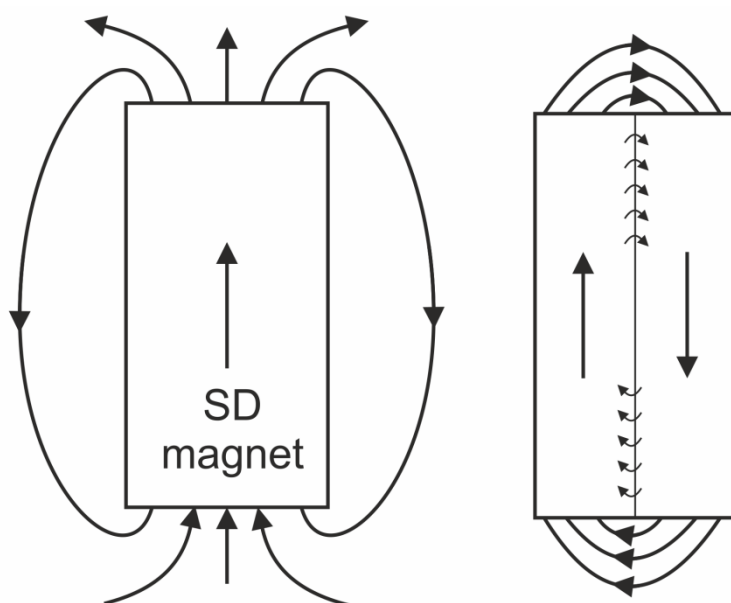


Figure 1.3. Illustration of the magnetic field in and around a material, from Blundell (2001).²⁵ Arrows represent direction of magnetisation. The shape, magnetostriction and magnetocrystalline anisotropies determine the direction of the easy axis of magnetisation shown in the centre of the rectangular material (left). When the field intersects the edge of the material, it diverges, which costs demagnetisation energy. The demagnetisation energy can be significantly reduced if the magnet splits into domains (right), but as this requires domain wall energy, these competing energies must be minimised.

Within a material, magnetic domains can be randomly ordered, or orientated into alignment by an externally applied magnetic field.²⁵ In the domain wall, the direction of magnetisation is rotated between those of the adjacent magnetic domains. When an external field is applied, the direction of magnetisation of domains can be re-orientated to align with the applied field.¹ Magnetic domains which are favourably orientated with the external field may grow at the expense of unfavourably orientated areas, as domain walls migrate within the material (Figure 1.4).²⁶ Therefore, the size, shape and number of domains within a material

depend on the temperature, crystal structure, and shape of a crystal, as well as minimising the competing magnetostatic, domain wall and demagnetisation energies for that material.

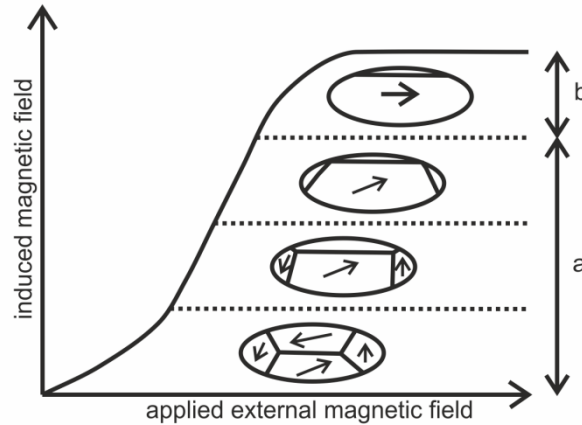


Figure 1.4. Schematic of domain growth and rotation of magnetisation from Newey & Weaver (1990).²⁶ (a) When an external magnetic field is applied, domains re-orientate themselves to become aligned. Domains orientated in a similar direction to the applied field can grow until at (b) they dominate the material.

1.3.1.2 Magnetic Hysteresis

When an external magnetic field is applied to a material, such as during vibrating sample magnetometry (VSM), the magnetic response of the material can be recorded. Figure 1.5 shows a diagram of a magnetic hysteresis loop measured from a sample when subjected to an externally applied magnetic field (H). The applied field induces a flux (M) in the material, which increases in a sigmoidal curve.¹ The slope of this curve is a measure of how easy it is to magnetise the sample, and is called the relative permeability (μ_r) of the material.¹ Relative permeability can be dependent on both the alignment of the atomic moments and the shape controlled easy axes of magnetisation. A steeper slope means it is easier to magnetise the sample, so the material has a higher relative permeability:¹

$$\mu_r = \frac{M}{H} \quad (1.1)$$

The plateau of this curve (at point 3) is the maximum flux density, or magnetic saturation (M_s). When saturated, all magnetic domains should be aligned with the external field.

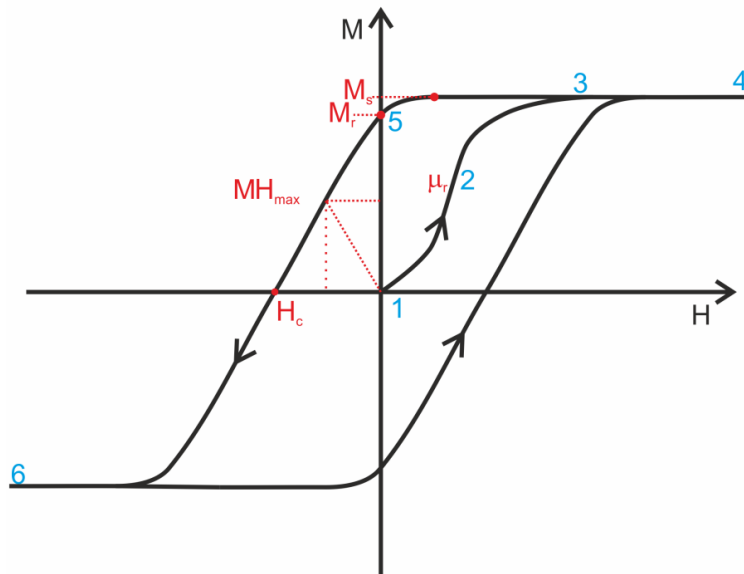


Figure 1.5. A diagram of a magnetic hysteresis loop. External field (H) is increased between points 1-4, then reduced to zero and reversed until point 6 is reached. The field is then reduced back to zero before returning to the original direction of magnetisation. The field induces a magnetic flux (M) in the sample, which is measured as the applied field is varied to record the magnetic hysteresis. Also labelled are: the relative permeability (μ_r); the magnetic saturation (M_s); the magnetic remanence (M_r); the coercivity (H_c); and a measure of the magnetic hardness (MH_{max}).

When M_s is reached, H is gradually reduced back to zero, then increased in the opposite direction and the flux recorded. Figure 1.5 shows the remanent magnetisation (M_r) at point 5, which is the flux from the sample at zero applied field. The magnetic domains of the material are then gradually realigned in the direction of the reversing field. The rate of reordering depends upon the demagnetisation energy from the applied field as well as the magnetic hardness of the sample. If it is easy to reorder the material, only a small amount of field reversal is required to realign the magnetic domains, and the material is magnetically soft. If a large external field is required to reorder the domains within the material, it is difficult to switch the magnetism, and the material is magnetically hard.

When the magnetic flux of the material is saturated by the reversed field (point 6 in Figure 1.5), the field is then returned to zero and increased again in the original direction. Then the measured flux records the lower curve and closes the hysteresis loop. The wider a hysteresis loop, the harder the magnetic material. The area enclosed by the loop is a measure of the energy required to align the magnetisation within the sample.¹ The coercivity (H_c) of the magnetic material is measured at the point where the externally applied field reorders the magnetic flux of the material to zero. MH_{max} is used to assess the magnetic hardness of the material, as a hard material may have high M_s and high H_c .¹

The relative ease of reordering magnetic domains is energy dependent, and thus can be affected by the temperature of a measurement, as well as the magnetocrystalline anisotropy and domain wall energy of the material. At higher temperatures, the thermal energy disrupts the exchange interactions between the electrons in the material, which reduces the magnetic ordering.²⁵ Hard magnetic materials are used to form permanent magnets for use in generators and electric motors. Magnetically soft materials require small applied fields to switch their direction of magnetisation, so are useful in transformers and sensors.¹ For data storage purposes, re-writable media, such as cassette tapes, require more magnetically soft materials than those used for permanent data storage, because information may need to be over-written.¹

Figure 1.6 shows schematic hysteresis loops of materials used for different applications. Hysteresis loops are wide and cover a large area for materials used for data storage and in permanent magnets. This is because more energy is required to reorder the direction of magnetisation within these materials. As the material in a transformer needs to switch its direction of magnetisation quickly, it has a narrow hysteresis loop, usually with a high saturation magnetisation. This provides a strong signal for little energy loss upon switching, as the material is magnetically soft. Materials used in sensors can show a gradual change in magnetic flux in response to an applied field, so produce a sloped hysteresis.

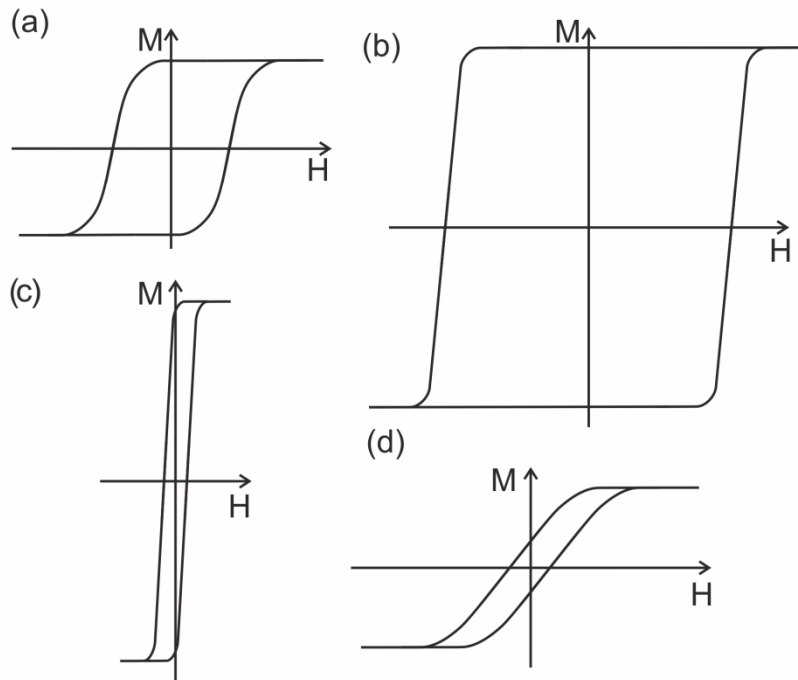


Figure 1.6. Diagram to show examples of hysteresis loops of materials used for different applications. (a) Data storage has high M_s and H_c so recorded information is retained. (b) A permanent magnet produces a very wide hysteresis loop and (c) a transformer switch has a very narrow hysteresis loop. (d) A sensor may need to produce a gradual change in magnetisation, so it has a sloped hysteresis loop.

1.3.1.3 Magnetic Ferrites

Magnetite is a mixed valence ferrite, and has the highest saturation magnetisation of all the magnetic iron containing oxides.³¹ However, the coercivity is low, making it magnetically soft. Magnetite forms an inverse spinel structure (see Figure 1.7),³² with ferrous (Fe^{2+}) and ferric (Fe^{3+}) ions randomly arranged at the octahedral sites, and all tetrahedral sites occupied by ferrous iron.^{33,34} This $[Fe^{3+}]_A[Fe^{2+}, Fe^{3+}]_B O_4$ structure allows electrons to hop between closely spaced, randomly ordered species of iron at the B sites (see Equation 1.2).³³⁻³⁵ This movement of electrons creates the net magnetic moment of magnetite.



When bulk magnetite is cooled below 120 K, there is a spontaneous drop in the saturation magnetisation and conductivity.^{33,34} This is accompanied by an increase in resistivity, a specific heat anomaly and elongation along some crystallographic axes.³⁴ This is called the Verwey Transition (T_V),³⁶ and is a phase transition that is thought to involve the magnetite inverse spinel structure re-crystallising to a monoclinic structure, creating ordering at the B sites upon cooling below the transition temperature.³³⁻³⁵

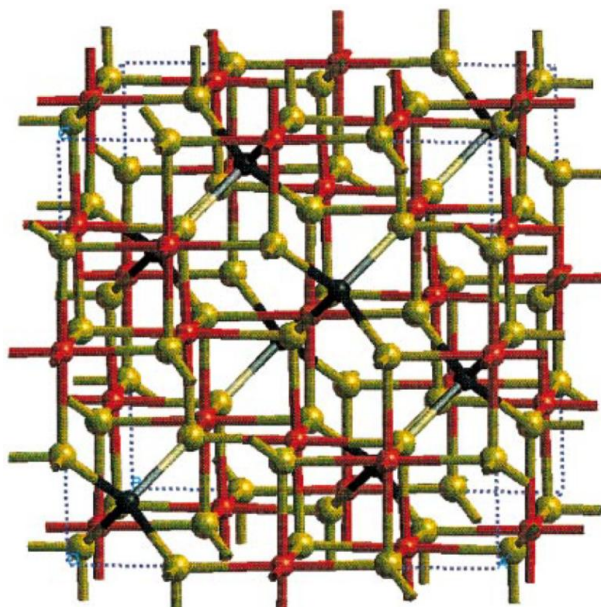


Figure 1.7. Diagram of the inverse spinel structure of magnetite from Sorescu (1998).³² Iron atoms on tetrahedral A sites are black, and red on octahedral B sites. Oxygen atoms are coloured yellow, and the unit cell (lattice parameter 8.397 Å) is outlined with a blue dotted line.

The temperature of the Verwey Transition can be measured using a VSM by recording M for a fixed applied field, as temperature is varied. The material can be cooled in zero applied field (ZFC) or an applied field (FC). The Verwey Transition appears as a sharp change in the sample magnetic flux as the sample is heated or cooled past 120 K. The introduction of small amounts of impurities, non-stoichiometry or oxidation of magnetite can significantly depress the temperature of the Verwey Transition, or obscure it completely.^{34,35,37,38} Therefore, the Verwey Transition is an extremely sensitive diagnostic tool for the identification of pure, crystalline magnetite.³⁴ Shifting of the transition to a lower temperature, blurring or a stepped transition indicates the material is not pure, bulk stoichiometric magnetite.

The Fe^{2+} in magnetite can be replaced with Co^{2+} to make cobalt ferrite (CoFe_2O_4), which has low saturation magnetisation and high coercivity.^{39,40} These two materials form the two end members of undoped and cobalt doped ferrites, and the magnetic properties of these ferrites can be tuned from high M_s /low H_c (pure magnetite, 0% Co) to low M_s /high H_c (pure cobalt ferrite, 33% Co).^{40,41} Magnetite has an isotropic crystal structure, so has three easy axes of magnetisation, making it magnetically soft. This means that magnetite has a high saturation magnetisation and a narrow hysteresis loop. Co^{2+} substitutes for Fe^{2+} at the octahedral B sites, and introduces a preferred magnetic orientation. The addition of cobalt increases the coercivity and reduces M_s , which creates a shorter, wider hysteresis loop.^{41,42} However, as adding cobalt acts as an impurity, cobalt doping can obscure the Verwey Transition of magnetite.^{34,35,38}

1.3.2 Nanoparticles (NPs)

Nanoparticles (NPs) are extremely useful for many applications, and often exhibit properties different to those of the parent bulk material. As NPs are small, they have a large surface area to volume ratio. This means that their properties are dominated by surface atom contributions, so small changes in size and shape of NPs can significantly alter their properties, as can small changes in purity or surface functionalisation of NPs.⁴³ The large surface area of silver NPs are thought to aid in their antimicrobial properties.^{44,45} This also helps many NPs (e.g. gold,⁴⁶ platinum,⁴⁷ and palladium)⁴⁸ to be good catalysts, be effective in sunscreens (e.g. zinc oxide),⁴⁹ or be useful in solar cells (e.g. titanium dioxide).⁵⁰ Other NPs absorb or emit different wavelengths of light depending on the particle size (e.g. semiconductor NPs^{51,52} or gold NPs).^{53,54} The magnetic properties of a material can also be changed by altering the particle size, which is discussed in more detail in Section 1.3.3. NPs for the majority of applications must be uniform to ensure they have reliably consistent properties.

1.3.3 Magnetic Nanoparticles (MNPs)

The size and shape of magnetic domains that are formed within a magnet are dependent on the size, shape and material that magnet is made from. If it is small enough, it is not energetically favourable for a magnetic material to partition into domains as it would in a larger bulk crystal, so it forms a single domain (SD). Smaller magnetic nanoparticles can be too small to maintain their magnetisation against thermal fluctuations, which means they behave superparamagnetically (SP) as they are unable to maintain a SD at room temperature.⁵⁵ As such, MNPs that behave as single domain magnets at room temperature are termed 'SD', and 'SP' is used to refer to MNPs that behave superparamagnetically in this study. The lower size limit for a spherical magnetite MNP to be able to maintain a single domain at room temperature is ≈ 25 nm.⁵⁵⁻⁵⁷ Particles larger than this lower limit are able to maintain a single domain at room temperature, and behave as ferrimagnets.⁵⁵

MNPs can also be larger than the SD upper size limit (≈ 85 nm for spherical magnetite) and form multi-domain (MD) magnetic particles.⁵⁸ In MD particles the direction of magnetisation is rotated between domains in domain walls, and some domains are aligned in different directions to achieve balance between domain wall energy and the demagnetisation energy. Therefore, the magnetisation of the material is not saturated in a single direction in the absence of an applied field, so MD particles usually have a lower remanent magnetisation than SD nanoparticles. Due to shape anisotropy, acicular MNPs usually have a preferred axis of magnetisation (along the long axis) which can stabilise the SD zone over a larger range. As with bulk magnetite, doping in controlled quantities of cobalt into

magnetite MNPs can alter the magnetic properties of the MNPs. This is because Co introduces a preferred magnetic orientation into the MNP, thus increasing the coercivity as more energy is required to switch the direction of magnetisation within the nanoparticle. The effect of cobalt doping into magnetite is investigated in Chapter 4 with Mms6 biotemplated MNPs.

The magnetic properties of an MNP determines which applications it may be useful for. Magnetically hard SD MNPs are used for spintronics and in high density data storage (e.g. FePt nanoparticles can self-assemble into superlattices that can store ≈ 225 Gbits in⁻¹).⁵⁹ Magnetically softer nanoparticles, such as FeCo MNPs, can be used in high frequency electronic circuits as they are able to rapidly flip their direction of magnetisation in response to an applied field.⁶⁰ SP nanoparticles are used in medical applications, such as contrast agents in magnetic resonance imaging (MRI),^{61,62} drug delivery⁶³ or cancer therapy by hyperthermia.⁶⁴⁻⁶⁸ SP suspensions of MNPs are also used to separate catalysts from reactants,^{69,70} recover pollutants⁷¹ and in ferrofluids.⁷² As with other NPs, the size, shape and purity of the MNPs must be consistent to ensure the NPs have an uniform magnetic response to an externally applied magnetic field.

This study is designed to template magnetic nanoparticles onto patterned surfaces, which are most likely to be useful in developing information storage devices. As such particles should be magnetically hard to retain the stored data, biotemplated MNPs should have a high coercivity if they are to be used for this purpose. Current magnetic data storage in hard disc drives use sputtered thin-films of ferromagnetic materials, where the direction of magnetisation within the film is used to record information.⁷³ In granular recording media, a write head is used to align the magnetism of a number of magnetic grains within a small area of the thin-film. This forms a single bit of information as a multi-particle magnetic domain (see Figure 1.8).⁷⁴ By exchange coupling multiple particles, the stability of the direction of magnetisation recorded in the magnetic domain is much higher than for a single particle.⁷⁵ This means that the integrity of the recorded information is high, as the multi-particle magnetic domains are more stable against demagnetisation (and therefore information loss) than individual SD MNPs.⁷³

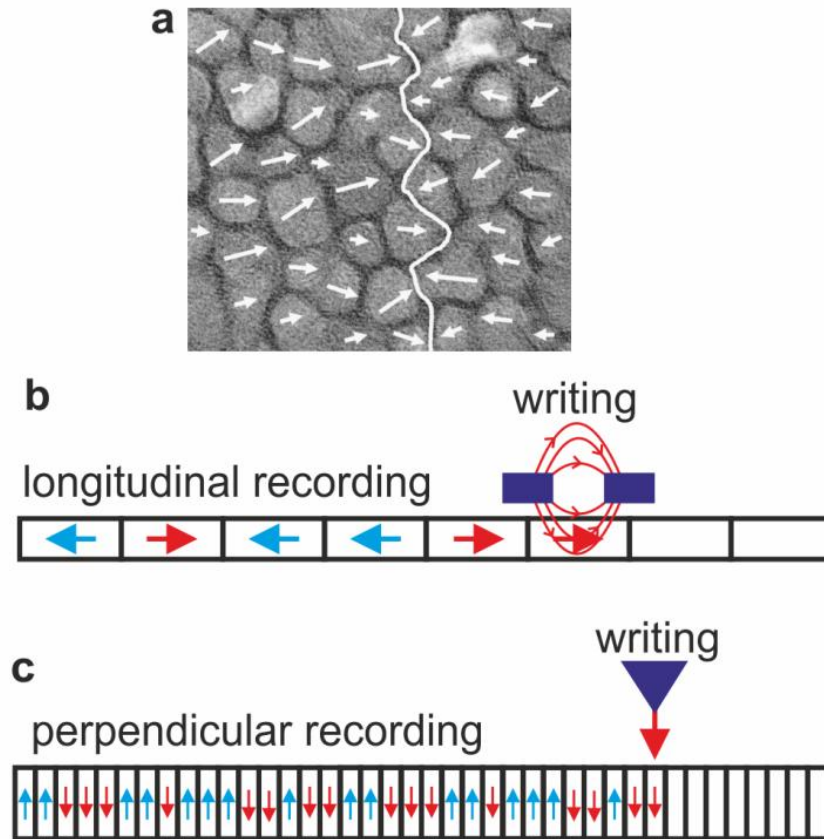


Figure 1.8. Schematic illustration of longitudinal and perpendicular granular recording for magnetic data storage, based on Piramanayagam (2007).⁷⁴ (a) Illustration of an LMR bit boundary (not to scale). Schematic of (b) longitudinal and (c) perpendicular recording.

In longitudinal magnetic recording (LMR), the easy axis of magnetisation of the film is parallel to the long axis of the film. In perpendicular magnetic recording (PMR), the easy axis of magnetisation of the film is perpendicular to the long axis of the film, so magnetisation can either be aligned 'up' or 'down'.⁷⁵ Perpendicular recording allows higher density data storage than longitudinal granular recording, as the magnetic domains in PMR take up less room than in LMR.⁷⁵ The materials used to make the films for high density data storage must have a high coercivity, to avoid loss of recorded information. If the recorded bit is not stable against thermal demagnetisation, the signal to noise ratio is poor, and much of the information can be lost.⁷⁴ However, if the coercivity is too high, the magnetic write head is not able to write information to the magnetic material, as the field required to switch the direction of magnetisation in the film is too high.⁷⁴ To achieve a high density of 500 Gbits in⁻² using PMR, the magnetic thin-film should have a coercivity of ≈ 6 kOe.⁷⁴ A magnetic thin film can be lithographically patterned to form nano-islands, each of which can record a bit of information that is more stable against thermal demagnetisation than an individual grain in PMR.⁷⁶ This is called bit patterned media (BPM), and offers an even higher density data storage solution for lower coercivity magnetic thin-films (e.g. ≈ 4 kOe).⁷⁶

1.3.4 Formation of Magnetic Nanoparticles

There are many methods available for the synthesis of magnetic nanoparticles, and each has advantages and disadvantages. For high density data storage, MNPs should have long-term stability (of magnetism, upon heating/cooling and against degradation/oxidation), a uniform size distribution, and be of high purity.^{60,65} This is necessary to ensure consistent and predictable recording, retention and recall of digital information. MNPs used in suspensions (e.g. SP MNPs in ferrofluids) should also avoid agglomeration and be stable over a wide pH range.^{4,59,60,69,70,77} For biomedical applications, MNPs should also be biocompatible.^{16,63,65} The biomineralisation protein Mms6 is discussed in detail in Section 1.4.4, as it evolved to template uniform magnetite nanoparticles in nature. Methods of magnetite synthesis that may be suited to biotemplating with Mms6 are discussed below.

The phase diagram for the formation of iron oxides is complex (see Figure 1.9).⁷⁸ The iron oxide/oxyhydroxide that is formed during mineralisation depends strongly upon: the level of oxidation; effective concentration of iron (activity); the type and activity of counter ions; and pH of the reactant solution. If the conditions are correct (low oxygen, high activity Fe^{2+} , pH 8-10) magnetite should be produced. If not, other iron mineral phases, which can also form as intermediates during magnetite mineralisation, can be produced. These include (but are not limited to): hydrated oxides (ferrihydrite, $x\text{Fe}_2\text{O}_3 \cdot y\text{H}_2\text{O}$), oxyhydroxides (goethite, $\alpha\text{-FeOOH}$; akaganéite, $\beta\text{-FeOOH}$; and lepidocrocite, $\gamma\text{-FeOOH}$), and oxides (maghemite, $\gamma\text{-Fe}_2\text{O}_3$ and haematite, $\alpha\text{-Fe}_2\text{O}_3$). Therefore, small perturbations in reaction conditions can change the phase of the iron mineral that is formed.

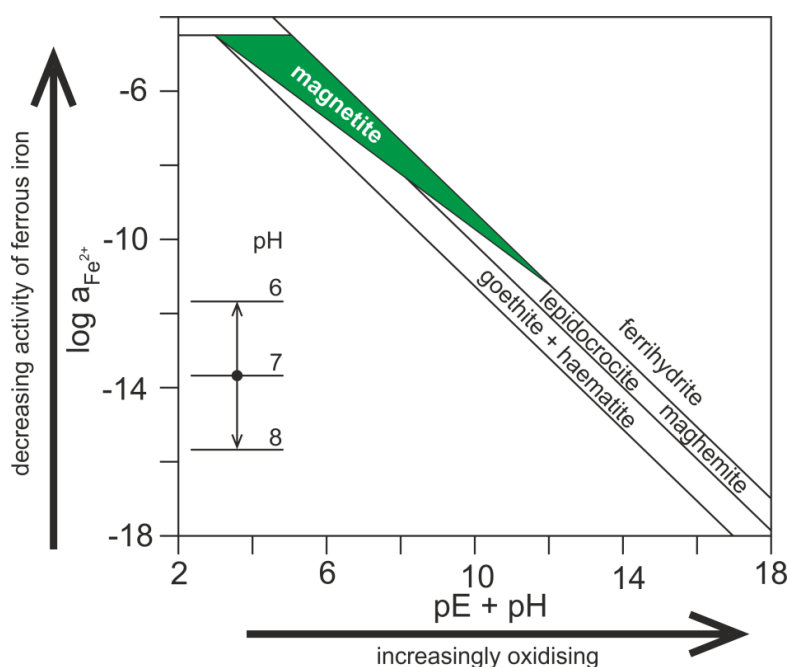


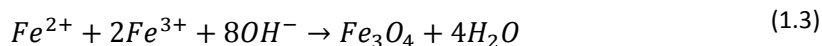
Figure 1.9. Phase diagram of iron oxides and oxyhydroxides formed under variable $pE + pH$ and activity of iron, after Cornell & Schwertmann (2003).⁷⁸ Magnetite is formed between $\approx pH$ 8-10, low oxidation conditions (low pE), and at higher relative concentrations of iron (higher activity of Fe^{2+}). If the system is too oxidising, or the concentration of the reactants is varied too much, a wide range of other iron oxides and oxyhydroxides can be formed instead of magnetite.

1.3.4.1 Thermal Decomposition

Thermal decomposition of organometals is used to synthesise metal and metal oxide MNPs with a narrow size distribution and consistent morphology for many current applications.^{4,79} The size and shape of the MNPs produced by thermal decomposition is dependent on the ratio of reactants and temperature of the reaction, as well as the duration of the reaction and aging time after synthesis.^{4,79} By varying these conditions, the size, shape and magnetic properties of the MNPs can be tuned.^{4,79} However, this method requires high temperatures (≈ 250 - 300°C) and harsh chemical surfactants and solvents (e.g. benzyl ether, toluene, hexane and chloroform).^{4-6,59,79} Therefore, thermal decomposition is not very environmentally friendly, and the particles may have residual coatings preventing their use for biomedical applications.⁸⁰ Importantly, the particles are not patterned onto a surface, and most thermal decomposition methods of MNP synthesis only produce small SP particles, which is not suited for use in data storage applications. It is highly unlikely that Mms6 will be stable at the high temperatures or in the harsh chemical reactants required for the thermal decomposition method of synthesis. This is because proteins, even those from thermophilic organisms, are not stable much above $\approx 100^\circ\text{C}$,⁸¹ nor are they designed to work in non-aqueous environments, so Mms6 would be unable to biotemplate magnetite during thermal decomposition. Therefore other 'greener' methods of magnetite synthesis have been used in this study.

1.3.4.2 Room Temperature Co-precipitation (RTCP)

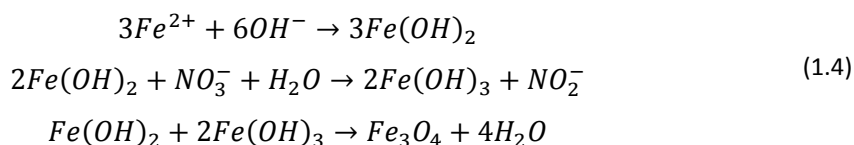
MNPs can be formed from a mixture of ferrous and ferric salts by co-precipitation at room temperature (RTCP). The salts are mixed under an inert atmosphere whilst adding a base to increase pH, which produces magnetic iron oxides, such as maghemite and magnetite, see Equation 1.3:⁴



Particles produced by RTCP usually have a small size and large size and shape distribution, as MNP formation occurs very quickly after the base is added to the iron salts (14.6±9.9 nm).²⁴ This rapid precipitation means that there are large local variations in the pH and reactant concentrations due to incomplete mixing, which allows a range of iron oxides to be precipitated. Coating RTCP particles in a thin oxide layer, surfactants, polymers, precious metals, silicon or carbon helps to stabilise these MNPs against agglomeration.⁴ The biomineralisation protein Mms6 has been shown to template uniform magnetite RTCP MNPs *in vitro*.²² The RTCP MNPs templated by Mms6 are high purity magnetite, with a narrow grainsize distribution (e.g. 21.2±8.3 nm)²⁴ and consistent cubo-octahedral morphology, similar to the MNPs formed by the parent bacterium. This avoids the use of the high temperatures and harsh chemicals required for thermal decomposition, so Mms6 templated RTCP particles are far more environmentally friendly to produce. As Mms6 is able to biotemplate MNPs under the RTCP reaction conditions, it may still be able to form MNPs when attached to a surface using this method.

1.3.4.3 Partial Oxidation of Ferrous Hydroxide (POFH)

The partial oxidation of ferrous hydroxide (POFH) requires a mild oxidant and some heating to form magnetite particles.^{24,82-85} During POFH, ferrous hydroxide forms from a ferrous salt, which is then partially oxidised with nitrate at 80-90°C. This forms a mixture of ferrous and ferric hydroxides which are dehydrated to form magnetite as per Equation 1.4:⁸⁴



This method requires careful control of the reaction conditions, as varying the iron salt, the type of base, the ratio of the reactants and the temperature of the reaction can alter the size, shape and iron mineral produced by the reaction.⁸⁵ Mms6, and a peptide based on Mms6, have also been shown to template uniform, cubo-octahedral magnetite MNPs using the POFH method.^{24,84} Therefore, this method may also be suited to producing biotemplated nanomagnets on patterned arrays using Mms6.

1.4 Proteins and Biomineralisation

1.4.1 Biomineralisation

Prokaryotic life is thought to have appeared on Earth about 3.5 billion years ago.⁷ Prokaryotes are simple organisms which are not internally compartmentalised, and many are able to survive and thrive in extreme living conditions. Originally, prokaryotes were likely to be chemotrophic or photosynthetic rather than oxic respirators. This is because the Earth's early atmosphere was not thought to contain oxygen, but was probably composed of methane, carbon dioxide ammonia, hydrogen and water.^{7,86} More complex eukaryotic life emerged about 1.5 billion years later, probably by the ingestion of specialised prokaryotic cells, which were retained rather than digested by the predator cell.⁷ These are thought to have formed the specialised organelles which perform specific tasks for the eukaryotic cell.⁸⁶ Eukaryotes are able to form multicellular organisms, with different cells containing only those organelles necessary to perform tasks for the specialised cells. Examples of organelles include the nucleus (containing a cell's genetic information), mitochondria (for respiration), chloroplasts (for photosynthesis), and other specialised organelles for biomineralisation.

The fossil record of the early Cambrian indicates that the major animal phyla began biomineralising hard-parts in a relatively short geological timeframe at about 525 Ma.⁸⁷ It is thought that an unstable, changeable climate and the appearance of mineralised teeth in predators, triggered an explosion in defensive mineralised tissue formation in many divergent taxa.⁸⁷ Magnetic bacterial biomineralisation is thought to pre-date the 'Cambrian Explosion' at ≈ 700 Ma, but may even be older than eukaryote evolution at ≈ 2.0 Ga.⁸⁸ It is possible that magnetic bacterial mineralisation acted as a template for biomineralisation in other organisms.⁸⁸

There is a diverse range of biominerals (about 60),⁸⁹ which form mineral reservoirs for the organism. Some biominerals have additional useful properties, such as aiding predation and maceration (e.g. apatite in teeth);⁹⁰ providing support and allowing locomotion (e.g. calcium phosphate in bone);⁹¹ or help to protect the animal (e.g. exoskeletons made of calcium carbonate).⁹² Silica not only provides structural support, but may also have light guiding properties (e.g. in sponges^{93,94} and diatom frustules).⁹⁵ Other biominerals sense magnetic fields and allow passive alignment of the organism with the field lines (e.g. magnetite in bacteria).²¹ Biominerals often have excellent materials properties when compared to man-made minerals, but are formed under physiological reaction conditions.⁴³

The mineralising organisms use proteins, which are genetically encoded, to help form the biomaterials.¹⁷ Different biomineralisation proteins have evolved to direct mineralisation by transporting ions, providing crystal nucleation sites and assembling lipid vesicles in which reactions can be contained, concentrated or confined.^{17,19,96-98} Other proteins may interact with specific crystallographic planes to direct crystal morphology and/or organise the biomaterials into larger, composite structures.⁴³ Biomineralisation of magnetic iron compounds may have evolved as a mechanism to reduce intracellular iron concentrations and/or to store iron for times of scarcity.⁸⁸ The ability of magnetic bacteria to align with the magnetic field of the Earth may have created a competitive advantage over non-magnetic bacteria (see Section 1.4.2).²¹

1.4.2 Magnetic Bacteria

Magnetic bacteria (sometimes called magnetotactic bacteria) were first identified by Blakemore in 1975.¹¹ They are prokaryotic, gram-negative bacteria, motile by flagellae, and tend to inhabit the region around the oxic-anoxic transition in sediments and the water column.^{8,99} Magnetic bacteria biomineralise magnetite ($\alpha\text{-Fe}_3\text{O}_4$) or greigite (Fe_3S_4)⁸ magnetic nanoparticles within lipid and protein bounded vesicles called magnetosomes. Most magnetic bacteria are sensitive to variation in oxygen levels, and will usually only produce magnetosome MNPs within a narrow range of low oxygen concentrations.²¹ As such, they are either microaerobic or anaerobic respirators, with some strains able to grow and biomineralise under both conditions.²¹ Magnetic bacteria can move in response to an externally applied magnetic field, which is called magnetotaxis.^{11,100} There is a wide diversity of bacteria that exhibit magnetotaxis, which includes: coccoid (spherical), vibrioid (curved rod shaped), spirilloid (spiral shaped) (Figure 1.10), and even some multicellular species.^{14,15,100}

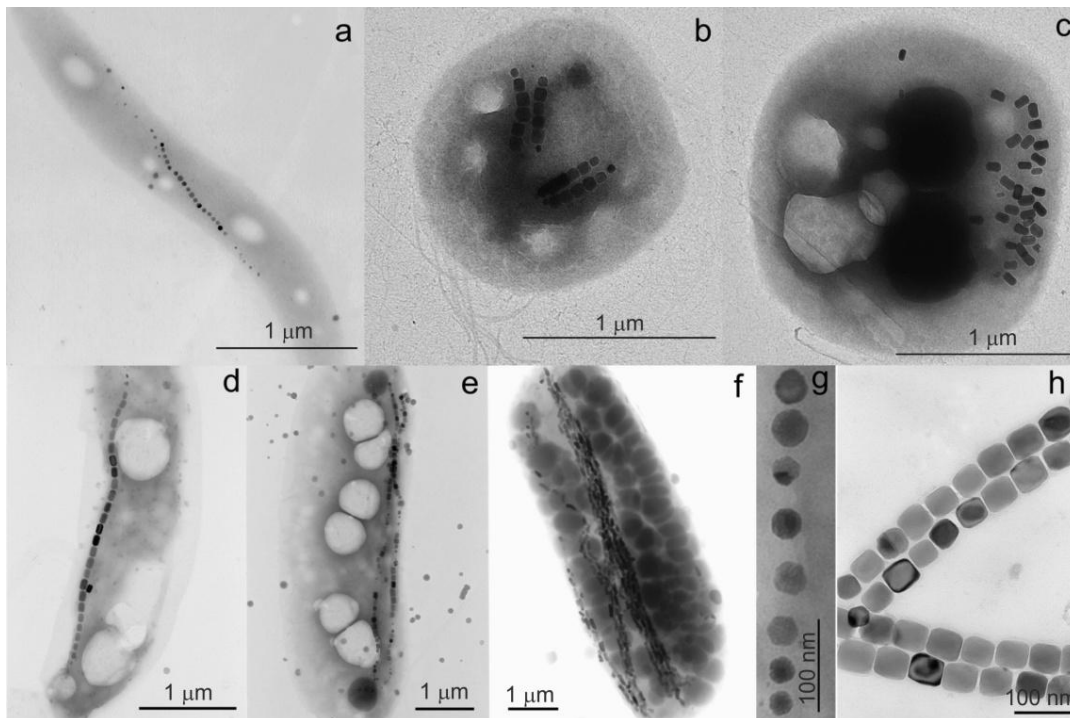


Figure 1.10. TEM images of magnetic bacteria from Faivre & Schüler (2008).¹⁵ (a) Single chain of cubo-octahedral magnetosomes within a spirillum and (b) a coccus with two double chains of elongated prism shaped magnetosomes. (c) A coccus with unordered prismatic magnetosomes, (d) a vibrio with one and (e) two chains of prismatic magnetosomes. (f) Multiple chains of bullet shaped magnetosomes in a rod shaped bacterium. (g) Detail of cubo-octahedral magnetosomes from a spirillum similar to image a, and (h) detail of two double chains of elongated prisms from a coccus, similar to image b.

Many different species of magnetic bacteria have been isolated from sediment and water samples, as they will tend to swim towards or away from an applied magnetic field.²⁰ Further study of many of these bacteria has not been possible as few species have been successfully cultured in a laboratory.²¹ This may be because many magnetic bacteria occupy a narrow chemical window in nature, so are highly adapted to their niche. This means that small changes in oxygenation or chemical gradients can prevent magnetosome formation and growth in many species.²¹ Recently, advances in sequencing uncultured strains of magnetic bacteria have been able to add a wealth of information to the genetic relationships between these diverse organisms.¹⁰¹⁻¹⁰³ Figure 1.11 is a transmission electron microscope (TEM) image of a magnetic bacterium *Magnetospirillum magneticum* AMB-1 from Matsunaga *et al.* (2004).¹⁰⁴ The majority of magnetic bacteria isolated in pure culture are of the genus *Magnetospirillum*,¹⁰⁵ although a *Magnetococcus* and a *Magnetovibrio*¹⁰ have also been isolated, cultured and described.

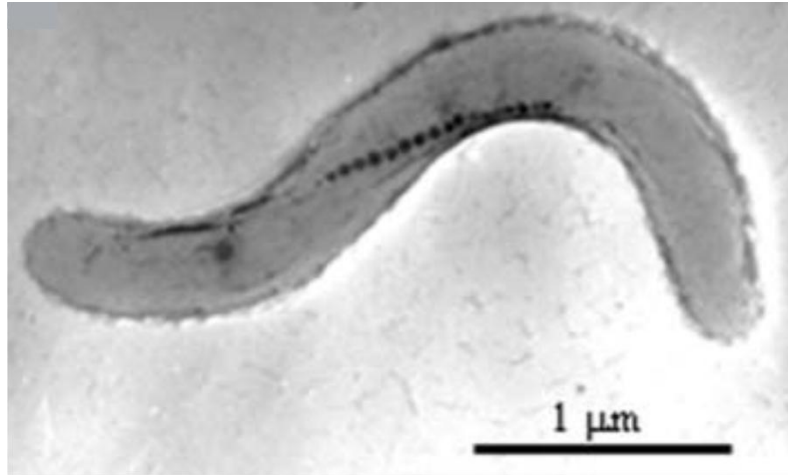


Figure 1.11. TEM image of magnetic bacterium *M. magneticum* AMB-1 from Matsunaga *et al.* (2005).¹² The magnetosomes appear as dark contrast in the centre of the image, and are arranged in a line. The biomineralisation protein Mms6 was identified by Arakaki *et al.* (2003)²² as it was tightly bound to the magnetosome MNPs extracted from AMB-1.

Most magnetic bacteria contain 20-40 magnetosomes.¹⁰⁶ A magnetosome is an intracellular protein and lipid membrane surrounding a single domain magnetic crystal, typically 30-120 nm in length.^{21,107} The magnetosomes are often arranged into chains (Figure 1.11) that aligns the [111] easy axis of magnetisation for magnetite NPs along the chain axis.¹⁰⁸ This allows the MNPs to act as a single magnetic dipole within the cell, and maximises the magnetic moment of the bacterium.¹⁰⁸ This enables the multiple single domain MNPs to behave as a single magnetic dipole as the magnetisation of the MNPs is aligned by the protein scaffold.^{21,108} The bacterial cells passively align with the Earth's magnetic field rather than being attracted or repelled. The bacteria then use their flagellae to propel themselves along the Earth's magnetic field lines by magnetotaxis.²¹ This allows many magnetic bacteria to be isolated from an environmental sample using a magnet, as only the magnetic bacteria will swim along the field lines.

It is proposed that magnetotaxis is used in conjunction with oxygen sensing to allow these bacteria to seek optimal redox conditions using magneto-aerotaxis.¹³ Magnetotaxis may also be used in conjunction with chemotaxis, where the bacteria seek optimal conditions within chemical gradients.¹² The magnetotaxis can help when seeking optimal chemical and redox conditions for the bacteria to thrive (Figure 1.12). By aligning with the Earth's magnetic field, the bacteria reduce the search for their ideal living conditions from three dimensions to one dimension, as they can follow nutrient gradients along the field lines.

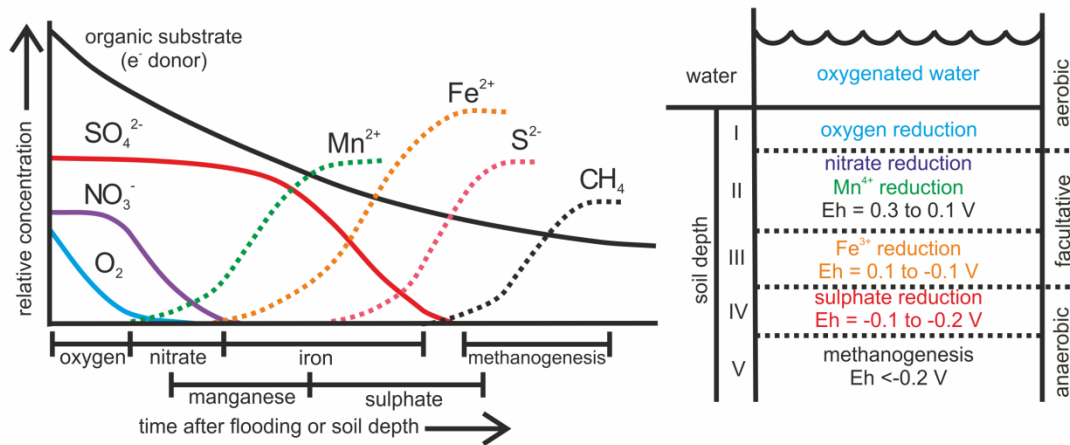


Figure 1.12. Sequence in time (left) and depth (right) of redox dependent chemical gradients in stratified sediments, redrawn from Reddy & DeLaune (2008)¹⁰⁹ and Charman (2002).¹¹⁰ When oxygen is not available, different anaerobes can use other available species as terminal electron acceptors for respiration.

However, magnetic bacteria are usually unable to mineralise their magnetosomes when outside micro-aerobic or anaerobic conditions. If the sediment or water column the bacteria live in is disturbed (e.g. by aeolian mixing or bioturbation), they may be displaced into a more oxygenated environment, or away from the primary electron acceptor for their optimal respiration pathway. As the magnetic bacteria need low oxygen conditions to live, this means they are unable to synthesise nanomagnets when they would need them the most, to return to the oxic-anoxic interface. This implies that the evolutionary origin of the magnetosome within the magnetic bacteria is unlikely to be magnetotaxis.

It may be that the magnetosome originally evolved as an iron storage mechanism, as iron ions can form extremely reactive and toxic species when in solution, i.e. in the cell cytoplasm.¹¹¹ Many organisms store iron in specialised, self-assembled protein cages, called ferritins. These ferritins contain ferrihydrite, a fully oxidised, bio-available hydrated iron oxide mineral.¹¹¹ Using ferric iron as a terminal electron acceptor is one of the most energy efficient anaerobic respiration pathways (Figure 1.12).^{109,110} However, iron is often very limited in sediments and natural stratified waters, especially in anaerobic environments.^{112,113} It is possible that magnetic bacteria utilise magnetosome stored iron for respiration if displaced from their niche environment. The energy released by respiring with Fe^{3+} may be then used to return to the nitrate or sulfate reduction zone that the magnetic bacterium usually occupies. It may be that prokaryotic magnetosomes are not as efficient at oxidising ferrous iron, so form partially oxidised iron minerals (magnetite and greigite) to store iron. The magnetic properties of these iron minerals would therefore be a coincidence, one that these bacteria have later exploited to their advantage when seeking their optimal redox conditions.

1.4.3 Magnetosome Formation

The shape and size of magnetosomes can vary significantly between different species of magnetic bacteria (see Figure 1.10).^{14-16,100} However, within a single species, the crystals have a narrow grainsize distribution and consistent aspect ratios.¹⁴ Uniformity of size and shape of MNPs ensures they also have consistent magnetic properties (see Section 1.3.3). This indicates the bacteria have a strong genetic control on the morphology of the MNPs formed in their magnetosomes.¹⁴⁻¹⁶ The genetic control is exerted via proteins, which help to form the magnetosomes, anchor them into chains, transport iron into the vesicles and template magnetite crystallisation (see Figure 1.13).¹⁷ One of these biomineralisation proteins from AMB-1 (Mms6) was identified by Arakaki *et al.* (2003).²²

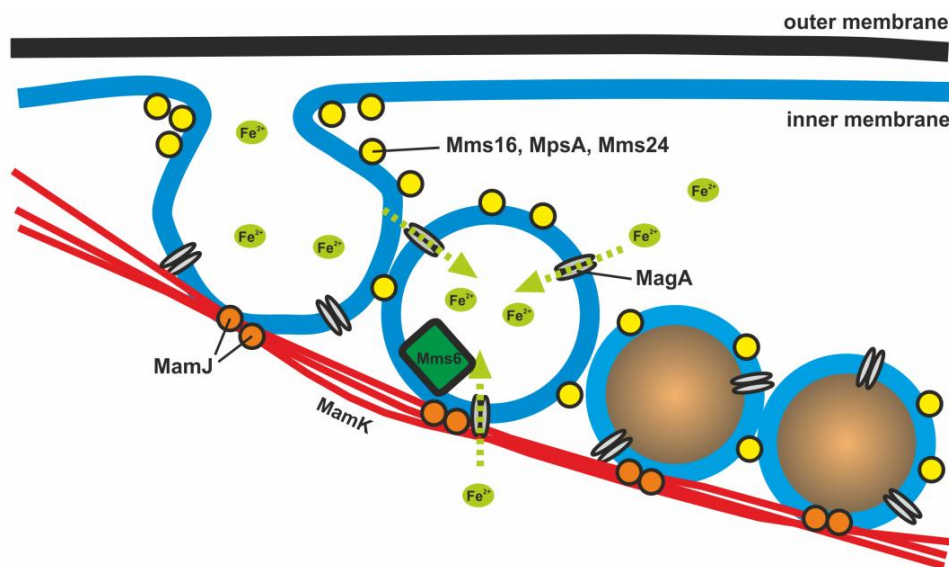
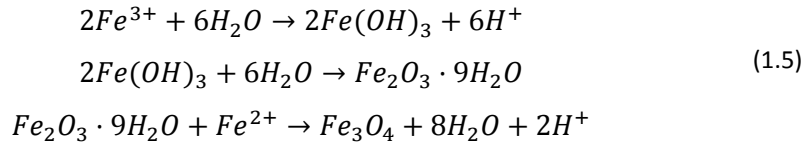


Figure 1.13. Schematic illustration of bacterial MNP formation in AMB-1, adapted from Arakaki *et al.* (2008).¹⁷ The formation and mineralisation of magnetosomes is thought to occur in three stages. First, a vesicle is formed by invagination of the inner membrane using proteins Mms16, MpsA and Mms24, which are then anchored onto a chain of MamK using MamJ. Then MagA transports Fe^{2+} into the magnetosome vesicle. Mms6 controls magnetite crystal morphology and habit during crystallisation, which ensures the consistent size and cubo-octahedral morphology. It is likely that there are many more proteins involved in magnetite biomineralisation in AMB-1 alone which are yet to be identified.

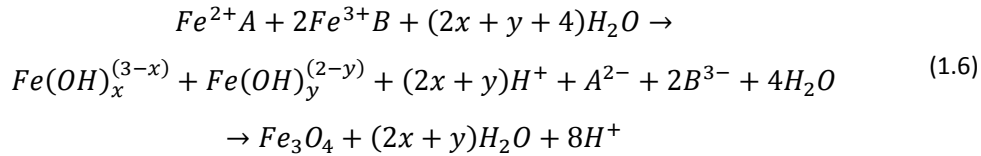
The entire genome of *M. Magneticum* AMB-1 was identified by Matsunaga *et al.* (2005).¹² The use of reverse genetics has allowed the identification of other genes which encode magnetosome membrane proteins in other bacterial strains.^{114,115} These strains include *M. gryphiswaldense* strain MRS-1,^{116,117} *M. magnetotactum* strain MS-1, and a magnetic coccus strain MC-1 (references in Arakaki *et al.*, 2008).¹⁷ Despite these bacteria belonging to very different families, Schübbe *et al.* (2003)¹¹⁸ found that genes encoding for magnetosomes all exist on a 'magnetosome island' (MAI).^{118,119} Comparison of MAIs from AMB-1, MRS-1, MS-1 and MC-1 by Richter *et al.* (2007)¹¹⁴ found that these strains share 891 genes, 28 of which are unique to magnetic organisms. It is not known if the strong genetic

similarity between the many very diverse species of magnetic bacteria is due to a common ancestor, or the lateral transfer of genetic information between species much later during their evolution.

Two pathways have been proposed for magnetite formation within magnetosome vesicles. The earlier model of Frankel *et al.* (1983)¹²⁰ for *M. magnetotacticum* assumes that ferrihydrite forms as a precursor to magnetite within the vesicle, Equation 1.5, adapted from Faivre *et al.* (2007):¹²¹



An alternative pathway has been proposed by Faivre *et al.* (2007),¹²¹ and is based on a study of *M. gryphiswaldense*. They found that cells uptake either ferric or ferrous iron with the help of organic ligands A (unknown) and B (ferritin). This is then converted to an intracellular ferrous species in the membrane. The ligands are released, and the ferrous species imported into the magnetosome vesicle, where co-precipitation of magnetite occurs rapidly, with no mineral precursor via Equation 1.6:¹²¹



Their more recent investigation did not detect any ferrihydrite during the formation of magnetosomes. As many magnetic bacteria live in disoxic or anoxic conditions, it is probable that iron will not be oxidised, but will exist as ferrous iron in their natural environment. This indicates that the reaction pathway for magnetite formation within the magnetosome is more complex than those proposed so far.

It is thought that the interior of the magnetosome vesicle is slightly basic and slightly reducing, which should stabilise magnetite formation (see Figure 1.14).¹⁵ As shown in Equations 1.5 & 1.6, magnetite formation is likely to produce protons, which would cause the pH of the magnetosome vesicle to drop during mineralisation. This means the magnetosome must buffer the reaction to ensure the formation of magnetite is favourable. If not buffered by the magnetosome, a range of iron oxide minerals could be formed within the bacterium, and it would not be able to form high quality magnetite nanoparticles. This buffering is most likely to be facilitated by proteins that pump protons out of the magnetosome to maintain a basic pH. The oxygen in magnetite is derived from water rather than molecular oxygen,¹²² and some magnetic bacteria are able to form magnetite in the absence of oxygen.¹²³

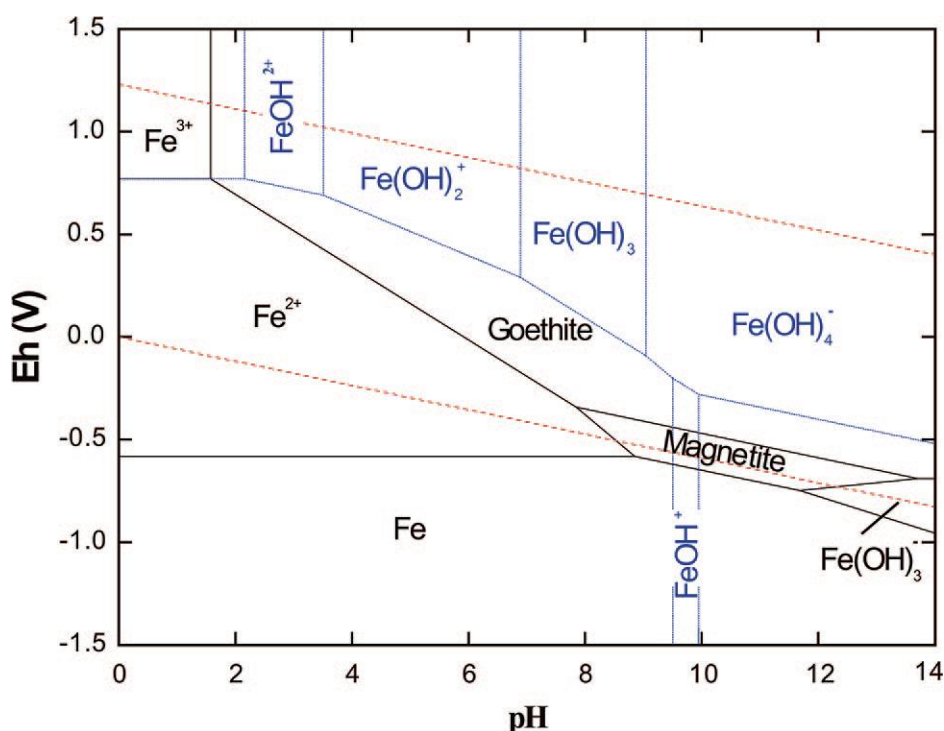


Figure 1.14. Phase stability (Eh-pH) Pourbaix diagram for the iron-water system likely to exist within the magnetosome (total concentration $\text{Fe}=10\ \mu\text{M}$) from Faivre & Schüler (2008).¹⁵ This represents a model system for within a mineralising magnetosome. At this concentration, magnetite formation is thermodynamically stable in a zone around $\text{pH}=10$ (basic) and $\text{Eh}=-0.5$ (reducing). If the redox conditions or pH are varied too much, other iron mineral phases, such as goethite, are more likely to form.

1.4.4 Biomineralisation Protein Mms6

Mms6 is a small protein ($\approx 6.4\ \text{kDa}$)¹²⁴ which has been shown to template uniform, cubo-octahedral magnetite MNPs both *in vivo*²³ and *in vitro*.^{22,24} Mms6 was identified as a biomineralisation protein because it was found tightly bound to magnetosome magnetite MNPs from AMB-1 by Arakaki *et al.* in 2003.²² Recently, the gene that encodes for *mms6* within AMB-1 was deleted to study the effect of Mms6 on magnetosome MNP formation *in vivo*.²³ Tanaka *et al.* (2011)²³ found that the $\Delta mms6$ mutant was still able to form magnetic particles, but they did not have the cubo-octahedral morphology observed in the wild type AMB-1. Instead, the MNPs from the $\Delta mms6$ mutant were smaller, less equidimensional, and consisted of many more crystal faces than those from the wild type AMB-1 bacterium.

As shown in Figure 1.13, Mms6 is one of many magnetosome associated proteins identified from AMB-1. The *N*-terminal region of Mms6 is hydrophobic, and thought to integrate the protein into the lipid membrane of the magnetosome vesicle.²² In aqueous solution, the hydrophobic residues may cause Mms6 to aggregate, and allow the hydrophilic *C*-terminal region to face outwards.²⁴ This hydrophilic section contains many carboxyl and hydroxyl amino acids, which are likely to bind iron and/or interact strongly with the magnetite nanoparticle surface.²² The *C*-terminal section is thought accumulate iron ions, initiate crystal nucleation and/or bind to

specific crystallographic planes of magnetite during crystal growth.^{22,23,106,125,126} However, the precise role of Mms6 in biotemplated magnetite MNP formation is still not well understood, as the crystal structure of this small protein has not been solved.

Mms6 forms cubo-octahedral magnetite nanoparticles *in vitro* with a similar morphology to those formed by the bacteria *in vivo*.^{22,24,127} Short peptide sequences based on the C-terminus of Mms6 have also been shown to perform a similar function.⁸⁴ In these studies, magnetite particles formed in the absence of Mms6 show a range of sizes and morphologies (see Figure 1.15).²⁴ Those formed in the presence of the Mms6 protein (or the C-terminus peptide) were of a cubo-octahedral morphology and had a narrow grain-size distribution, similar to those formed by the bacterium *in vivo*. The precise genetic control on magnetosome morphology by magnetic bacteria allows the organism to form consistent single domain, cubo-octahedral MNPs under ambient conditions. If the magnetic particles were of a variable size and shape, then their magnetic properties would also be varied (see Section 1.3.3). This would reduce the magnetic moment of the bacterium and hamper magnetotaxis.

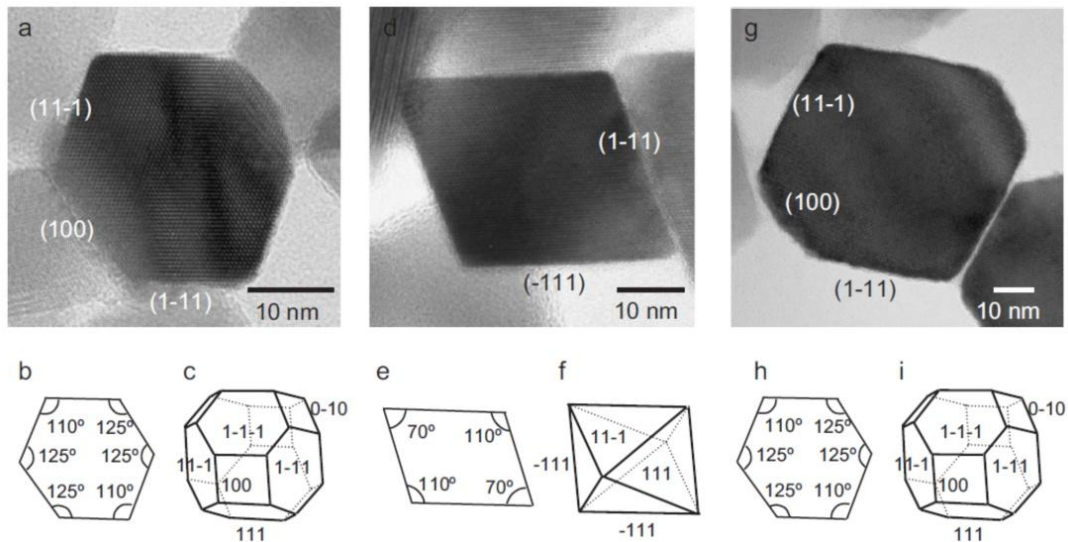


Figure 1.15. High resolution transmission electron microscopy (HRTEM) images of magnetite crystals from Amemiya *et al.* (2007).²⁴ Magnetite crystals formed by partial oxidation of ferrous hydroxide at 90°C (a-c) in the presence of Mms6, (d-f) the absence of Mms6. (g-i) Magnetosome magnetite nanoparticles from *M. magneticum* AMB-1. For comparison, (b, e & h) outline and (c, f & i) morphology of ideal magnetite crystals, showing both the internal angles and the crystal faces respectively.

1.4.5 Recombinant Protein Synthesis and Purification

Proteins are made up of amino acids, and synthesised by cells to perform functions such as catalysis, protection and support. The structure and function of deoxyribose nucleic acid (DNA) was described by Watson & Crick in 1953.^{128,129} DNA acts as a readable code for the production of proteins, and can self-replicate, thus allowing the code to be passed on to daughter cells during mitosis. Proteins are encoded in sections of DNA (genes) by an alphabet of four nucleotide bases which form triplet codons.¹³⁰ Each triplet codon acts as a three letter word that can correspond to an amino acid. By reading the DNA code correctly, an organism is able to assemble amino acids in the order encoded in the DNA, and thus produce a specified protein. As this information can be replicated and passed onto daughter cells, genes and DNA are able to effectively explain the mechanism behind Mendelian inheritance.¹³¹ Research into DNA and genomics is vast, and includes the Human Genome Project¹³² and the DOE Joint Genome Institute.¹³³

Genomics involves determining the base sequence, function and pattern of expression of genes.¹³⁴ In most bacteria, the DNA chromosome forms a closed loop which contains the information required for the bacterium to function and reproduce.¹³⁴ Bacteria may also contain extra pieces of DNA, such as plasmids. Plasmids tend to encode information that is useful to the bacterium rather than essential, including antibiotic resistance, pathogenesis and alternative metabolic pathways.¹³⁴ During conjugation, plasmids are passed between individual bacteria as vectors, and thus introduce new genes to a host cell.¹³⁵ Some phages are able to transfer DNA between host cells by transduction.¹³⁵ Bacteria are also able to take up genetic information from their surroundings via transformation.¹³⁵ These methods of sharing genetic information may explain how similarities in MAIs occur between magnetic bacteria from very different families. The ability of bacteria to transfer genetic information has disadvantages for humans, such as the development of multiple-antibiotic resistant strains of pathogenic bacteria.¹³⁶ However, there are also advantages, such as recombinant DNA uptake by bacteria during transformation, which allows recombinant proteins to be manufactured (e.g. insulin, Mms6).

Recombinant protein synthesis requires that the gene encoding for the desired protein is identified. The gene is then inserted into a vector plasmid to be introduced into an expression bacterial strain (Figure 1.16). The polymerase chain reaction (PCR)¹³⁷ amplifies a target gene using forward and reverse thermostable primers. During PCR, these primers replicate the desired section of DNA only, thus amplifying it. Heating DNA causes it to denature (melt) and unzip. This allows the complementary primers to locate and replicate the required gene.¹³⁸ When cooled,

the DNA zips back together (anneals), and releases the primers and the copied gene. Repeated thermal cycling allows many copies of the target gene to be replicated, which can be analysed using agarose gel electrophoresis.¹³⁸

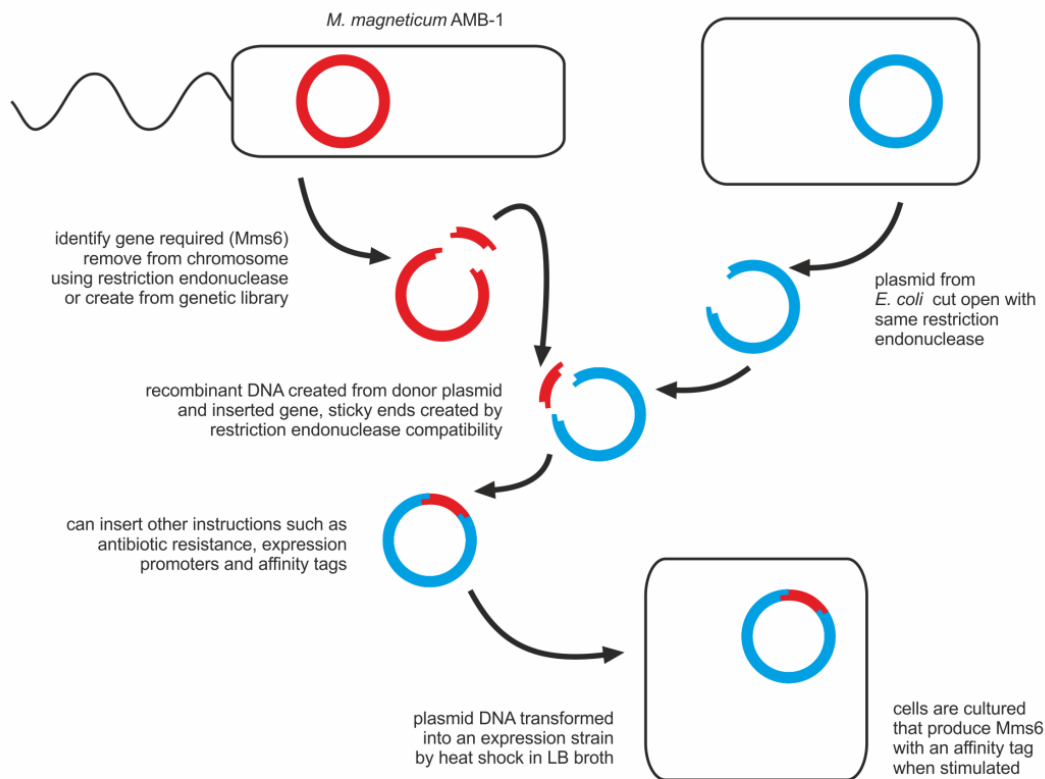


Figure 1.16. Schematic summary of Mms6 manufacture, based on Singleton (2004)¹³⁴ & Pruden *et al.* (2002).¹³⁹ The Gene that encodes Mms6 is identified and inserted into a vector plasmid. Expression promoters, (e.g. the *lac* promoter) are inserted to ensure the gene is switched on when stimulated to over-express the desired protein. Antibiotic resistance is also contained on the plasmid, and affinity tag(s) (e.g. polyhistidine) are inserted to allow the expressed protein to be isolated during purification. The recombinant plasmid is then transformed into a culture strain of bacteria. The antibiotic resistance ensures that only those bacteria that contain the recombinant DNA are cultured.

Recombinant DNA, which contains the *mms6* gene, is introduced into an expression strain by transformation (Figure 1.16). The vector plasmid also contains instructions for assembling an affinity tag at the *N*-terminus of Mms6, enzymatic cleavage sites, an expression promoter and antibiotic resistance. The transformed bacteria are cultured in media containing appropriate antibiotics to ensure only bacteria containing the *mms6* plasmid are able to grow. Over-expression of the Mms6 protein can then be switched on by exposing the bacteria to a chemical stimulus. A *lac* promoter switches on the expression of a specific protein when the bacteria are exposed to isopropyl- β -D-thiogalactopyranoside (IPTG) or lactose.¹⁴⁰

The affinity tag allows the over-expressed recombinant protein to be isolated from the mixture of proteins made by the culture bacteria.¹⁴¹ Polyhistidine (His_x-Mms6) tags are small and able to reversibly bind with immobilised transition metal ions,

such as nickel.¹⁴² Other recombinant tags include the small ubiquitin-like modifier (SUMO),¹⁴³ FLAG™, strep II, maltose binding protein (MBP) and glutathione-S-transferase (GST), see Arnau *et al.* (2006)¹⁴⁴ for more detail on affinity tags. Some tags not only offer a mechanism to purify the recombinant protein, but may also improve the physical properties of the expressed protein. For example, they may improve the overall protein yield, or, in the case of MBP or SUMO, they can also increase the solubility of the expressed protein.^{143,145}

His_x-tagged proteins are purified from the expressed proteins by passing the mixture through a column containing nickel or cobalt. The transition metal is immobilised onto a resin by chelation with nickel or cobalt *N*-nitrilo-triacetic acid (NTA) in the column during immobilised metal-ion affinity chromatography (IMAC).^{141,144} Two histidine residues in a tag chelate with each NTA, so tags containing six or eight histidines are used to create multiple bonds, and thus firmly bind the tagged protein to the metal in the column (Figure 1.17). Unwanted proteins wash through the column, and the recombinant, tagged protein is retained on the metal-NTA resin. By washing an NTA column with imidazole, the tagged protein is eluted, as the imidazole out-competes histidine, and displaces it from the immobilised metal ion. Ethylenediaminetetraacetic acid (EDTA) is also able to elute His_x-tagged proteins as it scavenges the transition metal from the NTA resin to release the bound protein.

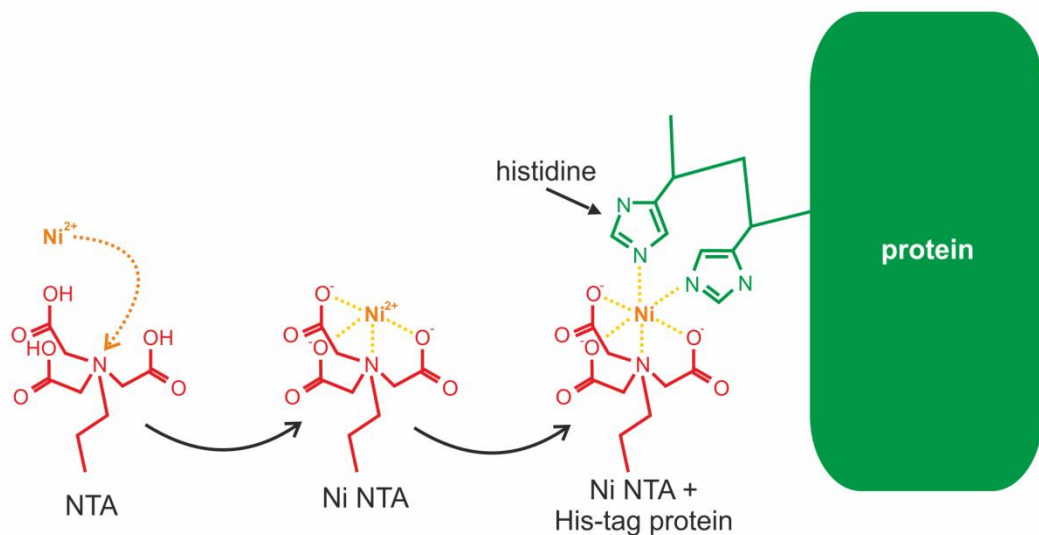


Figure 1.17. Diagram to show His_x-tag interaction with Ni²⁺-NTA during IMAC after Ludden *et al.* (2008),¹⁴⁶ Abad *et al.* (2005)¹⁴⁷ and Mrksich & Whitesides (1995).¹⁴⁸ A transition metal ion, such as Ni²⁺, is chelated with the NTA ligand on the resin. The Ni²⁺-NTA complex has a strong affinity for the histidine functional group in polyhistidine tagged proteins. The proteins are removed from the IMAC resin by imidazole or EDTA.

In many cases, the affinity tags are not needed after they have been used for protein purification. When designing vectors for recombinant protein synthesis, enzymatic cleavage sites can be inserted between tags and a target protein sequence. Many enzymes will only cleave a specific sequence of residues, so the cleavage can be localised to ensure that only the tag is cleaved from the expressed protein. For this work, thrombin¹⁴⁹ and the tobacco etch virus protease (TEV)¹⁵⁰ were used to remove tags from the Mms6 protein sequence. The protease and cleaved tags can be removed from the cleaved protein if the protease is also tagged with polyhistidine, leaving the pure, untagged Mms6 protein. Below is an example of a recombinant protein amino acid sequence, with the polyhistidine tag in green, the thrombin cleavage site in pink and the Mms6 mature protein sequence in blue:

**MGSSHHHHHSSGLVPRGSHMVGGTIWTGKGLGLGLGLG-
LGAWGPILGVVGAGAVYAYMKSRDIESAQSDEEVELRDALA**

1.5 Self-Assembled Monolayers (SAMs)

Self-assembled monolayers (SAMs) are formed by self-assembly of long chain hydrocarbons from a dilute solution or vapour phase.¹⁵¹ These are functionalised at the surface/air interface and attached to a suitable substrate by chemisorption (Figure 1.18).¹⁵² The head group attaches to the substrate, and the hydrocarbon chains order in the monolayer on the surface.¹⁵³ The chains tilt and twist to balance the intermolecular forces, such as Van der Waals (VDW) and electrostatic forces, between the hydrocarbon chains.¹⁵³ The degree of tilt and twist varies depending on the structure of the chain and the distance between surface attachment sites.¹⁵³ SAMs make good model systems for the study of physical chemistry and intermolecular interactions of surfaces with solvents and solutes.¹⁵² This is because a range of wetting behaviours and functionalities can be introduced to a SAM surface by appropriately functionalising the surface group (ω -group) of the SAM forming molecule.

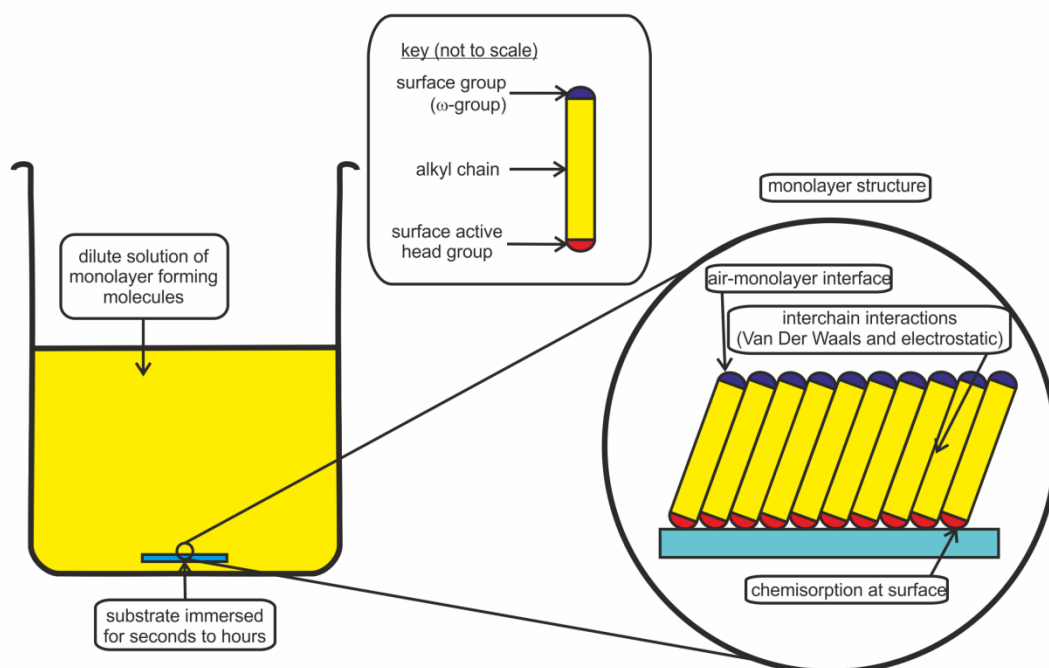


Figure 1.18. Illustration of formation of a SAM from a dilute solution, after Ulman (1996).¹⁵² An appropriate clean substrate is immersed in a dilute solution of SAM forming molecules. The head group bonds to the surface, and intermolecular forces order the alkane chains. The ω -group is presented at the surface of the SAM and provides the surface functionality.

1.5.1 Types of SAMs

There are two main types of SAMs that are commonly used to functionalise surfaces: organosilanes on silicon and alkanethiols on gold. Organosilanes self-assemble onto a silica surface via a polysiloxane head group, which connect to silanol groups ($-\text{SiOH}$) on the substrate by Si-O-Si bonds.¹⁵² Organosilane SAMs are excellent for surface functionalisation applications, as once formed they are very stable in organic solvents or acids and when heated.^{152,154} However, the formation of organosilane SAMs can be difficult, as the amount of water present during deposition must be carefully controlled to produce a high quality monolayer.¹⁵⁵⁻¹⁵⁷ This is because the ordering in organosilane SAMs is determined by the structure of the surface polysiloxane chain, rather than the underlying amorphous substrate (Figure 1.19).¹⁵² More SiOH groups form on the surface if there is more water.¹⁵² This distorts the polysiloxane chain, and leads to a more disordered monolayer when more water is present.¹⁵⁸ Temperature can also affect the formation of these monolayers, which means that it is difficult to form consistently reproducible organosilane SAMs.

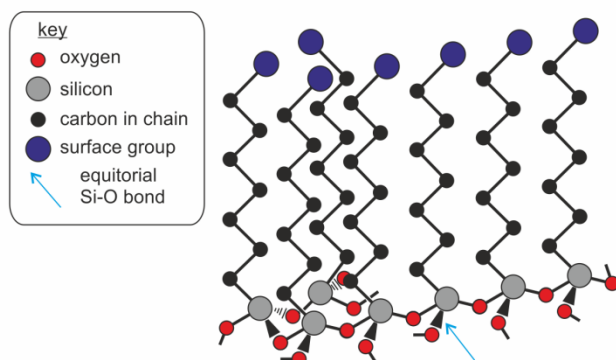


Figure 1.19. Stick and ball diagram to show polysiloxane structure at the monolayer-substrate surface after Ulman (1991).¹⁵³ Blue arrow indicates an equatorial Si-O bond that can be connected to either the substrate or the polysiloxane chain.

Alkanethiol SAMs on gold were first examined in detail by Nuzzo & Allara (1983),¹⁵⁹ with the alkanethiol on the Au [111] surface the most studied system to date.^{152,160} There are numerous alkanethiol compounds that are able to form monolayers on gold surfaces (see Figure 1.20).¹⁵² The sulfur head groups are also able to form self-assembled monolayers on surfaces of silver, copper, platinum, mercury, iron, GaAs, InP; and nanoparticles of maghemite and gold.¹⁶¹ As shown in Figure 1.18, a dilute solution (1-10 mM) is required to form a SAM from solution. The chemisorption of sulfur to the gold begins within seconds of immersion, and is completed within minutes to achieve $\approx 90\%$ of monolayer thickness.¹⁶²⁻¹⁶⁴ The kinetics of this reaction are controlled by the substrate-head group reaction, and the Au-S bond formed is very strong ($\approx 184 \text{ kJ mol}^{-1}$).¹⁶⁵

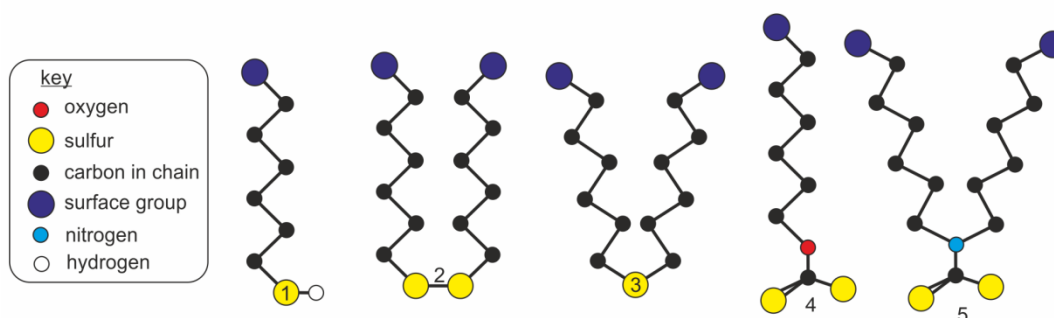
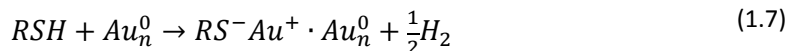


Figure 1.20. Stick and ball diagrams to show some organosulfur compounds that form SAMs on gold surfaces, from Ulman (1996).¹⁵² (a) Alkanethiol, (b) dialkyl disulfide, (c) dialkyl sulfide, (d) alkyl xanthate and (e) dialkyl thiocarbamate.

The chemisorption of alkanethiols and dialkyl disulfides is probably due to the formation of the Au^+ thiolate RS^- species.¹⁵² Alkanethiol monolayers may form on a clean gold surface by oxidative addition of the S-H bond to the gold substrate, and reductive loss of hydrogen as a gas by Equation 1.7:^{148,152,163}



The second stage of monolayer formation usually takes a few hours, and involves chain ordering by balancing inter-chain interactions.^{152,166} The chains usually tilt at approximately 30° from perpendicular to the surface when the ordering is complete.¹⁴⁸ From the disordered state at initial sorption, the chains form a two-dimensional crystal structure on the gold substrate.¹⁵² The time taken for chains to order is dependent on chain length, with longer chains ordering more rapidly due to greater VDW forces.^{152,162} The ω -group can also affect the structure of the SAM, as different groups interact in various ways to produce a diverse range of conformations.¹⁶⁷ There may also be some surface migration of alkanethiols on the gold surface as recrystallisation processes act to heal defects in the SAM, such as pinholes.¹⁵²

Silane monolayers show good stability, but Si-O bonds can be degraded thermally or under alkaline conditions, and may be prone to hydrolysis, which can introduce disorder into the SAM.^{158,168} Also, reproducibility in these monolayers can be problematic due to the concentration of water during monolayer formation, and there is not currently a large range of surface functionalities available.^{148,152,156,169,170} Monolayers of thiols on gold can be disordered and desorbed by heating in vacuum¹⁷¹ or in solvents.¹⁷² SAMs of alkanethiols on gold and organosilanes on silica are compared in Table 1.1.

Table 1.1. Table of advantages and disadvantages for each SAM system, based on in text references.

SAM type		silane-SiO ₂	alkanethiol-Au
production & analysis	positives	optically transparent	quick, simple, does not require organic solvents, ambient synthesis conditions, wide range of ω -functionalities
	difficulties	complex method, poor reproducibility, hydrolyses rapidly in weak base, low range of ω -functionalities	requires metal deposition, optically opaque
patternable		photolithography, e-beam, FIB, eCBL, probe methods	as silanes, but also μ CP
stability after formation	air	good	good
	water	poor	good
	organic solvents	poor	poor
	temperature	< \approx 140°C	< \approx 70°C
order		less ordered than alkanethiols	highly ordered, used as a template to compare to other systems
reproducibility		poor, water/temperature dependent, can require clean-room	good, most studied SAM, used as standard to compare to other systems

1.5.2 Functionalising SAMs

To control the surface properties of a monolayer, different ω -terminal functional groups can be employed. The hydrophobic/hydrophilic nature of a SAM surface is mainly determined by the chemical behaviour of the chosen surface group. Hydrophobic groups, such as methyl (-CH₃) and fluorinated groups (-CF₃) repel water. Hydrophilic groups, such as carboxylic acids (-COOH) can become charge polarised and interact with water through hydrogen bonding. It is also possible to functionalise SAMs to fluoresce, or facilitate the attachment of particles, molecules or proteins to a monolayer surface.

1.5.3 Attachment of Proteins to Surfaces

There are many methods that are used to attach proteins to surfaces, e.g. see Rusmini *et al.* (2007).¹⁷³ Although physisorption can inactivate proteins by unfolding them,¹⁷⁴ hydrophobic interactions of the *N*-terminal section of Mms6 with a hydrophobic -CH₃ surface was found to both attach the protein to a SAM surface and retain some of its' functionality.¹²⁵ They showed that the Mms6 was able to biotemplate multi-layers of MNPs when immobilised onto a surface via hydrophobic interactions. To attach Mms6 to a patterned surface and better maintain functionality of the biomineralisation protein, the protein should be selectively attached via the *N*-terminus. As in the magnetosome, this will allow the *C*-terminal

section to interact with iron in solution and template magnetite nucleation and growth onto the patterned protein. This may allow the formation of better templated MNPs by the immobilised protein, as it is less likely that immobilisation will deform the Mms6, which could significantly impair its function.

To create patterns of biomineralised MNPs onto surfaces, it is also necessary to functionalise areas to resist Mms6 protein binding. Surfaces can be blocked using sticky proteins, such as bovine serum albumin (BSA), to prevent non-specific binding of Mms6 in certain areas. However, it has recently been shown that BSA is able to biotemplate acicular iron oxide nanoparticles from a bulk solution.¹⁷⁵ This means that BSA, and possibly other sticky blocking proteins, may nucleate iron oxide mineralisation onto areas that should be functionalised to resist mineralisation. An alternative is to use a SAM forming molecule functionalised to resist protein binding. Poly-ethylene glycol (PEG) ω -terminated SAMs are good at resisting biofouling, and should be excellent for creating protein resistant surfaces. Therefore, appropriate surface functionalisation to resist or promote protein attachment can be achieved using self-assembled monolayers. Patterning of these SAMs should create areas that resist or promote particle immobilisation and/or mineralisation to fabricate biomineralised arrays of MNPs.

1.5.3.1 Affinity Tag Immobilisation

As detailed in Section 1.4.5, there are a wide variety of affinity tags that are used to purify proteins. These can also be used to immobilise proteins onto patterned surfaces, and some that are more commonly used are highlighted here. A polyhistidine affinity tag at the *N*-terminus of Mms6 could be used to pattern appropriately functionalised surfaces with the biomineralisation protein. As the tag is at the *N*-terminus, the His_x-Mms6 should retain its biomineralisation functionality. His_x-tagged proteins have been immobilised onto copper, gold and nickel metal surfaces, with nickel forming the strongest bond.^{142,176} As nickel is magnetic, a patterned surface of nickel is not ideal for this study, as it may affect the magnetic interactions between the biotemplated nanomagnets. To avoid this, patterned gold could be used, but as the affinity for the His_x-tag is less for Au, further surface functionalisation may be required.

The NTA moiety used in the purification of proteins during IMAC can also be used to immobilise His_x-tagged proteins onto patterned surfaces. Abad *et al.* (2005)¹⁴⁷ successfully attached His₆-tagged enzymes to gold nanoparticles functionalised with Co²⁺-NTA. As it has been demonstrated¹⁶ by Staniland *et al.* (2008)¹⁶ that magnetosomes can be doped with cobalt *in vivo*, a cobalt chelate may also attract the C-terminal portion of the Mms6 protein, which would misorientate the protein. In a study that investigated other dopants, Cu²⁺ and Mn²⁺ were also doped into

magnetosome magnetites.¹⁷⁷ However, their study found that the magnetic bacteria were not able to incorporate nickel into their magnetosomes. This indicates that Ni²⁺ is the best chelator for His₆-Mms6, as not only will it form the strongest bond with the polyhistidine tag, but it is unlikely that the C-terminal section of the protein will interact with a Ni²⁺-NTA surface. Ni²⁺-NTA has been used to attach His_x-tagged proteins to alkanethiols on gold and silane on silica self-assembled monolayers.^{146,147,178-183} The attachment of the protein is strongest at a mildly alkaline pH (≈pH 8), and involves the chelation of two histidines with each immobilised nickel ion (see Figure 1.17).

Single molecule experiments using His₆-tagged proteins found that the bond is quite weak, with just a 42% probability of a binding event occurring.¹⁸⁴ A force of only 153±57 pN was able to disrupt a single Ni²⁺-NTA-His₆-tag interaction.^{185,186} As a single Ni²⁺-NTA only interacts with two histidines, bis-Ni²⁺-NTA and tri-Ni²⁺-NTA have also been investigated. Bis-Ni²⁺-NTA was found to bind the His₆-tagged protein more strongly (316±50 pN) than mono-Ni²⁺-NTA,^{186,187} with tri-Ni²⁺-NTA binding more strongly still (468±44 pN).^{186,188} Careful spacing of the Ni²⁺-NTA head group is required to ensure unfavourable protein immobilisation is avoided.^{135,174,183,187-189} Usually, a mixed SAM involving a few mole percent of NTA moieties dispersed within an anti-biofouling molecule, such as a PEG, is used.^{146,148,190-193}

Other affinity tags could be introduced at the N-terminus of Mms6, which may also be used to pattern the protein onto a surface. Cysteine is an amino acid that contains sulfur, and the sulfur in cysteine can form a bond directly with gold. As Mms6 has no native cysteines, adding one or more cysteine residue(s) at the N-terminus should allow direct immobilisation of the protein onto a gold surface.¹⁹⁴⁻¹⁹⁸ This would avoid the need for SAMs specifically engineered for protein immobilisation, so could be a cost effective way of creating these biomineralised MNP arrays. Biotin has a strong affinity for avidin and streptavidin, so can also be used as a protein binding affinity tag.¹⁹⁹ However, the bond is so strong that harsh chemicals and denaturing conditions are required to elute the protein. This led to the development of the strep²⁰⁰ and strep II²⁰¹ affinity tags, which bind to the same area of avidin/streptavidin as biotin, but can be displaced from a column by biotin under physiological buffering conditions.²⁰¹ By functionalising a surface with biotin, and treating it with streptavidin, strep II tagged proteins could be immobilised onto a surface. However, biotin and NTA terminated SAM forming molecules can be very expensive to buy commercially, and mutating the protein to introduce affinity tags can alter the structure and function of a protein, both of which are undesirable.

1.5.3.2 EDC/NHS Activated Ester Linkage

Covalent protein binding, such as the use of activated esters to bind amines, can be used to try and bind the *N*-terminus of a protein without the need for affinity tags. Ethyl(dimethylaminopropyl) carbodiimide (EDC) and *N*-hydroxysuccinimide (NHS), or the more soluble sulfo-NHS, form an activated ester on a carboxylic acid surface (Figure 1.21).²⁰²⁻²⁰⁵ This will preferentially bind to the *N*-terminal amine of a protein if the protein is buffered to ≈ 1 pH point below its' isoelectric point (pI).^{173,203} However, amines on other residues may also be attached to the surface, which could misorientate the Mms6 protein. EDC/NHS activated ester linkage may also be used to attach molecules with other functionalities to a carboxylic acid surface. For example the lysine in *N*_α,*N*_α-bis(carboxymethyl)-L-lysine (*L*-NTA) can be covalently bound to a carboxylic acid SAM using EDC/NHS to form an NTA functionalised SAM far more cheaply than buying an NTA functionalised SAM forming molecule.

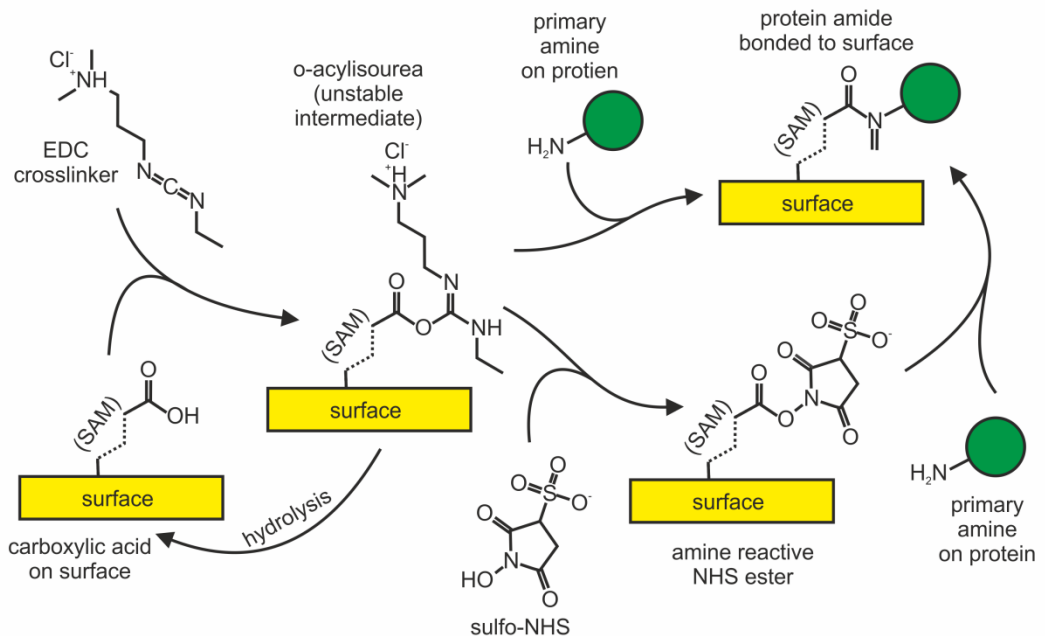


Figure 1.21. Reaction scheme for protein immobilisation onto a carboxylic acid surface using EDC/NHS, based on the Thermo Scientific website.²⁰⁵ The EDC and NHS convert a carboxylic acid on a surface into an activated ester. Here, the more soluble sulfo-NHS is shown. This covalently binds with an amine in the protein of interest to immobilise it onto the surface. Careful buffering of the protein can ensure the *N*-terminal amine is attached to the surface.

1.5.4 Patterning SAMs

The ability to selectively and precisely functionalise a monolayer surface has increased the applications of SAMs, for examples see Love *et al.* (2005).²⁰⁶ Lithographic techniques for patterning SAMs can be termed either hard or soft. Hard lithography can use light (photolithography) or an electron-beam (e-beam), to selectively irradiate a photoresist to create patterns on surfaces. Soft lithography employs two major techniques for patterning monolayers. The first damages the substrate prior to SAM formation, or removes part of the monolayer after SAM formation, to introduce an alternate functionality onto the patterned areas.²⁰⁶ The second involves the physical transfer of a SAM forming molecule to a clean surface as an ink. The ink can be drawn on using a probe as a pen, or transferred in a pattern over a large area using a stamp.²⁰⁶ Techniques that use masks and stamps tend to be higher throughput, as large areas can be patterned on the micro or nanoscale.²⁰⁷ The techniques that do not use masks but use serial writing (e.g. with a probe) provide high resolution of patterns on the nanoscale, but are time-consuming to use, so are difficult to scale-up for industrial production.²⁰⁷ The advantages and disadvantages of the methods for creating patterned SAMs are summarised in Table 1.2 at the end of this section.

1.5.4.1 Photolithography

Conventional photolithography is currently the main technique used to pattern organosilane monolayers on the microscale,²⁰⁸ and is used in industry to produce devices such as microchips.²⁰⁷ A photoresist is irradiated through a mask to form a pattern, before the treated resist is removed to expose the underlying silicon/gold surface.^{148,207,208} When an organosilane SAM is formed on the exposed areas, the remaining photoresist can then be removed to apply a SAM with a different functionality. Unfortunately, the photoresist can leave residue on the surface and lead to poor monolayer formation.²⁰⁸ The size of features produced by photolithography are dependent on the wavelength of the light used to irradiate the photoresist. The development of lenses to focus patterns post mask in projection printing photolithography improves the resolution of the patterns to a few tens of nanometers, but requires an even more expensive setup than for conventional photolithography.²⁰⁷ As organosilane monolayers do not have a great deal of variety in available functionalities, and the process is quite expensive for SAM patterning, alternative methods have been sought to pattern monolayers on substrates.²⁰⁸ Photolithography patterns are only available for use once, and require clean-room conditions to create each pattern, which means that it is an expensive technique for producing patterned SAMs. Researchers have been seeking faster, simpler and

more reusable methods of patterning SAM functionalities on surfaces to bring down the cost.

1.5.4.2 Electron Beam (e-beam) and Focussed Ion Beam (FIB) Lithography

E-beam and FIB lithography are the main techniques used for nanoscale patterning of surfaces, and both are serial techniques.²⁰⁷ E-beam lithography uses a focussed beam of electrons (spot size ≈ 2 nm, typically at energies of 50-100 keV) to write a pattern into a resist, which is then treated as in photolithography to form patterned SAMs.²⁰⁹ Fabrication of patterns using a FIB involves removing material or depositing material onto a surface with a focussed beam of heavy ions.²¹⁰ A thin film of metal can be etched away or deposited by serial writing of the FIB onto the surface to reveal the underlying substrate. This avoids the use of toxic developers and there are no resist residues, but the milled material can itself contaminate beam milled areas. E-beam and FIB lithography are able to produce precise nanopatterns, but are much slower than photolithography.²⁰⁷ However, the cost of e-beam lithographic nanopatterning has been reduced recently by fitting scanning electron microscopes (SEMs) with patterning capabilities.²⁰⁷

1.5.4.3 E-beam Chemical Lithography (eBCL)

Lower energy electrons (≈ 0.5 - 6.0 keV)^{211,212} than those used in e-beam lithography can be used to alter terminal functionality of a SAM using e-beam chemical lithography (eBCL). This technique has been successfully applied to altering a SAM functionalised with a nitro terminal group to an aromatic amine terminal group.^{211,213} EBCL has been used to pattern both alkanethiols on gold^{213,214} and organosilanes on silica^{211,212} to a resolution of ≈ 20 nm. This avoids residues that can be a problem for surfaces patterned by conventional photolithography, e-beam or FIB, but the functionalities that can be generated are still fairly limited.

1.5.4.4 Soft UV Photolithography

Soft UV photolithography uses specific wavelengths of light to alter the surface functionality of a SAM by cleaving part of the SAM forming molecule.²¹⁵ A range of photocleavable groups have been developed for SAMs on silica or gold. The most common of which is the *o*-nitrobenzyl group.²¹⁶⁻²²¹ When the photocleavable group is removed, a protected functional group, such as a carboxylic acid,^{216,217,221} an amine^{216,220,222} or a fluorescent group,²¹⁸ is exposed. As this method uses existing photolithographic technology, but removes the need for a photoresist, the patterning is far simpler than in conventional photolithography. Also, as only the lithographic mask needs to be made in a clean-room, this method is cheaper than conventional photolithography. However, there is a much greater level of complexity and

expense in the initial synthesis of the SAM forming molecule to create the appropriate functionalities.

1.5.4.5 Probe Patterning Methods

The most widely used probe patterning approach is dip-pen nanolithography, where a probe is inked with a SAM forming molecule, and then written onto the surface to create a pattern.^{223,224} More recently, arrays of polymer pyramids, similar to the elastomer stamps used in micro-contact printing (see Section 1.5.4.6), have been used to write many copies of the same pattern in parallel.²²⁵ Probes can also be used to physically remove parts of a SAM to form a serially written pattern.⁷⁷ The removed monolayer is replaced with a molecule with an alternate functionality to nanopattern the SAM.

Scanning near-field optical microscopy (SNOM) uses an optical probe to deliver light to nanopattern a SAM surface.²²⁶ Due to the diffraction limit of light, the feature size of patterns created using conventional photolithography cannot achieve nanoscale patterning. The SNOM probe is scanned a few nanometers from the surface, so uses near-field light, which only extends a few nanometers from the source, to modify the SAM surface.²²⁷ As the near-field is not subject to diffraction limitation, nanoscale patterns can be created using the SNOM.²²⁶ The recent development of the multi-probe SNOMipede to deliver many repeats of the same pattern in parallel may significantly improve throughput of near-field SAM patterning.²²⁸

1.5.4.6 Micro-Contact Printing (μ CP)

Micro-contact printing (μ CP) can currently only be used to pattern SAMs of alkanethiols on gold.²⁰⁸ A flexible elastomer stamp is created from a master and used to transfer an alkanethiol ink to a clean gold surface.²⁰⁸ The flexible stamp forms a conformal contact with the surface and transfers the alkanethiol ink to those areas it comes into contact with.²⁰⁸ Any area of clean gold can then be backfilled with an alternate alkanethiol SAM, which creates patterned functionality on the surface. μ CP can easily produce features down to $\approx 1 \mu\text{m}$,¹⁴⁸ but features as small as 50 nm have been produced.²⁰⁶ Creating the reusable stamp master is the only part of the process which requires a clean-room, and commercially available alkanethiols can be used for patterning. This makes μ CP one of the cheapest and simplest methods of patterning SAMs.^{208,229,230} However, the resolution and reproducibility of μ CP patterns depend on the flexibility and thickness of the elastomer stamp, and the pressure applied to the stamp during printing. Too much pressure, and the pattern can become distorted, not enough, and the full pattern is not transferred to the surface.

1.5.4.7 Patterning SAMs for Biotemplated MNP Array Formation

There are many techniques available for patterning SAMs on the micro and nanoscale, each with different advantages and disadvantages (see Table 1.2). Micro-contact printing was selected to form the patterns for the micropatterned arrays of biotemplated MNPs, as it is fairly simple to create micro-scale patterns using this technique. It only works for the thiolate-gold system, but there are a wide range of ω -functionalities available commercially for alkanethiol SAM forming molecules. This means that a diverse range of protein immobilisation strategies are available for a μ CP patterned thiolate on gold surface. As clean-room facilities are only required to create the masters for μ CP, every other stage of fabricating the biomineralised arrays can be carried out in a regular laboratory. This makes μ CP an inexpensive technique for creating micro-patterns when compared to the other methods of patterning SAMs.

Table 1.2. Summary of techniques for patterning self-assembled monolayers to functionalise substrates.

technique	scale	SAM system	advantages	disadvantages
conventional photolithography ^{148,207,208}	a few μ m	organosilane & alkanethiol	high throughput, micropattern large areas	expensive, clean-room, developer toxicity, residue
projection printing photolithography ²⁰⁷	tens of nm	organosilane & alkanethiol	quite high throughput, nanopattern large areas	as above, but even more expensive and slower
e-beam lithography ^{207,209}	\approx 5 nm	organosilane & alkanethiol	precise nanoscale patterning, fitting SEM reduces cost	slow and expensive, developer toxicity, residue
FIB lithography ²¹⁰	\approx 20 nm	organosilane & alkanethiol	precise nanopatterns, no toxic developer or resists	very slow and expensive, milled material can contaminate surface.
e-beam chemical lithography ²¹¹⁻²¹⁴	\approx 20 nm	organosilane & alkanethiol	precise nanopatterns, no toxic developer or resists, quick & efficient patterning	limited range of surface functionalities available
soft UV photolithography ^{216-218,220-222}	a few μ m	organosilane & alkanethiol	quite high throughput micropatterns on large areas, no resist residue, cheaper.	complex molecule synthesis
probe patterning ^{77,223-228}	\approx 5 nm	organosilane & alkanethiol	precise nanoscale patterning, no resists or residues, speed up using multiple-probe arrays	slow process, can only pattern small areas.
micro-contact printing ^{148,206,208,229,230}	<1 μ m	alkanethiol	quite high throughput micropatterns on large areas, no resist residue, cheapest.	reproducibility and resolution issues

1.6 Summary of Chapters

In the following chapters, the ideas and background introduced so far are used to show how arrays of nanomagnets can be templated using the biomineralisation protein Mms6. The second part of this section details the methods used during this study. The second section contains the results obtained on Mms6 structure and patterning proteins onto surfaces, the synthesis and characterisation of magnetite MNPs from a bulk solution, and the patterning of magnetite MNPs onto micropatterned surfaces, and the discussion of these results. There are also results and discussion on the effect of cobalt doping on the properties of these biotemplated MNPs. The third section contains the conclusions drawn from these discussions, and an outline of future directions this research could proceed in.

1.7 References

1. Braithwaite, N. & Weaver, G. (1990). *Electronic Materials* (Materials Department, Open University, Milton Keynes, UK).
2. Crowell, B. (2001). *Simple Nature [Online Version]*.
http://www.lightandmatter.com/html_books/0sn/ch11/ch11.html 22/03/2009.
3. Neckers, D.C. (1990). Stereolithography- An introduction. *Chem. Tech.* **20**, pp 615-619.
4. Lu, A.-H., Salabas, E.L. & Schüth, F. (2007). Magnetic nanoparticles: Synthesis, protection, functionalization, and application. *Angew. Chem. Int. Ed.* **46**, pp 1222-1244.
5. Park, J., An, K., Hwang, Y., Park, J.-G., Noh, H.-J., Kim, J.-Y., Park, J.-H., Hwang, N.-M. & Hyeon, T. (2004). Ultra-large-scale syntheses of monodisperse nanocrystals. *Nat. Mater.* **3**, pp 891-895.
6. Redl, F.X., Black, C.T., Papaefthymiou, G.C., Sandstrom, R.L., Yin, M., Zeng, H., Murray, C.B. & O'Brien, S.P. (2004). Magnetic, electronic, and structural characterization of non-stoichiometric iron oxides at the nanoscale. *J. Am. Chem. Soc.* **126**, pp 14583-14599.
7. Stanley, S.M. (1993). *Exploring Earth and Life Through Time* (W.H. Freeman, New York, USA).
8. Bazylinski, D.A., Frankel, R.B., Heywood, B.R., Mann, S., King, J.W., Donaghay, P.L. & Hanson, A.K. (1995). Controlled biomineralisation of magnetite (Fe₃O₄) and greigite (Fe₃S₄) in a magnetotactic bacterium. *Appl. Environ. Microbiol.* **61**, pp 3232-3239.
9. Gorby, A., Beveridge, T.J. & Blakemore, R.P. (1988). Characterisation of the bacterial magnetosome. *J. Bacteriol.* **170**, pp 834-841.
10. Amann, R., Peplies, J. & Schüler, D. (2007). Diversity and taxonomy of magnetotactic bacteria, pp 25-36. in *Magnetoreception and Magnetosomes in Bacteria* (ed. Schüler, D.). (Springer-Verlag, Berlin, DE).
11. Blakemore, R. (1975). Magnetotactic bacteria. *Science.* **190**, pp 377-379.

12. Matsunaga, T., Okamura, Y., Fukuda, Y., Wahyudi, A.T., Murase, Y. & Takeyama, H. (2005). Complete genome sequence of the facultative anaerobic magnetotactic bacterium *Magnetospirillum* sp strain AMB-1. *DNA Res.* **12**, pp 157-166.
13. Taylor, B.L., Zhulin, I.B. & Johnson, M.S. (1999). Aerotaxis and other energy-sensing behavior in bacteria. *Annu. Rev. Microbiol.* **53**, pp 103-128.
14. Devouard, B., Posfai, M., Hua, X., Bazylnski, D.A., Frankel, R.B. & Buseck, P.R. (1998). Magnetite from magnetotactic bacteria; Size distributions and twinning. *Am. Mineral.* **83**, pp 1387-1398.
15. Faivre, D. & Schüler, D. (2008). Magnetotactic bacteria and magnetosomes. *Chem. Rev.* **108**, pp 4875-4898.
16. Staniland, S., Williams, W., Telling, N., Van Der Laan, G., Harrison, A. & Ward, B. (2008). Controlled cobalt doping of magnetosomes in vivo. *Nat. Nanotechnol.* **3**, pp 158-162.
17. Arakaki, A., Nakazawa, H., Nemoto, M., Mori, T. & Matsunaga, T. (2008). Formation of magnetite by bacteria and its application. *J. R. Soc. Interface.* **5**, pp 977-999.
18. Lohße, A., Ullrich, S., Katzmann, E., Borg, S., Wanner, G., Richter, M., Voigt, B., Schweder, T. & Schüler, D. (2011). Functional analysis of the magnetosome island in *Magnetospirillum gryphiswaldense*: The mamAB operon is sufficient for magnetite biomineralization. *PLoS ONE.* **6**, pp e25561.
19. Uebe, R., Junge, K., Henn, V., Poxleitner, G., Katzmann, E., Pnitzko, J.M., Zarivach, R., Kasama, T., Wanner, G., Pósfai, M., Böttger, L., Matzanke, B. & Schüler, D. (2011). The cation diffusion facilitator proteins MamB and MamM of *Magnetospirillum gryphiswaldense* have distinct and complex functions, and are involved in magnetite biomineralization and magnetosome membrane assembly. *Mol. Microbiol.* **82**, pp 818-835.
20. Moench, T.T. & Konetzka, W.A. (1978). Novel method for isolation and study of a magnetotactic bacterium. *Arch. Microbiol.* **119**, pp 203-212.
21. Bazylnski, D.A. & Frankel, R.B. (2004). Magnetosome formation in prokaryotes. *Nat. Rev. Microbiol.* **2**, pp 217-230.
22. Arakaki, A., Webb, J. & Matsunaga, T. (2003). A novel protein tightly bound to bacterial magnetic particles in *Magnetospirillum magneticum* strain AMB-1. *J. Biol. Chem.* **278**, pp 8745-8750.
23. Tanaka, M., Mazuyama, E., Arakaki, A. & Matsunaga, T. (2011). Mms6 protein regulates crystal morphology during nano-sized magnetite biomineralization in vivo. *J. Biol. Chem.* **286**, pp 6386-6392.
24. Amemiya, Y., Arakaki, A., Staniland, S.S., Tanaka, T. & Matsunaga, T. (2007). Controlled formation of magnetite crystal by partial oxidation of ferrous hydroxide in the presence of recombinant magnetotactic bacterial protein Mms6. *Biomaterials.* **28**, pp 5381-5389.
25. Blundell, S. (2001). *Magnetism in Condensed Matter* (Oxford University Press, Oxford, U.K.).
26. Newey, C. & Weaver, G. (1990). *Materials Principles and Practice* (Butterworth Heinemann, Oxford).

27. Gambardella, P., Rusponi, S., Veronese, M., Dhési, S.S., Grazioli, C., Dallmeyer, A., Cabria, I., Zeller, R., Dederichs, P.H., Kern, K., Carbone, C. & Brune, H. (2003). Giant Magnetic Anisotropy of Single Cobalt Atoms and Nanoparticles. *Science*. **300**, pp 1130-1133.
28. Wolf, W.P. (1961). Ferrimagnetism. *Rep. Prog. Phys.* **24**, pp 212-303.
29. Weiss, P. (1907). L'hypothèse du champ moléculaire et la propriété ferromagnétique (The hypothesis of the molecular field and the property of ferromagnetism). *J. Phys. Théorique et Appliquée*. **6**, pp 661-690.
30. Bitter, F. (1931). On inhomogeneities in the magnetization of ferromagnetic materials. *Phys. Rev.* **38**, pp 1903-1905.
31. Peters, C. & Dekkers, M.J. (2003). Selected room temperature magnetic parameters as a function of mineralogy, concentration and grain size. *Phys. Chem. Earth*. **28**, pp 659-667.
32. Sorescu, M. (1998). Phase transformations induced in magnetite by high energy ball milling. *J. Mater. Sci. Lett.* **17**, pp 1059-1061.
33. Verwey, E.J., Haayman, P.W. & Romeijn, F.C. (1947). Physical properties and cation arrangement of oxides with spinel structures I. Cation arrangement in spinels. *J. Chem. Phys.* **15**, pp 181-187.
34. Walz, F. (2002). The Verwey transition - A topical review. *J. Phys. Condens. Matter*. **14**, pp R285.
35. Ozdemir, O., Dunlop, D.J. & Moskowitz, B.M. (1993). The effect of oxidation on the Verwey transition in magnetite. *Geophys. Res. Lett.* **20**, pp 1671-1674.
36. Verwey, E.J.W. (1939). Electronic conduction of magnetite (Fe_3O_4) and its transition point at low temperatures. *Nature*. **144**, pp 327-328.
37. Aragón, R. (1992). Magnetization and exchange in nonstoichiometric magnetite. *Phys. Rev. B*. **46**, pp 5328.
38. Aragón, R., Buttrey, D.J., Shepherd, J.P. & Honig, J.M. (1985). Influence of nonstoichiometry on the Verwey transition. *Phys. Rev. B*. **31**, pp 430.
39. Berkowitz, A.E. & Schuele, W.J. (1959). Magnetic properties of some ferrite micropowders. *J. Appl. Phys.* **30**, pp S134-S135.
40. Chinnasamy, C.N., Senoue, M., Jeyadevan, B., Perales-Perez, O., Shinoda, K. & Tohji, K. (2003). Synthesis of size-controlled cobalt ferrite particles with high coercivity and squareness ratio. *J. Colloid Interface Sci.* **263**, pp 80-83.
41. Sorescu, M., Grabias, A., Tarabasanu-Mihaila, D. & Diamandescu, L. (2001). From magnetite to cobalt ferrite. *J. Mater. Synth. Process.* **9**, pp 119-123.
42. Sorescu, M., Grabias, A., Brand, R.A., Voss, J., Tarabasanu-Mihaila, D. & Diamandescu, L. (2002). A Mössbauer study of the Verwey transition in cobalt-doped magnetite. *J. Magn. Magn. Mater.* **246**, pp 399-403.
43. Galloway, J.M. & Staniland, S.S. (2012). Protein and peptide biotemplated metal and metal oxide nanoparticles and their patterning onto surfaces. *J. Mater. Chem.* **22**, pp 12423-12434.

44. Currie, H.A., Deschaume, O., Naik, R.R., Perry, C.C. & Kaplan, D.L. (2011). Genetically engineered chimeric silk–silver binding proteins. *Adv. Funct. Mater.* **21**, pp 2889-2895.
45. Monteiro, D.R., Gorup, L.F., Takamiya, A.S., Ruvollo-Filho, A.C., Camargo, E.R.d. & Barbosa, D.B. (2009). The growing importance of materials that prevent microbial adhesion: antimicrobial effect of medical devices containing silver. *Int. J. Antimicrob. Agents.* **34**, pp 103-110.
46. Daniel, M.-C. & Astruc, D. (2003). Gold nanoparticles: Assembly, supramolecular chemistry, quantum-size-related properties, and applications toward biology, catalysis, and nanotechnology. *Chem. Rev.* **104**, pp 293-346.
47. Subban, C.V., Zhou, Q., Hu, A., Moylan, T.E., Wagner, F.T. & DiSalvo, F.J. (2010). Sol–gel synthesis, electrochemical characterization, and stability testing of $Ti_{0.7}W_{0.3}O_2$ nanoparticles for catalyst support applications in proton-exchange membrane fuel cells. *J. Am. Chem. Soc.* **132**, pp 17531-17536.
48. Espinet, P. & Echavarren, A.M. (2004). The mechanisms of the Stille reaction. *Angew. Chem. Int. Ed.* **43**, pp 4704-4734.
49. Mitchnick, M.A., Fairhurst, D. & Pinnell, S.R. (1999). Microfine zinc oxide (Z-Cote) as a photostable UVA/UVB sunblock agent. *J. Am. Acad. Dermatol.* **40**, pp 85-90.
50. Yella, A., Lee, H.-W., Tsao, H.N., Yi, C., Chandiran, A.K., Nazeeruddin, M.K., Diao, E.W.-G., Yeh, C.-Y., Zakeeruddin, S.M. & Grätzel, M. (2011). Porphyrin-sensitized solar cells with cobalt (II/III)–based redox electrolyte exceed 12 percent efficiency. *Science.* **334**, pp 629-634.
51. Gansen, E.J., Rowe, M.A., Greene, M.B., D, R., Harvey, T.E., Su, M.Y., Hadfield, R.H., Nam, S.W. & Mirin, R.P. (2007). Photon-number-discriminating detection using a quantum-dot, optically gated, field-effect transistor. *Nat. Photon.* **1**, pp 585-588.
52. Likovich, E.M., Jaramillo, R., Russell, K.J., Ramanathan, S. & Narayanamurti, V. (2011). High-current-density monolayer CdSe/ZnS quantum dot light-emitting devices with oxide electrodes. *Adv. Mater.* **23**, pp 4521-4525.
53. Xie, J., Zheng, Y. & Ying, J.Y. (2009). Protein-directed synthesis of highly fluorescent gold nanoclusters. *J. Am. Chem. Soc.* **131**, pp 888-889.
54. Zheng, J., Nicovich, P.R. & Dickson, R.M. (2007). Highly fluorescent noble-metal quantum dots. *Annu. Rev. Phys. Chem.* **58**, pp 409-431.
55. Dunlop, D.J. (1973). Superparamagnetic and single-domain threshold sizes in magnetite. *J. Geophys. Res.* **78**, pp 1780-1793.
56. Moskowitz, B. & Banerjee, S. (1979). Grain size limits for pseudosingle domain behavior in magnetite: Implications for paleomagnetism. *IEEE Trans. Magn.* **15**, pp 1241-1246.
57. Cedeño-Mattei, Y., Perales-Perez, O., Tomar, M.S., Roman, F., Voyles, P.M. & Stratton, W.G. (2008). Tuning of magnetic properties in cobalt ferrite nanocrystals. *Proceedings of the 52nd Annual Conference on Magnetism and Magnetic Materials.* **103**, pp 07E512-513.
58. Kneller, E.F. & Luborsky, F.E. (1963). Particle size dependence of coercivity and remanence of single-domain particles. *J. Appl. Phys.* **34**, pp 656-658.

59. Sun, S., Murray, C.B., Weller, D., Folks, L. & Moser, A. (2000). Monodisperse FePt nanoparticles and ferromagnetic FePt nanocrystal superlattices. *Science*. **287**, pp 1989-1992.
60. Desvaux, C., Amiens, C., Fejes, P., Renaud, P., Respaud, M., Lecante, P., Snoeck, E. & Chaudret, B. (2005). Multimillimetre-large superlattices of air-stable iron-cobalt nanoparticles. *Nat. Mater.* **4**, pp 750-753.
61. Berry, C.C. & Curtis, A.S.G. (2003). Functionalisation of magnetic nanoparticles for applications in biomedicine. *J. Phys. D: Appl. Phys.* **36**, pp R198-R206.
62. Weissleder, R., Bogdanov, A., Neuwelt, E.A. & Papisov, M. (1995). Long-circulating iron oxides for MR imaging. *Adv. Drug Delivery Rev.* **16**, pp 321-334.
63. Gupta, A.K. & Gupta, M. (2005). Cytotoxicity suppression and cellular uptake enhancement of surface modified magnetic nanoparticles. *Biomaterials*. **26**, pp 1565-1573.
64. Mornet, S., Vasseur, S., Grasset, F., Veverka, P., Goglio, G., Demourgues, A., Portier, J., Pollert, E. & Duguet, E. (2006). Magnetic nanoparticle design for medical applications. *Prog. Solid State Chem.* **34**, pp 237-247.
65. Reiss, G. & Hütten, A. (2005). Magnetic nanoparticles: Applications beyond data storage. *Nat. Mater.* **4**, pp 725-726.
66. Alphanbéry, E., Carvallo, C., Menguy, N. & Chebbi, I. (2011). Chains of cobalt doped magnetosomes extracted from AMB-1 magnetotactic bacteria for application in alternative magnetic field cancer therapy. *J. Phys. Chem. C*. **115**, pp 11920-11924.
67. Alphanbéry, E., Faure, S., Seksek, O., Guyot, F. & Chebbi, I. (2011). Chains of magnetosomes extracted from AMB-1 magnetotactic bacteria for application in alternative magnetic field cancer therapy. *ACS Nano*. **5**, pp 6279-6269.
68. Alphanbéry, E., Guyot, F. & Chebbi, I. (2012). Preparation of chains of magnetosomes, isolated from *Magnetospirillum magneticum* strain AMB-1 magnetotactic bacteria, yielding efficient treatment of tumors using magnetic hyperthermia. *Int. J. Pharm.* **434**, pp 444-452.
69. Lu, A.H., Schmidt, W., Matoussevitch, N., Bonnemann, H., Spliethoff, B., Tesche, B., Bill, E., Kiefer, W. & Schuth, F. (2004). Nanoengineering of a magnetically separable hydrogenation catalyst. *Angew. Chem. Int. Ed.* **43**, pp 4303-4306.
70. Tsang, S.C., Caps, V., Paraskevas, I., Chadwick, D. & Thompsett, D. (2004). Magnetically separable, carbon-supported nanocatalysts for the manufacture of fine chemicals. *Angew. Chem. Int. Ed.* **43**, pp 5645-5649.
71. Geng, Z., Lin, Y., Yu, X., Shen, Q., Ma, L., Li, Z., Pan, N. & Wang, X. (2012). Highly efficient dye adsorption and removal: a functional hybrid of reduced graphene oxide-Fe₃O₄ nanoparticles as an easily regenerative adsorbent. *J. Mater. Chem.* **22**, pp 3527-3535.
72. Mehta, R.V. & Upadhyay, R.V. (1999). Science and technology of ferrofluids. *Current Sci.* **76**, pp 305-312.
73. Lister, S.J., Thomson, T., Kohlbrecher, J., Takano, K., Venkataramana, V., Ray, S.J., Wismayer, M.P., Vries, M.A.d., Do, H., Ikeda, Y. & Lee, S.L. (2010). Size-dependent reversal of grains in perpendicular magnetic recording media measured by small-angle polarized neutron scattering. *Appl. Phys. Lett.* **97**, pp 112503.

74. Piramanayagam, S.N. (2007). Perpendicular recording media for hard disk drives. *J. Appl. Phys.* **102**, pp 011301.
75. Richter, H.J. (2007). The transition from longitudinal to perpendicular recording. *J. Phys. D.* **40**, pp R149.
76. Hellwig, O., Berger, A., Thomson, T., Dobisz, E., Bandic, Z.Z., Yang, H., Kercher, D.S. & Fullerton, E.E. (2007). Separating dipolar broadening from the intrinsic switching field distribution in perpendicular patterned media. *Appl. Phys. Lett.* **90**, pp 162516.
77. Liu, G.-Y. & Amro, N.A. (2002). Positioning protein molecules on surfaces: A nanoengineering approach to supramolecular chemistry. *Proc. Natl. Acad. Sci.* **99**, pp 5165-5170.
78. Cornell, R.M. & Schwertman, U. (2003). *The Iron Oxides: Structure, Properties, Reactions, Occurrences and Uses* (Wiley-VCH, Weinheim, DE).
79. Kim, D., Lee, N., Park, M., Kim, B.H., An, K. & Hyeon, T. (2009). Synthesis of uniform ferrimagnetic magnetite nanocubes. *J. Am. Chem. Soc.* **131**, pp 454-455.
80. Li, X., Xu, H., Chen, Z.-S. & Chen, G. (2011). Biosynthesis of nanoparticles by microorganisms and their applications. *J. Nanomater.* **2011**, pp Article ID 270974.
81. Kumar, S. & Nussinov, R. (2001). How do thermophilic proteins deal with heat? *Cell. Mol. Life Sci.* **58**, pp 1216-1233.
82. Regazzoni, A.E., Urrutia, G.A., Blesa, M.A. & Maroto, A.J.G. (1981). Some observations on the composition and morphology of synthetic magnetites obtained by different routes. *J. Inorg. Nucl. Chem.* **43**, pp 1489-1493.
83. Sorescu, M., Oberst, T., Gossett, K., Tarabasanu, D. & Diamandescu, L. (2000). Direct evidence for cobalt substitution effects in magnetite. *Solid State Commun.* **113**, pp 573-575.
84. Arakaki, A., Masuda, F., Amemiya, Y., Tanaka, T. & Matsunaga, T. (2010). Control of the morphology and size of magnetite particles with peptides mimicking the Mms6 protein from magnetotactic bacteria. *J. Colloid Interface Sci.* **343**, pp 65-70.
85. Sugimoto, T. & Matijevic, E. (1980). Formation of uniform spherical magnetite particles by crystallization from ferrous hydroxide gels. *J. Colloid Interface Sci.* **74**, pp 227-243.
86. Clarkson, E.N.K. (1998). *Invertebrate Palaeontology and Evolution* (Blackwell Science, Oxford, UK).
87. Kirschvink, J.L. & Hagadorn, J.W. (2000). A grand unified theory of biomineralization., pp 139-150. in *Biomineralization* (ed. Bäuerlein, E.). (Wiley-VCH Verlag GmbH, Weinheim, DE).
88. Chang, S.B.R. & Kirschvink, J.L. (1989). Magnetofossils, the magnetization of sediments, and the evolution of magnetite biomineralization. *Earth Planet. Sci. Lett.* **17**, pp 169-195.
89. Metzler, R.A., Kim, I.W., Delak, K., Evans, J.S., Zhou, D., Beniash, E., Wilt, F., Abrecht, M., Chiou, J.-W., Guo, J., Coppersmith, S.N. & Gilbert, P.U.P.A. (2008). Probing the organic–mineral interface at the molecular level in model biominerals. *Langmuir.* **24**, pp 2680-2687.

90. Reid, D.G., Duer, M.J., Murray, R.C. & Wise, E.R. (2008). The organic–mineral interface in teeth is like that in bone and dominated by polysaccharides: Universal mediators of normal calcium phosphate biomineralization in vertebrates? *Chem. Mater.* **20**, pp 3549-3550.
91. Fratzl, P. & Weinkamer, R. (2007). Nature's hierarchical materials. *Prog. Mater. Sci.* **52**, pp 1263-1334.
92. Addadi, L. & Weiner, S. (1992). Control and design principles in biological mineralization. *Angew. Chem. Int. Ed.* **31**, pp 153-169.
93. Cattaneo-Vietti, R., Bavestrello, G., Cerrano, C., Sarà, M., Benatti, U., Giovine, M. & Gaino, E. (1996). Optical fibres in an Antarctic sponge. *Nature.* **383**, pp 397-398.
94. Sundar, V.C., Yablon, A.D., Grazul, J.L., Ilan, M. & Aizenberg, J. (2003). Fibre-optical features of a glass sponge. *Nature.* **424**, pp 899-900.
95. Hildebrand, M. (2008). Diatoms, biomineralization processes, and genomics. *Chem. Rev.* **108**, pp 4855-4874.
96. Mann, S., Hannington, J.P. & Williams, R.J.P. (1986). Phospholipid vesicles as a model system for biomineralization. *Nature.* **324**, pp 565-567.
97. Meldrum, F.C. & Cölfen, H. (2008). Controlling mineral morphologies and structures in biological and synthetic systems. *Chemical Reviews.* **108**, pp 4332-4432.
98. Oaki, Y., Kotachi, A., Miura, T. & Imai, H. (2006). Bridged nanocrystals in biominerals and their biomimetics: Classical yet modern crystal growth on the nanoscale. *Adv. Funct. Mater.* **16**, pp 1633-1639.
99. Simmons, S.L., Sievert, S.M., Frankel, R.B., Bazylinski, D.A. & Edwards, K.J. (2004). Spatiotemporal distribution of marine magnetotactic bacteria in a seasonally stratified coastal salt pond. *Appl. Environ. Microbiol.* **70**, pp 6230-6239.
100. Blakemore, R.P. (1982). Magnetotactic bacteria. *Annu. Rev. Microbiol.* **36**, pp 217-238.
101. Lefèvre, C.T., Frankel, R.B., Abreu, F., Lins, U. & Bazylinski, D.A. (2011). Culture-independent characterization of a novel, uncultivated magnetotactic member of the Nitrospirae phylum. *Environ. Microbiol.* **13**, pp 538-549.
102. Lefèvre, C.T., Menguy, N., Abreu, F., Lins, U., Pósfai, M., Prozorov, T., Pignol, D., Frankel, R.B. & Bazylinski, D.A. (2011). A cultured greigite-producing magnetotactic bacterium in a novel group of sulfate-reducing bacteria. *Science.* **334**, pp 1720-1723.
103. Lefèvre, C.T., Vilorio, N., Schmidt, M.L., Pósfai, M., Frankel, R.B. & Bazylinski, D.A. (2012). Novel magnetite-producing magnetotactic bacteria belonging to the Gammaproteobacteria. *ISME J.* **6**, pp 440-450.
104. Matsunaga, T., Okamura, Y. & Tanaka, T. (2004). Biotechnological application of nano-scale engineered bacterial magnetic particles. *J. Mater. Chem.* **14**, pp 2099-2105.
105. Frankel, R., Williams, T. & Bazylinski, D. (2007). Magneto-aerotaxis, pp 1-24. *in Magnetoreception and Magnetosomes in Bacteria* (ed. Schüler, D.). (Springer-Verlag, Berlin, DE).

106. Staniland, S., Ward, B., Harrison, A., van der Laan, G. & Telling, N. (2007). Rapid magnetosome formation shown by real-time X-ray magnetic circular dichroism. *Proc. Natl. Acad. Sci.* **104**, pp 19524-19528.
107. Bazylinski, D.A., Garratt-Reed, A.J. & Frankel, R.B. (1994). Electron microscopic studies of magnetosomes in magnetotactic bacteria. *Microsc. Res. Tech.* **27**, pp 389-401.
108. Dunin-Borkowski, R.E., McCartney, M.R., Frankel, R.B., Bazylinski, D.A., Pósfai, M. & Buseck, P.R. (1998). Magnetic microstructure of magnetotactic bacteria by electron holography. *Science*. **282**, pp 1868-1870.
109. Reddy, K.R. & DeLaune, R.D. (2008). *Biogeochemistry of Wetlands: Science and Applications* (CRC Press, Taylor & Francis Group, Florida, USA).
110. Charman, D. (2002). *Peatlands and Environmental Change* (J. Wiley & Sons, Chichester, UK).
111. Brun, N.E.L., Crow, A., Murphy, M.E.P., Mauk, A.G. & Moore, G.R. (2010). Iron core mineralisation in prokaryotic ferritins. *Biochim. Biophys. Acta.* **1800**, pp 732-744.
112. Ross, S.M. (1995). Overview of the hydrochemistry and solute processes in British wetlands, pp 133-181. in *Hydrology and Hydrochemistry of British Wetlands* (eds. Hughes, J.M.R. & Heathwaite, A.L.). (J. Wiley & Sons, Chichester, UK).
113. Kolber, Z.S., Barber, R.T., Coale, K.H., Fitzwater, S.E., Greene, R.M., Johnson, K.S., Lindley, S. & Falkowski, P.G. (1994). Iron limitation of phytoplankton photosynthesis in the equatorial Pacific Ocean. *Nature*. **371**, pp 145-149.
114. Richter, M., Kube, M., Bazylinski, D.A., Lombardot, T., Glockner, F.O., Reinhardt, R. & Schüler, D. (2007). Comparative genome analysis of four magnetotactic bacteria reveals a complex set of group-specific genes implicated in magnetosome biomineralization and function. *J. Bacteriol.* **189**, pp 4899-4910.
115. Tanaka, M., Okamura, Y., Arakaki, A., Tanaka, T., Takeyama, H. & Matsunaga, T. (2006). Origin of magnetosome membrane: Proteomic analysis of magnetosome membrane and comparison with cytoplasmic membrane. *Proteomics*. **6**, pp 5234-5247.
116. Grünberg, K., Müller, E.-C., Otto, A., Reszka, R., Linder, D., Kube, M., Reinhardt, R. & Schüler, D. (2004). Biochemical and proteomic analysis of the magnetosome membrane in *Magnetospirillum gryphiswaldense*. *Appl. Environ. Microbiol.* **70**, pp 1040-1050.
117. Grünberg, K., Wawer, C., Tebo, B.M. & Schüler, D. (2001). A large gene cluster encoding several magnetosome proteins is conserved in different species of magnetotactic bacteria. *Appl. Environ. Microbiol.* **67**, pp 4573-4582.
118. Schübbe, S., Kube, M., Scheffel, A., Wawer, C., Heyen, U., Meyerdierks, A., Madkour, M.H., Mayer, F., Reinhardt, R. & Schüler, D. (2003). Characterization of a spontaneous nonmagnetic mutant of *Magnetospirillum gryphiswaldense* reveals a large deletion comprising a putative magnetosome island. *J. Bacteriol.* **185**, pp 5779-5790.
119. Ullrich, S., Kube, M., Schübbe, S., Reinhardt, R. & Schüler, D. (2005). A hypervariable 130-kilobase genomic region of *Magnetospirillum gryphiswaldense* comprises a magnetosome island which undergoes frequent rearrangements during stationary growth. *J. Bacteriol.* **187**, pp 7176-7184.

120. Frankel, R.B., Papaefthymiou, G.C., Blakemore, R.P. & O'Brien, W. (1983). Fe₃O₄ precipitation in magnetotactic bacteria. *Biochim. Biophys. Acta, Mol. Cell. Res.* **763**, pp 147-159.
121. Faivre, D., Böttger, L.H., Matzanke, B.F. & Schüler, D. (2007). Intracellular magnetite biomineralization in bacteria proceeds by a distinct pathway involving membrane-bound ferritin and an iron(II) species. *Angew. Chem. Int. Ed.* **46**, pp 8495-8499.
122. Mandernack, K.W., Bazylinski, D.A., Shanks III, W.C. & Bullen, T.D. (1999). Oxygen and iron isotope studies of magnetite produced by magnetotactic bacteria. *Science*. **285**, pp 1892-1896.
123. Bazylinski, D.A., Frankel, R.B. & Jannasch, H.W. (1988). Anaerobic magnetite production by a marine magnetotactic bacterium. *Nature*. **334**, pp 518-519.
124. (2012). *ExpASY ProtParam tool by the Swiss Institute of Bioinformatics*. <http://web.expasy.org/protparam/> 16/01/2012.
125. Arakaki, A., Masuda, F. & Matsunaga, T. (2009). Iron oxide crystal formation on a substrate modified with Mms6 protein from magnetotactic bacteria. *MRS Proc.* **1187**, pp KK03-08.
126. Galloway, J.M., Arakaki, A., Masuda, F., Tanaka, T., Matsunaga, T. & Staniland, S.S. (2011). Magnetic bacterial protein Mms6 controls morphology, crystallinity and magnetism of cobalt-doped magnetite nanoparticles in vitro. *J. Mater. Chem.* **21**, pp 15244-15254.
127. Prozorov, T., Mallapragada, S.K., Narasimhan, B., Wang, L.J., Palo, P., Nilsen-Hamilton, M., Williams, T.J., Bazylinski, D.A., Prozorov, R. & Canfield, P.C. (2007). Protein-mediated synthesis of uniform superparamagnetic magnetite nanocrystals. *Adv. Funct. Mater.* **17**, pp 951-957.
128. Watson, J.D. & Crick, F.H.C. (1953). Molecular structure of nucleic acids - A structure for deoxyribose nucleic acid. *Nature*. **171**, pp 737-738.
129. Watson, J.D. & Crick, F.H.C. (1953). Genetical implications of the structure of deoxyribose nucleic acid. *Nature*. **171**, pp 964-967.
130. Roberts, M.B.V. (1976). *Biology: A Functional Approach* (Nelson, Sunbury-on-Thames, UK).
131. Mendel, G. (1866). Experiments in plant hybridization (in English in 1901, J. R. Hortic. Soc. 26: 1-32). *Proc. Nat. Hist. Soc. Brünn.* **4**, pp 3-47.
132. Roberts, L., Davenport, R.J., Pennisi, E. & Marshall, E. (2001). A history of the human genome project. *Science*. **291**, pp 1195.
133. DOE Joint Genome Institute. <http://www.jgi.doe.gov/> 11/05/2009.
134. Singleton, P. (2004). *Bacteria in Biology, Biotechnology and Medicine* (Wiley, Chichester, UK).
135. Snyder, L. & Champness, W. (2007). *Molecular Genetics of Bacteria* (ASM Press, Washington D.C., USA).
136. Arias, C.A. & Murray, B.E. (2009). Antibiotic-resistant bugs in the 21st Century - A clinical super-challenge. *N. Eng. J. Med.* **360**, pp 439-443.

137. Saiki, R.K., Scharf, S., Faloona, F., Mullis, K.B., Horn, G.T., Erlich, H.A. & Arnheim, N. (1985). Enzymatic amplification of β -globin genomic sequences and restriction site analysis for diagnosis of sickle cell anemia. *Science*. **230**, pp 1350-1354.
138. Nicholl, D.S.T. (2008). *An Introduction to Genetic Engineering* (Cambridge University Press, Cambridge, UK).
139. Pruden, V., Burnett, J., Crane, J. & Woodward, C. (2002). *AQA GCSE Biology* (Hodder & Stoughton, London, UK).
140. Baneyx, F. (1999). Recombinant protein expression in *Escherichia coli*. *Curr. Opin. Biotech.* **10**, pp 411-421.
141. Porath, J., Carlsson, J., Olsson, I. & Belfrage, G. (1975). Metal chelate affinity chromatography, a new approach to protein fractionation. *Nature*. **258**, pp 598-599.
142. Soong, R.K., Stelick, S.J., Bachand, G.D. & Montemagno, C.D. (1999). Evaluating adhesion strength of biological molecules to nanofabricated substrates. *1999 Int. Conf. Model. Simul. Microsys.*, pp 95-98.
143. Marblestone, J.G., Edavettal, S.C., Lim, Y., Lim, P., Zuo, X. & Butt, T.R. (2006). Comparison of SUMO fusion technology with traditional gene fusion systems: Enhanced expression and solubility with SUMO. *Prot. Sci.* **15**, pp 182-189.
144. Arnau, J., Lauritzen, C., Petersen, G.E. & Pedersen, J. (2006). Current strategies for the use of affinity tags and tag removal for the purification of recombinant proteins. *Protein Expres. Purif.* **48**, pp 1-13.
145. Kapust, R.B. & Waugh, D.S. (1999). *Escherichia coli* maltose-binding protein is uncommonly effective at promoting the solubility of polypeptides to which it is fused. *Prot. Sci.* **8**, pp 1668-1674.
146. Ludden, M.J.W., Mulder, A., Schulze, K., Subramaniam, V., Tampé, R. & Huskens, J. (2008). Anchoring of histidine-tagged proteins to molecular printboards: Self-assembly, thermodynamic modeling, and patterning. *Chem. Eur. J.* **14**, pp 2044-2051.
147. Abad, J.M., Mertens, S.F.L., Pita, M., Fernandez, V.M. & Schiffrin, D.J. (2005). Functionalization of thioctic acid-capped gold nanoparticles for specific immobilization of histidine-tagged proteins. *J. Am. Chem. Soc.* **127**, pp 5689-5694.
148. Mrksich, M. & Whitesides, G.M. (1995). Patterning self-assembled monolayers using microcontact printing: A new technology for biosensors? *Trends Biotechnol.* **13**, pp 228-235.
149. Jenny, R.J., Mann, K.G. & Lundblad, R.L. (2003). A critical review of the methods for cleavage of fusion proteins with thrombin and factor Xa. *Protein Expres. Purif.* **31**, pp 1-11.
150. Kapust, R.B., Tözsér, J., Fox, J.D., Anderson, D.E., Cherry, S., Copeland, T.D. & Waugh, D.S. (2001). Tobacco etch virus protease: Mechanism of autolysis and rational design of stable mutants with wild-type catalytic proficiency. *Prot. Eng.* **14**, pp 993-1000.
151. Wasserman, S.R., Tao, Y.T. & Whitesides, G.M. (1989). Structure and reactivity of alkylsiloxane monolayers formed by reaction of alkyltrichlorosilanes on silicon substrates. *Langmuir*. **5**, pp 1074-1087.
152. Ulman, A. (1996). Formation and structure of self-assembled monolayers. *Chem. Rev.* **96**, pp 1533-1554.

153. Ulman, A. (1991). *An Introduction to Ultrathin Organic Films: From Langmuir-Blodgett to Self-Assembly* (Academic Press, London, UK).
154. Cohen, S.R., Naaman, R. & Sagiv, J. (1986). Thermally induced disorder in organized organic monolayers on solid substrates. *J. Phys. Chem.* **90**, pp 3054-3056.
155. Angst, D.L. & Simmons, G.W. (1991). Moisture absorption characteristics of organosiloxane self-assembled monolayers. *Langmuir.* **7**, pp 2236-2242.
156. Silberzan, P., Leger, L., Ausserre, D. & Benattar, J.J. (1991). Silanation of silica surfaces. A new method of constructing pure or mixed monolayers. *Langmuir.* **7**, pp 1647-1651.
157. Tripp, C.P. & Hair, M.L. (1992). An infrared study of the reaction of octadecyltrichlorosilane with silica. *Langmuir.* **8**, pp 1120-1126.
158. Allara, D.L. (1995). Critical issues in applications of self-assembled monolayers. *Biosens. Bioelectron.* **10**, pp 771-783.
159. Nuzzo, R.G. & Allara, D.L. (1983). Adsorption of bifunctional organic disulfides on gold surfaces. *J. Am. Chem. Soc.* **105**, pp 4481-4483.
160. Ulman, A. (1998). *Self-Assembled Monolayers of Thiols* (Academic Press, San Diego, USA).
161. van de Weert, M. & Stella, L. (2011). Fluorescence quenching and ligand binding: A critical discussion of a popular methodology. *J. Mol. Struct.* **998**, pp 144-150.
162. Bain, C.D., Troughton, E.B., Tao, Y.T., Evall, J., Whitesides, G.M. & Nuzzo, R.G. (1989). Formation of monolayer films by the spontaneous assembly of organic thiols from solution onto gold. *J. Am. Chem. Soc.* **111**, pp 321-335.
163. Biebuyck, H.A., Bain, C.D. & Whitesides, G.M. (1994). Comparison of organic monolayers on polycrystalline gold spontaneously assembled from solutions containing dialkyl disulfides or alkanethiols. *Langmuir.* **10**, pp 1825-1831.
164. Camillone, N. (2004). Diffusion-limited thiol adsorption on the gold (111) surface. *Langmuir.* **20**, pp 1199-1206.
165. Dubois, L.H. & Nuzzo, R.G. (1992). Synthesis, structure and properties of model organic surfaces. *Annu. Rev. Phys. Chem.* **43**, pp 437-463.
166. Bain, C.D., Evall, J. & Whitesides, G.M. (1989). Formation of monolayers by the coadsorption of thiols on gold: variation in the head group, tail group, and solvent. *J. Am. Chem. Soc.* **111**, pp 7155-7164.
167. Gorman, C.B., He, Y. & Carroll, R.L. (2001). The influence of headgroup on the structure of self-assembled monolayers as viewed by scanning tunneling microscopy. *Langmuir.* **17**, pp 5324-5328.
168. Calistri-Yeh, M., Kramer, E.J., Sharma, R., Zhao, W., Rafailovich, M.H., Sokolov, J. & Brock, J.D. (1996). Thermal stability of self-assembled monolayers from alkylchlorosilanes. *Langmuir.* **12**, pp 2747-2755.
169. McGovern, M.E., Kallury, K.M.R. & Thompson, M. (1994). Role of solvent on the silanization of glass with octadecyltrichlorosilane. *Langmuir.* **10**, pp 3607-3614.

170. Sieval, A.B., Demirel, A.L., Nissink, J.W.M., Linford, M.R., van der Maas, J.H., de Jeu, W.H., Zuilhof, H. & Sudholter, E.J.R. (1998). Highly stable Si-C linked functionalized monolayers on the silicon (100) surface. *Langmuir*. **14**, pp 1759-1768.
171. Tam-Chang, S.-W., Biebuyck, H.A., Whitesides, G.M., Jeon, N. & Nuzzo, R.G. (1995). Self-assembled monolayers on gold generated from alkanethiols with the structure RNHCOCH₂SH. *Langmuir*. **11**, pp 4371-4382.
172. Tillman, N., Ulman, A. & Penner, T.L. (1989). Formation of multilayers by self-assembly. *Langmuir*. **5**, pp 101-111.
173. Rusmini, F., Zhong, Z. & Feijen, J. (2007). Protein immobilization strategies for protein biochips. *Biomacromolecules*. **8**, pp 1775-1789.
174. Tinazli, A., Tang, J., Valiokas, R., Picuric, S., Lata, S., Piehler, J., Liedberg, B. & Tampé, R. (2005). High-affinity chelator thiols for switchable and oriented immobilization of histidine-tagged proteins: A generic platform for protein chip technologies. *Chem. Eur. J.* **11**, pp 5249-5259.
175. Hadley, M.J., Wright, A.J., Rowson, N.A. & Grover, L.M. (2011). Acicular nanoparticles formed through coprecipitation of iron salts in the presence of bovine serum albumin. *J. Mater. Chem.* **21**, pp 13769-13771.
176. Montemagno, C. & Bachand, G. (1999). Constructing nanomechanical devices powered by biomolecular motors. *Nat. Nanotechnol.* **3**, pp 225-231.
177. Tanaka, M., Brown, R., Hondow, N., Arakaki, A., Matsunaga, T. & Staniland, S. (2012). Highest levels of Cu, Mn and Co doped into nanomagnetic magnetosomes through optimized biomineralisation. *J. Mater. Chem.* **22**, pp 11919-11921.
178. Gupta, M., Caniard, A., Touceda-Varela, A., Campopiano, D.J. & Mareque-Rivas, J.C. (2008). Nitrilotriacetic acid-derivatized quantum dots for simple purification and site-selective fluorescent labeling of active proteins in a single step. *Bioconjugate Chem.* **19**, pp 1964-1967.
179. Keller, T.A., Duschl, C., Kröger, D., Sévin-Landais, A.-F., Vogel, H., Cervigni, S.E. & Dumy, P. (1995). Reversible oriented immobilization of histidine-tagged proteins on gold surfaces using a chelator thioalkane. *Supramol. Sci.* **2**, pp 155-160.
180. Le, T.T., Wilde, C.P., Grossman, N. & Cass, A.E.G. (2011). A simple method for controlled immobilization of proteins on modified SAMs. *Phys. Chem. Chem. Phys.* **13**, pp 5271-5278.
181. Lee, J.K., Kim, Y.-G., Chi, Y.S., Yun, W.S. & Choi, I.S. (2004). Grafting Nitrilotriacetic Groups onto Carboxylic Acid-Terminated Self-Assembled Monolayers on Gold Surfaces for Immobilization of Histidine-Tagged Proteins. *J. Phys. Chem. B.* **108**, pp 7665-7673.
182. Maury, P., Escalante, M., Péter, M., Reinhoudt, D.N., Subramaniam, V. & Huskens, J. (2007). Creating nanopatterns of his-tagged proteins on surfaces by nanoimprint lithography using specific NiNTA-histidine interactions. *Small*. **3**, pp 1584-1592.
183. Sigal, G.B., Bamdad, C., Barberis, A., Strominger, J. & Whitesides, G.M. (1996). A self-assembled monolayer for the binding and study of histidine-tagged proteins by surface plasmon resonance. *Anal. Chem.* **68**, pp 490-497.
184. Conti, M., Falini, G. & Samori, B. (2000). How strong is the coordination bond between a histidine tag and Ni - nitrilotriacetate? An experiment of mechanochemistry on single molecules. *Angew. Chem. Int. Ed.* **112**, pp 221-224.

185. Kienberger, F., Kada, G., Gruber, H.J., Pastushenko, V.P., Riener, C., Trieb, M., Knaus, H.-G., Schindler, H. & Hinterdorfer, P. (2000). Recognition force spectroscopy studies of the NTA-His6 bond. *Single Mol.* **1**, pp 59-65.
186. Verbelen, C., Gruber, H.J. & Dufrêne, Y.F. (2007). The NTA-His₆ bond is strong enough for AFM single-molecular recognition studies. *J. Mol. Recognit.* **20**, pp 490-494.
187. Valiokas, R., Klenkar, G., Tinazli, A., Tampé, R., Liedberg, B. & Piehler, J. (2006). Differential protein assembly on micropatterned surfaces with tailored molecular and surface multivalency. *ChemBioChem.* **7**, pp 1325-1329.
188. Huang, Z.H., Hwang, P., Watson, D.S., Cao, L.M. & Szoka, F.C. (2009). Tris-nitrilotriacetic acids of subnanomolar affinity toward hexahistidine tagged molecules. *Bioconjugate Chem.* **20**, pp 1667-1672.
189. Lata, S., Reichel, A., Brock, R., Tampe, R. & Piehler, J. (2005). High-affinity adaptors for switchable recognition of histidine-tagged proteins. *J. Am. Chem. Soc.* **127**, pp 10205-10215.
190. Blawas, A.S. & Reichert, W.M. (1998). Protein patterning. *Biomaterials.* **19**, pp 595-609.
191. Prime, K.L. & Whitesides, G.M. (1993). Adsorption of proteins onto surfaces containing end-attached oligo(ethylene oxide): A model system using self-assembled monolayers. *J. Am. Chem. Soc.* **115**, pp 10714-10721.
192. Sui, G., Wang, J., Lee, C.-C., Lu, W., Lee, S.P., Leyton, J.V., Wu, A.M. & Tseng, H.-R. (2006). Solution-phase surface modification in intact poly(dimethylsiloxane) microfluidic channels. *Anal. Chem.* **78**, pp 5543-5551.
193. Yin, H.B., Brown, T., Greef, R., Wilkinson, J.S. & Melvin, T. (2004). Chemical modification and micropatterning of Si (100) with oligonucleotides. *Microelectron. Eng.* **73-74**, pp 830-836.
194. Bizzarri, A.R., Bonanni, B., Costantini, G. & Cannistraro, S. (2003). A combined atomic force microscopy and molecular dynamics simulation study on a plastocyanin mutant chemisorbed on a gold surface. *ChemPhysChem.* **4**, pp 1189-1195.
195. Kanno, S., Yanagida, Y., Haruyama, T., Kobatake, E. & Aizawa, M. (2000). Assembling of engineered IgG-binding protein on gold surface for highly oriented antibody immobilization. *J. Biotechnol.* **76**, pp 207-214.
196. Lee, J.M., Park, H.K., Jung, Y., Kim, J.K., Jung, S.O. & Chung, B.H. (2007). Direct immobilization of protein G variants with various numbers of cysteine residues on a gold surface. *Anal. Chem.* **79**, pp 2680-2687.
197. Prisco, U., Leung, C., Xirouchaki, C., Jones, C.H., Heath, J.K. & palmer, R.E. (2005). Residue-specific immobilization of protein molecules by size-selected clusters. *J. R. Soc. Interface.* **2**, pp 169-175.
198. Wang, J., Luck, L.A. & Suni, I.I. (2007). Immobilization of the glucose-galactose receptor protein onto a Au electrode through a genetically engineered cysteine residue. *Electrochem. Solid St.* **10**, pp J33-J36.
199. de Boer, E., Rodriguez, P., Bonte, E., Krijgsveld, J., Katsantoni, E., Heck, A., Grosveld, F. & Strouboulis, J. (2003). Efficient biotinylation and single-step purification of tagged transcription factors in mammalian cells and transgenic mice. *Proc. Natl. Acad. Sci.* **100**, pp 7480-7485.

200. Korndörfer, I.P. & Skerra, A. (2002). Improved affinity of engineered streptavidin for the Strep-tag II peptide is due to a fixed open conformation of the lid-like loop at the binding site. *Protein Sci.* **11**, pp 883-893.
201. Schmidt, T.G.M. & Skerra, A. (2007). The strep-tag system for one-step purification and high-affinity detection or capturing of proteins. *Nat. Protocols.* **2**, pp 1528-1535.
202. Duevel, R.V. & Corn, R.M. (1992). Amide and ester surface attachment reactions for alkanethiol monolayers at gold surfaces as studied by polarization modulation Fourier transform infrared spectroscopy. *Anal. Chem.* **64**, pp 337-342.
203. Lahiri, J., Isaacs, L., Tien, J. & Whitesides, G.M. (1999). A strategy for the generation of surfaces presenting ligands for studies of binding based on an active ester as a common reactive intermediate: A surface plasmon resonance study. *Anal. Chem.* **71**, pp 777-790.
204. Lahiri, J., Ostuni, E. & Whitesides, G.M. (1999). Patterning ligands on reactive SAMs by microcontact printing. *Langmuir.* **15**, pp 2055-2060.
205. (2012). *Carbodiimide Crosslinker Chemistry*.
<http://www.piercenet.com/browse.cfm?fldID=F3305493-0FBC-93DA-2720-4412D198A9C9> 22/07/2012.
206. Love, J.C., Estroff, L.A., Kriebel, J.K., Nuzzo, R.G. & Whitesides, G.M. (2005). Self-assembled monolayers of thiolates on metals as a form of nanotechnology. *Chem. Rev.* **105**, pp 1103-1170.
207. Pimpin, A. & Srituravanich, W. (2012). Review on micro- and nanolithography techniques and their applications. *Eng. J.* **16**, pp 37-56.
208. Xia, Y. & Whitesides, G.M. (1998). Soft lithography. *Angew. Chem. Int. Ed.* **37**, pp 550-575.
209. Grigorescu, A.E. & Hagen, C.W. (2009). Resists for sub-20-nm electron beam lithography with a focus on HSQ: state of the art. *Nanotechnol.* **20**, pp 292001-292032.
210. Tseng, A.A. (2004). Recent developments in micromilling using focused ion beam technology. *J. Micromech. Microeng.* **14**, pp R15-R34.
211. Jung, Y.J., La, Y.-H., Kim, H.J., Kang, T.-H., Ihm, K., Kim, K.-J., Kim, B. & Park, J.W. (2003). Pattern formation through selective chemical transformation of imine group of self-assembled monolayer by low-energy electron beam. *Langmuir.* **19**, pp 4512-4518.
212. Mendes, P.M., Jacke, S., Critchley, K., Plaza, J., Chen, Y., Nikitin, K., Palmer, R.E., Preece, J.A., Evans, S.D. & Fitzmaurice, D. (2004). Gold nanoparticle patterning of silicon wafers using chemical e-beam lithography. *Langmuir.* **20**, pp 3766-3768.
213. Eck, W., Stadler, V., Geyer, W., Zharnikov, M., Götzhäuser, A. & Grunze, M. (2000). Generation of surface amino groups on aromatic self-assembled monolayers by low energy electron beams - A first step towards chemical lithography. *Adv. Mater.* **12**, pp 805-808.
214. Götzhäuser, A., Eck, W., Geyer, W., Stadler, V., Weimann, T., Hinze, P. & Grunze, M. (2001). Chemical nanolithography with electron beams. *Adv. Mater.* **13**, pp 803-806.
215. Bochet, C.G. (2002). Photolabile protecting groups and linkers. *J. Chem. Soc., Perkin Trans.* **1**, pp 125-142.

216. Campo, A.d., Boos, D., Spiess, H.W. & Jonas, U. (2005). Surface modification with orthogonal photosensitive silanes for sequential chemical lithography and site-selective particle deposition. *Angew. Chem. Int. Ed.* **44**, pp 4707-4712.
217. Critchley, K., Zhang, L., Fukushima, H., Ishida, M., Shimoda, T., Bushby, R.J. & Evans, S.D. (2006). Soft-UV photolithography using self-assembled monolayers. *J. Phys. Chem. B.* **110**, pp 17167-17174.
218. McGall, G.H., Barone, A.D., Diggelmann, M., Fodor, S.P.A., Gentalen, E. & Ngo, N. (1997). The efficiency of light-directed synthesis of DNA arrays on glass substrates. *J. Am. Chem. Soc.* **119**, pp 5081-5090.
219. Pillai, R.V.N. (1980). Photoremovable protecting groups in organic synthesis. *Synthesis.* **1980**, pp 1-26.
220. Ryan, D., Parviz, B.A., Linder, V., Semetey, V., Sia, S.K., Su, J., Mrksich, M. & Whitesides, G.M. (2004). Patterning multiple aligned self-assembled monolayers using light. *Langmuir.* **20**, pp 9080-9088.
221. Zhao, X.M., Xia, Y.N. & Whitesides, G.M. (1997). Soft lithographic methods for nanofabrication. *J. Mater. Chem.* **7**, pp 1069-1074.
222. Critchley, K., Jeyadevan, J.P., Fukushima, H., Ishida, M., Shimoda, T., Bushby, R.J. & Evans, S.D. (2005). A mild photoactivated hydrophilic/hydrophobic switch. *Langmuir.* **21**, pp 4554-4561.
223. Hong, S., Zhu, J. & Mirkin, C.A. (1999). Multiple ink nanolithography: Toward a multiple-pen nano-plotter. *Science.* **286**, pp 523-525.
224. Piner, R.D., Zhu, J., Xu, F., Hong, S. & Mirkin, C.A. (1999). "Dip-Pen" nanolithography. *Science.* **283**, pp 661-663.
225. Huo, F., Zheng, Z., Zheng, G., Giam, L.R., Zhang, H. & Mirkin, C.A. (2008). Polymer pen lithography. *Science.* **321**, pp 1658-1660.
226. Leggett, G.J. (2012). Light-directed nanosynthesis: near-field optical approaches to integration of the top-down and bottom-up fabrication paradigms. *Nanoscale.* **4**, pp 1840-1855.
227. Betzig, E. & Trautman, J.K. (1992). Near-field optics: Microscopy, spectroscopy, and surface modification beyond the diffraction limit. *Science.* **257**, pp 189-195.
228. ul Haq, E., Liu, Z., Zhang, Y., Ahmad, S.A.A., Wong, L.-S., Armes, S.P., Hobbs, J.K., Leggett, G.J., Micklefield, J., Roberts, C.J. & Weaver, J.M.R. (2010). Parallel scanning near-field photolithography: The Snomipede. *Nano Lett.* **10**, pp 4375-4380.
229. de la Fuente, J.M., Andar, A., Gadegaard, N., Berry, C.C., Kingshott, P. & Riehle, M.O. (2006). Fluorescent aromatic platforms for cell patterning. *Langmuir.* **22**, pp 5528-5532.
230. Kumar, A. & Whitesides, G.M. (1993). Features of gold having micrometer to centimeter dimensions can be formed through a combination of stamping with an elastomeric stamp and an alkanethiol 'ink' followed by chemical etching. *Appl. Phys. Lett.* **63**, pp 2002-2004.

Chapter 2

Methods

In this chapter the methods used to fabricate and characterise the samples for this project are described in detail. All water used in the methods was ultrapure MilliQ (18.2 M Ω cm).

2.1 Protein Synthesis and Purification

The expression and purification of recombinant Mms6 was optimised to obtain untagged Mms6 (Mms6), and *N*-terminal hexahistidine tagged Mms6 (His₆-Mms6). Protocols for the optimisation of the expression and purification of these proteins are courtesy of personal communications from A. Rawlings, S. Baldwin and J. Ingram, University of Leeds. All culture media were autoclaved prior to use.

2.1.1 His₈-MBP-Mms6 Production by Auto Induction

Mms6 was prepared by auto induction, which uses two different carbon sources, the first allows the bacteria to grow to a high cell density before the second induces protein expression.¹ To over-express Mms6, the carbenicillin resistant plasmid, referred to as pBPTNHOMT-*mms6*, was used (see vector map in Figure 2.1). This plasmid encodes for an octahistidine (His₈) metal ion affinity tag^{2,3} and a solubility enhancing maltose binding protein⁴ at the *N*-terminus of the Mms6 fusion protein. There is an encoded tobacco etch virus protease cleavage site between the tags and the Mms6 sequence, which should allow the Mms6 to be cleaved from the tags using TEV. This plasmid also contains a *lac* promoter, which switches on transcription to produce His₈-MBP-Mms6 when the *E. coli* ingests lactose. The plasmid was introduced into chemically competent *E. coli* BL21 (DE3) star cells via a transformation protocol. This cell strain harbours the chloramphenicol resistant plasmid pRare, which compensates for rare codon usage. Heat-shock (heating and cooling between 4°C and 42°C) allows the pBPTNHOMT-*mms6* plasmid to enter the cells. Only those cells resistant to both carbenicillin and chloramphenicol antibiotics after the transformation will be able to over-express His₈-MBP-Mms6 at high levels.

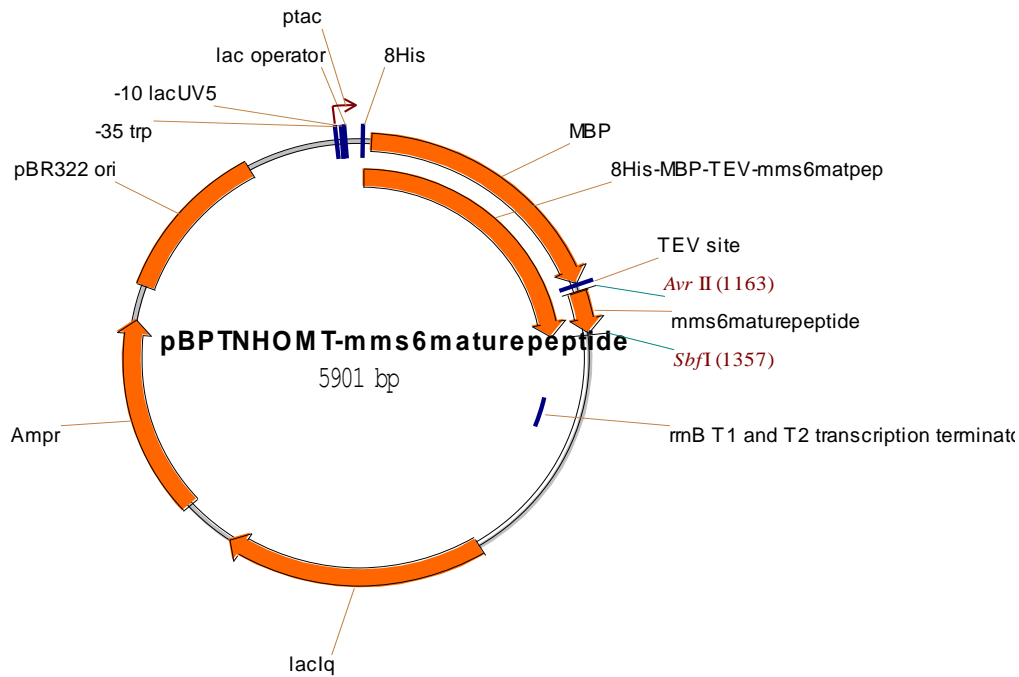


Figure 2.1. Vector diagram of pBPTNHOMT-*mms6* plasmid, arrows indicate read direction.* When lactose is not present, the *lac* repressor protein is bound to the *lac* operator, switching off protein expression. His₈-MBP-Mms6 is expressed when the *lac* repressor protein (encoded on *lacIq*) detaches from the *lac* operator at sites -10lacUV5 and -35 trp to bind to lactose. This allows expression of the His₈-MBP-*mms6* RNA sequence, as a protein that promotes expression can now bind to the promoter. Expression is terminated at the transcription terminator, and the RNA transcribed to produce the recombinant protein. The plasmid contains restriction sites (*italics*) for cloning the mature *mms6* sequence into the vector, and the TEV cleavage site is encoded between the tags and the mature Mms6 sequence. The plasmid also contains a section for replicating the entire plasmid (pBR322 ori) and carbenicillin/ampicillin antibiotic resistance (Ampr).

The transformed cells were plated onto Luria Bertani (LB)-Agar (for 100 mL: 1 g tryptone; 0.5 g yeast extract; 1 g NaCl; 1.5 g agar; prepared in water; pH 7.4) containing antibiotics (34 µg mL⁻¹ chloramphenicol and 100 µg mL⁻¹ carbenicillin), and incubated overnight at 37°C to generate colonies. 4 mL of LB (for 100 mL: 1 g tryptone; 0.5 g yeast extract; 1 g NaCl; prepared in water; pH 7.4) containing antibiotics as before was inoculated with a colony from the LB-Agar and incubated for 8 hours at 37°C and 200 rpm. This was transferred to the auto induction medium¹ (400 mL 2xZY (in 400 mL: 4 g yeast; 8 g tryptone); 20 mL 20xNPSC (in 1 L: 71 g Na₂HPO₄; 68 g KH₂PO₄; 14.2 g Na₂SO₄; 53.3 g NH₄Cl); 8 mL 50x5052 (in 100 mL: 25 g glycerol; 2.5 g glucose; 10 g α-lactose); 400 µL 1 M MgSO₄; antibiotic) before incubation at 37°C and shaking at 200 rpm for 36 hours. The bacteria preferentially use the glycerol and glucose in the 5052 component as a carbon source first, and so grow without induction. The concentration of the primary carbon source allows the bacteria to reach a consistently high cell density before it is all consumed and the α-lactose induces target protein over-expression.¹

* Vector diagram courtesy of A. Rawlings, University of Leeds.

The cells were separated from the supernatant by centrifugation using a Beckman Avanti centrifuge and a JLA 8.1000 rotor for 15 minutes at 4°C and 3500 rpm. The resulting cell pellet was stored at -80°C. Thawed cells were resuspended to form a 20% w/v suspension with TBS (25 mM tris; 100 mM NaCl; pH 7.4). An Ultra Turrex cell homogeniser was used to thoroughly resuspend the pellet prior to cell disruption at 30 kPsi using a Constant Systems cell disruptor. Centrifugation using a Beckman Avanti centrifuge and J-20XP JA 25.50 rotor for 20 minutes at 4°C and 12,000 rpm was used to separate the soluble cell lysate from the insoluble cell debris. The soluble fraction should contain any soluble His₆-MBP-Mms6 that was over-expressed by the bacteria.

2.1.2 His₆-Mms6 Production by IPTG Induction

His₆-Mms6 was over-expressed by isopropyl- β -D-thiogalactopyranoside (IPTG) induction, which is added to the bacterial culture to induce protein expression once a high cell density is reached.^{5,6} The kanamycin resistant pET28b-*mms6* plasmid encodes for a hexahistidine (His₆) tag at the *N*-terminus of the *mms6* sequence. The plasmid also encodes for a thrombin cleavage site between the His₆ tag and the *mms6* sequence, and a *lac* promoter to ensure protein transcription occurs when IPTG is added to the culture. Heat-shock is used to transform the pET28b-*mms6* plasmid into *E. coli* BL21 (DE3) star, which contains the chloramphenicol resistant plasmid pRare. The addition of IPTG to cells harbouring pET28b-*mms6* induces over-expression of *N*-terminal hexahistidine tagged Mms6.

The pET28b-*mms6* plasmid (see vector diagram in Figure 2.2) was transformed into the BL21 (DE3) star cells by heat-shock, as above. Post transformation, only those cells resistant to both kanamycin and chloramphenicol harbour both plasmids, so are the only ones that should be able to produce His₆-Mms6 at high levels. The cells harbouring the plasmid were cultured overnight at 37°C on antibiotic LB-Agar (30 $\mu\text{g mL}^{-1}$ chloramphenicol and 50 $\mu\text{g mL}^{-1}$ kanamycin). A colony was picked and used to inoculate 3 mL antibiotic LB and incubated for 8 hours at 37°C and 200 rpm. 1 mL of this starter culture was transferred to 100 mL antibiotic containing LB and incubated overnight at 37°C and 200 rpm. 50 mL of the overnight culture was then transferred to 450 mL LB and incubated for 2-3 hours at 37°C and 100 rpm, until the optical density at $\lambda = 600 \text{ nm}$ is ≈ 0.6 .

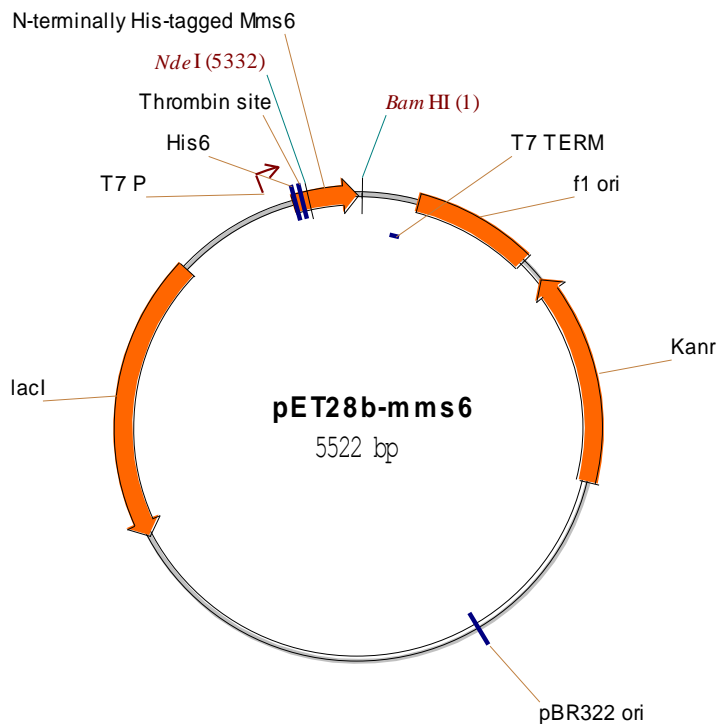


Figure 2.2. Vector diagram for pET28b-*mms6* plasmid, arrows indicate read direction.* When IPTG is not present, the *lac* repressor protein is bound to the *lac* operator (T7P), switching off protein expression. His₆-Mms6 is expressed when the *lac* repressor protein (encoded on *lacI*) detaches from TP7 to bind to IPTG. This allows expression of the His₆-*mms6* RNA sequence, as a protein that promotes expression can now bind to the promoter. The f1 ori site also allows this plasmid to produce single stranded RNA if required. Expression is terminated at the transcription terminator (T7 TERM), and the RNA is transcribed to produce the recombinant protein. There are restriction sites (italics) for cloning the mature *mms6* sequence into the vector, and the thrombin cleavage site is encoded between the tag and the mature Mms6 sequence. There is also a section for replicating the entire plasmid (pBR322 ori) and antibiotic resistance (Kanr).

Over-expression of the *mms6* gene was induced by addition of 250 μL of 1 M IPTG, and the culture incubated for another 3 hours (37°C and 100 rpm). The cells were pelleted as described above (Section 2.1.1) and disrupted by sonication. The thawed cells were resuspended in sonication buffer (50 mM tris; 150 mM NaCl; 1 mM EDTA; pH 8.0) and 100 μL 12 mg mL⁻¹ 4-(2-aminoethyl) benzenesulfonyl fluoride hydrochloride (AEBSF) and 250 μL of 40 mg mL⁻¹ lysozyme in TE buffer (10 mM tris; 1 mM EDTA; pH 8.0) were added before mixing at room temperature for \approx 20 minutes. This was immersed in an ice bath and sonicated in short bursts to disrupt the cells. The lysate was incubated with \approx 2% Triton-X-100 at 4°C for 30 minutes before centrifugation as described for auto induction (Section 2.1.1). This separates the insoluble cell debris from the soluble protein fraction, which contains the soluble His₆-Mms6 fusion protein. To further clarify the soluble fraction if it remained cloudy, the solution was passed through a sterile 0.45 μm filter.

* Vector diagram courtesy of A. Rawlings, University of Leeds.

2.1.3 Immobilised Metal-ion Affinity Chromatography (IMAC)^{3,7}

Resin slurry containing nitrilo-triacetic acid immobilised nickel or cobalt was used to separate the *N*-terminally histidine affinity tagged Mms6 from the soluble cell lysate by IMAC.^{3,7,8} Histidine has an affinity for transition metal ions, each of which can chelate two histidines.^{9,10} Ni²⁺-NTA has a stronger affinity for histidine than Co²⁺-NTA. Therefore, Ni²⁺-NTA resin usually has a higher overall protein yield, but this may contain more impurities than if Co²⁺-NTA is used.¹¹ Approximately 1.5 mL HisPur slurry (Thermo) was washed in water and washing TBS (50 mM tris; 150 mM NaCl; 10 mM imidazole; pH 8.0) before incubating with the soluble cell lysate for ≈2 hours at 4°C. The resin was transferred to a gravity flow column and rinsed to remove loosely bound proteins with 20 mL washing TBS. The immobilised Mms6 fusion was eluted using 10 mL elution TBS (50 mM tris; 150 mM NaCl; 250 mM imidazole; pH 8.0). Imidazole was removed by overnight dialysis at 4°C against 3 L TBS for His₈-MBP-Mms6 before tag cleavage can be carried out. His₆-Mms6 was dialysed against 3 L water then concentrated using a 2 kDa molecular weight cut-off centrifugal concentrator.

2.1.4 Affinity Tag Cleavage Using the Tobacco Etch Virus (TEV) Protease¹²

The affinity and solubility enhancing *N*-terminal tags on the His₈-MBP-Mms6 fusion are removed by cleavage using an octahistidine tagged tobacco etch virus (His₈-TEV). The His₈-TEV was produced from the Addgene plasmid 822, using the auto induction method (Section 2.1.1). The concentration of the tagged Mms6 fusion was estimated by measuring the absorbance at $\lambda=280$ nm, and His₈-TEV added in a 5:1 molar ratio of Mms6 fusion to His₈-TEV. Then 1 mM dithiothreitol (DTT) was added, before incubating the cleavage mixture at 4°C for 48 hours, with a further 1 mM DTT added after 24 hours incubation.

The resin and column used in the initial purification of the Mms6 fusion protein (Section 2.1.3.1) was washed using 20 mL washing TBS to remove excess imidazole. The cleaved tags, uncleaved fusion protein and His₈-TEV were separated from the cleaved Mms6 by passage through the cleaned resin two times. The absence of a polyhistidine tag on the cleaved Mms6 protein means it flows through the column and is present in the unbound fraction. The Mms6 was then dialysed against 3 L of water and concentrated using a 2 kDa molecular weight cut-off centrifugal concentrator.

2.1.5 Sodium Dodecyl Sulfate-Polyacrylamide Gel Electrophoresis (SDS-PAGE) with Tricine¹³

During sodium dodecyl sulfate-polyacrylamide gel electrophoresis (SDS-PAGE), proteins are separated on a polymer gel. Proteins bind negatively charged SDS as a function of protein mass, so larger proteins bind more SDS and *vice versa*.¹⁴ The SDS ensures a constant charge to mass ratio, as well as denaturing the protein in the presence of reducing agents and heat. The treated samples are transferred to the wells at the top of the vertical gel, and a potential difference applied to cause migration of the charged proteins through the gel matrix. Smaller proteins are able to move more rapidly through the gel matrix towards the cathode, and larger proteins are impeded. This acts to separate proteins by mass when a potential difference is applied. Due to the small size of Mms6 (≈ 6.4 kDa)¹⁵, proteins were analysed on low molecular weight tricine gels,¹³ and compared to low molecular weight protein markers of known mass (Spectra LMW markers, Fermentas).

The following method was used to prepare 2 x 1.0 mm minigels (see Figure 2.3). First the resolving gel was mixed [2.5 mL gel buffer (3 M tris; 0.3% SDS; pH 8.5); 3.0 mL ethylene glycol; 4.5 mL resolving acrylamide (40%; 19:1 acrylamide:bis-acrylamide)]. To polymerise the gel, 40 μ L of 10% ammonium persulfate (APS) and 10 μ L tetramethylethylenediamine (TEMED) was gently mixed in just before casting, and then it is covered with water until set. The water was removed, and the stacking gel was prepared [1.2 mL gel buffer; 0.65 mL stacking acrylamide (40%; 29:1 acrylamide:bis-acrylamide); 3.2 mL water]. This was gently mixed with 20 μ L APS and 20 μ L TEMED just before casting, the gel was poured and the combs inserted. Once set, the gels can be wrapped in damp paper and sealed (e.g. with Clingfilm) for storage at 4°C until required.

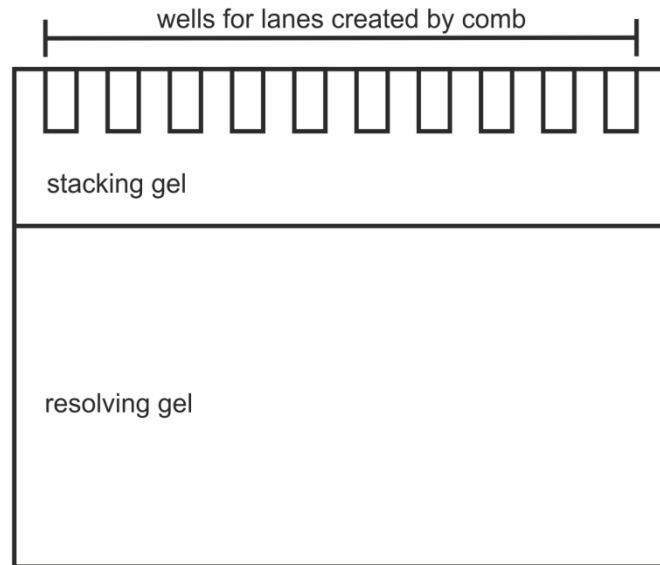


Figure 2.3. Schematic of tricine minigel for SDS-PAGE. First the resolving gel is mixed and poured, before allowing to set under a layer of water. The water is then removed, and the freshly mixed stacking gel poured and a comb inserted. The comb moulds the wells for 10 lanes. Once the comb is removed, up to 25 μ L of sample can be loaded into each lane using a pipette.

Each 5-10 μ g protein sample was mixed with 2x loading buffer (100 mM tris; 8% w/v SDS; 20% v/v glycerol; 20 mM DTT; pH 6.8) and between 10-25 μ L loaded onto each lane for analysis. The electrophoresis cell was assembled and cathode buffer (0.1 M tris; 1 M tricine; 3 mL 10% w/v SDS; pH 8.25) and anode buffer (0.2 M tris; pH 8.9) added. This was run at 200 V for \approx 1 hour, until the dye-front reached the bottom of the gel. Gels can then be stained or blotted (see below).

2.1.5.1 Coomassie Stain

Proteins in the polymer gels were stained with Coomassie Brilliant Blue R, thus showing the location of the protein bands.¹⁶ Gels are immersed in a fixing solution (25% v/v acetic acid; 10% v/v isopropanol) for 1-2 hours, then transferred to the Coomassie stain (for 2 L: 200 mL acetic acid; 500 mL isopropanol; 1300 mL water; 625 mg Coomassie Blue R) overnight. After a few changes of de-stain (for 2 L: 200 mL acetic acid; 100 mL isopropanol; 1700 mL water) the gel can be imaged or preserved.

2.1.5.2 Western Blot for Hexahistidine¹⁷

Whereas Coomassie staining indicates the presence of all proteins on the gel, Western blotting uses antibody recognition to selectively label a specific protein sequence (e.g. His₆). The antibody for hexahistidine is supplied pre-conjugated with horseradish peroxidase (HRP) (R & D Systems). The gel was soaked in transfer buffer (for 1 L: 25 mM tris; 192 mM glycine; 800 mL water; 200 mL methanol; pH should be between pH 8.0-8.8) with filter paper; nitrocellulose and Scotchbrite

foam. The gel was sandwiched (foam; 2x filter paper; gel; nitrocellulose; 2x filter paper; foam) before mounting in a gel tank with ice and transfer buffer. The proteins were transferred to the nitrocellulose by applying 100 V for 1 hour. The nitrocellulose was blocked overnight at 4°C using 20 mL TBST (for 1 L: 25 mM tris; 100 mM NaCl; 2 mL Tween-20) containing 3% w/v BSA. The BSA binds to areas of the nitrocellulose that are still able to bind protein, and blocks them from non-specifically binding to the antibody. The anti-hexahistidine HRP conjugate was added to the blocking solution (anti-6xpolyHis Mab HRP; used at 1:5000), and the nitrocellulose incubated for 1 hour at room temperature. Excess antibody conjugate was rinsed off using 3x TBST 10 minute washes, before incubating the nitrocellulose for 5 minutes in 4 mL Pierce SuperSignal West Pico Chemiluminescent dye. The HRP enzymatically breaks down the peroxide in the substrate solution, which activates a luminescent dye, luminol, thus showing the location of His₆ tagged proteins on the membrane. Excess dye was removed, and the labelled membrane viewed and/or imaged on a GeneGnome Imager (Syngene).

2.2 Protein Activity and Stability

2.2.1 Modelling Mms6 Structure

Mms6 has so far eluded structural characterisation and, as a result, the conformation of the protein at a molecular level is not well understood. As there are also no solved structures for homologues of Mms6, it is difficult to use conventional protein modelling software to define a structural model for Mms6. It may be that, due to the hydrophobic residues at the *N*-terminus, and its small size, Mms6 may not be able to form ordered crystals that are able to diffract X-rays sufficiently well to form a good diffraction pattern. Therefore, modelling of the structure based solely on the primary amino acid sequence was used to form a prediction of the structure of Mms6. Quark is a protein structural prediction algorithm which builds models from short amino acid sequences (between 1-20 amino acids long).¹⁸ This then uses Monte Carlo simulation to create a protein structure based on *ab initio* protein folding.¹⁸ The amino acid sequence for Mms6 was sent to the Quark server (<http://zhanglab.ccmb.med.umich.edu/QUARK/>),* and a model of the Mms6 structure produced. This model can then be viewed in programs such as PyMOL,¹⁹ which allows the structure of any protein to be displayed.

* Computational model requested by J. Bramble, University of Leeds.

2.2.2 Iron Binding by Mms6

Different concentrations of iron citrate were incubated with the Mms6 protein to investigate the amount of iron that the protein is able to bind, and also if any conformation changes occur upon binding iron.

2.2.2.1 Chemical Detection of Iron Bound by Mms6*

To detect iron that is bound to a protein, the protein must first be stripped of any metals that may be bound to it already. That way, only metal ions deliberately added to the solution can be bound by the protein and thus detected in the assay. The protein was dialysed overnight against 5 mM EDTA in TBS to remove any metals bound to the protein. Then, the protein was dialysed against TBS overnight to remove any EDTA, then further dialysed overnight against TBS treated with Chelex 100 (Sigma). Chelex 100 should remove any metal ions from the TBS buffer, and thus ensure that the protein is free of bound metals. The protein was diluted with Chelex treated TBS to 150 μ M concentration, and 75 μ L aliquots used for each experiment. This was made up to 100 μ L using up to 15 μ L of water and up to 10 μ L of an appropriately concentrated ferric citrate stock (stored in an amber Eppendorf tube to prevent photo degradation). The amount of iron added was varied between 0 mM and 3.3 mM (protein:iron ratio between 1:0 and 1:30) to study the effect of adding different concentrations of iron to the amount bound by the Mms6. Once the iron was added, the samples were wrapped in foil to exclude light, and incubated for two hours at room temperature.

Desalting columns (Thermo) were washed with Chelex treated TBS, and the incubated protein sample was spun through the column (1500 g, 1 minute) twice to remove any excess iron that was not bound to the protein. Any iron bound to the protein was then released by denaturing the protein by adding 5 μ L of 8 M urea to 2 μ L of the desalted, incubated protein. To detect the iron, 10 μ L of a luminol working reagent was added (aqueous luminol reagent contains 11 mM luminol, 500 mM NaCO₃ and 1% w/v H₂O₂)²⁰ and the luminescence recorded on a FLUOstar Optima (BMG Labtech) using a 384 well black fluorescence plate. Measurements were recorded across a range of wavelengths between λ =260 and 700 nm, and the total luminescence calculated by fitting under the peak emission. A standard luminescence curve for iron citrate incubated with luminol was also recorded.

* Iron binding data collection by S. Corbett, University of Leeds.

2.2.2.2 Tryptophan Fluorescence*

The amino acids tryptophan (W), tyrosine (Y) and phenylalanine (F) are all aromatic molecules that fluoresce. Tryptophan typically absorbs at a wavelength of $\lambda=280$ nm and emits at $\lambda=348$ nm, and has a higher quantum yield than the other fluorescent amino acids.^{21,22} The fluorescence of tryptophan is strongly dependent on the environment around the residue, and small changes in local conditions can cause the emission profile to change. For example, tryptophan fluorescence can be quenched by proximity to acidic residues, or shifted by up to 20 nm if buried in hydrophobic residues in a protein.^{21,22} Therefore the fluorescence of this residue can be used to monitor changes in the structure of a protein e.g. upon binding to a substrate. As the Mms6 protein contains one tryptophan, its fluorescence was used to see if there were changes in the intensity and/or emission peak position when iron citrate was added to the protein.

The purified protein was dialysed against buffer (200 mM NaCl, 25 mM tris, pH 7.4) then concentrated to ≈ 30 μM to ensure there was a good signal for the fluorescence experiments. For each sample, 25 μL of protein was transferred to a well in a 384 well black fluorescence plate, and up to 5 μL iron citrate (stored in an amber Eppendorf tube to prevent photo degradation) or a water blank added to make a total reaction volume of 30 μL . A range of concentrations of iron in ratios of protein:iron between 1:0 and 1:20 were investigated. After about 30 minutes incubation the absorbance and fluorescence intensity was measured at a wavelength of $\lambda=290$ and 340 nm on the FLUOstar Optima (BMG Labtech). As iron citrate can absorb at the excitation and emission wavelengths of tryptophan, these data were corrected for any absorbance using the following equation:²³

$$F_{obs} = F_{corr} * 10^{-((A_{ex} * d_{ex} / 2) - (A_{em} * d_{em} / 2))} \quad (2.1)$$

Here F_{obs} is the fluorescence measured and F_{corr} is the corrected fluorescence intensity. d is the cuvette pathlength and A is the change in absorbance caused by the addition of the ligand at the excitation (ex) and emission (em) wavelengths.

* Tryptophan fluorescence collected in collaboration with A. Rawlings, University of Leeds.

2.2.2.3 Circular Dichroism (CD)*

In circular dichroism (CD), plane polarised light is passed through an aqueous protein sample. Plane polarised light can be considered to consist of two circularly polarised components, one rotating anti-clockwise (left-handed polarisation) and one rotating clockwise (right-handed polarisation). If the protein is optically active (i.e. chiral), different proportions of these two components are absorbed by the sample. This creates elliptical polarisation of the transmitted light, which is recorded and used to produce a spectrum across a range of wavelengths (see Figure 2.4).²⁴ By recording the spectrum of a sample protein across a range of wavelengths, the spectra can be fitted to determine the proportion of different chiral protein secondary structure types that are present. CD spectra are typically recorded between wavelengths of $\lambda=190$ to 260 nm, but can be scanned up to ≈ 350 nm to monitor wavelengths affected by the excitation and emission of light due to tryptophan fluorescence.

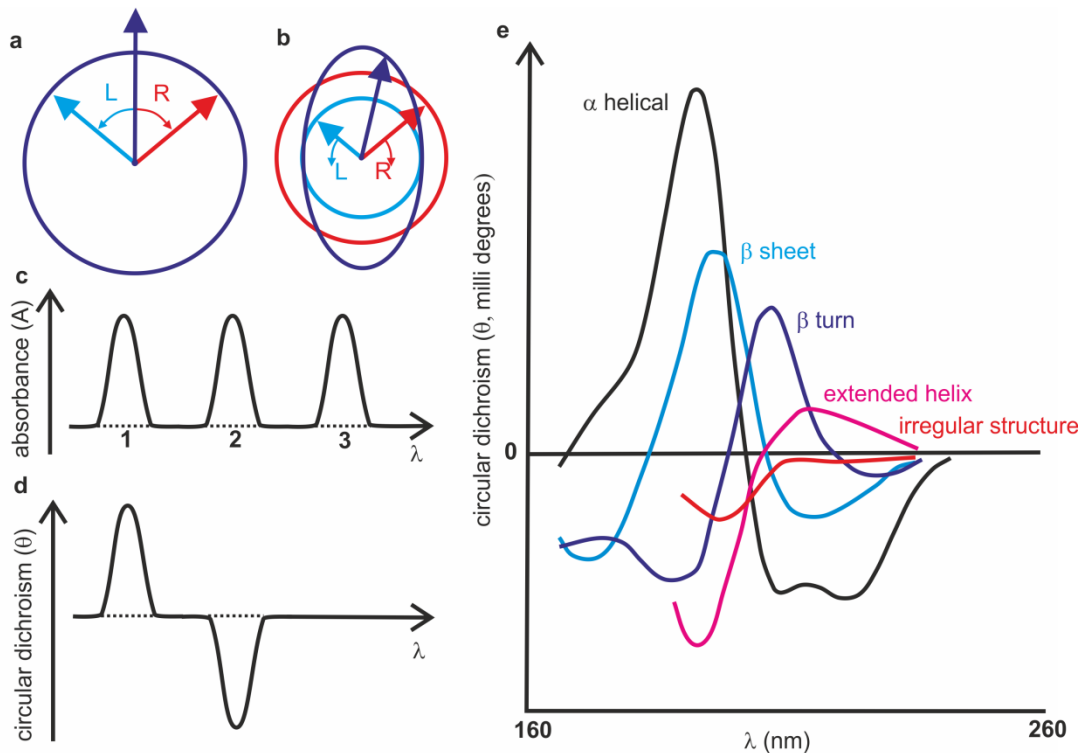


Figure 2.4. Circular dichroic effect and signal detected after transmission, after Kelly *et al.* (2005).²⁴ (a) Plane polarised light consists of left (L) and right (R) circularly polarised light of the same amplitude. (b) The left polarised light is of a lower magnitude than the right component, which combine to create elliptically polarised light. (c) The total absorption for three different samples are all the same. However, (d) shows that the signal is different for the three samples when the two polarisation directions are detected. Sample 1 shows a positive CD spectrum (more L absorbed than R), sample 2 a negative spectrum (more R absorbed than L) and sample 3 shows an achiral response, where both L & R are absorbed equally. (e) Typical CD spectra from different sorts of optically active protein structures.

* CD collected in collaboration with A. Rawlings, University of Leeds.

The purified protein was dialysed against CD buffer (250 mM NaCl, 25 mM tris, pH 7.4) at a concentration of 150 μ M to ensure there was a good signal for the CD experiments. The spectrometer (ChirascanTM, Applied Photophysics) was set up, and spectra collected, first with an empty sample chamber, then with the cleaned glass cuvette containing CD buffer to act as a blank. After cleaning the cuvette, the buffered protein was loaded into the sample chamber, and a spectrum recorded between the wavelengths λ =190 to 320 nm in 1 nm intervals and 1 second per point. The light from the 150 W Xe lamp was monochromated using the F/7 split-Wollaston prism before the protein sample, and detected using a high performance UV-Vis photomultiplier tube after the sample. The average of three CD spectra was taken for each sample. Iron was added in small volumes of 10 mM iron citrate (stored in an amber Eppendorf tube to prevent photo degradation) to the protein and the buffer blank to see if iron addition caused a change in the CD spectrum. The spectra were fitted using DichroWeb²⁵ to determine the secondary structure likely to be present in the protein sample.

2.2.3 Accessibility of the His-tag on Pre-formed MNPs

The accessibility of the His₆ affinity tag was tested after MNP formation, as the tag would need to be accessible to attach preformed MNPs to patterned surfaces. MNPs were formed by room temperature co-precipitation (see Section 1.5.1) with Mms6 (as a control) and with His₆-Mms6. Washed particles were resuspended in degassed water so that 1 mL of washed sample contained the particles from \approx 1 mL of iron/cobalt salts mixed in the reaction vessel before the addition of NaOH. For each sample, 100 μ L MNPs were resuspended in 1 mL TSBT containing 3% BSA and mixed for 1 hour to block any non-specific binding of antibody to the nanoparticles. Then an antibody specific to hexahistidine (anti-6xpolyHis Mab HRP; used at 1:5000) was added into the blocking solution, which should bind specifically to any accessible His₆ tags. After an hour, the unbound antibody was washed from the particles using 5 x 1 mL TBST washes, and any excess liquid was removed.

The antibody is conjugated to HRP, which catalyses the breakdown of hydrogen peroxide. Therefore, any His₆-Mms6 that is accessible is bound to an antibody, which, through the conjugated HRP, is able to catalyse the breakdown of H₂O₂. The TMB-Ultra reagent (Pierce Thermo) contains hydrogen peroxide, and a dye which turns blue upon the breakdown of H₂O₂. 50 μ L of TMB-Ultra was added to the protein templated MNPs and incubated for 30 minutes on a mixer. The particles were magnetically separated, and a 25 μ L aliquot of the incubated TMB reagent transferred to a well in a 384 well plate. The absorbance was recorded on a FLUOstar Optima (BMG Labtech) at λ =355 nm (the absorbance maxima of TMB are at a wavelength of λ =370 and 652 nm). As the HRP should only be conjugated

to accessible His₆-tags, a greater absorbance indicates more peroxide breakdown and therefore more accessible His₆-tags.

2.3 SAMs of Alkanethiols on Gold

2.3.1 Gold Substrate Preparation

Gold films of between 50 and 200 nm were prepared on clean silicon or glass microscope slides. The substrates were cleaned by sonicating for 10 minutes in 1% Decon 90, then rinsed thoroughly in water before drying under N₂. They were then sonicated with isopropanol for 10 minutes, dried with N₂ and immersed in dichloromethane (DCM) for 10 minutes, before drying with N₂. The slides were immersed in piranha solution in the fume hood (70% H₂SO₄; 30% H₂O₂) before thorough rinsing in water and drying with N₂. The slides are washed in this order of surfactants and solvents to ensure as many contaminants as possible are removed prior to metal deposition.

The cleaned substrates were mounted inside the evaporator (Edwards Auto 360 thermal evaporator) and 99.99% 0.75 mm diameter gold wire was coiled inside an evaporation boat. The chamber was sealed and pumped to pressure $< 2 \times 10^{-6}$ mbar before a chromium adhesion layer (3-5 nm) was evaporated onto the glass at 0.1 nm s⁻¹. The gold was then evaporated at the same deposition rate to achieve the desired film thickness. The chamber was cooled, vented, and the gold coated substrates removed and used as soon as possible.

2.3.2 Preparation of Uniform and Mixed SAMs

Gold coated substrates were cut to an appropriate size (≈ 1 cm²) and either ozone or piranha cleaned. For ozone cleaning, the substrates were rinsed in isopropanol, dried with N₂, and put into UV/ozone cleaner (UVOCS) for 20 minutes. The substrates were then immersed in ethanol for 40 minutes to reduce the gold surface back to metallic Au⁰, and dried with N₂. To piranha clean the gold substrates, they were sonicated with isopropanol for 10 minutes, dried with N₂, immersed in piranha solution for 2 minutes, then thoroughly rinsed in water, dried with N₂, before rinsing in ethanol and drying with N₂. The substrate final rinse was ethanol, as the self-assembled monolayers form from ethanolic solutions. Cleaned substrates were then used for the self-assembly of alkanethiols from solution, either with or without patterning (see Section 2.3.3 below). To prepare an unpatterned SAM, a clean gold substrate was immersed in a 1 mM ethanolic solution of the desired alkanethiol(s) overnight. The thiol at the head group attaches to the gold surface from the solution, and the alkane chains order into a monolayer over a few hours by balancing inter-chain interactions.²⁶ This presents the surface group of the

alkanethiol at the SAM/air interface, which functionalises the substrate accordingly (see Section 1.5). The SAMs were rinsed in ethanol, dried with N₂, then rinsed with water and dried with N₂.

2.3.3 Micro-Contact Printing (μ CP)²⁷

SAMs can be patterned by soft-lithography, using a patterned polymer stamp to transfer an alkanethiol to parts of the gold surface, before filling the unstamped areas with a differently ω -functionalised SAMs (Figure 2.5).²⁸ Poly(dimethyl)siloxane (PDMS) stamps were prepared by thoroughly mixing Sylguard 184 base with \approx 10% w/w curing agent, before degassing under vacuum to remove any bubbles. Silicon master(s) were rinsed in isopropanol, dried with N₂ and the PDMS poured on to a depth of a few millimetres. After degassing under vacuum, the PDMS was cured at 60°C overnight. Stamps were then cut out and soaked in ethanol overnight prior to use.

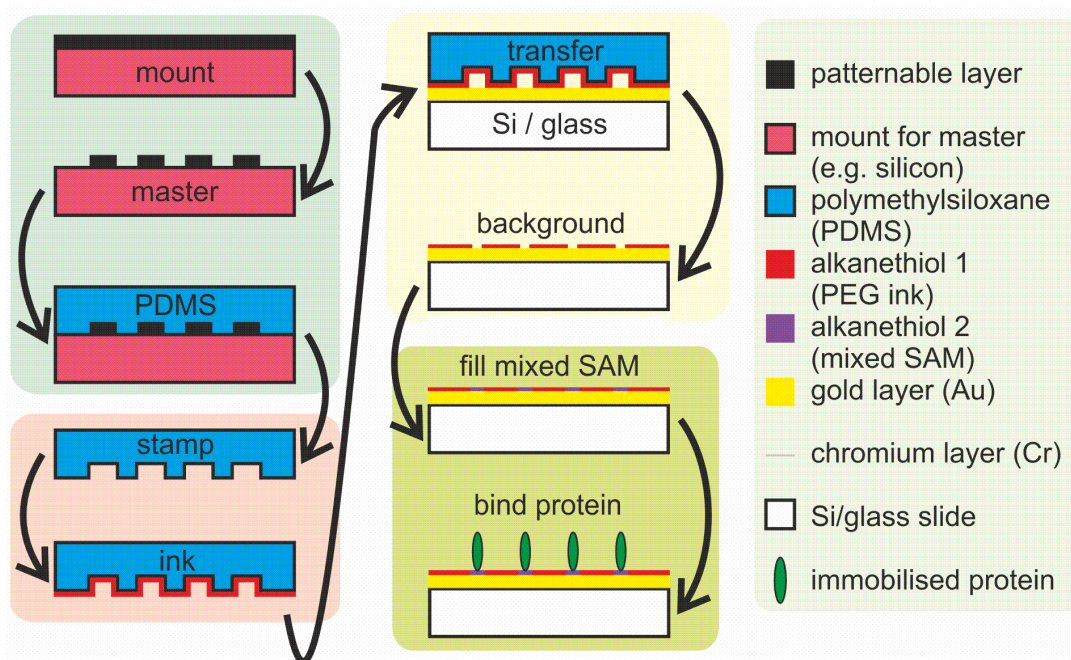


Figure 2.5. Diagram to show stages of micro-contact printing, based on Mrksich & Whitesides (1995).²⁸ A master is produced (e.g. by photolithography) and used to template the PDMS to form an elastomer stamp. The stamp is used to transfer the alkanethiol ink (PEG to resist protein binding) to the clean gold surface, with bare areas functionalised with a different SAM (mixed SAM to attach protein).

Dried stamps were inked with 5 mM alkanethiol (usually the biofouling resistant 11-mercaptoundecyl tetra(ethylene)glycol, formula: HS(CH₂)₁₁(OCH₂CH₂)₃OCHOH (PEG-OH, Sigma))²⁹ in ethanol for a few minutes. The excess liquid was removed before gentle drying with N₂. The stamp was carefully laid onto the cleaned gold substrate to form a conformal contact which transfers the alkanethiol to form the pattern over a few minutes. The stamp was then removed, and the patterned gold immersed in a different 1 mM alkanethiol ethanolic solution overnight to

appropriately functionalise the clean gold left bare by the stamp. This was usually a mixed SAM for attaching the desired protein via the *N*-terminus using EDC/NHS (see Section 2.4.1.2). The mixed SAM consisted of 1 mM total alkanethiol concentration, containing 90% PEG-OH and 10% 11-mercaptoundecyl hexa(ethylene)glycol acetic acid, with the formula $\text{HS}(\text{CH}_2)_{11}(\text{OCH}_2\text{CH}_2)_6\text{OCHCOOH}$ (PE-COOH, Sensopath Technologies). The ethanol used to make the PEG and PE-COOH SAM solutions also contained 1 drop HCl per 25 mL, which should prevent deprotonation of the COOH moiety, and form better monolayers. The PEG molecules space out the carboxylic acid attachment sites on the mixed SAM surface, which should avoid deformation of the protein upon attachment. The SAMs were rinsed in ethanol and dried with N_2 , then they were rinsed with water and dried with N_2 .

2.3.4 Characterisation of SAMs

The surface and bulk properties of SAMs can be characterised in numerous ways. The SAM should form a uniform (or uniformly patterned) thin film with homogenous surface properties and uniform thickness. Here, ellipsometry has been used to assess monolayer thickness, and water contact angle measurements have been used to determine surface wetting properties. X-ray photoemission spectroscopy (XPS) was used to assess elemental ratios of the SAMs. These were all compared to published data to determine the quality of the monolayers formed. The SAMs used for characterisation were all unpatterned. Patterning can introduce a great deal of inhomogeneity as different SAMs are used to create the pattern. Therefore, it has been assumed that μCP SAMs and backfills have similar properties to those of the unprinted ones tested here.

2.3.4.1 Ellipsometry

In ellipsometry, plane polarised light is analysed after reflection from a surface to determine thickness and vertical and lateral uniformity of an organic film on a given substrate (see Figure 2.6).²⁶ The ellipsometer (JY Horiba UVISEL) contains a mercury arc lamp source, providing light at wavelengths between 300-1200 nm. The sample was mounted on an X-Y stage, and the Z component manually adjusted to focus onto the sample and maximise the signal at the detector.

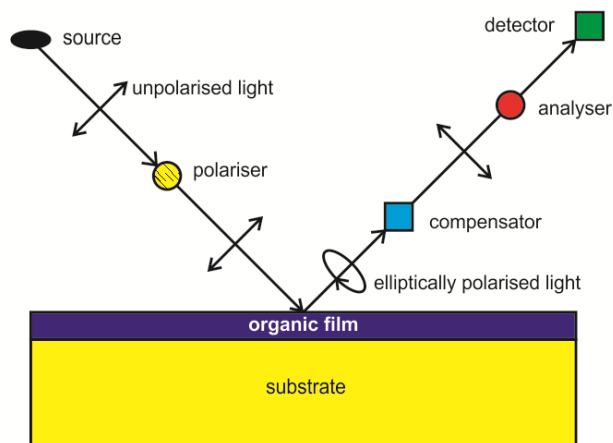


Figure 2.6. Schematic of an ellipsometer, from Ulman (1991).²⁶ First, the light is plane polarised, then reflected from the surface. Reflection of the beam causes the light to become elliptically polarised, which is analysed and detected by the apparatus.

The parallel (s) and perpendicular (p) components of the polarised source are reflected at different amplitudes and phases.²⁶ The total phase shift after reflection (Δ), and the ratio of the amplitudes of the two components ($\tan\psi$) is determined by the equation:²⁶

$$\frac{R_p}{R_s} = e^{i\Delta} \tan\psi \quad (2.2)$$

Where R_p and R_s are the Fresnel reflection coefficients. To estimate the thickness of a SAM on gold, measurements of Δ and ψ are taken for both a clean gold reference substrate and the SAM of interest. JY $\Delta\Psi 2$ software uses the difference between the two curves to model SAM thickness across the spectral range, and uses the Cauchy relation (Equation 2.3)³⁰ to model the dispersion of the monolayer:

$$n(\lambda) = n_f + \frac{A}{\lambda^2} + \frac{B}{\lambda^4} \quad (2.3)$$

Here the refractive index (n_f), co-efficients A and B , as well as the thickness of the SAM are fitted by the software. The refractive index is usually estimated as 1.45 for shorter alkyl chains ($C < 9$) 1.50 for longer alkyl chains ($C > 10$).³¹ As the molecules in SAMs usually tilt to tightly pack on the surface to form a monolayer, the thickness of an alkanethiol monolayer on gold is usually less than the individual molecule length.³² Measurements taken from at least three different areas were fitted for each sample to assess the lateral continuity of the monolayers.

2.3.4.2 Water Contact Angle

Surface wetting properties of a substrate were determined using a First-Ten-Angstrom 2000 goniometer and a suitable solvent. A droplet of water was applied to the sample surface to be analysed, and the angle of the contact between the surface, the water and the air (θ) recorded. The wetting of a monolayer by a liquid can be used to establish the lateral continuity of a SAM, as the shape of the droplet on the surface is related to the surface free energies (γ) between the air (V), liquid (L) and the substrate (S) via Young's equation:²⁶

$$\gamma_{SV} = \gamma_{SL} + \gamma_{LV} \cos \theta \quad (2.4)$$

Where θ is the angle of the contact between the surface and the liquid droplet in air (Figure 2.7).³² The contact angle was measured for advancing (θ_a), receding (θ_r) and static (θ_s) water droplets for each sample in at least 3 different locations. The contact angle is very high between water and a hydrophobic surface (e.g. a methyl terminated SAM $\theta_s \approx 111^\circ$), and very low on a hydrophilic surface (e.g. a very clean carboxylic acid terminated SAM $\theta_s < 10^\circ$).²⁶ If there is a difference between the static, advancing and receding contact angles, this creates an hysteresis which is due to surface roughness, and indicates the SAM is not homogeneous.

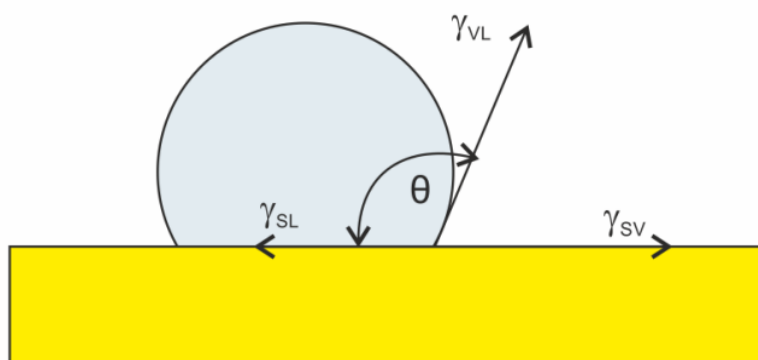


Figure 2.7. Schematic of a water contact angle on a hydrophobic surface, after Ulman (1996).³² For the definition of the symbols, see Equation 2.4.

2.3.4.3 X-ray Photoelectron Spectroscopy (XPS)

XPS detects low energy range electrons (20-1300 eV) photoemitted from an atom after excitation by soft X-rays (Figure 2.8).³³ The samples were earthed to avoid charging and thus ensure that a good signal could be obtained, before loading into the XPS (Thermo Electron Corporation ESCA lab 250 spectrometer). The atmosphere in the entrance chamber was pumped down for about 1 hour, before transferring the samples to the analysis chamber, which was maintained at an atmosphere of $\approx 1 \times 10^{-9}$ mbar. Monochromated Al K α (1.5 keV, 150 W) X-rays were focussed onto the sample at a spot diameter of ≈ 0.5 mm, and the signal at the detector maximised to ensure the surface was in focus. Survey scans were

recorded at a pass energy of 150 eV, and detailed scans obtained at 20 eV, with an electron take-off angle of 90°. Data were normalised to the Au 4f_{7/2} peak at 84.0 eV, then the detailed spectra fitted using the Advantage (Thermo VG software package) peak fitting algorithms.

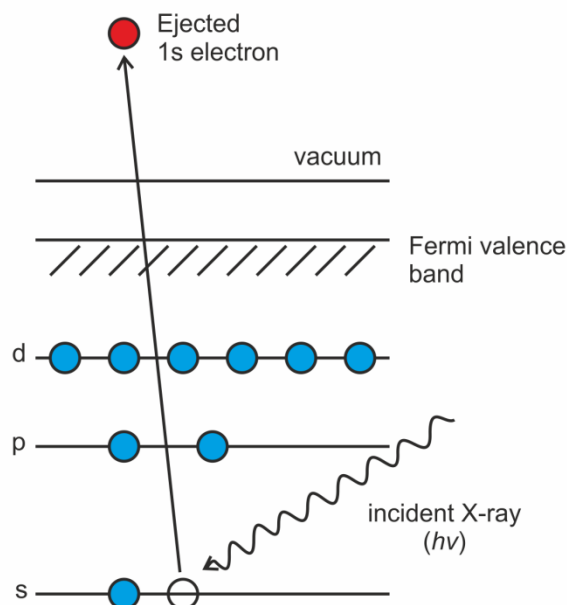


Figure 2.8. Schematic of photoelectron emission during XPS from Watts & Wolstenholme (2002).³³ Photoionisation of the atom is caused here by the ejection of a 1s electron.

The energy emitted as a photon ($h\nu$) has a kinetic energy (E_k) recorded in the spectrometer, and is related to the binding energy of the electron to the atom by the spectrometer work function (W) via the following equation:³³

$$E_B = h\nu - E_k - W \quad (2.5)$$

The spectrometer work function is automatically accounted for in output data, and determined by calibration with standards. The binding energy of an electron to an atom is an intrinsic material property. This binding energy undergoes a chemical shift due to the density of the electrons from nearby atoms.³³ When an electron is able to escape without energy loss, a characteristic peak is recorded in the XPS spectrum, with the background made up by inelastically scattered electrons.³³ By fitting the area under a peak (and dividing by the element sensitivity factor), the relative abundance of different elements, and what that element is bonded to, can be calculated for a detailed spectrum of a surface. These data should be regarded as qualitative for SAMs, as elements at the monolayer surface will shield those buried in the SAM.²⁶ Therefore, the signal from the sulfur in the head group of a monolayer will be lower than that of a sulfur at the surface/air interface of a SAM. After emission of the photoelectron, the ionised atom relaxes by either emitting an X-ray photon by X-ray fluorescence, or by emitting an Auger electron, which can also be detected.

2.4 Protein Attachment to Surfaces

2.4.1 Methods for Protein Attachment

There are many methods available for the attachment of proteins to surfaces (see Section 1.5.3). Previously, non-specific binding of Mms6 to a surface was shown to be able to template multi-layers of iron oxide magnetic nanoparticles.³⁴ As non-specific binding is likely to deform the Mms6 protein, this may have reduced its templating ability and prevented the protein from forming a single layer of MNPs. Therefore, to try and generate single layers of biotemplated MNPs, methods to attach Mms6 via the *N*-terminus were explored, as the *C*-terminal section should remain active. Sulfur in cysteine is able to bind proteins directly to gold surfaces. In nature, Mms6 does not contain any cysteines, so expression trials of *N*-terminally cysteine tagged Mms6 (Cys-Mms6) were explored. Unfortunately, it was not possible to purify the Cys-Mms6 protein, as it did not remain soluble, and precipitated from solution. *N*-terminally poly-histidine tagged Mms6 expressed and purified well. Therefore, a SAM functionalised with Ni²⁺-NTA should be able to specifically immobilise His₆-Mms6 in the desired orientation. Chemical linkage of the *N*-terminus of Mms6 directly to a patterned substrate was also explored.

2.4.1.1 Histidine to Ni²⁺-NTA Terminated SAM

NTA functionalised alkanethiols are expensive to buy commercially, therefore protocols to introduce the NTA functionalisation to cheaper, more commonly available SAMs were sought. Self-assembled monolayers were prepared as above, with the mixed SAM containing 90% PEG-OH/ 10% PE-COOH, for molecules see Figure 2.9. Carboxylic acids in the mixed SAM form activated esters when immersed in aqueous EDC (0.8 mg mL⁻¹) and NHS (0.1 mg mL⁻¹) for ≈15 minutes. The EDC/NHS solutions were mixed just prior to use, as the activity of these reagents decays exponentially over time. The activated esters are able to bind with amines in solution, and thus should immobilise a desired molecule. The amine in the lysine group of *N*_α,*N*_α-bis(carboxymethyl)-L-lysine, with the formula H₂N(CH₂)₄C(COOH)N(CH₂COOH)₂ (*L*-NTA) should attach to the activated ester surface to form an NTA functionalised SAM, if buffering is conducive to *L*-NTA immobilisation. Therefore, activated surfaces were then directly transferred from the EDC/NHS solution to a solution containing a between 0.5 and 5 mM of *L*-NTA hydrate (Sigma). This NTA functionalised surface was then rinsed with water and immersed in a Ni²⁺ salt solution to try and functionalise the surface for His_x-tagged protein immobilisation. Immobilisation of a protein by complexation of the Ni²⁺-NTA surface with a multi-histidine tagged protein (as used to purify such proteins using IMAC, see Section 2.1.3.1) should ensure the correct orientation of the desired

protein. Various protocols, buffers, concentrations, incubation times and pH conditions were used to try to create an Ni²⁺-NTA functionalised surface for protein immobilisation, as per references^{9,35-40} (see Section 3.3.1).

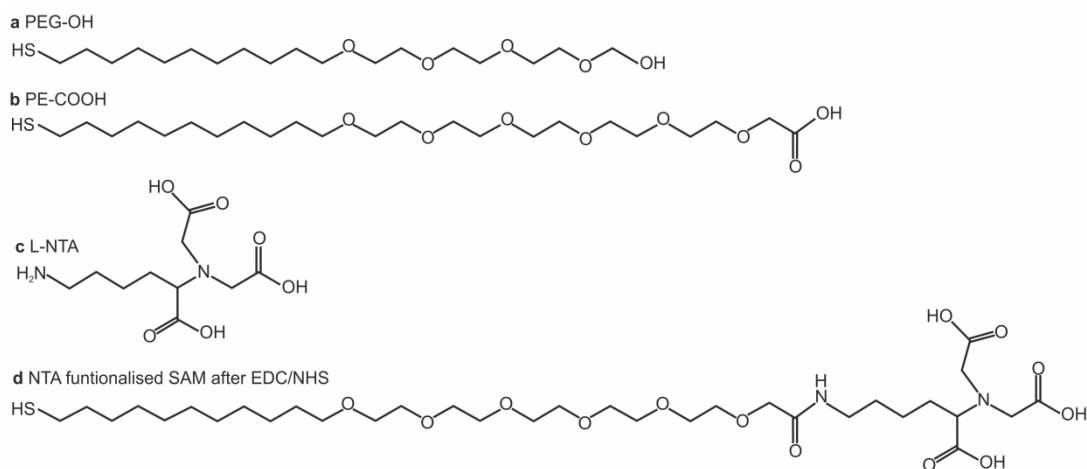


Figure 2.9. Structures of molecules used to form SAM and functionalise SAM with NTA for protein attachment. Molecules used to form mixed SAM are a) PEG-OH and b) PE-COOH. c) shows *L*-NTA before attachment to carboxylic acid in mixed SAM and d) shows PE-COOH after EDC/NHS reaction to bind *L*-NTA.

2.4.1.2 EDC/NHS onto Carboxyl Terminated SAM⁴¹

Self-assembled monolayers are prepared as above (Section 2.3.2 for unpatterned and 2.3.3 for patterned SAMs). The PEG SAM resists protein attachment, and the mixed SAM of 10% PE-COOH/90% PEG forms the protein immobilisation areas. The SAM was rinsed in ethanol to remove unbound thiol molecules, dried with N₂, then rinsed in water and dried with N₂. The SAM was then immersed in aqueous EDC/NHS (0.8 mg mL⁻¹/ 0.1 mg mL⁻¹, 15 minutes) to form activated esters, before transferring to a buffered protein solution for between 30 minutes and 2 hours. The protein should preferentially attach via the *N*-terminus (see Figure 1.21) if buffered to ≈1 pH point below its pI,⁴¹ with more concentrated protein attaching more rapidly. Just below the pI, a protein will have a slight net positive charge, and many of the lysine residues (the ε-amines) will be protonated, and therefore blocked from reacting with the activated ester surface.⁴¹ This ensures the primary amine (α-amine) at the *N*-terminus is the most likely to bind with the surface, thus immobilising the protein via the *N*-terminus. The pI of Mms6 is ≈4.7,⁵ so 20 mM sodium acetate at pH 4.0 was used to buffer 10 μg mL⁻¹ Mms6 in the protein attachment solution. After immobilisation, the protein patterned substrate was rinsed in water and transferred to the reaction vessel for magnetite mineralisation (see Section 2.5).

2.4.2 Monitoring Protein Attachment

2.4.2.1 Quartz Crystal Microbalance with Dissipation (QCM-D)⁴²

A quartz crystal microbalance (QCM) uses the piezoelectric properties of a quartz crystal, which is oscillated by applying an AC voltage. When a voltage is applied, the crystal changes in size at the same frequency as the applied voltage, which is used to oscillate the crystal at its resonant frequency (4.95 MHz). The frequency and dissipation of the crystal is altered by the addition or removal of material on the surface. QCM-D monitors both the frequency and the energy dissipation changes of the oscillating sensor. Quartz crystals coated with gold (Qsense AB, Gothenburg) were ozone cleaned and SAMs formed on the surface as in Section 2.3.2. These were loaded into the Q Sense E4 sensor (Qsense AB, Gothenburg), sealed in the chambers and locked in place. The frequency (f) and dissipation (d) of the 3rd to 13th overtones were checked in air and water. A zero baseline was set using water/buffer, as changes in buffer composition alter the density and viscosity of the fluid, and can cause frequency and dissipation shifts that are not due to the adhesion of a layer to the surface.

To carry out an experiment, the solutions required to form a protein layer (with washing steps as necessary) were degassed and flowed through at a suitable rate (i.e. 100 $\mu\text{L min}^{-1}$). The changes in frequency (Δf) and dissipation (Δd) of all overtones are recorded. The order and types of buffers and solutions used depends upon the process to be followed. For example, to monitor Mms6 attachment with EDC/NHS, the timings and solutions used in Section 2.4.2.1 should be followed. Air bubbles need to be excluded from the sensor chambers, so degassed solutions are used and the flow stopped when changing solutions. The final stage (i.e. after protein attachment) should always use the same water or buffer used to set the initial experimental baseline, which removes the influence of varying fluid viscosities on the frequency and dissipation recorded. Therefore, Δf and Δd shifts should only be due to the changes caused by the protein adhering to the crystal surface.

Layer thickness and the mass of protein attached to the surface can be modelled using the Qtools software (Qsense AB, Gothenburg). The resonant frequency (f) decreases proportionally with mass when a rigid thin film is attached to the sensor. If the layer is thin and rigid (i.e. $\Delta d \approx 0$), the mass adsorbed on the surface (Δm) can be calculated using the Sauerbrey Equation:⁴³

$$\Delta m = -\frac{\Delta f \rho_q v_q}{2n\sqrt{f_{fun}}} = -\frac{\Delta f \rho_q t_q}{n f_{fun}} \quad (2.6)$$

Where Δf is the change in frequency due to mass absorption in Hz, ρ_q is the density of quartz (2648 kg m^{-3}), v_q the speed of sound in quartz (3340 m s^{-1}) and t_q the thickness of the quartz crystal. n is the number of the overtone, and f_{fun} the fundamental resonant frequency of the quartz crystal (4.95 MHz). The model contained in the Qtools software also has a correction (based on the QCM-D crystal thickness, ≈ 0.081)⁴⁴ to convert the mass adsorbed onto the crystal into ng cm^{-2} . As the proteins modelled here are in a hydrated environment, their size, even when properly folded on the surface, is probably larger than would be predicted from the crystal structure.⁴⁵ Therefore the molecular mass of a protein should be multiplied by 1.25 to take into account the mass increase due to water, and the size should be rounded up to the nearest nanometer.⁴⁴ If a single layer of correctly folded protein has formed, this mass can be converted into moles of protein per square centimetre for an ideal protein layer using:

$$\text{moles cm}^{-2} = \frac{(1 \times 10^7 / l_{\text{hydrated}}) * (1 \times 10^7 / w_{\text{hydrated}})}{N_A} \quad (2.7)$$

Where l_{hydrated} is the estimated length and w_{hydrated} the width of the hydrated protein in nm, and N_A is Avogadro's number. This can then be compared to estimates of the coverage of the hydrated protein on the surface from the QCM-D Sauerbrey mass:

$$\text{pico moles cm}^{-2} = \frac{\Delta m}{M_{\text{hydrated}}} \quad (2.8)$$

Where Δm is the Sauerbrey mass, calculated using Equation 2.7, and M_{hydrated} is the estimated molecular mass of the hydrated protein in kDa (i.e. 1.25 times the predicted mass from ProtParam).

However, protein layers are not always rigid, so viscoelastic Voight model may need to be used to estimate layer thickness.⁴⁶ The model, in the Qtools software, uses the frequency and dissipation shifts from all the overtones (3rd to the 13th) recorded during protein layer formation (see Figure 2.10).⁴⁷ The Voight modelling allows unknown parameters (e.g. the thickness of the protein layer) to be estimated.⁴⁷ The protein layers were modelled based on the methods in Krzemiński *et al.* (2011).⁴⁵ The fluid density and viscosity were fixed at 1000 kg m^{-3} and $0.0089 \text{ kg m s}^{-1}$ respectively, with a layer density of 1200 kg m^{-3} used. This is less than would be predicted from protein crystal structures ($\approx 1370 \text{ kg m}^{-3}$), as the protein is hydrated. The layer properties were fitted with 6 steps, and within the ranges for layer viscosity of 0.001 to 0.02 kg m s^{-1} , layer shear of 1×10^{-4} to $1 \times 10^{-8} \text{ Pa}$ and thickness between 1×10^{-7} to $1 \times 10^{-10} \text{ m}$. For a good fit to the data, the χ^2 of the fit should be less than 1×10^5 .

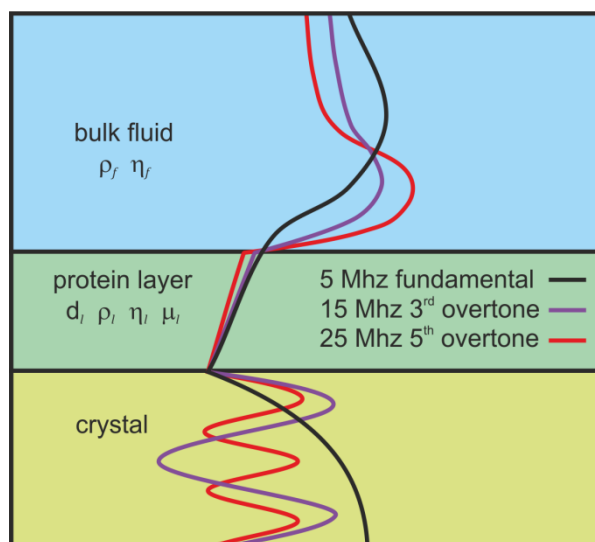


Figure 2.10. Schematic of Voigt viscoelastic model, redrawn from the QSense website.⁴⁷ This assumes the layer has a uniform thickness and density, and f and d are described as functions of the parameters shown. The parameters include the density (ρ) and viscosity (η) of both the fluid (f) and the protein layer (l), as well as the layer thickness (d) and elasticity (μ).

2.4.2.2 Fluorescence Microscopy

Fluorescent protein (such as hexahistidine tagged enhanced green fluorescent protein, (eGFP) and the tagged red fluorescent protein mCherry)* was used as a proxy for Mms6. As Mms6 is not fluorescent, the fluorescence of the proteins should allow immobilised protein patterns to be imaged. eGFP has a peak excitation and emission of $\lambda=488/507$ nm respectively, and the peak ex/em for mCherry are $\lambda=587/610$ nm respectively.⁴⁸ For patterned SAMs on gold, the SAMs were μ CP (Section 2.3.3) and protein attached using EDC/NHS (Section 2.4.1.2). The pH of the protein attachment buffer (20 mM sodium acetate) was adjusted to pH 4.6 for eGFP (pI=5.67), and pH 5.2 for mCherry (pI=6.23). The protein patterned SAMs were rinsed in phosphate buffered saline (PBS) (Invitrogen, 1 tablet makes 500 mL, 10 mM sodium phosphate, 2.68 mM KCl, 140 mM NaCl, pH 7.4). Then the patterns were mounted in a flow cell containing PBS. The fluorescent microscope used was the Nikon E600, equipped with a Hamamatsu (ORCA-ER) digital camera. eGFP patterns were excited and imaged through the FITC filter block (ex/em of $\lambda=465-495$ nm/515-555 nm), and mCherry patterns using the TxRed block (ex/em of $\lambda= 540-580$ nm/600-660 nm).

* His-tagged eGFP and mCherry courtesy of J Roth, Molecular and Nanoscale Physics, University of Leeds

2.5 Magnetic Nanoparticle Synthesis

There are many methods available for the synthesis of magnetic nanoparticles (see Section 1.3.4). Here, methods that involve the synthesis of magnetite (and other metal doped ferrites) have been used, as they were the most likely to be compatible with Mms6 biomineralisation. One of the major advantages of biomineralisation is that high quality materials are synthesised at relatively low temperatures (e.g. < 90°C), thus higher temperature synthetic methods have not been used. Also, high temperatures may denature the protein, which is likely to reduce or erase any biotemplating action of the Mms6 of magnetite MNP formation. As Mms6 has been shown to biotemplate MNPs for both room temperature co-precipitation^{5,6,49} and partial oxidation of ferrous hydroxide,^{5,6} these methods were explored for the mineralisation of the immobilised Mms6 patterns.

The type of iron salt used and the rate of addition of the reactants, can alter the mineral phase formed, see Section 1.3.4. This is because the activity of the reactants can be altered by the presence of different counter ions, which can divert the mineralisation down alternative pathways. When reactants are added quickly, localised effects due to inhomogeneous mixing can also alter the reaction pathways, and produce different iron minerals.⁵⁰ Thus, deoxygenated (anaerobic) water is used in all magnetite mineralisation reactions, and a range of reaction conditions were explored to ensure magnetite was mineralised onto the Mms6 patterns. Anaerobic water should be thoroughly degassed and N₂ sparged (at least 1 hour for each) before being used for magnetite synthesis.

2.5.1 Room Temperature Co-precipitation (RTCP)

When ferrous and ferric iron salts are mixed under an inert atmosphere and a base added, small magnetite MNPs are formed, see Equation 1.3. Equation 1.3 is an exceedingly simplified reaction scheme, as many other iron oxides and (oxy)hydroxide intermediates may also be formed, and remain as impurities in the final product.^{50,51} Arakaki *et al.* (2003)⁴⁹ found that larger magnetite MNPs, with a narrower grainsize distribution and less impurities were formed by RTCP in the presence of Mms6.

Unless specified otherwise in the text, this is the protocol followed to synthesise RTCP MNPs. 10 mM stock solutions of Fe²⁺ (FeSO₄·7H₂O), Fe³⁺ (FeCl₃·4H₂O) and Co²⁺ (CoCl₂·6H₂O) and a 100 mM solution of OH⁻ (NaOH) were prepared with anaerobic water and sparged with N₂. To make magnetite, a 2:1 ratio of Fe²⁺ to Fe³⁺ was mixed and stirred using N₂ flow. Despite magnetite containing one Fe²⁺ for every two Fe³⁺ ions, excess ferrous iron was used as some oxidation can occur during the reaction (see Figure 1.9). For a total 10 mL reaction volume, 6.6 mL Fe²⁺

(6.6 mM) and 3.4 mL Fe³⁺ (3.4 mM) was used. To make 6% cobalt doped magnetite, 6.3 mL Fe²⁺ (6.3 mM), 3.1 mL Fe³⁺ (3.1 mM) and 0.6 mL Co²⁺ (0.6 mM) were mixed. To this, the Mms6 or His₆-Mms6 protein (10 µg mL⁻¹) or Mms6 immobilised on a patterned substrate was added and incubated for a few minutes.

An excess of sodium hydroxide (≈3.0 mL, 30 mM) is gradually added dropwise over ≈10 minutes. The solution first turned orange, before a dark green precipitate was formed as different hydrated iron (oxy)hydroxide and iron oxide magnetite precursors were precipitated. This was matured for ≈30 minutes, and it gradually turned from green to black as magnetite was crystallised. If present, patterned substrates were removed with tweezers and thoroughly rinsed with anaerobic water, before drying with N₂. The base was removed from the bulk precipitate and the particles washed by magnetically separating the MNPs to the side of the reaction vessel, removing the solution, and resuspending the MNPs in anaerobic water between 3 and 5 times. The MNPs were then dried under N₂, or kept sealed in anaerobic water.

2.5.2 Partial Oxidation of Ferrous Hydroxide with Potassium Hydroxide (POFHK)^{5,6,51-53}

Ferrous hydroxide was formed by mixing a ferrous iron salt with potassium hydroxide, which was then partially oxidised by potassium nitrate, as per Equation 1.4. The ratio of the reactants, as well as the temperature and duration of the reaction were all found to affect the mineral phase formed. Stock solutions of 0.5 M FeSO₄·7H₂O and CoCl₂·6H₂O, and 1.0 M KOH and 0.1 M KNO₃ were prepared with anaerobic water and N₂ sparged. For a total 1 mL reaction volume, the ferrous and cobaltous stocks were mixed (percentage cobalt as a ratio of metal ions) as per Table 2.1.

Table 2.1. Ratio of stock solutions used to prepare POFHK MNPs.

% Co	volume of Fe ²⁺ (µL)	volume of Co ²⁺ (µL)
0%	100	0
2%	98	2
6%	94	6
10%	90	10
15%	85	15

To this, either 400 µL anaerobic water, or 400 µL anaerobic water containing 10 µg Mms6 or His₆-Mms6 were added and incubated for a few minutes. Then 100 µL KOH and 400 µL KNO₃ were gradually added over a few minutes to form ferrous hydroxide. The dark green mixtures were transferred to an oil bath heated to 90°C for 4 hours, with N₂ sparging used to both mix the reactants and maintain anoxia in the reaction vessel. The nitrate slowly oxidises the ferrous hydroxide to form black

magnetite and/or Co doped magnetite MNPs. The particles were then washed and stored (see RTCP method above).

2.5.3 POFHK on a Patterned Surface⁵²⁻⁵⁴

The reaction conditions for POFHK were systematically varied to optimise the reaction towards the formation of magnetite nanoparticles onto the micro-patterned Mms6 arrays. As for POFHK above, an excess of nitrate was used to mineralise magnetite on the patterned Mms6 surface. However, it was not possible to use a large excess of KOH due to the caustic nature of the solution, which etched the surfaces and destroyed the patterning. The choice of ferrous salt (e.g. chloride, sulfate, fumarate, oxalate, acetylacetonate) was also explored, as the type and morphology of the mineral phase formed was found to be altered by the salt counter ion. Also, as this method involves mineralisation of a flat surface, a reaction vessel with a flat bottom and removable lid was used, so the immobilised Mms6 pattern could be removed with minimal damage (see Figure 2.11).⁵⁴

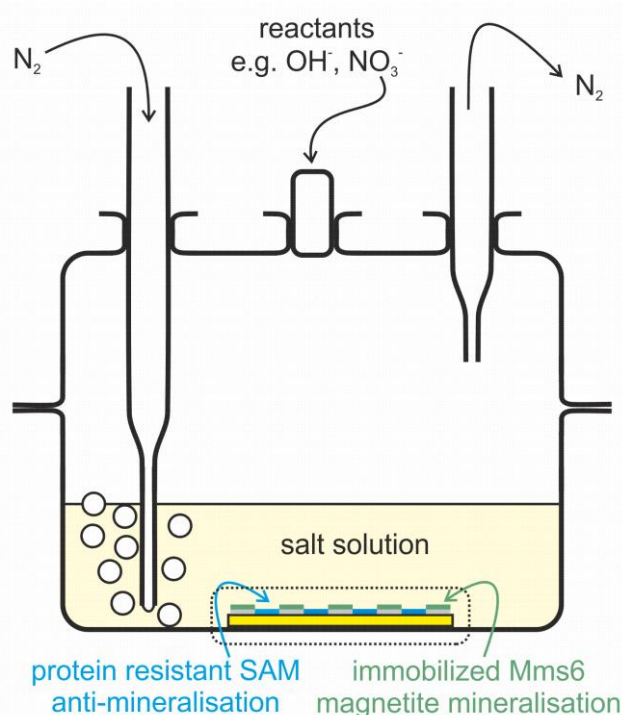


Figure 2.11. Diagram of the reaction vessel for mineralisation of a protein patterned surface after Galloway *et al.* (2012a).⁵⁴ The Mms6 patterned substrate is placed at the bottom of the reaction vessel, before it is sealed and an N₂ atmosphere maintained by gentle sparging. Anaerobic solutions can then be added, the vessel heated and the mineralised sample removed without scratching the patterned substrate.

The following is for an optimised method to ensure magnetite (or 6% cobalt doped magnetite), rather than other iron mineral phases, was mineralised onto the Mms6 pattern. Stock solutions of 0.5 M FeSO₄·7H₂O and CoSO₄·7H₂O, and 1.0 M KOH and 1.0 M KNO₃ were prepared with anaerobic water and N₂ sparged. For a total 50 mL reaction volume, 2.5 mL Fe²⁺ (25 mM) was pipetted into 24.75 mL anaerobic

water under gentle N₂ flow to mix. If 6% Co doping was desired, 2.35 mL Fe²⁺ (23.5 mM) and 0.15 mL Co²⁺ (1.5 mM) were added to 24.75 mL of anaerobic water. When mineralising a protein patterned surface, or using Mms6 in the bulk solution, this should be added at this stage and incubated for a few minutes, maintaining gentle N₂ sparging. Reaction volumes can be scaled down to 10 mL for the Mms6 in bulk solution controls.

A slight excess of base (2.75 mL, 55 mM) was then added over about 1 minute, which formed dark green ferrous hydroxide. The reaction vessel was then transferred to an oil bath at 80°C, and a large excess (20 mL, 400 mM) of KNO₃ was gradually added over a few minutes. The N₂ bubbling and heating was maintained for 4 hours, as the green ferrous hydroxide was slowly oxidised to black magnetite. The bulk precipitated MNPs were then washed and stored as for the RTCP method above. Biotemplated patterned surfaces were thoroughly washed with anaerobic water, and dried with N₂.

2.5.4 Partial Oxidation of Ferrous Hydroxide with Ammonia and Hydrazine (POFHN)^{6,52}

For this method, ammonia was used as the base to form the ferrous hydroxide in the presence of hydrazine, which helps to prevent the formation of ferric oxide impurities during mineral nucleation.⁵² As with the POFHK method, the type of ferrous salt, ratio of reactants, and the temperature and duration of the mineralisation was found to alter the type and morphology of the iron mineral phase formed.

Again, stock solutions of 0.5 M FeSO₄·7H₂O and CoCl₂·6H₂O, and 0.2 M KNO₃ were prepared with anaerobic water and N₂ sparged, with 65% N₂H₄ and 25% NH₄OH used as purchased. For a total 1 mL reaction volume, the Fe²⁺ and Co²⁺ were mixed (percentage of cobalt expressed as a ratio of the metal ions) as per Table 2.2.

Table 2.2. Ratio of stock solutions used to prepare POFHN MNPs.

% Co	volume of Fe ²⁺ (μL)	volume of Co ²⁺ (μL)
0%	100	0
2%	98	2
4%	96	4
6%	94	6
8%	92	8
10%	90	10

Then 400 μL anaerobic water or 400 μL anaerobic water containing 10 μg Mms6 or His₆-Mms6 were added and incubated for a few minutes under N₂ sparging. 4 μL hydrazine was added, which formed a pale green precipitate, followed by 20 μL ammonium hydroxide, which turned the precipitate dark green as ferrous hydroxide was formed. Whilst continuing N₂ sparging, 500 μL KNO₃ was gradually pipetted into the reaction vessel over a few minutes. Once thoroughly mixed (using the N₂ sparging), the reactant vessel was transferred to an oil bath at 90°C for 2 hours, and N₂ flow was maintained. During heating, the green ferrous hydroxide was gently oxidised to black magnetite. The precipitated magnetite or Co doped magnetite MNPs were then washed and stored as per the RTCP method.

2.5.5 POFHN on a Patterned Surface^{54,55}

As for the POFHK method, the following is for the optimised POFHN method of magnetite mineralisation onto surface immobilised Mms6. Stock solutions of 0.5 M FeSO₄·7H₂O and CoSO₄·7H₂O, and 0.2 M KNO₃ were prepared with anaerobic water and N₂ sparged, with 26% NH₄OH and 50-60% N₂H₄ used as purchased. For a total 50 mL reaction volume, 5.0 mL Fe²⁺ (50 mM) was added to 19.3 mL anaerobic water under gentle N₂ sparging. If using 6% Co doping, 4.7 mL Fe²⁺ (47 mM) and 0.3 mL Co²⁺ (3 mM) were pipetted into 19.3 mL anaerobic water. When mineralising a patterned substrate, or using Mms6 in the bulk solution, this should also be added at this stage and incubated for a few minutes, maintaining N₂ bubbling. Again, if Mms6 is scarce, reaction volumes can be scaled down to form the controls using Mms6 in the aqueous bulk solution.

Conversely to the POFHK method, it was found that the metal salt should be in slight stoichiometric excess to form magnetite with POFHN on a surface.⁵⁴ 200 μL of hydrazine and 1.0 mL of ammonium hydroxide were then added to the metal salts in the reaction vessel, and incubated for \approx 1 minute to form a dark green ferrous hydroxide. The vessel was then transferred to an oil bath at 80°C, and an excess of 25 mL KNO₃ (100 mM) gradually added over a few minutes. Gentle nitrogen bubbling was maintained during 2 hours heating, as the ferrous hydroxide matured to form black magnetite MNPs. The surfaces and/or bulk precipitated MNPs were then washed and stored as per the POFHK surface method (Section 2.5.3).

2.6 Characterisation of Magnetic Nanoparticles

A number of methods were used to image and characterise the particles formed both from the bulk solution and on the patterned substrates. Where appropriate, samples have been imaged with transmission electron microscopy (TEM), scanning electron microscopy (SEM) and atomic force microscopy (AFM). They have also undergone elemental analysis using electron energy loss spectroscopy (EELS), energy dispersive X-ray (EDX), and inductively coupled plasma-atomic emission spectroscopy (ICP-AES). Crystallographic measurements were recorded by selected area electron diffraction (SAED) and powder X-ray diffraction (XRD), and the magnetic properties of the arrays were probed using vibrating sample magnetometry (VSM) and magnetic force microscopy (MFM).

2.6.1 Transmission Electron Microscopy (TEM)*

To prepare MNPs for TEM, the particles were resuspended in anaerobic water and $\approx 10 \mu\text{L}$ transferred to a carbon coated copper grid before drying. The grids were loaded into a Phillips CM200 Field Emission (FEG)TEM and imaged with a 0.24 nm point resolution using Digital Micrograph software. TEM is only suitable for analysing thin samples and/or nanoparticles, as thicker materials can fully attenuate the incident electron beam. As thicker materials contain more atoms, the likelihood of an electron being scattered increases with sample thickness. Also, the electrons are likely to be scattered more if they encounter a heavier atom, so electrons are not transmitted by thick or heavy samples for detection.

The TEM used produces electrons with a Schottky style field emission gun (FEG).⁵⁶ This uses an electric field to lower the work function of the tungsten source, thus requiring less heat to achieve electron emission than with a traditional thermionic source.⁵⁶ The electrons were accelerated towards the sample at 200 keV. The beam is kept under vacuum and is focussed onto the sample with a series of electro-magnetic lenses (Figure 2.12).⁵⁶ The images are created by projecting the transmitted beam onto a phosphor screen or charge coupled device (CCD) digital camera. Electron dense materials, such as crystalline magnetic nanoparticles, diffract, absorb and scatter electrons, and appear as dark contrast in bright field images (i.e. the central portion of the transmitted beam).

* TEM imaging, EELS, EDX and SAED recorded in collaboration with M. Ward and A. Walton, University of Leeds.

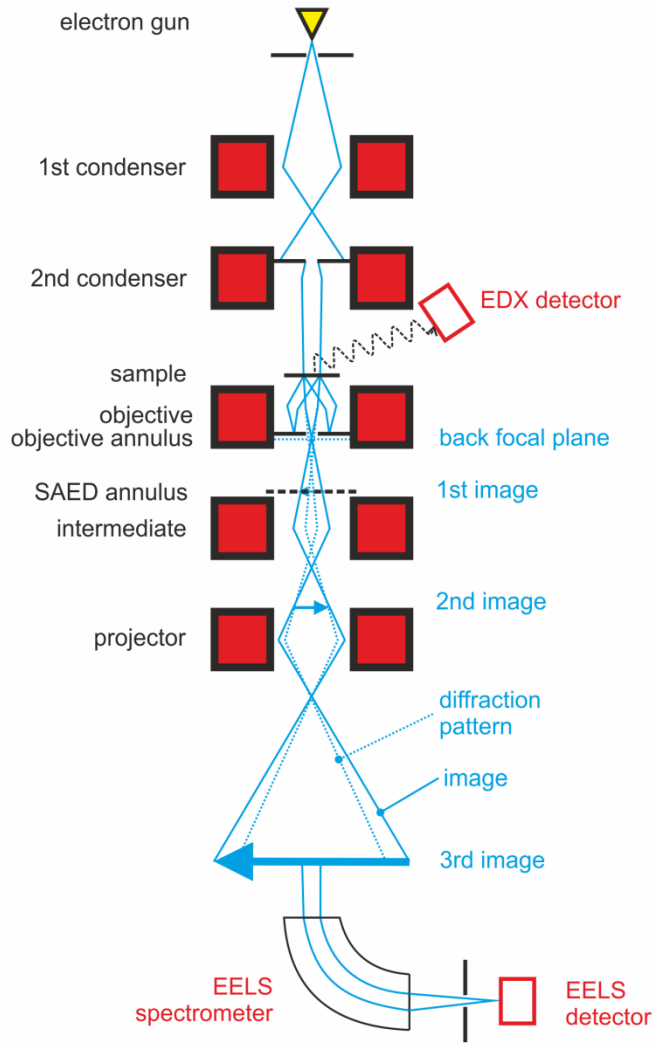


Figure 2.12. Schematic of TEM showing ray path, adapted from Reimer & Kohl (2010).⁵⁶ Electromagnetic optics (red shaded boxes) focus and control the beam in the vacuum and focus the electrons onto the sample. Post sample, the optics are used to either focus on the sample to produce an image (solid blue line), or the back focal plane to image the diffraction pattern of the sample (dotted blue line). Also shown are typical detector locations (red outlined boxes) for EDX and EELS data collection.

Crystalline MNPs diffract the electron beam, which forms a Fourier transform of the image on the back focal plane. The diffraction pattern for single crystals can be imaged on photographic film by refocusing to the back focal plane and using the selected area electron diffraction annulus.⁵⁷ The spacing of the dots (single crystal) or rings (polycrystalline material) on the photographic film are converted to the d spacings of the diffracted crystal using the following equations:⁵⁸

$$\frac{\lambda}{d} = 2\sin\theta_B \approx \tan 2\theta_B = \frac{r}{l} \quad (2.9)$$

$$d \approx \frac{\lambda l}{r} = \frac{23}{r} \quad (2.10)$$

Where d is the lattice spacing, λ the wavelength of the electrons, θ_B the Bragg angle of the diffraction (which is very small), l the camera focal length, and r the distance between the spot/ring and the zero order spot.⁵⁶ λl is also called the camera constant, and it is determined using standards (it is 23 for the CM200). Interplanar spacings and angles can then be related to zone axes using formulae contained in tables 1a & 1b in Andrews *et al.* (1971)⁵⁸ for comparison to crystallographic databases (such as those used in Section 2.6.5).

Electron energy loss spectra are collected post transmission, and show element specific absorption, which can be used to form elemental maps in the TEM.⁵⁷ Energy is also lost during ionisation, when an incident electron excites and ejects an electron from an atom. As different elements require a characteristic quantity of energy to eject a particular electron, peaks in the EELS spectrum are used to identify which elements are present in a sample.⁵⁷ EELS spectra were collected in diffraction mode using a Gatan GIF200 imaging filter and processed with the Digital Micrograph software to form elemental maps.

X-ray emission occurs when an electron in the beam ejects a core electron of an element, and a higher energy electron emits a characteristic X-ray photon to fill the vacancy.⁵⁷ An energy dispersive X-ray detector in the chamber is used to collect EDX spectra, in which elements present can be identified by the peaks in the energy spectrum. EDX spectra were collected using the UWT Oxford Instruments EDXS detector and processed using the ISIS software.

2.6.2 Scanning Electron Microscopy (SEM)

Samples that are too thick for TEM (such as the patterned biomineralised MNPs) were imaged using SEM. Samples were attached and earthed onto an aluminium stub, and up to 8 loaded into the LEO 1530 Gemini FEG(SEM). The chamber was pumped to $<2 \times 10^{-5}$ mbar, and the sample positioned at a working distance (WD) of ≈ 3 mm for imaging, and ≈ 8.5 mm for X-ray mapping. Electrons are generated and focussed in the same manner as in TEM, but use a much lower accelerating voltage (≈ 3 -20 keV). The electrons interact with the sample to a depth and volume dependent on the atomic number of the sample and the energy of the beam.^{59,60} Lower atomic number materials and higher beam acceleration create a larger volume of interaction, see Figure 2.13.^{59,60} The incident beam penetrates the surface of a sample, and electrons are attenuated by elastic and inelastic scattering in the substrate. Each collision causes the electrons to lose energy and change direction, which can cause a number of effects.

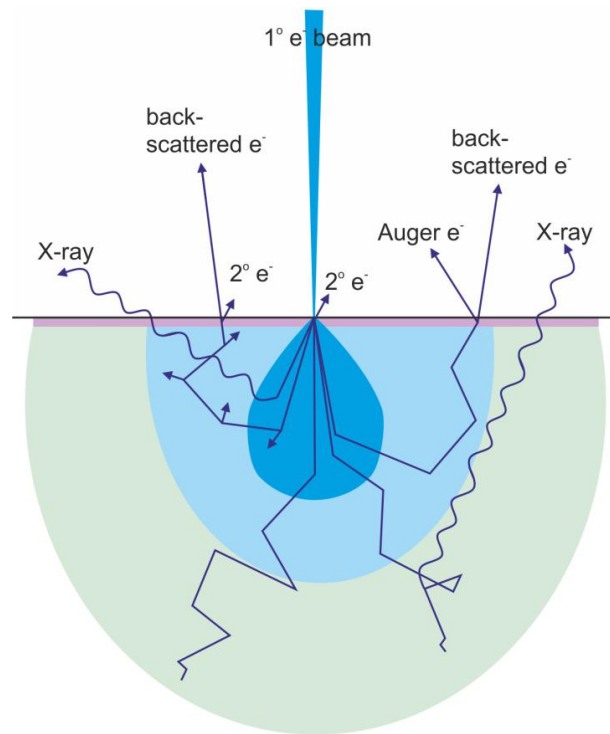


Figure 2.13. Schematic showing interaction of electrons with a substrate during SEM, based on Reimer (1998)⁶⁰ and Goldstein *et al.* (2003).⁵⁹ Primary electrons ($1^\circ e^-$) are focussed onto the surface, and a tear-drop shaped volume of interaction of the electrons with the substrate is formed. Backscattered e^- are detected after one or more scattering events. Secondary electrons ($2^\circ e^-$) are generated by 1° and backscattered e^- , but can only be detected from $<1\text{nm}$ depth into the sample. Auger electrons are also easily attenuated, so can only be detected from the $<10\text{ nm}$. X-rays can be detected from anywhere in the interaction volume. For a 20 keV beam interacting with a silicon substrate, Monte Carlo simulations predict that the total depth of interaction is $\approx 5\ \mu\text{m}$.

Backscattered electrons were originally primary electrons that are scattered back towards the detector by one or more scattering events. As they have quite high energy, they interact with a large volume of the substrate before detection. Low energy secondary electrons ($<50\text{ eV}$) can be emitted by the outer orbitals of atoms in the sample, by primary or backscattered electrons. Secondary electrons can only travel short distances within a material due to their low energy, thus only those emitted near the substrate surface ($<1\text{ nm}$) can escape the sample.⁵⁹ The in lens secondary electron detector collected image information ($\text{WD} \approx 3\text{ mm}$, 3 keV), which was processed using the Zeiss SmartSEM software to produce digital SEM micrographs of the biomineralised patterned gold substrates. An SEM image is built up by sequential detection of secondary electrons as the focussed beam of electrons is sequentially scanned across the sample surface.

Auger electrons are emitted when the energy lost by relaxation of a higher energy electron to fill a core vacancy is passed to a third electron.⁶⁰ The electron energy is characteristic of the three electron energy levels involved, therefore the energy of an Auger electron is element specific. This is also an extremely surface sensitive technique, as Auger electrons are quite low energy (100-1000 eV), they can only be detected from <10 nm depth.⁶⁰ A higher energy electron can also relax to fill the ionised core vacancy by emission of an X-ray. As energy dispersive X-rays interact with matter much less than electrons, they can be detected from anywhere in the interaction volume.⁵⁹

The Oxford Instruments AZtecEnergy EDX system on the LEO was used (WD \approx 8.5 mm, 10-20 keV) to collect X-ray spectra and elemental surface maps of the biomineralised patterned substrates. EDX maps have a lower resolution than the 2° electron images, due to the large effective spot size created by the volume of interaction of the electrons with the substrate. A lower scan energy (e.g. 10 keV) has a smaller volume of interaction, but as less energetic electrons are entering the sample, fewer X-rays are emitted. This means the peaks in the detected spectra are smaller, making mapping for elements with similar X-ray intensities, such as iron and cobalt, difficult. Therefore, scan energy selection is key to ensuring a good elemental map with EDX in the SEM for these biomineralised patterned samples.

2.6.3 Particle Size Analysis of Electron Microscope Images

Particle size and morphological analysis of the imaged nanoparticles involved recording the longest and shortest axis of \approx 500 nanoparticles per sample using Image J.⁶¹ To allow for comparison of TEM and SEM images, the length (longest) and width (shortest) axes were measured on the projection of the image of a particle. The aspect ratio was taken as the width:length ratio of the particles. Only particles with an aspect ratio >0.5 were used for grainsize distribution analysis. Using Origin, these data were fitted with a 1 or 2 peak Gaussian distribution, or with the Asym2Sig asymmetric function, see Equation below:

$$y = y_0 + A \left(\frac{1}{1 + e^{\frac{-(x-x_c+\omega_1)/2}{\omega_2}}} \right) \left(\frac{1}{1 + e^{\frac{-(x-x_c+\omega_1)/2}{\omega_3}}} \right) \quad (2.11)$$

Where y_0 is the offset, A is the amplitude, x_c is the peak centre and ω width measurements. The best peak fit was selected based on the optimum r^2 and χ^2 of each grainsize distribution.

2.6.4 Inductively Coupled Plasma-Atomic Emission Spectroscopy (ICP-AES)*

The quantity of iron and cobalt as a ratio of metal ions was measured using ICP-AES for the bulk synthesised MNPs. Approximately 1 mg of dried MNPs were resuspended in aqua regia (150 μ L HCl, 150 μ L HNO₃) and sonicated for 16 hours to dissolve them. The solutions were made up to 10 mL with water and 0.22 μ m filtered before analysis on a Perkin Elmer Optima 5300 DV spectrometer. The solutions were pumped into a nebuliser to create an aerosol that is carried to the spray chamber by humidified argon gas.⁶² This is then injected into the torch assembly and the Ar plasma. The plasma excites electrons, and relaxation of the ionised Fe and Co in the samples emits energy at element specific wavelengths.⁶² This is detected on a spectrometer, allowing the relative abundance of Fe:Co to be determined.

2.6.5 Powder X-ray Diffraction (XRD)

Powder X-ray diffraction utilises constructive interference of monochromated X-rays with a crystalline lattice. The crystal lattice spacing (d) is related to the scattering angle (θ) by the Bragg Equation:⁶³

$$n\lambda = 2d\sin\theta \quad (2.12)$$

Where n is the order, and λ the wavelength of the incident X-ray. Therefore, crystallographic planes in the powdered sample produce characteristic peaks in an XRD spectrum at precise angles. The angle at which a peak is located can be converted back to a d -spacing, and the full spectrum compared to standards to identify an unknown sample.

A Bruker-AXS D8 Series 2 diffractometer, set to a Bragg Brentano Parafocussing geometry, was used to obtain XRD spectra. X-rays were generated at 40 kV at room temperature using a Cu K α_1 source ($\lambda=1.54056$ Å). Monochromated X-rays were passed through a 2 mm exit slit and an automatic divergence slit of 0.2° and onto the sample. Dried bulk precipitated samples were spread onto a silica flat-plate, or mineralised patterned substrates were mounted directly onto the sample stage. X-ray intensities were collected between $2\theta=5^\circ$ and 80° with a Braun position sensitive detector (0.010° and 7.5 seconds per step). These data were analysed with Bruker-AXS and EVA software to compare the spectra obtained to d -spacings from crystallographic databases (pattern numbers in Table 2.3). Powdered samples were normalised to a silica standard, and patterned

* ICP-AES protocol courtesy of S. Staniland, University of Leeds.

substrates normalised to the Au (111) peak from the gold substrate. The grainsize of particles D was calculated using the Debye-Scherrer Equation:⁶⁴

$$D = \frac{k\lambda}{\beta \cos\theta} \quad (2.13)$$

Here, k is the shape constant (0.89), and β the full width half maximum (FWHM) of the peak in radians.

Table 2.3. Details of spectra used from EVA software to fit XRD patterns.

Mineral	Formula	Pattern number
gold	Au	00-004-0784
silicon oxide	SiO ₂	00-051-1380
chromium oxide	Cr ₈ O ₂₁	00-047-1312
eskolaite	Cr _{1.9} V _{0.09} Fe _{0.01} O ₃	00-011-0354
graphite 2H	C	01-075-1621
maghemite	γ-Fe ₂ O ₃	00-004-0755
magnetite	Fe ₃ O ₄	00-011-0614
cobalt ferrite	CoFe ₂ O ₄	00-022-1086

2.6.6 Vibrating Sample Magnetometry (VSM)

Vibrating sample magnetometry⁶⁵ was carried out using an Oxford Instruments Maglab VSM. Dried bulk precipitated MNPs were weighed and packed into a gelatine capsule. The capsule, or the biomineralised patterned sample, was mounted onto the end of a rigid carbon rod and vibrated at 55 Hz next to a pair of pick-up coils inside the VSM. Sample magnetisation causes a magnetic flux to induce an AC voltage across the pick-up coils, the amplitude of which is proportional to the magnetic moment of the sample.⁶⁵ The vibration of the sample is perpendicular to any applied external field (maximum range of -20 kOe to 20 kOe). This allows the magnetic response of the material to be measured over an applied field range to record a magnetic hysteresis loop at a fixed temperature. Alternatively, by fixing the applied field (here between 0 Oe and 1000 Oe), and recording the magnetic flux induced voltage in the pick-up coils over a temperature range (e.g. 10 K to 250 K), sample moment versus temperature can also be measured. The sample mass can be used to convert the moment readings to emu g⁻¹ (e.g. for bulk precipitated MNPs) or normalised if it is not possible to take a mass (for mineralised substrates).

2.6.7 Atomic/Magnetic Force Microscopy (AFM/MFM)⁶⁶

Atomic force microscopy uses an extremely sharp probe mounted onto a cantilever to build up an image of a surface in sequential line scans. This can be done in full contact with the surface, by tapping the probe on the surface, or by interactions between the probe and the surface at a short separation distance. The sample was mounted on the stage of a Multimode Nanoscope III AFM (Veeco). The topography was imaged when the tip was tapped across the surface at the resonant frequency of the cantilever (tapping-mode). For magnetic force microscopy, non-contact mode AFM is used with a magnetised tip (Cr/Co coated tips (MESP probe, Veeco)). Prior to use, the silicon cantilever was clasped in a tip holder and the MFM tip magnetised perpendicular to the sample surface using a permanent magnet. Magnetic interactions between the magnetised tip and the surface are recorded in non-contact mode at a constant distance above the topographical line retrace. Magnetic interactions between sample and tip cause phase shifts in the oscillation of the cantilever, which should be independent of the topographical height (see Figure 2.14).⁶⁶

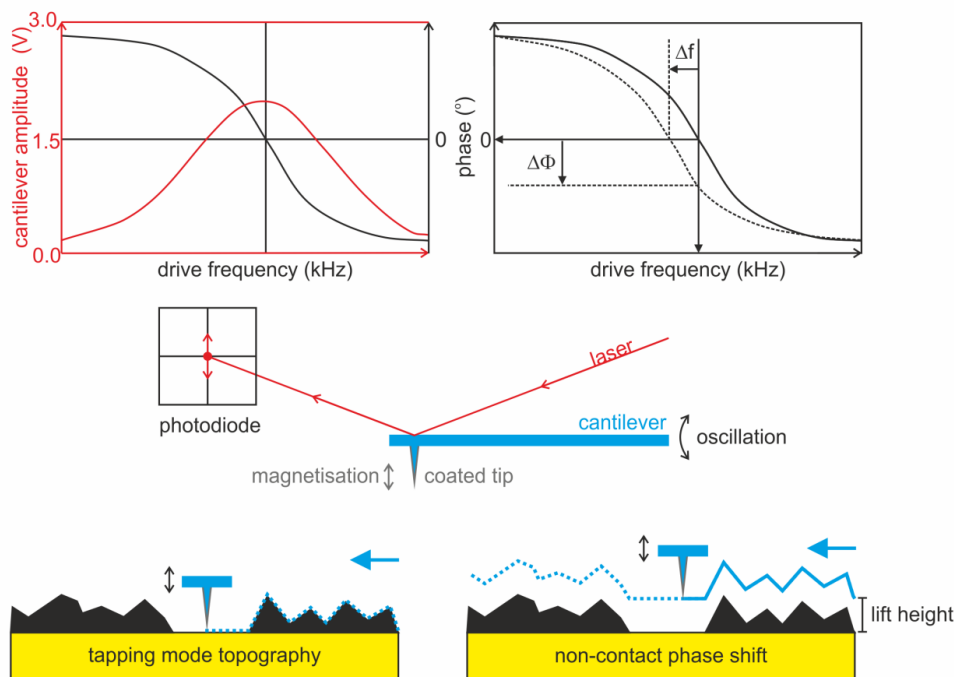


Figure 2.14. Schematic of imaging with AFM/MFM, based on the MultimodeTM SPM Instruction Manual.⁶⁶ A laser is focussed onto the end of a silicon cantilever, which has a sharp, magnetised MFM tip (grey arrow indicates direction of magnetisation). The laser is then focussed onto a four quadrant photodiode to detect deflection of the cantilever by interactions with a sample. The drive frequency is set at the resonant frequency of the cantilever (oscillation direction black arrows), and the phase shift between piezo drive frequency and cantilever zeroed. For each scan line, the surface topography is traced and retraced in tapping mode, where the resonating tip taps across the surface. The piezo stack then lifts the tip and a trace and retrace of the topographical retrace is followed at this fixed distance. Blue arrows indicate retrace direction, and therefore the direction of the recorded scan. Attraction of the magnetised tip towards the surface causes a negative phase shift ($-\Delta\Phi$), and repulsion a positive phase shift ($+\Delta\Phi$).

The tip assembly was mounted onto the piezo stack and positioned above the biomineralised sample. The piezo stack consists of a number of piezoelectric crystals that control the height, oscillation and raster-scanning motion of the probe cantilever. To detect movement of the cantilever, a laser is reflected off the end of the cantilever and focussed onto a detector. The detector consists of four photodiodes, and the laser is focussed at its centre. This means that any deflection in the cantilever by the sample surface (or magnetic interactions) when imaging will deflect the laser and thus be detected. The cantilever was then tuned to its resonant frequency in air (typically ≈ 80 kHz for MFM probes) using the Nanoprobe software. A maximum in the amplitude of the laser signal at the detector indicates resonance of the cantilever, so the drive frequency was set to the centre of the resonant peak. The phase curve should decrease with increasing frequency, and cross the centre line at the peak drive frequency, which corresponds to a 90° phase lag. Therefore, shifts in the phase curve occur when the lag between the drive frequency and the cantilever frequency is altered. Vertical deflection of the tip by the surface causes a shift in resonant frequency (Δf), and thus the phase shift ($\Delta\Phi$). These settings allow both attractive and repulsive magnetic interactions between the sample and the tip to be differentiated in non-contact mode.

Initially the microscope should be set up to form a good topographical image. Once the tip was engaged, the amplitude set point was gradually reduced to lightly contact the surface, and the image area selected. The feedback controls (integral gain and proportional gain) were adjusted to ensure the forward (trace) and reverse (retrace) of the tapping mode topographical line traces overlaid well. To record magnetic interactions, the interleave mode was engaged. An appropriate lift height (between 50 and 200 nm) was selected to avoid contact between the tip and the surface as the topography is traced and retraced during non-contact magnetic imaging. For both tapping mode and non-contact mode, the retrace scan line should be recorded. These data were processed using WSxM software⁶⁷ and 3D output compiled in "R" using the rgl package.*

* 3D composite plots rendered in 'R' by J. Bramble, University of Leeds.

2.7 References

1. Sturdier, F.W. (2005). Protein production by auto-induction in high density shaking cultures. *Protein Express. Purif.* **41**, pp 207-234.
2. Arnau, J., Lauritzen, C., Petersen, G.E. & Pedersen, J. (2006). Current strategies for the use of affinity tags and tag removal for the purification of recombinant proteins. *Protein Express. Purif.* **48**, pp 1-13.
3. Porath, J. (1992). Immobilized metal ion affinity chromatography. *Protein Express. Purif.* **3**, pp 263-281.
4. Kapust, R.B. & Waugh, D.S. (1999). Escherichia coli maltose-binding protein is uncommonly effective at promoting the solubility of polypeptides to which it is fused. *Prot. Sci.* **8**, pp 1668-1674.
5. Amemiya, Y., Arakaki, A., Staniland, S.S., Tanaka, T. & Matsunaga, T. (2007). Controlled formation of magnetite crystal by partial oxidation of ferrous hydroxide in the presence of recombinant magnetotactic bacterial protein Mms6. *Biomaterials.* **28**, pp 5381-5389.
6. Galloway, J.M., Arakaki, A., Masuda, F., Tanaka, T., Matsunaga, T. & Staniland, S.S. (2011). Magnetic bacterial protein Mms6 controls morphology, crystallinity and magnetism of cobalt-doped magnetite nanoparticles in vitro. *J. Mater. Chem.* **21**, pp 15244-15254.
7. Porath, J., Carlsson, J., Olsson, I. & Belfrage, G. (1975). Metal chelate affinity chromatography, a new approach to protein fractionation. *Nature.* **258**, pp 598-599.
8. Snyder, L. & Champness, W. (2007). *Molecular Genetics of Bacteria* (ASM Press, Washington D.C., USA).
9. Abad, J.M., Mertens, S.F.L., Pita, M., Fernandez, V.M. & Schiffrin, D.J. (2005). Functionalization of thioctic acid-capped gold nanoparticles for specific immobilization of histidine-tagged proteins. *J. Am. Chem. Soc.* **127**, pp 5689-5694.
10. Ludden, M.J.W., Mulder, A., Schulze, K., Subramaniam, V., Tampé, R. & Huskens, J. (2008). Anchoring of histidine-tagged proteins to molecular printboards: Self-assembly, thermodynamic modeling, and patterning. *Chem. Eur. J.* **14**, pp 2044-2051.
11. (2011). *HisPur Resins and Kits*.
<http://www.piercenet.com/browse.cfm?fldID=BAD4ABB2-E9D4-4D94-9058-70499F5F73A9> 14/12/2011.
12. Kapust, R.B., Tózsér, J., Fox, J.D., Anderson, D.E., Cherry, S., Copeland, T.D. & Waugh, D.S. (2001). Tobacco etch virus protease: Mechanism of autolysis and rational design of stable mutants with wild-type catalytic proficiency. *Prot. Eng.* **14**, pp 993-1000.
13. Schägger, H. (2006). Tricine-SDS-PAGE. *Nat. Protocols.* **1**, pp 16-22.
14. Shapiro, A.L., Viñuela, E. & Maizel Jr, J.V. (1967). Molecular weight estimation of polypeptide chains by electrophoresis in SDS-polyacrylamide gels. *Biochem. Biophys. Res. Commun.* **28**, pp 815-820.
15. (2012). *ExpASy ProtParam tool by the Swiss Institute of Bioinformatics*.
<http://web.expasy.org/protparam/> 16/01/2012.

16. Meyer, T.S. & Lamberts, B.L. (1965). Use of Coomassie brilliant blue R250 for the electrophoresis of microgram quantities of parotid saliva proteins on acrylamide-gel strips. *Biochim. Biophys. Acta.* **107**, pp 144-145.
17. von Strandmann, E.P., Zoidl, C., Nakhei, H., Holewa, B., von Strandmann, R.P., Lorenz, P., Klein-Hitpaß, L. & Ryffel, G.U. (1995). A highly specific and sensitive monoclonal antibody detecting histidine-tagged recombinant proteins. *Prot. Eng.* **8**, pp 733-735.
18. Xu, D. & Zhang, Y. (2012). Ab initio protein structure assembly using continuous structure fragments and optimized knowledge-based force field. *Proteins.* **80**, pp 1715-1735.
19. Schrödinger, LLC. (2012). *The PyMOL Molecular Graphics System, Version 1.5.0.1.*
20. Högbom, M., Ericsson, U.B., Lam, R., Bakali H., M.A., Kuznetsova, E., Nordlund, P. & Zamble, D.B. (2005). A high throughput method for the detection of metalloproteins on a microgram scale. *Mol. Cell. Proteomics.* **4**, pp 827-834.
21. (2012). *Intrinsic Fluorescence of Proteins and Peptides.*
<http://dwb.unl.edu/Teacher/NSF/C08/C08Links/pps99.cryst.bbk.ac.uk/projects/gmoczf/fluor.htm> 23/07/2012.
22. Subramaniam, V., Steel, D.G. & Gafni, A. (2002). Room temperature tryptophan phosphorescence as a probe of structural and dynamic properties of proteins, pp 43-65. *in Topics in Fluorescence Spectroscopy, vol. 6, Protein Fluorescence* (ed. Lakowicz, J.R.). (Kluwer Academic / Plenum Publishers, New York, USA).
23. van de Weert, M. & Stella, L. (2011). Fluorescence quenching and ligand binding: A critical discussion of a popular methodology. *J. Mol. Struct.* **998**, pp 144-150.
24. Kelly, S.M., Jess, T.J. & Price, N.C. (2005). How to study proteins by circular dichroism. *Biochim. Biophys. Acta.* **1751**, pp 119-139.
25. Whitmore, L. & Wallace, B.A. (2004). DICHROWEB, an online server for protein secondary structure analyses from circular dichroism spectroscopic data. *Nucleic Acids Res.* **32**, pp W668-W673.
26. Ulman, A. (1991). *An Introduction to Ultrathin Organic Films: From Langmuir-Blodgett to Self-Assembly* (Academic Press, London, UK).
27. Kumar, A., Biebuyck, H.A. & Whitesides, G.M. (1994). Patterning self-assembled monolayers: Applications in materials science. *Langmuir.* **10**, pp 1498-1511.
28. Mrksich, M. & Whitesides, G.M. (1995). Patterning self-assembled monolayers using microcontact printing: A new technology for biosensors? *Trends Biotechnol.* **13**, pp 228-235.
29. Prime, K.L. & Whitesides, G.M. (1993). Adsorption of proteins onto surfaces containing end-attached oligo(ethylene oxide): A model system using self-assembled monolayers. *J. Am. Chem. Soc.* **115**, pp 10714-10721.
30. Tompkins, H.G. & Irene, E.A. (2005). *Handbook of Ellipsometry [Electronic Resource]* (Knovel/William Andrews Publishing/Noyes).
31. Nuzzo, R.G. & Allara, D.L. (1983). Adsorption of bifunctional organic disulfides on gold surfaces. *J. Am. Chem. Soc.* **105**, pp 4481-4483.

32. Ulman, A. (1996). Formation and structure of self-assembled monolayers. *Chem. Rev.* **96**, pp 1533-1554.
33. Watts, J.F. & Wolstenholme, J. (2002). *An Introduction to Surface Analysis by XPS and AES* (Wiley, Chichester, UK).
34. Arakaki, A., Masuda, F. & Matsunaga, T. (2009). Iron oxide crystal formation on a substrate modified with Mms6 protein from magnetotactic bacteria. *MRS Proc.* **1187**, pp KK03-08.
35. Graff, R.A., Swanson, T.M. & Strano, M.S. (2008). Synthesis of nickel–nitrilotriacetic acid coupled single-walled carbon nanotubes for directed self-assembly with polyhistidine-tagged proteins. *Chem. Mater.* **20**, pp 1824-1829.
36. Gupta, M., Caniard, A., Touceda-Varela, A., Campopiano, D.J. & Mareque-Rivas, J.C. (2008). Nitrilotriacetic acid-derivatized quantum dots for simple purification and site-selective fluorescent labeling of active proteins in a single step. *Bioconjugate Chem.* **19**, pp 1964-1967.
37. Le, T.T., Wilde, C.P., Grossman, N. & Cass, A.E.G. (2011). A simple method for controlled immobilization of proteins on modified SAMs. *Phys. Chem. Chem. Phys.* **13**, pp 5271-5278.
38. Lee, J.K., Kim, Y.-G., Chi, Y.S., Yun, W.S. & Choi, I.S. (2004). Grafting Nitrilotriacetic Groups onto Carboxylic Acid-Terminated Self-Assembled Monolayers on Gold Surfaces for Immobilization of Histidine-Tagged Proteins. *J. Phys. Chem. B.* **108**, pp 7665-7673.
39. Thomson, N.H., Smith, B.L., Almqvist, N., Scmitt, L., Kashlev, M., Kool, E.T. & Hansma, P.K. (1999). Orientated, active Escherichia coli RNA polymerase: An atomic force microscopy study. *Biophys. J.* **76**, pp 1024-1033.
40. Zhen, G., Falconnet, D., Kuennemann, E., Vörös, J., Spencer, N.D., Textor, M. & Zürcher, S. (2006). Nitrilotriacetic acid functionalized graft copolymers: A polymeric interface for selective and reversible binding of histidine-tagged proteins. *Adv. Funct. Mater.* **16**, pp 243-251.
41. Lahiri, J., Isaacs, L., Tien, J. & Whitesides, G.M. (1999). A strategy for the generation of surfaces presenting ligands for studies of binding based on an active ester as a common reactive intermediate: A surface plasmon resonance study. *Anal. Chem.* **71**, pp 777-790.
42. Zhang, Y., Du, B., Chen, X. & Ma, H. (2009). Convergence of dissipation and impedance analysis of quartz crystal microbalance studies. *Anal. Chem.* **81**, pp 642-648.
43. Sauerbrey, G. (1959). Verwendung von schwingquarzen zur wägung dünner schichten und zur mikrowägung. *Z. Phys.* **155**, pp 206-222.
44. Rodahl, M., Hook, F., Fredriksson, C., A. Keller, C., Krozer, A., Brzezinski, P., Voinova, M. & Kasemo, B. (1997). Simultaneous frequency and dissipation factor QCM measurements of biomolecular adsorption and cell adhesion. *Faraday Discuss.* **107**, pp 229-246.
45. Krzemiński, Ł., Cronin, S., Ndamba, L., Canters, G.W., Aartsma, T.J., Evans, S.D. & Jeuken, L.J.C. (2011). Orientational control over nitrite reductase on modified gold electrode and its effects on the interfacial electron transfer. *J. Phys. Chem. B.* **115**, pp 12607-12614.

46. Höök, F., Kasemo, B., Nylander, T., Fant, C., Sott, K. & Elwing, H. (2001). Variations in coupled water, viscoelastic properties, and film thickness of a Mefp-1 protein film during adsorption and cross-linking: A quartz crystal microbalance with dissipation monitoring, ellipsometry, and surface plasmon resonance study. *Anal. Chem.* **73**, pp 5796-5804.
47. Q-sense. *QCM-D Technology Note*. <http://www.q-sense.com/qcm-d-technology> 01/12/2011.
48. Shaner, N.C., Patterson, G.H. & Davidson, M.W. (2007). Advances in fluorescent protein technology. *J. Cell Sci.* **120**, pp 4247-4260.
49. Arakaki, A., Webb, J. & Matsunaga, T. (2003). A novel protein tightly bound to bacterial magnetic particles in *Magnetospirillum magneticum* strain AMB-1. *J. Biol. Chem.* **278**, pp 8745-8750.
50. Ahn, T., Kim, J.H., Yang, H.-M., Lee, J.W. & Kim, J.-D. (2012). Formation pathways of magnetite nanoparticles by coprecipitation method. *J. Phys. Chem. C.* **116**, pp 6069-6076.
51. Cornell, R.M. & Schwertman, U. (2003). *The Iron Oxides: Structure, Properties, Reactions, Occurrences and Uses* (Wiley-VCH, Weinheim, DE).
52. Regazzoni, A.E., Urrutia, G.A., Blesa, M.A. & Maroto, A.J.G. (1981). Some observations on the composition and morphology of synthetic magnetites obtained by different routes. *J. Inorg. Nucl. Chem.* **43**, pp 1489-1493.
53. Sugimoto, T. & Matijevic, E. (1980). Formation of uniform spherical magnetite particles by crystallization from ferrous hydroxide gels. *J. Colloid Interface Sci.* **74**, pp 227-243.
54. Galloway, J.M., Bramble, J.P., Rawlings, A.E., Burnell, G., Evans, S.D. & Staniland, S.S. (2012). Nanomagnetic arrays formed with the biomineralization protein Mms6. *J. Nano Res.* **17**, pp 127-146.
55. Galloway, J.M., Bramble, J.P., Rawlings, A.E., Burnell, G., Evans, S.D. & Staniland, S.S. (2012). Biotemplated magnetic nanoparticle arrays. *Small.* **8**, pp 204-208.
56. Reimer, L. & Kohl, H. (2010). *Transmission Electron Microscopy: Physics of Image Formation* (ed. Rhodes, W.T.). (Springer, New York, USA).
57. Brydson, R. (2001). *Electron Energy Loss Spectroscopy* (Taylor & Francis Ltd, Oxford, UK).
58. Andrews, K.W., Dyson, D.J. & Keown, S.R. (1971). *Interpretation of Electron Diffraction Patterns* (Adam Hilger Ltd, London, UK).
59. Goldstein, J., Newbury, D., Joy, D., Lyman, C., Echlin, P., Lifshin, E., Sawyer, L. & Michael, J. (2003). *Scanning Electron Microscopy and X-ray Microanalysis* (Springer, New York, USA).
60. Reimer, L. (1998). *Scanning Electron Microscopy: Physics of Image Formation and Microanalysis* (ed. Lotsch, H.K.V.). (Springer, Berlin, DE).
61. Abramoff, M.D., Magalhaes, P.J. & Ram, S.J. (2004). Image processing with Image J. *Biophotonics Int.* **11**, pp 36-42.

62. Murray, R.W., Miller, D.J. & Kryc, K.A. (2000). Analysis of major and trace elements in rocks, sediments and interstitial waters by inductively coupled plasma-atomic emission spectroscopy (ICP-AES). *ODP Tech. Note.* **29**, pp 1-27.
63. Bragg, W. (1913). The diffraction of short electromagnetic waves by a crystal. *Proc. Cambridge Philos. Soc.* **17**, pp 43-57.
64. Patterson, A.L. (1939). The Scherrer formula for X-Ray particle size determination. *Phys. Rev.* **56**, pp 978.
65. Foner, S. (1959). Versatile and sensitive vibrating-sample magnetometer. *Rev. Sci. Instrum.* **30**, pp 548-557.
66. (Oct. 1997). *MultimodeTM SPM Instruction Manual (4.31ce)* (Digital Instruments Veeco Metrology Group).
67. Horcas, I., Fernandez, R., Gomez-Rodriguez, J.M., Colchero, J., Gomez-Herrero, J. & Baro, A.M. (2007). WSXM: A software for scanning probe microscopy and a tool for nanotechnology. *Rev. Sci. Instrum.* **78**, pp 013705.

Part II
Results
and
Discussion

Chapter 3

Mms6 and Patterning onto Surfaces

In this chapter the optimisation of the expression and purification of the Mms6 protein, and the possible structure of the protein both in the absence and presence of iron, is explored. Then the attachment of Mms6 to patterned surfaces is optimised in preparation for the formation of biotemplated arrays of MNPs.

3.1 Protein Expression and Purification

The expression and purification of a number of differently tagged recombinant forms of Mms6 were optimised. Mms6 is a small protein (see Figure 3.1), and the *N*-terminal region contains mainly hydrophobic residues (e.g. leucine, *L*; isoleucine, *I*; and valine, *V*). Both the hydrophobicity and small size make the Mms6 protein difficult to express and purify in a soluble untagged (mature) form as it is likely to aggregate when in solution. The *C*-terminal region of Mms6 is rich in acidic residues (e.g. aspartic acid, *D*; and glutamic acid, *E*) and is hydrophilic, which improves the solubility of Mms6.

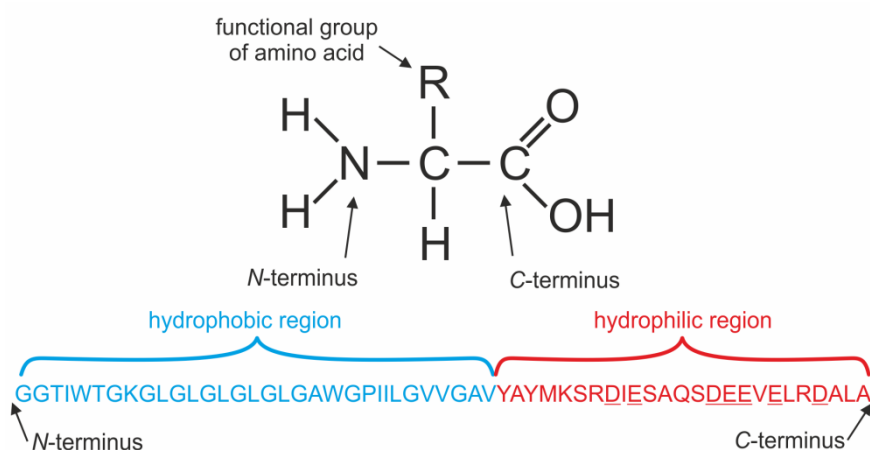


Figure 3.1. Stick diagram of an amino acid and the primary amino acid sequence of Mms6. The amino acid has an amino group at one end (the *N*-terminus) and a carboxylic acid group at the other end (the *C*-terminus). To assemble a protein, the amino acids are linked by peptide bonds between the carboxylic acid and amine groups. There are ≈ 20 different amino acids used in nature,¹ which have different 'R' groups that give the amino acids their different properties (e.g. hydrophobic/hydrophilic, acidic, basic, aromatic, etc). Below this is the primary amino acid sequence of Mms6,² with the region consisting of mainly hydrophobic residues highlighted in blue. The region consisting of mainly hydrophilic residues is highlighted in red, and acidic amino acid residues are underlined.

3.1.1 Mms6*

A high yield of recombinant Mms6 was achieved by inserting the maltose binding protein at the *N*-terminus of the Mms6 protein, as this tag increases the solubility of recombinant protein constructs.³ An octahistidine tag was also inserted at the *N*-terminus of the recombinant construct to create a vector for the expression of His₈-MBP-Mms6 in *E. coli*. The octahistidine sequence allowed the His₈-MBP-Mms6 to be isolated from the expressed protein mixture using immobilised metal ion affinity chromatography.^{4,5} During IMAC, the His₈-tag chelates with Co²⁺ on nitrilo-triacetic acid resin (Co²⁺-NTA), thus isolating the tagged protein from a mixture. Once isolated, the His₈-MBP-tag was cleaved from the mature Mms6 sequence using the tobacco etch virus protease.⁶ As there is a proteolytic cleavage site for TEV between the His₈-MBP and the Mms6, incubation of the expressed and purified His₈-MBP-Mms6 with His₈-TEV releases the Mms6 sequence from the tags. The cleaved mixture was passed through the rinsed Co²⁺-NTA column to remove the tags and protease from the mature Mms6 protein sequence.

Figure 3.2⁷ shows a tricine SDS-PAGE⁸ analysis of the resultant purified fusion protein, the cleaved protein mixture and the isolated mature Mms6. Using this method to produce the protein ensures a yield of ≈0.5 mg of Mms6 per 400 mL culture. The tricine SDS-PAGE analysis shows that the Mms6 produced by this method contains few impurities (Figure 3.2). The Mms6 was dialysed into water and concentrated so it could be used in mineralisation reactions (see Chapters 4 and 5). The theoretical pI of the mature Mms6 sequence (see Figure 3.1 for sequence) is 4.72, and its mass 6.4 kDa,⁹ which is relatively acidic and small for a protein. The size and pI of mature Mms6 may be important for the structure and/or biomineralisation function of the protein.

* Genetic manipulation and optimisation of expression and purification in collaboration with A. Rawlings, University of Leeds.

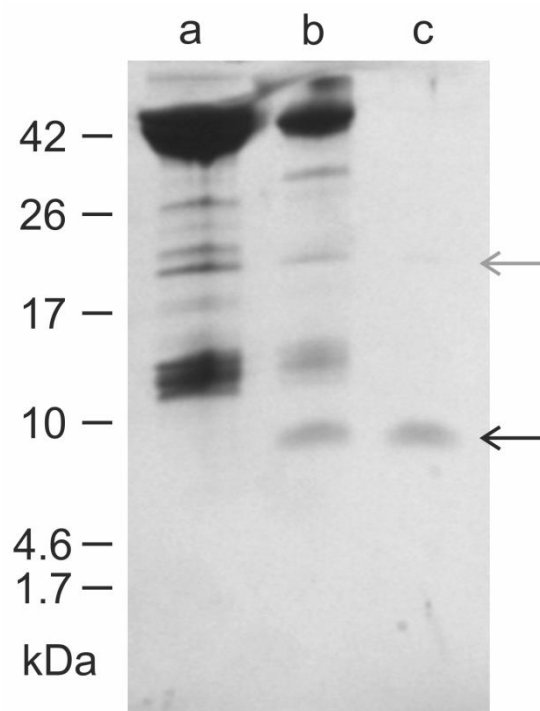


Figure 3.2. Tricine SDS-PAGE analysis of Mms6 expression and purification, from Galloway *et al.* (2012a).⁷ Marked on left are positions of low molecular weight markers, and their weight in kDa. Lane (a) contains the eluted fractions from the IMAC column (dense band above 42 kDa marker is His₈-MBP-Mms6 (theoretical molecular weight 49.2 kDa). Lane (b) is the protein mixture after His₈-TEV proteolysis, the Mms6 band appears below the 10 kDa marker (marked with an arrow). Lane (c) is the protein remaining after passing the cleaved mixture through the Co²⁺-NTA column. A strong Mms6 band (black arrow, theoretical molecular weight 6.4 kDa) appears below the 10 kDa marker, with a faint band (grey arrow) just visible that may be an oligomer of Mms6.

3.1.2 His₆-Mms6

N-terminally tagged His₆-Mms6 was expressed and purified to use in a number of experiments, as there are fewer stages in the purification of this construct. Therefore His₆-Mms6 is cheaper and simpler to synthesise than Mms6. One 400 mL culture pellet produced ≈4 mg His₆-Mms6 when purified and dialysed into water, so it is higher yield than the Mms6 purification shown above. The Western Blotted and Coomassie stained tricine SDS-PAGE (see Figure 3.3) show the final product is quite pure as few impurities appear on the gel. The theoretical pI of the His₆-Mms6 construct (sequence shown in Section 1.4.5) is 6.34, and the mass 8.4 kDa.⁹ This is a larger size and more pH neutral than the mature Mms6 sequence, so the templating ability of the protein may be altered by the addition of a tag. Therefore, particles synthesised by RTCP in the presence of His₆-Mms6 were compared to those synthesised without protein, and with the mature Mms6 protein, to see if the presence of the His₆-tag alters the biotemplating ability of the protein (see Section 4.3).

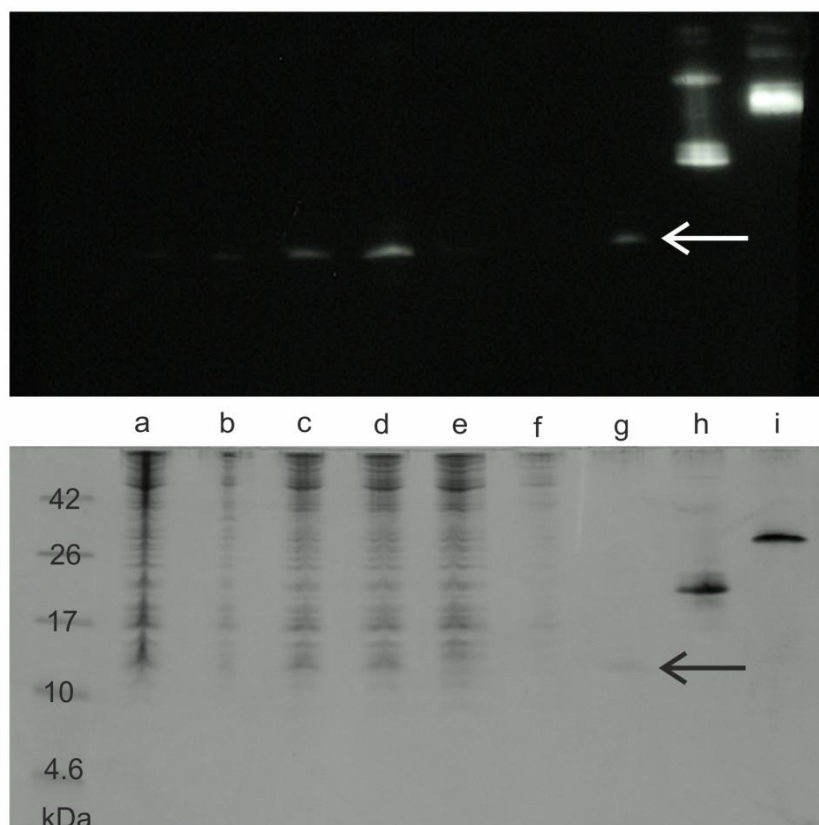


Figure 3.3. Western blot (upper image) and Coomassie stained SDS-PAGE (lower image) analysis of His₆-Mms6 purification. On left of gel are low molecular weight markers (non-fluorescent). Lane (a) is the total cell lysate; (b) the resuspended insoluble fraction (pellet); and (c) the soluble fraction (supernatant) of the centrifuged cell lysate. Lane (d) is the filtered supernatant; (e) the supernatant after incubation with Ni²⁺-NTA (i.e. IMAC column flow-through); and (f) is a sample of the column wash. Lane (g) is the eluted His₆-Mms6 (theoretical weight 8.4 kDa, marked with arrows); (h) is His₆-SUMO-Mms6; and (i) His₆-eGFP. Lanes (h) & (i) are positive controls for the anti-6xpolyHis Mab HRP antibody.

In a trial cleavage experiment, thrombin was incubated with the His₆-Mms6 protein in thrombin cleavage buffer (2.5 mM CaCl₂, 20 mM tris, 150 mM NaCl) overnight to try to cleave the affinity tag from the Mms6 protein sequence. Unfortunately, the SDS-PAGE analysis of the cleavage trial became too destained to clearly image the protein bands. When viewed before the destaining was completed, the thrombin appeared to be able to cleave a large proportion of the His₆-tag from the Mms6 protein sequence. This experiment has not been scaled up and repeated because there was no affinity tag on the thrombin, so it could not be removed easily from the cleaved protein mixture. However, if the thrombin protease could be separated from the cleaved mixture (e.g. using an affinity tag on the thrombin) the cleaved tags and the protease could be removed to yield the pure Mms6 protein. This would provide an alternative, and possibly simpler route to synthesising untagged Mms6 protein.

The auto induction method was also used to try and produce a number of differently tagged recombinant Mms6 proteins.* A His₈-Mms6 construct with a TEV protease cleavage site between the tag and the mature Mms6 sequence was successfully produced. However, it was not possible to cleave the tag from the Mms6 using the TEV protease, even when very large concentrations of TEV was incubated with the His₈-Mms6. This is despite the TEV protease cleaving the His₈-MBP-Mms6 tags well to liberate the mature Mms6 sequence (see Section 4.1.1). The SUMO tag has been shown to enhance solubility, yield and purity of difficult to express fusion proteins.¹⁰ The His₆-SUMO-Mms6 expressed and purified well, but the SUMO protease was unable to cleave the His₆-SUMO tag from the fusion protein.

Mms6 is likely to self-assemble via hydrophobic interactions between the *N*-terminal regions of the protein when in aqueous solution. It may be that the smaller His₈-Mms6 (9.6 kDa) and His₆-SUMO-Mms6 constructs (21.5 kDa) are still able to self-assemble in this manner, but the larger His₈-MBP-Mms6 construct (49.2 kDa) is not able to. In self-assembling, the accessibility of the cleavage recognition sites between the tags and the Mms6 sequence (e.g. the His₈-Mms6 and His₆-SUMO-Mms6) may be blocked. This means that the SUMO protease and TEV protease are unable to recognise their respective cleavage sites, so they are unable to cleave the tags to yield the mature Mms6 protein. In the MBP tagged construct (His₈-MBP-Mms6) the tag is much larger and extremely soluble. This may disrupt the self-assembly at the hydrophobic *N*-terminal region of Mms6, which would allow the TEV protease to access the cleavage site and to remove the tags from the mature Mms6 sequence. Auto induction of a His₈-MBP-Cys-Mms6 construct was used to try and produce a cysteine tagged Mms6 (Cys-Mms6) to facilitate protein immobilisation directly onto gold. It was found that the *N*-terminally cysteine tagged Mms6 precipitated from solution when the solubility enhancing His₈-MBP tag was cleaved from the Cys-Mms6 sequence. The work to produce these tagged proteins to facilitate MNP patterning on surfaces is still ongoing, as they may offer better alternatives to immobilise the Mms6 protein on patterned surfaces to form biotemplated magnetic arrays.

* Genetic manipulation and optimisation of expression and purification in collaboration with A. Rawlings, University of Leeds.

3.2 Protein Structure and Activity

The structure of Mms6 is not currently well understood. This means it is not clear how Mms6 is able to template highly crystalline cubo-octahedral magnetite with a narrow grainsize distribution. As it is a small protein, with hydrophilic and hydrophobic motifs, it is difficult to achieve the high levels of purity required for structural analysis. For example, the crystallographic protein structure has not been solved, as it has not yet been possible to produce the high purity crystals of Mms6 that would be necessary for diffraction studies. As there are no proteins with a similar primary amino acid sequence that have been solved, reliable computational modelling of the structure of Mms6 based on the primary amino acid sequence alone is also difficult.

An iron binding assay was completed to try to quantify how much iron from solution could be bound by Mms6. Mms6 contains one tryptophan residue (W), which has been used to probe possible conformational changes of Mms6, both with and without ferric iron. CD spectra were recorded and fitted to estimate the different chirally optically active secondary structures (e.g. β -sheet, α -helix, etc) present in a sample of Mms6, in the presence and absence of ferric citrate. The accessibility of the *N*-terminal poly-histidine tag was assessed after magnetic particle synthesis. This is because the tag must be accessible on the particle if it is to be used to attach pre-formed MNPs to a functionalised, patterned surface.

3.2.1 Model Structure of Mms6

As the crystal structure for Mms6 has not been solved, and there are no known homologues that have been solved either, a prediction of the protein structure was made* based on the primary amino acid sequence using Quark.¹¹ This model can then be viewed in programs that are able to display crystallographic structural files, such as PyMOL¹². The modelled prediction can then be compared and contrasted with the structural information extracted from other techniques, such as CD (see Section 3.2.2.3).

The Quark model predicts that the *N*-terminal region of Mms6 is hydrophobic, which was expected from the high concentration of hydrophobic amino acid residues in this section (Figure 3.4). This also predicts that these residues should form a small β -sheet like structure. This may help to incorporate the Mms6 protein into the magnetosome membrane *in vivo*. It may also help constrain the *C*-terminal region and facilitate iron binding and/or magnetite mineralisation. The *C*-terminal region is predicted to form two small helices, which are folded together to position acidic

* Computational model requested by J. Bramble, University of Leeds.

residues in close proximity with a methionine (sulfur containing) amino acid. This appears to form a pocket, which would be an ideal binding site for positively charged ions, such as ferrous or ferric iron. There are other regions that are also rich in acidic residues around the C-terminal helices, which may also bind iron.

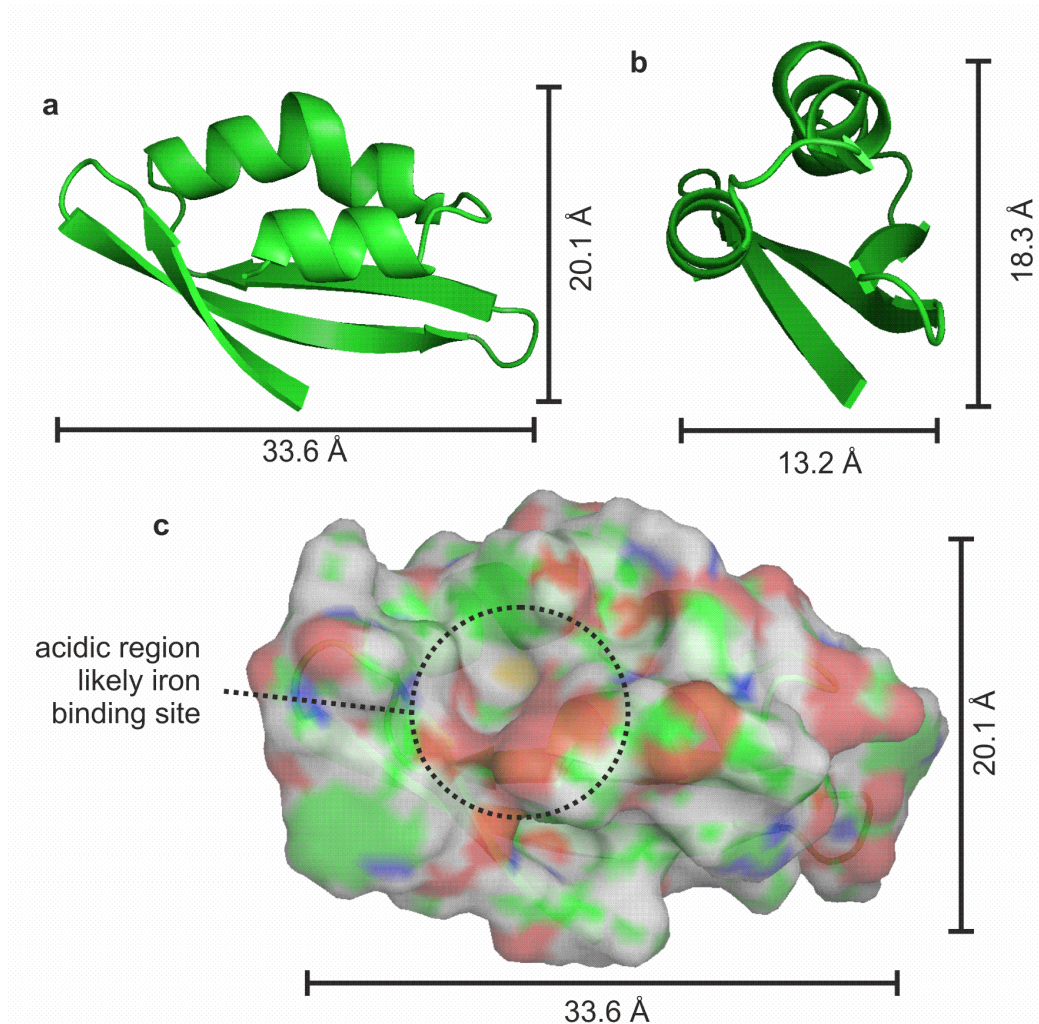


Figure 3.4. Cartoon and surface of model based on the Mms6 primary amino acid sequence. (a & b) Cartoons of predicted Mms6 structure from two different viewpoints to show the (a) long and (b) short axes of the protein. Arrows represent β -sheet type structures, and are mainly situated in the *N*-terminal region. Unstructured or turn regions are represented by strings. Helical structures appear mainly towards the *C*-terminus. (c) Surface of the modelled protein (hydrogen is grey, carbon is green, oxygen is red, nitrogen is blue and sulfur is yellow). The model predicts that there is a pocket towards the *C*-terminus which is surrounded by acidic residues (circled), and the only sulfur containing residue in Mms6. Structural model produced using Quark¹¹ and images created in PyMOL.¹²

3.2.2 Aqueous Iron Binding to Mms6

3.2.2.1 Chemical Detection of Iron Bound by Mms6*

De-metallicised His₆-SUMO-Mms6 protein buffered with TBS at pH 7.4 was incubated with different concentrations of ferric citrate. As this is not a standard assay, these data were collected to establish good working concentrations for the amounts of protein and iron to use for studying aqueous iron binding to proteins in future work. The His₆-SUMO-Mms6 protein remained stable in the presence of ferric citrate up to a molar ratio of protein to iron of $\approx 1:25$. Higher molar ratios of 1:30 and above caused the protein to precipitate from solution. Figure 3.5 shows the luminescence change of the luminol reagent due to the iron bound by the His₆-SUMO-Mms6 protein. Different amounts of iron citrate were added to the protein to try and determine how much iron the His₆-SUMO-Mms6 protein was able to bind. These data show that the protein was able to bind an increasing amount of iron as more ferric citrate was added. At low molar ratios, there is a rapid increase in the amount of iron bound by the Mms6 protein, which levels off as the higher concentrations of iron are reached. When a control protein that should not preferentially bind iron (His₈-eGFP) was used, there was very little bound iron detected (luminescence $\approx 1 \times 10^{-6}$). This shows that the iron detected from the His₆-SUMO-Mms6 is unlikely to be due to iron binding to the histidine tag, so can be attributed to iron binding by the Mms6 section.

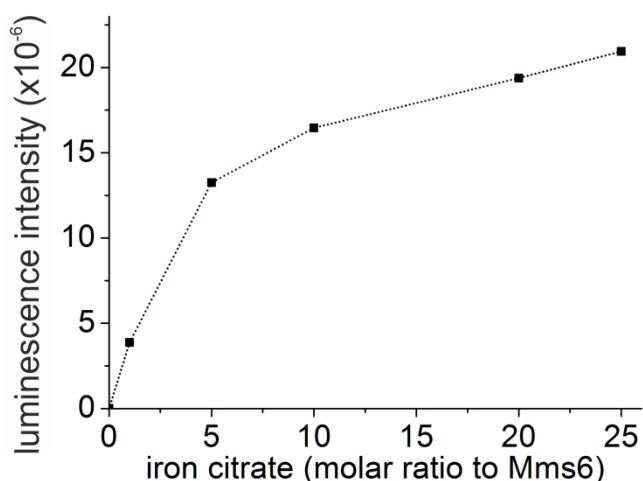


Figure 3.5. Luminescence due iron bound by His₆-SUMO-Mms6 for different concentrations of iron added to the protein.

A standard curve of iron citrate was prepared to try and convert this luminescence into a molar concentration of iron bound by the protein (Figure 3.6). It was not possible to fit the curve with a simple function to convert luminescence recorded to a concentration of iron. This may be because the luminescence appears to saturate

* Iron binding data courtesy of S. Corbett, University of Leeds.

the detector and/or the luminol reagent at the higher iron concentrations. Another factor is that the dissociation of ferric iron from citrate varies with concentration and pH, thus the activity of iron in solution is not directly proportional to the concentration of iron citrate added to the assay.¹³ Also, as it was not expected that all of the iron added to the His₆-SUMO-Mms6 protein would be bound for the higher concentrations, the standard curve was only recorded for values up to 1 mM iron. It was found that the best fit to the standard iron curve data was complex (see equation on Figure 3.6). Unfortunately, it was not possible to rearrange this fit to allow the luminescence to be converted to a concentration of iron. However, the curve can be used to estimate the amount of iron bound by the His₆-SUMO-Mms6 protein for the lower concentrations of iron used.

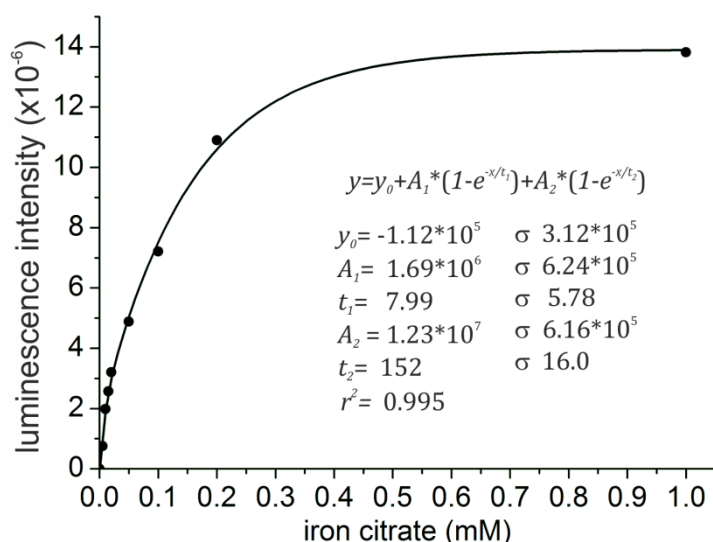


Figure 3.6. Plot of concentration of ferric iron citrate against the luminescence due to the reaction of luminol with iron. Equation on graph is the best curve fit from Origin, and is the ExpAssoc non-linear curve fit function. As can be seen, the luminescence rapidly reaches a plateau at higher iron concentrations.

When iron is added to the His₆-SUMO-Mms6 in a 1:1 molar ratio (110 μ M), the standard curve shows that the protein binds \approx 32 μ M of iron. From the 1:5 ratio, where 550 μ M iron is added to 110 μ M His₈-Mms6, the standard curve indicates that 615 μ M iron is detected after binding to the protein, which is more than was added to the protein. The higher molar ratios of iron to protein produced luminescence that was well above that recorded to create the standard curve, so the luminescence cannot be converted into a concentration of iron for these measurements using this curve. Also, as the two values that can be estimated from the standards are at the opposite limits of the standard curve, the concentration of iron may not be very accurately determined using the curve.

These preliminary data indicate that His₆-SUMO-Mms6 protein is able to bind the majority (if not all) of the iron from a solution with a protein to iron ratio of 1:5. To determine if His₆-SUMO-Mms6 is able to efficiently bind even higher proportions of iron, it may be necessary to create a more detailed standard curve, and to use lower concentrations of protein and/or serial dilution of the bound iron. This would allow the amount of iron that can be bound by physiologically buffered His₆-SUMO-Mms6 to be determined. It may also allow the effect of temperature changes, varying pH and point mutation of the Mms6 sequence to be studied for iron binding to the Mms6 protein. This may require the use of the untagged Mms6 sequence, as the SUMO tag is designed to enhance solubility, this tag may alter the effect of iron binding on the Mms6 protein.

3.2.2.2 Tryptophan Fluorescence of Mms6*

Tryptophan (w) is a fluorescent amino acid, and the peak position and intensity of emission of this fluorescence is extremely sensitive to the conditions in the localised region around the residue. If the local environment around the residue is changed by a protein altering its structure, the fluorescence signal from tryptophan should change. This means that any conformational changes due to ligand binding may be detected by quenching or shifting of the fluorescence intensity from tryptophan. Mms6 contains one tryptophan residue (highlighted in Figure 3.7), so fluorescence intensity measurements were recorded for His₈-Mms6 at $\lambda=340$ nm, which is extremely close to the peak in emission of tryptophan ($\lambda=348$ nm). The absorbance was also recorded at the excitation and emission wavelengths used, so the readings could be corrected for the inner filter effect (Equation 2.1). For these experiments, His₈-Mms6 was used, as mature Mms6 was not available. The His₈-tag is smaller than the His₆-SUMO-tag, and is not designed to increase the solubility of the protein. Therefore, the folding and assembly of the His₈-Mms6 in solution should be closer to that of pure Mms6 than His₆-SUMO-Mms6 construct.

* Tryptophan fluorescence data recorded in collaboration with A. Rawlings, University of Leeds.

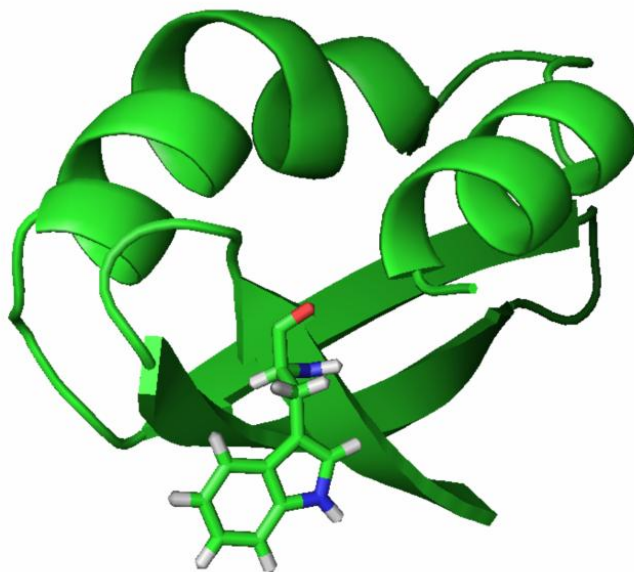


Figure 3.7. Cartoon of Mms6 model to show the position of the tryptophan residue. The tryptophan residue is in the *N*-terminal region, and appears to be folded close to many hydrophobic residues within the Mms6 predicted structure. Structural model produced using Quark¹¹ and image created in PyMOL.¹²

It was found that it was not possible to obtain reliable readings for the tryptophan fluorescence. There appeared to be no correlation in the fluorescence intensity levels with differing protein concentration or upon the addition of iron. In some cases, the intensity of the fluorescence signal from the buffer blank, a water blank or an empty cell was higher than from the samples containing the protein. Also, the fluorescence intensity generally decreased over time, whether buffer, protein or iron was present in the sample or not. As such, a number of scans were recorded on a single sample spectrofluorimeter (e.g. QuantaMasterTM, PTI) with excitation at $\lambda=290$ nm and emission recorded in 1 nm steps between 310 nm and 410 nm. Again, the peak intensity in emission seemed to randomly change in intensity and position, generally decreasing over time, whether iron citrate was added to the protein or not.

In His₈-Mms6, the tryptophan residue is in the hydrophobic part of the protein, towards the *N*-terminus. The predicted structure of Mms6 indicates that the aromatic rings of the residue should be displayed on the outer surface of the folded protein (Figure 3.7). However, if the tryptophan residue was rotated through 180°, the aromatic rings would be buried inside the hydrophobic area and be in close proximity to the acidic residues in the *C*-terminal section of the protein. The hydrophobicity could significantly shift the peak in emission, and the proximity to the acidic residues could also quench the fluorescence from the aromatic amino acid.^{14,15} If the His₈-Mms6 protein does self-assemble via the hydrophobic residues in the *N*-terminal region, this could further enhance any quenching of the signal from the tryptophan. As the signal from the tryptophan may be extremely low, this could

explain why background measurements of empty cells, water and buffer sometimes showed higher fluorescence intensity than if the protein was present, as it may be within error for the system measured. Therefore, tryptophan fluorescence is not well suited to monitoring iron binding to His₈-Mms6 (and probably pure Mms6), as the signal intensity is not high enough to be easily monitored.

3.2.2.3 Circular Dichroism of Mms6*

CD measurements were taken for His₈-Mms6 protein at various concentrations. It was found that a high protein concentration (150 μM) was necessary to obtain a clear spectrum (see Figure 3.8). When a small amount of ferric citrate was added to create a $\approx 1:1$ ratio of protein to iron (160 μM , 4.0 μL of 10 mM ferric citrate added to 250 μL protein), there was a change in the spectrum recorded using CD. However, the protein rapidly began precipitating from the solution, which could have caused a loss in signal intensity. The His₆-SUMO-Mms6 remained stable in solution up to a molar ratio of 1:25 protein to iron during the iron binding assay (Section 3.2.2.1). This difference between the His₆-SUMO-Mms6 and the His₈-Mms6 constructs shows that the SUMO tag does significantly enhance the solubility of the protein in the presence of iron. As the His₈-Mms6 construct only has a very small tag, it is likely that it behaves in a very similar manner to the untagged Mms6. Unfortunately, the untagged Mms6 protein was not for this study due to the SUMO and TEV proteases being unable to cleave the tags from the smaller Mms6 constructs (see Section 3.1.2).

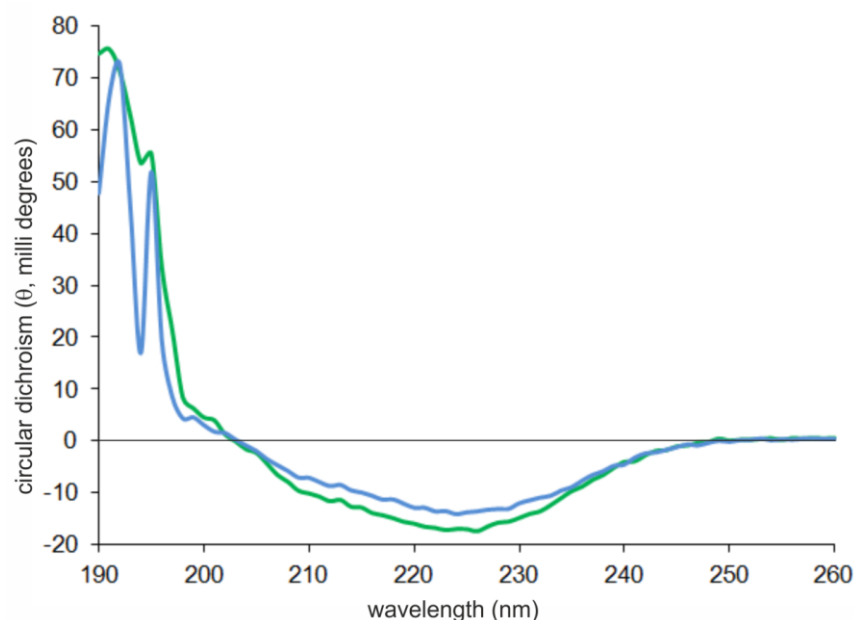


Figure 3.8. Circular dichroic spectra for His₈-Mms6 (green) and His₈-Mms6 with iron citrate (blue). There is a change in the spectrum when iron is added in a 1:1 molar ratio. These spectra have been fitted to extract protein structures using DichroWeb,¹⁶ see Table 3.1.

* CD data recorded in collaboration with A. Rawlings, University of Leeds.

Fitting of these spectra* using DichroWeb¹⁶ (see Table 3.1) determined that the CD shows far less helical structures than are found in the predicted model, with an increase in the stranded and unordered parts of the spectrum. As the computational model is designed to show a crystallographic structure, and CD is recorded using a dissolved, hydrated protein, it is not surprising that there are large differences in the structure of the Mms6 protein determined by these two methods. CD is unable to 'see' non-optically active chiral structures, the buffer used can also absorb a lot of light from CD, and it is a low resolution technique when compared to crystallography.¹⁷ However, as X-ray diffraction requires crystals of protein, it may be unable to predict how the structure of protein in solution would appear, and it is unable to resolve any dynamic areas of a proteins, as these do not diffract. As the structural model of Mms6 has been produced using a computational, any structures predicted using this model may be even further from the solvated structure of Mms6 when in solution.

Table 3.1. Summary of Mms6 protein structure based on fitting CD spectra using DichroWeb.¹⁶ Structure names: helix for helical structures; strand for sheet-like structures; turn for bends or turns; and unordered for structures that are not well defined in CD, i.e. are not chirally optically active. The values for the predicted model are based on the structure predicted by the model and not on fitting of a CD spectrum. Normalised root mean square standard deviation of His₈-Mm6 fit is 2.7%, and is 7.7% for the spectrum taken with iron present.

structure	predicted model	His ₈ -Mms6	His ₈ -Mms6 + Fe ³⁺
helix (%)	22	9	9
strand (%)	26	35	36
turn (%)	10	24	23
unordered (%)	42	32	32

There was a small change in the structures present when the iron citrate was added, with a decrease in turn (-1%) and an increase in stranded structures (+1%). The protein began precipitating from solution when the ferric citrate was added in a 1:1 molar ratio. This shows that the addition of iron causes the His₈-Mms6 protein to aggregate enough to become insoluble. This level of aggregation with only a small amount of iron may be due to the extremely high protein concentration required to obtain a good CD spectrum. When this is coupled with the large amounts of iron that Mms6 is able to bind, it may cause the protein to rapidly precipitate in the presence of iron. As the protein began precipitating as soon as iron was added, it was not possible to obtain a good CD spectrum for His₈-Mms6 with iron. This is illustrated by the increase in the error on the fitted spectra for the His₈-Mms6 + Fe³⁺

* CD fitting using DichroWeb courtesy of A. Rawlings, University of Leeds.

sample (7.7%). This means that the changes in the structure from fitting the CD spectrum after the addition of iron may not be reliable. The precipitated protein may scatter more of the beam, and the precipitated protein settles from the solution, so much of it may not be analysed by the CD beam passing through the sample.¹⁷ This removal of protein by precipitation could explain the similarities in the two spectra taken in the presence and absence of iron, as it would only be the un-precipitated Mms6 that would be analysed by the beam.

3.2.2.4 The Structure and Function of Mms6

His₈-Mms6 has a very similar structure to the untagged Mms6 protein, so it is likely that its structure and function, both in the presence and absence of iron, are also very similar. The high levels of iron that can be bound by the His₆-SUMO-Mms6 construct demonstrates the high affinity that the Mms6 protein has for ferric iron. However, the absence of the SUMO tag shows that iron also causes the His₈-Mms6 to precipitate from solution. Fitting of the CD spectra indicate that the His₈-Mms6 becomes more stranded as some of the turn structure is lost upon iron binding. It may be that the structure containing more turns facilitates the initial binding of Fe³⁺, which is followed by a conformational change that leads to the precipitation of the protein from an aqueous solution in the presence of iron. The more stranded structure could help the Mms6 protein to form the solid magnetite from the iron bound from solution. However, as these changes are well within the error of the DichroWeb fits to the data, there may not be any significant change in the structure of Mms6 upon the binding of iron.

The Mms6 protein firmly binds to magnetosome MNPs, which may be specific to certain crystallographic faces to template the cubo-octahedral morphology of the MNPs. The cubo-octahedral particles synthesised in the presence of Mms6 by Amemiya *et al.* (2007)¹⁸ are bounded by [111] and [100] faces (Figure 1.15). In the absence of Mms6 protein, the system forms octahedra bounded by [111] faces. It is likely that the Mms6 protein binds to the [100] faces to direct the morphology of the magnetite particles, and prevents growth in the [111] direction. The evidence from the CD suggests that this may involve a slight conformational change, from a structure containing more turns to a slightly more stranded structure, which could allow the Mms6 protein to bind to the [100] type magnetite crystallographic planes. In the study of Arakaki *et al.* (2010)¹⁹ a peptide based on the C-terminus of Mms6 was shown to direct the morphology of magnetite particles towards the same cubo-octahedral morphology formed by the mature Mms6 protein. Therefore, it is likely that iron binding and conformational changes upon binding to magnetite (maybe to the [100] crystal faces) are located around the C-terminal section of Mms6.

Short peptide sequences that preferentially bind to iron oxides and magnetite have been identified using biopanning. Biopanning involves the use of a randomised peptide library, which displays many different short peptide sequences on the surface of a cell or a virus.²⁰⁻²² When the library is exposed to a target, such as magnetite nanoparticles, cells or viruses displaying peptide sequences that bind to the particle surface are collected, and those that do not bind are rinsed away.²³ The DNA/RNA that encodes for the peptides that became bound to the particles are then amplified, before this new library is re-exposed to the desired target. This is then repeated for a number of rounds, as this allows those sequences that bind more strongly to the target to out-compete the weaker binders, and thus become enriched in the sample.

Mutation of the strongly bound sequences can also be used to direct the evolution of the peptide sequences towards those that have an even higher affinity for the target. Brown (1992)²⁰ and Barbas *et al.* (1993)²⁴ identified the sequence RSKLR as binding to magnetite using biopanning. The Mms6 protein contains a similar motif of 'KSR' (see Figure 3.9) which may be involved in binding the protein to the nanoparticle surface. In the Mms6 sequence, the KSR sequence is bounded by the sulfur containing methionine on one side and an aspartic acid on the other, therefore it is in close proximity to the proposed binding pocket labelled in Figure 3.9. Unfortunately, the authors do not specify what type of magnetite MNP they used as the target material for the biopanning, or if they tried to avoid surface oxidation of the MNPs, so it is unclear if this motif binds to a specific magnetite crystallographic face, or to oxidised magnetite MNP surfaces.

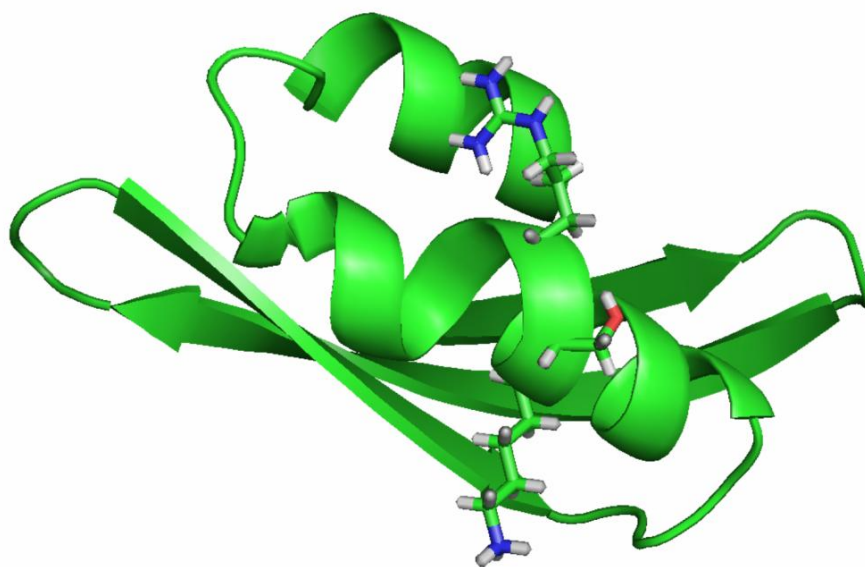


Figure 3.9. Cartoon of Mms6 model to show the position of the 'KSR' motif. This sequence of amino acids may be involved in binding the Mms6 protein to the [100] surface of a magnetite nanoparticle. Structural model produced using Quark¹¹ and image created in PyMOL.¹²

3.2.3 Accessibility of His₆-tag on Pre-formed MNPs

It has been assumed that it is the C-terminal section of Mms6 that interacts with the magnetite surface and is involved in biotemplating cubo-octahedral magnetite particles, and that the N-terminus integrates the protein into the hydrophobic magnetosome lipid membrane.^{2,18,19,25,26} The peptide based study by Arakaki *et al.* (2010)¹⁹ demonstrated that the N-terminus of Mms6 is not essential for the biotemplating control of this protein. Therefore, for this project, methods of immobilising the Mms6 protein via the N-terminus (either before or after MNP formation) have been sought. However, this assumes that the N-terminus of Mms6 is still accessible after MNP formation.

The accessibility of the N-terminus of Mms6 after particle formation was assessed using an immunological assay. MNPs were synthesised using RTCP in the presence of Mms6 and His₆-Mms6, and thoroughly washed. They were incubated with an antibody that binds to hexahistidine, and is able to catalyse a change in the colour of TMB-Ultra reagent from clear to blue. Iron is also able to catalyse this colour change in TMB-Ultra, so the Fe₃O₄ particles synthesised without the histidine tag also caused the indicator to change colour. The absorbance of the indicator after incubation with the Mms6 templated MNPs was 0.657 at a wavelength of $\lambda=355$ nm. However, there was a much stronger signal from the His₆-Mms6 MNPs, with an absorbance of 1.093. This shows that the N-terminal His-tag on the His₆-Mms6 templated MNPs is able to conjugate the antibody, and thus further catalyse the colour change in the indicator, so is accessible on the particle surface. In the future, it may be possible to create a standard curve using the antibody, and estimate the concentration of antibody (and therefore accessible His-tags) on the particle surfaces. However, it may be necessary to reduce the background signal from the iron catalysis of the TMB-Ultra reagent, possibly by incubating the particles with the reagent for a shorter period of time.

3.3 Protein Attachment to Self-Assembled Monolayers

A number of SAMs were investigated, both for protein attachment and to resist non-specific protein binding. Some methods used to fabricate the arrays of magnetic particles require the patterned SAMs to be heated in aqueous solutions to 80-90°C (see Chapter 5). Many SAMs of alkanethiols on gold are not thought to be stable upon heating above $\approx 70^\circ\text{C}$.²⁷ Therefore, the stability of a range of SAMs after heating to 90°C for four hours in water was also investigated.

There are a number of methods that can be used to immobilise proteins onto surfaces. Two of these methods were attempted, chemical binding of the protein directly to an appropriately functionalised SAM, and Ni²⁺-NTA functionalisation of a SAM to immobilise protein using histidine-Ni²⁺ chelation. PEG-OH SAMs were used to functionalise areas to resist biofouling, as this is recommended to resist non-specific protein binding.²⁷⁻³⁶ Finally, the patterning of SAMs using micro-contact printing and subsequent protein attachment was studied using AFM and fluorescent microscopy.

3.3.1 EDC/NHS binding of Protein to a SAM

EDC/NHS can be used to directly immobilise proteins onto patterned surfaces by chemically linking an amine on the protein to a carboxylic acid surface (see Section 1.5.3.2). However, it can be difficult to ensure that the protein is immobilised in a particular orientation. By buffering a protein to about 1 pH point below its pI, a wide range of proteins have been successfully immobilised by their *N*-terminal amine.³⁰ Therefore, EDC/NHS should be able to selectively bind Mms6 at its *N*-terminus when buffered appropriately. As the active portion of the Mms6 protein is thought to be the *C*-terminal section, binding the protein via its *N*-terminus should not prevent Mms6 from biomineralising magnetite on the patterns *in situ*. In this section, protein attachment to surfaces is monitored using QCM-D and modelled using the Qtools software. SAMs are characterised using XPS, and also tested for stability (before and after heating in water) by ellipsometry and water contact angle measurements.

3.3.1.1 Monitoring Protein Attachment to SAMs using QCM-D

A number of SAMs were prepared to test for protein binding affinity or protein binding resistance (with His₆-TEV as a proxy for Mms6) using QCM-D. His₆-TEV was used to preserve the stock of Mms6. Also, as His₆-TEV is larger than Mms6 (His₆-TEV ≈28.6 kDa, Mms6 ≈6.4 kDa)⁹ it should produce a larger negative frequency shift when bound to the SAM on the QCM-D crystal, and thus be easier to detect in QCM-D. Firstly, His₆-TEV was passed over different SAM surfaces in a physiological buffer (10 mM HEPES buffer, pH 7.2) to see which surfaces resisted non-specific protein binding well. Figure 3.10 shows four SAMs tested to resist protein binding (in order of increasing hydrophobicity), 11-mercaptoundecanoic acid (MUA); 11-mercaptoundecanol (MU-OH); octadecane thiol (C18); and 1H,1H,2H,2H, perfluorodecane thiol (PFDT).

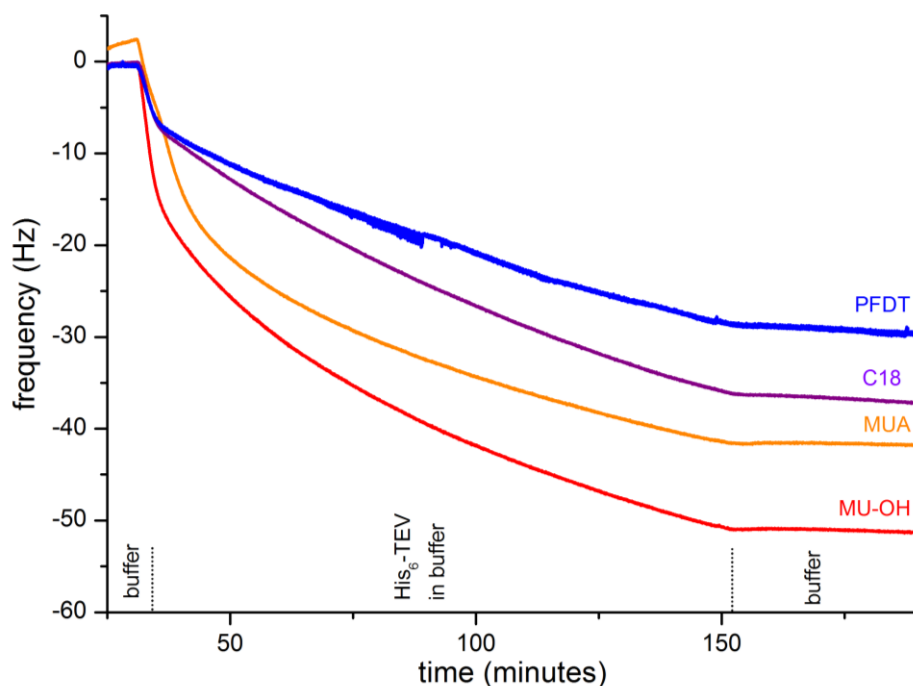


Figure 3.10. Frequency shift during non-specific binding of proteins to SAMs, monitored with QCM-D, only 9th overtone shown for clarity. Largest negative shift indicates greatest mass of bound protein to surface (see Table 3.2). Traces shown are PFDT (blue); C18 (purple); MUA (orange); and MU-OH (red), larger negative frequency shifts indicate a greater mass bound to the surface.

In all cases, some protein bound to the SAM surfaces, with the most binding to the MU-OH ($\approx 914 \text{ ng cm}^{-2}$) and least to the very hydrophobic PFDT ($\approx 525 \text{ ng cm}^{-2}$), see Table 3.2. Hydrated His₆-TEV can be assumed to be slightly larger than the size of His₆-TEV calculated from its' crystal structure³⁷⁻³⁹ (see Figure 3.11). From the crystal structure, each single molecule of correctly folded, hydrated His₆-TEV should take up between $\approx 12.9 \text{ nm}^2$ and 18.9 nm^2 depending on the orientation of the protein when bound to the surface. The mass of a His₆-TEV molecule is $\approx 27 \text{ kDa}$,^{9,37} which is multiplied by 1.25 to allow for the mass of water in hydrated His₆-TEV (33.8 kDa). These values can be used to convert the mass adsorbed to the surface of the QCM-D crystal to a molar value per square centimetre, see Section 2.4.2.1.

Table 3.2. Modelling fits to data from QCM-D shown in Figure 3.10. Sauerbrey mass assumes the protein layer is laterally consistent and rigid. The mass is converted to moles, assuming each molecule of His₆-TEV takes up a slightly larger area than predicted based on the crystal structure ($\approx 4.3 \text{ nm}^2$) due to hydration with water (here 5 nm^2 was used). The thickness, layer shear and viscosity modelled were with Voight visco-elastic model in Qtools.

SAM	Sauerbrey mass (ng cm ⁻²)	Protein on surface (pM cm ⁻²)	Voight thickness (nm)	Layer shear (x 10 ⁵ Pa)	Layer viscosity (kg m ⁻¹ s ⁻¹)	χ^2 of visco-elastic model fit
MUA	745	22.1	12.0	5.5	0.0017	7.5×10^5
MU-OH	914	27.1	8.4	6.9	0.0017	0.5×10^5
C18	659	19.5	14.0	1.6	0.0013	0.5×10^5
PFDT	525	15.6	14.2	3.6	0.0018	0.7×10^5

For His₆-TEV, a single layer of correctly folded, hydrated His₆-TEV should contain $\approx 8.8 \text{ pM cm}^{-2}$ if attached on its longest axis (Figure 3.11a). If the protein is attached via the *N*-terminus as a monomer (Figure 3.11b), a single layer should contain 12.9 pM cm^{-2} . If the TEV dimerises on the surface, the double layer will be twice this amount, which is 25.8 pM cm^{-2} . Modelling of the QCM-D data from the SAM surfaces tested have a higher surface coverage than would be expected from a single layer of correctly folded His₆-TEV (Table 3.2). In fact, if the protein is assumed to attach via the *N*-terminus, these surfaces have non-specifically bound between just over one monolayer (PFDT) and two layers (MU-OH). Therefore, the Sauerbrey Equation (Equation 2.6) indicates that either highly deformed, thickened layers of His₆-TEV have been formed on these surfaces, or single to double layers of protein have been formed.

Visco-elastic Voight modelling of these data shows that the thickest layer formed on the MU-OH (14.2 nm thick) and the thinnest on the PFDT (8.4 nm thick). Even when hydrated, a single layer of correctly folded His₆-TEV should only be $\approx 5 \text{ nm}$ thick. Therefore, multi-layers or unfolded, deformed, thickened layers of His₆-TEV were formed on these SAM surfaces. Both the Sauerbrey and Voight models indicate that the mass and thickness of protein on the surfaces, due to non-specific binding, is greater than would be expected of a single layer of hydrated His₆-TEV. Therefore, none of these commonly available SAMs are suitable to resist protein binding for this project.

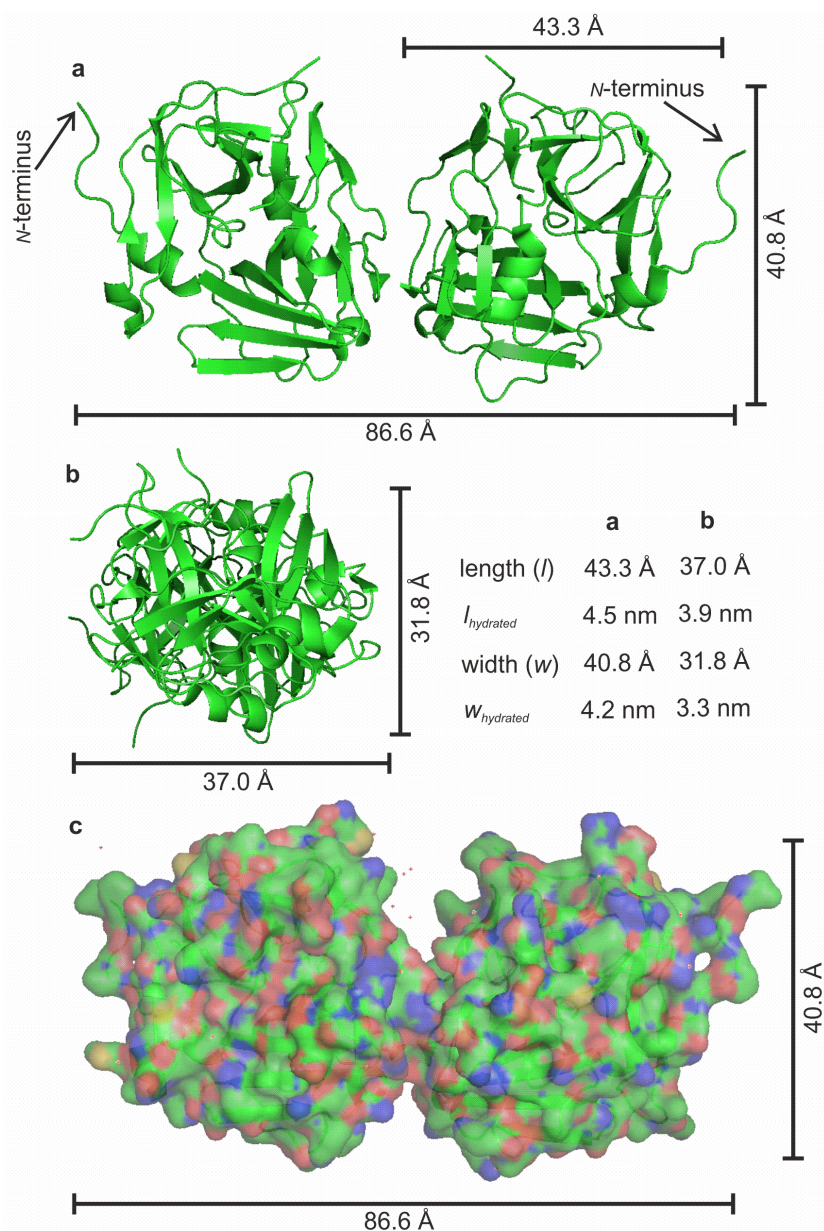


Figure 3.11. Cartoons of the protein crystal structure of TEV (pdb file 1q31).³⁹ (a) Long axis view of dimerised TEV, measurements show full length, length of a monomer and width of the protein structure. (b) View of *N*-terminus of TEV with width and length dimensions. (c) Surface of the protein (carbon is green, oxygen is red, nitrogen is blue and sulfur is yellow). Images are produced using PyMOL.¹²

A number of authors recommend polyethylene glycol terminated SAMs to resist non-specific protein binding and biofouling, see Section 1.5.3.^{27,28,30-34,36,40} EDC/NHS binding to a mixed SAM containing some carboxylic acid moieties should allow *N*-terminal immobilisation of Mms6. Therefore, mixed SAMs containing between 0% PE-COOH/100% PEG-OH and 20% PE-COOH/80% PEG-OH were used to bind Mms6 to the surface using EDC/NHS. QCM-D showed that 100% PEG-OH was the best at resisting Mms6 protein adsorption, and 10% PE-COOH/90% PEG-OH (called 'mixed SAM') the most suited to specific Mms6 protein immobilisation, Figure 3.12.

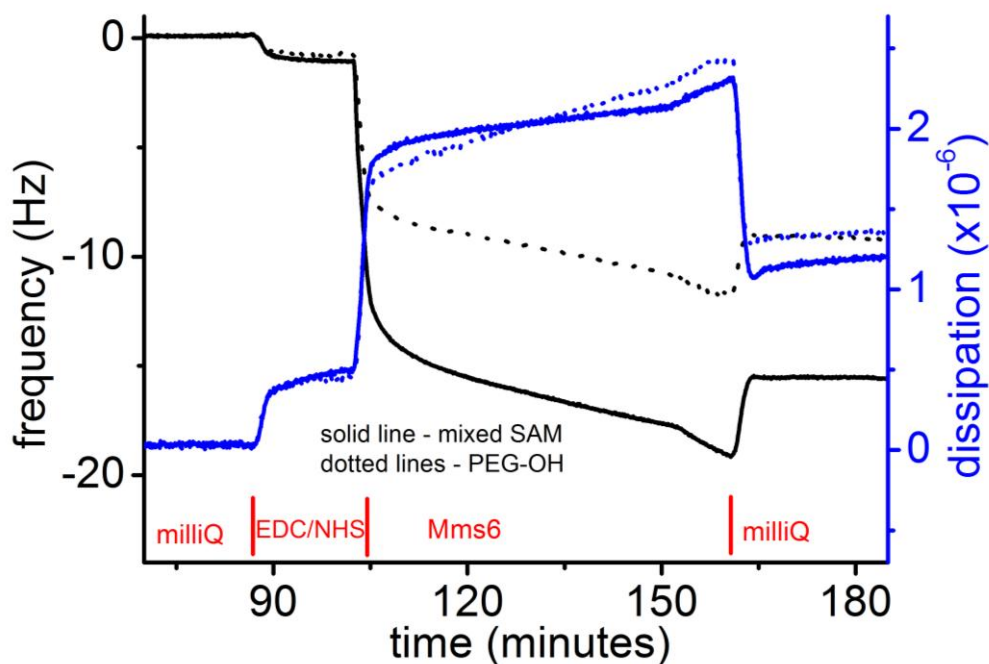


Figure 3.12. QCM-D data for Mms6 attachment to PEG-OH SAM (dotted lines) and mixed SAM of 10% PE-COOH/90% PEG-OH (solid lines). Black lines show frequency and blue dissipation. Reaction conditions used here as per Mms6 attachment protocol (Section 2.4.1.2). EDC/NHS (0.8 mg mL^{-1} / 0.1 mg mL^{-1} , in water) and Mms6 in 20 mM sodium acetate at pH 4.0 was used to buffer $10 \mu\text{g mL}^{-1}$. Final stage and initial baseline set with MilliQ water to allow Sauerbrey and Voight modelling of immobilised Mms6. A greater negative frequency shift between the initial and final baselines is due to a greater mass of protein binding to the QCM-D crystal surface.

The mass adhering to the surface of the PEG-OH SAM when modelled with the Sauerbrey equation (Equation 2.6, Table 3.3) is less than found for other SAMs (172 ng cm^{-2}). Based on the predicted structural model of Mms6 (Section 3.2.1), if hydrated Mms6 is attached via the *N*-terminus, it should take up $1.6 \times 2.2 \text{ nm}$ on the SAM surface. This is based on the dimensions from the predicted structural model (Figure 3.4b, dimensions are $13.2 \text{ \AA} \times 18.3 \text{ \AA}$). The values from the model have been rounded up slightly to allow for swelling due to hydration with water (Mms6 = 6.4 kDa, therefore hydrated Mms6 = 8.0 kDa).

Table 3.3. Modelling fits to data from QCM-D shown in Figure 3.12. Sauerbrey mass assumes the protein layer is laterally consistent and rigid. The mass is converted to moles, assuming each molecule of hydrated Mms6 takes up more space than the crystal structure (predicted from simulations). Here, a monolayer formed by *N*-terminal attachment should occupy $\approx 2 \text{ nm}^2$, and a non-specifically bound monolayer should occupy $\approx 2 \text{ nm} \times \approx 4 \text{ nm}$. The thickness, layer shear and viscosity modelled with Voight visco-elastic modelling in Qtools software.

SAM	Sauerbrey mass (ng cm^{-2})	Protein on surface ($\mu\text{M cm}^{-2}$)	Voight thickness (nm)	Layer shear ($\times 10^5 \text{ Pa}$)	Layer viscosity ($\text{kg m}^{-1} \text{ s}^{-1}$)	χ^2 of visco-elastic model fit
PEG-OH	172	21.5	2.4	1.4	0.0014	2.3×10^5
mixed SAM	310	38.8	3.2	2.6	0.0022	2.6×10^5

The concentration of Mms6 attached to the PEG-OH surface was $21.5 \mu\text{M cm}^{-2}$, which is far less than a single monolayer of Mms6 when attached by the *N*-terminus ($47.2 \mu\text{M cm}^{-2}$). However, during non-specific binding, the Mms6 may be binding on its' long axis (as per Figure 3.4a, hydrated dimensions $3.5 \text{ nm} \times 2.2 \text{ nm}$). The surface coverage for this is $21.6 \mu\text{M cm}^{-2}$, which is a very close match. The Sauerbrey model indicates the hydrated Mms6 layer on the mixed SAM is $38.8 \mu\text{M cm}^{-2}$, which is far closer to the expected value ($47.2 \mu\text{M cm}^{-2}$) for a single monolayer of *N*-terminally attached Mms6. The dissipation shift for both PEG-OH and the mixed SAM is very close to zero, indicating more rigid layers are formed by Mms6 than the His₆-TEV. Therefore, the molar coverage from these data for hydrated Mms6 may be more reliable than for the His₆-TEV protein used above.

Voight modelling of these data show the protein layer on the PEG-OH is quite thick (2.4 nm). However, the low layer shear and layer viscosity indicate this may be due to this film being water rich and protein poor. Also, this is a very close match to the expected thickness of an Mms6 layer bound via its long axis ($\approx 2.2 \text{ nm}$). The layer on the mixed SAM is thicker (3.2 nm), with a higher shear and viscosity. Based on the predicted structure, the thickness of a well packed monolayer of *N*-terminally attached hydrated Mms6 should be $\approx 3.5 \text{ nm}$. Recently, Wang *et al.* (2012)⁴¹ found that a layer of a 10.3 kDa tagged Mms6 was $31.4 \pm 0.3 \text{ \AA}$ thick when compressed on the surface of a buffer solution. This indicates that the Mms6 layer on the SAM surface is probably thicker than Mms6 self-assembled at the liquid-air interface in their study. Higher concentrations of attachment sites on the SAM surface (i.e. >10% PE-COOH) formed layers much thicker than this. Therefore, it is likely the Mms6 would be deformed by attachment to the surfaces with a higher concentration of attachment sites. As the function of a protein is strongly dependent on its structure, the higher concentration mixed SAMs were ruled out for Mms6

attachment to avoid protein deformation, so the mixed SAM containing 10% PE-COOH was used for protein attachment.

It is likely that the Mms6 on the PEG-OH is unfolded by non-specific binding to form a thinner, water rich layer than would be expected from a well packed and folded Mms6 protein layer. Therefore, the PEG-OH SAM was the most resistant SAM to non-specific protein binding, and any protein bound there is likely to have impaired function due to structural deformation. Thus, this was selected to form the protein resistant areas on the patterned surfaces. Both the Voight and Sauerbrey models indicate that the 10% PE-COOH/90% PEG-OH mixed SAM is likely to have formed about a monolayer of *N*-terminally attached Mms6. As this should allow the Mms6 protein to fold correctly, and therefore still biomineralise magnetite, this was used to form the protein attachment areas. In all future sections, the 10% PE-COOH/90% PEG-OH SAM is the attachment SAM or mixed SAM, unless otherwise indicated.

3.3.1.2 XPS of PEG SAMs

XPS spectra were recorded for the SAMs used for protein attachment (mixed SAM) and protein resistance (PEG-OH). As this involved a mixed SAM, measurements were taken of a range of SAMs formed from solutions containing between 100% PEG-OH and 100% PE-COOH. The SAM forming molecules were expected to contain carbon, oxygen and sulfur on the gold surface. Therefore, survey scans were performed to ensure there was no contamination, and detailed scans of the C 1s, O 1s, S 2p3 and Au 4f peaks were also recorded. These spectra were normalised to the Au 4f peak (84.0 eV) to compensate for any charge shifting. This allows comparisons to be made between the different peaks in the C 1s spectra due to the different bonding environments for carbon in these SAMs. These detailed spectra were then fitted with the Advantage software, using the relative intensity correction factors in the program (Table 3.4).

Table 3.4. Details of fitted peaks and relative atomic percentages for PEG-OH and PE-COOH mixed SAMs. Mixed SAMs labelled as a percentage of PE-COOH in the SAM forming solution. Peaks were fitted with the Advantage software (labelled 'eV') and assigned based on Beamson & Briggs (1992)⁴² and the NIST XPS database C 1s.⁴³ Relative atomic percentages (labelled '%') were calculated from the fitted peaks using the relative sensitivity factors in the fitting software.

Peak	0%		10%		50%		100%		
	eV	%	eV	%	eV	%	eV	%	
S 2p	162.1	3.4	161.7	3.2	161.9	3.7	161.8	2.5	
O 1s	533.3	18.9	533.1	17.7	533.0	20.3	533.0	24.4	
C 1s	C-C	285.0	44.7	285.0	45.0	284.8	38.4	284.9	26.5
	C-O-C	286.9	29.5	286.8	31.8	286.6	31.3	286.7	39.5
	C-S	288.2	3.5	288.2	3.2	287.5	5.1	287.7	2.6
	COOH	-	-	-	-	289.4	1.3	289.5	4.5

Peak assignment was based on literature values in Beamson & Briggs⁴² and the NIST XPS database: C 1s.⁴³ The S 2p peaks occurred between 161.7-162.1 eV, which agrees well with the expected values for an Au-S thiol bond. The O 1s peak positions (533.0-533.3 eV) also agree well with the values expected for oxygen bound to carbon. The C 1s spectra showed multiple peaks, as the carbon can be bonded to carbon (C-C), and sulfur (C-S), as well as oxygen in the PEG chain (C-O-C) and carboxylic acid (COOH) in the PE-COOH. The C 1s detailed spectra shown in Figure 3.13 have been baseline corrected and normalised to show the relative peak intensities due to the different species bonded to carbon in the SAMs.

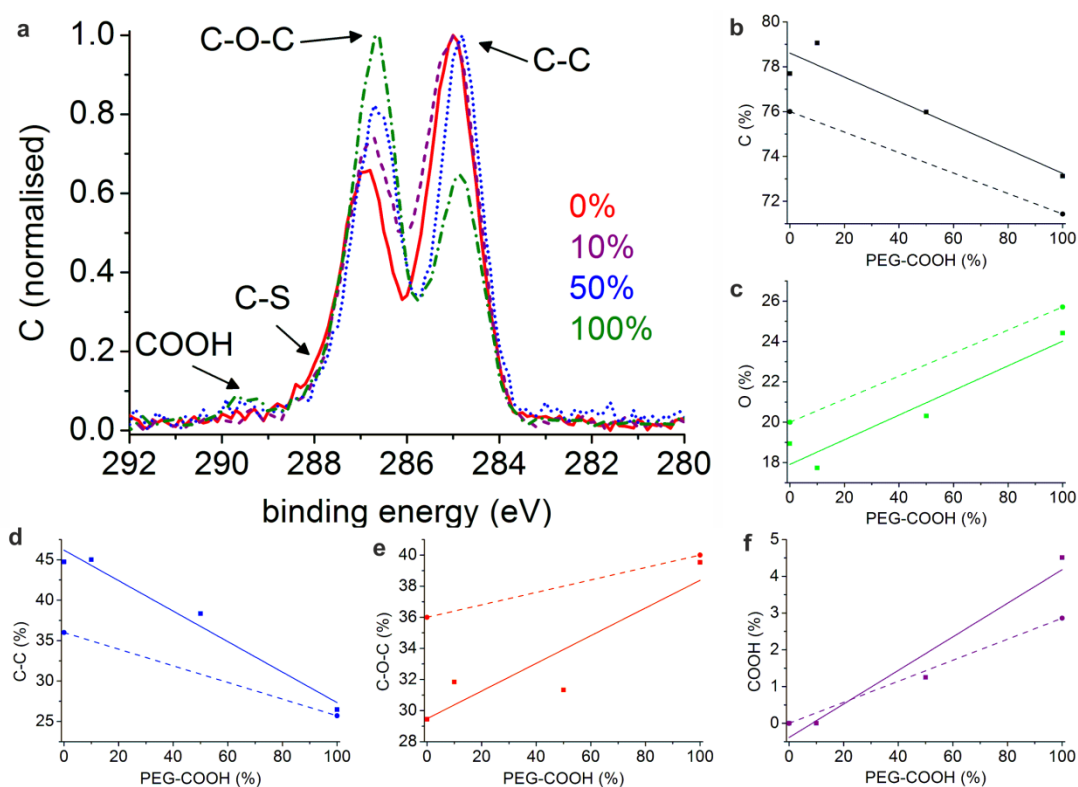


Figure 3.13. XPS spectra and relative abundances of elements in mixed PEG-OH and PE-COOH SAMs. Detailed XPS spectra of (a) baseline subtracted and normalised C 1s peaks for PEG SAMs. Trace colours are as a percentage of PE-COOH in the mixed SAM: 0% (red); 10% (purple); 50% (blue); and 100% (green). Relative abundance of (b) carbon and (c) oxygen from fitting the detailed spectra from the C 1s and O 1s peaks. Relative abundances of (d) C-C bonds, (e) C-O-C bonds and (f) COOH carbon bonds from fitting of the detailed C 1s spectra. (b-f) Concentration of the mixed SAMs are plotted on the x axes as a percentage of PE-COOH in the mixed SAM forming solution. Solid lines are fits to the measured data, dotted lines link theoretical values expected from the molecular structure of the SAM forming molecule end members.

The trend in the relative abundances for each C 1s carbon species in the mixed SAM is the same as predicted from the stoichiometry of the molecules. As the concentration of PE-COOH in the mixed SAM forming solution is increased, there is an increase in the relative abundance of oxygen, and a decrease in carbon. However, the relative abundance of carbon is overestimated when compared to the PEG-OH and PE-COOH molecules (see Figure 2.9 for structures), and the oxygen is underestimated in the measured samples. This may be due to the tilt and packing of the SAM molecules on the surfaces, as the alkane backbone should form a crystalline monolayer, tilting at $\approx 30^\circ$ from the vertical.²⁷ The PEG chains on the molecules may be less ordered, which helps resist non-specific protein binding, but may not give as strong a signal in XPS. However, as the slopes of the trends are also very similar to the predicted values, it is more likely the excess carbon is due to contamination.

There is good agreement between the 100% PE-COOH measured and calculated values for the C-C and C-O-C relative abundances, which is not as good for the 0% PEG-OH end member of the series. As the PE-COOH has a longer polyethylene glycol spacer than the PEG-OH, this indicates that SAM tilt and order is not causing the difference in the relative abundances of carbon and oxygen. Therefore, the overestimate of carbon and with respect to oxygen in the measured samples is most likely due to carbon contamination of the surface. As carbon tape is used to immobilise and earth the samples in the XPS, it is difficult to avoid some contamination on these small samples. However, the trends in these data are as expected, and the differences in relative abundances between the theoretical and measured values are only $\approx 2\%$, the composition of the mixed SAMs on the surfaces are very close to that of the molar ratio in the SAM forming solution.

3.3.1.3 Aqueous Heat Stability of SAMs

Some of the methods used to mineralise the patterns of immobilised protein involve heating the reagents to 80-90°C in aqueous solutions. Therefore, the stability of SAMs used to form the patterned substrates for protein attachment and resistance were investigated. Bare gold, and any carboxylic acid SAMs (e.g. see Section 5.3.2) can become mineralised by magnetite precipitation solutions. This means it was not possible to test the stability of the SAMs after heating in the mineralisation solutions. However, it was possible to compare the ellipsometric thickness and water contact angles of SAMs before and after heating in MilliQ water (Figure 3.14). SAMs with a range of lengths and hydrophobicities were selected for comparison. Acid terminated MUA and PE-COOH, alcohol terminated MU-OH and PEG-OH, and two hydrophobic alkanethiols, the shorter dodecane thiol (C12) and the longer C18.

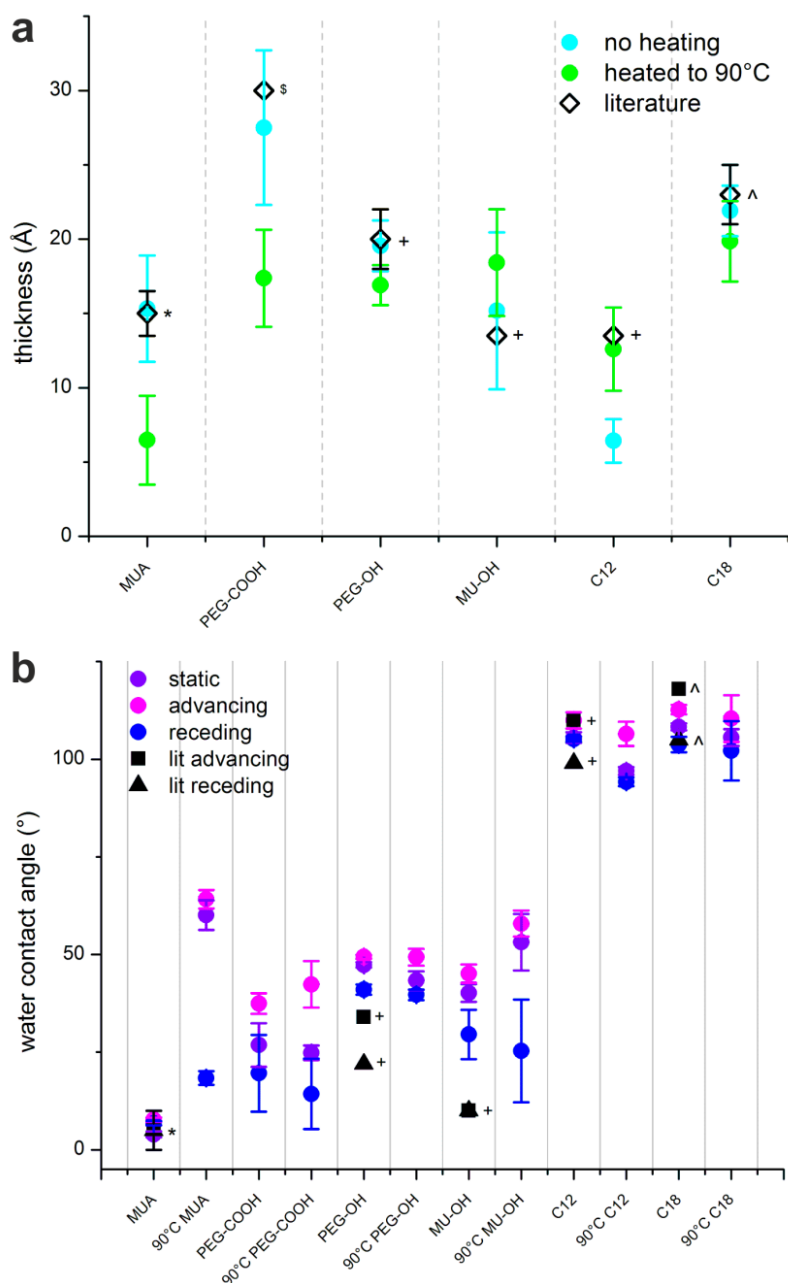


Figure 3.14. (a) Ellipsometric thickness and (b) water contact angle of SAMs before and after heating in water to 90°C for 4 hours. Thicknesses fitted from ellipsometry data, and water contact angles recorded for static, advancing and receding water droplets. Error on ellipsometric thicknesses is the standard deviation (σ) of the error on each individual fit. The error on water contact angles is the σ of the measurements taken. References for literature values: (*) Bain *et al.* (1989),⁴⁴ (\$) Lahiri *et al.* (1999),³⁰ (+) Pale-Grosdemange *et al.* (1991),⁴⁵ and (^) Biebuyck *et al.* (1994).⁴⁶ Note: water contact angle data not available for PE-COOH in literature, but would be expected to be less than PEG-OH, and more than MUA.

The mixed SAM of 10% PE-COOH/90% PEG-OH was not tested. This is because mixed SAMs, especially those formed from molecules with different chain lengths, may have increased surface roughness and be thicker/thinner than predicted based on mixing of the molecules on the surface. For many mixed monolayers, one of the molecules may preferentially attach to the surface from solution. This means that the relative concentration of molecules in the monolayer may not be the same as

their concentration when in the SAM forming solution. This should be minimised by using molecules with similar structures (e.g. the eleven carbon long alkane chains and similar PEG chains in both molecules). The QCM-D results (3.3.1.1) show the optimal mixed SAM to use for Mms6 protein attachment based on the concentration in the SAM forming solution. Therefore, the exact composition of the mixed SAM when on the surface is not important for this study.

A single batch of gold substrates (100 nm Au, 5 nm Cr on glass slides) was used to form these data to minimise substrate variability. For each type of SAM, a gold covered glass slide was split in half. Both halves were immersed in the same SAM solution, and one half used as a control (unheated) SAM. The other half was heated to 90°C in MilliQ water for four hours. First, the ellipsometric thicknesses were recorded at three different locations on the surface of the dried samples. Then advancing (θ_a), receding (θ_r) and static (θ_s) water contact angle measurements were recorded to check the hydrophobicity and surface roughness of the SAMs (Figure 3.14). A large difference between the advancing and receding contact angles ($\theta_a - \theta_r = \theta_h$) indicates a large hysteresis (θ_h), and significant surface roughness.

The longer, hydrophobic SAM (C18) shows very little change in hydrophobicity or thickness after the aqueous heating. Also, there is very little hysteresis in the water contact angles before ($\theta_h = 8.9^\circ$) or after heating ($\theta_h = 8.3^\circ$). Both indicate that the C18 SAM is very homogenous, and therefore stable, even after heating in water. The shorter hydrophobic SAM (C12) appears to swell slightly after aqueous heating, as does the more hydrophilic MU-OH. Despite the increase in thickness after heating, there is little effect on the water contact angle hysteresis of C12 (before $\theta_h = 4.8^\circ$, after $\theta_h = 12.3^\circ$) which remains small, indicating a laterally consistent SAM.

This is in contrast to the more hydrophilic SAMs (MUA and MU-OH). Before heating $\theta_h = 15.6^\circ$ for MU-OH, whereas after heating $\theta_h = 32.6^\circ$, indicating an increase in surface roughness after heating. MUA is more hydrophilic than MU-OH, and it is significantly thinned by aqueous heat treatment (before was $15.3 \pm 3.6 \text{ \AA}$, after was $6.5 \pm 3.0 \text{ \AA}$). As the water contact angle hysteresis on MUA is significant only after heating (before $\theta_h = 0.9^\circ$, after $\theta_h = 45.8^\circ$), it is likely that a lot of the MUA monolayer has been removed by heating in water. Therefore, longer, more hydrophobic molecules appear to be more resistant to thermal degradation in water. As the more hydrophobic SAMs are likely to be better at repelling the heated solvent, the higher degree of degradation of the hydrophilic SAM is to be expected.

Before heating, the PE-COOH SAM is quite hydrophilic ($\theta_s=26.8^\circ$, $\theta_r=17.8^\circ$), but also quite thick ($27.5\pm 5.2 \text{ \AA}$). After heating, this SAM was thinned to $17.4\pm 3.3 \text{ \AA}$, and the water contact angle hysteresis increased slightly ($\theta_r=28.1^\circ$). The PEG-OH was far more stable, with the thickness only decreasing from $19.6\pm 1.7 \text{ \AA}$ to $16.9\pm 1.4 \text{ \AA}$ upon heating. The water contact angle hysteresis was only increased slightly (from $\theta_r=8.4^\circ$ before heating, to $\theta_r=9.3^\circ$ after). Both factors indicate that the PEG-OH is very stable upon aqueous heating. This may be due to both the shorter PEG chain in PEG-OH allowing better packing of this SAM, coupled with the slightly less hydrophilic nature of PEG-OH, preventing heated water from degrading the monolayer. The majority of the SAMs used to form the patterned self assembled monolayers for protein attachment are PEG-OH (protein resistant is 100% PEG-OH, attachment mixed SAM is 90% PEG-OH/10% PE-COOH). Therefore, the patterned SAMs should be stable upon heating in water, even when containing a small amount of the PE-COOH in the mixed SAM.

3.3.2 Functionalising SAMs with Nitrilo-triacetic Acid (NTA)

During IMAC, NTA forms a complex with transition metals, such as Ni^{2+} or Co^{2+} , which immobilises polyhistidine tagged proteins at neutral to slightly basic pH. As an *N*-terminally tagged His₆-Mms6 purified well, complexation between the tagged protein and an immobilised transition metal ion could be used to pattern the biomineralisation protein onto a surface via the *N*-terminus. Unfortunately, despite investigating a wide range of reaction conditions and published protocols, it was not possible to functionalise a SAM with the NTA moiety. Detailed below are some of the main findings from ≈ 15 different attempts to functionalise a SAM with the Ni^{2+} -NTA moiety for His-tagged protein attachment. EDC/NHS forms an activated ester on a carboxylic acid SAM, which should be able to chemically link a target molecule to the surface via an amine on that molecule (Section 1.5.3.2). Therefore, *L*-NTA should be attached via the amine in the lysine to a carboxylic acid SAM using EDC/NHS. This would then create an NTA functionalised SAM, that can be treated with nickel to form a surface for the reversible attachment of any polyhistidine tagged protein.

SAMs of pure MUA, 16-mercaptohexadecanoic acid (MHA) and PE-COOH were used. However, as the SAM molecules are far smaller than the protein to be attached, the carboxylic acid sites are usually diluted on the surface by forming mixed SAMs with another molecule. Therefore, mixed SAMs containing MUA and MU-OH, MHA with PEG-OH, and PE-COOH with PEG-OH were used. A range of incubation times with different EDC/NHS ratios, concentrations, buffer types and pH were used by different authors to form the activated ester on the carboxylic acid SAM (see Table 3.5). There were also differences in the buffer and concentration of the *L*-NTA used during the attachment step, as well as variations in the transition metal salt and buffer used in the metal ion immobilisation step. Therefore, a variety of combinations were used to try to attach the *L*-NTA to the SAMs, using mixed SAMs ranging between 100% X-OH to 100% X-COOH (Table 3.6).

Table 3.5. Summary of reaction conditions for *L*-NTA coupling to carboxylic acid SAMs and subsequent metal ion functionalisation, based on literature cited in table. A range of buffers, pH, reaction times, and metal salts have been used.

system	EDC:NHS/ buffer/ time (mins)	<i>L</i> -NTA/ buffer/ time (mins)	Salt/ buffer/ time (mins)	comments
NTA on quantum dots (not flat) ⁴⁷	3:3 mM/ 20 mM HEPES pH 7.5/ 30	4.4 mM/ 20 mM HEPES pH 7.5/ 1440	NiCl ₂ 0.2 mM / water/ 60	9 mg QDs
Au NPs (not flat) ⁴⁸	3:3 mM/ 20 mM HEPES pH 7.5/ 1440	CoCl ₂ 20 mM + <i>L</i> -NTA (no amount)/ 20 mM HEPES (increase to pH 10 then filter removes excess Co ²⁺ / no time		Co ²⁺ before NTA attach
Au surface ⁴⁹	10:10 mM/ water/ 30	3 mg mL ⁻¹ / 12 mM PBS/ 720	NiSO ₄ 200 mM/ water/ 60	1 mM NaOH after <i>L</i> -NTA
Au surface ⁵⁰	1 M:1 M / water/ 15/ PBS rinse	1 mg mL ⁻¹ / 10 mM sodium carbonate pH 6-8/ 30/ PBS rinse	(1 M ethanol-amine/ pH 8.5/ 15 mins) NiCl ₂ 200 mM/ water/ 30	PBS rinses (no pH), Ni ²⁺ needs to be basic ⁵¹

Table 3.6. Summary of range of reaction conditions used to try and couple *L*-NTA to carboxylic acid SAMs for transition metal functionalisation based on Table 3.5. Range of buffers, pH, incubation times, concentrations and nickel salts used, many were repeated without success.

	EDC/NHS	rinse	<i>L</i> -NTA	Ni ²⁺
1	1 mL 0.2 mM/5 mL 0.2 mM in water, 20 minutes	water	1 mM in water, 2 hours	50 mM SO ₄ ²⁻ in HEPES pH 7.5, 1 hour
2	1 mL 0.2 mM/5 mL 0.2 mM in water, 30 minutes	water	0.5 mM in HEPES pH 7.5, 2 hours	50 mM SO ₄ ²⁻ HEPES pH 7.5, 1 hour
3	1 mL 0.2 mM/5 mL 0.2 mM in water, 20 minutes	HEPES pH 7.5	0.5 mM in HEPES pH 7.5, 16 hours	50 mM SO ₄ ²⁻ HEPES pH 7.5, 1 hour
4	1 mL 0.2 mM/5 mL 0.2 mM in water, 30 minutes	HEPES pH 7.5	0.5 mM in HEPES pH 7.5, 16 hours	50 mM SO ₄ ²⁻ HEPES pH 7.5, 1 hour
5	1.6 mg mL ⁻¹ /0.2 mg mL ⁻¹ in water, 15 minutes	water	1 mM in 20 mM sodium acetate pH 5.2, 2 hours	50 mM SO ₄ ²⁻ in water, 16 hours
6	10 mM/10 mM in water, 30 minutes	-	1 mM in 20 mM sodium acetate pH 5.2, 7 hours	40 mM SO ₄ ²⁻ in 1 mM NaOH, 16 hours
7	0.8 mg mL ⁻¹ /0.1 mg mL ⁻¹ in water, 30 minutes	-	5 mM in water, 3 hours	100 mM Cl ⁻ in 1 mM NaOH, 1 hour
8	10 mM/10 mM in water, 10 minutes	water	3 mg mL ⁻¹ in PBS pH 8.3, 16 hours	100 mM Cl ⁻ in 1 mM NaOH, 1 hour

A large number of the Ni²⁺-NTA coupling experiments were carried out to try to produce SAMs for QCM-D protein attachment experiments and XPS characterisation. It was not expected that the *L*-NTA would couple to the -OH terminated SAMs, as a carboxylic acid is required to for the activated ester to bind the protein. The QCM-D experiments (discussed in more detail in Section 3.3.1.1) showed small negative frequency shifts (between \approx -1 and -4 Hz), which indicates that only partial layer formation occurred on these surfaces. Patchy, incomplete layers indicate that the protein is non-specifically binding to the SAMs on the QCM-D crystals. However, it was not possible to detect *L*-NTA coupling to the -COOH terminated or mixed SAMs either.

The QCM-D for these SAMs only showed non-specific binding. The example shown in Figure 3.15 shows protein immobilisation on SAMs of 100% PEG-OH and 10% MHA/90% PEG-OH treated with EDC/NHS and *L*-NTA, prior to nickellation and protein immobilisation in the QCM-D. His₆-TEV protease was used as a proxy for Mms6, as it also has an *N*-terminal hexahistidine tag and it is larger, so it should produce a stronger signal when attached to the SAM surface. The 100% PEG-OH resists protein binding well, with a small frequency shift to \approx -4 Hz. The method followed here should have functionalised the mixed SAM with Ni²⁺-NTA, which then should immobilise the His-tagged protein via the chelated nickel. The protein was able to bind to the treated SAM containing 10% MHA, but was not removed by treatment with EDTA elution buffer. As EDTA should elute all of the chelated nickel

from the surface, it should also remove any of the His-tagged protein immobilised onto Ni^{2+} -NTA. As the protein was not removed by EDTA, this means that it was not bound to the surface via the His₆-tag, but the His₆-TEV was also non-specifically bound to the surface. This means that either the NTA, the nickel or both were not successfully functionalised onto the SAM surface.

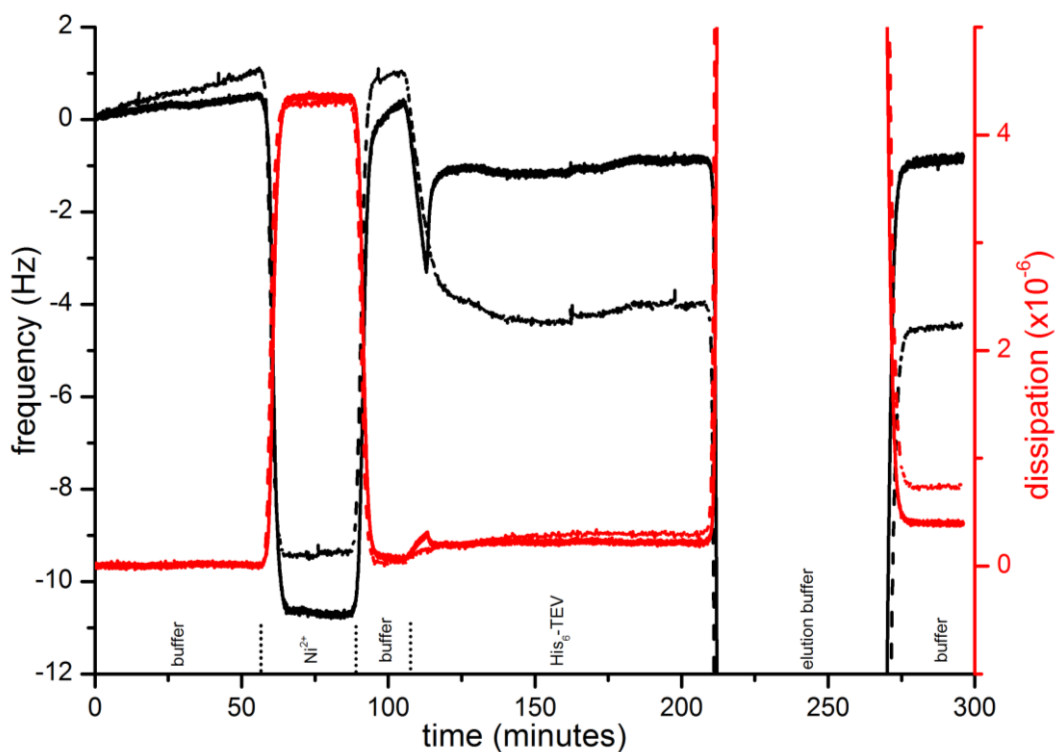


Figure 3.15. QCM-D trace from protein attachment to SAMs treated with aqueous EDC (1 mL, 0.2 mM) and NHS (5 mL, 0.2 mM) for 30 minutes before immersing in *L*-NTA (0.5 mM in buffer) overnight. Only 9th overtone shown for clarity (3rd-13th recorded). Dotted line trace from 100% PEG-OH SAM, solid line from 10% MHA/90% PEG-OH mixed SAM. Buffer is 10 mM HEPES, 150 mM NaCl, 50 μM EDTA (elution buffer contains 200 mM EDTA), Ni^{2+} is 50 mM $\text{NiSO}_4 \cdot 6\text{H}_2\text{O}$ in buffer, His₆-TEV is 2 $\mu\text{g mL}^{-1}$ in buffer, run at 20 $\mu\text{L min}^{-1}$. The negative shift in frequency between the buffer baseline (set at zero minutes) and the final buffer wash (after ≈ 270 minutes) indicates that a small mass of protein is adhering to the SAM surface. As the protein is not removed with high concentrations of EDTA, it is not bound to the surface via the His₆-tag.

This was investigated further using XPS to determine the elements present in the treated and untreated SAMs. In all cases, there was no detection of an N 1s peak at ≈ 400.0 eV in the XPS spectra (Figure 3.16). As both -OH and -COOH SAMs should not contain nitrogen, an N 1s peak would indicate that *L*-NTA had coupled to the SAM surface. However, there was a weak Ni 2p_{3/2} peak visible, despite the lack of *L*-NTA coupling to the surface, when NiCl_2 was used for the nickellation in weak sodium hydroxide. It may be that some nickel ions were immobilised by the unreacted carboxylic acid groups in the SAMs. All protein immobilisation QCM-D experiments only showed non-specific protein adsorption. This supports the XPS data in that *L*-NTA and/or Ni^{2+} was not bound to the surface, so the SAM was unable to chelate polyhistidine for protein immobilisation. This is unsuitable for

maintaining Mms6 functionality, as the activity of the protein may be seriously hampered if distorted by non-specific binding. As it was not possible to develop a protocol that was able to form a Ni^{2+} -NTA functionalised surface, alternative protein immobilisation strategies were attempted.

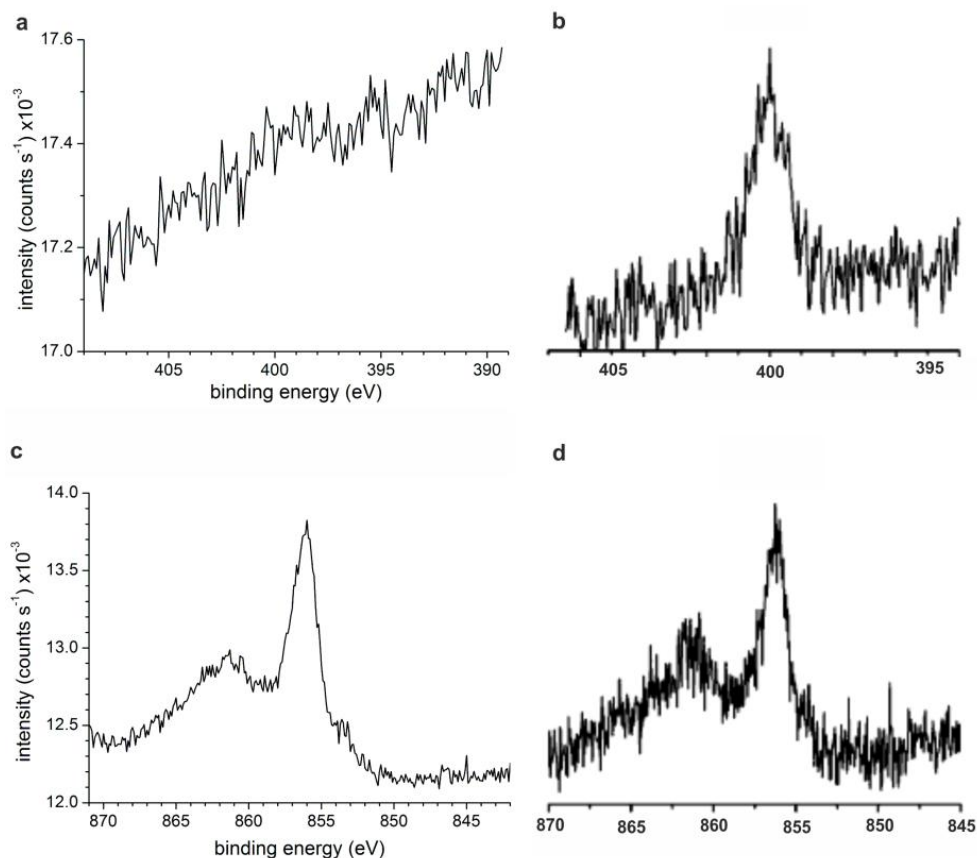


Figure 3.16. Detailed XPS spectra of Ni^{2+} -NTA SAM peaks. Plots (a, c) from 100% PE-COOH SAM after EDC/NHS ($0.8:0.1 \text{ mg mL}^{-1}$ in water, 30 minutes); *L*-NTA (5 mM in water, 180 minutes); NiCl_2 (100 mM in 1 mM NaOH; 60 minutes). Plots (b, d) from Lee *et al.* 2004⁴⁹ for comparison (intensity not available). N 1s detailed spectra around 400.0 eV ⁵² (a, b) show no N 1s peak for the SAMs treated in this study. Therefore, it is highly unlikely the *L*-NTA has coupled with the PE-COOH SAM, as there is no nitrogen signal. However, there is still an Ni 2p3 peak around 856.0 eV ⁵² in both data sets (c, d). These data suggest that nickel was still able to bind to the carboxylic acid terminated SAM in the absence of the NTA moiety.

In Abad *et al.* (2004),⁴⁸ the protocol for *L*-NTA binding to a carboxylic acid functionalised surface creates the cobalt and *L*-NTA complex before binding to the activated ester on the gold nanoparticle surface. It is possible that nickellating the *L*-NTA before attachment to the patterned carboxylic acid could help the binding of *L*-NTA to the surface. EDC/NHS chemistry creates activated esters using carboxylic acids (see Figure 1.21), which can then bind to the amine on the *L*-NTA. Unfortunately, *L*-NTA contains three carboxylic acids, which can also form activated esters which could bind amines.⁵³ This would create many cross-linked NTA molecules in the bulk solution, and prevent their immobilisation onto the surface. When a transition metal ion, such as cobalt or nickel, chelates with the NTA moiety,

the three carboxylic acids are used to create the complexation bonds. If the nickel is chelated with the *L*-NTA prior to the attempted binding to the carboxylic acid surface, the carboxylic acids on the *L*-NTA should be unable to interact with the EDC/NHS to form the activated esters. This could prevent polymerisation of *L*-NTA in the bulk solution, and thus allow the amine to bind and create an NTA functionalised surface.

3.3.3 Imaging Protein Attachment

As demonstrated above, the SAMs used to attach/resist Mms6 binding are fairly stable when heated in an aqueous environment. Modelling of the QCM-D data shows the Mms6 protein forms a consistent, hydrated layer on an unpatterned SAM. Next, the attachment of protein to patterned surfaces was investigated to show that protein is immobilised onto the correct parts of the patterned SAM surfaces.

3.3.3.1 AFM of Protein Patterns

Tapping mode AFM was used to image patterned surfaces. Fluorescent protein was attached to the patterned SAM surfaces (PEG-OH to resist protein binding and the mixed SAM containing 10% PE-COOH/90%PEG-OH to form attachment areas). Fluorescent proteins (eGFP and mCherry) were attached to a patterned surface using EDC/NHS.* Fluorescent proteins were buffered appropriately and attached to the patterned SAMs using EDC/NHS linking chemistry. The optimal attachment of the *N*-terminus of a protein is dependent upon buffering the protein to ≈ 1 pH point below its *pI*. Therefore, eGFP and mCherry were attached as per the Mms6 protocol (Section 2.4.1.2), but the 20 mM sodium acetate buffer for the protein attachment was pH=4.6 for eGFP (*pI*=5.67)⁹ and pH=5.2 for mCherry (*pI*=6.23).⁹ As they are larger than Mms6, they should have been easier to detect on the patterned surfaces, even when dried. The protein patterns were rinsed thoroughly in water and dried before imaging in tapping mode with AFM. Unfortunately, it was not possible to resolve the patterned protein on the surface, as the evaporated gold has greater relief than any dried protein (Figure 3.17). In future, this could be avoided if the protein patterns were imaged under buffer. As it was not possible to clearly image the protein patterns using tapping mode AFM, fluorescent microscopy was used to try to image the protein patterns.

* Fluorescent protein courtesy of J. Roth, Molecular and Nanoscale Physics, University of Leeds.

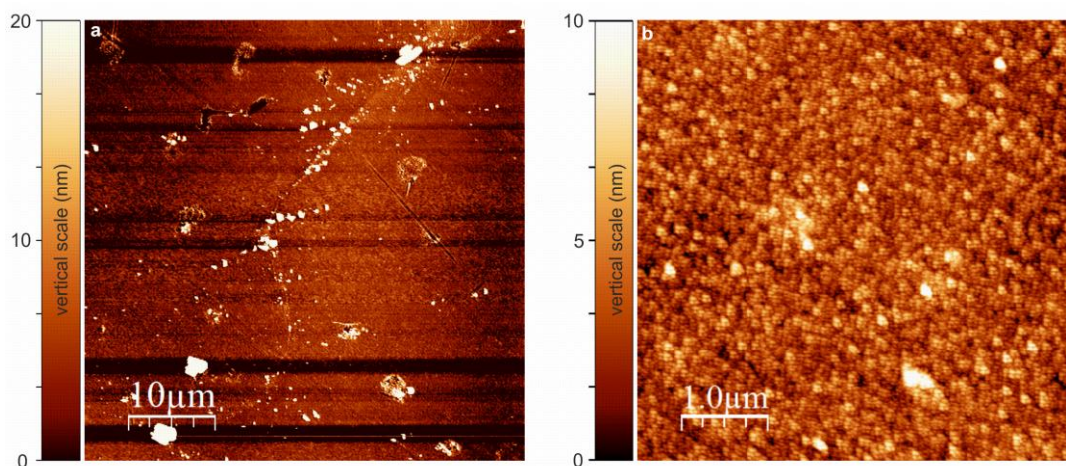


Figure 3.17. Tapping mode AFM images of patterned SAM after protein attachment by EDC/NHS. (a) $50 \mu\text{m}^2$ scan area and (b) $5 \mu\text{m}^2$ scan area typical of samples imaged. Cannot see protein pattern on dried surface. Texture of evaporated gold can be seen in image b. These data were processed using WSxM.⁵⁴

3.3.3.2 Fluorescent Microscopy

eGFP (peak excitation/emission (ex/em) of $\lambda=488/507 \text{ nm}$) and mCherry (peak ex/em of $\lambda=587/610 \text{ nm}$)⁵⁵ were attached to the patterned SAMs as above (3.3.1.1). In fluorescent proteins, folding brings together amino acid residues (usually containing π -electrons in the R-group) to form the chromophore, which is surrounded by a β -sheet barrel.⁵⁵ Therefore, the structure of the folded protein is extremely important in maintaining their fluorescent properties. Thus, if protein attachment deforms the protein structure, the fluorescence may be shifted or quenched. Unfortunately, as the patterned SAMs are on gold, the metallic Au may also quench some or all of the fluorescence from the proteins. Equally, surface plasmon resonance on thin films of gold can enhance fluorescence if the excited fluorophore is able to couple with the resonance.⁵⁶ Therefore, a number of mechanisms could act to enhance or quench fluorescence of these patterned proteins.

As can be seen in Figure 3.18, the signal from the patterned eGFP is about an order of magnitude lower than that from the patterned mCherry. This is despite forming the image for eGFP over a longer collection time (2400 ms collection for eGFP, 1200 ms for mCherry). As eGFP is usually two times as bright as mCherry (and more photostable),⁵⁵ this difference was not expected. The differences in intensities may be due to lower detection of the fluorescence from eGFP, as the filter block used to excite and detect emission for this image (FITC) is not optimised to image eGFP. The peak emission ($\lambda=507 \text{ nm}$) falls outside the FITC detection

* Fluorescent protein courtesy of J. Roth, Molecular and Nanoscale Physics, University of Leeds.

filter range ($\lambda=515-555$ nm). However, the peak excitation for mCherry ($\lambda=587$ nm) is just outside the range of the filter block used to create those images (TxRed, excitation $\lambda=540-580$ nm). Therefore, there may also be other factors that have caused this difference in intensity.

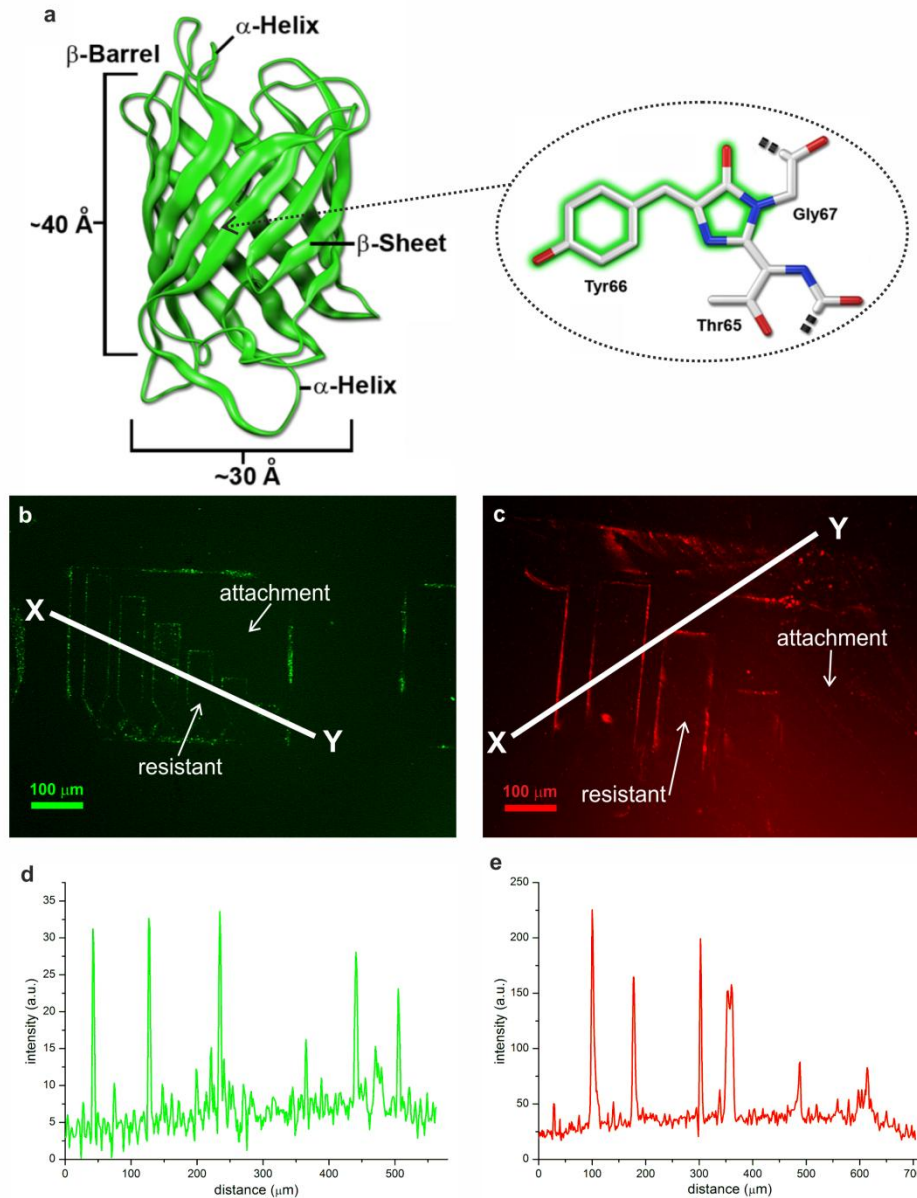


Figure 3.18. Cartoon of the structure of eGFP, and fluorescent microscopy images of patterned eGFP and mCherry fluorescent proteins. (a) Cartoon of GFP structure and stick diagram of chromophore of eGFP as an example of a β -barrel structure of a fluorescent protein, adapted from Shaner et al. (2007).⁵⁵ Fluorescent microscope images of (b) patterned eGFP and (c) patterned mCherry. Fluorescence intensity along transects X-Y (X is at 0 nm) for (d) image b, and (e) image c. Fluorescence can only be seen at pattern edges, with no discernible signal observed on the areas that should have a fluorescent protein layer (labelled attachment) or should resist protein binding (labelled resistant). Fluorescence can only be seen at pattern edges, and the intensity of the fluorescence is much lower from patterned eGFP than from the mCherry.

The gold surface may be more effective when quenching the fluorescence from eGFP than from mCherry, which could explain the differences in the fluorescence signal intensity. It is also possible that the mCherry β -barrel is more stable than that of eGFP when attached to a surface. This would allow mCherry to be better able to maintain its morphology, thus protecting the activity of the chromophore when attached to the surface. However, these possibilities do not explain why the only observable signal from the fluorescent proteins is from the pattern edges, and not on the areas where the SAM should be functionalised for protein attachment. The schematic in Figure 3.19 shows some possible causes of this phenomenon.

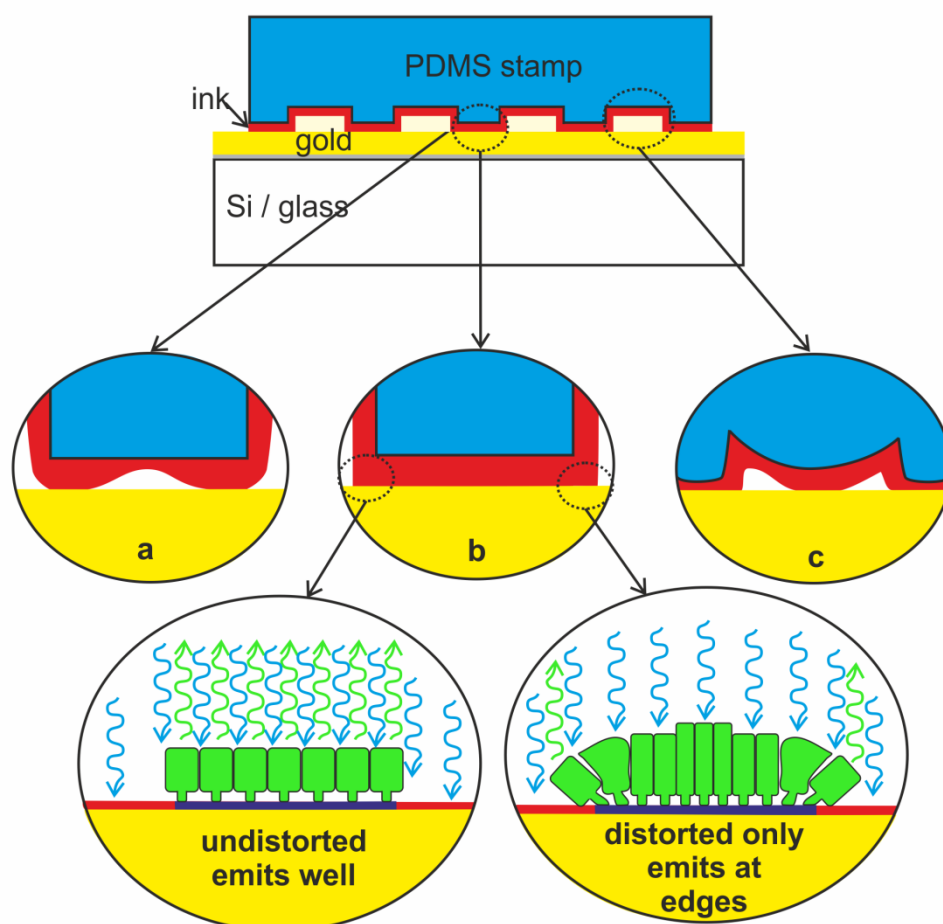


Figure 3.19. Schematic illustration of micro-contact printing and fluorescent protein attachment to SAMs. Above is a PDMS stamp that has been inked with PEG-OH thiol to print protein resistance onto a gold surface. Below (a) only transfers part of the pattern, and occurs if the ink on the stamp is too dry. In case (b) an appropriate amount of ink and pressure ensures a good conformal contact of the stamp with the surface, and thus a good transfer of the printed pattern. (c) Shows stamp touch-down, which happens if the stamp is too wet, or if too much pressure is applied to the stamp during printing. Below is a diagram to show how correctly orientated and undistorted GFP could attach to a surface and emit well, and how distortion of the β -barrel structure could prevent emission on the patterned surface, except at the edges of the pattern.

The concentration of attachment sites for protein in the mixed SAM used for Mms6 protein attachment (10% PE-COOH, 90% PEG-OH) may be too dense for the larger fluorescent proteins. This would cause the proteins to deform in order to attach to the surface, thus preventing them from fluorescing. As proteins at the pattern edges would be less confined, they may be better able to properly fold, and therefore produce the fluorescent signal observed in Figure 3.18. The lines at the pattern edges could also be due poor printing of the pattern, which may have only allowed the protein attachment SAM to form at the pattern edges (see Figure 3.19). The PDMS stamps used for μ CP are soft, and can sometimes touch-down on the surface in the areas that should not form a conformal contact with the gold surface. In the protein attachment system used here, this could functionalise lines at pattern edges for protein attachment, and leave all other areas resistant to protein binding.

As any combination of these factors (excitation/emission detection, quenching, deformation of folding or touch-down) may have caused the line patterns observed in the fluorescence images. It is difficult to conclude what is happening to the protein when it is attached to the patterned surface from the AFM and fluorescent microscopy. The fluorescence images do show that there is protein patterned on the surface, and the QCM-D shows that the Mms6 protein should preferentially attach to the mixed SAM. Therefore, the EDC/NHS immobilisation should be suitable to immobilise Mms6 to form biotemplated magnetic nanoparticles onto micro-patterned surfaces.

3.4 References

1. Nicholl, D.S.T. (2008). *An Introduction to Genetic Engineering* (Cambridge University Press, Cambridge, UK).
2. Arakaki, A., Webb, J. & Matsunaga, T. (2003). A novel protein tightly bound to bacterial magnetic particles in *Magnetospirillum magneticum* strain AMB-1. *J. Biol. Chem.* **278**, pp 8745-8750.
3. Kapust, R.B. & Waugh, D.S. (1999). *Escherichia coli* maltose-binding protein is uncommonly effective at promoting the solubility of polypeptides to which it is fused. *Prot. Sci.* **8**, pp 1668-1674.
4. Porath, J. (1992). Immobilized metal ion affinity chromatography. *Protein Express. Purif.* **3**, pp 263-281.
5. Porath, J., Carlsson, J., Olsson, I. & Belfrage, G. (1975). Metal chelate affinity chromatography, a new approach to protein fractionation. *Nature.* **258**, pp 598-599.
6. Kapust, R.B., Tözsér, J., Fox, J.D., Anderson, D.E., Cherry, S., Copeland, T.D. & Waugh, D.S. (2001). Tobacco etch virus protease: Mechanism of autolysis and rational design of stable mutants with wild-type catalytic proficiency. *Prot. Eng.* **14**, pp 993-1000.

7. Galloway, J.M., Bramble, J.P., Rawlings, A.E., Burnell, G., Evans, S.D. & Staniland, S.S. (2012). Nanomagnetic arrays formed with the biomineralization protein Mms6. *J. Nano Res.* **17**, pp 127-146.
8. Schagger, H. (2006). Tricine-SDS-PAGE. *Nat. Protocols.* **1**, pp 16-22.
9. (2012). *ExpASY ProtParam tool by the Swiss Institute of Bioinformatics.* <http://web.expasy.org/protparam/> 16/01/2012.
10. Marblestone, J.G., Edavettal, S.C., Lim, Y., Lim, P., Zuo, X. & Butt, T.R. (2006). Comparison of SUMO fusion technology with traditional gene fusion systems: Enhanced expression and solubility with SUMO. *Prot. Sci.* **15**, pp 182-189.
11. Xu, D. & Zhang, Y. (2012). Ab initio protein structure assembly using continuous structure fragments and optimized knowledge-based force field. *Proteins.* **80**, pp 1715-1735.
12. Schrodinger, LLC. (2012). *The PyMOL Molecular Graphics System, Version 1.5.0.1.*
13. Warner, R.C. & Weber, I. (1953). The cupric and ferric citrate complexes. *J. Am. Chem. Soc.* **75**, pp 5086-5094.
14. (2012). *Intrinsic Fluorescence of Proteins and Peptides.* <http://dwb.unl.edu/Teacher/NSF/C08/C08Links/pp99.cryst.bbk.ac.uk/projects/gmocz/fluor.htm> 23/07/2012.
15. Subramaniam, V., Steel, D.G. & Gafni, A. (2002). Room temperature tryptophan phosphorescence as a probe of structural and dynamic properties of proteins, pp 43-65. *in Topics in Fluorescence Spectroscopy, vol. 6, Protein Fluorescence* (ed. Lakowicz, J.R.). (Kluwer Academic / Plenum Publishers, New York, USA).
16. Whitmore, L. & Wallace, B.A. (2004). DICHROWEB, an online server for protein secondary structure analyses from circular dichroism spectroscopic data. *Nucleic Acids Res.* **32**, pp W668-W673.
17. Kelly, S.M., Jess, T.J. & Price, N.C. (2005). How to study proteins by circular dichroism. *Biochim. Biophys. Acta.* **1751**, pp 119-139.
18. Amemiya, Y., Arakaki, A., Staniland, S.S., Tanaka, T. & Matsunaga, T. (2007). Controlled formation of magnetite crystal by partial oxidation of ferrous hydroxide in the presence of recombinant magnetotactic bacterial protein Mms6. *Biomaterials.* **28**, pp 5381-5389.
19. Arakaki, A., Masuda, F., Amemiya, Y., Tanaka, T. & Matsunaga, T. (2010). Control of the morphology and size of magnetite particles with peptides mimicking the Mms6 protein from magnetotactic bacteria. *J. Colloid Interface Sci.* **343**, pp 65-70.
20. Brown, S. (1992). Engineered iron oxide-adhesion mutants of the Escherichia coli phage lambda receptor. *Proc. Natl. Acad. Sci.* **89**, pp 8651-8655.
21. Brown, S. (1997). Metal-recognition by repeating polypeptides. *Nat. Biotech.* **15**, pp 269-272.
22. Sarikaya, M., Tamerler, C., Jen, A.K.Y., Schulten, K. & Baneyx, F. (2003). Molecular biomimetics: Nanotechnology through biology. *Nat. Mater.* **2**, pp 577-585.
23. Naik, R.R., Jones, S.E., Murray, C.J., McAuliffe, J.C., Vaia, R.A. & Stone, M.O. (2004). Peptide templates for nanoparticle synthesis derived from polymerase chain reaction-driven phage display. *Adv. Funct. Mater.* **14**, pp 25-30.

24. Barbas, C.F., Rosenblum, J.S. & Lerner, R.A. (1993). Direct selection of antibodies that coordinate metals from semisynthetic combinatorial libraries. *Proc. Natl. Acad. Sci.* **90**, pp 6385-6389.
25. Galloway, J.M., Arakaki, A., Masuda, F., Tanaka, T., Matsunaga, T. & Staniland, S.S. (2011). Magnetic bacterial protein Mms6 controls morphology, crystallinity and magnetism of cobalt-doped magnetite nanoparticles in vitro. *J. Mater. Chem.* **21**, pp 15244-15254.
26. Tanaka, M., Mazuyama, E., Arakaki, A. & Matsunaga, T. (2011). Mms6 protein regulates crystal morphology during nano-sized magnetite biomineralization in vivo. *J. Biol. Chem.* **286**, pp 6386-6392.
27. Mrksich, M. & Whitesides, G.M. (1995). Patterning self-assembled monolayers using microcontact printing: A new technology for biosensors? *Trends Biotechnol.* **13**, pp 228-235.
28. Kankate, L., Werner, U., Turchanin, A., Götzhäuser, A., Großmann, H. & Tampé, R. (2010). Protein resistant oligo(ethylene glycol) terminated self-assembled monolayers of thiols on gold by vapor deposition in vacuum. *Biointerphases.* **5**, pp 30-36.
29. Kim, P., Lee, S.E., Jung, H.S., Lee, H.Y., Kawai, T. & Suh, K.Y. (2006). Soft lithographic patterning of supported lipid bilayers onto a surface and inside microfluidic channels. *Lab on a Chip.* **6**, pp 54-59.
30. Lahiri, J., Isaacs, L., Tien, J. & Whitesides, G.M. (1999). A strategy for the generation of surfaces presenting ligands for studies of binding based on an active ester as a common reactive intermediate: A surface plasmon resonance study. *Anal. Chem.* **71**, pp 777-790.
31. Prime, K.L. & Whitesides, G.M. (1993). Adsorption of proteins onto surfaces containing end-attached oligo(ethylene oxide): A model system using self-assembled monolayers. *J. Am. Chem. Soc.* **115**, pp 10714-10721.
32. Sui, G., Wang, J., Lee, C.-C., Lu, W., Lee, S.P., Leyton, J.V., Wu, A.M. & Tseng, H.-R. (2006). Solution-phase surface modification in intact poly(dimethylsiloxane) microfluidic channels. *Anal. Chem.* **78**, pp 5543-5551.
33. Veiseh, M., Zareie, M.H. & Zhang, M. (2002). Highly selective protein patterning on gold-silicon substrates for biosensor applications. *Langmuir.* **18**, pp 6671-6678.
34. Yang, Z., Galloway, J.A. & Yu, H. (1999). Protein interactions with poly(ethylene glycol) self-assembled monolayers on glass substrates: Diffusion and adsorption. *Langmuir.* **15**, pp 8405-8411.
35. Zhen, G., Falconnet, D., Kuennemann, E., Vörös, J., Spencer, N.D., Textor, M. & Zürcher, S. (2006). Nitrilotriacetic acid functionalized graft copolymers: A polymeric interface for selective and reversible binding of histidine-tagged proteins. *Adv. Funct. Mater.* **16**, pp 243-251.
36. Zhen, G.L., Zürcher, S., Falconnet, D., Xu, F., Kuennemann, E. & Textor, M. (2005). NTA-functionalized poly(L-lysine)-g-poly(ethylene glycol): A polymeric interface for binding and studying 6xHis-tagged proteins. *27th Annu. Int. Conf. IEEE Eng. Med. Biol. Soc.* **1-7**, pp 1036-1038.
37. Rodahl, M., Hook, F., Fredriksson, C., A. Keller, C., Krozer, A., Brzezinski, P., Voinova, M. & Kasemo, B. (1997). Simultaneous frequency and dissipation factor QCM measurements of biomolecular adsorption and cell adhesion. *Faraday Discuss.* **107**, pp 229-246.

38. Krzemiński, Ł., Cronin, S., Ndamba, L., Canters, G.W., Aartsma, T.J., Evans, S.D. & Jeuken, L.J.C. (2011). Orientational control over nitrite reductase on modified gold electrode and its effects on the interfacial electron transfer. *J. Phys. Chem. B.* **115**, pp 12607-12614.
39. Nunn, C.M., Jeeves, M., Cliff, M.J., Urquhart, G.T., George, R.R., Chao, L.H., Tscuchia, Y. & Djordjevic, S. (2005). Crystal structure of tobacco etch virus protease shows the protein C terminus bound within the active site. *J. Mol. Biol.* **350**, pp 145-155.
40. Kim, D.-H., Fischer, P., Chao, W., Anderson, E., Im, M.-Y., Shin, S.-C. & Choe, S.-B. (2006). Magnetic soft X-ray microscopy at 15 nm resolution probing nanoscale local magnetic hysteresis. *J. Appl. Phys.* **99**, pp 08H303.
41. Wang, W., Bu, W., Wang, L., Palo, P.E., Mallapragada, S., Nilsen-Hamilton, M. & Vaknin, D. (2012). Interfacial properties and iron binding to bacterial proteins that promote the growth of magnetite nanocrystals: X-ray reflectivity and surface spectroscopy studies. *Langmuir.* **28**, pp 4274-4282.
42. Beamson, G. & Briggs, D. (1992). *High Resolution XPS of Organic Polymers: The Scienta ESCA300 Database* (Wiley, Chichester, UK).
43. Wagner, C.D., Naumkin, A.V., Kraut-Vass, A., Allison, J.W., Cedric J. Powell & Rumble, J.R. *NIST XPS database C1s*.
http://srdata.nist.gov/xps/EngElmSrchQuery.aspx?EType=PE&CSOpt=Retri_ex_dat&Elm=C 28/11/2010.
44. Bain, C.D., Evall, J. & Whitesides, G.M. (1989). Formation of monolayers by the coadsorption of thiols on gold: variation in the head group, tail group, and solvent. *J. Am. Chem. Soc.* **111**, pp 7155-7164.
45. Pale-Grosdemange, C., Simon, E.S., Prime, K.L. & Whitesides, G.M. (1991). Formation of self-assembled monolayers by chemisorption of derivatives of oligo(ethylene glycol) of structure HS(CH₂)₁₁(OCH₂CH₂)_mOH on gold. *J. Am. Chem. Soc.* **113**, pp 12-20.
46. Biebuyck, H.A., Bain, C.D. & Whitesides, G.M. (1994). Comparison of organic monolayers on polycrystalline gold spontaneously assembled from solutions containing dialkyl disulfides or alkanethiols. *Langmuir.* **10**, pp 1825-1831.
47. Gupta, M., Caniard, A., Touceda-Varela, A., Campopiano, D.J. & Mareque-Rivas, J.C. (2008). Nitrilotriacetic acid-derivatized quantum dots for simple purification and site-selective fluorescent labeling of active proteins in a single step. *Bioconjugate Chem.* **19**, pp 1964-1967.
48. Abad, J.M., Mertens, S.F.L., Pita, M., Fernandez, V.M. & Schiffrin, D.J. (2005). Functionalization of thioctic acid-capped gold nanoparticles for specific immobilization of histidine-tagged proteins. *J. Am. Chem. Soc.* **127**, pp 5689-5694.
49. Lee, J.K., Kim, Y.-G., Chi, Y.S., Yun, W.S. & Choi, I.S. (2004). Grafting Nitrilotriacetic Groups onto Carboxylic Acid-Terminated Self-Assembled Monolayers on Gold Surfaces for Immobilization of Histidine-Tagged Proteins. *J. Phys. Chem. B.* **108**, pp 7665-7673.
50. Le, T.T., Wilde, C.P., Grossman, N. & Cass, A.E.G. (2011). A simple method for controlled immobilization of proteins on modified SAMs. *Phys. Chem. Chem. Phys.* **13**, pp 5271-5278.

51. Thomson, N.H., Smith, B.L., Almqvist, N., Scmitt, L., Kashlev, M., Kool, E.T. & Hansma, P.K. (1999). Orientated, active Escherichia coli RNA polymerase: An atomic force microscopy study. *Biophys. J.* **76**, pp 1024-1033.
52. Moulder, J.F., Stickle, W.F., Sobol, P.E. & Bomben, K.D. (1995). *Handbook of X-ray Photoelectron Spectroscopy* (eds. Chastain, J. & King Jr., R.C.). (Physical Electronics Inc., Minnesota, USA).
53. (2012). *Carbodiimide Crosslinker Chemistry*. <http://www.piercenet.com/browse.cfm?fldID=F3305493-0FBC-93DA-2720-4412D198A9C9> 22/07/2012.
54. Horcas, I., Fernandez, R., Gomez-Rodriguez, J.M., Colchero, J., Gomez-Herrero, J. & Baro, A.M. (2007). WSXM: A software for scanning probe microscopy and a tool for nanotechnology. *Rev. Sci. Instrum.* **78**, pp 013705.
55. Shaner, N.C., Patterson, G.H. & Davidson, M.W. (2007). Advances in fluorescent protein technology. *J. Cell Sci.* **120**, pp 4247-4260.
56. Gryczynski, I., Malicka, J., Gryczynski, Z. & Lakowicz, J.R. (2004). Surface plasmon-coupled emission with gold films. *J. Phys. Chem. B.* **108**, pp 12568-12574.

Chapter 4

Magnetic Particles Formed from a Bulk Solution

In this section, the synthesis and characterisation of Mms6 biotemplated nanoparticles are investigated. Three methods of magnetite synthesis (RTCP, POFHK and POFHN) were used to synthesise both magnetite and cobalt doped magnetite, both in the presence and absence of Mms6, and the properties of these particles are assessed. This was done to investigate the effect of the addition of Mms6 to the mineralisation systems, and to establish an optimal level of cobalt doping to produce a large increase in coercivity for little loss of saturation magnetisation.

In the introduction, a number of methods of magnetite particle synthesis were discussed. In nature, Mms6 templates uniform cubo-octahedral magnetite under mild conditions, i.e. at room temperature and using non-toxic reagents. Therefore, it is unlikely that Mms6 will be able to biotemplate effectively at high temperatures (e.g. over 100°C) or in the presence of harsh chemicals, such as benzyl ether and toluene. Previously, Mms6 has been shown to direct both the RTCP¹ and the POFH² methods of magnetite synthesis *in vitro*. For both methods, Mms6 was able to template the cubo-octahedral morphology and nanoparticle size similar to the MNPs formed by AMB-1 *in vivo*. For RTCP, Mms6 templated particles were larger, and for POFH, Mms6 templated particles were smaller, than the controls made without protein. This shows the biotemplating control of Mms6 on magnetite nanoparticles, as uniform, cubo-octahedral particles of a similar size to those formed by the bacterium are templated whether the method produces smaller particles (RTCP) or larger MNPs (POFH) in the absence of protein.

Here, these methods of magnetite synthesis are investigated, with and without Mms6 protein, to compare to the previous studies. This is then expanded to include particles synthesised in the presence of His₆-Mms6, to see if the tag alters the ability of Mms6 to template uniform MNPs. Magnetite is magnetically soft, with high saturation magnetisation, and cobalt ferrite is magnetically hard with low saturation magnetisation. Thus, the effect of cobalt doping into these magnetite systems (without protein as a control, and with His₆-Mms6 and Mms6 in the bulk solution) is also studied, forming the key focus of this chapter. By controlled doping of Co into

magnetite, the magnetic properties of the biotemplated MNPs can be tuned to achieve optimum saturation magnetisation and coercivity. The main part of this work is published in Galloway *et al.* (2011).³

4.1 Effect of Cobalt Doping on Non-biotemplated MNPs

As mentioned above, it is known that cobalt doping increases the coercivity and decreases the saturation magnetisation of magnetite. However, literature values of M_s and H_c of MNPs with specific levels of cobalt doping into magnetite were not known for the $\text{Co}_x\text{Fe}_{3-x}\text{O}_4$ system. Therefore, hysteresis loops were measured using VSM for non-biotemplated MNPs. This was completed for POFHK and POFHN on dried MNPs. A wide range of morphologies of MNPs are known to be produced by room temperature co-precipitation in the absence of biomineralisation protein Mms6. The variation of the size and shape of MNPs produced by RTCP would not produce consistent magnetic behaviour, so it would be difficult to establish the effect of varying Co doping levels on RTCP MNPs. Many of the MNPs produced by RTCP in the absence of any protein are much smaller than the SD limit, so will behave superparamagnetically. SP MNPs tend to have a lower saturation magnetisation than SD particles, and very little coercivity. The range of particle sizes and shapes would produce complex magnetic hysteresis loops due to the different signals from the magnetic nanoparticles spanning the SP and SD size ranges. As the size effects may dominate the signal from the RTCP MNPs, this would make the effect of doping in different amounts of cobalt to the magnetite very difficult to interpret. As such, only the particles produced using the POFH methods were used for this preliminary work to establish the effect of doping different levels of cobalt into magnetite on the magnetic hysteresis of non-biotemplated MNPs.

4.1.1 VSM of POFHK MNPs

Levels of cobalt between 0% and 15% (i.e. Fe_3O_4 (magnetite) to $\text{Co}_{0.45}\text{Fe}_{2.55}\text{O}_4$ (15% cobalt doped magnetite) were synthesised by POFHK and dried for VSM* (see Figure 4.1).³ Higher levels of Co doping were not investigated, as this did not produce a black, magnetic precipitate, but a green coloured non-magnetic material. The green material is not likely to be cobalt doped magnetite, but is probably a different iron-cobalt oxide. This may be because the addition of higher levels of cobalt could alter the reaction conditions enough to make the formation of cobalt doped magnetite thermodynamically unfavourable.

* MNP synthesis and VSM measurements courtesy of S. Staniland, University of Leeds.

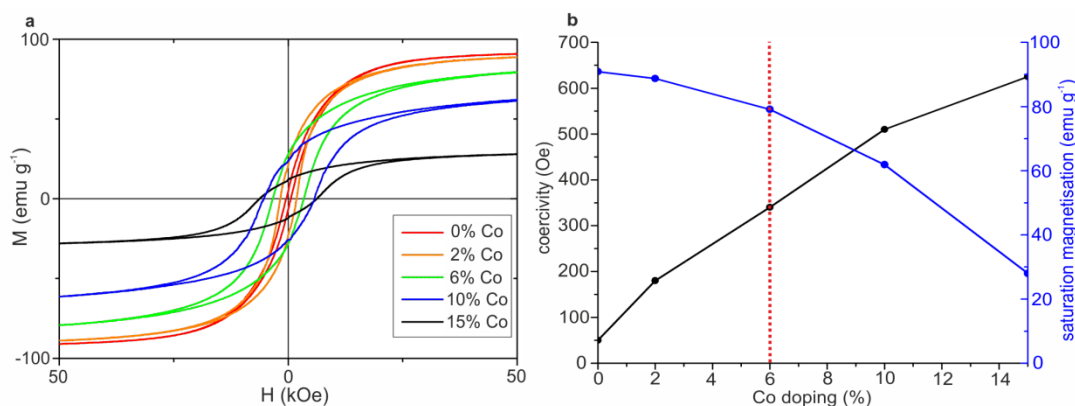


Figure 4.1. Hysteresis loops of POFHK MNPs, recorded at 10 K, H applied between ± 10 kOe, redrawn from Galloway *et al.* (2011).³ (a) Full hysteresis loops and (b) comparison of saturation magnetisation and coercivity of POFHK MNPs (crossover point is arbitrary). H_c increases and M_s decreases with the addition of cobalt as expected. Red dotted line on (b) marks 6% Co doping, selected as the optimum as there is little loss of M_s for a significant increase in H_c .

The coercivity (H_c) was measured from the centre to the intersection of the hysteresis loop with the x axis at $M=0$. As expected, the coercivity of the POFHK MNPs increases as cobalt is doped into the magnetite, from $H_c=53$ Oe for 0% Co to 622 Oe for 15% Co doping (see Table 4.1). The saturation magnetisation also varied as expected, with $M_s=90.7$ emu g⁻¹ for pure magnetite and $M_s=28.2$ emu g⁻¹ for 15% Co doping. As can be seen in Figure 4.1b, between 0% and 6% Co there is relatively little loss in saturation magnetisation (a reduction of 11.5 emu g⁻¹, which is 12.7%) for a 6.4 fold increase in coercivity from 52.3 to 334.7 Oe. However, between 6% and 15% Co doping there is a larger reduction in the saturation magnetisation (a difference of 51.0 emu g⁻¹, which is 64.4%), for only a 1.9 fold increase in the coercivity from 334.7 to 621.7 Oe. This indicates that 6% Co doping has an optimal increase in coercivity for relatively little loss of saturation magnetisation for POFHK MNPs.

4.1.2 VSM of POFHN MNPs

MNPs containing levels of cobalt between 0% and 10% were synthesised by POFHN and dried for VSM* (see Figure 4.2).³ A range between 0% and 10% Co doping was investigated, as higher levels of cobalt doping did not produce a black magnetic precipitate. The green, non-magnetic precipitate produced was similar to the precipitate produced at $\text{Co} > 15\%$ in POFHK. As expected, the coercivity of the POFHN MNPs increases as cobalt is doped into the magnetite, from $H_c=63$ Oe for 0% Co to 367 Oe for 10% Co doping (see Table 4.1). However, the saturation magnetisation was not altered by varying the amount of cobalt added to the MNPs, which remained level at ≈ 83 emu g⁻¹.

* MNP synthesis and VSM measurements courtesy of S. Staniland, University of Leeds.

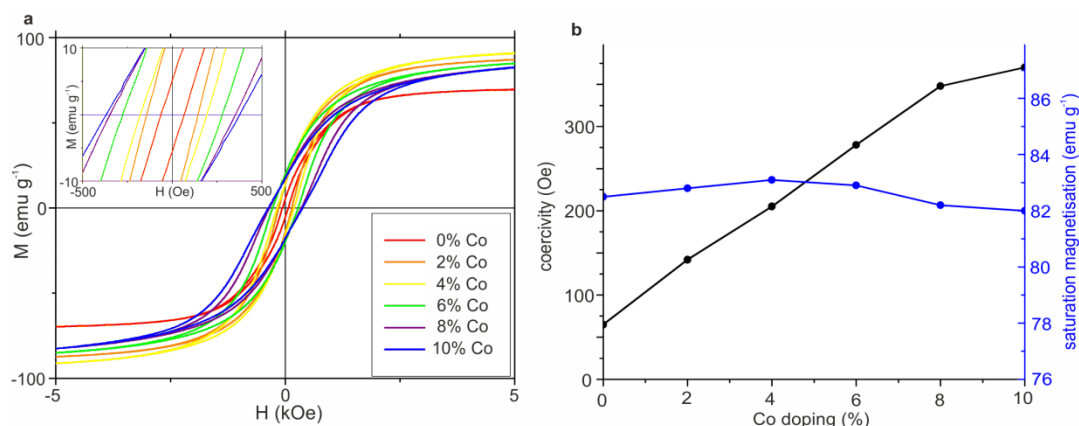


Figure 4.2. Hysteresis loops from VSM of POFHN MNPs, recorded at 10 K, H applied between ± 10 kOe, redrawn from Galloway *et al.* (2011).³ (a) Hysteresis loops, and inset close-up of centre of hysteresis loops. (b) Comparison of saturation magnetisation and coercivity of POFHN MNPs (crossover point arbitrary as it is scale dependent). H_c increases with the addition of cobalt as expected. However, M_s does not change significantly with increased cobalt doping.

Table 4.1. Summary of magnetic properties of non-biotemplated MNPs from both POFH methods. MNPs synthesised by the POFHK method shows expected trends in coercivity and saturation magnetisation. POFHN MNPs show expected trend in H_c but not M_s .

Co doping (%)	POFHK		POFHN	
	H_c (Oe)	M_s (emu g^{-1})	H_c (Oe)	M_s (emu g^{-1})
0.0	52.9	90.7	62.6	82.0
2.0	176.0	88.6	141.0	82.2
4.0	-	-	176.4	82.9
6.0	334.7	79.2	273.6	83.1
8.0	-	-	345.3	82.8
10.0	565.7	61.7	366.5	82.5
15.0	621.7	28.2	-	-

4.1.3 ICP-AES of POFH MNPs

By doping in different quantities of cobalt, the magnetic properties of these MNPs can be tuned between those of magnetite and cobalt ferrite. For the POFHK method, 6% Co doping was found to be the optimum amount of cobalt to add to the magnetite, as this increased the coercivity the most for the least loss in saturation magnetisation. The lack of change in the M_s of MNPs synthesised by the POFHN method could be due to a number of factors. One reason could be that cobalt is not incorporated well into the magnetite particles formed by POFHN. Therefore, the levels of cobalt and iron included in the MNPs produced by each method were analysed by ICP-AES* (Table 4.2).³ These data show that MNPs formed by both POFH methods preferentially incorporate cobalt in the MNPs rather than iron from

* ICP-AES measurements courtesy of S. Staniland, University of Leeds.

the mineralisation solutions. Also, this effect appears to be more pronounced for the lower levels of cobalt doping than the higher levels. The MNPs formed from 2% cobalt by POFHK actually contain $4.0 \pm 0.6\%$ Co, and POFHN MNPs contain $3.9 \pm 0.6\%$ Co. For the higher initial concentrations, there is still more cobalt included in the MNPs than expected from the stoichiometry of the reactants (POFHK 15% Co MNPs contain $20.0 \pm 3.3\%$ Co, and POFHN 10% Co MNPs contain $17.1 \pm 2.7\%$ Co).

Table 4.2. ICP-AES results for relative abundance of cobalt as a ratio of the total metal ions in the MNPs, from Galloway *et al.* (2011).³ Comparison of POFHK and POFHN methods show that both preferentially incorporate cobalt rather than iron into MNPs.

method	Co in reactants (%)	Co in particles (%)	error (\pm)	difference (%)
POFHK	0.0	0.0	-	-
	2.0	4.0	0.6	200
	6.0	10.6	1.7	177
	10.0	15.7	2.5	157
	15.0	20.0	3.3	133
POFHN	0.0	0.0	-	-
	2.0	3.9	0.6	195
	4.0	8.0	1.3	200
	6.0	9.6	1.5	160
	8.0	14.3	2.3	176
	10.0	17.1	2.7	171

It was not possible to find a literature value for the standard energy of formation ($\Delta_f G^0$) of cobalt ferrite ($\Delta_f G^0$ for CoFe_2O_4) to compare to that of magnetite ($\Delta_f G^0$ of magnetite $\text{Fe}_3\text{O}_4 = -1015.4 \text{ KJ mol}^{-1}$).⁴ This would have provided a thermodynamic explanation for the preferential inclusion of cobalt into the ferrite lattice during mineralisation by partial oxidation at 90°C . However, the ICP-AES data shows that the unexpected magnetic behaviour of the POFHN MNPs cannot be due to cobalt deficiency in the ferrite MNPs, as the MNPs are actually enriched in cobalt.

4.1.4 XRD of POFH MNPs

Another possible reason for the unexpected magnetic behaviour of the POFHN MNPs with changing levels of Co doping could be poor crystallinity or the presence of non-magnetite iron oxide mineral phases. Therefore, XRD of undoped magnetite MNPs formed by the POFHN and POFHK methods were recorded and compared* (see Figure 4.3).³ The position of the peaks obtained from powder XRD were then converted to d spacings to compare to the EVA crystallographic data base, and are

* Powder XRD data courtesy of S. Staniland, University of Leeds.

summarised in Table 4.3. The peaks from the POFHK sample are much higher and sharper than those from the POFHN particles. This may indicate that POFHK MNPs have a larger grainsize than POFHN particles. Maghemite and magnetite have very similar crystal structures, so produce similar X-ray diffraction patterns. As can be seen in Table 4.3, the peaks produced by the POFHK sample are an extremely close match to magnetite, therefore it is likely POFHK MNPs consist of magnetite. The POFHN peaks are also a close match to magnetite, but some (e.g. the (111), (220) and (311) peaks) are a closer match to maghemite. This indicates that MNPs produced by POFHN may contain some maghemite, which may explain the reduced saturation magnetisation of 0% Co doped POFHN magnetite. The presence of maghemite may also be why the saturation magnetisation of POFHN MNPs does not vary with changing levels of Co doping. Maghemite nanoparticles are often acicular (needle shaped), so the low aspect ratio can help stabilise magnetic domains along the long axis.

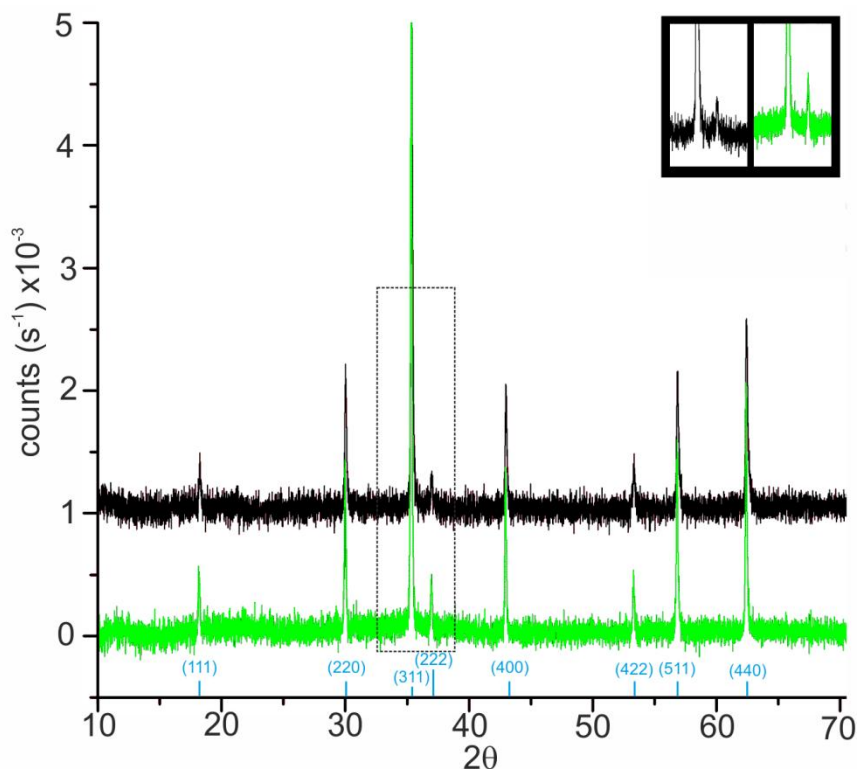


Figure 4.3. Powder XRD of magnetite MNPs synthesised by POFHN (black) and POFHK (green), after Galloway *et al.* (2011).³ The traces are offset so peaks can be seen more clearly. Higher, sharper peaks indicate a larger grainsize, and magnetite peak position is labelled in blue.

Table 4.3. Summary of d spacing for magnetite, maghemite and POFH MNPs. Pattern numbers for magnetite and maghemite shown in Section 2.6.5, POFHK and POFHN calculated by converting peak position recorded in powder XRD (2θ) to d spacing (in Å) using the Bragg Equation (Equation 2.12).

peak	d spacing			
	magnetite	maghemite	POFHK	POFHN
(111)	4.850	4.820	4.854	4.814
(220)	2.966	2.950	2.960	2.955
(311)	2.530	2.520	2.526	2.523
(222)	2.419	2.410	2.419	2.416
(440)	2.096	2.080	2.096	2.093
(422)	1.712	1.700	1.712	1.711
(511)	1.614	7.610	1.615	1.613
(440)	1.483	1.480	1.483	1.482
(533)	1.279	1.270	1.280	1.279

4.2 Cobalt Doping and Mms6 in the POFH System

To determine if magnetic particles formed by partial oxidation of ferrous hydroxide can be templated by Mms6 to form cobalt doped magnetite MNPs, grain size analysis of TEM images was completed. It has been previously shown that POFHK MNPs templated by Mms6 are smaller and more uniform than those formed in the absence of protein.² As 6% Co doping POFHK particles had the greatest increase in H_c for the least loss of M_s , MNPs formed in the presence and absence of Mms6, both with and without 6% Co doping, were analysed for both POFH methods. From here on, all undoped particles are referred to as 'Fe' and all particles containing 6% cobalt doping as 'Co' followed by a subscript. 'Mms6' identifies Mms6 protein templated MNPs and 'no protein' indicates controls formed in the absence of protein. Table 4.4 contains a summary of these grain size analysis data from the TEM images of POFH MNPs. The length and width of ≈ 500 particles were recorded for each sample, and those with an aspect ratio greater than 0.5 were deemed equidimensional and used for grain size analysis.

Table 4.4. Summary of grainsize analysis data for POFH MNPs, averages, errors and detail of fitted peaks, from Galloway *et al.* (2011).³ Best fit is a single Gaussian (1) or double Gaussian (2) based on the lowest χ^2 of the fitted peaks.

method	particle	average (nm)	peak fitting details			
			best fit	centre (nm)	error on fit (\pm)	FWHM (nm)
POFHK	Fe _{no protein}	234	1	164.3	6.6	143.3
	Co _{no protein}	336	2	102.3	5.2	75.2
				427.9	12.9	277.1
	Fe _{Mms6}	86	2	42.9	2.7	53.4
				136.4	4.6	65.5
	Co _{Mms6}	132	2	39.0	3.4	34.4
151.3				3.2	92.2	
POFHN	Fe _{no protein}	315	2	59.0	3.5	19.8
				400.2	16.8	172.1
	Co _{no protein}	207	2	48.3	1.9	41.6
				327.2	28.	346.2
	Fe _{Mms6}	145	1	134.7	6.3	162.3
	Co _{Mms6}	60	2	24.4	1.4	22.0
58.9				7.7	54.8	

4.2.1 POFHK TEM and Grainsize Analysis

TEM* images were taken of MNPs formed by the POFHK method, and the width and length of ≈ 500 particles recorded in Image J⁵ (see Figure 4.4).³ As can be seen in the TEM images, there are very few acicular particles, but there is a fairly wide range of particle sizes. POFHK Fe_{no protein} MNPs range in size from 20 to 730 nm in diameter, with the size of Co_{no protein} particles ranging even higher to ≈ 820 nm. When the particles are doped with 6% Co, a higher proportion of the particles appear at the larger end of the grainsize distribution. When Mms6 is added to the reactants, the maximum particle grainsize achieved is significantly suppressed (≈ 200 nm for Fe_{Mms6} and ≈ 290 nm for Co_{Mms6} MNPs). The Co_{Mms6} MNPs are larger than the Fe_{Mms6} MNPs for POFHK. This indicates that Co doping increases the particle size, both with and without the Mms6 biomineralisation protein. These results suggest that Mms6 suppresses the maximum grainsize of MNPs, both with and without cobalt doping, but is unable to form MNPs with a single narrow, grainsize distribution using this POFHK method.

* TEM images courtesy of S. Staniland, University of Leeds.

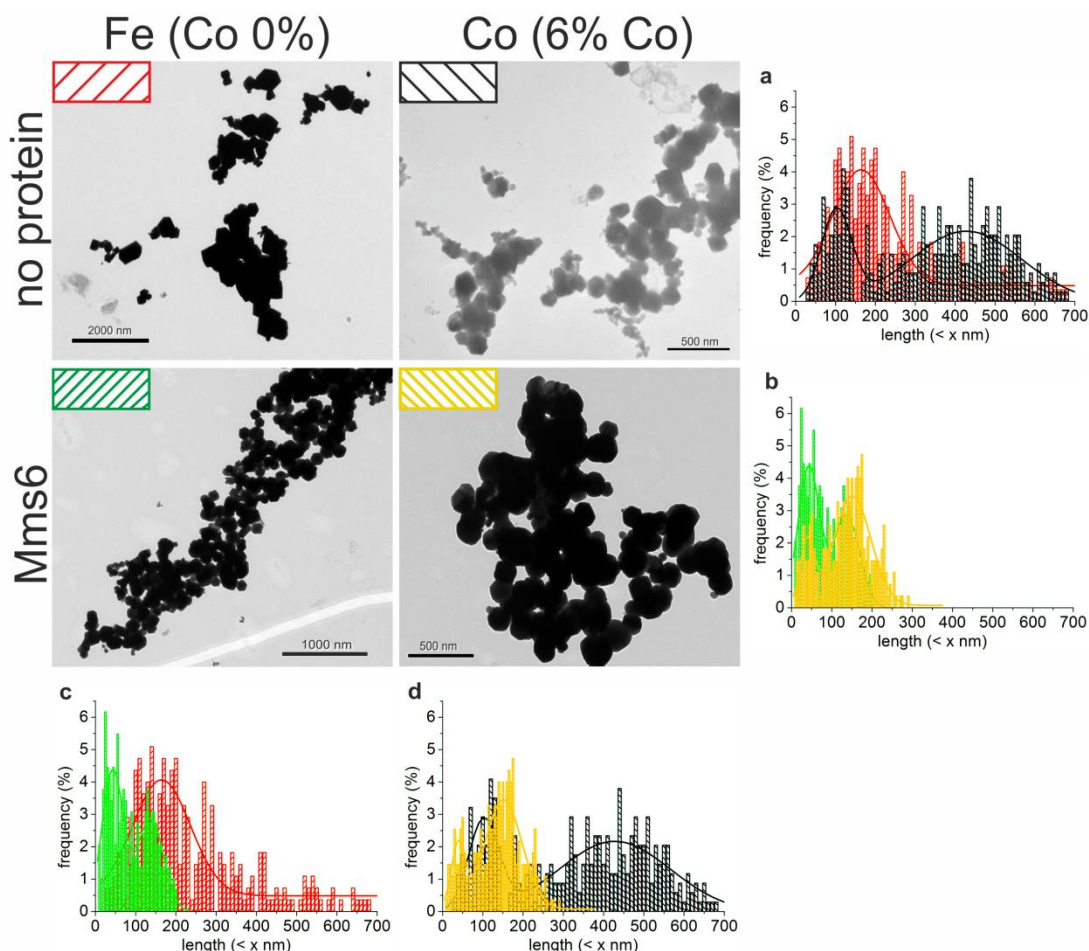


Figure 4.4. TEM images and grain size analysis of POFHK MNPs, from Galloway *et al.* (2011).³ Graphs (a-d) summarise particle grain size analysis of equidimensional particles (aspect ratio >0.5). Particles formed without protein are larger and frequency distributed into a bin size of 10, and fitted with a single Gaussian peak for Fe_{no protein} (red) and a double Gaussian peak for Co_{no protein} (black). Particles formed with Mms6 are smaller and frequency distributed into a bin size of 5, and both Fe_{Mms6} (green) and Co_{Mms6} (yellow) are fitted with 2 peak Gaussian distributions.

4.2.2 POFHN TEM and Grain size Analysis

The TEM* and particle analysis of MNPs formed by the POFHN method are shown in Figure 4.5.³ The majority of the POFHN MNPs formed without protein or cobalt (Fe_{no protein}) were found to have low aspect ratios, as such only ≈60 of the MNPs analysed were included in the grain size analysis for this sample. The addition of Mms6 or cobalt both dramatically reduced the occurrence of acicular particles for the POFHN method, with far more rounded MNPs appearing for Co_{no protein} than seen in the other samples. In the absence of Mms6, the maximum MNP size for equidimensional particles is ≈700 nm, with a two peak distribution occurring for the Co_{no protein} MNPs. The grain size distribution of the non-biologically mediated MNPs is broad, with the 6% Co doping appearing to again increase the grain size of the MNPs. When Mms6 is added during MNP formation, the particle size distributions

* TEM images courtesy of S. Staniland, University of Leeds.

are again shifted to much smaller grainsize. The addition of Mms6 reduced the maximum particle size to ≈ 390 nm for Fe_{Mms6} and ≈ 240 nm for Co_{Mms6} MNPs. Despite a double peak best fitting the Co_{Mms6} particle grainsize data, the grainsize distribution of the POFHN Co_{Mms6} particles is narrower than for the other POFHN particles. This is the opposite trend to all other grainsize measurements, in which Co doping appears to shift the MNPs to larger grainsizes.

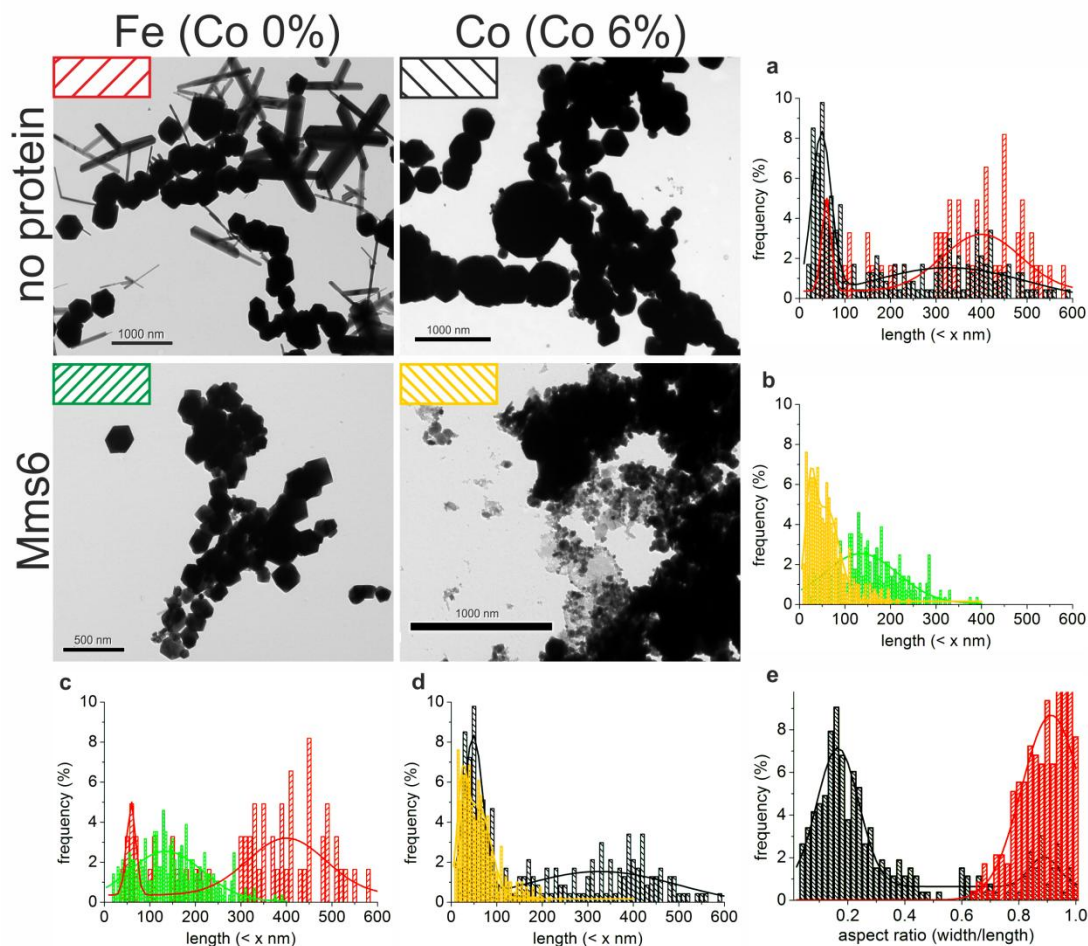


Figure 4.5. TEM images and grainsize analysis of POFHN MNPs, from Galloway *et al.* (2011).³ Graphs (a-d) summarise particle grainsize analysis of equidimensional particles (aspect ratio >0.5). Particles formed without protein are frequency distributed into a bin size of 10, and fitted with a Gaussian double peak for both $\text{Fe}_{\text{no protein}}$ (red) and $\text{Co}_{\text{no protein}}$ (black). Particles formed with Mms6 are frequency distributed into a bin size of 5, and Fe_{Mms6} (green) is fitted with a single Gaussian distribution, and Co_{Mms6} (yellow) is fitted with 2 peak Gaussian distribution. Graph (e) compares the aspect ratio (width/length) of $\text{Fe}_{\text{no protein}}$ (red) and $\text{Co}_{\text{no protein}}$ (black).

4.2.3 Quality of POFH MNPs

POFHK MNPs showed the expected trends in magnetic properties (increased coercivity and decreased saturation magnetisation) with increased levels of cobalt doping. However, the saturation magnetisation for MNPs synthesised by POFHN remains at $\approx 83 \text{ emu g}^{-1}$ between 0% and 10% Co doping. This is slightly lower than the 88.5 emu g^{-1} of 150 nm spherical magnetite particles of Goya *et al.* (2003),⁶ but higher than the 10% Co doped POFHK MNPs, which are $\approx 63 \text{ emu g}^{-1}$. This lower M_s of the POFHN MNPs may be due to poorer crystallinity of particles made by this method in the absence of cobalt. The addition of cobalt has been shown to improve the crystallinity of spinel structured ceramics.⁷ Therefore, the doping of cobalt may improve the crystallinity of the POFHN MNPs, and thus allow the saturation magnetisation to stay high when cobalt is incorporated into the spinel structure of the MNPs. However, the particle size and shape is changed when cobalt is added to the POFHN mineralisation solution. As morphology and particle size also significantly influences the magnetic properties of nanoparticles, this may also cause the unexpected trend in the saturation magnetisation of the POFHN MNPs.

The particle size distribution of POFHN MNPs is narrower in the presence of 6% Co doping, and there is a smaller average particle size. When cobalt is added to the POFHN mineralisation, the MNPs appear to be more rounded than the faceted particles formed in the absence of cobalt. Also, the shape anisotropy of the elongated MNPs produced by POFHN $\text{Fe}_{\text{no protein}}$ may dominate the magnetic hysteresis of the undoped particles. As cobalt is added, there is a reduction in the occurrence of needle-shaped particles. The XRD data (Section 4.4.1) indicated that there may be some maghemite present in the POFHN sample, which could be the acicular particles seen in Figure 4.5. Itoh & Sugimoto (2003)⁸ found that nanoscale crystals of maghemite with an aspect ratio of 0.25 have a greater coercivity than magnetite MNPs of the same morphology. When the aspect ratio is more equidimensional, the coercivity of the maghemite is greatly reduced.⁸ Therefore, the stability of the saturation magnetisation as up to 10% cobalt is doped into the POFHN MNPs could be due to the presence of different levels of maghemite, or variations in the crystallinity, particle size or shape across the range.

For both POFH methods, there is a wide size distribution of MNPs formed, whether doped with cobalt or formed with Mms6 in the bulk solution. The MNPs in the Amemiya *et al.* (2007)² study of Mms6 templating with POFHK found a much smaller grain size of both Mms6 templated ($\approx 20 \text{ nm}$) and untemplated MNPs ($\approx 32 \text{ nm}$). The crystal size and shape of MNPs formed by POFHK is very sensitive to the ratio of the reactants in the mineralisation solution.⁹ MNPs formed with a slight excess of iron tend to be large ($\approx 1 \mu\text{m}$) and rounded⁹ similar to the particles

formed in this study. However, if there is an excess of hydroxide, the MNPs are much smaller (≈ 100 nm) and show an octahedral morphology.⁹ The MNPs in the Amemiya *et al.* (2007)² study were formed with an excess of OH⁻ in the reaction (30 mM FeSO₄, 100 mM KOH, 400 mM KNO₃), so exhibit the octahedral morphology in the absence of Mms6, and the cubo-octahedral morphology in the presence of Mms6.

The reaction used to form MNPs for this study was closer to stoichiometry (50 mM FeSO₄, 100 mM KOH, 400 mM KNO₃), which explains why the average grainsize of MNPs formed were much larger (up to ≈ 820 nm). The propensity for the reaction conditions to form larger particles can also explain why Mms6 was unable to template uniform MNPs for the POFH methods. As the reaction conditions favour the formation of much larger MNPs than Mms6 is able to template, the biomineralisation protein was unable to fully control the mineralisation reaction. This led to the bimodal grainsize distributions, with Mms6 only able to template some of the POFH MNPs towards the smaller grainsizes. Therefore, the POFH methods, due to their sensitivity to the reaction conditions, are not suitable for the formation of uniform biotemplated cobalt doped magnetite from a bulk solution. However, adjustment of the mineralisation conditions towards conditions that suit Mms6 templating could be used to improve the size distribution of the MNPs produced by this method. Optimisation of the reaction conditions towards forming uniform MNPs has been investigated, but for Mms6 when immobilised onto a patterned surface rather than when in the bulk solution (Chapter 5).

4.3 Cobalt Doping, Mms6 and the RTCP System

In all cases, the MNPs templated by the POFH methods presented above span quite a large range of grainsizes, whether Mms6 is present or absent. This means MNPs produced using the POFH methods here, either with or without cobalt doping, would be unsuitable for many applications. This is because the magnetic properties of mixed grainsizes and shapes of particles will not be uniform, but will have mixture of magnetic behaviours. Therefore, the room temperature co-precipitation method was also investigated to establish if this is more suitable to produce bio-mediated uniform, cobalt doped MNPs.

Again, all undoped particles are referred to as 'Fe' and all particles containing 6% cobalt doping as 'Co' followed by a subscript. 'Mms6' identifies Mms6 protein templated MNPs, 'His₆-Mms6' identifies tagged protein templated MNPs, and 'no protein' indicates controls formed in the absence of protein. To determine if magnetic particles formed by room temperature co-precipitation can be templated by Mms6 to form uniform cobalt doped magnetite MNPs, grainsize analysis of the

TEM images was recorded using Image J.⁵ It has been shown previously that MNPs formed by RTCP in the presence of Mms6 are larger and more uniform than those formed without Mms6 protein. As 6% Co doping POFHK particles had the greatest increase in H_c for the least loss of M_s , RTCP MNPs formed in the presence and absence of Mms6, RTCP MNPs formed both with and without 6% Co doping, were analysed.

The MNPs formed with the tagged Mms6 protein were characterised, as MNPs formed by His₆-Mms6 may be suitable for attachment to patterned surfaces after MNP synthesis. Also, the expression and purification of His₆-Mms6 is simpler, and therefore less expensive, than the untagged Mms6 protein. Table 4.5 contains a summary of the grainsize analysis data from the TEM images discussed below. The length and width of ≈ 500 particles were recorded for each sample, and those with an aspect ratio greater than 0.5 were deemed 'equidimensional' and used for the grainsize analysis. The magnetic properties and crystallinity of the RTCP particles were also characterised to see if the cobalt doping and/or biotemplating has an effect on the properties of the MNPs.

Table 4.5. Summary of grainsize analysis data for RTCP MNPs, averages, errors and detail of fitted peaks, from Galloway *et al.* (2011).³ Best fit is Asymmetric (A) or a single Gaussian (1) based on the lowest χ^2 of the fitted peaks for each data set.

particle	average (nm)	peak fitting details			
		best fit	centre (nm)	error on fit (\pm)	FWHM (nm)
Fe _{no protein}	23.1	A	8.7	0.3	n/a
Co _{no protein}	19.6	A	11.7	0.8	n/a
Fe _{His6-Mms6}	21.9	1	18.2	0.4	14.1
Co _{His6-Mms6}	26.8	1	23.2	0.5	15.4
Fe _{Mms6}	22.3	1	21.9	0.3	12.2
Co _{Mms6}	31.1	1	31.7	0.2	15.3

4.3.1 TEM and Grainsize Analysis of RTCP MNPs

TEM and particle grainsize analysis for undoped and 6% Co doped MNPs formed by RTCP are shown in Figure 4.6,³ for 'no protein,' 'His₆-Mms6' and 'Mms6'. RTCP MNPs formed in the absence of any biomineralisation protein have a range of particle sizes and shapes, which could be due to the presence of different iron oxides or hydroxides, as well as the desired magnetite phase. The control MNPs have an asymmetric grainsize distribution, which is biased towards the smaller particle sizes. The peak for Fe_{no protein} MNPs centres on 8.7 ± 0.3 nm, and Co_{no protein} on 11.7 ± 0.8 nm. Particles synthesised with His₆-Mms6 are larger than the controls (Fe_{His6-Mms6} peak centres on 18.2 ± 0.4 nm, and Co_{His6-Mms6} on 23.2 ± 0.5 nm). MNPs

templated by untagged Mms6 are larger still (the Fe_{Mms6} peak centres on 21.9 ± 0.3 nm, and Co_{Mms6} on 31.7 ± 0.2 nm). This agrees with the trend found for increasing particle size with the addition of 6% Co for the POFHK method, and for non-biotemplated POFHN MNPs. It can also be seen that cobalt doping increases the size of MNPs across the range of RTCP synthesised particles investigated here.

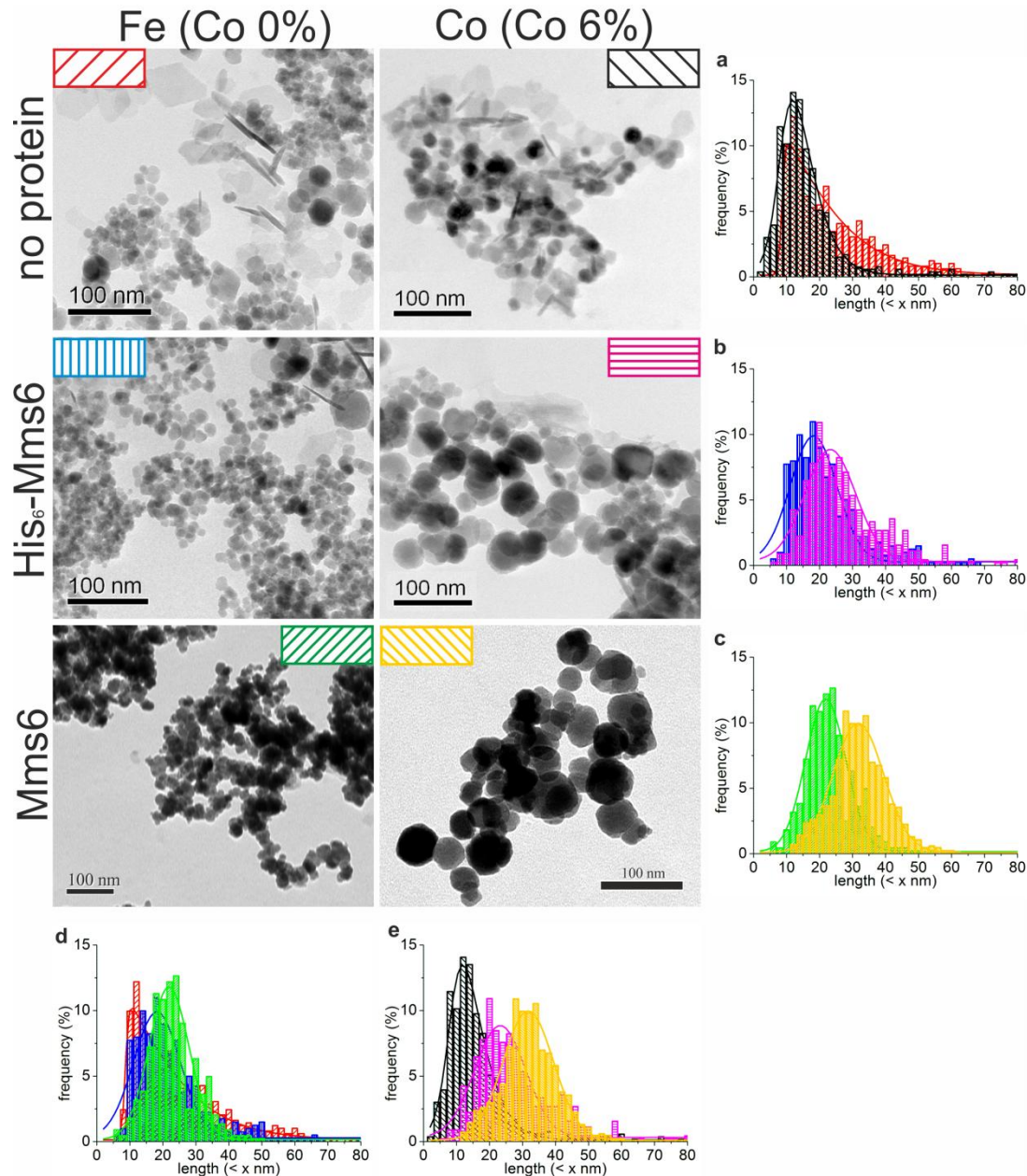


Figure 4.6. TEM and grainsize analysis of RTCP MNPs, from Galloway *et al.* (2011).³ Graphs (a-e) show grainsize distribution and fits for MNPs formed in the presence and absence of 6% Co doping for controls formed in the absence of any protein (no protein), His₆-Mms6 templated MNPs and Mms6 templated particles. The particles are frequency distributed into 2 nm bins and fitted with asymmetric curves for both $\text{Fe}_{\text{no protein}}$ (red) and $\text{Co}_{\text{no protein}}$ (black) MNPs. Single Gaussian distributions are fitted to MNPs formed with tagged Mms6 ($\text{Fe}_{\text{His6-Mms6}}$ are shown in blue and $\text{Co}_{\text{His6-Mms6}}$ in pink) and with Mms6 (Fe_{Mms6} are shown in green and Co_{Mms6} in yellow).

4.3.2 Elemental Analysis of RTCP MNPs

4.3.2.1 ICP-AES of RTCP MNPs

The levels of cobalt and iron included in the MNPs produced by RTCP were analysed by ICP-AES.* This showed that RTCP MNPs formed from the reaction solution containing 6% Co/ 94% Fe contained only 4.8% Co.³ This is the opposite trend to that seen in the POFH methods, as cobalt does not appear to be preferentially included in the RTCP MNPs. It is possible that the platy and acicular particles (see TEM in Figure 4.6) may not be magnetite. The range of MNPs morphologies formed by RTCP may not be able to include cobalt into their crystal structures as easily as the larger MNPs formed by the POFH methods. This could lead to zonation of cobalt within individual particles, or particles with different morphologies containing different levels of cobalt.

4.3.2.2 EELS and EDX of RTCP MNPs

The elemental analysis above indicated that some of the different particles formed by RTCP may not be able to include cobalt into the MNPs as well as the particles formed by POFH. Therefore, elemental analysis of $\text{Co}_{\text{His6-Mms6}}$ and $\text{Co}_{\text{no protein}}$ MNPs was performed in the TEM using EDX and EELS, see Figure 4.7.³ Although very few were present, an area containing some acicular particles from the biotemplated sample ($\text{Co}_{\text{His6-Mms6}}$) was selected. This was done so the Co distribution could be checked in all the different particle morphologies found.

* ICP-AES measurements courtesy of S. Staniland, University of Leeds.

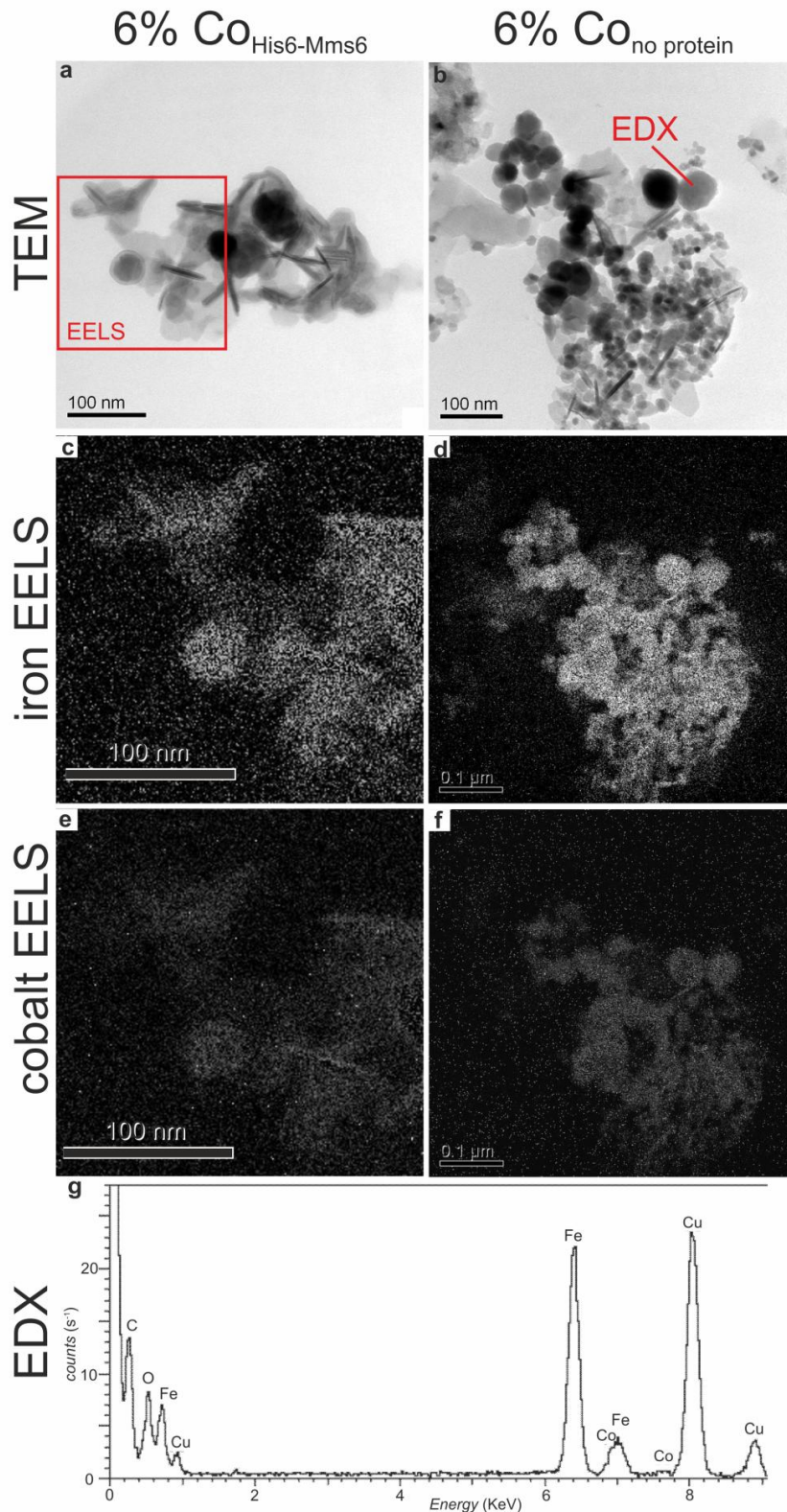


Figure 4.7. TEM images, EELS maps and EDX analysis* of $\text{Co}_{\text{His6-Mms6}}$ and $\text{Co}_{\text{no protein}}$ MNPs, from Galloway *et al.* (2011).³ (a) TEM of $\text{Co}_{\text{His6-Mms6}}$, selected for analysis as, although rare in this sample, it contained some different particle morphologies. (b) TEM of $\text{Co}_{\text{no protein}}$. Iron EELS map of (c) $\text{Co}_{\text{His6-Mms6}}$ and (d) $\text{Co}_{\text{no protein}}$ on TEM images shown in (a) and (b) respectively. Cobalt EELS map of same TEM images for (e) $\text{Co}_{\text{His6-Mms6}}$ and (f) $\text{Co}_{\text{no protein}}$. (g) plot of EDX obtained from centre of large particle annotated in image b.

* TEM, EDX and EELS data in collaboration with M. Ward, University of Leeds.

As expected, the signal from the cobalt in the EELS maps is lower than the signal from the iron in both non-templated ($\text{Co}_{\text{no protein}}$) and biotemplated ($\text{Co}_{\text{His6-Mms6}}$) MNPs. The elemental signals detected by EELS are due to the electron beam interacting with the elements encountered by the beam during transmission. Different elements attenuate different energies of electrons in the beam. This means that the more an electron beam can interact with a sample, or the more abundant a particular element is within that sample, the greater the signal for that element. Despite the low signal from cobalt, the maps show that Co appears to be fairly evenly distributed between all particle morphologies.

The Co signal shows up most clearly on the EELS maps from the equidimensional MNPs. This is probably because these are the thickest particles, so are able to interact with the TEM beam for longer periods as the beam passes through the samples. There is also some cobalt detected in the acicular particles, which are thinner than the equidimensional MNPs. The platy particles also seem to contain some cobalt, as there is even some signal in the EELS map from these very thin materials. Cobalt and iron have very similar peak positions in EDX analysis, but can be clearly distinguished in the spectrum shown in Figure 4.7g. The EDX analysis (annotated on Figure 4.7b) also shows that cobalt and iron are present at the centre of the large particle selected. These data indicate that cobalt is evenly distributed within all of the RTCP MNPs.

4.3.3 Crystallinity of RTCP MNPs

The RTCP MNPs were dried and analysed using XRD,* as particles made by this method usually show polydispersity and poor crystallinity. Figure 4.8³ shows the diffraction patterns obtained for undoped and 6% Co doped RTCP MNPs, synthesised both with and without Mms6 protein. The peaks from these MNPs are broader than those from the POFH method, which is due to the small size of the MNPs. The low height of the peaks may also indicate poor crystallinity and/or a more dispersed size distribution. Based on the standard spectrum for magnetite, the (311) peak at $2\theta \approx 35.4^\circ$ should be the most intense, and thus the easiest to distinguish in each spectrum. The Debye-Scherrer equation (Equation 2.13) can be used to measure the grain size of the particles, and assumes the particles are perfectly crystalline with a narrow grain size distribution. The (311) peak was fitted for each sample, and used to calculate the grain size from XRD to compare with the values measured from TEM (Table 4.6).³

* XRD data courtesy of S. Staniland, University of Leeds.

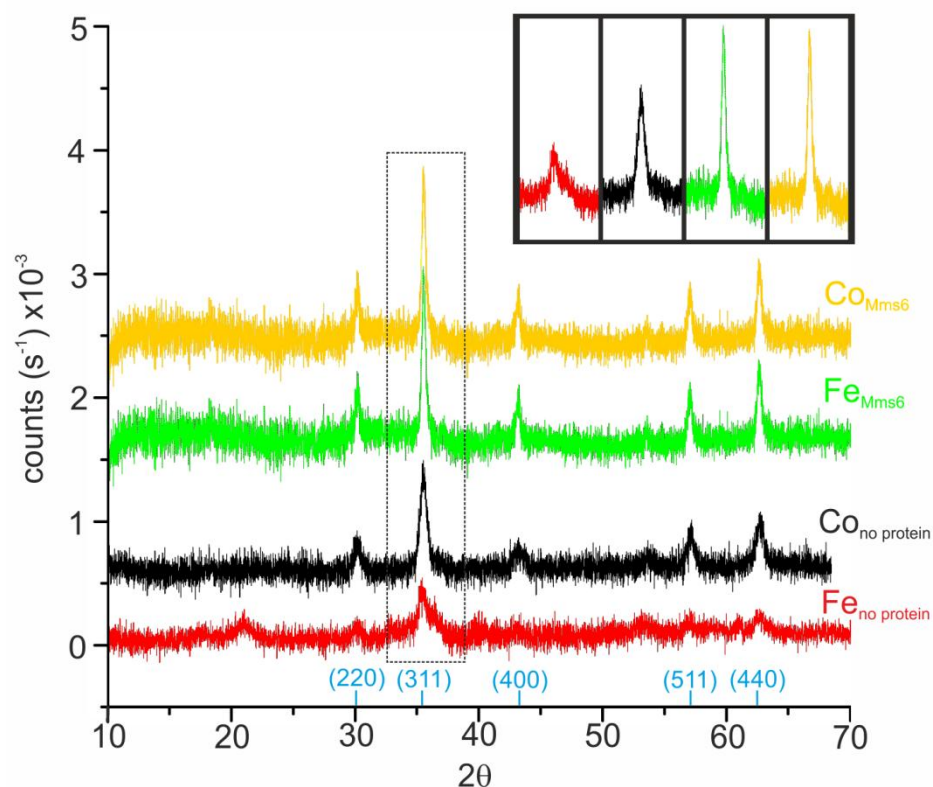


Figure 4.8. Powder XRD diffraction patterns for RTCP MNPs, from Galloway *et al.* (2011).³ Traces are offset so peaks can be seen clearly for each sample. Traces are coloured as $\text{Fe}_{\text{no protein}}$ (red), $\text{Co}_{\text{no protein}}$ (black), Fe_{Mms6} (green) and Co_{Mms6} (yellow). Magnetite ideal peak positions are labelled in blue. The magnetite (311) peak¹⁰ at $2\theta=35.4^\circ$ is highlighted (inset) is used to calculate grainsize based on Equation 2.13. This is then used to estimate crystallinity (see Table 4.6).

Table 4.6. Analysis of RTCP XRD peaks and grainsize, from Galloway *et al.* (2011).³ Peaks are fitted, and the grainsize estimated using Equation 2.13. Comparison between TEM and XRD values used to estimate crystallinity.

sample	(311) peak FWHM ($^\circ$)	(311) peak FWHM (rad)	Calculated from XRD (nm)	average from TEM (nm)	agreement (%)
$\text{Fe}_{\text{no protein}}$	1.6877	0.0295	4.9	23.1	21.2
$\text{Co}_{\text{no protein}}$	0.7446	0.0130	11.1	19.6	56.6
Fe_{Mms6}	0.6845	0.0102	14.1	22.3	63.2
Co_{Mms6}	0.4124	0.0072	20.1	31.1	64.6

The agreement between the grainsize from XRD and TEM measurements has been used to assess the crystallinity of the RTCP MNPs, although a broad grainsize distribution could also lead to poor agreement between these values. Control $\text{Fe}_{\text{no protein}}$ RTCP MNPs have a broad peak, and a low size agreement of 21.1%, which indicates they have a broad size distribution and/or poor crystallinity, as expected. The $\text{Co}_{\text{no protein}}$ RTCP MNPs, which contain 6% Co doping, have an improved agreement of 56.6%. This is despite the peak being quite low and wide. The agreement indicates the addition of 6% cobalt to RTCP MNPs may improve

their crystallinity as the grainsize analysis from TEM shows that they have a broader size distribution. Previously, it has been shown that Co doping can improve the crystallinity of ceramic materials with a spinel structure.⁷ Therefore, these XRD data show that cobalt doping improves the crystallinity of RTCP MNPs.

The peaks are the most intense and narrowest for the Mms6 templated MNPs, and both biotemplated samples have a good agreement between TEM and XRD grainsizes ($Fe_{Mms6}=63.2\%$, $Co_{Mms6}=64.6\%$). The agreement may not be perfect (i.e. 100%) due to some of the assumptions of the Debye-Scherrer equation (Equation 2.13), which uses a correction factor (the shape constant) and assumes that the powder has perfectly uniform grainsize distribution. As can be seen in TEM, the grainsize distribution of the biotemplated MNPs is narrow (FWHM of $Fe_{Mms6}=12.2$ nm and $Co_{Mms6}=15.3$ nm), but is not a single value. The increased sharpness in the XRD peaks and improved agreement between the XRD and TEM grainsizes of the biotemplated RTCP MNPs show that the addition of Mms6 significantly increases the quality of these nanocrystals.

4.3.4 VSM of RTCP MNPs

RTCP MNPs were dried, weighed, and packed into capsules to record magnetic measurements. VSM was used to record FC and ZFC measurements for all six RTCP MNP samples. A series of hysteresis loops were also recorded at a range of temperatures for the RTCP samples.

4.3.4.1 Magnetisation with Temperature

The samples were cooled in a zero field to 10 K. Then the change in magnetisation was recorded as the temperature was increased at 1 K minute^{-1} to 250 K in an applied field of 1 kOe to record ZFC measurements. The samples were then cooled in the same applied field at the same rate to record FC measurements (see Figure 4.9).³ The smaller $Fe_{no \text{ protein}}$ MNPs show the lowest magnetisation, with the slightly larger $Fe_{His6-Mms6}$ MNPs having slightly higher values. The largest (and likely more crystalline) Fe_{Mms6} MNPs have the highest magnetisation values for FC and ZFC in this regime.

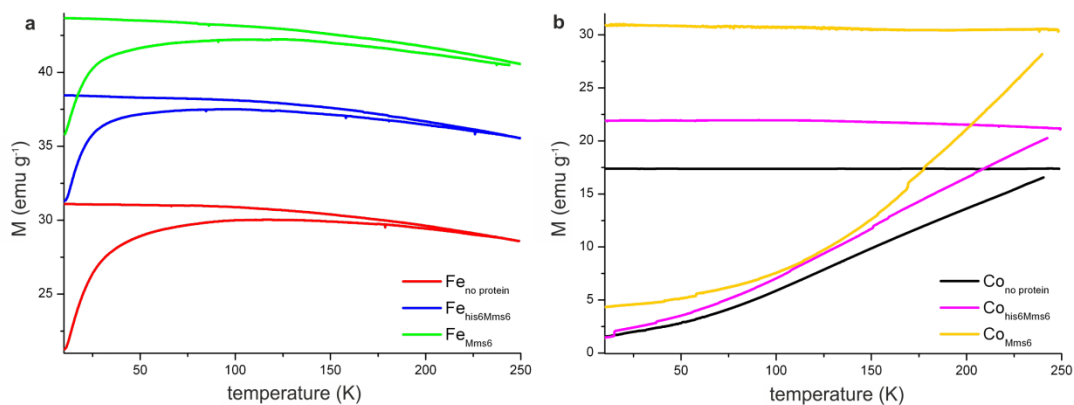


Figure 4.9. VSM of ZFC (lower trace) and FC (upper trace) measurements for RTCP MNPs, from Galloway *et al.* (2011).³ Samples were heated/cooled at 1 K minute⁻¹ between 10 K and 250 K in an applied field of 1 kOe. (a) Undoped magnetite MNPs and (b) 6% Co doped particles.

The undoped magnetite MNPs have a blocking temperature of between 100-200 K. Above T_B , the MNPs behave paramagnetically, as the thermal disorder dominates over the ferrimagnetism of the small magnetite particles. T_B cannot be more accurately determined with the VSM used, as the temperature of the sample usually lags behind the temperature of the chamber, creating an offset between the FC and ZFC measurements. However, this range for T_B is consistent with spherical magnetite particles of the grainsizes recorded from TEM. For example, Goya *et al.* (2003)⁶ found that the blocking temperature of their 10 nm magnetite is ≈ 107 K and 50 nm magnetite is ≈ 300 K. Figure 4.9b shows that the 6% Co doped particles have a much higher blocking temperature, probably at about room temperature ($T_B > 250$ K). Unfortunately, the VSM used to record these data is not able to remain stable when recording measurements up to temperatures ≈ 300 K. Therefore, it was not possible to determine a more accurate blocking temperature for these 6% Co doped MNPs.

There is no evidence of a Verwey transition in the ZFC or FC measurements, which is as expected. The sharp drop in magnetisation is completely suppressed by small, SP magnetite particles.¹¹⁻¹³ As the RTCP Fe_{Mms6} MNPs are likely to be below the SD size for magnetite ($SD \approx 25$ nm, $Fe_{Mms6} = 21.9 \pm 0.3$ nm) there should not be a visible transition. Magnetic measurements across T_V of dried magnetic bacteria have shown that the Verwey Transition is at about 100 K for magnetosome magnetite particles.^{12,14} Magnetosome MNPs are usually in the SD size for magnetite, between 25-50 nm in diameter.^{15,16}

Goya *et al.* (2003)⁶ found that the Verwey Transition is weakened, and suppressed from ≈ 98 K for 150 nm particles to ≈ 16 K for 50 nm diameter magnetite particles. The higher T_v of magnetosome MNPs when compared to the artificially synthesised particles of Goya *et al.* (2003)⁶ could be due to surface oxidation. The magnetosome membrane may protect the biogenic MNPs from exposure to oxygen, and thus prevent alteration by air. The particles of Goya *et al.* (2003)⁶ were dried in air, so may well have been subjected to surface oxidation, and thus depression of T_v . Although every care was taken to reduce the exposure of the MNPs to air during drying, it is possible that some surface oxidation may have occurred. Impurities have also been found to significantly suppress or obscure the Verwey Transition.^{13,17-19} The doping of 6% Co into magnetite can be expected to introduce a significant level of impurity into the magnetite inverse spinel structure. This means that the cobalt doping should completely obscure the Verwey Transition in the larger Co_{Mms6} (31.1 ± 0.2 nm) and $\text{Co}_{\text{His6-Mms6}}$ (26.8 ± 0.5 nm) RTCP MNPs. Therefore, a combination of the small grain size of the Fe_{Mms6} MNPs (probably smaller than the SD/SP boundary) and their possible surface oxidation may combine to completely suppress T_v in these undoped biotemplated particles. For the Co_{Mms6} particles, the Verwey transition could also be completely suppressed by the 6% cobalt doping acting as an impurity.

4.3.4.2 Magnetic Hysteresis

Spherical and cubic magnetite nanoparticles below ≈ 25 nm are superparamagnetic,²⁰ with the upper size limit of the SD zone at ≈ 85 nm.^{21,22} Cobalt ferrite is able to maintain a single domain at room temperature in particles between about 5 nm¹⁰ and 70 nm.²³ Below the SD zone, MNPs will behave superparamagnetically, and above they will form multiple domains. The SD size limits were not known for 6% Co doped ferrite, so a linear relationship between the two end-members has been assumed to estimate these values, see Figure 4.10.³ Based on the grain size analysis above, this indicates that Co_{Mms6} RTCP MNPs should fall within the lower part of the SD zone ($\text{Co}_{\text{Mms6}} = 31.7 \pm 0.2$ nm). Also, $\text{Co}_{\text{His6-Mms6}}$ RTCP MNPs may also be SD ferrites ($\text{Co}_{\text{His6-Mms6}} = 23.2 \pm 0.5$ nm).

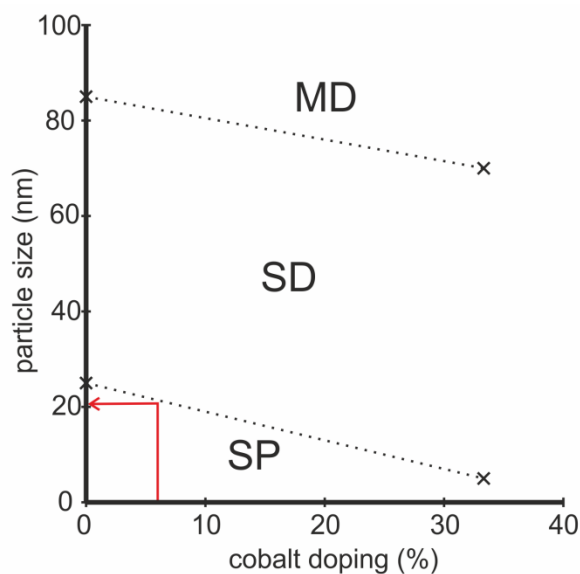


Figure 4.10. Summary of data used to estimate upper size limit of SD and SP particles for different levels of cobalt doping into magnetite, from Galloway *et al.* (2011).³ Graph plotted of limits of SD magnetite^{20,21,24} (0% Co doping) and cobalt ferrite²²⁻²⁴ (33.3% Co doping). A linear relationship between the two end-members is assumed to estimate lower size limit of the SD zone (below which particles are superparamagnetic) for 6% Co doped magnetite. The red arrow shows 6% Co doping estimates SD/SP threshold of ≈ 20 nm.

VSM was used to measure hysteresis loops for the RTCP samples, both with and without 6% Co doping. Both MNP compositions were prepared for the no protein controls, the His₆-Mms6 and the Mms6 biotemplated MNPs. Figure 4.11³ shows hysteresis loops recorded for the RTCP samples at a range of temperatures for the RTCP MNPs. The Fe_{no protein} MNPs have a lower saturation magnetisation than the other undoped, biotemplated RTCP MNPs (see Table 4.7). This is another indication that the crystallinity of the MNPs is improved by mineralisation in the presence of His₆-Mms6, and more so by Mms6, in the synthesis of magnetite nanoparticles by RTCP. The coercivity of the Fe_{no protein} RTCP MNPs is also lower than the coercivity of the Fe_{Mms6} MNPs at room temperature. However, there is a complex hysteresis involving a softer and harder magnetic behaviour seen at 10 K in the Fe_{Mms6} MNPs. This may be due the size distribution of these particles spanning the SP/SD boundary for magnetite. As some of the MNPs behave superparamagnetically, and others are larger and therefore able to maintain a single domain, it is difficult to assess the coercivity of these particles. The Fe_{His6-Mms6} MNPs show a single hysteresis at 10 K ($H_c=390.1$ Oe), which is about three times greater than the smaller Fe_{no protein} magnetite particles ($H_c=127.4$ Oe). This may be due to the Fe_{His6-Mms6} particles being at the upper end of the SP size zone, so having increased coercivity over the smaller Fe_{no protein} particles.

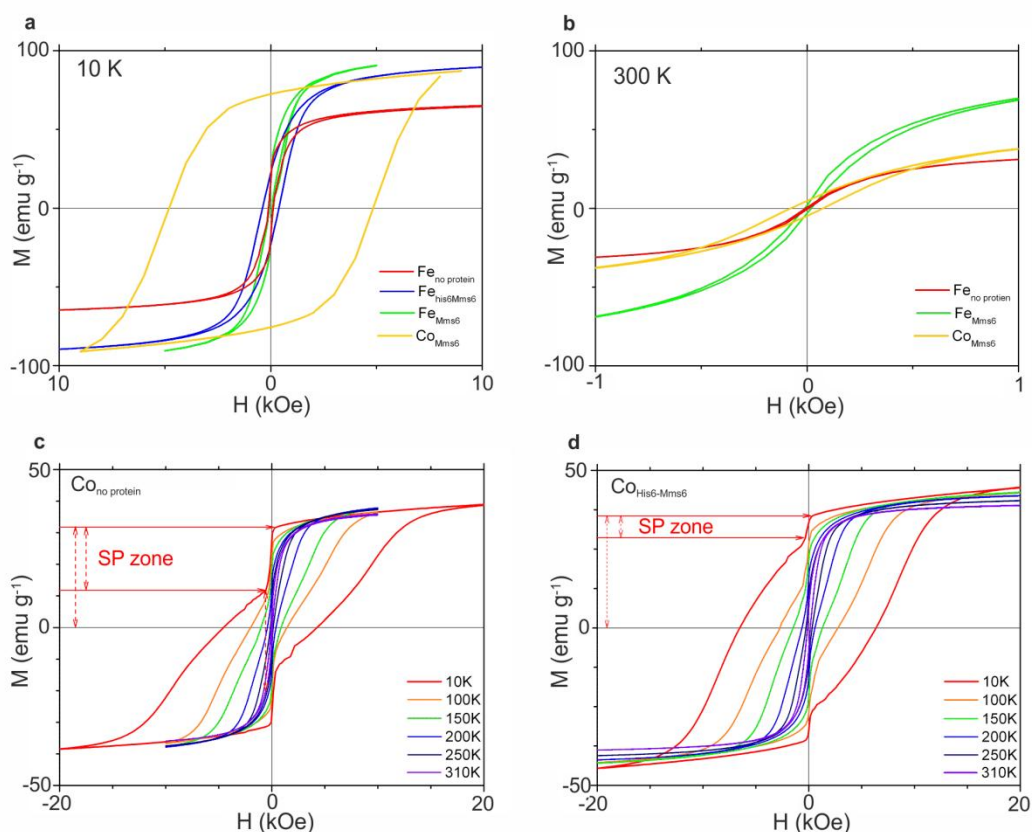


Figure 4.11. Hysteresis loops recorded using VSM of dried MNPs formed by RTCP, from Galloway *et al.* (2011).³ (a) Hysteresis loops recorded at 10 K and (b) at 300 K for $\text{Fe}_{\text{no protein}}$ (red), $\text{Fe}_{\text{His6-Mms6}}$ (blue), Fe_{Mms6} (green) and Co_{Mms6} (yellow). Loops recorded at varying temperatures for (c) $\text{Co}_{\text{no protein}}$ and (d) $\text{Co}_{\text{His6-Mms6}}$ (colours of loops labelled with temperatures on graph). Both show a more complex hysteresis, involving at least two different magnetic behaviours. Magnetically soft zone, labelled as ‘SP zone,’ makes up $\approx 62\%$ of the $\text{Co}_{\text{no protein}}$ and $\approx 20\%$ of the $\text{Co}_{\text{His6-Mms6}}$ plots at 10 K.

Table 4.7. Summary of magnetic properties of RTCP MNPs from VSM hysteresis loops. Saturation magnetisation (M_s) and coercivity (H_c), (*) denotes value from complex hysteresis (more than one type of magnetic behaviour), (-) for data not available, as VSM no longer able to operate at room temperature.

sample	10 K		300 K	
	M_s (emu g^{-1})	H_c (Oe)	M_s (emu g^{-1})	H_c (Oe)
$\text{Fe}_{\text{no protein}}$	64.1	127.4*	38.8	5.8
$\text{Co}_{\text{no protein}}$	38.8	4597*	36.0	63.6*
$\text{Fe}_{\text{His6-Mms6}}$	89.0	390.1	-	-
$\text{Co}_{\text{His6-Mms6}}$	71.5	6544*	71.5	129.4*
Fe_{Mms6}	91.6	77.3*	90.6	12.8
Co_{Mms6}	86.7	4792	56.1	78.3

As expected, the Co_{Mms6} MNPs have a reduced saturation magnetisation and increased coercivity when compared to the undoped particles. At both 10 K and 300 K they show a uniform hysteresis, with the room temperature $H_c=78.3$ Oe, over six times greater than coercivity of the Fe_{Mms6} MNPs (12.8 Oe). The average particle size, and the single, uniform magnetic hysteresis indicate that these MNPs are SD particles of 6% cobalt doped ferrite. As many of the Fe_{Mms6} MNPs may be smaller than the SD limit of magnetite (≈ 25 nm for magnetite cubes),²⁰ the room temperature coercivity of Fe_{Mms6} MNPs may be significantly lower than would be found for SD magnetite MNPs. There is a similar trend of increased coercivity with 6% Co doping seen for the $\text{Co}_{\text{His6-Mms6}}$ and $\text{Co}_{\text{no protein}}$ doped particles, but the hysteresis loops shows at least two different magnetic behaviours. The hysteresis of the $\text{Co}_{\text{no protein}}$ particles have a large magnetically soft zone, which takes up about 62% of the hysteresis plot at 10 K. There is also a soft zone in the hysteresis of the $\text{Co}_{\text{His6-Mms6}}$ MNPs, but it is much smaller ($\approx 20\%$ of the plot at 10 K). As the soft zones distort the hysteresis loops, the coercivity measured from these complex hystereses cannot be directly compared to the single hysteresis of the Co_{Mms6} MNPs.

The different magnetic behaviours of these particles could be due to zonation of cobalt within particles, or between different particle morphologies, or simply due to the size of the magnetic particles. The TEM images in Figure 4.6 show that the $\text{Co}_{\text{His6-Mms6}}$ particles are very equidimensional. This means that the mixture of soft and hard magnetic behaviour from the MNPs is unlikely to be due to different particle morphologies. The EDX and EELS data (Section 4.3.2.2) show iron and cobalt are fairly evenly distributed between and within the 6% Co doped MNPs, whether His₆-Mms6 is present or not. Therefore, this mixed magnetic behaviour is most likely due to these samples consisting of MNPs with particle sizes spanning the SD/SP limit for 6% Co doped magnetite. Interestingly, the TEM grainsize analysis shows that 61.8% of $\text{Co}_{\text{no protein}}$ and 22.7% of $\text{Co}_{\text{His6-Mms6}}$ MNPs are less than 18 nm. This is extremely close to the lower SD threshold of ≈ 20 nm for 6% Co doped magnetite estimated by the linear approximation between the magnetite and cobalt ferrite end members in Figure 4.10.³ As these grainsize values closely correspond to the proportion of a hysteresis that exhibits the soft magnetic behaviour, it is likely that the SD/SP threshold in 6% Co doped magnetite is ≈ 18 nm. MNPs below this limit contribute to the soft SP zone of the hysteresis, with the larger MNPs able to maintain a single domain, and thus contribute to the magnetically hard part of the signal.

4.3.5 RTCP, 6% Co, Mms6 and His₆-Mms6

The addition of Mms6 or His₆-Mms6 to the formation of RTCP MNPs increases the size of the particles and narrows the size distribution, which is desirable for many applications. However, the magnetic behaviour of RTCP Fe_{Mms6} MNPs is not uniform, which may be due to this narrow grainsize distribution spanning the SP/SD zones for magnetite. The Fe_{His6-Mms6} MNPs formed by RTCP, which are of a smaller average grainsize, show a single magnetic hysteresis. These Fe_{His6-Mms6} MNPs are likely to be at the larger end of the SP zone for magnetite, and could be useful for applications that require SP MNPs, such as MRI contrast agents. As the His₆-tag is accessible on the particles (see Section 2.2.3), it may also be possible to functionalise the MNPs for drug delivery using the affinity tag. But, why does the addition of a very small affinity tag (the His₆ tag adds < 2 kDa to the 6.4 kDa mass of Mms6) alter the size of the MNPs produced during RTCP? Previous *in vitro* studies of Mms6^{1,2,25} proposed that Mms6 agglomerates via its hydrophobic *N*-terminal region to help stabilise the protein when in aqueous solution, and allow the *C*-terminal section to interact with the solution to form magnetite. If this is the case, it is logical that any tag at the *N*-terminus could alter the ability of the protein to agglomerate, and thus affect its templating ability.

By adding 6% cobalt to the RTCP biotemplated MNPs, the grainsize is increased, and the crystallinity of the MNPs is also improved. Cobalt doping of magnetosome MNPs *in vivo* was found to increase the size of the crystallites formed by magnetic bacteria.²⁶ The Co_{no protein} and Co_{His6-Mms6} MNPs both produced complex hysteresis loops, with magnetically soft and hard components. The size of the magnetically soft zone correlates extremely closely with the proportion of MNPs that are below ≈18 nm (from TEM measurements). This indicates that the soft behaviour is likely to be due to smaller particles exhibiting SP behaviour, with the larger particles able to maintain a SD, and thus maintain a higher coercivity. In a study of cobalt ferrite (CoFe₂O₄) nanoparticles that span the SD zone, Chinnasamy *et al.* (2003)²⁷ showed that smaller SD CoFe₂O₄ MNPs have a greater coercivity than the larger particles at the upper end of the SD zone. This phenomenon was also observed by Maaz *et al.* (2007),²⁸ which they attribute to surface effects. The surface anisotropy is greater than the bulk anisotropy for CoFe₂O₄.²⁸ As smaller SD particles have a greater surface area to volume ratio than larger NPs, they have a high coercivity as their magnetism is dominated by surface contributions. The larger SD particles have a lower coercivity, as these MNPs are dominated by contributions from the weaker bulk anisotropy of CoFe₂O₄, thus the direction of magnetisation requires less energy to be switched. If this effect holds for cobalt doped magnetite nanoparticles, it should be expected that 6% Co doped MNPs that are just large

enough to maintain a single domain (i.e. just above 18 nm) would have the highest coercivity for MNPs with this level of cobalt doping.

The Co_{Mms6} RTCP MNPs show a single magnetic hysteresis with a much increased room temperature coercivity (78.3 Oe) over the undoped Fe_{Mms6} MNPs (12.8 Oe). This increased coercivity may mean these MNPs could be more suited to applications such as treating cancer using hyperthermia. Cobalt doped magnetosome MNPs have been shown to have an increased efficacy over undoped magnetosome MNPs when targeting cell death to *in vivo* cancers.²⁹⁻³¹ Although the chain structure of bacterial magnetosomes can facilitate cell uptake,³¹ the increase in coercivity of the Co_{Mms6} and their uniform magnetic behaviour, indicate that the Mms6 templated MNPs may also be suited to this purpose. The Mms6 protein on the MNP surface could be further functionalised to improve cell uptake, or for targeted drug delivery. Also, the synthesis of the Co_{Mms6} MNPs is simpler, easier, higher yield and cheaper than culturing and doping magnetic bacteria to extract their biomineralised magnetosomes. Therefore, Co_{Mms6} MNPs may be a better alternative to the cobalt doped magnetosome MNPs for such medical applications.

4.4 References

1. Arakaki, A., Webb, J. & Matsunaga, T. (2003). A novel protein tightly bound to bacterial magnetic particles in *Magnetospirillum magneticum* strain AMB-1. *J. Biol. Chem.* **278**, pp 8745-8750.
2. Amemiya, Y., Arakaki, A., Staniland, S.S., Tanaka, T. & Matsunaga, T. (2007). Controlled formation of magnetite crystal by partial oxidation of ferrous hydroxide in the presence of recombinant magnetotactic bacterial protein Mms6. *Biomaterials.* **28**, pp 5381-5389.
3. Galloway, J.M., Arakaki, A., Masuda, F., Tanaka, T., Matsunaga, T. & Staniland, S.S. (2011). Magnetic bacterial protein Mms6 controls morphology, crystallinity and magnetism of cobalt-doped magnetite nanoparticles *in vitro*. *J. Mater. Chem.* **21**, pp 15244-15254.
4. (2008). *CRC Handbook of Chemistry and Physics, 89th Edition* (ed. Lide, D.R.). (CRC Press, Cleveland, USA).
5. Abramoff, M.D., Magalhaes, P.J. & Ram, S.J. (2004). Image processing with Image J. *Biophotonics Int.* **11**, pp 36-42.
6. Goya, G.F., Berquo, T.S., Fonseca, F.C. & Morales, M.P. (2003). Static and dynamic magnetic properties of spherical magnetite nanoparticles. *J. Appl. Phys.* **94**, pp 3520-3528.
7. Malyarevich, A.M., Denisov, I.A., Yumashev, K.V., Dymshits, O.S. & Zhilin, A.A. (2002). Optical absorption and luminescence study of cobalt-doped magnesium aluminosilicate glass ceramics. *J. Opt. Soc. Am. B.* **19**, pp 1815-1821.

8. Itoh, H. & Sugimoto, T. (2003). Systematic control of size, shape, structure, and magnetic properties of uniform magnetite and maghemite particles. *J. Colloid Interface Sci.* **265**, pp 283-295.
9. Sugimoto, T. & Matijevic, E. (1980). Formation of uniform spherical magnetite particles by crystallization from ferrous hydroxide gels. *J. Colloid Interface Sci.* **74**, pp 227-243.
10. Moumen, N., Bonville, P. & Pileni, M.P. (1996). Control of the size of cobalt ferrite magnetic fluids: Mossbauer spectroscopy. *J. Phys. Chem.* **100**, pp 14410-14416.
11. Moskowitz, B.M., Frankel, R.B. & Bazylinski, D.A. (1993). Rock magnetic criteria for the detection of biogenic magnetite. *Earth Planet. Sci. Lett.* **120**, pp 283-300.
12. Moskowitz, B.M., Frankel, R.B., Bazylinski, D.A., Jannasch, H.W. & Lovley, D.R. (1989). A comparison of magnetite particles produced anaerobically by magnetotactic and dissimilatory iron-reducing bacteria. *Geophys. Res. Lett.* **16**, pp 655-688.
13. Ozdemir, O., Dunlop, D.J. & Moskowitz, B.M. (1993). The effect of oxidation on the Verwey transition in magnetite. *Geophys. Res. Lett.* **20**, pp 1671-1674.
14. Fischer, H., Mastrogiacomo, G., Löffler, J.F., Warthmann, R.J., Weidler, P.G. & Gehring, A.U. (2008). Ferromagnetic resonance and magnetic characteristics of intact magnetosome chains in *Magnetospirillum gryphiswaldense*. *Earth Planet. Sci. Lett.* **270**, pp 200-208.
15. Moisescu, C., Bonneville, S., Staniland, S., Ardelean, I. & Benning, L.G. (2011). Iron uptake kinetics and magnetosome formation by *Magnetospirillum gryphiswaldense* as a function of pH, temperature and dissolved iron availability. *Geomicrobio. J.* **28**, pp 590-600.
16. Fischer, A., Schmitz, M., Aichmayer, B., Fratzl, P. & Faivre, D. (2011). Structural purity of magnetite nanoparticles in magnetotactic bacteria. *J. R. Soc. Interface.* **8**, pp 1011-1018.
17. Walz, F. (2002). The Verwey transition - A topical review. *J. Phys. Condens. Matter.* **14**, pp R285.
18. Aragón, R., Buttrey, D.J., Shepherd, J.P. & Honig, J.M. (1985). Influence of nonstoichiometry on the Verwey transition. *Phys. Rev. B.* **31**, pp 430.
19. Aragón, R. (1992). Magnetization and exchange in nonstoichiometric magnetite. *Phys. Rev. B.* **46**, pp 5328.
20. Dunlop, D.J. (1973). Superparamagnetic and single-domain threshold sizes in magnetite. *J. Geophys. Res.* **78**, pp 1780-1793.
21. Moskowitz, B. & Banerjee, S. (1979). Grain size limits for pseudosingle domain behavior in magnetite: Implications for paleomagnetism. *IEEE Trans. Magn.* **15**, pp 1241-1246.
22. Schmidbauer, E. & Schembera, N. (1987). Magnetic hysteresis properties and anhysteretic remanent magnetization of spherical Fe_3O_4 particles in the grain size range 60-160 nm. *Phys. Earth Planet. Inter.* **46**, pp 77-83.
23. Berkowitz, A.E. & Schuele, W.J. (1959). Magnetic properties of some ferrite micropowders. *J. Appl. Phys.* **30**, pp S134-S135.

24. Cedeño-Mattei, Y., Perales-Perez, O., Tomar, M.S., Roman, F., Voyles, P.M. & Stratton, W.G. (2008). Tuning of magnetic properties in cobalt ferrite nanocrystals. *Proceedings of the 52nd Annual Conference on Magnetism and Magnetic Materials*. **103**, pp 07E512-513.
25. Arakaki, A., Masuda, F., Amemiya, Y., Tanaka, T. & Matsunaga, T. (2010). Control of the morphology and size of magnetite particles with peptides mimicking the Mms6 protein from magnetotactic bacteria. *J. Colloid Interface Sci.* **343**, pp 65-70.
26. Staniland, S., Williams, W., Telling, N., Van Der Laan, G., Harrison, A. & Ward, B. (2008). Controlled cobalt doping of magnetosomes in vivo. *Nat. Nanotechnol.* **3**, pp 158-162.
27. Chinnasamy, C.N., Senoue, M., Jeyadevan, B., Perales-Perez, O., Shinoda, K. & Tohji, K. (2003). Synthesis of size-controlled cobalt ferrite particles with high coercivity and squareness ratio. *J. Colloid Interface Sci.* **263**, pp 80-83.
28. Maaz, K., Mumtaz, A., Hasanain, S.K. & Ceylan, A. (2007). Synthesis and magnetic properties of cobalt ferrite (CoFe_2O_4) nanoparticles prepared by wet chemical route. *J. Magn. Magn. Mater.* **308**, pp 289-295.
29. Alphandéry, E., Carvallo, C., Menguy, N. & Chebbi, I. (2011). Chains of cobalt doped magnetosomes extracted from AMB-1 magnetotactic bacteria for application in alternative magnetic field cancer therapy. *J. Phys. Chem. C.* **115**, pp 11920-11924.
30. Alphandéry, E., Faure, S., Seksek, O., Guyot, F. & Chebbi, I. (2011). Chains of magnetosomes extracted from AMB-1 magnetotactic bacteria for application in alternative magnetic field cancer therapy. *ACS Nano.* **5**, pp 6279-6269.
31. Alphandéry, E., Guyot, F. & Chebbi, I. (2012). Preparation of chains of magnetosomes, isolated from *Magnetospirillum magneticum* strain AMB-1 magnetotactic bacteria, yielding efficient treatment of tumors using magnetic hyperthermia. *Int. J. Pharm.* **434**, pp 444-452.

Chapter 5

Optimisation of Magnetic Array Synthesis

In the previous chapter, different methods of magnetite synthesis from an aqueous bulk solution using the biomineralisation protein Mms6 were characterised. In this chapter, these methods of magnetite mineralisation are explored to establish optimal conditions for the formation of biotemplated arrays of magnetite, cobalt doped magnetite and cobalt ferrite. For the RTCP method, Mms6 in the bulk solution was able to template uniform magnetite SP MNPs using His₆-Mms6. It was also able to template uniform cobalt doped SD MNPs using untagged Mms6. The POFH methods were not able to solely form uniform MNPs for 6% doped or undoped systems in the presence of Mms6 in the bulk solution. This may have been due to the reaction conditions used for the formation of these MNPs not being optimised towards forming uniform particles from a bulk solution. Here, these methods are investigated so that arrays of uniform biotemplated nanomagnets can be formed.

There are two main routes to form patterned arrays of biotemplated nanomagnets. The MNPs can be formed before patterning, and subsequently attached selectively to a patterned surface. Alternatively, the Mms6 protein can be patterned onto a substrate before mineralisation, and used to template MNP formation *in situ* (see Figure 1.1). As a reaction proceeds at the surface, localised chemical gradients may develop as the reactants are used up. This can cause different phases to become stable at different stages during the mineralisation as diffusion limits the availability of reactants at the surface. In this study, this may cause non-magnetite iron minerals to be formed, which is undesirable as this would significantly affect the magnetism of the biotemplated arrays. Therefore, any mineralisation reactions on surfaces may need to be carefully controlled to ensure that immobilised Mms6 is able to biotemplate magnetite nanomagnets onto patterned arrays.

In this chapter, the attachment of preformed RTCP MNPs to surfaces was explored first, as this may offer the simplest route to biotemplated magnetic array formation. Next, Mms6 protein was selectively immobilised onto micro-patterned substrates, and the RTCP and POFH methods used to form biotemplated MNPs *in situ*. The mineralisation conditions were varied for both POFH methods to optimise selective

magnetite mineralisation onto the immobilised Mms6. The optimised mineralisation methods were then used to form 6% Co doped magnetite and cobalt ferrite onto immobilised, patterned Mms6. Much of this work is published in Galloway *et al.* 2012a¹ & b².

5.1 Attachment of Preformed Biotemplated MNPs

For this section, the RTCP method of magnetite synthesis was used. The MNPs are formed before their attachment to surfaces, and the Mms6 protein should still be attached to the surface of the particles. Mms6 was identified as it was found to be tightly bound to the surface of magnetosome MNPs from *M. magneticum* AMB-1.³ It is the C-terminus of Mms6 that is thought to template the MNP formation and interact with the crystal surface. If the C-terminus remains firmly attached to MNPs biotemplated with Mms6 *in vitro*, the N-terminus may be able to bind these particles to surfaces. Therefore, as the tags on the N-terminus of the Mms6 protein are still accessible, they could be used to bind biotemplated MNPs to appropriately functionalised surfaces.

During RTCP, the MNPs are templated by Mms6 at room temperature, rather than at 90°C for the POFH methods. As heating usually degrades or destroys proteins, the RTCP method should avoid the Mms6 protein, or any tags, being degraded during mineralisation. Unfortunately, the size of the RTCP Fe_{Mms6} MNPs are quite small (see Section 4.3.5), so they are unable to maintain a single domain at room temperature. This means that RTCP Fe_{Mms6} particles patterned in a surface will behave superparamagnetically at room temperature. SP nanoparticles only respond to an externally applied field, which could make imaging them with a magnetised MFM probe very difficult. However, the RTCP Co_{Mms6} MNPs are large enough to be SD nanomagnets, and show a significant coercivity at room temperature (78.3 Oe). Any method that patterns protein templated magnetite MNPs should also be able to pattern the cobalt doped MNPs onto surfaces. This should allow the magnetic behaviour of micro-patterned arrays of biotemplated RTCP Co_{Mms6} nanomagnets to be imaged with MFM.

The mature Mms6 sequence expressed and purified well (Section 3.1.), but this construct does not contain any tags that would enable it to be specifically immobilised onto a surface. Non-specific binding of Fe_{Mms6} particles to surfaces showed little difference between biotemplated MNPs and non-biotemplated controls. Also, the particles also appeared to adhere to surfaces that should resist biofouling, such as the PEG-OH SAM. Therefore, more specific methods of preformed, biotemplated MNPs were investigated. EDC/NHS linkage of preformed Mms6 templated particles was not tried, as the acidic buffer conditions required to

immobilise Mms6 may have significantly abraded the MNPs. Magnetite, and cobalt doped magnetite, is the most stable under basic conditions, so the acid treatment required could damage the Mms6 templated MNPs. This abrasion would have significantly reduced the particle quality, and could have also reduced the size of the MNPs.

A number of methods for specific immobilisation of tagged Mms6 to patterned surfaces were investigated. The sulfur in a cysteine residue should be able to directly link a protein to a clean gold surface. Mms6 does not contain a native cysteine, and the attempts to introduce a cysteine residue at the *N*-terminus of Mms6 were unsuccessful (Section 3.1). This work to produce a Cys-Mms6 mutant is still ongoing, so this strategy for immobilising preformed MNPs is not yet possible. It was also not possible to cleave the His₆-SUMO tag from the His₆-SUMO-Mms6 construct, which would have yielded strep II-Cys-Mms6. This could have been used to immobilise the protein onto gold via the cysteine, or onto a biotinylated surface via the strep II tag. Again, this may be something that is possible in the future, as this protein work is still ongoing.

His₆-Mms6 was successfully expressed and purified, and the tag is still accessible after MNP formation (see Section 3.2.3). However, it was not possible to generate an histidine specific immobilisation surface to bind His₆-Mms6 or preformed His₆-Mms6 templated MNPs (see Section 3.3.1). As histidine also has an affinity for gold,⁴ patterning of RTCP MNPs templated with Mms6 and His₆-Mms6 directly onto gold was attempted. Clean gold surfaces were stamped with PEG-OH for 10 minutes to resist non-specific protein immobilisation, then immersed in Fe_{no protein}, Fe_{His6-Mms6} and Fe_{Mms6} RTCP MNPs in degassed water for ≈1 hour. Fe_{no protein} and Fe_{Mms6} should not have an affinity for the gold surface. The hexahistidine tag on the Fe_{His6-Mms6} particles should preferentially bind to the exposed gold on the patterned surface. Figure 5.1 shows SEM images of the different patterned surfaces after incubation with the MNPs. Despite thorough washing of the particles before the incubation of the patterned surfaces, and of the surfaces after the incubation, there appeared to be a lot of black coloured material adhering to the surfaces. It is possible this black material could be removed by washing the MNPs with solvents other than water before incubation with the surfaces. However, the particles also do not seem to attach to the gold surface, but to the PEG-OH, which was not expected as this should resist non-specific protein binding.

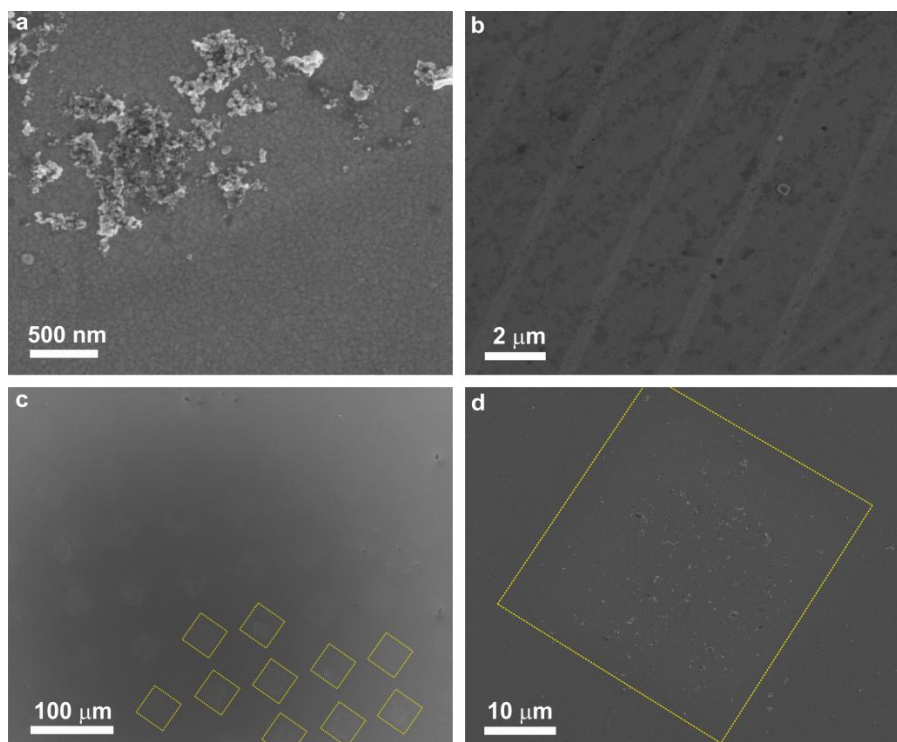


Figure 5.1. SEM images of patterned surfaces after incubation with preformed RTCP MNPs. (a) $\text{Fe}_{\text{no protein}}$ MNPs at pattern edge, more attached to PEG-OH surface than clean gold. (b) $\text{Fe}_{\text{His6-Mms6}}$ MNPs were not attached to the clean gold areas and surface functionalised with PEG-OH (wide lines) show a lot black coloured material. (c) Fe_{Mms6} MNPs attach on squares functionalised with PEG-OH rather than attaching to the clean gold surface. (d) Close-up of PEG-OH square on surface with Fe_{Mms6} RTCP MNPs attached. Edge of pattern highlighted with yellow line for clarity in c & d.

The PEG-OH surface should resist protein binding, and therefore MNP binding, to the areas functionalised with the PEG-OH. However, in all three cases (no protein; Mms6 and His₆-Mms6) the MNPs preferentially attached to the stamped SAM rather than the clean gold. It is possible that the histidine tag has chelated iron during the mineralisation of the nanoparticles. However, the tag on the His₆-Mms6 was still accessible on the surface of MNPs synthesised in the same way in the immunological assay. This suggests that the His₆-tag is not blocked with iron. An alternative possibility is that the histidine-gold interaction is too weak to immobilise the $\text{Fe}_{\text{His6-Mms6}}$ MNPs preferentially onto the gold surface. As the PEG-OH SAM was only stamped for 10 minutes before particle attachment, it may not have been fully ordered. This disorder may have made the stamped SAM better able to attach iron oxides and particles than the clean gold surface.

There was also a lot of a black material adhering to the stamped SAM. This was observed in all the RTCP synthesised MNPs, whether templated with protein or not. This material may be very small particles of magnetite, or another iron mineral formed at the same time as the magnetite MNPs. Despite thorough washing of the particles before incubation with the patterned surface, this black material may be a surface contaminant from the MNPs, or a PM or SP mineral that is co-purifying with the biotemplated MNPs. These results indicate that preformed RTCP MNPs may not be suitable for the fabrication of arrays of nanomagnets, because the attachment to the SAM is non-specific, and the particles on the surface contain a mixture of MNPs and other materials. This is highly undesirable, as the particles do not attach specifically to either the SAM or the gold surfaces, and there is also non-magnetite contamination (i.e. the black material).

5.2 RTCP Mineralisation of Immobilised Mms6

Mms6 was attached to a patterned SAM using EDC/NHS linkage to form protein patterned substrates for magnetite mineralisation. The substrates were micro-contact printed with a PEG-OH SAM, and back filled with the mixed SAM (10% PE-COOH/90% PEG-OH) to create areas that resist or promote protein binding respectively. After Mms6 binding, these substrates were immersed in a mixture of iron (II) and iron (III) salts, under an inert atmosphere, and base was added gradually to increase the pH and form magnetite. The method described in Section 2.5.1 to form RTCP from a bulk solution uses ferrous sulfate and ferric chloride, which are mixed in a 2:1 ratio, incubated for a few minutes with Mms6, before the addition of sodium hydroxide over a ≈ 10 minutes. This was adapted to try and mineralise the protein patterned substrates.

Figure 5.2¹ shows SEM images of some substrates that were mineralised under different conditions using the RTCP method. 'Mms6 usual' used the timings of the RTCP bulk precipitation method described above, for a mixture iron salts (SO_4/Cl_3) and single counter ion (Cl_2/Cl_3). For 'Mms6 slow' the timings were slowed, so the protein patterned substrate was incubated in the iron salts for ≈ 1 hour, and the base was added gradually over a 2 hour period. Controls of the patterned SAM with no protein attachment, and a clean gold substrate were also mineralised using the 'slow' method.

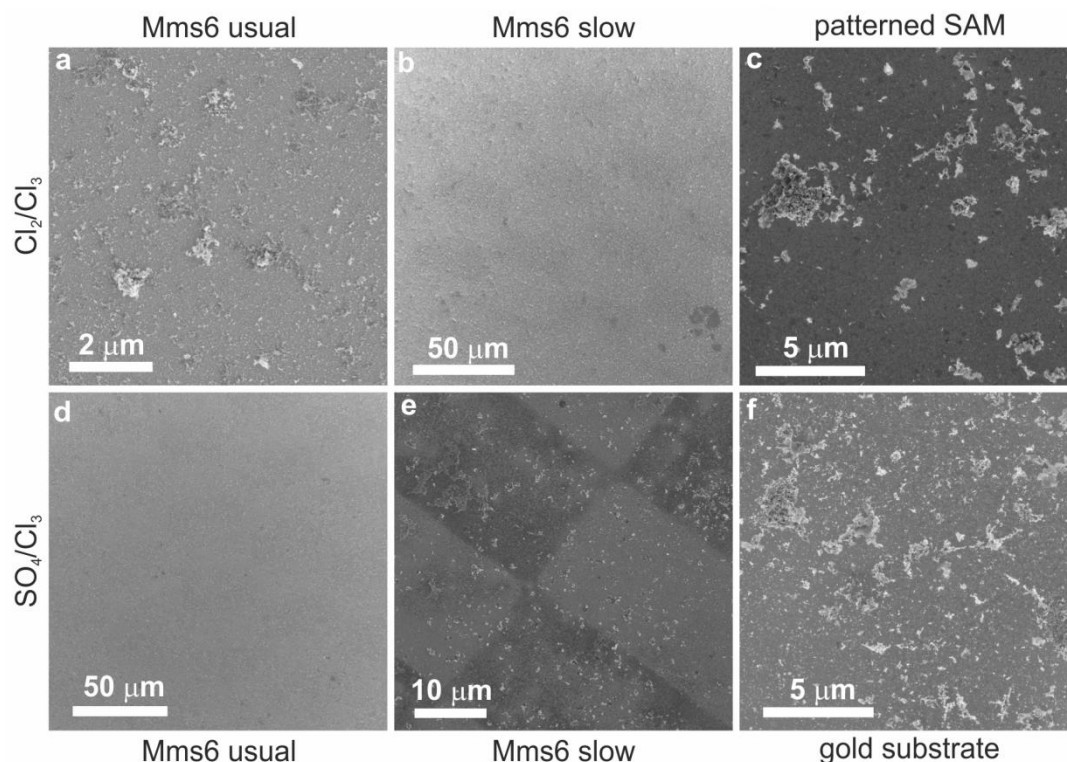


Figure 5.2. SEM images of RTCP and Mms6 protein patterned surfaces, from Galloway *et al.* (2012a).¹ (a-c) chloride counter ions used to mineralise (a) patterned Mms6 using usual timings and (b) slow timings, and (c) a patterned SAM using the slow timings. (d-f) mixed sulfate and chloride counter ions used to mineralise (d) patterned Mms6 using usual timings and (e) slow timings, and (f) a clean gold surface using the slow timings.

For the ‘usual’ timings of the RTCP method, there was no evidence of patterned mineralisation on the surfaces. When the reactants were added more slowly, there is some patterning that can be seen on the immobilised Mms6, which is much clearer for the mixed counter ions than the chloride only system. However, the Mms6 protein immobilised on the surface was not able to template nanoparticles onto the pattern. Figure 5.2e shows dark areas where the Mms6 is immobilised, and light areas where the PEG-OH resisted protein binding. A black non-particulate material has formed on the immobilised Mms6, with MNPs appearing to be randomly deposited onto the surface rather than templated onto the protein. There are also some MNPs on the controls (a patterned SAM with no protein attachment and a clean gold surface). This suggests that MNPs on the Mms6 pattern, and on the controls, are not templated onto the surface, but have adhered to the surfaces despite thorough washing before imaging.

Nanoparticles form rapidly during RTCP, probably in close proximity to where the iron ions first come into contact with hydroxide near the solution surface. This means that MNPs will form near the point of base addition, even if hydroxide is added extremely slowly. When Mms6 is mixed with the reactants in the aqueous bulk solution, hydrophobic interactions may cause it to aggregate via its *N*-terminal sections. This could form aggregates of Mms6 suspended in the bulk solution, or

self-assemble the protein at the liquid-air interface of the reactant solution. In either case, the C-terminal section is able to interact with the reactant solution as the base is added to help template RTCP MNP formation. When immobilised onto a patterned surface, the Mms6 substrate is at the bottom of the mineralisation vessel, which is away from the surface of the reactant solution (see Figure 2.10). This may prevent the patterned Mms6 from interacting with MNP formation for the RTCP method, as the co-precipitation reaction occurs before reaching the protein at the bottom of the reaction vessel.

5.3 POFHK Mineralisation of Immobilised Mms6

As Mms6 was not able to template magnetite MNPs when immobilised on a substrate using the RTCP method, partial oxidation of ferrous hydroxide was also investigated. The reactants for POFH are thoroughly mixed and in contact with the patterned surfaces, both before and during magnetite formation. As magnetite takes a few hours to mature, the Mms6 protein may be better able to interact with the iron ions and/or magnetite precursors during MNP formation, even when immobilised onto a patterned substrate. POFH with potassium hydroxide is a fairly well studied method of magnetite synthesis, and is able to be templated by Mms6 during particle formation, e.g. Amemiya *et al.* (2007).⁵ The POFHK method produces different sizes and shapes of MNPs when the temperature or duration of mineralisation is altered, or ratio of the reactants or the type of iron salt used is changed.⁶ As such, a range of reaction conditions were explored for the POFHK method to try and optimise biomineralisation of magnetite onto the immobilised Mms6 patterns.

5.3.1 Effect of Varying Counter Ions on POFHK

Firstly, a range of five different ferrous salts (chloride, sulfate, fumarate, oxalate and acetylacetonate) were used to try and mineralise magnetite biotemplated magnetic arrays. For these reactions, a total volume of 10 mL was used, and N₂ sparging was maintained throughout the mineralisation process. Mms6 patterned substrates were immersed in 25 mM Fe²⁺ before 60 mM KOH, followed by 250 mM KNO₃ were gradually added over a few minutes. The reactants were incubated at 80°C for 4 hours, then thoroughly washed and dried. Figure 5.3 shows SEM images of these mineralised substrates. Iron chloride formed MNPs onto the surface, but there was no clear patterning visible. Iron sulfate formed patterns of MNPs mainly on the immobilised Mms6, with a few on the PEG-OH protein resistant background. The pattern immersed in fumarate was not able to template MNPs, but formed a dark material similar to that formed by RTCP in Figure 5.2e. Both the acetylacetonate and oxalate also showed no patterning on the surface. As such, only chloride and

sulfate were investigated further as the particles appeared to be fairly regular in size and shape and templated *in situ* by the patterned Mms6 protein.

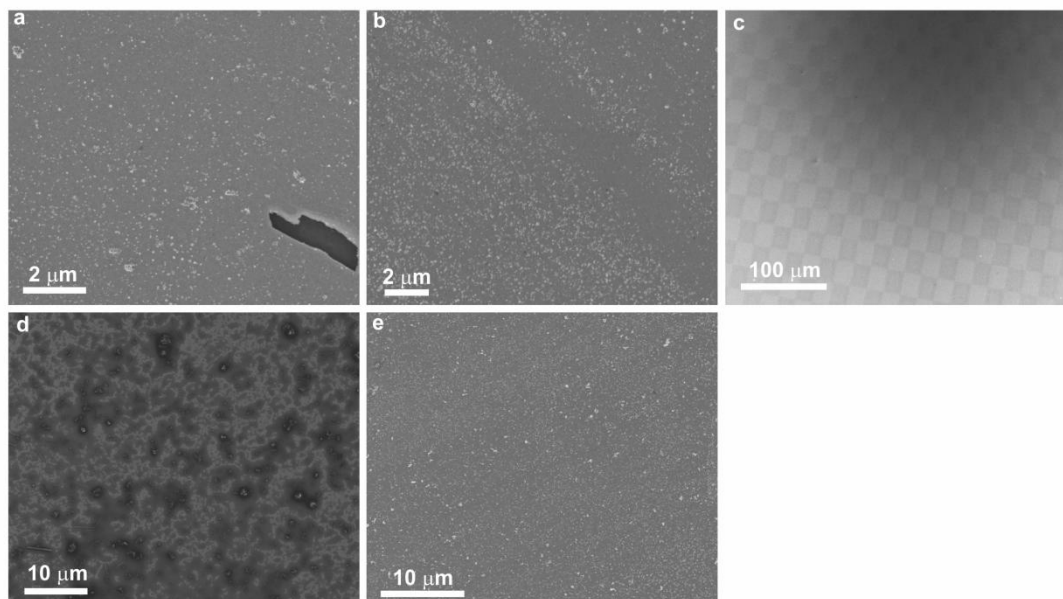


Figure 5.3. SEM images of Mms6 patterned substrates after POFHK with varying salt counter ions. (a) Chloride shows no discernible pattern whereas (b) sulfate allows Mms6 to template patterns of individual MNPs onto areas with protein, and resists MNP formation in the area without protein. (c) Fumarate shows a dark material on the immobilised Mms6 pattern. (d) Acetylacetonate and (e) oxalate show no difference between immobilised Mms6 and PEG-OH patterned surface.

5.3.2 Effect of Incubation Time and Temperature on POFHK

As the reactants used above were quite dilute, a more concentrated solution of reactants was used to investigate the effect of incubation time and temperature. Again, a total 10 mL reaction volume was used, and N₂ sparging maintained throughout the mineralisation process for the heated samples. The substrates mineralised at room temperature for five days were sparged with N₂ for half an hour before being sealed, and mixed on a tilt-table for the duration of the mineralisation. Mms6 patterned substrates were immersed in 50 mM Fe²⁺, before 100 mM KOH, followed by 400 mM KNO₃ were gradually added over a few minutes. The reactants were incubated at 80°C for 4 hours, or five days at room temperature. The substrates were then thoroughly washed and dried before imaging with SEM (see Figure 5.4).¹

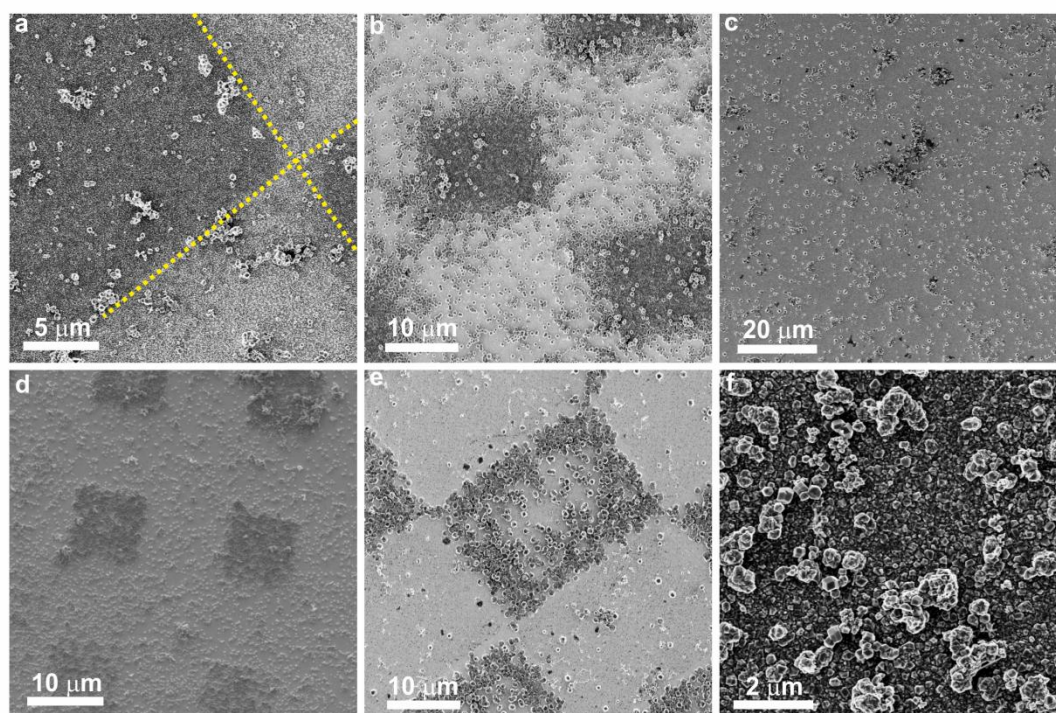


Figure 5.4. SEM images of patterned surfaces mineralised using POFHK and under varying mineralisation incubation times and temperatures, adapted from Galloway *et al.* (2012a).¹ Chloride incubated with (a) immobilised Mms6 for 4 hours at 80°C, areas patterned with Mms6 appear darker as they are mineralised more heavily than PEG-OH background (pattern edge highlighted with yellow line). (b) Shows patterned Mms6 incubated for 5 days at room temperature and (c) a patterned SAM with no protein attached, mineralised for 4 hours at 80°C with POFHK using iron chloride. Sulfate incubated with (d) immobilised Mms6 for 4 hours at 80°C and (e) for 5 days at room temperature, in both cases there is less mineralisation on the PEG-OH background than seen in those surfaces mineralised with iron chloride. (f) Clean gold surface incubated with sulfate for 4 hours at 80°C.

When ferrous chloride is used, the Mms6 functionalised surface templates many intergrown particles (dark coloured areas), with the PEG-OH background being covered in a less dense, less intergrown layer of MNPs (lighter coloured areas). The PEG-OH should resist protein binding (Section 3.3.2) therefore it should resist magnetite mineralisation. There are less MNPs on the PEG-OH background when the chloride mineralisation performed at room temperature over five days, but there are still a lot of MNPs on the areas that should resist mineralisation, which is not ideal. The patterned SAM control shown in Figure 5.4c has not had any protein attached to the pattern, and this still shows mineralisation of nanoparticles by the chloride solution across the whole surface. When ferrous sulfate is used to mineralise the patterned Mms6 at 80°C for four hours, there are still some MNPs formed on the PEG-OH background. However, there are many less than formed by the chloride POFHK salt. The slower, cooler mineralisation conditions reduces the occurrence of particles on the background for the sulfate salt. The mineralisation of MNPs on the PEG-OH background cannot be solely due to non-specifically bound Mms6, as the non protein treated surface was also mineralised with some MNPs

(Figure 5.4c). Therefore, it may be that the ferrous chloride is better able to form MNPs onto the PEG-OH background than the ferrous sulfate, whether there is protein bound to the surface or not.

Figure 5.4e shows that there are not many MNPs templated in the middle of the Mms6 immobilised areas. As shown in Figure 3.19, it is possible that a protein can be distorted by surface immobilisation, if the attachment sites are too close together, but still fold properly at the edges of the protein attachment area. As much of a protein's function is dependent on proper folding, deformation upon attachment to the surface may prevent Mms6 biotemplating MNPs properly in the middle of the micro-patterned areas. This would allow the Mms6 to biomineralise the MNPs at the edges of the micro-patterned areas, but prevent effective templating of particles in the middle of the protein attachment areas. Another possibility is that surface diffusion of the mineralisation reactants may be restricted during the biomineralisation of the Mms6 patterned surfaces. This effect could be further enhanced by the Mms6 at the edge of the pattern, removing a lot of the reactants from the solution by accumulating iron ions or magnetite precursors. Either mechanism, or a combination of the two, could prevent the formation of MNPs at the centre of the immobilised Mms6 patterns. The protein towards the edge of the features may use up reactants to make MNPs at the edges before they can reach the deformed Mms6 at the centre.

Another alternative is that the middle of the patterned rectangles may have accidentally been functionalised to resist protein attachment if the stamp touched-down in the middle of these areas (see Figure 3.19). The mineralisation of some MNPs on the PEG-OH background, and the lack of MNP mineralisation in the middle of patterned Mms6 areas indicates that the POFHK method may not be ideally suited to forming micro-patterned arrays of nanomagnets. As many more MNPs were mineralised onto the PEG-OH background when ferrous chloride was used, only ferrous sulfate was focussed on for further optimisation.

5.3.3 Reactant Ratios for POFHK

Mms6 evolved naturally within *M. magneticum* to template cubo-octahedral magnetite nanoparticle formation within the bacterial magnetosome (i.e. reducing and slightly basic conditions). Therefore, it is unlikely that Mms6 will be able to template magnetite formation if the reaction conditions heavily favour the formation of other iron oxide phases. Thus, the ratio of the Fe^{2+} , HO^- and NO_3^- reactants were varied to study the effect on the templating ability of the immobilised Mms6. In this section, the iron oxides are identified based on the morphology observed in SEM images, and their comparison to sources such as Cornell & Schwertmann (2003).⁷ The likely position that the reaction precipitated the minerals at on the iron oxide

phase diagram (see Figure 1.9) can also be used to clarify mineralogical identification.

When a large excess of KOH was used, the POFHK system forms smaller, more uniform magnetite MNPs than those characterised in Section 4.2. The addition of Mms6 to the bulk solution during mineralisation with excess base in the POFHK system has been shown to template smaller, even more uniform MNPs.⁵ At stoichiometric concentrations, or slight excesses of Fe^{2+} , the system will form much larger MNPs,⁶ and the templating ability of Mms6 is significantly reduced (see Section 4.2).⁸ When a large excess of base was used with the immobilised Mms6 patterns, the caustic solutions scoured deep pits in the substrates and removed the gold film from the surfaces. Figure 5.5¹ shows the effect of different levels of excess iron (i.e. low hydroxide) in reactant solutions and the effect of low levels of the oxidant, nitrate.

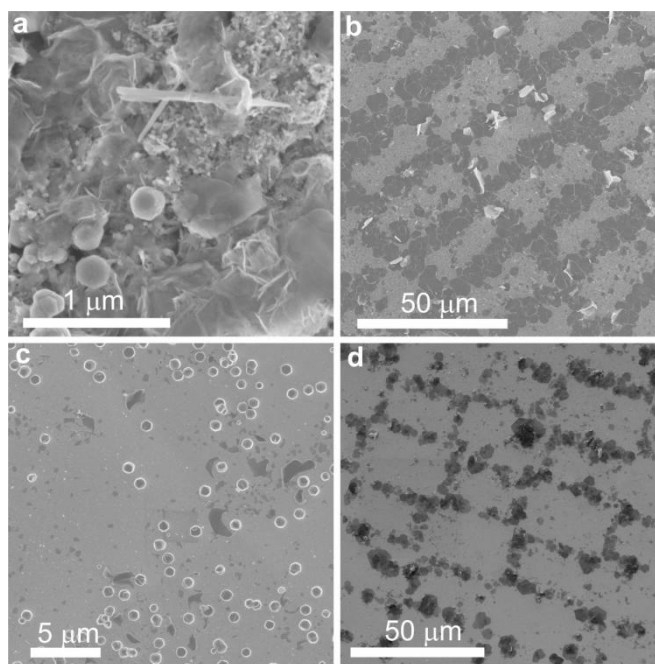


Figure 5.5. SEM images of substrates with varied ratios of reactants for POFHK and Mms6 patterned surfaces, redrawn from Galloway *et al.* (2012a).¹ (a-c) Shows mineralised Mms6 patterns, formed at 80°C with increasing excess iron (II) sulfate in the reactant solution containing 27 mM KOH and 150 mM KNO_3 . (a) 15 mM FeSO_4 forms magnetite, lepidocrocite and goethite, then (b) 20 mM FeSO_4 forms platy lepidocrocite before (c) 25 mM FeSO_4 forms mainly spherical maghemite. (d) Low nitrate concentration (13 mM FeSO_4 , 27 mM KOH, 10 mM KNO_3) forms platy lepidocrocite, similar to image b.

When there is a slight excess of iron (15 mM Fe^{2+} , 27 mM KOH, Figure 5.5a), needles (likely to be goethite, $\alpha\text{-FeOOH}$) and a platy mineral (lepidocrocite, $\gamma\text{-FeOOH}$) are formed at the same time as magnetite MNPs with a range of grain sizes. When the excess of iron is increased (to 20 mM Fe^{2+} , Figure 5.5b), patterns of platy lepidocrocite form at the edges of the patterned Mms6. When increased further (to 25 mM Fe^{2+} , Figure 5.5c) some platy lepidocrocite and MNPs that look like rolled up balls (likely to be maghemite), are formed on the patterned Mms6.

For all these reactions, there was a large excess of nitrate in the system, which was found to be necessary to ensure that magnetite MNPs were formed. Figure 5.5d shows Mms6 templated lepidocrocite, which formed with an appropriate concentration of iron and hydroxide (13 mM FeSO₄, 27 mM KOH), but with a low nitrate concentration (10 mM KNO₃). When the level of nitrate is low, the oxidation of iron (which is necessary to form magnetite using the POFH methods) is slow.^{6,7} In fact, the formation of magnetite seems to occur very soon after the oxidation of iron during POFHK, almost immediately after the ferric species is formed.⁹ Therefore, a large excess of nitrate allows the immobilised Mms6 to form patterns of magnetite, if there is a slight excess of hydroxide in the system.

5.3.4 Nanopatterns Mineralised Using POFHK

Although micro-contact printing has been used to create the patterns for protein attachment, nanopatterning was also tried repeatedly. An old stamp master that was patterned to stamp lines of between 200 and 800 nm wide was used to try and create nanolines of biotemplated magnetic particles. Many of the attempts to create the nanoline pattern did not work, which may be due to the age of the stamp master. However, Figure 5.6 shows one occasion when the nanoline pattern was successfully created onto the gold surface and biomineralised with magnetite. The MNPs biomineralised onto the patterned surfaces are fairly spread out, and there is some undesirable mineralisation onto the PEG-OH background, but the line pattern is clearly discernible. This shows that the POFHK method is also effective for nanopatterning biomineralised magnetite onto surfaces, but may require that new stamp masters are created to ensure reproducible patterning on the nanoscale.

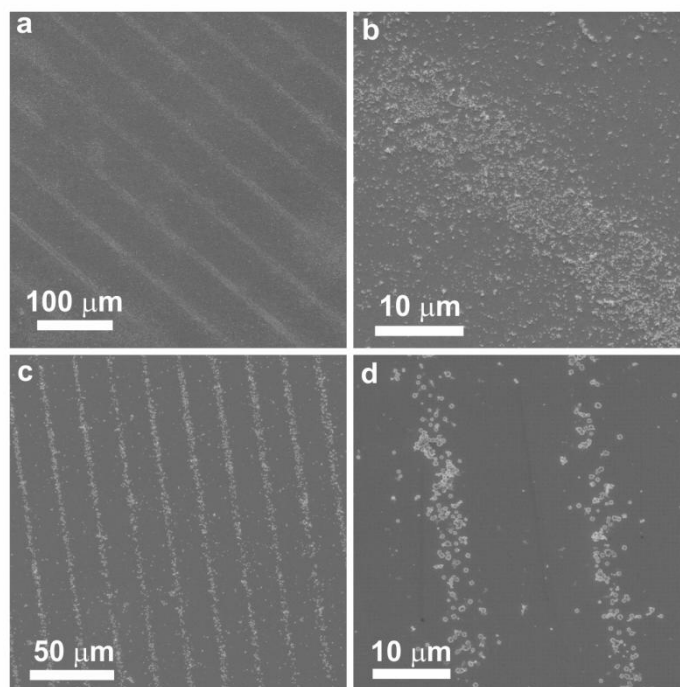


Figure 5.6. SEM of microscale and nanoscale patterned lines of magnetite formed by POFHK onto immobilised Mms6 (25 mM FeSO_4 , 55 mM KOH , 250 mM KNO_3). (a-b) Micropatterned lines biomaterialised with magnetite onto the immobilised Mms6 pattern, with some undesirable mineralisation onto the PEG-OH background. (c-d) Nanolines pattern biomaterialised with magnetite. The MNPs formed on these patterns are fairly spread out on the Mms6 areas.

5.3.5 Total Concentration of Reactants for POFHK

To try and reduce the intergrowth of MNPs onto the Mms6 surface, and reduce the occurrence of MNPs on the PEG-OH background, different total concentrations of the reactants were used for the optimised reactant ratio. The optimised conditions were found to require a slight excess of hydroxide and large excess of nitrate. The ratio was found to be $\text{Fe}^{2+}:\text{OH}^{\ominus}:\text{NO}_3^{\ominus}$ of $\approx 5:11:25$, although higher excesses of nitrate were also used, there was no observable difference in the mineralised patterns formed. If the total concentration of reactants was too low (i.e. > 10 mM Fe^{2+}) there was little consistency in the minerals formed by the patterned Mms6. This is likely to be due to some oxygen entering the reaction vessel during mineralisation, which would have a more significant effect on the redox conditions during the reaction at these lower reactant concentrations.

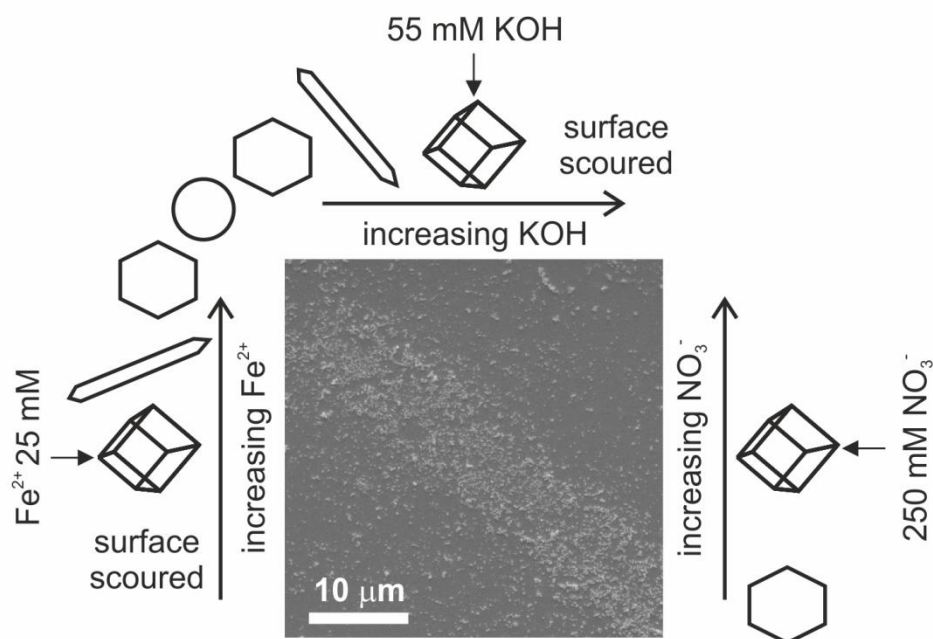


Figure 5.7. SEM image of micro-patterned line of magnetite on immobilised Mms6 using optimum conditions for POFHK method, and schematic of mineral phases produced under varying reactant ratios. Image also shown in Figure 5.6b, and optimum reaction conditions labelled on diagram. Shapes represent mineral phases as follows: cube for cubic magnetite; needle shape for acicular goethite; hexagon for platy lepidocrocite; circle for spherical maghemite ($\gamma\text{-Fe}_2\text{O}_3$).

Figure 5.4d shows mineralisation both on the Mms6 pattern, and on the PEG-OH background, and was formed from a concentrated solution (50 mM FeSO_4 , 100 mM KOH, 400 mM KNO_3). The degree of mineralisation on the PEG-OH background was significantly reduced if a lower concentration of iron (25 mM), with an excess of hydroxide (55 mM) and nitrate (250 mM) was used, see Figure 5.7. When the ratio of the reactants was varied to find these optimised conditions, altering pH seems to have the greatest effect on the mineral phase formed by POFHK. The iron oxide phase diagram shown in Figure 1.9 shows the effect of varying the activity of iron when compared varying oxidation conditions at pH 7. From this diagram, low iron activity and very reducing conditions should produce magnetite, with increasing the effective concentration of iron and increasing oxidation levels producing the other iron oxides and oxyhydroxides.

When more Fe^{2+} is added to the system, the pH is also reduced, as iron sulfate forms an acidic solution. It is likely that for the POFHK system, the decrease in pH caused by introducing excess iron, and the increase in ferrous iron activity by this addition, shifts the phase diagram away from the formation of magnetite. Therefore, the pH, iron concentration and redox potential of the POFHK system dictates the iron mineral formed, with magnetite forming at high pH, low iron and highly reducing conditions. As the concentration of iron, the pH, and the oxidation level is increased, first goethite, then lepidocrocite, and then maghemite are formed by the

POFHK system. It is possible that the size and proximity of MNPs formed on the Mms6 pattern could be altered by adjusting the total concentration of the reactants and the ratio of the reactants within these boundaries. However, it may be difficult to ensure MNPs are only formed onto the immobilised Mms6 patterns for the POFHK method. Therefore, the POFHN method was also investigated and optimised towards the formation of magnetite MNPs on the immobilised Mms6 and not on the PEG-OH background.

5.4 POFHN After Mms6 Immobilisation

The POFHN method is similar to the POFHK method, but is far less well studied. POFHN uses hydrazine to avoid the formation of ferric oxides, and ammonia to further adjust the pH of the solution. Previous authors have found that POFHN was a reliable method to synthesising polydisperse stoichiometric magnetite MNPs. However, the control particles synthesised in the previous chapter using POFHN were found to contain many acicular MNPs, and the XRD data indicated that these may be maghemite. Mms6 in the bulk solution is able to interact with the mineralisation of magnetite and cobalt doped magnetite during POFHN, but not as well as for the POFHK method (see Chapter 4). The level of control that Mms6 exerts over the POFHN towards the formation of magnetite may also be strongly dependent on the reaction conditions, as was found for POFHK above. Therefore, a range of salt counter ions, mineralisation times and temperatures, and iron, base and hydrazine ratios have also been investigated for the formation of magnetite onto patterned Mms6 array surfaces using POFHN.

5.4.1 Effect of Varying Counter Ions on POFHN

The same salts used for POFHK were also used to try and mineralise Mms6 patterns using the POFHN method. For these reactions, a total 10 mL reaction volume was used, and N₂ bubbling of the reactants maintained throughout mixing and heating. The patterned Mms6 was immersed in 25 mM Fe²⁺ for a few minutes, before 30 µL of 50-60% N₂H₄ and 300 µL of 26% NH₄OH were added. A few minutes later, 100 mM KNO₃ was added gradually, and the reaction heated to 80°C for 2 hours. When thoroughly washed and dried, the substrates were imaged using SEM (Figure 5.8).¹

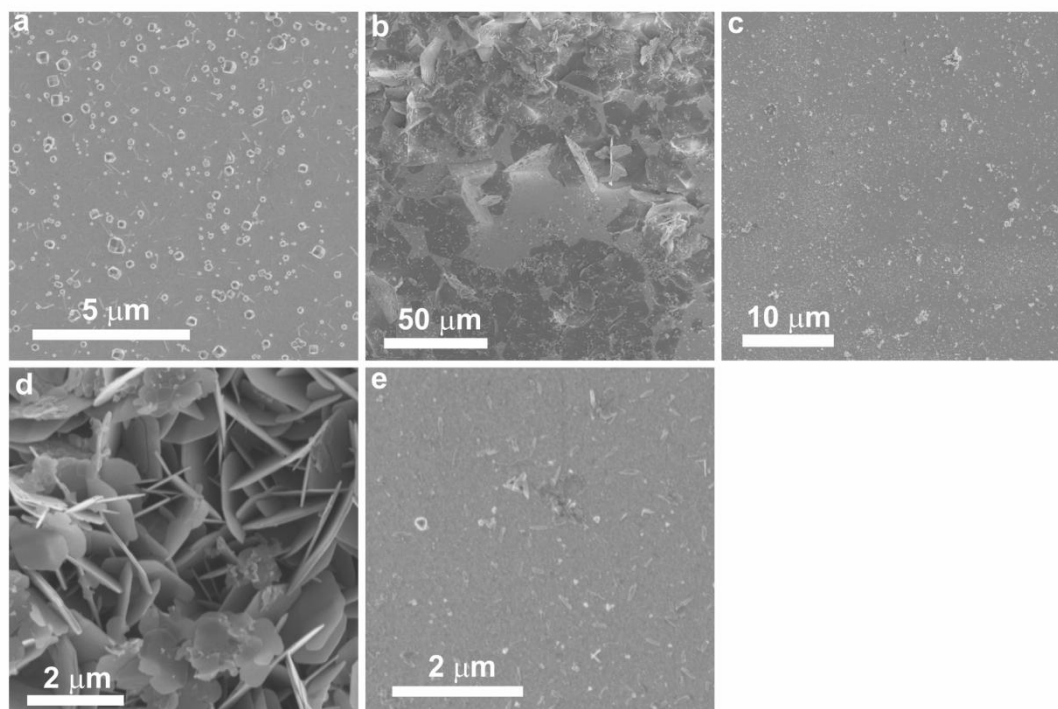


Figure 5.8. SEM images of Mms6 micropatterned surfaces after mineralisation with a range of iron salts using POFHN, redrawn from Galloway et al. (2012a).¹ (a) Chloride mineralised onto the Mms6 pattern, but forms magnetite and goethite, and (b) platy lepidocrocite forms on patterned Mms6 with ferrous sulfate. (c-e) No mineralisation onto Mms6 pattern, but there was still some mineralisation onto the substrates. (c) Fumarate mainly forms euhedral magnetite, (d) oxalate forms expanses of intergrown tabular lepidocrocite laths, and (e) acetylacetonate forms squat needles of goethite.

The only salts that were able to mineralise on the patterned Mms6 were the chloride and sulfate reactions. However, the chloride reaction formed equidimensional magnetite and some acicular particles (likely to be goethite) on the Mms6 pattern. The patterned Mms6 was only able to form a platy material, likely to be lepidocrocite, with the ferrous sulfate. The other salts used did mineralise onto the surfaces, but not onto a pattern, so this mineralisation is not likely to be templated by the immobilised Mms6. Fumarate formed mainly equidimensional crystals, which are probably magnetite, oxalate formed intergrown tabular laths, which are likely to be lepidocrocite, and acetylacetonate formed short needles, which are probably goethite. Only chloride and sulfate were investigated further to form biotemplated arrays, as these salts appeared to be able to interact with the Mms6 during mineralisation to form particles onto the patterned protein. However, as the reactions did not form just magnetite, the reaction conditions were systematically varied to optimise POFHN towards magnetite formation.

5.4.2 Effect of Incubation Time and Temperature on POFHN

The POFHN mineralisation solution was found to be unsuitable for longer, cooler mineralisation. As for POFHK, reactions were set up to mineralise for five days at room temperature, and compared to reactions that were heated to 80°C for a shorter period (2 hours). The ratio of the reaction in the total 10 mL reaction volume were 50 mM Fe²⁺, 40 µL 50-60% N₂H₄, 200 µL 26% NH₄OH and 100 mM KNO₃. The heated solutions were sparged with N₂ for the duration of the mineralisation, whereas the room temperature reactions bubbled with N₂, then sealed after combining the reactants and mixed on a tilt table for 5 days.

Figure 5.9^{1,2} shows SEM images of some of the substrates after mineralisation using POFHN. When heated for 2 hours using ferrous sulfate, the Mms6 patterned substrate mineralised a layer of euhedral magnetite MNPs onto the Mms6 immobilised areas. The PEG-OH background resisted mineralisation well, creating excellent contrast on the micropatterned array (Figure 5.9a). However, if the solution was left at room temperature for five days, there was virtually no mineralisation onto the patterned surface, despite the patterned SAM still just being visible (Figure 5.9b). It may be that the ammonium hydroxide, or the hydrazine, are able to remove the Mms6 protein and/or and MNPs that form on the surface over extended exposure periods. This may also explain why the POFHN method is able to form very few MNPs onto the PEG-OH background. If a short exposure to heated POFHN solution is able to remove loosely bound protein or MNPs, any particles that may be templated onto the PEG-OH background by non-specifically bound Mms6 would be removed from these surfaces. This indicates that the duration of the POFHN reaction is critical to ensuring the formation of good patterns of biotemplated MNPs.

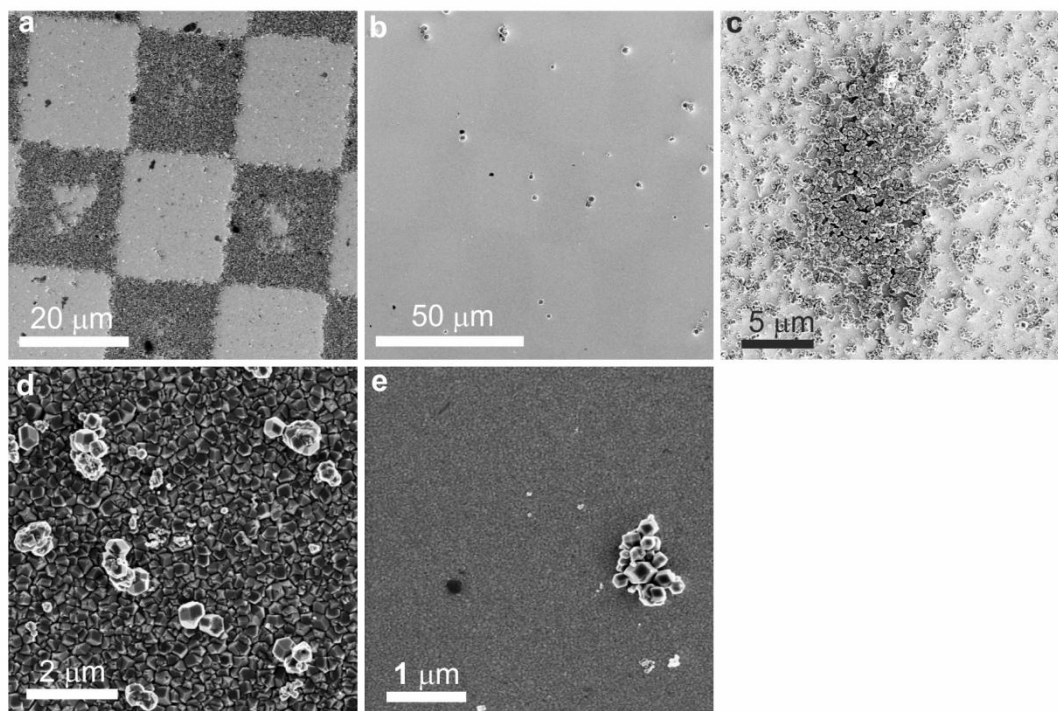


Figure 5.9. SEM images of POFHN mineralised substrates with varying reaction conditions, total 10 mL reaction volume, redrawn from Galloway et al. (2012a & b).^{1,2} Mineralisation reactants were 50 mM FeSO_4 , 40 μL 50-60% N_2H_4 , 200 μL 26% NH_4OH and 100 mM KNO_3 . (a)¹ When heated for 2 hours at 80°C, Mms6 mineralised magnetite with excellent contrast between Mms6 immobilised areas and PEG-OH background. (b)¹ However, when incubated for 5 days at room temperature only a faint SAM pattern can be seen. (c)¹ If ferrous chloride was used, mineralisation occurred on a patterned SAM with no Mms6 attached. (d)¹ Gold control immersed in same conditions as in image a, shows extensive areas of intergrown magnetite crystals, but (e)² patterned SAM shows no mineralisation with the same conditions.

When ferrous chloride was used, MNPs were formed on the patterned SAM without any Mms6 protein attachment, mainly on the mixed SAM areas (Figure 5.9c). It may be that the carboxylic acid groups in the mixed SAM are able to act as nucleation sites for FeCl_2 POFHN, creating MNP patterns with no Mms6 protein attachment. As MNPs are also templated onto the PEG-OH background, ferrous chloride is not suitable for the formation of micro-patterned arrays of magnetite. Figure 5.9d shows the mineralisation which occurred on a clean gold substrate when immersed in the same reaction conditions as for Figure 5.9a. There is extensive mineralisation of intergrown euhedral MNPs on the gold surface. When patterned SAMs of the PEG-OH and the mixed SAM are immersed in the same POFHN solution, there was virtually no mineralisation onto the SAM surface (Figure 5.9e). This indicates that the SAM layer shields the gold surface from the mineralisation solution when ferrous sulfate is used. As the chloride reaction formed MNPs on both the PEG-OH background and the mixed SAM containing 10% PE-COOH, only the sulfate reaction was investigated further to study the effect of varying the reactant ratios.

5.4.3 Reactant Ratios for POFHN

Similar to the POFHK method, low levels of KNO_3 produced platy lepidocrocite instead of magnetite for the POFHN system. However, the POFHN method is more complex than the POFHK method, as there are both ammonium hydroxide (NH_4OH) and hydrazine (N_2H_4) as alkalis in the mineralisation reaction. Variation in the concentration of these alkalis seemed to favour the formation of iron oxy-hydroxides rather than magnetite (see Figure 5.10). When the concentration of hydrazine was low, magnetite MNPs and the ferric oxyhydroxide goethite form on the patterned Mms6 (Figure 5.10a). At slightly higher hydrazine concentrations, platy lepidocrocite forms in an assemblage with magnetite and goethite. At the optimum concentration, cubic magnetite is formed by the POFHN system. As hydrazine is thought to prevent the formation of ferric oxides,¹⁰ such as haematite, the concentration of hydrazine is critical to ensuring the POFHN method forms magnetite.

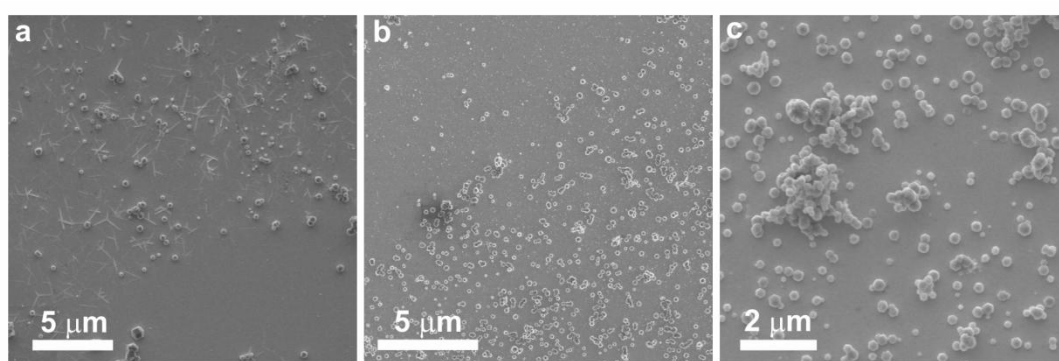


Figure 5.10. SEM images of MNPs mineralised using POFHN, total 10 mL reaction volume, from Galloway et al. (2012a & b).^{1,2} Image (a)¹ shows low hydrazine (18 mM FeSO_4 , 10 μL 50-60% N_2H_4 , 100 μL 26% NH_4OH and 150 mM KNO_3 for 2 hours at 80°C) which forms goethite needles and magnetite onto the Mms6 pattern. (b)¹ Dilute system (30 mM FeSO_4 , 21 μL 50-60% N_2H_4 , 165 μL 26% NH_4OH and 150 mM KNO_3 for 2 hours at 80°C) shows more dispersed MNP packing on Mms6 patterned substrate than in Figure 5.9a. (c)² Bovine serum albumin protein (BSA) immobilised onto patterned SAM mineralised using 50 mM FeSO_4 , 40 μL 50-60% N_2H_4 , 200 μL 26% NH_4OH and 100 mM KNO_3 . There is little mineralisation of MNPs, and the particles have variable sizes.

If the concentration of ammonia is too high, POFHN seems to form platy lepidocrocite onto the patterned Mms6. If the concentration of ammonia was significantly reduced, the reaction again favoured the formation of acicular goethite (see Figure 5.11). This is a different trend to that seen when the hydrazine is varied, as a slight deficiency of N_2H_4 causes the platy mineral to be formed. This may be because hydrazine is used to prevent the formation of ferric species, so hydrazine concentration is more important for the redox potential of the POFHN system than the pH. The mineral assemblage trend seen when ammonium hydroxide is varied is also different to the trend seen when the iron/base concentration was varied in the POFHK system. In POFHN, the concentration of iron needs to be in slight excess to

ensure good mineralisation of magnetite MNPs on the surface, which is the opposite of the trend seen in POFHK.

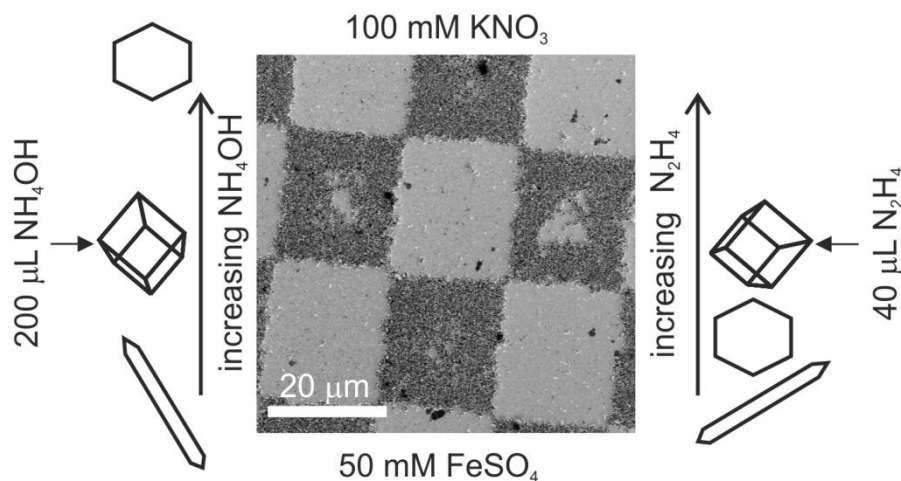


Figure 5.11. SEM image of micro-patterned chessboard of magnetite on immobilised Mms6 using optimum conditions for POFHN method, and schematic of varying mineral phases produced under different reactant ratios. Image also shown in Figure 5.9a, and optimum reaction conditions labelled on diagram. Shapes represent mineral phases as follows: cube for cubic magnetite; needle shape for acicular goethite; and hexagon for platy lepidocrocite.

5.4.4 Total Concentration of Reactants for POFHN

The effect of varying the total concentration of the reactants was also investigated for the POFHN method. When a reduced total concentration of reactants was used (Figure 5.10b, 30 mM FeSO_4) the MNPs formed on the immobilised Mms6 pattern are not as closely packed together as in the arrays formed with the more concentrated solutions. This may be because the lower concentration of reactants reduces the frequency of collisions between the reactants and the mineralising nanoparticles, forming smaller crystals. Very similar mineralisation occurs if the concentration of nitrate is increased to large excesses, which should induce rapid crystallisation of magnetite. The optimised conditions are shown in Figure 5.11 (50 mM FeSO_4), where a good contrast between Mms6 biotemplated MNPs and the PEG-OH background can be seen.

5.5 Summary of Magnetite Formation by POFH

When another protein (BSA) was bound to the patterned SAM surface before mineralisation, few, irregular sized MNPs are templated onto the surface (Figure 5.10c). Recently, it has been shown that BSA is able to template the formation of acicular iron oxide particles for the RTCP method from a bulk solution.¹¹ This control sample shows that BSA is also able to template magnetite MNPs when immobilised on a patterned substrate for the POFHN method. However, the particles are less uniform in size than those formed by immobilised

Mms6, so BSA is less suited to the formation of magnetite micro-patterned arrays. The immobilised Mms6 is able to form closely spaced magnetite MNPs with little mineralisation on the PEG-OH background for the ideal reaction conditions shown in Figure 5.9a. For these optimised conditions, the patterned SAM with no protein attached does not mineralise MNPs onto the patterned surface for POFHN when ferrous sulfate is used (Figure 5.9e). Therefore, it can be concluded that the immobilised Mms6 protein is responsible for the formation of the MNPs on the micro-patterned surfaces from ferrous sulfate POFHN.

Balancing the reactants to produce magnetite for the POFHN system is more complex than for the POFHK system. Variation in the levels of hydrazine alters both the pH and redox potential, as it is used to prevent the formation of ferric oxides and is also a base. POFHN seems to form good magnetite patterns with a slight excess of iron and hydrazine. If there is less hydrazine, the POFHN system forms the ferric oxyhydroxides of lepidocrocite and goethite. If there is too much ammonium hydroxide, lepidocrocite is formed, if there is too little, goethite is formed. Therefore, the changes in the relative concentrations different reactants cause the redox, pH and activity of the different elements to direct the reaction towards the formation of different iron minerals if not carefully controlled.

The timing of the POFHN mineralisation is also important, as the reaction needs time to form magnetite from the ferrous and ferric hydroxide precursors. If left for too long, there is no mineralisation on the surface. This may be due to the ammonium hydroxide and/or hydrazine removing Mms6 or mineralised MNPs from the surfaces over time. It is possible that these nitrogen based alkalis are able to break the bond between the Mms6 protein and the surface. This would explain why there is no mineralisation on the patterned surfaces when incubated for long periods (e.g. Figure 5.9b). It may also help the POFHN system to avoid the formation of MNPs on any non-specifically bound Mms6 on the PEG-OH background, and create the excellent contrast on the chessboard pattern. If the duration of the mineralisation is too short, the reaction produces patterns of platy lepidocrocite. Despite the increase in the complexity of the system, the POFHN method produces excellent contrast between the lack of mineralisation on the PEG-OH background, and the closely spaced magnetite cubes on the immobilised Mms6. Therefore, the optimum reaction conditions (total 10 mL reaction volume, 50 mM FeSO_4 , 40 μL 50-60% N_2H_4 , 200 μL 26% NH_4OH and 100 mM KNO_3 , 2 hours heating at 80°C) have been chosen as the ideal method for the synthesis of biotemplated micro-patterned arrays of magnetite nanoparticles.

5.6 Cobalt Doping of POFH Biomineralised Patterns

One of the main applications for magnetic nanoparticles patterned onto surfaces is for electronic data storage. To store data, the magnetic particles must be able to retain their magnetic orientation, so should have a high coercivity. As magnetite is magnetically soft, its magnetism can easily be altered by applying an external magnetic field. This means that patterns of magnetite nanoparticles may not be suitable for data storage applications. Magnetite biotemplated by Mms6 from a bulk solution can be doped with cobalt to increase the coercivity (see Chapter 4). Therefore, Mms6 may also be able to template magnetically harder MNPs of cobalt doped magnetite or cobalt ferrite when immobilised onto a patterned surface. As the RTCP method was unable to allow Mms6 to template nanoparticles when immobilised onto a patterned surface, only the POFH methods were used to try and form magnetically harder Mms6 biotemplated micro-patterned nanoparticles. Here, both POFH methods have used to synthesise 6% Co doped magnetite and cobalt ferrite MNPs onto micro-patterned Mms6 substrates.

5.6.1 POFHN and 6% Cobalt Doping of Immobilised Mms6 Patterns

A number of attempts were made to mineralise 6% Co doped magnetite onto the immobilised Mms6 patterns using POFHN. When 6% Co was added to the ideal magnetite mineralisation solution for POFHN (i.e. 47 mM FeSO_4 , 3 mM CoSO_4), platy lepidocrocite was formed on the patterns instead of equidimensional MNPs. The reaction only seemed able to mineralise 6% cobalt doped magnetite MNPs onto the Mms6 patterns if a lower concentration of metal salt was used than was necessary for the magnetite reaction (i.e. 23.5 mM FeSO_4 , 1.5 mM CoSO_4 , Figure 5.12). However, the patterning is difficult to see, as the MNPs are quite small and very spread out on the immobilised Mms6 pattern. This is not ideal for creating biotemplated micro-patterned MNPs, as it is likely that multiple particles in close proximity will be required for applications such as electronic data storage. This is discussed in greater detail in Chapter 6, where the properties of these arrays are characterised. The proportion of cobalt in the reactants was increased to 33% (17 mM FeSO_4 , 8 mM CoSO_4 , Figure 5.12) to try and form cobalt ferrite (CoFe_2O_4) onto the patterned Mms6. However, the solutions were only able to precipitate a platy mineral, likely to be a cobalt containing lepidocrocite, on expanses of the surface, and no patterning was visible. Therefore, the POFHN method is not suited to forming high coercivity biotemplated MNPs onto arrays.

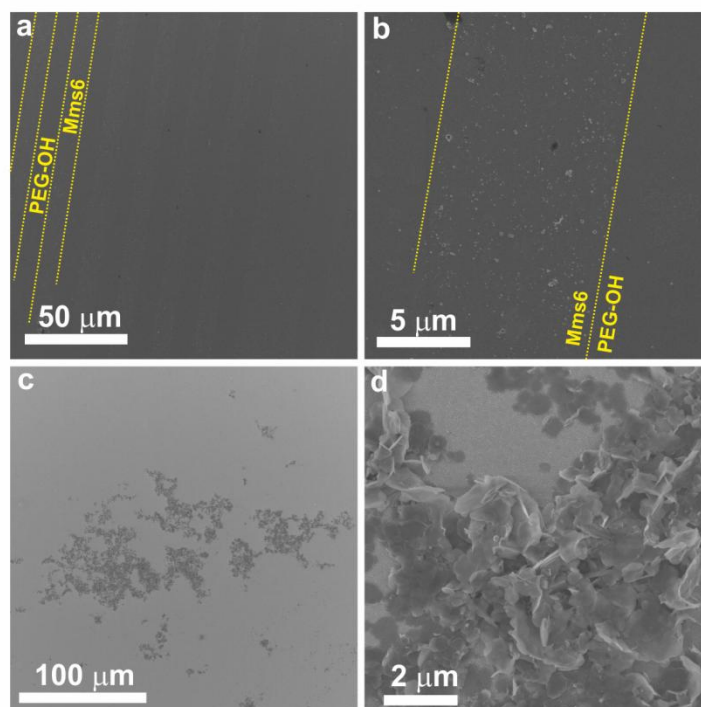


Figure 5.12. SEM images of Mms6 patterned surfaces mineralised using POFHN with (a-b) 6% cobalt doped magnetite and (c-d) cobalt ferrite on micro-patterned Mms6. The mineralisation solution for a total 10 mL reaction volume was 25 mM XSO_4 (where X is either Co^{2+} or Fe^{2+}), 40 μL 50-60% N_2H_4 , 100 μL 26% NH_4OH and 100 mM KNO_3 . (a-b) 6% Co doping (23.5 mM $FeSO_4$, 1.5 mM $CoSO_4$) shows small, sparse MNPs form on immobilised Mms6 (yellow lines show pattern edges). (c-d) Cobalt ferrite (17 mM $FeSO_4$, 8 mM $CoSO_4$) formed extensive networks of platy lepidocrocite, and no patterning could be seen.

The element cobalt has similar properties to iron (e.g. atomic radius, atomic mass). This means that the Co^{2+} is able to substitute into the magnetite lattice at the octahedral B sites in place of Fe^{2+} to form cobalt doped magnetite or cobalt ferrite. However, the properties of cobalt are not the same as iron, hence the increased coercivity and reduced saturation magnetisation of cobalt ferrite when compared to stoichiometric magnetite. Unfortunately, it was not possible to find a value for the standard energy of formation ($\Delta_f G^0$) for cobalt ferrite. This would have allowed a Pourbaix diagram (Eh vs. pH diagram) to be plotted for an aqueous Fe/Co system, which could then be compared to an aqueous Fe system (e.g. Figure 1.9). This would show how the addition of cobalt to the mineralisation system alters the stability zones of the different mineral phases.

When magnetite is formed by POFH, ferrous and ferric hydroxide are dehydrated to form the desired mineral, see Equation 1.4. The crystal structure of lepidocrocite facilitates the formation of spinel structures (such as the inverse spinel magnetite) when OH^- is removed.⁷ The formation of the oxyhydroxide lepidocrocite occurs when too little N_2H_4 or too much NH_4OH is added to the POFHN system. As this also happens when cobalt is added to the POFHN system in place of iron, this indicates that cobalt may prevent full dehydroxylation to magnetite, forming

lepidocrocite instead. As the POFHN system is complex, it is difficult to know how to alter the reactant ratios to ensure the formation of cobalt doped magnetite or cobalt ferrite. Therefore, the simpler POFHK system was investigated to try to form cobalt containing magnetic iron oxides.

5.6.2 POFHK and 6% Cobalt Doping of Immobilised Mms6 Patterns

When mineralising magnetite onto the immobilised Mms6, there were quite a lot of MNPs that also formed on the PEG-OH background that should resist MNP mineralisation (e.g. Figure 5.4d). When the patterned Mms6 was mineralised with 6% cobalt doped magnetite using POFHK, there are less particles on the PEG-OH background (Figure 5.13). Also, the MNPs formed onto the patterned Mms6 are closely spaced and seem to be equidimensional. This may be because the ratio of the reactants was slightly different for this 6% Co doping POFHK onto patterned Mms6. For magnetite, 50 mM of FeSO_4 was used with 100 mM KOH and 400 mM KNO_3 , but this was adjusted to 23.5 mM of FeSO_4 , 1.5 mM of CoSO_4 with 55 mM KOH and 400 mM KNO_3 . Although not perfect, the greater excess of potassium nitrate may have minimised the formation of MNPs onto the PEG-OH background for the 6% Co doped Mms6 patterned arrays. This may have the same effect for the undoped magnetite, which could be investigated in the future to further optimise the POFHK method of biotemplating magnetite onto arrays. These 6% Co doped biotemplated nanomagnets are characterised in Chapter 6.

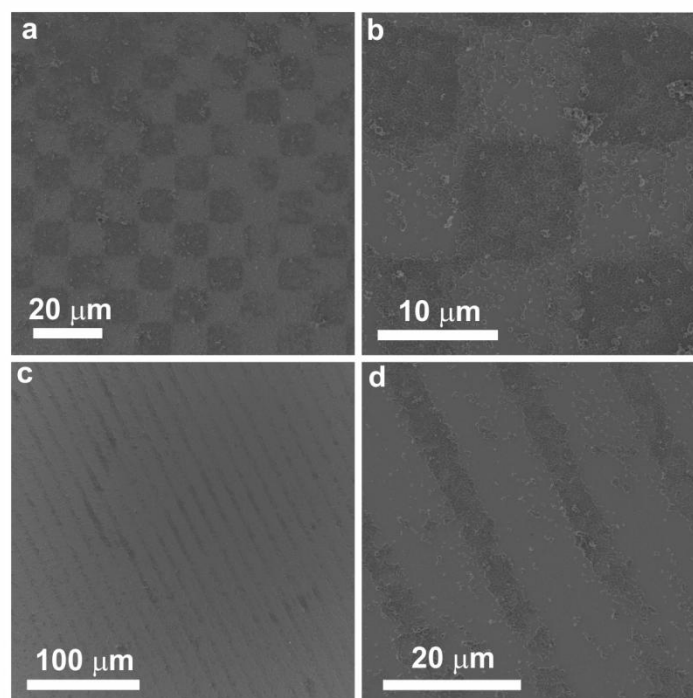


Figure 5.13. SEM images of Mms6 patterned surfaces mineralised using POFHK with 6% Co doping onto micro-patterned Mms6. Reactant ratios in total 10 mL reaction volume were 23.5 mM FeSO_4 , 1.5 mM CoSO_4 , 55 mM KOH , 400 mM KNO_3 . (a) Shows chessboard pattern of closely packed equidimensional MNPs on immobilised Mms6 patterned surface, and (b) a close up. (c) Closely packed MNPs on line pattern of Mms6, and (d) a close up. Although there are some MNPs on the PEG-OH background, there are less than were formed for the magnetite POFHK mineralisation (e.g. see Figure 5.4d).

5.6.3 POFHK and 33% Cobalt Ferrite Mineralisation of Immobilised Mms6 Patterns

When the proportion of cobalt in the reactants was increased to 33% to try and form cobalt ferrite onto the patterned Mms6, platy lepidocrocite was formed (Figure 5.14). As the POFHK system is less complex than the POFHN system, and the Mms6 seemed able to template the platy mineral onto the patterned surface, some optimisation of the POFHK method to template CoFe_2O_4 was attempted. By slightly increasing the concentration of base in the system, the reaction was able to form equidimensional MNPs onto the Mms6 surface, which are likely to be CoFe_2O_4 . Further optimisation of this system is still needed to ensure the formation of closely packed cobalt ferrite MNPs onto the immobilised Mms6, similar to those formed for magnetite and 6% Co doped ferrite. The nanoline patterned Mms6 was also successfully biomineralised to form lines of cobalt ferrite particles. The nanoscale patterning appears to have allowed the immobilised Mms6 to form larger MNPs than those formed on the microscale patterns. This may be due to the smaller feature size allowing reactants to diffuse to the biomineralising Mms6 more easily on the surface than for protein immobilised on a larger pattern. The nanopatterning, and any effect on biomineralisation, could be further studied in the future if new masters are created.

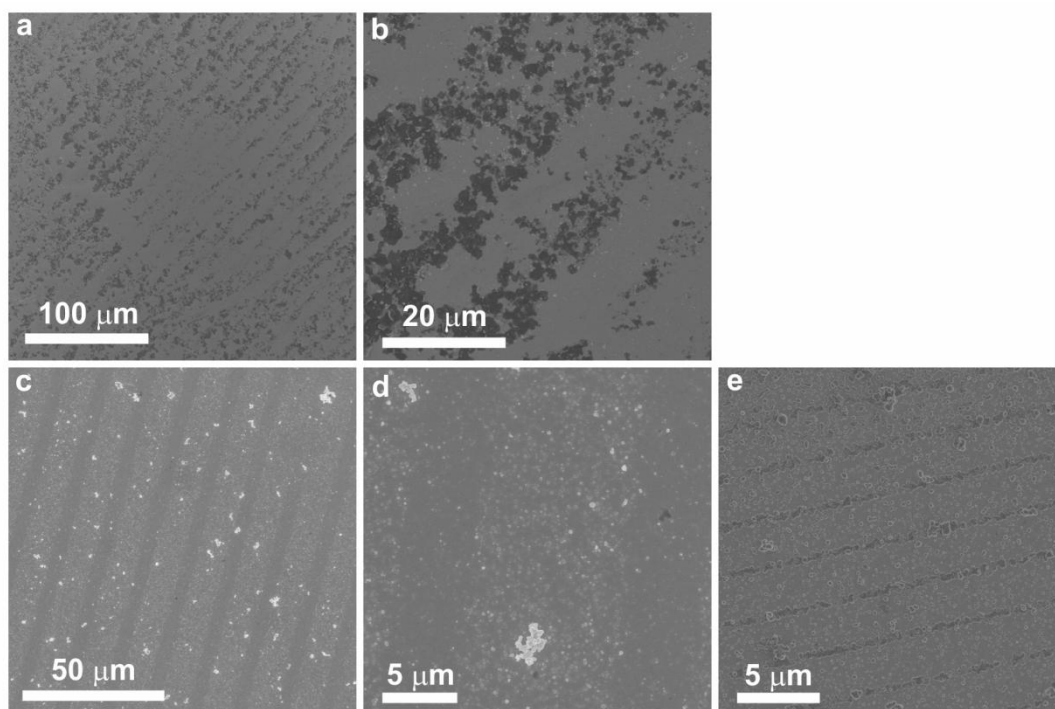


Figure 5.14. SEM images of Mms6 patterned surfaces mineralised using POFHK with 33% Co doping (i.e. to form cobalt ferrite, CoFe_2O_4) onto patterned Mms6. Reactant ratios in total 10 mL reaction volume was 17 mM FeSO_4 , 8 mM CoSO_4 , 55 mM KOH, 400 mM KNO_3 . (a) Shows line pattern of platy lepidocrocite formed on immobilised Mms6 patterned surface, and (b) a close up. When the concentration of KOH was increased to 60 mM, (c) small MNPs formed on the line pattern of Mms6, and (d) a close up. The CoFe_2O_4 MNPs formed by slightly increasing the concentration of alkali are quite sparse on the Mms6 surface. (e) Nanopatterned biotemplated cobalt ferrite particles are much closer together on the patterned surface, which were formed under same reaction conditions as images c & d.

The addition of 33% cobalt to the POFHK system requires an increase in the concentration of KOH to form cobalt ferrite instead of the platy mineral. It is possible that the pH and solubility of cobalt sulfate is different to that of ferrous sulfate. As an excess of the acidic iron sulfate solution produces a similar shift, it may be that the cobalt sulfate solution is more acidic than the iron sulfate solution, so causes a similar shift in the phases formed. The oxidation of iron is more favourable in basic solutions,¹² so reducing the pH by substituting cobalt for iron may retard the partial oxidation of ferrous hydroxide to form magnetite. Therefore, by adding a slightly greater excess of base to the POFHK system, the cobalt ferrite phase can be formed by the immobilised Mms6 on the patterned surface.

5.7 References

1. Galloway, J.M., Bramble, J.P., Rawlings, A.E., Burnell, G., Evans, S.D. & Staniland, S.S. (2012). Nanomagnetic arrays formed with the biomineralization protein Mms6. *J. Nano Res.* **17**, pp 127-146.
2. Galloway, J.M., Bramble, J.P., Rawlings, A.E., Burnell, G., Evans, S.D. & Staniland, S.S. (2012). Biotemplated magnetic nanoparticle arrays. *Small.* **8**, pp 204-208.
3. Arakaki, A., Webb, J. & Matsunaga, T. (2003). A novel protein tightly bound to bacterial magnetic particles in *Magnetospirillum magneticum* strain AMB-1. *J. Biol. Chem.* **278**, pp 8745-8750.
4. Montemagno, C. & Bachand, G. (1999). Constructing nanomechanical devices powered by biomolecular motors. *Nat. Nanotechnol.* **3**, pp 225-231.
5. Amemiya, Y., Arakaki, A., Staniland, S.S., Tanaka, T. & Matsunaga, T. (2007). Controlled formation of magnetite crystal by partial oxidation of ferrous hydroxide in the presence of recombinant magnetotactic bacterial protein Mms6. *Biomaterials.* **28**, pp 5381-5389.
6. Sugimoto, T. & Matijevic, E. (1980). Formation of uniform spherical magnetite particles by crystallization from ferrous hydroxide gels. *J. Colloid Interface Sci.* **74**, pp 227-243.
7. Cornell, R.M. & Schwertman, U. (2003). *The Iron Oxides: Structure, Properties, Reactions, Occurrences and Uses* (Wiley-VCH, Weinheim, DE).
8. Galloway, J.M., Arakaki, A., Masuda, F., Tanaka, T., Matsunaga, T. & Staniland, S.S. (2011). Magnetic bacterial protein Mms6 controls morphology, crystallinity and magnetism of cobalt-doped magnetite nanoparticles in vitro. *J. Mater. Chem.* **21**, pp 15244-15254.
9. Sidhu, P.S., Gilkes, R.J. & Posner, A.M. (1978). The synthesis and some properties of Co, Ni, Zn, Cu, Mn and Cd substituted magnetites. *J. Inorg. Nucl. Chem.* **40**, pp 429-435.
10. Regazzoni, A.E., Urrutia, G.A., Blesa, M.A. & Maroto, A.J.G. (1981). Some observations on the composition and morphology of synthetic magnetites obtained by different routes. *J. Inorg. Nucl. Chem.* **43**, pp 1489-1493.
11. Hadley, M.J., Wright, A.J., Rowson, N.A. & Grover, L.M. (2011). Acicular nanoparticles formed through coprecipitation of iron salts in the presence of bovine serum albumin. *J. Mater. Chem.* **21**, pp 13769-13771.
12. Cotton, F.A. & Wilkinson, G. (1980). *Advanced Inorganic Chemistry: A Comprehensive Text, 4th Edition* (John Wiley & Sons, Chichester, UK).

Chapter 6

Characterisation of Biotemplated Magnetic Arrays

Both the POFHK and POFHN method of magnetite synthesis have been optimised to form equidimensional particles onto a surface patterned with immobilised Mms6. The reaction conditions used during particle formation, as well as the morphology of the MNPs, indicate that these particles should be magnetite, 6% cobalt doped magnetite or cobalt ferrite. In this chapter, the subscript 'Fe' indicates MNPs formed from a magnetite mineralisation solution, '6%Co' is used for particles formed from a mineralisation solution containing 6% Co, which should form cobalt doped magnetite, and '33%Co' for MNPs formed from a solution containing 33% cobalt, that should form cobalt ferrite. However, the biotemplated minerals need to be characterised to ensure that uniform, crystalline MNPs of the appropriate iron (cobalt) oxide mineral were formed by the immobilised Mms6 protein. In this chapter, EDX is used to map the elements present in the undoped magnetite, the 6% cobalt doped magnetite and cobalt ferrite arrays that were formed. Grainsize analysis of SEM images of the patterned arrays are compared to TEM images of controls to establish the particle size distributions. The crystallinity of the MNPs was studied using powder XRD, and the bulk magnetic behaviour of the arrays recorded using VSM. Finally, the magnetic interactions of the biotemplated, patterned MNPs were imaged and analysed using MFM.

6.1 Magnetite Templated by Immobilised Mms6

In this section, no cobalt was added to the reactant solutions when mineralising particles onto the patterned Mms6 substrates. Therefore, the system should have been optimised towards forming magnetite, rather than any other iron oxide mineral phase. The morphology of the particles indicates that they are magnetite, but further characterisation is required to confirm this. The micropatterned biomineralised substrates have been analysed to determine if uniform nanomagnets of magnetite were formed by the Mms6 protein *in situ*. Much of the work in this section is published in Galloway *et al.* (2012a)¹ & (2012b).²

6.1.1 Grainsize Analysis from SEM and TEM

The grainsize and shape of MNPs from SEM and TEM images of a number of the biomineralised patterned arrays were analysed. The results were used to compare the grainsize distributions of a selection of biomineralised arrays, which were selected because of their good contrast between the immobilised Mms6 and the PEG-OH background. Figure 6.1 shows the SEM images of samples mineralised using three different reaction conditions for magnetite formation. There are also TEM images of MNPs formed from the respective bulk solution with no protein present, and the grainsize distributions of the samples recorded in Image J.³ These data were fitted with Gaussian distributions in Origin, and the results are summarised in Table 6.1. 'POFHN' refers to the optimum mineralisation (50 mM FeSO₄, 40 µL 50-60% N₂H₄, 200 µL 26% NH₄OH and 100 mM KNO₃, first shown in Figure 5.9a). 'Dilute POFHN' refers to a less concentrated reaction solution (30 mM FeSO₄, 21 µL 50-60% N₂H₄, 165 µL 26% NH₄OH and 150 mM KNO₃, first shown in Figure 5.10b). Finally, the sample labelled 'RT POFHK' was mineralised at room temperature using potassium hydroxide as the base (50 mM Fe²⁺, 100 mM KOH, and 400 mM KNO₃ for five days at room temperature, first shown in Figure 5.4e). The subscript 'Fe_Mms6_surface' refers to the micro-patterned surface that has been biomineralised with magnetite onto the immobilised Mms6. The subscript 'Fe_no protein_bulk' is used to denote control particles formed under the same reaction conditions as for the mineralised surface, but in the absence of any protein in the bulk solution.

Table 6.1. Summary of grainsize data comparing different methods of biomineralising magnetite onto patterned Mms6 arrays shown in Figure 6.1, from Galloway *et al.* (2012a).¹

colour	sample	peak centre (nm)	σ (nm)	FWHM (nm)
black	POFHN _{Fe_Mms6_surface}	340	54	126
grey	POFHN _{Fe_no protein_bulk}	230	121	285
dark pink	dilute POFHN _{Fe_Mms6_surface}	231	47	110
light pink	dilute POFHN _{Fe_no protein_bulk}	154	63	149
dark blue	RT POFHK _{Fe_Mms6_surface}	836	107	252
light blue	RT POFHK _{Fe_no protein_bulk}	126	66	154

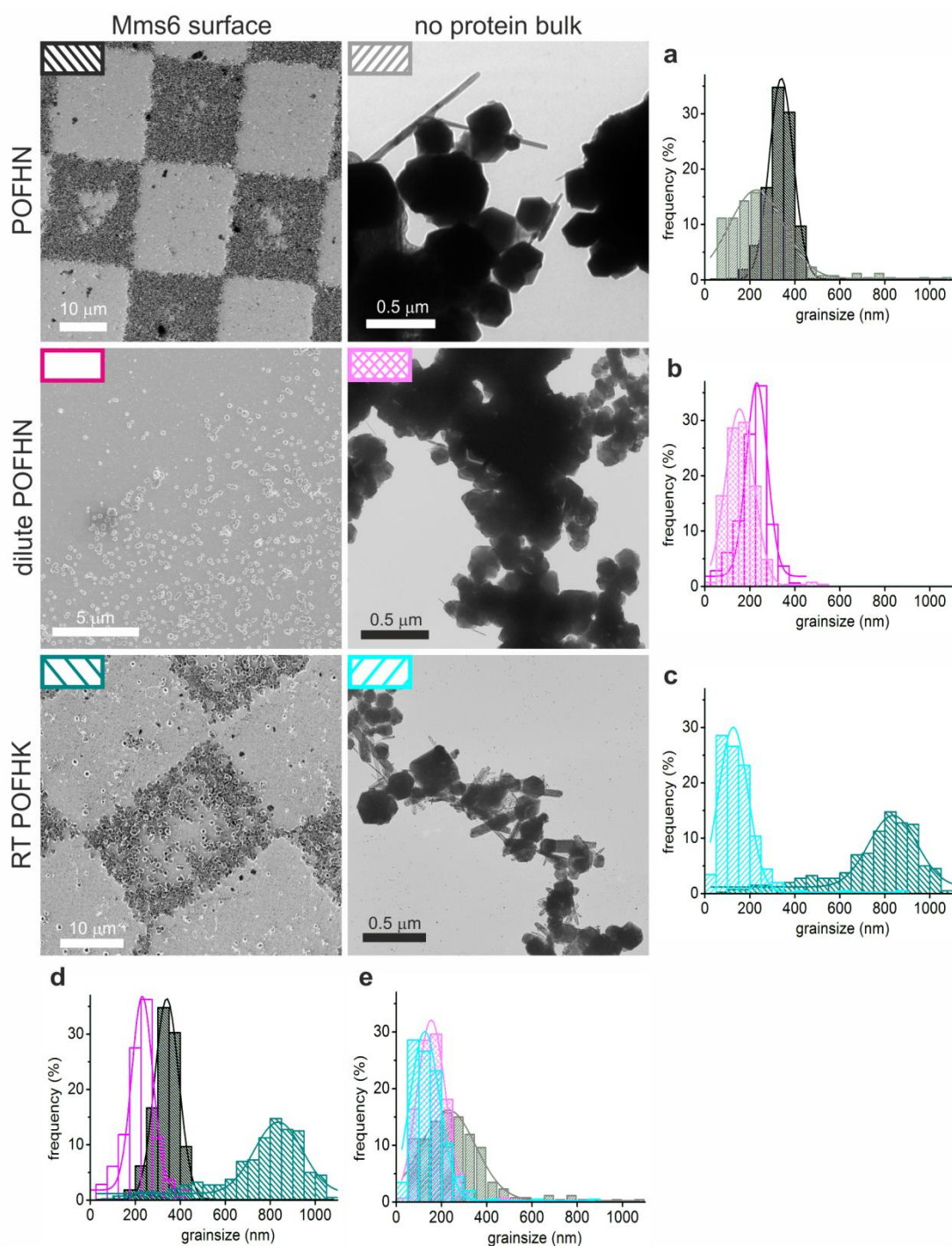


Figure 6.1. SEM (left column), TEM (centre column) and grainsize analysis (right column and bottom) of MNPs formed on an Mms6 patterned array, redrawn from Galloway *et al.* (2012a).¹ Reactant conditions for POFHN as in Figure 5.9a, dilute POFHN as in Figure 5.10b and RT POFHK as in Figure 5.4e. Grainsize measured using Image J³ (bin size 50 nm), and fitted with single Gaussian distributions using Origin. Colour key for grainsize analysis shown on respective electron microscope images.

In all cases, MNPs formed by the immobilised Mms6 are larger than the controls formed from the same mineralisation solution in the absence of protein. The FWHM and σ of the fits show that the Mms6 templated MNPs on the surfaces also have a narrower size distribution than the controls. RT POFHK_{Fe_Mms6_surface} MNPs formed over a long period, and are much larger (836 ± 107 nm) than those formed using POFHN_{Fe_Mms6_surface} (340 ± 54 nm) and dilute POFHN_{Fe_Mms6_surface} (231 ± 63 nm), which were mineralised more rapidly at higher temperatures (80°C). Therefore, the most uniform MNPs mineralised onto the immobilised Mms6 patterned surface were formed by the POFHN_{Fe_Mms6_surface}, with the dilute POFHN_{Fe_Mms6_surface} MNPs being slightly smaller and having a slightly broader grainsize distribution.

MNPs templated by Mms6 from the bulk solution (POFHN_{Fe_Mms6_bulk}) were also synthesised to compare to the POFHN mineralised surface (POFHN_{Fe_Mms6_surface}) and those mineralised from the bulk solution with no protein (POFHN_{Fe_no protein_bulk}). $10\mu\text{g mL}^{-1}$ Mms6 was added to a bulk reaction solution of POFHN, with the same reaction conditions used to form the POFHN_{Fe_Mms6_surface} MNPs. Figure 6.2 shows SEM and TEM images, and the grainsize analysis of these MNPs. The POFHN_{Fe_Mms6_surface} MNPs are more equidimensional than either the POFHN_{Fe_no protein_bulk} or POFHN_{Fe_Mms6_bulk} MNPs. POFHN_{Fe_Mms6_surface} MNPs have an aspect ratio of 0.899 ± 0.066 , and there are no acicular particles. When no protein was present in the mineralisation solution, the MNPs have a broad grainsize distribution (232 ± 121 nm) and the needle shaped MNPs that have formed skew the aspect ratio towards a more elongated average (0.753 ± 0.074). When Mms6 was present in the bulk solution, the particles are also fairly equidimensional (average 0.856 ± 0.081). However, they are not monodisperse, but they have a bimodal grainsize distribution, with peaks for POFHN_{Fe_Mms6_bulk} MNPs centred on 73 ± 38 nm and 203 ± 121 nm.

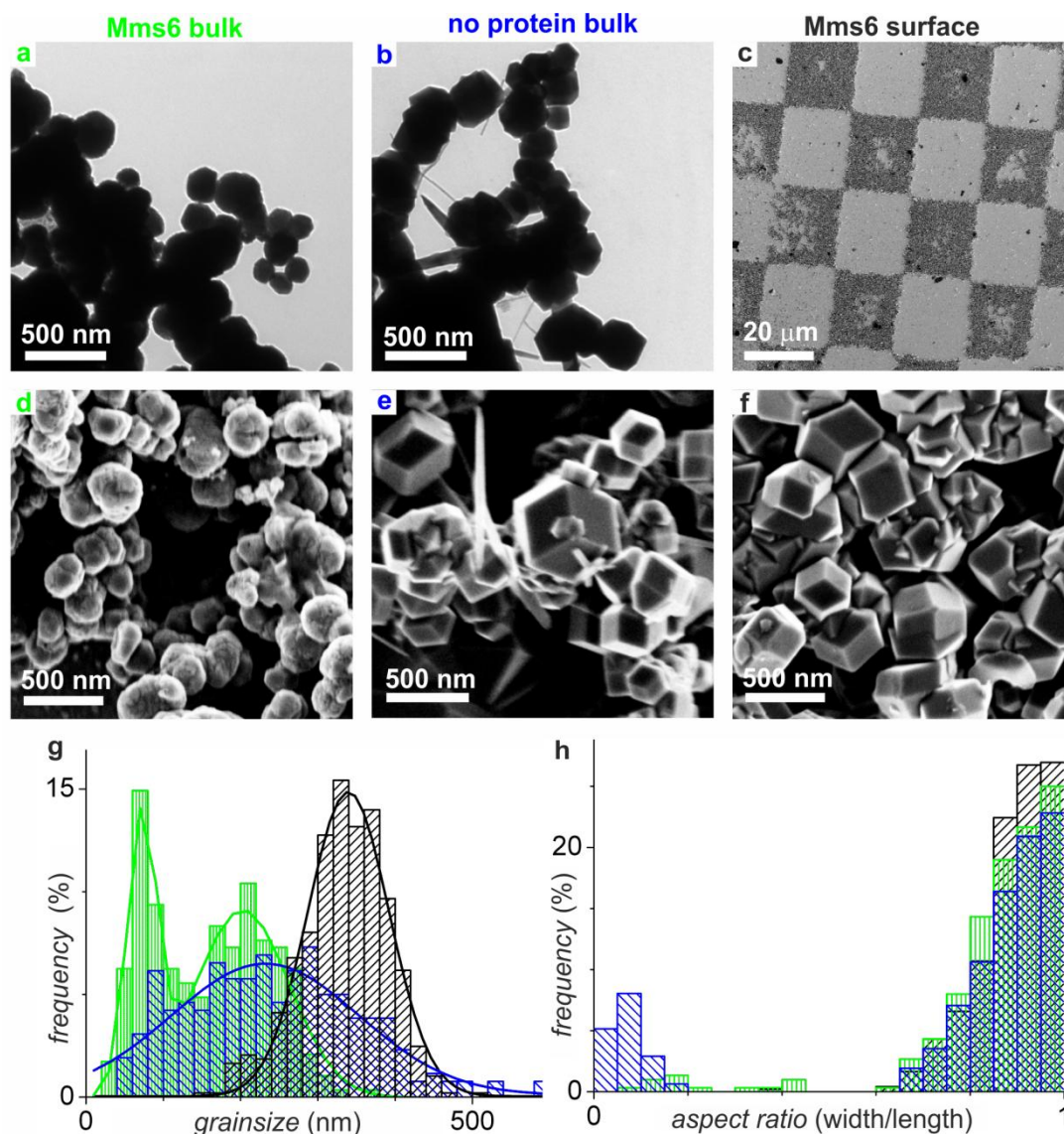


Figure 6.2. (a-b) TEM and (c-f) SEM images of POFHN MNPs, redrawn from Galloway *et al.* (2012b).² (a & d) POFHN_{Fe_Mms6_bulk} MNPs (green), (b & e) POFHN_{Fe_no_protein_bulk} MNPs (blue) and (c & f) POFHN_{Fe_Mms6_surface} MNPs (black). (g) Grainsize analysis (bin size 50 nm) and (h) aspect ratio of MNPs (bin size 0.05) measured in Image J³ and fitted with single/double Gaussian distributions based on the lowest χ^2 of the fit in Origin.

The POFHN MNPs mineralised onto the patterned surface are of a similar size and size distribution to magnetite MNPs synthesised using a very high temperature method. Kim *et al.* (2009)⁴ synthesised magnetite cubes at 290°C using thermal decomposition, with an edge length of 160 ± 40 nm, which is $\approx 280 \text{ nm} \pm 70 \text{ nm}$ along the diagonal. This shows that the POFHN method is well suited to forming uniform sized magnetite MNPs onto the Mms6 patterned surfaces. In fact, attachment to the patterned surface seems to allow the Mms6 protein to template more uniform particles than those formed in the presence of Mms6 in the bulk solution for the POFHN method. It may be that attachment to the surface helps to stabilise the Mms6 protein during the mineralisation process. This would allow the patterned Mms6 to form more uniform MNPs when attached to a surface than when in a bulk

solution. As these reaction conditions are optimised to form MNPs on the patterned surface, the protein in the bulk solution may not be as well suited to the formation of uniform MNPs from these conditions. The next stage of the characterisation is to determine if the equidimensional MNPs are made from magnetite.

6.1.2 EDX Elemental Mapping of Biotemplated Magnetite Arrays

The X-rays produced by some electrons that penetrate a sample during SEM can be used to map which elements are present in the substrate. The wavelength of the X-rays that are emitted are element specific, so can be used to determine which elements are present in the sample being scanned. The signal strength of the EDX signal is increased with increasing beam current, as more energetic incident electrons create more X-ray emissions for detection. However, increasing the beam current also increases the volume of interaction of the electrons with the sample. Unfortunately, as the X-rays can be detected from anywhere in the interaction volume of the electron beam with the sample, increasing the beam current also increases the effective spot size for EDX mapping. This means that a low beam current is desirable for good surface specific resolution to form an accurate elemental map of the sample. Therefore, a careful balance between signal strength at the detector and spot size is required to build up good EDX images. Point spectra were taken on both the biomineralised areas and the unmineralised PEG-OH background, and the sample surface was scanned to build up elemental maps (Figure 6.3).

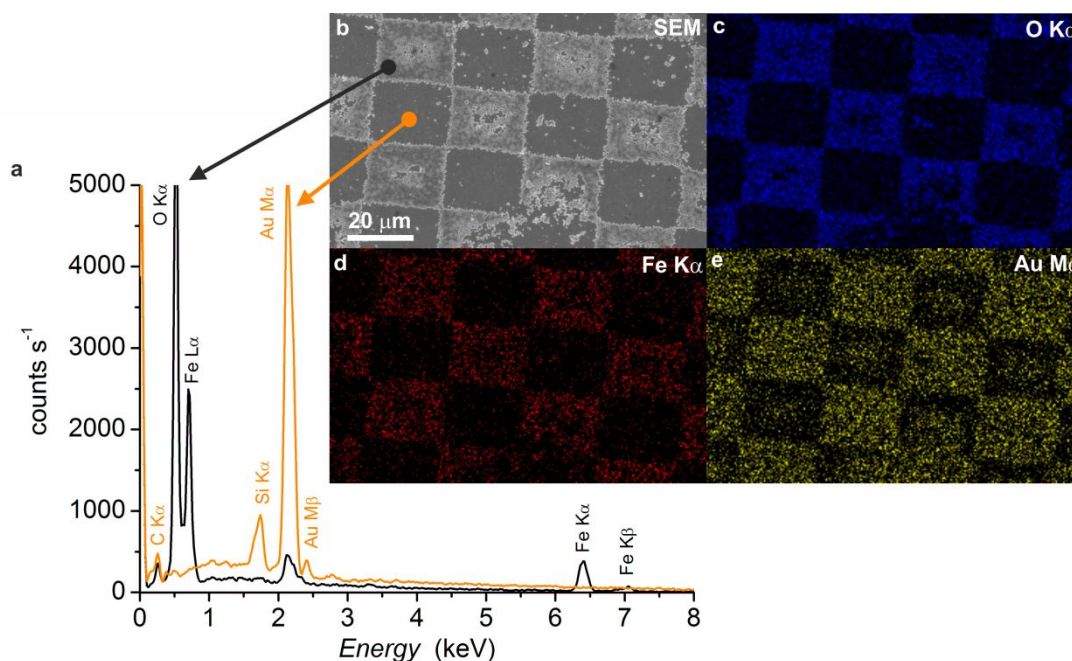


Figure 6.3. EDX spectra and elemental maps from SEM of micro-patterned biomineralised magnetite surface. Sample imaged is POFHN_{Fe_Mms6_surface} (50 mM FeSO₄, 40 μ L 50-60% N₂H₄, 200 μ L 26% NH₄OH and 100 mM KNO₃, Figure 5.11) (a) EDX spectra recorded at 10 keV at the points marked on the biomineralised magnetite (black) and PEG-OH background (orange). Peaks from oxygen and iron are clearly discernible from the biomineralised magnetite, with the gold and silicon from the substrate more prominent on the PEG-OH background. (b) 2° electron image of the sample shows the biomineralised chessboard pattern. EDX elemental maps of (c) O K α , (d) Fe K α and (e) Au M α X-ray peaks show the localisation of iron and oxygen in biomineralised magnetite, and a much stronger signal from the gold on the PEG-OH background.

The two spectra show a clear difference in the magnitude and location of many of the detected EDX peaks due to the different elements present at the point scanned. On the biomineralised magnetite areas, there are strong peaks due to the presence of oxygen and iron, which show that an iron oxide is biomineralised onto these areas. The PEG-OH background has resisted mineralisation well, as there is no clear peak for iron or oxygen in this spectrum. However, the signal from the gold layer deposited onto the glass slide has produced a peak for both gold and silicon. The elemental maps distinctly show the contrast between the biomineralised areas, where X-rays from Fe and O are strongly detected, and the mineralisation resistant areas, where X-rays from gold are dominant. These data show that iron oxide is present on the biomineralised areas, but as there are many different oxides of iron, it cannot be concluded that it is magnetite. Further characterisation of the properties of the Mms6 biomineralised arrays is required to determine that the iron oxide nanoparticles are magnetite.

6.1.3 Crystallinity of Biotemplated Magnetite Arrays

6.1.3.1 Selected Area Electron Diffraction (SAED)

The crystallinity of the control samples for the POFHN_{Fe} method (i.e. no protein bulk and Mms6 bulk) was assessed using SAED in the TEM. As the biomineralised substrates are far too thick to be imaged using TEM, it was not possible to characterise the biomineralised arrays using this technique. Figure 6.4 shows TEM images of the area selected using the diffraction annulus, and the corresponding diffraction patterns. The no protein bulk control contained a lot of thin acicular particles that were heavily agglomerated, so it was not possible to select a single crystal for diffraction. Therefore, an area containing many of the needle shaped particles was selected, which produced the polycrystalline diffraction pattern seen in Figure 6.4b. It was possible to select a single crystal for diffraction from the Mms6 bulk sample, which produced the single crystal diffraction shown in Figure 6.4d. The spacing of the spots was converted to *d* spacings for the diffracted crystal using the camera constant of the TEM (see Equation 2.10). The distances, and angles between the spots were a very good match for magnetite viewed along the [1 $\bar{1}$ 0] axis (see Table 6.2).

Table 6.2. Summary of SAED data from Figure 6.4 with comparison to magnetite & maghemite peaks from EVA software (see Table 2.3), and goethite peaks from Cornell & Schwertmann (2003).⁵ *d* spacings are measured in Å.

line	POFHN Fe no protein bulk	closest match (<i>d</i> in Å)
1	3.243	(120) goethite (3.383)
2	2.945	(220) maghemite (2.950)
3	2.444	(311) maghemite (2.520)
4	2.318	(320) maghemite (2.320)
5	1.912	(041) goethite (1.920)
6	1.814	(420) maghemite (1.870)
7	1.520	(160) & (250) goethite (1.561) & (1.509)
8	1.378	(301) goethite (1.369)
9	1.252	(622) maghemite (1.260)
10	1.186	(4412) maghemite (1.204)

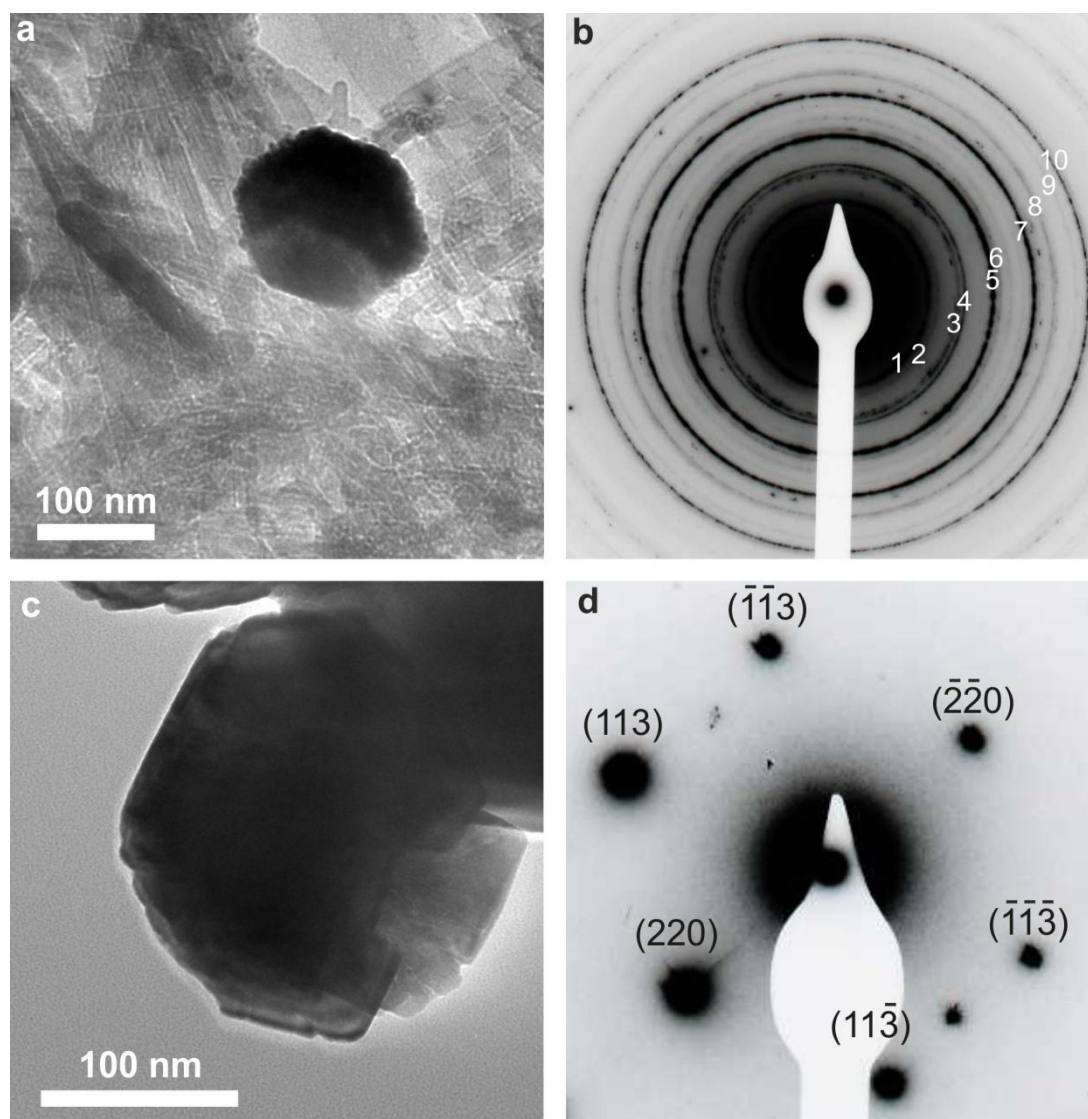


Figure 6.4. TEM images and SAED patterns* for POFHN_{Fe} controls, redrawn from Galloway *et al.* (2012b).² (a) TEM image of no protein bulk control and (b) SAED pattern shows polycrystalline pattern, line numbers assigned in Table 6.2 are mainly maghemite and goethite. (c)² TEM image of Mms6 bulk control and (d)² SAED single crystal diffraction pattern of the MNP in the TEM image, viewed along the $[1\bar{1}0]$ axis. Diffraction spots are labelled with crystallographic planes of magnetite based on the measured d spacings and Andrews *et al.* (1971).⁶

The camera constant for the TEM was also used to convert the distance between the diffracted lines in Figure 6.4b and the central beam into a d spacing, which was compared to diffraction data from different iron oxides (Table 6.2). Despite the similar structures of magnetite and maghemite, the crystallographic data from the no protein bulk sample was a much better match to maghemite than magnetite. There were also some other planes recorded, which were a much better match to goethite rather than maghemite or magnetite. The TEM images shown in Figure 6.4 were selected as they are representative of the range of particles seen in TEM from

* TEM images and SAED taken in collaboration with M. Ward and A. Walton, University of Leeds.

that sample. As the acicular particles were probably not magnetite, but an unidentified iron oxide, an area consisting mainly of the acicular particles was selected for the diffraction study.

The area selected for SAED from the POFHN_{Fe_no protein_bulk} sample contained mainly thin acicular particles, very few of the more opaque acicular particles, and one equidimensional particle. It is likely that the single equidimensional particle is magnetite, and may be responsible for some of the spots on the diffraction pattern in Figure 6.4b. In fact, some of the *d* spacings measured from the spots are a close match to the magnetite standard. Therefore, the mixture of peaks for goethite and maghemite that dominate the lines generated by the polycrystalline diffraction may be due to a mixture of these minerals in the diffracted area. Based on these diffraction data for both POFHN_{Fe} controls, it is likely that equidimensional particles are magnetite, whether formed in the presence or absence of Mms6. The POFHN_{Fe_Mms6_bulk} MNP formed a good quality single crystal diffraction pattern, indicating that the presence of Mms6 facilitated the formation of high quality magnetite over other iron oxide mineral phases for the POFHN method. The acicular particles seen in the POFHN_{Fe_no protein_bulk} samples could be either goethite or maghemite in keeping with the characteristic morphology.

6.1.3.2 Powder X-ray Diffraction (XRD)

The crystallinity of the biotemplated magnetite surfaces made by POFHN_{Fe_Mms6_surface} and RT POFHK_{Fe_Mms6_surface} were assessed using powder XRD,* see Figure 6.5 and Table 6.3.^{1,2} Controls of POFHN_{Fe_no protein_bulk}, POFHN_{Fe_Mms6_bulk} and a gold coated substrate control that was heated to 90°C for 4 hours in water were also analysed. The glass in the substrates produces the broad hump in the spectra between $2\theta \approx 15^\circ$ to 35° , and the gold (111) and (200) peaks are clearly visible in the unmineralised gold slide (labelled orange), as well as in the spectra from the biomineralised Mms6 patterns. The peaks for magnetite or maghemite are labelled in black. The peaks labelled with grey arrows on the traces are probably due to carbon, which may be from the carbon tape used to earth the samples for SEM imaging. However, it is possible that these grey labelled peaks are due to oxidation of the chromium adhesion layer beneath the gold surface. The chromium could be readily oxidised, either during evaporative deposition to form the adhesion layer, or by the oxidising magnetite mineralisation solution. This is because these unknown peaks are also a close match to the Cr₈O₂₁ ($\bar{1}\bar{1}2$) and (205) peaks. Thus, the peaks labelled in grey cannot be assigned to a specific mineral using these XRD data.

* XRD collected and analysed in collaboration with L. Neve, University of Leeds.

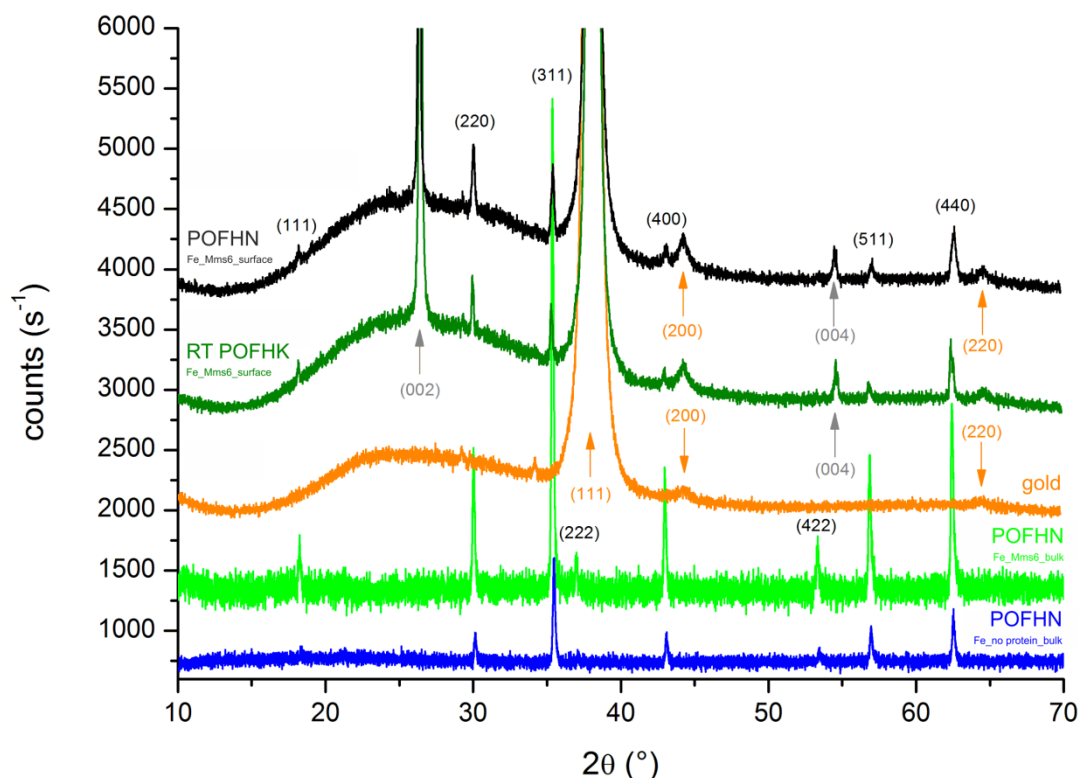


Figure 6.5. Powder XRD of biomineralised micro-patterned arrays of magnetite and controls, from Galloway *et al.* (2012a & b).^{1,2} POFHN_{Fe_no_protein_bulk} (blue), POFHN_{Fe_Mms6_bulk} (green), heat treated gold (orange), RT POFHK_{Fe_Mms6_surface} (dark green) and POFHN_{Fe_Mms6_surface} (black). The traces are offset for clarity. Magnetite peaks labelled in black, gold peaks labelled in orange, and probable carbon peaks labelled in grey. Peak positions for magnetite and maghemite are summarised in Table 6.3.

Table 6.3. Table of peak positions for magnetite and maghemite (based on spectra from EVA software, see Table 2.3) and peak positions from samples shown in Figure 6.5, measured in Å.^{1,2} The particles templated by Mms6 show a much closer match to magnetite than other iron oxide minerals, for MNPs templated both on the patterned surfaces and from a bulk solution. However, some peaks from POFHN_{Fe_no_protein_bulk} (e.g. (220) and (311) peaks) are a closer match to maghemite.

peak	magnetite	maghemite	RT POFHK Fe Msm6 surface	POFHN Fe no protein bulk	POFHN Fe Mms6 bulk	POFHN Fe Msm6 surface
(111)	4.850	4.820	4.888	4.825	4.884	4.889
(220)	2.966	2.950	2.974	2.958	2.982	2.971
(311)	2.530	2.520	2.543	2.572	2.535	2.534
(222)	2.419	2.410			2.426	
(400)	2.096	2.080	2.140	2.095	2.103	2.100
(422)	1.712	1.700		1.713	1.718	
(511)	1.614	1.610	1.618	1.614	1.618	1.618
(440)	1.483	1.480	1.485	1.482	1.488	1.482

Maghemite and magnetite have very similar crystal structures, so their crystals produce very similar diffraction patterns. The MNPs made in the presence of Mms6 (i.e. RT POFHK_{Fe_Mms6_surface}, POFHN_{Fe_Mms6_surface} and POFHN_{Fe_Mms6_bulk}) produce peaks that are a much closer match to magnetite than maghemite (see Table 6.3). Interestingly, this was still found to be true of the POFHN_{Fe_Mms6_surface} arrays after

12 months storage in air. This resistance to oxidation in air demonstrates that the biotemplated magnetite on the patterned surface is extremely stable. The non-biotemplated control (POFHN_{no protein_bulk}) has some peaks that are a closer match to maghemite than to magnetite (e.g. the (220) and (311) peaks). As can be seen in Figure 6.2 and 6.4, there are a lot of acicular particles formed by both POFHN and RT POFHK in the absence of protein when these methods are optimised for the formation of magnetite onto the immobilised Mms6 patterns.

In the SAED study above, the acicular MNPs produced by POFHN_{Fe_no protein_bulk} are likely to be a mixture of maghemite and goethite. However, there are no goethite peaks in the powder XRD diffraction patterns. It may be that any goethite present in the sample is poorly crystalline, so does not produce clear diffraction peaks in XRD. As the SAED annulus was used to select mainly needle shaped particles, any diffraction of electrons due to goethite may have been easier to detect. From both the SAED and XRD data, it is likely that at least some of the needle shaped particles are maghemite, and are responsible for the shift in some of the XRD peaks towards the structure of maghemite for POFHN_{Fe_no protein_bulk}. These data strongly indicate that the uniform MNPs templated by the immobilised Mms6 are magnetite, rather than any other iron oxide mineral phase. Even after 12 months storage in air, the position of the peaks from the POFHN_{Fe_Mms6_surface} sample were still found to closely match magnetite. This also shows that the magnetite nanoparticles biomineralised onto the micro-patterned arrays are stable against oxidation or degradation to other iron oxide minerals when stored in air for long periods.

6.1.4 VSM of Biotemplated Magnetite Arrays

6.1.4.1 Magnetisation with Temperature

VSM was used to try and measure the POFHN_{Fe_Mms6_surface} sample for FC and ZFC measurements, see Figure 6.6. As it was not possible to determine a mass of magnetite particles on the biotemplated patterned surfaces, the data from each sample was normalised so they could be compared. An unmineralised gold substrate shows an antiferromagnetic response at low temperatures for both the ZFC and FC measurements. This is probably due to the chromium adhesion layer evaporated onto the glass slides to affix the gold to the substrates. This thin layer (a few nm) may easily be oxidised by oxygen present in the evaporation chamber during metal deposition, either under vacuum or after gold deposition. Cr₈O₂₁ is antiferromagnetic below ≈ 100 K, and paramagnetic above this temperature.⁷ The XRD data may have shown the presence of chromium oxide from the biomineralised substrates. However, the XRD did not show a clear signal for chromium oxide from the unmineralised gold substrate, so it may be that this thin

layer is not easily detected in XRD due to the Au layer evaporated on top. These magnetic measurements do show the presence of an antiferromagnetic signal at low temperatures, which is most likely to be due to the chromium adhesion layer, whether it is oxidised or not. This means that the peaks labelled grey on the XRD (Figure 6.5) could still be due to either chromium oxide or carbon contamination.

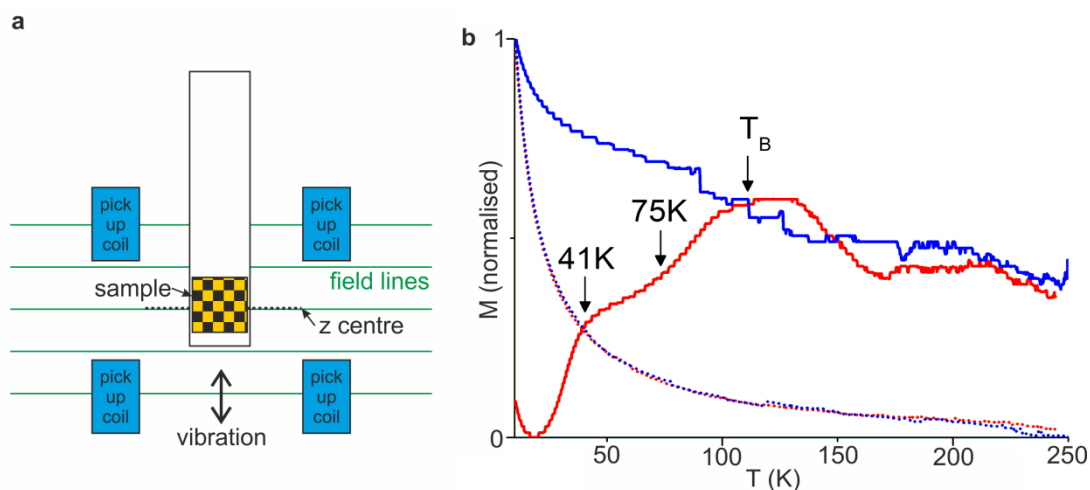


Figure 6.6. Schematic of a biomaterialised sample in the VSM, and temperature versus moment for ZFC (red) and FC (blue) VSM measurements with an applied field of 200 Oe, from Galloway *et al.* (2012b).² (a) A biomaterialised sample is difficult to centre in the VSM due to its size and shape, so it is not always possible to maximise the sample signal. (b) Temperature versus moment data, dotted trace is an unmineralised gold substrate, and the solid trace is $\text{POFHN}_{\text{Fe_Mms6_surface}}$. A divergence in the traces from $\text{POFHN}_{\text{Fe_Mms6_surface}}$ indicates a possible blocking temperature ($T_B \approx 111$ K), and sudden changes in slope at 41 K and 75 K may be evidence of the Verwey transition.

It was difficult to obtain clear data for the biomaterialised magnetite surfaces using the VSM as there were issues with the stability of the instrument at higher temperatures. Also, the sample holder used to mount the biomaterialised arrays in the magnetometer makes it difficult to centre the sample to maximise the magnetic signal at the pick-up coils. Powdered samples can be packed into a small area, so can be positioned fairly easily to maximise the signal at the z centre. However, as the biomaterialised substrates are flat, the shape of the substrates causes the sample to be elongated in the z direction, making it difficult to position the sample to maximise the signal. The $\text{POFHN}_{\text{Fe_Mms6_surface}}$ shows an antiferromagnetic signal below ≈ 15 K, which is most likely due to the antiferromagnetic signal from the chromium adhesion layer. As the temperature is increased, there is a clear difference in the ZFC and FC behaviour up until ≈ 111 K, which may indicate the blocking temperature for the surface biotemplated magnetite nanoparticles.

There are changes in slope which can be seen in the ZFC measurements, at ≈ 41 K and ≈ 75 K, which may be evidence of the Verwey Transition. The Verwey Transition is characteristic of stoichiometric magnetite,^{8,9} and T_V has been recorded at ≈ 98 K for 150 nm diameter spherical magnetite nanoparticle powders.¹⁰ The

biotemplated micropatterned MNPs are larger (340 ± 54 nm), and cubic rather than spherical, so direct comparison between these data are difficult. The two different transition temperatures may be due to two distinct magnetic behaviours of magnetite nanoparticles on the biomineralised surfaces. The grainsize distribution of the biotemplated MNPs is fairly narrow, so the two different transitions are unlikely to be due to two distinct particle grainsize populations.

Figures 5.9 and 6.3 show the micropatterns of $\text{POFHN}_{\text{Fe_Mms6_surface}}$ MNPs. Some of the MNPs on the micropatterned areas are closely packed with other MNPs in two dimensions, so may be exchange coupled with numerous many close neighbours. The MNPs at the edge of a patterned area have fewer neighbours, so have fewer MNPs they could couple with. The magnetism of the individual particles, or smaller groups of MNPs, may be more easily destabilised by increasing temperatures than the larger groups in the more densely mineralised areas. Therefore, the more densely mineralised MNPs may be responsible for the higher temperature transition, and the less densely packed MNPs at the pattern edges may produce the lower transition. However, this assessment is fairly tentative, as the positioning of the sample in the VSM is difficult to optimise, and the measured data is quite noisy.

6.1.4.2 Magnetic Hysteresis

Magnetic hysteresis loops were recorded at a range of temperatures for the $\text{POFHN}_{\text{Fe_Mms6_surface}}$, RT POFHN , $\text{POFHN}_{\text{Fe_Mms6_bulk}}$ and $\text{POFHN}_{\text{Fe_no protein_bulk}}$ samples. As the mass of MNPs on the biomineralised surfaces cannot be accurately quantified, the magnetisation of the all the samples were normalised to allow the coercivity of the different samples to be measured, see Figure 6.7. At low temperatures (i.e. 10 K), the antiferromagnetic signal from the substrate creates a complicated hysteresis, making comparison of the coercivity between controls and the biomineralised surfaces difficult. The substrate is not antiferromagnetic above ≈ 100 K, so the magnetic hysteresis loops are far easier to compare with each other and the controls when measured at higher temperatures. At 300 K, the coercivity of the $\text{POFHN}_{\text{Fe_Mms6_surface}}$ sample is 112.5 Oe, much higher than the controls ($\text{POFHN}_{\text{Fe_Mms6_bulk}}$ is 98.2 Oe, and $\text{POFHN}_{\text{Fe_no protein_bulk}}$ is 95.9 Oe) and a little higher than the RT $\text{POFHN}_{\text{Fe_Mms6_surface}}$ sample (106.1 Oe). This increase in coercivity for the MNPs mineralised onto the micropatterned Mms6 surfaces could be due to their larger grainsize and/or the improved crystallinity of these particles.

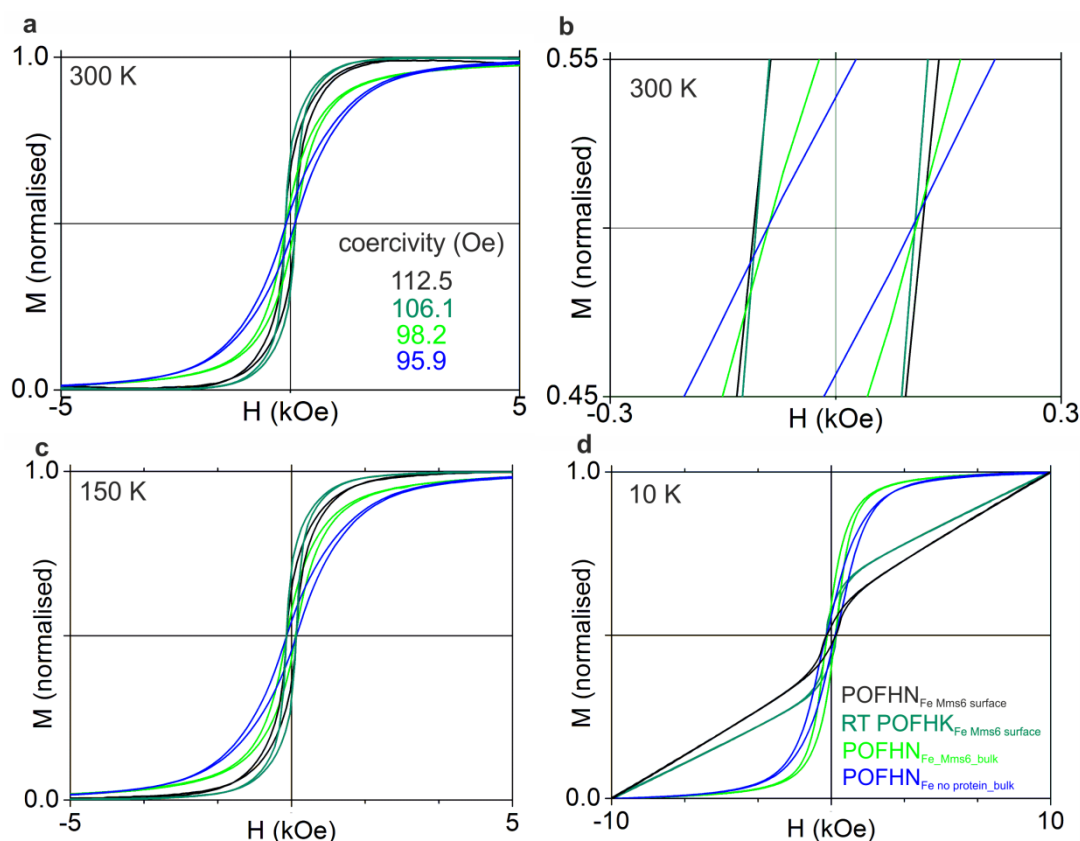


Figure 6.7. Magnetic hysteresis loops from biomaterialised samples and controls from Galloway *et al.* (2012a & b).^{1,2} (a) Shows full hysteresis and (b) is a close-up of the origin to show the coercivity of the different samples at room temperature (300 K). Hysteresis loops also recorded at (c) 150 K and (d) 10 K. Key for colours is as previously: POFHN_{Fe_Mms6_surface} (black); RT POFHK_{Fe_Mms6_surface} (dark green); POFHN_{Fe_Mms6_bulk} (green); and POFHN_{Fe_no_protein_bulk} (blue).

At 300 K and 150 K there is a very rapid change in slope for the MNPs formed by biomaterialisation onto the surfaces when compared to the POFHN_{Fe_Mms6_bulk} and POFHN_{Fe_no_protein_bulk} controls. This indicates that the magnetic behaviour of the RT POFHK_{Fe_Mms6_surface} and POFHN_{Fe_Mms6_surface} surface mineralised particles are extremely uniform, which is highly desirable for use in applications such as data storage. The room temperature coercivity of the surface biomaterialised MNPs is slightly greater than the magnetite nanocubes synthesised by thermal decomposition.⁴ Their synthesis method requires toxic chemicals, such as toluene and chloroform, and high temperatures (290°C) to produce magnetite particles with a coercivity of ≈ 100 Oe⁴ at room temperature, whereas the Mms6 templated MNPs are formed under far less harsh conditions. The immobilisation of the Mms6 templated MNPs onto a surface, and the uniform magnetic switching behaviour, indicates that these biomaterialised arrays could be adapted for use in data storage. However, the coercivity of magnetite is probably far too low for data storage purposes, as the films used in data storage have a coercivity of ≈ 4 kOe.^{11,12} Also, the MNPs formed by this method may also be too large for efficient measurement of the magnetic orientation of the MNPs on the surfaces. The thin-films used currently

for data storage are up to a few 10's of nanometres thick,¹³ so form surfaces that are less rough than formed by these Mms6 biotemplated MNPs. To study the properties of these Mms6 biotemplated magnetite particles on the surface, AFM and MFM were combined to image the particles and to examine the magnetic interactions of the MNPs on the nanoscale.

6.1.5 MFM of Biotemplated Magnetite Arrays

Tapping mode AFM images a surface by tapping a sharp tip across a substrate to record the topographic height of features on that surface. When a magnetised tip is used, the topographical line trace can then be followed at a fixed distance, or lift height, above the surface. In lift mode, magnetic interactions of the surface with the tip cause deflection of the tip, with attractive forces causing a negative shift in the phase of the resonating cantilever, and repulsive forces causing a positive shift. The magnitude of the shift in the resonance is dependent on many factors, including the strength and direction of the magnetisation of the particles on the surface, as well as the strength of the magnetisation of the tip and the distance between the tip and the surface. If the magnetic moment of the tip was known, it would be possible to compare the relative strengths of magnetic interactions between different samples and different tips. However, it was not possible to measure the strength of the magnetisation of the MFM tip, so any comparisons between MFM plots are qualitative.

Figure 6.8 shows MFM plots and SEM images of representative areas of the same samples. The RT POFHK_{Fe_Mms6_surface} sample was very difficult to image due to the large variations in the topography introduced by the large MNPs biomineralised onto the micro-patterned Mms6 on this surface. The large lift height used (200 nm) not only decreases the magnitude of interactions between the surface and the magnetised tip, but the interactions are also more diffuse. Despite these limitations, the RT POFHK MFM plot shows that the magnetic particles on this surface form zones of attraction or repulsion that extend over multiple particles, when on the closely packed Mms6 patterned MNPs. This shows that the MNPs are able to maintain their magnetic moment at room temperature, so are ferrimagnetic. The MNPs on the PEG-OH background are more spread out, and do not seem to have any interactions between adjacent particles. When MFM was attempted on the nanolines of MNPs formed by POFHK_{Fe_Mms6_surface} (25 mM FeSO₄, 55 mM KOH, 400 mM KNO₃, Figures 5.6c & d), magnetic interactions between the particles could not be seen. This may be due to increased distances between the less closely packed biomineralised MNPs on the Mms6 patterned surface when formed using the POFHK_{Fe_Mms6_surface} reaction conditions. Therefore, the MNPs must be quite closely packed on the surface for multi-particle zones of interaction to form.

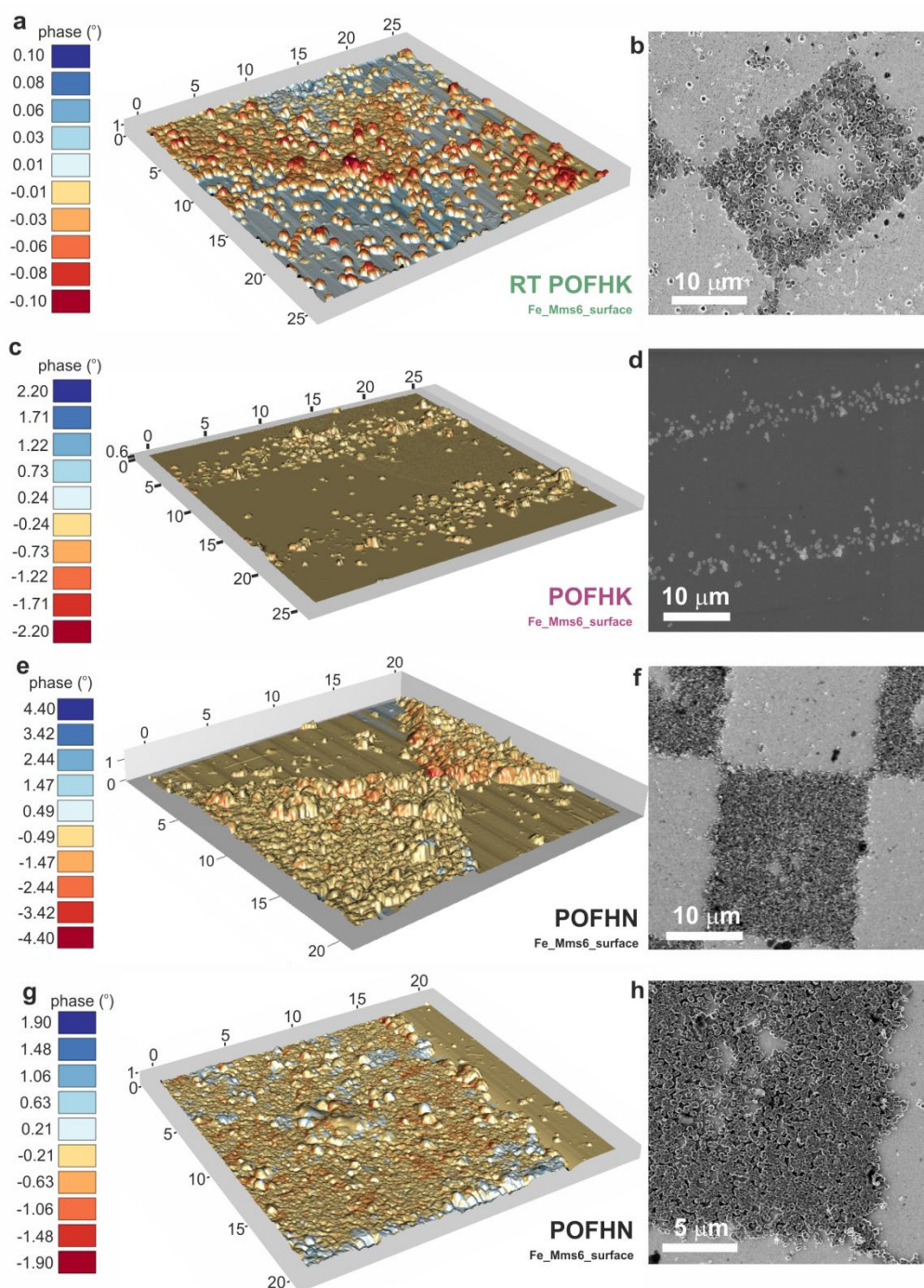


Figure 6.8. Composite of tapping mode AFM topography and non-contact 200 nm lift height MFM plots,^{*} and representative SEM images of biotemplated magnetite patterns, from Galloway *et al.* (2012a & b).^{1,2} (a)¹ 25 μm^2 MFM plot of RT POFHK, and (b)¹ SEM image of representative area. Despite difficulty with imaging the large particles, the MFM plot shows multi-particle zones of attraction (red) or repulsion (blue). (c) MFM composite of nano patterned POFHK surface, particles do not appear to magnetically interact and (d) SEM of representative area. (e)² 20 μm^2 MFM composite plot and (f)² SEM of the POFHN sample shows smaller MNPs than formed on the RT POFHK surface. Multi-particle zones of attraction and repulsion can again be seen in the MFM plot. (g)¹ 20 μm^2 MFM plot and (h)¹ SEM of representative area of different part of POFHN sample surface, again shows multi-particle zones of magnetic attraction and repulsion. AFM and MFM data were processed using WSxM.¹⁴

^{*} 3D composite plots rendered in 'R' by J. Bramble, University of Leeds.

The $\text{POFHN}_{\text{Fe_Mms6_surface}}$ MNPs are much smaller than the MNPs on the RT $\text{POFHK}_{\text{Fe_Mms6_surface}}$ surface, and are very closely packed together on the micro-patterned Mms6. The multi-particle zones of attraction or repulsion are also formed on these areas, but the $\text{POFHN}_{\text{Fe_Mms6_surface}}$ multi-particle zones seem to have a very low aspect ratio. The long axis of these features align with the long axis of the 2D micro-patterned rectangles onto which the MNPs were biotemplated by the immobilised Mms6. Figure 6.9 shows a close up of two different areas of MNPs on the $\text{POFHN}_{\text{Fe_Mms6_surface}}$ biotemplated MNPs taken after 12 months storage in air, and an SEM image of a similar area. Importantly, repeated MFM measurements after 12 months storage in air showed that the MNPs are still ferrimagnetic. Again, the zones of attraction and repulsion can be seen to extend over multiple nanoparticles in one direction, but are only about one nanoparticle wide. These magnetic features alternate between attraction and repulsion, and the long axis of the magnetic zones often align with the long axis of the 2D micro-patterned rectangles.

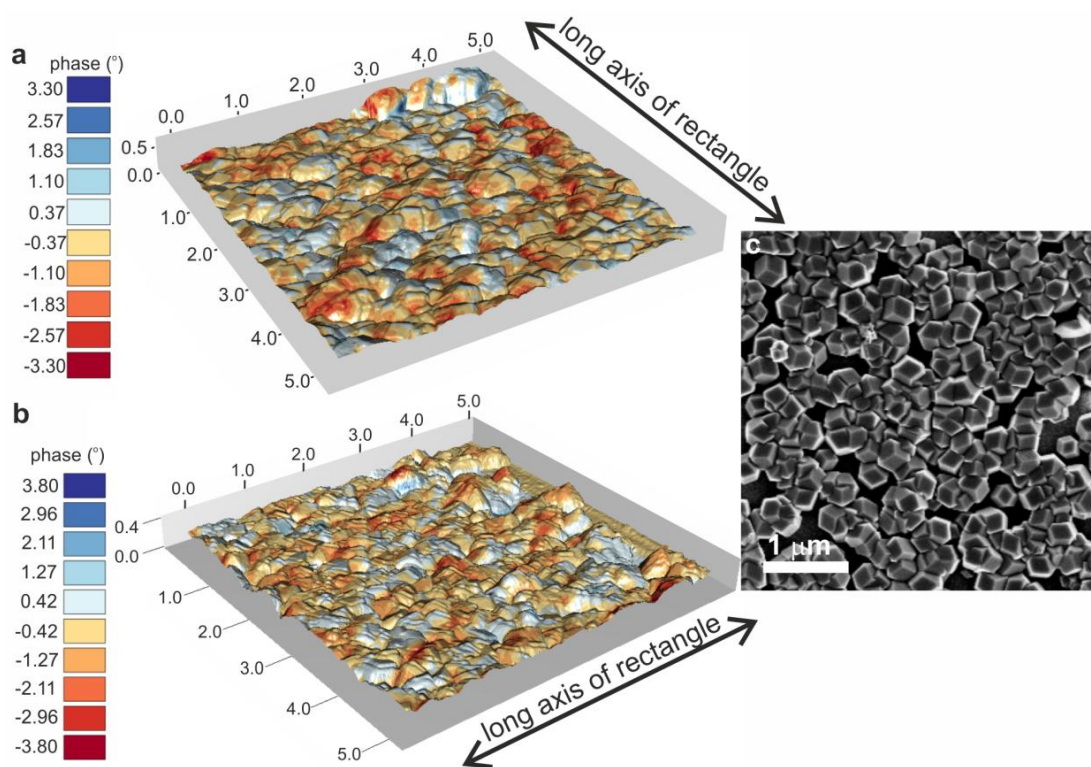


Figure 6.9. Composite of tapping mode AFM topography and non-contact 50 nm lift height MFM plots,* and representative SEM image of $\text{POFHN}_{\text{Fe_Mms6_surface}}$, from Galloway *et al.* (2012a & b).^{1,2} (a)¹ $5 \mu\text{m}^2$ MFM plot from middle of area of closely packed biotemplated MNPs shows more detail of magnetic interactions between particles. (b)² $5 \mu\text{m}^2$ MFM plot of from a different area of closely packed MNPs also shows low aspect ratio multi-particle zones of attraction and repulsion. (c)¹ Representative SEM image of similar areas imaged in a & b. AFM and MFM data were processed using WSxM, as per Horcas *et al.* (2007).¹⁴

* 3D composite plots rendered in 'R' by J. Bramble, University of Leeds.

Fresnel-Lorentz microscopy and electron holography were used by Yamamoto *et al* (2011)¹⁵ to image magnetic domains in single layers of closely packed, small superparamagnetic magnetite MNPs. These authors found that the closely packed MNPs were able to maintain multi-particle magnetic domains up to 575°C. They also observed that the shape of the magnetic domains formed by the multi-particle interactions were strongly linked to the shape of the assembly of nanoparticles, with the long axis of a domain running parallel with the long axis of the MNP assembly.¹⁵ As these biotemplated nanomagnets are closely packed onto a 2D surface, they may also be exchange coupled, just as the particles in continuous granular recording media are to record a bit of information during perpendicular recording.¹¹ It is likely that the shape of the multi-particle zone of attraction or repulsion formed by the exchange coupled MNPs is dictated by the overall shape of the MNP assembly, which is micro-patterned to form rectangles. This creates the low aspect ratio exchange coupled zones, with the long axis running parallel to the long axis of the rectangular assembly.

MFM measurements on the samples after 12 months storage in air showed that there are still zones of magnetic attraction and repulsion on the biotemplated MNP arrays. This demonstrates that the biotemplated magnetite areas are able to resist oxidation and degradation well, to maintain their ferrimagnetic characteristics. Single layers of SP magnetite MNPs can form multi-particle domains which are stable, even upon heating up to 575°C.¹⁵ The biomineralised magnetite SD/MD MNPs created here may also be able to retain their multi-particle magnetic domains up to similar (or higher) temperatures, and so remain stable upon heating. However, it is unlikely that these multi-particle magnetic domains remain in the same places for this length of time, due to the low coercivity of magnetite. The magnetic orientation of the MNPs must be extremely stable for use in data storage. If the MNPs are not able to maintain their magnetic orientation over time, any data written to the memory will be lost when the MNPs re-orientate themselves. Therefore, materials with much greater magnetic hardness are required to ensure the long-term stability of digital memory written to a magnetic surface.

Cobalt doping of magnetite increases the coercivity of the MNPs formed, but reduces the saturation magnetisation.^{16,17} Controlled doping of 6% Co into magnetite biotemplated by Mms6 from the bulk solution formed MNPs with a large increase in coercivity for relatively little reduction in saturation magnetisation (Chapter 4).¹⁸ The increase in coercivity should allow the MNPs to be more stable against switching their magnetic orientation over time than undoped magnetite. The cobalt doped magnetite may also be able to form multi-particle magnetic domains that should also be stable at room temperature, or when heated to higher

temperatures. Both high coercivity and stability upon heating are required for materials used in magnetic data storage, so the 6% Co doped magnetite Mms6 biotemplated micro-patterned surfaces formed in Chapter 5^{1,2} are characterised below.

6.2 6% Cobalt Doped Magnetite Templated by Immobilised Mms6

In this section, cobalt was added to the reactant solutions when mineralising particles onto the patterned Mms6 substrates. This system should have been optimised towards forming 6% cobalt doped magnetite ($\text{Co}_{0.18}\text{Fe}_{2.82}\text{O}_4$), rather than any other iron oxide mineral phase using the POFHK method. The samples characterised in this section were formed using the optimised reaction conditions (23.5 mM FeSO_4 , 1.5 mM CoSO_4 , 55 mM KOH, 400 mM KNO_3 , see Figure 5.13). As such, POFHK_{6%Co} refers to samples prepared using these reaction conditions, either on the immobilised Mms6 (Mms6_surface) or with no protein in the bulk solution (no protein_bulk). The 6% Co doped magnetite arrays are compared to the magnetite arrays biotemplated by POFHN, which are characterised above. In the section below, the magnetite arrays are referred to as POFHN_{Fe}, and are formed using the reactants in the ratio 50 mM FeSO_4 , 40 μL 50-60% N_2H_4 , 200 μL 26% NH_4OH and 100 mM KNO_3 . Again, the MNPs formed onto the immobilised Mms6 are 'Mms6_surface' and those formed as a control in the absence of protein 'no protein_bulk.' The morphology of the POFHK_{6%Co_Mms6_surface} particles indicates that they are cobalt doped magnetite, but further characterisation is required to confirm this. The micropatterned biomineralised substrates have been analysed to determine if uniform nanomagnets of cobalt doped magnetite were formed by the Mms6 protein immobilised on the micro-patterned surfaces.

6.2.1 Grainsize Analysis from SEM and TEM

The grainsize and shape of the surface biotemplated MNPs, for both POFHN_{Fe} and POFHK_{6%Co} were measured using Image J.³ The same was performed for controls formed from a bulk solution where no protein was present during mineralisation, see Figure 6.10. These data were fitted with single Gaussian distributions in Origin based on the χ^2 of the fit, which are summarised in Table 6.4. The only sample that contained any low aspect ratio MNPs was the POFHN_{Fe_no protein_bulk} sample (Figure 6.10d) which is more fully characterised in Section 6.1. The POFHK_{6%Co_Mms6_surface} MNPs (245±41 nm) are larger than the POFHK_{6%Co_no protein_bulk} MNPs, which have many small particles (31±28 nm). As can be seen in Figure 6.10d, the POFHK_{6%Co_no protein_bulk} MNPs consist of a few larger MNPs about 100-400 nm in diameter, with many smaller particles also visible. This

is similar to the distribution seen for the 6% Co doped POFHK MNPs characterised in Chapter 4, but the control particles are much smaller here. This was expected, as the MNPs formed in Chapter 4 did not have an excess of hydroxide, but were formed using 47 mM FeSO₄, 3 mM CoSO₄, 100 mM KOH, 400 mM KNO₃. When an excess of base and iron sulfate is used during POFHK, the MNPs formed tend to be smaller than if there is an excess of metal salt in the reaction solution.¹⁹ As the control POFHK_{6%Co_no protein_bulk} particles are formed under the same reaction conditions as those used to form the POFHK_{6%Co_Mms6_surface} arrays, the slight excess of base in the reaction seems to favour the formation of smaller MNPs.

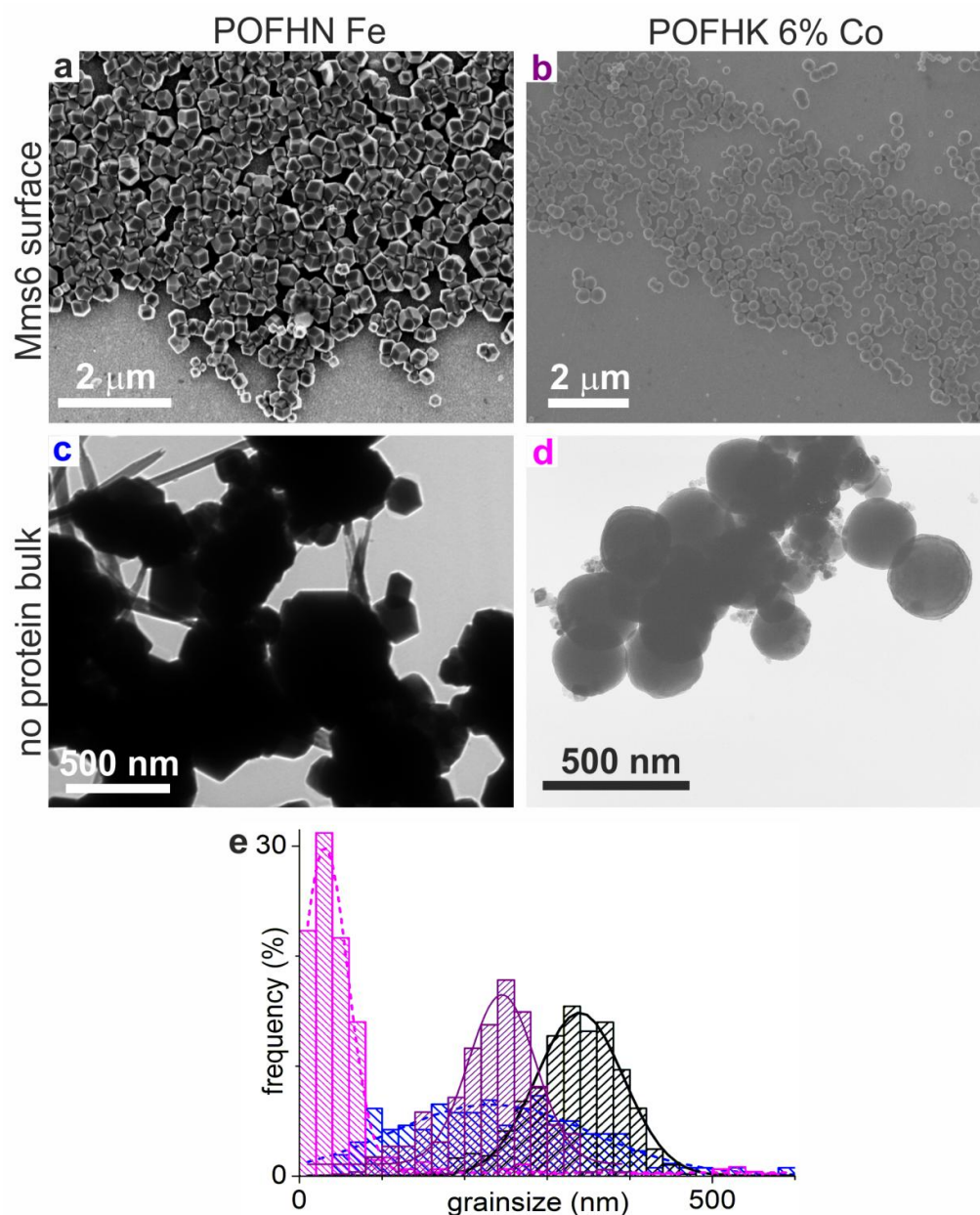


Figure 6.10. (a-b) SEM and (c-d) TEM images of POFHN_{Fe} (reactant conditions as in Figure 5.11) and POFHK_{6%Co} MNPs (reactant conditions as in Figure 5.13). Images show (a) POFHN_{Fe_Mms6_surface} (black), (b) POFHK_{6%Co_Mms6_surface} (purple), (c) POFHN_{Fe_no protein_bulk} (blue) and (d) POFHK_{6%Co_no protein_bulk} (pink) MNPs. (e) Grainsize measurements (50 nm bins), recorded using Image J³ and fitted with a single Gaussian distribution using Origin.

Table 6.4. Summary of grainsize data presented in Figure 6.10, comparing undoped and 6% Co doped MNPs both templated by Mms6 on a surface, and formed with no protein from the bulk solution.

colour	sample	average (nm)	peak centre (nm)	σ (nm)	FWHM (nm)
black	POFHN _{Fe_Mms6_surface}	333	340	54	126
purple	POFHK _{6%Co_Mms6_surface}	233	245	41	95
blue	POFHN _{Fe_no protein_bulk}	265	230	121	285
pink	POFHK _{6%Co_no protein_bulk}	60	31	28	66

When the grainsize of POFHK_{6%Co_Mms6_surface} MNPs are compared to that of the POFHN_{Fe_Mms6_surface}, the cobalt doped particles are smaller and have a narrower size distribution (245 ± 41 nm) than the magnetite MNPs (340 ± 54 nm). The difference in size and size distribution may be due to the presence of cobalt, but could also be due to the difference in the mineralisation conditions used to form the POFHN_{Fe} and POFHK_{6%Co} biotemplated arrays. Whether due to the presence of cobalt, or another change in the reaction conditions between the POFHN_{Fe_Mms6_surface} and POFHK_{6%Co_Mms6_surface} MNP formation conditions, the smaller POFHK_{6%Co_Mms6_surface} particles also have a narrower size distribution. Again, the size and size distribution of the biotemplated cobalt doped MNPs produced by the immobilised Mms6 are similar to the magnetite particles produced by the high temperature/harsh chemical thermal decomposition method.⁴ However, POFHK_{6%Co_Mms6_surface} particles have the advantage of not requiring harsh synthesis conditions to achieve this uniformity.

The size of the MNPs on the POFHK_{6%Co_Mms6_surface} array should allow the particles to behave as single domain magnets at room temperature. The magnetic properties of the 6% Co doped surface templated MNPs should be consistent, as the particles have a uniform size distribution. They should also have a significant increase in coercivity with little loss in saturation magnetisation when compared to the undoped magnetite controls. The increased coercivity may make the 6% Co doped biotemplated nanomagnets more suited to data storage applications than the POFHN_{Fe_Mms6_surface} undoped particles. The next stage of the characterisation is to determine if the POFHK_{6%Co_Mms6_surface} particles consist of cobalt doped magnetite, then to determine the magnetic properties of these biotemplated arrays.

6.2.2 EDX Elemental Mapping of Biotemplated 6% Cobalt Doped Magnetite Arrays

Figure 6.11 shows EDX point spectra and elemental maps for the POFHK_{6%Co_Mms6_surface} MNPs. As the binding energy of the Fe K α and Co K α electrons are very similar, the X-rays detected from these elements produce emission peaks that are also very close together. This, coupled with the low amount of cobalt present in the MNPs when compared to iron, means that higher energy primary electrons are required to ensure the signal from the cobalt is detectable. An accelerating voltage of 20 keV was used to ensure the signal from the X-rays was maximised at the detector, so a larger total count was achieved. As can be seen in the spectrum taken on the PEG-OH background, there is an increase in the detection of elements from the glass substrate when an accelerated voltage of 20 keV is used, including Na, Mg and Ca, as well as detection of the chromium adhesion layer. As can be seen in the spectrum taken on the PEG-OH background, there is an increase in the detection of elements from the glass substrate when an accelerated voltage of 20 keV is used, including Na, Mg and Ca, as well as detection of the chromium adhesion layer.

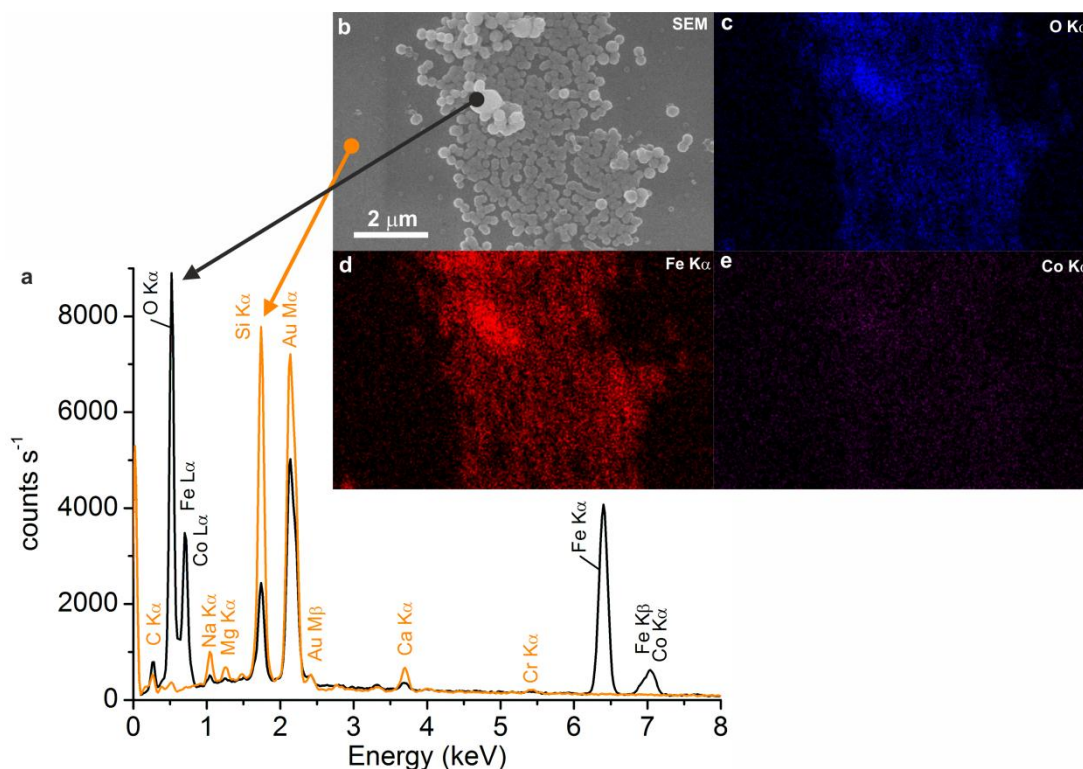


Figure 6.11. EDX spectra and elemental maps of micro-patterned biomineralised 6% Co doped magnetite on a surface. Sample is imaged and spectra recorded at 20 keV, and is POFHN_{6%Co_Mms6_surface} (23.5 mM FeSO₄, 1.5 mM CoSO₄, 55 mM KOH, 400 mM KNO₃, Figure 5.13). (a) EDX point spectra from biomineralised area (black) and PEG-OH background (orange). The cobalt peak is weak, but Co K α appears as a shoulder on the Fe K β peak. (b) 2° electron image of sample shows a micro-patterned line of mineralisation, and EDX maps of (c) O K α , (d) Fe K α and (e) Co K α . Oxygen and iron maps clearly show that the biomineralised areas contain iron and oxygen, with a weak signal also visible in the cobalt map of the biomineralised nanomagnets.

The higher accelerating voltage also significantly increased the signal from the O, Fe and Co in the MNPs biotemplated onto the immobilised Mms6 patterned surface. The elemental maps from the O K α and Fe K α show the signal from these elements are spatially localised to the biotemplated MNP pattern. Despite the signal from the cobalt being distinguishable in the EDX spectrum from the MNPs, the Co K α map shows that the detection of these X-rays is only slightly greater from the biotemplated MNPs than from the PEG-OH background. This is most likely due to the low concentration of cobalt doped into the system to form the POFHK_{6%Co_Mms6_surface} MNPs. Therefore, these EDX data show that iron, cobalt and oxygen are spatially associated with the biomineralised MNPs. Again, further characterisation is required to confirm the biomineral formed on the Mms6 patterns is cobalt doped magnetite, rather than any other iron/cobalt oxide.

6.2.3 Crystallinity of Biotemplated 6% Cobalt Doped Magnetite Arrays from XRD

The crystallinity of the 6% cobalt doped magnetite MNPs were studied using powder XRD* and compared to the POFHN_{Fe} MNP control and Mms6 surface templated samples, see Figure 6.12. The peak positions were then assigned based on the magnetite, maghemite, cobalt ferrite, gold and graphitic carbon spectra from the EVA software. The X-ray diffraction peak positions of magnetite, maghemite and cobalt ferrite are all very close to each other due to the similarity in crystal structures of these minerals. Both of the POFHK_{6%Co} sample spectra are a closer match to magnetite and/or cobalt ferrite than to maghemite. There were no acicular MNPs observed in the TEM and SEM images and grainsize analysis for the POFHK_{6%Co} MNPs (Figure 6.12). The shift towards maghemite peak positions for some peaks in the POFHN_{Fe_no protein_bulk} sample are likely to be due to the presence of acicular maghemite in the sample (see Section 6.1.3.2). The peak at $2\theta=65.719^\circ$ is not usually found in magnetite, but is found as a relatively low intensity peak from the (531) plane in cobalt ferrite. The (531) peak is not apparent in the POFHK_{6%Co_Mms6_surface} spectrum, but as this sample contains less mineralised MNPs than the POFHK_{6%Co_no protein_bulk} control, it may not have been detectable. Therefore, these XRD data shows that the crystallographic structure of biomineralised 6% Co doped MNPs is mainly that of magnetite, with some evidence of cobalt ferrite structuring due to the 6% cobalt doping.

* XRD collected and analysed in collaboration with L. Neve, University of Leeds.

Table 6.5. Table of peak positions for magnetite and cobalt ferrite (based on spectra from EVA software, see Table 2.3) and peak positions from samples shown in Figure 6.12, measured in Å.

peak	magnetite	cobalt ferrite	POFHN _{Fe_} no protein_bulk	POFHK _{6%Co_no} protein_bulk	POFHN _{Fe_} Mms6_surface	POFHK _{6%Co} Msm6_surface
(111)	4.850	4.847	4.825	4.840	4.889	
(220)	2.966	2.968	2.958	2.965	2.971	2.957
(311)	2.530	2.531	2.572	2.529	2.534	2.532
(222)	2.419	2.424		2.423		
(400)	2.096	2.099	2.095	2.098	2.100	2.096
(422)	1.712	1.713	1.713	1.714		
(511)	1.614	1.615	1.614	1.614	1.618	1.614
(440)	1.483	1.483	1.482	1.482	1.482	1.482
(531)		1.419		1.419		

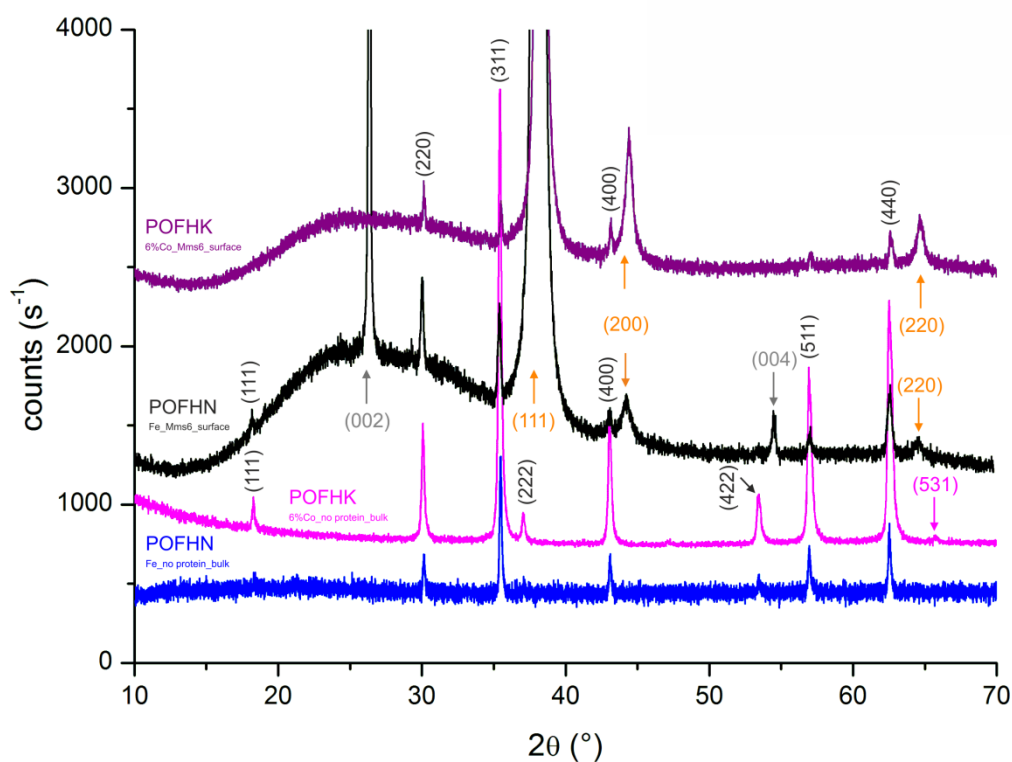


Figure 6.12. XRD of biomaterialised micro-patterned arrays of magnetite, cobalt doped magnetite and controls. POFHN_{Fe_no protein_bulk} (blue), POFHK_{6%Co_no protein_bulk} (pink), POFHN_{Fe_Mms6_surface} (black) and POFHK_{6%Co_Mms6_surface} (purple). Traces are offset for clarity. Magnetite peaks are labelled in black, cobalt ferrite peaks are labelled in pink, gold peaks are labelled in orange and carbon peaks are labelled in grey. Peak positions for magnetite and cobalt ferrite are summarised in table 6.5.

There is an absence of peaks at $2\theta=26.372^\circ$ and 54.442° in the $\text{POFHK}_{6\%Co_Mms6_surface}$ spectrum that are present in the $\text{POFHN}_{Fe_Mms6_surface}$ sample. The metal deposition and oxidant level of the mineralisation solutions should have been almost identical for both of these samples. As the peaks only appear the spectrum of one of these biomineralised arrays, they are highly unlikely to be due to the presence of chromium oxide, but more likely from graphitic carbon contaminating the surface of the samples. As conductive tape containing carbon was used to earth and attach samples to SEM stubs for imaging prior to subsequent characterisation, an amount of graphitic carbon must have remained attached to the $\text{POFHN}_{Fe_Mms6_surface}$ sample surface. The $\text{POFHK}_{6\%Co_Mms6_surface}$ sample was larger than the $\text{POFHN}_{Fe_Mms6_surface}$ sample. This means it may have been easier to focus the X-ray beam onto the centre of the cobalt doped magnetite particle patterned surface, thus avoiding picking up carbon contamination at the edge of the sample.

6.2.4 VSM of Biotemplated 6% Cobalt Doped Magnetite Arrays

Despite a number of attempts, it was not possible to collect reliable and reproducible ZFC and FC data for the cobalt doped MNP array or control. Therefore, the magnetic hysteresis was recorded at a fixed temperatures to allow the coercivity of the biomineralised arrays and their controls to be compared at low temperatures (10 K) and room temperature (300 K), see Figure 6.13. Again, as the mass of the particles on the surface were not known, the magnetisation has been normalised to allow comparison of the coercivity between samples.

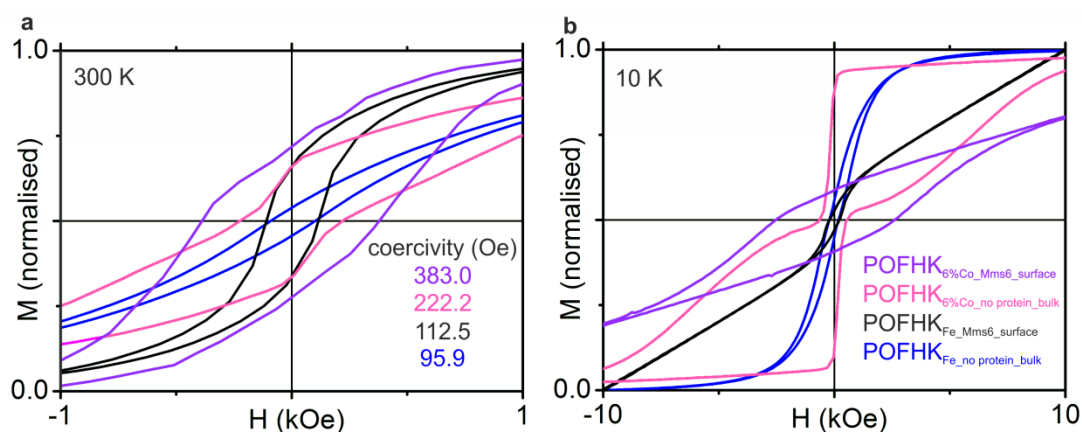


Figure 6.13. Magnetic hysteresis loops for 6% cobalt doped and undoped magnetite samples. (a) Shows the hysteresis at room temperature (300 K) and (b) at low temperature (10 K). Key for colours as previously: $\text{POFHN}_{Fe_no_protein_bulk}$ (blue); $\text{POFHK}_{6\%Co_no_protein_bulk}$ (pink); $\text{POFHN}_{Fe_Mms6_surface}$ (black); and $\text{POFHK}_{6\%Co_Mms6_surface}$ (purple).

The coercivity of the MNPs on the 6% cobalt doped array (383.0 Oe) is ≈ 1.7 times greater than the coercivity of the POFHK_{6%Co_no protein_bulk} MNPs (222.2 Oe). However, the hysteresis loops from the POFHK_{6%Co_no protein_bulk} MNPs are complex, as there are at least two different magnetic behaviours. This means it is not possible to directly compare the coercivity of the POFHK_{6%Co_no protein_bulk} MNPs with the cobalt doped biomineralised array. In Chapter 4 it was found that there is a strong correlation in 6% Co doped magnetite RTCP MNPs between the proportion of the magnetic hysteresis that shows magnetically soft behaviour, and the proportion of MNPs that are below ≈ 18 nm in diameter. This relationship does not hold for the POFHK_{6%Co_no protein_bulk} MNPs, as $\approx 50\%$ of the magnetic hysteresis shows the soft behaviour, but only 17.4% of the MNPs recorded in the grainsize analysis are below 18 nm in diameter (see Figure 6.10).

The TEM image in Figure 6.10d shows the MNPs from the POFHK_{6%Co_no protein_bulk} sample, in which there are a number of very large MNPs, surrounded by many smaller MNPs. It is possible that there are many smaller MNPs decorating the larger particles, only some of which can be seen in the TEM images. Due to the greater thickness of the larger MNPs, they are likely to fully attenuate the electron beam, thus only smaller MNPs at the circumference of these large particles are visible and able to be included in the grainsize analysis. This hypothesis could be checked if SEM was used to image the POFHK_{6%Co_no protein_bulk} MNPs, as an image of the surface of the larger particles could be recorded. However, the lower resolution of SEM images may not allow the very small particles to be imaged clearly, so it may still be difficult to include them in any grainsize analysis. Another option could be to use SAED to form a diffraction pattern of one of the larger particles. If a polycrystalline pattern is revealed (e.g. Figure 6.4b) there were multiple crystals diffracting the electron beam, if only spots are seen, the large particle is a single crystal (e.g. Figure 6.4d). Again, this would not allow the size and number of any possible MNPs on the larger particle surface to be determined, so could not be used to produce a more representative grainsize distribution for the POFHK_{6%Co_no protein_bulk} sample.

The room temperature coercivity of POFHK_{6%Co_Mms6_surface} sample (383.0 Oe) is ≈ 3.5 times greater than that of the POFHN_{Fe_Mms6_surface} sample (112.5 Oe). In the smaller RTCP MNPs characterised in Chapter 4, 6% cobalt doping of the Mms6 templated MNPs increased the coercivity at room temperature from 12.8 Oe in Fe_{Mms6} MNPs to 78.3 Oe in Co_{Mms6} MNPs, a greater than six-fold increase. This larger increase in coercivity between the undoped and 6% Co doped MNPs may have also been due to MNP size effects. Many of the undoped particles are likely to have been smaller than the SD limit for magnetite (≈ 25 nm), whereas the majority of

the Co_{Mms6} MNPs are likely to be larger, and therefore able to maintain a single domain at room temperature. Both of the biomineralised surfaces are patterned with equidimensional MNPs with a fairly uniform grainsize distribution well above the SD/SP size limit, so it is likely that both samples consist entirely of SD or MD MNPs. The increase in coercivity coincided with relatively little loss in saturation magnetisation for the Mms6 templated MNPs (90.6 emu g^{-1} for Fe_{Mms6} to 56.1 emu g^{-1} for Co_{Mms6}). As the mass of MNPs on the biomineralised arrays is not known, it is not possible to calculate the saturation magnetisation of the biotemplated arrays so it can be compared to other samples. Nonetheless, there is a significant increase in the coercivity of the $\text{POFHK}_{6\% \text{Co_Mms6_surface}}$ due to the introduction of 6% cobalt doping, which has a single hysteresis. Therefore, the uniform magnetic response of the biotemplated arrays with 6% cobalt doping may be more suited to retaining magnetic information for applications such as data storage. However, the coercivity of 383.0 Oe is still less than that of thin-films of materials currently used in data storage ($\approx 4 \text{ kOe}$).^{11,12}

6.2.5 MFM of 6% Cobalt Doped Magnetite Arrays

Tapping mode AFM was combined with non-contact mode MFM to image the topography and magnetic interactions of MNPs on the biomineralised 6% cobalt doped micro-patterned arrays. Figure 6.14 shows a representative SEM image of an area on the $\text{POFHK}_{6\% \text{Co_Mms6_surface}}$ sample, which shows the lines of Mms6 that have been biomineralised with cobalt doped magnetite nanoparticles. The MFM measurements show that zones of magnetic attraction or repulsion run along the length of the micro-patterned nanomagnet lines. The same area was imaged in two different orientations to ensure that the magnetic interactions in the image were not an artefact of the scan direction, but due to the magnetic interactions of the nanomagnets on the surface with the magnetised tip. As can be seen in Figures 6.14b & c, the zones of magnetic repulsion and attraction remain in the same location on the patterned surface when the scan direction is rotated through 90° . This shows that the biomineralised cobalt doped MNPs are able to maintain their magnetic orientation at room temperature, so are ferrimagnetic.

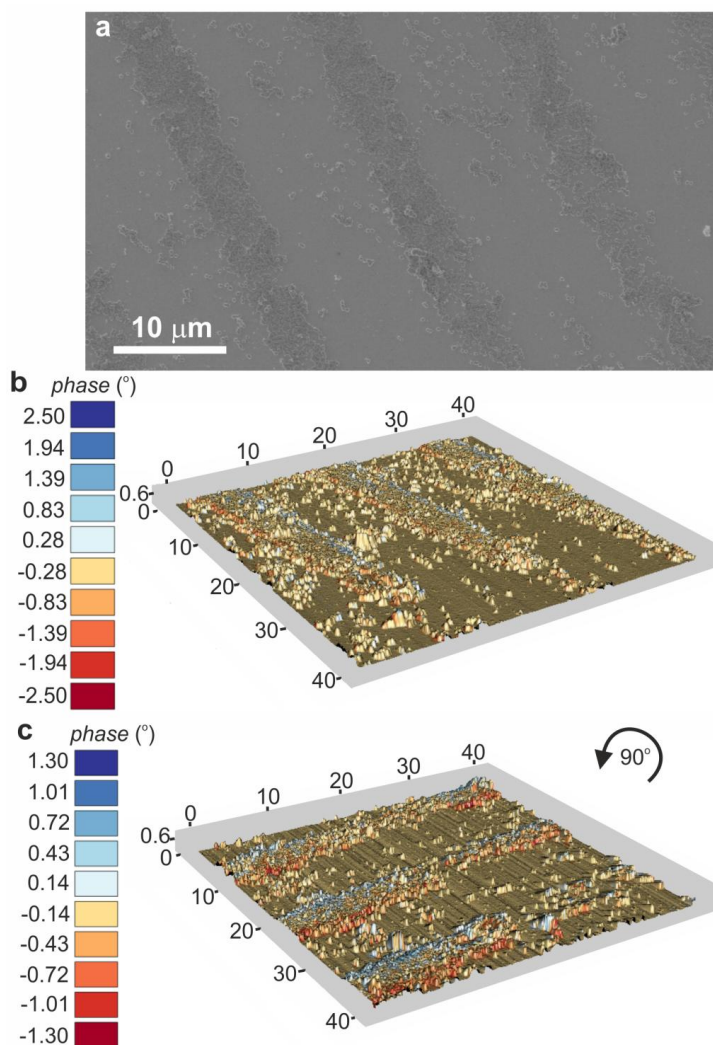


Figure 6.14. Composites of tapping mode AFM topography and non-contact 200 nm lift height MFM plots,^{*} and a representative SEM image of 6% Co doped magnetite patterns. (a) SEM image of 6% Co doped biotemplated magnetite micro-patterned lines (23.5 mM FeSO₄, 1.5 mM CoSO₄, 55 mM KOH, 400 mM KNO₃, Figure 5.13). (b) 40 μm² MFM composite of POFHK_{6%Co_Mms6_surface} and (c) the same area of the sample, but imaged when scan direction is rotated by 90° anti-clockwise. Both MFM images show areas of attraction (red) and repulsion (blue) following the long axis of the biomineralised lines of nanomagnets. AFM and MFM data were processed using WSxM).¹⁴

The magnetic zones of attraction/repulsion on the micro-patterned cobalt doped arrays extend over much longer distances than were seen in the micro-patterned magnetite samples (e.g. see Figure 6.9). This may be due to the 6% Co doping increasing the coercivity of the biotemplated MNPs. As the direction of magnetisation of the doped magnets is more difficult to perturb at room temperature, these 6% Co doped nanomagnets may be able to form more stable interactions on the 2D surface. Therefore, the closely packed cobalt doped nanomagnets could allow the zones of magnetic interactions to align over long distances, creating the interactions imaged here. However, the line pattern used to

^{*} 3D composite plots rendered in 'R' by J. Bramble, University of Leeds.

form these $\text{POFHK}_{6\% \text{Co_Mms6_surface}}$ is a different morphology to the rectangular pattern used to form the $\text{POFHN}_{\text{Fe_Mms6_surface}}$ patterns. The morphology of a multi-particle magnetic domain is dependent on the shape of the assembly for SP magnetite particles in a single layer.¹⁵ It is highly likely that the same is true for the biotemplated magnetite SD/MD particles characterised above, based on the MFM studies in Section 6.1.5. Therefore, the cobalt doped magnetite may also behave in the same manner, with the shape of the magnetic zones of interaction being dependent on the shape of the larger scale pattern. This means that the long lines of the micro-patterned cobalt doped MNPs may further elongate the long axis of the zones of magnetic interaction on the biotemplated particles on the surface.

When the magnetism of the nanomagnet arrays are examined in closer detail (Figure 6.15), the zones of magnetic attraction/repulsion do not appear to extend over the very long distances seen in the larger scale images (Figure 6.14). The length and width of the magnetic zones appear different to those imaged in the magnetite 2D array (see Figure 6.9, $\text{POFHN}_{\text{Fe_Mms6_surface}}$). The interaction zones from the $\text{POFHK}_{6\% \text{Co_Mms6_surface}}$ are ≈ 2 particles wide, rather than the ≈ 1 particle wide seen on the $\text{POFHN}_{\text{Fe_Mms6_surface}}$. The long axis of the magnetic interactions seems to extend over many more nanoparticles than was seen in the undoped magnetite arrays. This could be due to the smaller size of the MNPs on the $\text{POFHK}_{6\% \text{Co_Mms6_surface}}$ and the increased coercivity of the doped nanomagnets. However, the longer zones of interaction could also be due to the low aspect ratio of the patterned lines on the $\text{POFHK}_{6\% \text{Co_Mms6_surface}}$ when compared to the rectangles used to form the $\text{POFHN}_{\text{Fe_Mms6_surface}}$ pattern. The effect of doping versus pattern shape could be investigated in the future by carefully selecting the type and scale of patterns used to form the Mms6 patterned surface, which is discussed in more detail in Chapter 7.

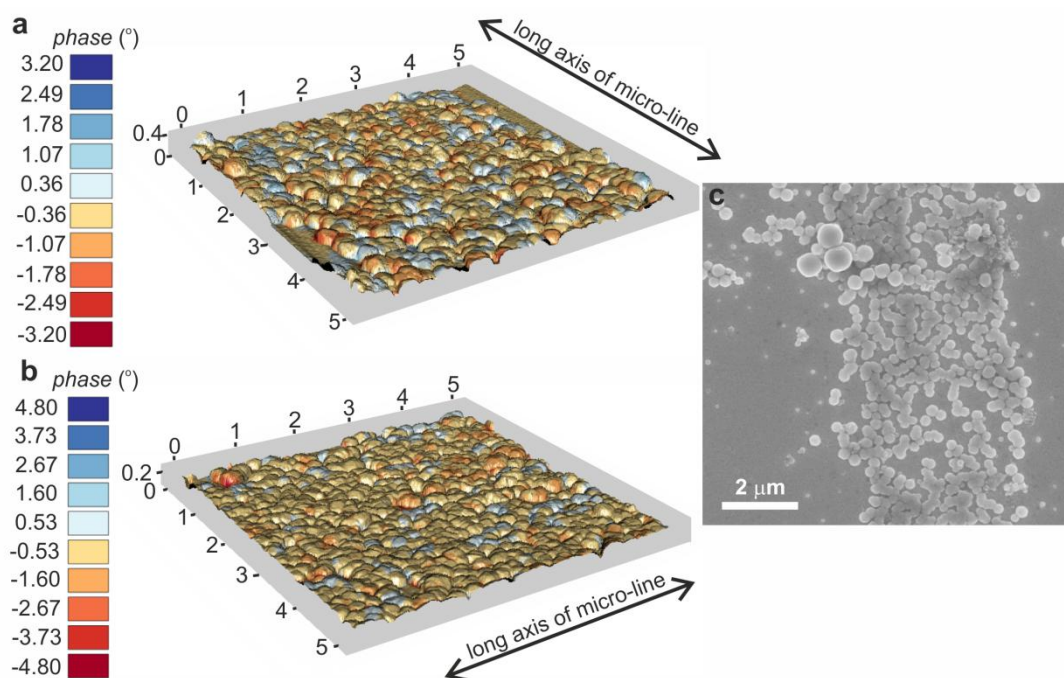


Figure 6.15. Composite of tapping mode AFM topography and non-contact mode 100 nm lift height MFM plots,* and representative SEM image of micro-patterned biotemplated 6% Co doped magnetite. (a) $5 \mu\text{m}^2$ MFM plot of $\text{POFHK}_{6\% \text{Co_Mms6_surface}}$ from middle of micro-patterned line of biomineralised nanomagnets. (b) $5 \mu\text{m}^2$ MFM plot of $\text{POFHK}_{6\% \text{Co_Mms6_surface}}$ on a different area of the sample. (c) Representative SEM image of a micro-patterned line of nanomagnets from the $\text{POFHK}_{6\% \text{Co_Mms6_surface}}$. Both MFM images show multi-particle zones of attraction and repulsion, with the long axis of the magnetic zone running parallel to the long axis of the micropatterned line. AFM and MFM data were processed using WSxM, as per Horcas *et al.* (2007).¹⁴

6.3 Cobalt Ferrite Templated by Immobilised Mms6

It is possible to form MNPs onto the immobilised Mms6 patterns using a reactant solution containing 33% cobalt sulfate and 67% ferrous sulfate (17 mM FeSO_4 , 8 mM CoSO_4 , 60 mM KOH, 400 mM KNO_3 , Figure 5.14c-e). The MNPs formed from this reactant solution should be cobalt ferrite (CoFe_2O_4), and their morphology indicates that they are cobalt ferrite. Due to time constraints, it was only possible to partially characterise the biomineralised cobalt ferrite arrays ($\text{POFHK}_{33\% \text{Co_Mms6_surface}}$). As such, elemental mapping and MFM imaging are included in this section for $\text{POFHK}_{33\% \text{Co_Mms6_surface}}$ samples. Further work to characterise these samples more thoroughly, such as grainsize analysis, VSM and XRD, with reference to appropriate controls, is ongoing.

* 3D composite plots rendered in 'R' by J. Bramble, University of Leeds.

6.3.1 EDX Elemental Mapping of Biotemplated Cobalt Ferrite Arrays

An SEM was used to record EDX point spectra and elemental maps for nanolines of Mms6 biomineralised using POFHK_{33%Co_Mms6_surface} reaction conditions. As for the 6% Co doped maps, a higher accelerating voltage of 20 keV was used to allow the Fe and Co peaks to be more easily distinguished. In Figure 6.16 the point spectrum from the PEG-OH background shows signals from elements in the glass substrate, as well as from the chromium and gold evaporated layers, as expected. In the spectrum recorded from the biomineralised cobalt ferrite nanoline, there is a good signal from all the expected elements (i.e. O, Fe & Co). This is despite there only being a thin layer of the biomineralised cobalt ferrite, which is only the thickness of a single nanoparticle. The EDX maps show that the elements from cobalt ferrite are indeed localised to the biomineralised nanolines on the patterned surface, with relatively little signal from the smaller MNPs that formed on the PEG-OH background. There appears to be a better signal in the cobalt map than seen in the 6% Co doped samples (Figure 6.11e), which is most likely due to the higher concentration of Co in the biomineralised nanoparticles. This is supported by the slightly weaker signal on the iron map, as there is also less iron in CoFe_2O_4 than $\text{Co}_{0.18}\text{Fe}_{2.82}\text{O}_4$.

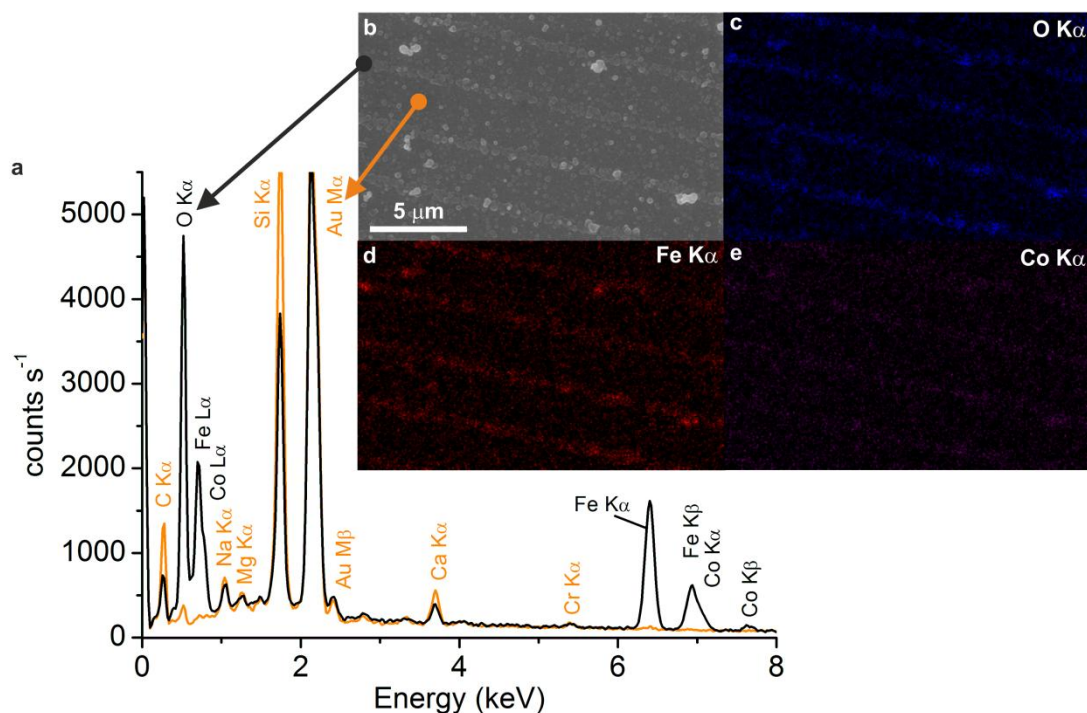


Figure 6.16. EDX spectra and elemental maps of nanolines of biomineralised cobalt ferrite, recorded at 20 keV. Sample imaged is POFHK_{33%Co_Mms6_surface} (17 mM FeSO₄, 8 mM CoSO₄, 60 mM KOH, 400 mM KNO₃, Figure 5.14e). (a) EDX spectra recorded at points shown on biomineralised cobalt ferrite (black) and PEG-OH background (orange). The peaks from oxygen, iron and cobalt are clear in the biomineralised cobalt ferrite spectrum. (b) 2° electron image of sample shows nanolines of MNPs. EDX maps show spatial location of (c) O K α , (d) Fe K α and (e) Co K α . The EDX signal from oxygen strongly localised onto the lines of cobalt ferrite, as is that of the iron and cobalt, despite the lower intensity of the peaks due to the transition metals.

6.3.2 MFM of Biotemplated Cobalt Ferrite Arrays

AFM and MFM were used to image the POFHK_{33%Co_Mms6_surface} MNPs on the nanoline pattern, see Figure 6.17. The MNPs biomineralised onto the nanoline pattern appear to mainly be magnetically attractive to the magnetised probe. The close spacing of the magnetically hard cobalt ferrite nanoparticles on the biotemplating areas may facilitate exchange coupling of these nanomagnets on the biomineralised lines. This was also found to be the case when the scan direction was rotated, or the scan area altered to image different areas of the sample. This shows that the magnetic attraction of the patterned MNPs to the magnetised MFM probe is highly unlikely to be an imaging artefact.

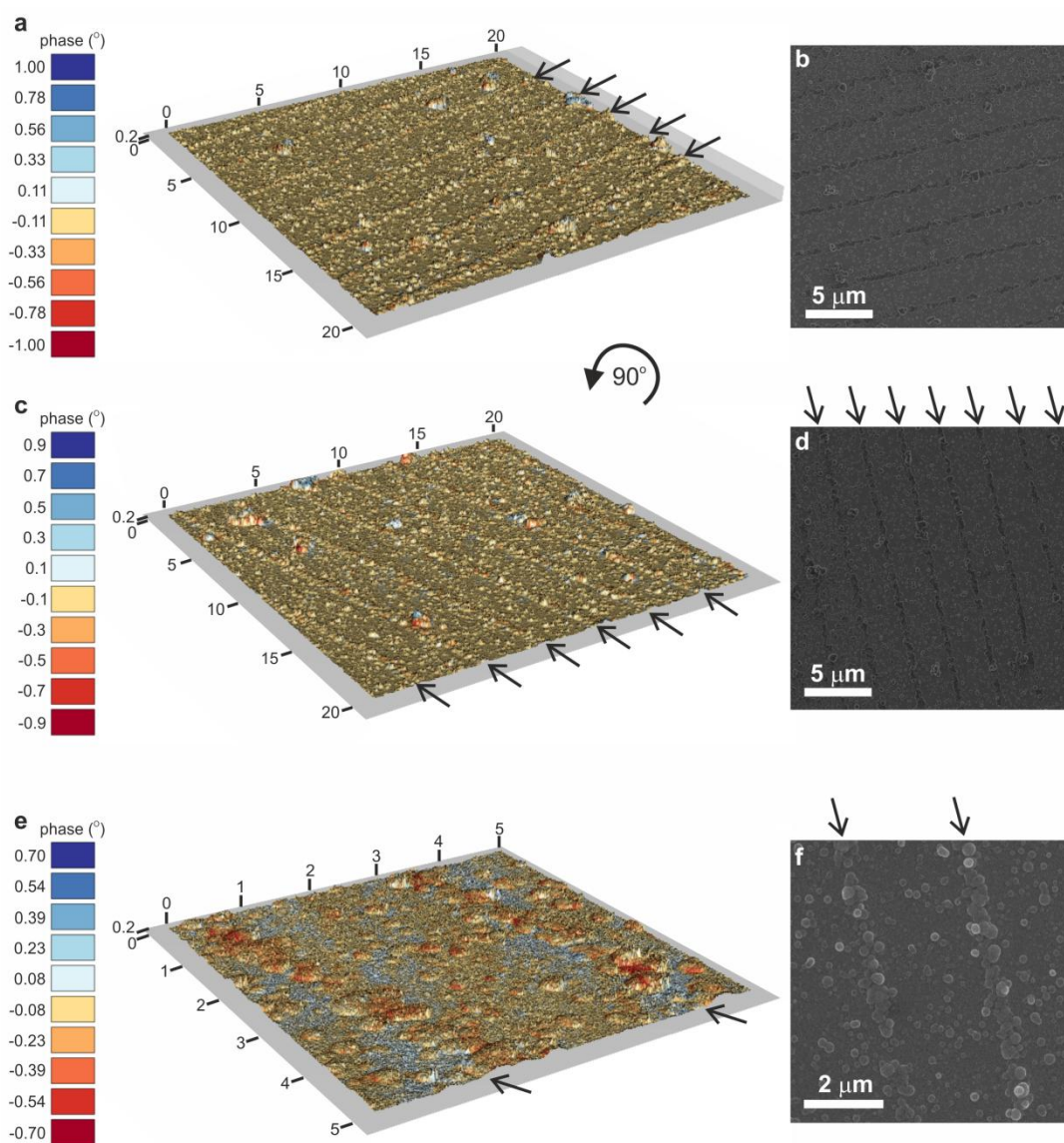


Figure 6.17. Composite MFM plots of cobalt ferrite biotemplated by Mms6 onto nanolines.* (a) 100 nm lift height, 20 μm^2 MFM of nanolines of cobalt ferrite appear to be mainly attractive to the magnetised probe, and (b) representative SEM image. (c) MFM same at image a, but scan direction is rotated by 90° anti-clockwise, which shows the same trend in magnetic phase data, and (d) SEM image. (e) 50 nm lift height, 5 μm^2 MFM plot of two nanolines, MNPs on nanoline appear to be mainly attractive to the magnetised probe, those on PEG-OH background do not appear to be exchange coupled. (f) Representative SEM image. Arrows used to highlight lines of biotemplated nanoparticles on nanopatterned surfaces AFM and MFM data were processed using WSxM.¹⁴

The nanolines are only 1-2 nanoparticles wide, and the interactions that maintain a magnetic attraction between the probe and the particles on the surface appear to run the full length of the imaged features. These magnetic interactions between the closely spaced biotemplated magnetic nanoparticles could be extended over these long distances by the extremely low aspect ratio of the patterned nanolines and/or the increased coercivity of cobalt ferrite over that of magnetite and cobalt doped

* 3D composite plots rendered in 'R' by J. Bramble, University of Leeds.

magnetite. These nanoscale features, whether patterned into 1D lines, or 2D arrays of squares or rectangles, may offer far more insight into whether high coercivity of ferrite MNPs, or the shape of the assembly, is the most important in controlling the shape of the multi-particle magnetic zones on the surfaces. By varying the size and spacing between nanoscale features, the effect on the exchange coupling of the biomineralised nanomagnets with their neighbours can be studied for magnetically soft particles, such as magnetite. This can then be extended to explore the effect of altering the coercivity of the MNPs by doping cobalt into the magnetite, right up to 33% Co to form cobalt ferrite. This is explored in more detail in the future work discussion in Chapter 7.

6.4 References

1. Galloway, J.M., Bramble, J.P., Rawlings, A.E., Burnell, G., Evans, S.D. & Staniland, S.S. (2012). Nanomagnetic arrays formed with the biomineralization protein Mms6. *J. Nano Res.* **17**, pp 127-146.
2. Galloway, J.M., Bramble, J.P., Rawlings, A.E., Burnell, G., Evans, S.D. & Staniland, S.S. (2012). Biotemplated magnetic nanoparticle arrays. *Small.* **8**, pp 204-208.
3. Abramoff, M.D., Magalhaes, P.J. & Ram, S.J. (2004). Image processing with Image J. *Biophotonics Int.* **11**, pp 36-42.
4. Kim, D., Lee, N., Park, M., Kim, B.H., An, K. & Hyeon, T. (2009). Synthesis of uniform ferrimagnetic magnetite nanocubes. *J. Am. Chem. Soc.* **131**, pp 454-455.
5. Cornell, R.M. & Schwertman, U. (2003). *The Iron Oxides: Structure, Properties, Reactions, Occurrences and Uses* (Wiley-VCH, Weinheim, DE).
6. Andrews, K.W., Dyson, D.J. & Keown, S.R. (1971). *Interpretation of Electron Diffraction Patterns* (Adam Hilger Ltd, London, UK).
7. Norby, P., Christensen Nørlund, A., Fjellvåg, H. & Nielsen, M. (1991). The crystal structure of Cr₈O₂₁ determined from powder diffraction data: Thermal transformation and magnetic properties of a chromium-chromate-tetrachromate. *J. Solid State Chem.* **94**, pp 281-293.
8. Verwey, E.J., Haayman, P.W. & Romeijn, F.C. (1947). Physical properties and cation arrangement of oxides with spinel structures I. Cation arrangement in spinels. *J. Chem. Phys.* **15**, pp 181-187.
9. Walz, F. (2002). The Verwey transition - A topical review. *J. Phys. Condens. Matter.* **14**, pp R285.
10. Goya, G.F., Berquo, T.S., Fonseca, F.C. & Morales, M.P. (2003). Static and dynamic magnetic properties of spherical magnetite nanoparticles. *J. Appl. Phys.* **94**, pp 3520-3528.
11. Hellwig, O., Berger, A., Thomson, T., Dobisz, E., Bandic, Z.Z., Yang, H., Kercher, D.S. & Fullerton, E.E. (2007). Separating dipolar broadening from the intrinsic switching field distribution in perpendicular patterned media. *Appl. Phys. Lett.* **90**, pp 162516.

12. Piramanayagam, S.N. (2007). Perpendicular recording media for hard disk drives. *J. Appl. Phys.* **102**, pp 011301.
13. Mosendz, O., Pisana, S., Reiner, J.W., Stipe, B. & Weller, D. (2012). Ultra-high coercivity small-grain FePt media for thermally assisted recording (invited). *J. Appl. Phys.* **111**, pp 07B729.
14. Horcas, I., Fernandez, R., Gomez-Rodriguez, J.M., Colchero, J., Gomez-Herrero, J. & Baro, A.M. (2007). WSXM: A software for scanning probe microscopy and a tool for nanotechnology. *Rev. Sci. Instrum.* **78**, pp 013705.
15. Yamamoto, K., Hogg, C.R., Yamamuro, S., Hirayama, T. & Majetich, S.A. (2011). Dipolar ferromagnetic phase transition in Fe₃O₄ nanoparticle arrays observed by Lorentz microscopy and electron holography. *Appl. Phys. Lett.* **98**, pp 072509.
16. Berkowitz, A.E. & Schuele, W.J. (1959). Magnetic properties of some ferrite micropowders. *J. Appl. Phys.* **30**, pp S134-S135.
17. Chinnasamy, C.N., Senoue, M., Jeyadevan, B., Perales-Perez, O., Shinoda, K. & Tohji, K. (2003). Synthesis of size-controlled cobalt ferrite particles with high coercivity and squareness ratio. *J. Colloid Interface Sci.* **263**, pp 80-83.
18. Galloway, J.M., Arakaki, A., Masuda, F., Tanaka, T., Matsunaga, T. & Staniland, S.S. (2011). Magnetic bacterial protein Mms6 controls morphology, crystallinity and magnetism of cobalt-doped magnetite nanoparticles in vitro. *J. Mater. Chem.* **21**, pp 15244-15254.
19. Sugimoto, T. & Matijevic, E. (1980). Formation of uniform spherical magnetite particles by crystallization from ferrous hydroxide gels. *J. Colloid Interface Sci.* **74**, pp 227-243.

Part III
Conclusions
and
Future Work

Chapter 7

Conclusions and Future Work

The synthesis and characterisation of biotemplated arrays of nanomagnets using the biomineralisation protein Mms6 involved using many different multi-disciplinary techniques. Here, the conclusions and future work are presented for the optimisation of the expression, purification and the activity of the Mms6 protein. The effect of the protein on the mineralisation of nanomagnets from a bulk solution is then discussed. Finally, the optimisation of the synthesis of patterns of nanomagnets, and their characterisation on surfaces are also examined. The main application for nanomagnets patterned onto surfaces is data storage. This currently involves the use of harsh chemicals, high temperatures, expensive equipment and clean-room facilities, which is not environmentally friendly. The work presented here does not require as harsh conditions or expensive patterning techniques, so may offer a 'greener' route towards magnetic memory device fabrication. However, the magnetic materials mineralised onto these micro-patterned surfaces may be too magnetically soft to be used for data storage purposes. Therefore, methods that could be used to fabricate biotemplated devices that should be better suited to applications in technology of the future are also presented.

7.1 The Mms6 Protein

This section focuses on the structure and function of Mms6. By examining the protein sequence and its likely structure under various different conditions, the possible mechanisms used by Mms6 to template uniform MNPs are explored.

7.1.1 Expression and Purification of Mms6

The mature Mms6 and the His₆-Mms6 tagged proteins were expressed and purified well, so were used for the majority of the experiments completed for this thesis. However, there was still some contamination of the purified protein, as there are some other weak bands just visible in the SDS-PAGE analysis. For the His₈-MBP-Mms6, a small amount of His₈-MBP remains in the mature Mms6 after cleavage with the TEV protease and subsequent purification (see Figure 3.2). When the His₆-Mms6 was purified, there were also a small amount of other protein

bands which can be seen in the Coomassie stained gel shown in Figure 3.3. The amount of contamination is small in both cases, so the purified proteins were suitable for use in the biomineralisation experiments. However, even this small level of contamination made structural analyses (such as CD or protein crystallography) of the Mms6 or His₆-Mms6 protein difficult, as signals from the contaminants also appear in the data. Therefore, further optimisation of the expression and purification of Mms6 is required to synthesise the high purity protein necessary for structural studies.

When purified, the His₈-Mms6 construct contains far less contamination than the His₆-Mms6. As there are two more histidine residues in the His₈ affinity tag, it has a higher binding affinity for the IMAC column, so less of the tagged protein was lost during the purification. This meant that Co²⁺-NTA could be used in the purification, as a lot of the His₈-Mms6 protein was still bound to the column. The process was still relatively high yield. Also, there tends to be less non-specific binding of proteins to the cobalt column than the Ni²⁺-NTA, so there was less contamination of the purified His₈-Mms6 protein. However, it was not possible to cleave the octahistidine tag from the mature Mms6 sequence using the TEV protease, so other methods were also explored to achieve a purer, untagged Mms6. The His₆-SUMO-Mms6 construct was also investigated to try and further improve the purity of the recombinant protein. This construct also expressed and purified extremely well, with no visible contamination on the SDS-PAGE analysis. However, it was not possible to cleave the solubility enhancing SUMO tag from the Mms6 sequence using the SUMO protease. It is likely that the SUMO and TEV cleavage recognition sites are not accessible to these proteases when part of a smaller construct containing Mms6.

In trials using the His₆-Mms6 protein, the thrombin cleavage site appears to be accessible to proteolytic cleavage in this small construct. The thrombin was able to cleave a large proportion of the mature Mms6 protein from the affinity tags. However, thrombin was not available with an affinity tag to remove it from the protein mixture after cleavage. From this protein expression work,* the His₈-tag has been shown to produce a less contaminated protein fraction after purification than the His₆-tag. The SUMO tag appears better suited to producing a pure, uncontaminated Mms6, as there are still some impurities in the purified product when His₈-MBP-Mms6 is used. Unfortunately, as the SUMO and TEV proteases were unable to cleave the tags from the smaller Mms6 constructs, it may be necessary to introduce a thrombin cleavage site into the His₆-SUMO-Mms6

* Optimisation of protein expression and purification in collaboration with A. Rawlings, University of Leeds.

construct. Based on the expression and purification work completed for this study, it is likely that a construct such as His₆-SUMO-Mms6, with a thrombin cleavage site between the tags and the mature sequence, may be suitable for producing high yields of very pure, untagged Mms6. As it is possible to purchase thrombin immobilised onto agarose beads or with affinity tags (e.g. from Sigma-Aldrich), the thrombin could also be separated from the Mms6 after the cleavage of the tag. This route towards the production of Mms6 may produce protein of a high enough purity to be suitable for crystallisation and structural studies.

7.1.2 Protein and Particle Attachment to SAMs

The His₈-Mms6 and His₆-Mms6 tagged fusions were expressed and purified well. The immunological assay demonstrated that the His₆-tag remains accessible after MNP formation by RTCP (see Section 3.2.3), thus this tag could be used to immobilise the Mms6 protein onto appropriately functionalised surfaces, either before or after MNP formation. However, it was not possible to form an NTA functionalised SAM surface for histidine tagged protein immobilisation. In the future, it may be possible to use EDC/NHS linking chemistry to bind nickellated *L*-NTA to form the desired surface functionality. This may require nickellation of the *L*-NTA prior to EDC/NHS linkage of the molecule to the surface. By chelating the *L*-NTA with Ni²⁺ before attachment, the carboxylic acid groups in the *L*-NTA should not be able to cross-link in the solution. This should allow the Ni²⁺-NTA to be covalently bound to the surface, and thus form a surface for His-tagged protein immobilisation. Another alternative would be to buy an expensive NTA functionalised SAM forming molecule, which would also generate SAM surfaces for protein and particle immobilisation.

As it is likely that any *N*-terminal tag will remain accessible on the biotemplated MNPs, it may be simpler to try and introduce different affinity tags to the *N*-terminus of Mms6. These tags could then be used to pattern biotemplated MNPs onto surfaces, or to immobilise the Mms6 before particle formation. Work is currently ongoing to try to produce a cysteine tagged Mms6 fusion,* as the sulfur in the cysteine should allow protein immobilisation directly onto a clean gold surface. The His₈-MBP-Cys-Mms6 remains soluble until the TEV protease cleaves the Cys-Mms6 from the His₈-MBP. Unfortunately, the Cys-Mms6 precipitates from solution when the tags are cleaved. It may be possible to use the SUMO tag to improve the solubility instead of the MBP tag. In fact, the His₆-SUMO-Mms6 construct contains a cysteine residue between the SUMO and Mms6 tags. It is

* Optimisation of protein expression and purification courtesy of A. Rawlings, University of Leeds.

much smaller than the His₈-MBP-Cys-Mms6, so it may be possible for this construct to maintain the biomineralisation function of Mms6 without removing the tags. The SUMO tag allows this recombinant protein to remain soluble, and the cysteine should still be able to attach to a gold surface for biomineralisation.

7.1.3 Self-assembly of Mms6 in Aqueous Solution

A predicted crystal structure of Mms6 was produced based on the primary amino acid sequence of the protein (e.g. see Figure 3.4). This was essential to gain some insight into the likely structure of Mms6, as it has not yet been possible to produce the pure crystals of Mms6 necessary to establish a crystallographic protein structure using X-ray diffraction. The computational structural model shows that the *N*-terminal region forms a hydrophobic multi-stranded β -sheet, and that the *C*-terminal section consists of two short helices. There is a potential high affinity iron binding site in the folded *C*-terminal region of Mms6, with many other acidic residues forming other potential binding sites on the protein surface. When this model is compared to a CD spectrum of the protein in solution under physiological buffer conditions, the His₈-Mms6 protein appears to fewer have helical structures, and more of the turn and strand conformations. It is likely that the Mms6 protein self-assembles via the hydrophobic *N*-terminal region when in aqueous solution. It may be that this self-assembly of the hydrated Mms6 protein causes it to form a more stranded, sheet-like structure than is predicted by the computational model.

The inability of the TEV and SUMO proteases to cleave the *N*-terminal tags from the mature Mms6 sequence indicates that the cleavage recognition sites are not accessible in the His₈-Mms6 and the His₆-SUMO-Mms6. This may be due to the self-assembly of the hydrophobic *N*-terminal region of Mms6, preventing accessibility of these sites. In the much larger His₈-MBP-Mms6 construct, the TEV protease is able to cleave the His₈-MBP from the Mms6 sequence effectively. Therefore it is likely that the large MBP tag is able to disrupt the hydrophobic self-assembly of the Mms6 protein in solution. However, the addition of *N*-terminal tags to Mms6 does appear to alter the ability of Mms6 to bind iron and template MNPs. For example, the *N*-terminal SUMO tag is able to significantly enhance the solubility of His₆-SUMO-Mms6 over that of His₈-Mms6 in the presence of iron (see Section 7.1.4). Also, His₆-Mms6 produces smaller MNPs than those templated by Mms6 using the RTCP method (see Section 4.3). It is likely that these differences are due to the *N*-terminal tags partially, or wholly, disrupting the hydrophobic self-assembly of Mms6 in aqueous solution, which may also disrupt the biotemplating action of tagged Mms6.

The study of Wang *et al.* (2012a)¹ used a Mms6 construct of 10.3 kDa, with a pI of 5.25 (pure Mms6 is 6.4 kDa, with a pI of 4.72)² to study the self-assembly of Mms6 in a physiological buffer. They used dynamic light scattering (DLS) and analytical ultra centrifugation to determine that the majority of their aqueous Mms6 existed in micelles, containing 20-40 monomers. They found that their Mms6 also self-assembled at the liquid-gas interface, and that proteolytic digestion of the micelles was not able to digest a hydrophobic core, which precipitated from solution.¹ In another study using the same Mms6 construct, Wang *et al.* (2012b)³ found that a layer of tagged Mms6 deposited onto a ferric chloride solution has a similar structure to the same protein when under compression in the absence of iron. They attribute this to the iron causing the Mms6 to form aggregates. Their study also found that the protein was better able to bind Fe³⁺ than Fe²⁺ at pH 3.0.³

In the magnetosome, it is likely that the *N*-terminal region integrates the Mms6 protein into the lipid membrane,⁴ which could provide some structural support during biomineralisation *in vivo*. This conformation allows the *C*-terminal region to be displayed on the interior of the vesicle, where the bacterium controls the chemistry and redox potential of the magnetosome to produce the conditions necessary for magnetite mineralisation. Therefore, the *C*-terminal region is able to interact with iron ions and the magnetite crystal surface to template cubo-octahedral magnetite MNP formation within the magnetosome. It appears that when recombinant Mms6 is in an aqueous solution, it self-assembles via the *N*-terminal hydrophobic region, even when hampered by smaller *N*-terminal tags, with the *C*-terminal region displayed on the external surface of the self-assembled structure. This means that the *C*-terminal section of the recombinant protein is able to interact with mineralisation solution to template the biomineralisation of cubo-octahedral magnetite MNPs *in vitro*. However, it is still not clear if the self-assembly of Mms6 at the liquid-gas interface or into micelles is the most important for the biotemplating action of recombinant Mms6 *in vitro*. Figure 7.1 is a schematic to illustrate the two possible methods of self-assembly of Mms6 in solution to form cubo-octahedral magnetite nanoparticles. As the *C*-terminal region interacts with the particle surface, the hydrophobic *N*-terminal section remains accessible on the outside of the particle after MNP formation.

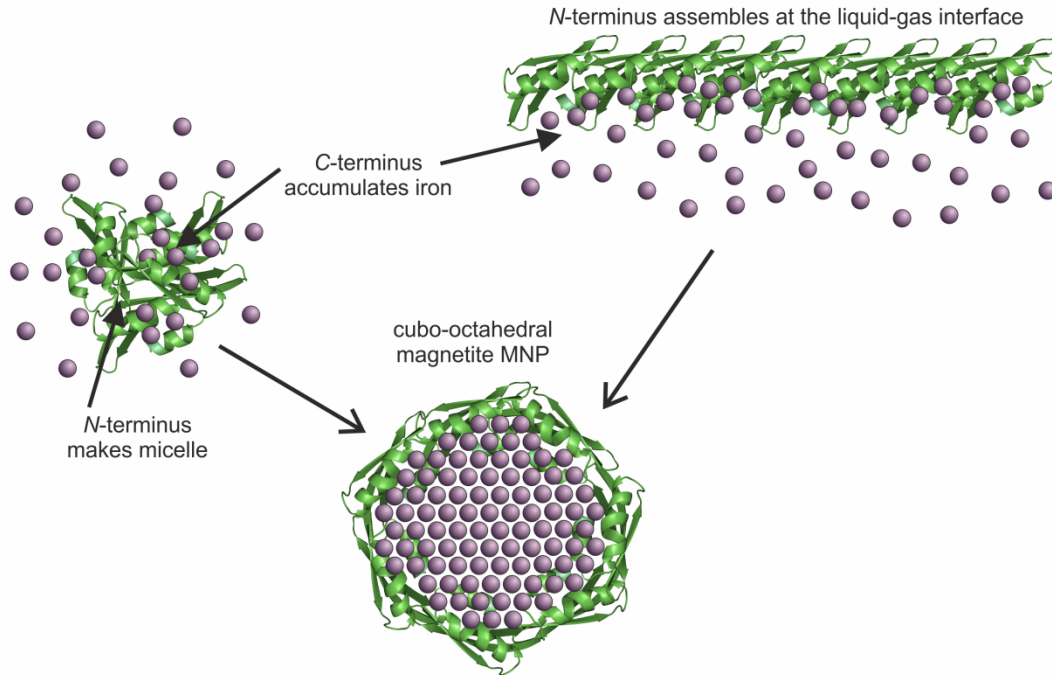


Figure 7.1. Illustration of self-assembly of Mms6 in an aqueous solution, not to scale. Model of Mms6 generated using Quark⁵ and cartoon rendered using PyMOL.⁶ It is likely that Mms6 self assembles via the hydrophobic *N*-terminal region, either into micelles or at the liquid-gas interface. Therefore, the *C*-terminal section is able to interact with the mineralisation solution to form cubo-octahedral magnetite nanoparticles *in vitro*.

7.1.4 Mms6 and Iron Binding

His₆-SUMO-Mms6 was shown to be able to bind large amounts of ferric iron under physiological buffer conditions (see Section 3.2.2.1). The protein was able to bind virtually all of the iron when added in a 1:5 protein to iron molar ratio. Based on the luminescence, it was found that the His₆-SUMO-Mms6 was able to bind more iron when higher concentrations were added. Unfortunately, it was not possible to determine the precise amount of iron bound by the protein for these higher concentrations. However, when iron was added to His₈-Mms6, there was rapid precipitation of the protein from solution. As the protein is likely to self-assemble via the hydrophobic *N*-terminal region in the absence of iron, the addition of iron may also cause the *C*-terminal areas of the Mms6 protein to aggregate. It is likely that the SUMO tag helps to maintain the solubility of the Mms6, even when it has bound large amounts of iron, and thus prevents much of this aggregation to form precipitates. In a recent study, it was found that recombinant Mms6 constructs were able to bind quite high concentrations of iron at pH 3.¹ It is likely that the protein structure may be distorted at such low pH, which may also prevent aggregation and precipitation of the recombinant protein. Further work is still necessary to gain a better understanding of the iron binding mechanisms of Mms6. Also, as these studies only used ferric iron to study the binding behaviour, it may not be representative of the behaviour of Mms6 inside the magnetosome.

It is likely that there is a reducing environment inside the magnetosome to facilitate magnetite formation.⁷ Therefore, it is probable that dissolved iron in the magnetosome is in the reduced ferrous form, rather than as oxidised ferric iron. If this is the case, determination of the binding affinity of Mms6 for ferrous and ferric iron in a basic and reducing environment would give far better understanding of how Mms6 may accumulate iron ions. In turn, this could establish how Mms6 may facilitate uniform MNP biomineralisation, both inside the magnetosome and *in vitro*. As Fe³⁺ is necessary for magnetite formation, it could be that Mms6 is better able to bind ferric iron than ferrous iron, especially if the oxidised form is scarce within the magnetosome. Mms6 may be able to oxidise ferrous iron to ferric species to allow it to form magnetite, or this could be done by another biomineralisation protein within the organism. A comparison of the binding affinity of Fe²⁺ and Fe³⁺ is necessary to resolve these questions regarding Mms6 and the binding of iron. For this, it may be necessary to stabilise the Mms6 protein against precipitation using the SUMO tag, as the His₈-Mms6 precipitated rapidly from solution upon the addition of iron. This may allow the effect of point mutation on the binding ability of Mms6 to be studied, which may establish which residues are necessary for effective iron binding in this protein.

When iron is added to the His₈-Mms6, the CD spectrum does change, but the fit of this spectrum may not be reliable, as the protein also precipitated from solution (see Section 3.2.2.3). However, if the protein does contain less turns and become more stranded when binding iron, this could lead to a conformational change in the protein to structures. As crystallographic planes are flat, a more stranded conformation may allow the C-terminal section of the Mms6 protein to interact with the MNP surface more effectively, and facilitate templating of the cubo-octahedral particle morphology. As a peptide based on the C-terminus of Mms6 is able to template cubo-octahedral MNPs,⁸ it is probable that conformational changes upon iron binding occur in this region.

Another route towards stabilisation of recombinant Mms6 in the presence of iron could be to integrate the protein into a lipid bilayer on a flat surface⁹ or in a synthetic vesicle.¹⁰ This may form a more life-like analogy for the protein, as it is thought that the hydrophobic region on the protein integrates it into the magnetosome lipid vesicle *in vivo*. This study shows that it is likely that the addition of solubility enhancing tags could significantly alter the structure, and therefore, the function of the Mms6 protein. By supporting the protein in a lipid layer, the structure of Mms6 would not have to be altered to study the effects of varying pH or iron concentrations on the activity of the protein. If Mms6 still aggregates when in a bilayer in the presence of iron, this aggregation is likely to be highly significant for

the biotemplating action of the protein. This would provide a more realistic picture of how Mms6 templates cubo-octahedral MNPs *in vivo*, as the protein would be in a more native state than if the structure was significantly altered by the addition of solubility enhancing sequences.

7.1.5 Interaction of Mms6 with Specific Crystallographic Planes of Magnetite When in an Aqueous Solution

Mms6 templates the formation of cubo-octahedral magnetite MNPs, probably by binding to the [100] type crystal faces of the magnetite nanoparticle to prevent growth in the [111] direction. The 'KSR' motif in Mms6 is likely to be involved in magnetite nanoparticle surface binding, which appears in the helical part of the C-terminal region in the modelled structure (see Figure 3.9). This mode of binding is supported by the similar 'RSKLR' sequence that was found to be important for iron oxide or magnetite binding in biopanned peptide sequences.^{11,12} However, further work is necessary to determine which parts of the Mms6 sequence are important for directing magnetite nanoparticle morphology. This could include biopanning using magnetite nanoparticles that present specific crystal faces (e.g. all [111] or all [100] type planes) on their surfaces. By carefully avoiding surface oxidation of the magnetite MNPs before and during the biopanning, it would be possible to identify amino acid sequences that strongly bind to a specific face of a magnetite nanoparticle. These peptides could then be compared and contrasted with Mms6, and other proteins important for iron binding and biomineralisation, to determine likely crystallographic binding motifs.

As mentioned above, the self-assembly of Mms6 via the hydrophobic *N*-terminal region may facilitate the biotemplating action of the Mms6 protein *in vivo*. It is likely that the *N*-terminal region integrates the protein into the magnetosome membrane *in vitro*, which may also help to template uniform MNPs within AMB-1. However, the biotemplating ability of the Mms6 C-terminus peptide⁸ shows that this self-assembly is not vital to the formation of cubo-octahedral MNPs. This study indicates that it is likely that the C-terminal region of Mms6 binds iron and interacts with the [100] crystal face during MNP growth, to direct iron oxide mineralisation towards uniform cubo-octahedral magnetite formation. The self-assembly of Mms6 micelles and/or monolayers at the surface of a reactant solution via the *N*-terminal region may allow the protein to template MNPs with a more uniform size distribution. As the hydrophobic self-assembly would bring many Mms6 C-terminal regions into close proximity, this may facilitate the assembly of iron ions onto the magnetite crystal structure.

That hydrophobic self-assembly of the *N*-terminal section of Mms6 may facilitate MNP formation is supported by His₆-Mms6 producing smaller, less monodisperse MNPs than untagged Mms6 during RTCP. The aromatic hexahistidine tag is likely to partially disrupt the ability of the hydrophobic *N*-terminal region to self-assemble, and thus reduce the templating ability of the Mms6 protein in an aqueous solution. If a strep II tag was introduced at the *N*-terminus, this may have a similar effect to the polyhistidine affinity tag on the assembly of recombinant Mms6 in an aqueous solution. The strep II sequence is also small (NWSHPQFEK)¹³ and contains many aromatic residues, which could disrupt the *N*-terminal assembly of Mms6 in a similar manner to the His_x tags. The addition of a Cys-tag at the *N*-terminus may facilitate self-assembly of the *N*-terminal region, as the sulfur in cysteine is able to form disulfide bridges with other cysteines. These sulfide bonds are very strong, and important in stabilising tertiary and quaternary protein structures.¹⁴ Therefore, any constructs containing new affinity tags should be fully characterised and compared to MNPs templated by the unmodified Mms6 sequence in an aqueous solution. However, if the tags are used to immobilise the protein onto a patterned surface before MNP formation, this should not be an issue. This is because the tags will be attached to the surface, and thus should provide stability for the *C*-terminal region as it interacts with the mineralisation solution to form MNPs *in situ*.

7.1.6 Mms6 Templating Magnetite MNPs When Immobilised on a Patterned Surface

This study has demonstrated that the Mms6 protein is able to biotemplate magnetite when immobilised onto a patterned surface. It is likely that self-assembly of the Mms6 protein via the *N*-terminal region facilitates biomineralisation of cubo-octahedral magnetite when in the magnetosome and *in vitro*. However, it is probably the *C*-terminal portion which interacts with the MNP surface and templates the cubo-octahedral morphology of the magnetite particles. When immobilised onto a solid substrate via the *N*-terminus, the *C*-terminal area remains able to interact with the mineralisation solution. This means that the immobilised Mms6 protein is also able to biomineralise uniform magnetite MNPs when attached via the *N*-terminus onto a patterned surface. However, these MNPs appear to be of a cubic rather than cubo-octahedral morphology, and are larger than MNPs templated by the protein from a bulk solution. This is probably because the Mms6 protein is only able to interact with the MNP on the underside of the particle, so cannot fully control the particle size or morphology (see Figure 7.2). However, the size control is still very good, as the particles are all templated in a similar manner during the nucleation and initial growth phases, creating the narrow MNP size distribution.

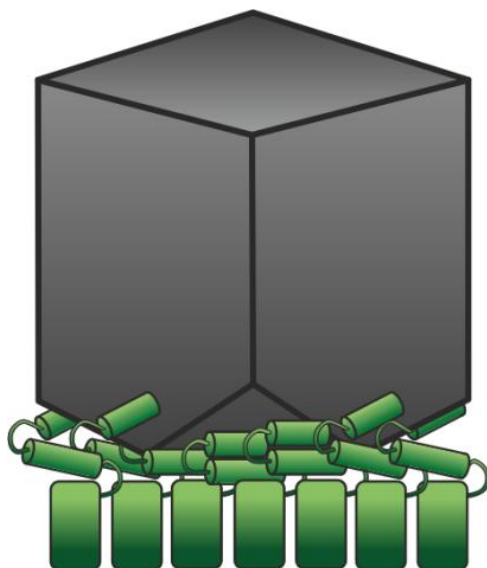


Figure 7.2. Illustration of Mms6 biotemplating magnetite cubes when immobilised onto a surface, not to scale. Mms6 protein is coloured green, the hydrophobic *N*-terminus is represented by a rectangle, and the hydrophilic *C*-terminus by two cylinders. The protein is attached to the substrate via the *N*-terminus, so the *C*-terminus is able to interact with the mineralisation solution to template the magnetite. Mms6 is likely to only be able to template the underside of the MNP, so the particles appear cubic when imaged in SEM from above.

On some of the micro-patterned biomineralised arrays, there was a greater density of MNPs mineralised at the edge of the micro-patterned protein attachment areas than in the middle (e.g. Figure 5.4e). It is possible that this is due to stamp touch-down (see Figure 3.19c), which would functionalise the centre of the protein attachment areas to resist protein binding. It is likely that stamp touch-down would produce two distinct functionalisations on the patterned surface: densely mineralised MNPs on the attached protein, with only a few MNPs on the PEG-OH surface. However, the density of the mineralised MNPs seems to gradually reduce as the centre of the pattern is approached, which indicates a different mechanism may be responsible.

Figure 7.3 is a schematic illustration of the possible cause of the gradual increase in MNP density towards the edge of the immobilised Mms6 patterned areas. Surface diffusion of the iron ions and magnetite precursors that form the MNPs is likely to be reduced as the centre of the protein attachment areas are approached. This is because the Mms6 at the edge of the patterned areas is likely to bind a lot of the iron from the solution. Also, if the Mms6 is too densely packed on the surface, the structure of the protein may be distorted as the centre of the immobilisation areas are approached. The QCM-D study found that Mms6 formed a 3.2 nm layer onto the mixed SAM surface (see Section 3.3.1.1), which is slightly thicker than the 10.3 kDa tagged Mms6 compressed layer on a buffer surface ($31.4 \pm 0.3 \text{ \AA}$) studied by Wang *et al* (2012b).³ As structure is usually important for protein function (e.g. see Section 3.3.3.2), improper folding, especially in the *C*-terminal region, may reduce the ability of Mms6 to biotemplate uniform MNPs. Therefore, the reduced

mineralisation density at the centre of some of the micro-patterned Mms6 areas could also be due to increased packing density of protein distorting the structure of Mms6 as the centre of the micro-patterned areas are approached.

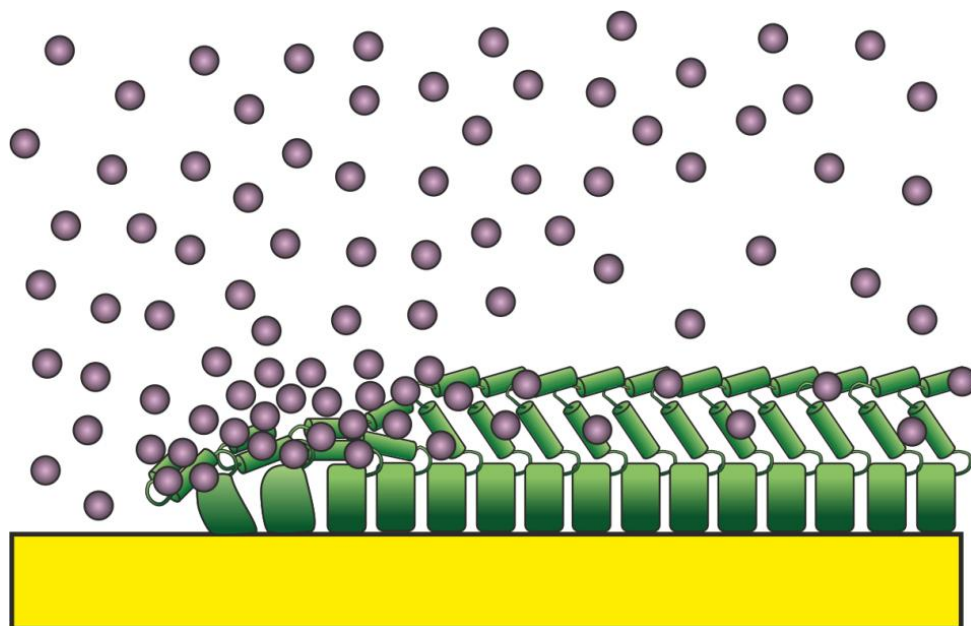


Figure 7.3. Schematic illustration of Mms6 biomimetic mineralisation of magnetite onto a patterned surface, not to scale. Mms6 is coloured green, the hydrophobic *N*-terminal region is represented by a rectangle, and the hydrophilic *C*-terminal area by two cylinders. Mms6 attached at the edge of the pattern may be slightly distorted towards the *N*-terminus to ensure attachment to the mixed SAM, but the *C*-terminal region is able to fold correctly. Towards the middle, the whole of the protein may be slightly distorted. This enables the Mms6 at the edge of the pattern to better scavenge iron ions and/or magnetite pre-cursors from solution. In turn, this reduces the concentration of the reactants at the surface towards the middle of the protein attachment areas. Therefore, the immobilised protein is able to mineralise more densely packed particles at the micro-pattern edges than at the centre.

If the protein is too densely packed onto the patterned surface, the concentration of PE-COOH in the attachment SAM could be reduced. If there were fewer attachment sites on the surface, the protein layer formed should be less densely packed, and therefore better able to fold correctly. However, surface diffusion may still prevent the Mms6 in the middle of micro-patterned attachment areas from forming as many MNPs as the protein at the edge of the patterned areas. If the protein is attached to smaller, nanoscale patterns on the surface, the effects of surface diffusion will also be minimised. Also, nanoscale patterns of biomimetic mineralised MNPs may allow the interactions between individual particles to be studied in detail.

7.2 Biotemplated MNPs Synthesised From a Bulk Solution

In this section, the MNPs formed by Mms6 from a bulk solution are examined. The POFH and RTCP methods of magnetite and cobalt doped magnetite synthesis in the presence of Mms6 are discussed. The quality of the particles formed by these methods were studied to enhance the understanding of how the Mms6 protein may interact with mineralisation solutions to template MNP formation *in vitro*.

7.2.1 POFHN and POFHK

Preliminary VSM work using the POFHK method established an optimum level of 6% cobalt doping for this study, which ensured the MNPs have high coercivity for relatively little loss of saturation magnetisation (see Section 4.1). However, depending on the application the MNPs are required for, their coercivity and saturation magnetisation can be tuned between the magnetite and cobalt ferrite end-members for this system. When templated with Mms6, the POFHK MNPs were smaller and of a narrower grainsize distribution when compared to controls. However, it was found that the protein was unable to template small particles with a narrow grainsize distribution, which were observed in previous work. The ratio of reactants used by Amemiya *et al.* (2007)¹⁵ to create Mms6 templated POFHK MNPs contained an excess of base. When the alkali is in excess, the POFHK method tends to produce small (≈ 32 nm), octahedral particles in the absence of Mms6.¹⁵ In the presence of Mms6, the particles are cubo-octahedral, and templated towards a smaller size (≈ 20 nm) and narrower size distribution.¹⁵ However, at stoichiometric ratios of iron and base, or for an excess of Fe^{2+} , the POFHK method produces very large particles of up to ≈ 1 μm .¹⁶ Therefore, it is likely that the tendency of the reaction towards producing larger particles under these reaction conditions overcomes the templating ability of the protein, thus producing MNPs with a range of grainsizes in the presence of Mms6.

The POFHN method was also found to be unsuitable for synthesising Mms6 biotemplated cobalt doped MNPs. In the absence of cobalt and protein, there are many particles with a low aspect ratio. Mainly equidimensional particles were produced when either Mms6 or 6% Co was added. This shows that Mms6 is able to direct the POFHN method away from the formation of acicular MNPs. However, the variation in particle shape and levels of cobalt doping made the interpretation of the magnetic hysteresis data difficult. Similar to the POFHK method, the addition of Mms6 was unable to produce uniform MNPs with a narrow size distribution for the POFHN method. Again, the reaction conditions are not optimised towards forming small particles in the absence of protein. This means that the tendency of the POFHN system towards forming larger particles under these reaction conditions

overcomes any size control of Mms6 on particle formation. Therefore, Mms6 was unable to control the mineralisation to direct it towards the formation of MNPs at the smaller end of the SD region. Therefore, optimisation of the POFH methods to produce biotemplated SD cobalt doped MNPs requires more careful control of the reaction conditions to ensure that the Mms6 is able to biotemplate cubo-octahedral MNPs. The objective of this study is to form biotemplated arrays of MNPs onto a patterned surface. Thus, the optimisation of the POFH method was investigated for Mms6 bound to a surface rather than when in an aqueous bulk solution (see Section 7.3).

7.2.2 RTCP

MNPs formed by RTCP in the absence of protein have a wide particle size and shape distribution. In the presence of His₆-Mms6, the magnetite particles have a very uniform magnetic behaviour and a narrow grainsize distribution, which is just below the lower SD size limit for magnetite. SP iron oxide MNPs such as these can be used to enhance contrast during MRI.^{17,18} As no harsh chemicals are used in the synthesis of RTCP Fe_{His6-Mms6} particles, they should not be coated in toxic residues, so are likely to be biocompatible. Also, the His₆-Mms6 protein is dual functional as it both templates the formation of uniform, cubo-octahedral MNPs with a consistent magnetic behaviour, but it also remains strongly bound to the particle surface. As the affinity tag on the RTCP particles is still accessible after MNP synthesis, this could allow the Fe_{His6-Mms6} MNPs to be easily functionalised with other biological molecules (see Figure 7.4). The *N*-terminal affinity tag could be used to attach molecules to the protein on the surface of the MNPs to add additional functionality to the magnetic particles. For example, fluorescent molecules could be attached to the MNPs which would allow the cargo and particles to be imaged, or medicinal molecules could be attached for use in drug delivery.

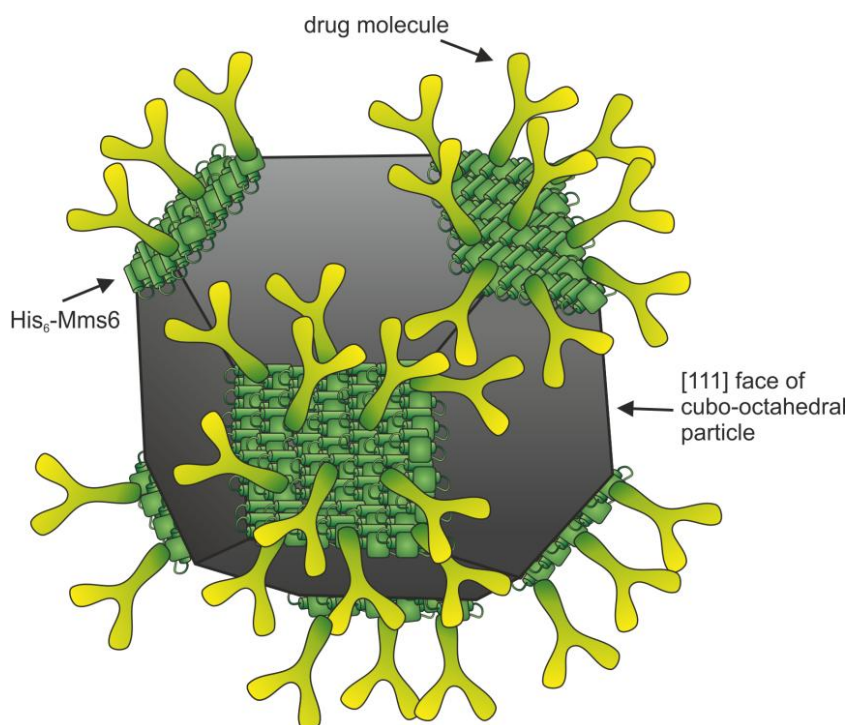


Figure 7.4. Illustration of $\text{Fe}_{\text{His6-Mms6}}$ templated magnetite nanoparticle functionalised with drug molecules. These biotemplated SP MNPs are likely to be biocompatible due to their mild method of synthesis, and may have potential uses as vehicles for drug delivery.

The RTCP MNPs synthesised from a solution containing 6% Co showed two different magnetic behaviours, one magnetically soft and the other hard. This is likely to be due to there being a range of particle sizes, with the smaller particles behaving superparamagnetically and thus producing the low coercivity magnetic response. The larger particles above ≈ 18 nm diameter are able to maintain a single domain at room temperature, so have a high coercivity and are magnetically hard. The Co_{Mms6} particles produce a single magnetic hysteresis loop with a coercivity of 78.3 Oe at room temperature. It is possible that Co_{Mms6} MNPs could be useful for hyperthermic cancer treatment. Recently, cobalt doped magnetosome MNPs have been found to be more effective than undoped particles in treating *in vivo* cancer by hyperthermia.¹⁹ They attribute the increased potency to the higher coercivity of the doped MNPs, which allows the particles to be heated more efficiently in an alternating magnetic field during the hyperthermic treatment. Unfortunately, the growth of magnetic bacteria and harvesting of magnetosome MNPs can be expensive, slow and there is often a low yield of particles. By using the more economical Co_{Mms6} templated MNPs synthesised here, a higher yield of MNPs for applications such as hyperthermia could be achieved. These particles could also be further functionalised by conjugation of molecules to the Mms6 protein tightly bound to the surface of the MNPs. In the future, work could be done to try and functionalise the MNPs with other biomolecules, and the efficacy of the Co_{Mms6} MNPs in cancer hyperthermia could be examined.

7.3 Patterning Mms6 Biotemplated MNPs

7.3.1 RTCP and Surface Patterning

The RTCP method was found to be unsuitable for forming arrays of magnetic nanoparticles onto a surface. When Mms6 templated MNPs were synthesised from a bulk solution, it was not possible to immobilise the preformed MNPs onto the pattern effectively. There was a lot of contamination of a black material, and the particles seemed to preferentially attach to the PEG-OH, which should resist protein binding, and therefore also resist MNP binding. It is probable that this method could be significantly improved to allow the immobilisation of preformed MNPs. A Cys-Mms6 templated MNP is likely to be better suited to immobilisation onto a patterned gold surface, so use of this mutant may make the attachment of preformed MNPs to a patterned surface more likely to succeed. It may also be possible to use another affinity tag, such as streptavidin or the strep II tag to immobilise preformed magnetite MNPs onto a biotinylated streptavidin patterned SAM. However, RTCP magnetite MNPs are superparamagnetic, which means they cannot be used for data storage as their magnetism is thermally unstable. Therefore, cobalt doping of the preformed MNPs may also be needed to ensure that magnetically stable single domain particles are patterned onto the surface.

It was not possible to use RTCP to mineralise MNPs onto an Mms6 functionalised surface, as a black deposit was formed onto the immobilised protein rather than magnetite particles. It is likely that the patterned protein was unable to interact with the RTCP mineralisation solution to template MNPs, but formed a fine grained iron oxide instead. This is because MNPs synthesised by RTCP form away from the surface, around the locus of base addition. The co-precipitation method forms particles rapidly upon the addition of hydroxide, just below the liquid-gas interface. This means that the Mms6 on the patterned surfaces was too far away from the site of MNP formation, as the patterned surfaces are at the bottom of the reaction vessel (see Figure 2.10). Therefore, methods that form magnetite more slowly were explored, as they should allow the immobilised Mms6 to interact with the mineralisation solution for longer periods, and thus to biotemplate patterns of MNPs.

7.3.2 Biotemplated Magnetite Formation on a Surface

Different phases of iron oxides and (oxy)hydroxides were mineralised on the immobilised Mms6 as the POFH reaction conditions were altered. The effect of varying the reaction conditions are discussed in detail in Chapter 5. For the POFHK method, excess Fe^{2+} and/or lower pH skewed the system towards the formation of ferric oxyhydroxides (e.g. goethite and lepidocrocite) and the ferric oxide maghemite. An excess of nitrate was also required to ensure that magnetite was formed rather than lepidocrocite (see Figure 5.7). Therefore, the immobilised Mms6 requires an excess of OH^- to synthesise magnetite MNPs for the POFHK system. This indicates that Mms6 protein function (i.e. to mineralise magnetite) is suited to operating in a basic environment, where there is a stoichiometric shortage of Fe^{2+} for a partial oxidation reaction.

It is likely that the magnetosome is basic and reducing,⁷ and that iron in the cell cytoplasm is also in the reduced ferrous form. If magnetosome mineralisation originally evolved as a method to store iron (as iron is limited in anaerobic environments),^{20,21} many of the proteins involved in this mineralisation may have originally evolved to template iron oxides under reducing conditions using low iron concentrations. Therefore, it is likely that the formation of magnetite within a magnetosome vesicle occurs under reaction conditions similar to the optimised POFHK conditions. Development of the suite of proteins involved in MNP formation in bacteria may have subsequently enhanced the ability of the magnetosome to form MNPs for magnetotaxis. These proteins are likely to help the magnetosome to maintain a basic pH and concentrate iron within the vesicle, to control MNP size and shape, as well as to arrange the magnetic MNPs into chains to maximise the magnetic moment of the bacterium.

The POFHN method is more complicated than the POFHK method, as there are more reactants, and therefore more variables, when mineralising magnetite using ammonia and hydrazine. Variation in the ratio of the different reactants also caused the reaction to mineralise different iron minerals. If there was too much ammonia, or not enough hydrazine, the POFHN method formed platy lepidocrocite. Too little ammonia, and acicular goethite formed (see Figure 5.11). POFHN seems to require a slight excess of Fe^{2+} , with the hydrazine being more important for controlling the redox of the solution, by preventing the formation of ferric oxides, rather than adjusting the pH of the mineralisation solution.

The optimum reaction conditions were able to allow the immobilised Mms6 protein to biotemplate uniform magnetite nanoparticles onto the protein attachment areas, with mineralisation resistance on the PEG-OH background. This occurred for the POFHN method (in 10 mL: 50 mM Fe^{2+} , 40 μL 50-60% N_2H_4 , 200 μL 26% NH_4OH and 100 mM KNO_3), and allowed the immobilised Mms6 areas to biotemplate uniform MNPs of magnetite with no mineralisation on the background (e.g. see Figure 5.11). When mineralised with POFHK, there was often some mineralisation onto the PEG-OH background (e.g. Figure 5.7). This is not ideal, as the background should resist mineralisation to allow the formation of high quality biomineralised particles only on the areas with immobilised protein. If clean gold was immersed in the reaction solution, an extensive, intergrown network of magnetite particles were formed on the surface. As the PEG-OH stamped SAM remained unmineralised after immersion in the optimised POFHN conditions, the PEG-OH SAM must have remained stable during heating in the reactant solution to protect the underlying gold surface from mineralisation.

It is possible that the POFHK reactant solution slightly degraded the PEG-OH SAM to cause the undesirable mineralisation on the background areas. However, the QCM-D data (Section 3.3.2.1) showed that it is likely that there was some non-specific binding of Mms6 to the PEG-OH background, which could be able to nucleate MNP formation. When patterned Mms6 was incubated in the POFHN reactants for a long period, there was no mineralisation on the protein patterned surface, and only the patterned SAM could be seen (Figure 5.9b). This indicates that the NH_4OH and/or the N_2H_4 in the POFHN solution is able to remove MNPs and/or Mms6 from the substrates over long exposure periods, whether covalently bound to the mixed SAM or non-specifically bound to the PEG-OH background. If non-specifically bound Mms6 is the easier to remove using ammonia and hydrazine, then a short incubation would remove non-specifically bound Mms6 from the PEG-OH for the POFHN method. This would prevent mineralisation on the background, but leave the Mms6 covalently bound to the mixed SAM able to biomineralise magnetite onto the protein attachment areas. This would create the excellent contrast between mineralised and unmineralised areas on the POFHN mineralised substrate. In the future, this could be tested using QCM-D to see if ammonia and hydrazine are able to remove Mms6 from a PEG-OH SAM (or a mixed attachment SAM) over time.

7.3.3 Biotemplated 6% Co Doped Magnetite Formation on a Surface

The addition of 6% Co to form cobalt doped magnetite using the POFHN method caused the reaction to either form much smaller particles, or to form a platy mineral, likely to be a cobalt doped lepidocrocite. As it was not possible to find a value for the standard energy of formation ($\Delta_f G^0$) for cobalt ferrite, it is difficult to establish how the inclusion of cobalt in the POFH mineralisation solutions would alter the stability of the different phases using an Eh-pH diagram. As the POFHN method is more complex than the POFHK method, it was unclear how to adjust the ratio of the other reactants to ensure that this method is able to mineralise cobalt doped magnetite instead of the other iron (cobalt) minerals. Therefore, the POFHK method, which is simpler, was also explored.

The optimum conditions for 6% Co doped magnetite biomineralisation onto immobilised Mms6 (23.5 mM of FeSO_4 , 1.5 mM of CoSO_4 , 55 mM KOH, 400 mM KNO_3) were also found to produce less non-specific mineralisation on the PEG-OH background than for the undoped samples. As this uses a higher proportion of nitrate, the rate of magnetite formation was probably faster, which may reduce MNP formation by any non-specifically bound Mms6 on the PEG-OH background. It is unlikely that Mms6 evolved to interact with cobalt during mineralisation, as cobalt is far less abundant than iron in natural waters (e.g. oceanic concentrations of $\text{Fe}=0.33$ ppb and $\text{Co}=0.008$ ppb).²² Therefore, the addition of cobalt to the POFHK reaction may also hamper how the Mms6 interacts with the mineralisation solution, especially if it's distorted by non-specific binding. Whether due to an increased rate of MNP formation or cobalt affecting the action of non-specifically bound Mms6, the reduction of MNP formation on the PEG-OH background produces a better contrast between biomineralised and unbiomineralised areas for 6% Co doping of the POFHK system, which is desirable.

7.3.4 Biotemplated Cobalt Ferrite Formation on a Surface

The POFHN method was also unable to template uniform cobalt ferrite MNPs onto the immobilised Mms6 protein when the optimum conditions for magnetite formation were used. Again, as the POFHK reaction is simpler to manipulate towards magnetite formation, this was investigated to form cobalt ferrite using the immobilised Mms6 to biotemplate the particles. The optimum conditions for the formation of cobalt ferrite by POFHK (17 mM FeSO_4 , 8 mM CoSO_4 , 60 mM KOH, 400 mM KNO_3) required a greater excess of base than for the 6% cobalt doped system. This indicates that the addition of cobalt may reduce the pH of the solution and reduce the ability of the nitrate to oxidise the iron to form CoFe_2O_4 . When this is countered by the addition of the greater excess of base, the system is restored to

the mineralisation of equidimensional cobalt ferrite nanoparticles by the immobilised Mms6. However, the MNPs formed by the micro-patterned Mms6 are very small and quite sparsely dispersed on the protein patterned areas (e.g. see Figure 5.14).

When the same reaction conditions were used to mineralise nanopatterned lines of Mms6 with cobalt ferrite, the biotemplated MNPs are much more closely spaced on the Mms6 immobilised areas. This supports the premise that Mms6 at the edge of the patterned areas is better able to interact with the mineralisation solution to form more densely packed MNPs, as illustrated in Figure 7.3. It is likely that the Mms6 will be better able to properly fold at the edges of the nano-lines, and thus template MNPs more effectively. As the nano-lines are much narrower than the micro-scale patterned protein immobilisation areas, a higher proportion of the Mms6 will be at the edge of these protein immobilisation areas. This means that there will also be less limitation on biomineralisation by surface diffusion of the reactants, which could also facilitate the nano-patterned Mms6 when biotemplating MNPs *in situ*. This is encouraging for any future work on nano-scale biomineralisation of surfaces, as nano-patterning seems better suited to maintaining protein functionality when Mms6 is immobilised onto a surface.

7.4 Properties of Mms6 Biotemplated Arrays of MNPs

7.4.1 Biotemplated Arrays of Magnetite

The magnetite mineralised by the immobilised Mms6 for the optimised conditions (in 10 mL: 50 mM Fe^{2+} , 40 μL 50-60% N_2H_4 , 200 μL 26% NH_4OH and 100 mM KNO_3) showed a narrow grainsize distribution (340 ± 54 nm) when compared to controls (e.g. $\text{POFHN}_{\text{Fe_no_protein_bulk}} = 232\pm 121$ nm) and high temperature magnetite synthesis methods (e.g. Kim *et al.* (2009)²³ = 280 ± 70 nm). The powder XRD data strongly suggests that the $\text{POFHN}_{\text{Fe_Mms6_surface}}$ MNPs are high quality magnetite. The good crystallinity of the MNPs biotemplated on the surface by POFHN is supported by the magnetic hysteresis of the $\text{POFHN}_{\text{Fe_Mms6_surface}}$ MNPs. Their coercivity at room temperature (112.5 Oe) is slightly higher than the coercivity of nanocubes synthesised by thermal decomposition (≈ 100 Oe).²³ The change in slope on the hysteresis loop is also very rapid for the $\text{POFHN}_{\text{Fe_Mms6_surface}}$ samples. These results show that the Mms6 biotemplated MNPs on the surface are superior quality magnetite particles with a very consistent magnetic behaviour. As their fabrication does not require the harsh chemicals or very high temperatures of the non-biotemplated particles, this is a much more environmentally friendly approach to high quality magnetite synthesis than the method of Kim *et al.* (2009).²³

Due to the different packing densities of MNPs on the micro-patterned arrays, the bulk magnetic behaviour of these samples is likely to be complex. This is highlighted by the two possible Verwey transitions in the ZFC and FC VSM measurements (see Section 6.1.4.1). The closely packed particles on the arrays are likely to be exchange coupled with many of their neighbours, which may be responsible for the higher temperature transition at ≈ 75 K. The less closely packed particles (at the centre of some, and at the very edge of all of the micropatterned areas) may not be exchange coupled to any neighbours. This may lead them to behave as individual nanomagnets, and create the lower temperature transition at ≈ 41 K. However, these data are very noisy, so more reliable temperature versus moment data for the biomineralised surfaces is required to establish if this is the case. Evidence of the Verwey transition would have demonstrated conclusively that the Mms6 surface templated MNPs are stoichiometric, highly crystalline magnetite. In the future, it may be possible to record more reliable ZFC, FC and remanence readings for these biotemplated samples. A new sample holder for the VSM that holds the substrate horizontally at the z centre could help to significantly reduce noise in the temperature versus moment data. Another alternative could be to use a superconducting quantum interference device (SQUID) magnetometer for ZFC, FC and remanence measurements, as this technique is extremely sensitive and less noisy.²⁴ Less noisy data across a wider temperature range could establish both a blocking temperature and if there is evidence of the Verwey transition for these uniform biotemplated nanoparticles.

The MFM plots of the POFHN_{Fe_Mms6_surface} arrays show that the MNPs are behaving as SD ferrimagnets (see Section 6.1.5). The small area MFM plots clearly show low aspect ratio multi-particle zones of magnetic repulsion and attraction running parallel to the long axis of the micro-patterned biotemplated MNPs. It is likely that this is due to exchange coupling between the closely packed magnetite particles biotemplated onto the surface. The shape and size of these multi-particle zones is likely to be strongly dependent on the shape of the micro-pattern, as assembly shape strongly influences the shape of multi-particle magnetic zones in single layers of magnetite.²⁵ This effect could be investigated in more detail by using different pattern shapes (e.g. square, circular, triangular, linear), pattern scales and by magnetisation of the samples in different directions before probing the magnetic interactions on the surfaces using MFM. Nano-patterning could be used to study the effect of spacing on the exchange coupling between small groups or even on individual nanoparticles.

This work with Mms6 biotemplated magnetite arrays demonstrates that high quality magnetite nanoparticles can be formed under far milder conditions than required for current industrial synthetic techniques. The biotemplating action of Mms6 not only allows the formation of uniform magnetite particles using milder chemicals and at lower temperatures, but also anchors the particles onto the micro-patterned surface. Further optimisation of the POFHK mineralisation conditions could allow the adaptation of this biotemplating method to form high quality MNPs at lower temperatures and with even less harsh chemicals. The expression and purification of Mms6 is still quite time consuming, and therefore expensive. The development of simpler protein expression and purification techniques, and the addition of affinity tags, such as cysteine that can immobilise proteins directly onto a gold surface, could help to simplify the fabrication of Mms6 biotemplated magnetic arrays, and thus reduce costs. Further improvements could also be made by using biotemplating peptides instead of the full length Mms6 protein, as shorter peptide sequences are cheaper to synthesise than a full length protein. Arakaki *et al.* (2010)⁸ found that a peptide based on the C-terminal segment of Mms6 was able to template uniform cubo-octahedral magnetite nanoparticles when in a bulk solution. In the future, this peptide could be selectively attached to appropriate substrates, possibly using an N-terminal cysteine for direct attachment to gold. This would provide a far simpler and more economical route to synthesising biotemplated arrays of nanomagnets.

7.4.2 Biotemplated Arrays of 6% Cobalt Doped Magnetite

The coercivity of the biotemplated magnetite nanoparticles on the micro-patterned arrays is quite low (112.5 Oe), and the particles are quite large. Therefore, it is unlikely that they will be able to be used for data storage, as any magnetic information may be easily lost, and the surface roughness created by the large particles may make reading and writing information difficult. However, as cobalt doping increases the coercivity of magnetite, this offers a promising route towards the development of biotemplated data storage devices. Mms6 templated magnetic nanoparticle patterns using 6% Co doping and the POFHK method produced smaller MNPs with a narrower grainsize distribution (245 ± 41 nm) than on the POFHN_{Fe_Mms6_surface}. The XRD shows that the crystallinity of the 6% Co doped MNPs is good, and the VSM showed a significant increase in coercivity from 112.5 Oe for undoped particles to 383.0 Oe with 6% Co doping at room temperature. However, these particles are still much larger, and the coercivity is less than that of nanoparticles used in cutting edge high density data storage (≈ 4 kOe).²⁶

The MFM plots of the POFHK_{6%Co_Mms6_surface} samples show much longer zones of multi-particle magnetic interactions (see Section 6.2.5). This could be due to the increased coercivity of the doped MNPs allowing stronger exchange coupling of the closely spaced MNPs biotemplated onto the micro-patterned surfaces. However, the elongation of the multi-particle magnetic domains could also be attributed to the shape of the micropatterned areas. As the micro-line patterns have a much lower aspect ratio than the chessboard rectangles of the POFHN_{Fe_Mms6_surface}, the shape of the assembly may have a strong influence on the shape of the multi-particle magnetic zones. Further study of the magnetic interactions of different patterns of biotemplated magnetite and cobalt doped magnetite are necessary. This could establish if the assembly shape or the level of cobalt doping is the most significant factor in controlling the length of these multi-particle magnetic zones.

7.4.3 Biotemplated Arrays of Cobalt Ferrite

Closely spaced nanoparticles of cobalt ferrite were also biotemplated onto nanolines of Mms6 using the POFHK method. When this method was used to mineralise a micro-patterned surface, the MNPs formed were very small and sparsely distributed on the areas of immobilised Mms6. This difference may be due to the Mms6 being better able to interact with the 33% Co POFHK mineralisation solution when patterned on the nanoscale. If Mms6 is better able to fold correctly at the edge of the protein immobilisation areas, a larger proportion of the patterned protein will be at the edge of patterned areas on the nanoline patterns. Also, the distance between the centre and edge of the nanopatterned lines is far less than for the micro-pattern. This means that surface diffusion is less likely to limit the delivery of reactants to all of the immobilised Mms6 protein. Therefore, any reduction of the biomineralisation ability of Mms6 due to misfolding or surface diffusion effects will be greatly reduced for the nanoscale patterns (Figure 7.3), allowing the immobilised protein to biotemplate MNPs more effectively.

SEM images show that the nanopatterned Mms6 templated lines of MNPs 1-2 nanoparticles wide on the POFHK_{33%Co_Mms6_surface}, and EDX maps show that cobalt is included in these equidimensional MNPs. It can be seen in the MFM plots of the POFHK_{33%Co_Mms6_surface} patterns that the closely spaced biotemplated MNPs are all attractive to the MFM tip. Again, this alignment of the direction of magnetisation across multiple nanoparticles could be due to the line shape on which the particles are patterned, or due to the high levels of cobalt present in the ferrite MNPs. As suggested above, further study using different levels of cobalt doping and different pattern morphologies could establish if the shape of the assembly or level of cobalt doping is most important for dictating the morphology of the multi-particle magnetic domains formed on these biotemplated arrays. Nanoscale patterning of individual

MNPs at different spacings could also be extremely important in establishing the range over which biotemplated MNPs are able to maintain magnetic interactions. MFM studies of biotemplated nanopatterns of magnetite and cobalt doped magnetite should be able to establish if exchange coupling between adjacent particles is strengthened by the addition of cobalt. It is only when the positioning of the particles can be controlled on the nanoscale that the suitability of biotemplated cobalt ferrite nanoparticles for data storage could be assessed.

It is likely that the coercivity of the POFHK_{33%Co_Mms6_surface} MNPs is higher than for 6% Co doped magnetite. Cobalt ferrite particles of between 30-40 nm in diameter have been shown to have a room temperature coercivity of 2 kOe.²⁷ In the future, grainsize, magnetic hysteresis and XRD crystallographic characterisation of these POFHK_{33%Co_Mms6_surface} MNPs can be carried out. This should allow the properties of the Mms6 biotemplated cobalt ferrite MNPs to be compared to those of the magnetite and 6% cobalt doped magnetite arrays. Even if the POFHK_{33%Co_Mms6_surface} MNPs do have a high coercivity and small grainsize, it is likely that the coercivity of the cobalt ferrite MNPs is still about half of that used in current magnetic data storage applications. Nanoscale patterning of small groups or individual cobalt ferrite MNPs may be able to be used to create bit patterned media. However, until the range of the interactions between nanopatterned MNPs can be established, the packing density of bits on a surface cannot be known. This means that other materials and biological templates may need to be used to create biotemplated magnetic data storage.

7.5 Future Directions for Biotemplated Arrays

Current methods used to synthesise magnetic thin-films for data storage applications require the use of sputtering equipment, high temperatures ($\approx 500^\circ\text{C}$) and vacuum conditions.^{28,29} If the materials also need to be patterned, e.g. to create bit patterned media, clean room facilities and photolithography or e-beam lithography are usually used.^{26,30} These requirements mean that expensive facilities and energy intensive equipment are essential for creating modern devices for data storage applications. The work presented in this study shows that it is possible to create patterns of uniform nanomagnets under far milder conditions when using bioinspired methods. Thus, biotemplating of magnetic materials onto surfaces offers more environmentally friendly, less energy intensive and therefore cheaper routes towards creating devices for magnetic data storage. However, the particles templated by Mms6 are too large and magnetically soft for data storage applications, so further work is necessary to develop biotemplated magnetic arrays for data storage applications.

Despite having a high coercivity, it is likely that cobalt ferrite MNPs templated by Mms6 are still too large to be used for magnetic data storage. Currently, the MNPs used in LMR and PMR to form multi-particle magnetic domains are ≈ 7 nm in diameter,²⁶ which are much smaller than the MNPs biotemplated by Mms6 onto the patterned surfaces. However, bioinspired materials synthesis may be adapted and further developed to form biotemplated magnetic materials even more suited to data storage applications. This work with iron and cobalt ferrites biotemplated by the Mms6 protein can be used as a foundation towards developing more environmentally friendly and cheaper methods to synthesise materials for electronic devices.

There are about 60 different biominerals that occur in nature,³¹ many of which are templated by genetically encoded proteins and peptides. Some of these biomineralisation proteins, such as Mms6, have been shown to also be able to biotemplate mineralisation *in vitro*.^{4,15,32} In this study, Mms6 has been shown to template magnetite, cobalt doped magnetite and cobalt ferrite when immobilised onto a patterned surface. It is possible that Mms6 will also be able to template MNPs of other ferrites that may be more suited to data storage. For example, ferrites doped with barium and strontium may have applications in PMR,²⁶ which could also be templated by Mms6 when immobilised onto a patterned surface. However, the magnetite and cobalt ferrite particles formed by patterned Mms6 are quite large, which could create problems with making high density data storage devices using Mms6 as the biotemplate. Fortunately, protein and peptide sequences have been identified that are able to template the mineralisation of high quality materials that are not biomineralised in nature, also under mild reaction conditions. These materials include nanoparticles of: antibacterial silver,^{33,34} catalytic platinum^{35,36} and palladium,^{37,38} conductive gold,³⁹⁻⁴¹ and magnetic platinum alloys.⁴²⁻⁴⁴

Some of these peptides and proteins are able to biotemplate mineralisation of nanoparticles or thin films of materials whilst immobilised onto a surface. A peptide based on a silica biomineralisation protein was patterned within a polymer substrate.⁴⁵ Once mineralised with silica under mild reaction conditions, the biomineralised polymer substrate was able to produce a hologram with a 50 fold increase in diffraction efficiency over the unmineralised control.⁴⁵ In another study, a different biomineralising peptide was shown to biotemplate autofluorescent silver NPs from an aqueous salt solution when non-specifically bound onto a patterned substrate.⁴⁶ These examples show that biomineralisation onto patterned surfaces could be used to create fluorescent silver patterns or silica optics for the transmission of light, all under mild reaction conditions.

The techniques used in this study to fabricate Mms6 biotemplated arrays of magnets could be combined with some of those used in these other studies to design methods to biosynthesise magnetic materials more suited to data storage. Due to the specificity of a peptide sequence towards their target material, they are able to control nanoparticle composition, structure, size and shape, often at room temperature and using benign chemical precursors. This may be less expensive, and is far more environmentally friendly, than current methods used to synthesise materials for applications. This is because these conventional methods often require very high temperatures and pressures, harsh chemicals and specialised equipment to synthesise high quality nanoparticles for applications. Some routes towards building biotemplated devices for applications such as magnetic data storage are presented below.

7.5.1 Patterning Pre-formed High Anisotropy Biotemplated MNPs

Ferritins are used by many eukaryotes to store iron *in vitro*.⁴⁷ They form self-assembled protein cages that are mineralised with the hydrated ferric oxyhydroxide, ferrihydrite.⁴⁸ Recently, ferritins were nano-patterned on a gold substrate using contact printing of SAMs to form hydrophobic and hydrophilic areas (Figure 7.5).⁴⁹ The mineralised ferritin cages self-assemble onto the hydrophilic lines and form a closely packed array of nanoparticles, which were then annealed at 500°C.⁴⁹ Annealing removed the protein coats from the ferrihydrite cores on the patterned surface, before the surfaces were imaged with MFM.⁴⁹ Unfortunately, the level of oxidation of the patterned ferrihydrite nanoparticles was not known, and the magnetic moment of the oxidised cores was thought to be very low at room temperature.⁴⁹ Therefore, it is unlikely that patterned ferritins mineralised with ferrihydrite could be used in biotemplated data storage. However, SAMs (similar to those used in this study to attach Mms6 onto a patterned surface) could be patterned with protein cages biomineralised with materials more suited to data storage applications. These could be characterised using many of the techniques used here, and may be able to form patterns far more suited to biotemplated magnetic data storage.

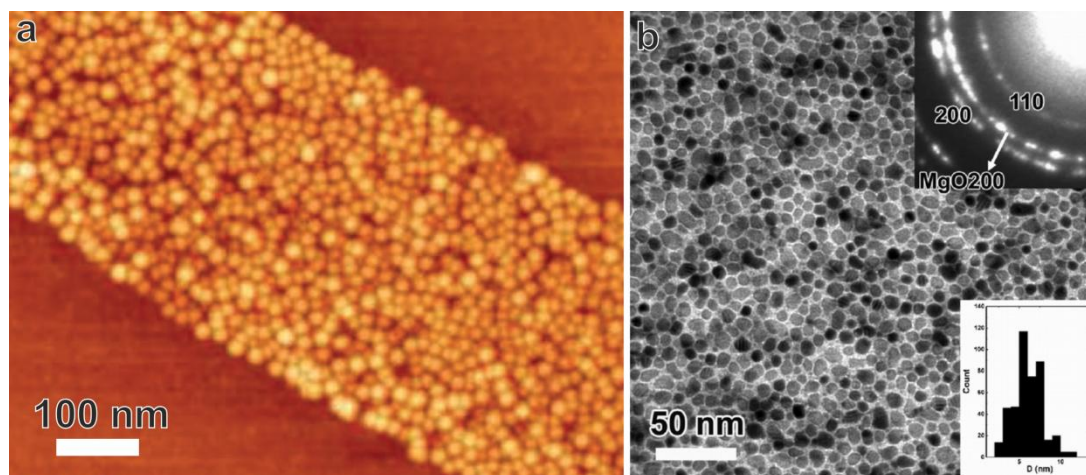


Figure 7.5. (a) AFM of ferritin attached to a patterned SAM from Martinez *et al.* (2011)⁴⁹ and (b) TEM of a sputtered thin-film of $\text{Fe}_{0.45}\text{Pt}_{0.45}\text{Ag}_{0.10}$ on a MgO seed layer from Zhang *et al.* (2011).²⁸ (a) The AFM shows that all the ferritin molecules are very closely packed in a single layer onto the hydrophilic nanoline pattern. (b) Inset SAED pattern from TEM shows significant $L1_0$ chemical ordering of the Pt alloy film, and grainsize distribution is narrow: 6.1 ± 1.8 nm.²⁸

Alloys of platinum with cobalt or iron of the $L1_0$ phase have an extremely high magnetic anisotropy, and are currently used in the development of high density perpendicular data storage.^{28,29,50} In recent work, an MgO seed layer was used to template the $L1_0$ chemical ordering in a sputtered Pt alloy thin-film of MNPs (see Figure 7.5).^{28,29} As with other MNPs, the particles need to be monodisperse in size and shape to ensure the magnetic properties are reliably consistent, and the c -axis of the nanocrystals is normal to the film plane. To achieve these conditions, the substrates are heated to between 450°C ²⁸ and 550°C ²⁹ during sputtering of the film. If the films are deposited at lower temperatures, the $\text{Fe}_{0.45}\text{Pt}_{0.45}\text{Ag}_{0.10}$ alloy forms a disordered phase instead of the high coercivity $L1_0$ phase. The perpendicular coercivity of the $\text{Fe}_{0.45}\text{Pt}_{0.45}\text{Ag}_{0.10}$ layers was measured at > 37 kOe for the film deposited at 450°C ,²⁹ and > 48 kOe for the 550°C deposition.²⁸ The deposited MNPs also have a narrow size distribution, with the 450°C deposition 6.1 ± 1.8 nm²⁸ and the 550°C deposition 7.2 ± 1.5 nm.²⁹

Klem *et al.* (2005)⁴⁴ genetically engineered heat-shock protein cages to biotemplate their interiors with a CoPt nanoparticles from an aqueous solution at 65°C . The heat-shock protein mutant self-assembles to form a protein cage, similar to ferritin, but it has a peptide sequence (KTHEIHSPLLHK) that binds strongly to $L1_0$ CoPt nanoparticles displayed on the interior surface of the protein cage.⁴⁴ This enabled the engineered heat-shock protein to template uniform CoPt MNPs from an aqueous solution of metal ions in the presence of a reducing agent.⁴⁴ These CoPt MNPs have a coercivity of ≈ 15 kOe at room temperature, which is increased to ≈ 61 kOe after a 650°C annealing step. The particles templated within the protein cage showed a significant amount of $L1_0$ chemical ordering before annealing, and

they have a narrower size distribution than the sputtered MNPs (6.5 ± 1.3 nm).⁴⁴ Also, the protein cage was still intact around the unannealed MNPs after metallisation. In both of the sputtered thin-films discussed above, there were also some small SP MNPs deposited, which is highly undesirable as this introduces heterogeneity into the magnetic behaviour of the material. By using the templating ability of the genetically engineered heat-shock protein, the formation of small SP MNPs should be avoided.

Aggregation during annealing increased the size of the biotemplated particles, which can also introduce heterogeneity into the magnetic properties of the MNPs. The technique used by Mosendz *et al.* (2012)²⁹ and Zhang *et al.* (2011)²⁸ to sputter $\text{Fe}_{0.45}\text{Pt}_{0.45}\text{Ag}_{0.10}$ films also used carbon, as this helps to segregate the Pt alloy particles into the small, exchange decoupled grains required for perpendicular magnetic data storage. These high coercivity protein cage templated CoPt MNPs could be patterned onto a hydrophobic/hydrophilic SAM pattern using a similar method to Martinez *et al.* (2011),⁴⁹ see Figure 7.5. If subsequent annealing is required to achieve a higher coercivity, the copious amounts of carbon from the protein cage template and the SAMs could help to prevent particle aggregation during annealing. Even if annealing is required, patterning of heat-shock CoPt nanoparticles would offer a far more environmentally friendly method of generating Pt alloy thin films of the $L1_0$ phase for high density data storage than using current argon sputtering techniques. Patterning MNPs using surface immobilisation of biotemplated CoPt requires far less energy and expensive equipment than is needed to sputter Pt alloy thin-films at high temperatures.

Even if the *c*-axis of the protein templated particles is not aligned to maximise the perpendicular coercivity of these surfaces, the biotemplated MNPs will still be far more suited to generating surfaces for high density data storage than Mms6 templated magnetite or cobalt ferrite. This is because the CoPt biotemplated nanoparticles have a much smaller grain size and a higher coercivity than would be expected from the Mms6 surface templated cobalt ferrite. It should be possible to optimise the expression, purification and mineralisation of the CoPt(Ag) protein cages using similar methods to those developed for this study. Also, the patterning, surface attachment and characterisation techniques used to form Mms6 templated patterns of magnets could be used to analyse these protein cage biotemplated nanomagnets. This would offer a far greener approach than is currently used to fabricate magnetic thin-films with high coercivity for PMR.

7.5.2 Biotemplating Thin-films of High Anisotropy Magnetic Materials

An alternative method to form thin-films of biotemplated magnetic materials could use any of a number of other peptide sequences that have been shown to template L1₀ Pt alloys. Immobilisation of the peptide onto a surface could be used to mineralise a thin-film of a Pt alloy *in situ*. One such peptide (HNKHLPTQPLA) was identified by Reiss *et al.* (2004)⁴³ using biopanning, and it is able to template mainly L1₀ FePt MNPs from an aqueous solution at 60°C in the presence of a reducing agent. They found that the peptide was better able to template the L1₀ phase of FePt at room temperature if many repeats of the peptide were displayed closely packed on the exterior surface of a virus. As the biomineralisation protein Mms6 seems to be stabilised by immobilisation onto a surface, attachment of a L1₀ templating peptide onto a surface before mineralisation may further stabilise the formation of the desired phase of Pt alloy for perpendicular magnetic recording (see Figure 7.6).

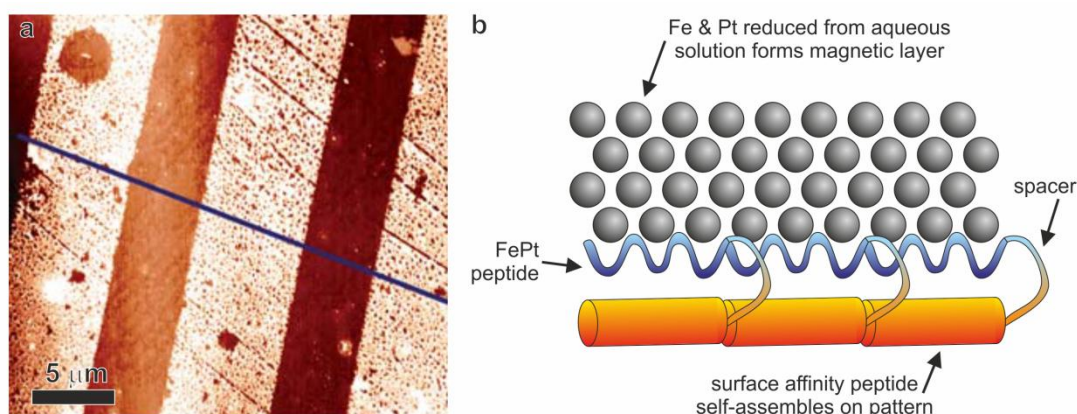


Figure 7.6. AFM image of biotemplated gold films on a patterned surface from Matmor & Ashkenasy (2011)⁴¹ and an illustration of a dual functional peptide which is biotemplating a metal thin-film onto a surface. (a) The AFM image shows 3-4 nm thick electrically conductive gold films biomineralised *in situ*.⁴¹ Schematic in (b) shows the dual functional peptide tightly bound to a surface by one end, and the other end able to biotemplate metal ions from solution to form a thin-film.

In a recent publication, Matmor & Ashkenasy (2011)⁴¹ used a dual functional peptide (DFP) which combines sequences identified by biopanning to biotemplate thin-films of electrically conductive gold onto a silicon surface. One end of the peptide has a strong affinity for silicon oxide (HPPMNASHPHMH),⁵¹ and is used to bind the peptide to a silicon oxide substrate in a pattern using micro-contact printing. The other end of the peptide (MHGKTQATSGTIQS)⁵² is able to reduce gold from an aqueous solution of HAuCl₄ to form an electrically conductive film onto the patterned peptide, under ambient conditions. This method, and the methods used in the formation of Mms6 biotemplated arrays, could be adapted to form a biotemplated, patterned thin-film of an L1₀ platinum alloy. Contact printing a dual

affinity peptide which can bind to silicon oxide and template FePt from an aqueous solution could be used to biotemplate a high coercivity magnetic thin-film onto a similar surface. This would allow patterning of the peptide on the micro and nanoscale to form biotemplated patterns of L1₀ Pt alloys, which may more be suited for use in perpendicular magnetic recording or bit patterned media than Mms6 templated particles.

The biomineralisation of a magnetic film may require the use of a reducing agent, such as NaBH₄, to reduce the metals onto the peptide on the surface. However, alternative methods of reducing platinum using methanol³⁵ may be adapted to make this reaction even more environmentally friendly. Some biopanned peptides, such as the gold templating peptide used by Matmor & Ashkenasy (2011),⁴¹ are able to reduce metal ions directly from solution without the need of a reducing agent. This may also be a possibility for a Pt alloy templating peptide, but no protocol could be found in the literature that would allow MNP formation without the addition of a reducing agent. This may require optimisation of the mineralisation reaction conditions, using techniques similar to those used to optimise the mineralisation of Mms6 on the patterned surfaces. This would also allow optimisation of the phase and orientation of the MNPs on the surface, and thus allow a maximisation of the perpendicular coercivity of the surfaces. Therefore, it may be possible to create biotemplated magnetic surfaces under mild reaction conditions that are far more suited for data storage purposes than the Mms6 templated ferrites synthesised for this study.

7.5.3 Magnetic Recording onto Biotemplated Magnetic Surfaces

The ultimate test of a material designed for use in a magnetic data storage device is to determine if it is able to record and retain information written to it. Static drag testing^{28,29,53} is often used to determine the stability and density that information can be written on to a magnetic material. The read/write heads used to record information are undergoing as rapid technological advances as the magnetic substrates on which a bit is recorded. This should allow researchers to achieve more accurate writing and reading of smaller bit sizes, to achieve higher and higher density data storage. A static drag test uses a write head to record smaller and smaller bits of information onto a magnetic surface (Figure 7.7).⁵³ As the head needs to be in contact with the surface, any surface roughness can create friction and cause the head to stick or abrade the surface. Therefore, the surface formed by the MNPs templated by Mms6 to create the patterned arrays for this study is probably far too rough to attempt drag testing, even if using very large bit sizes.

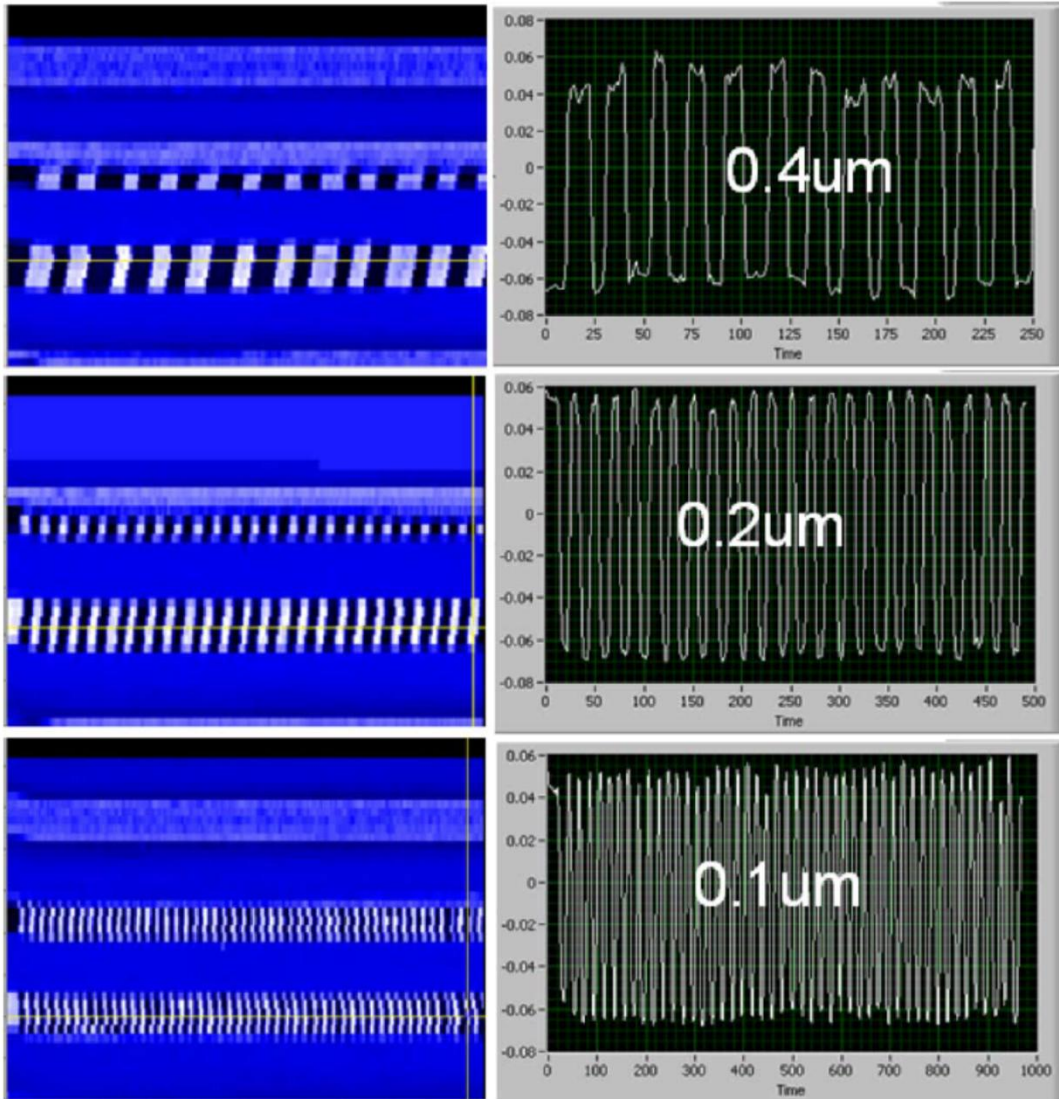


Figure 7.7. 2-D magnetic read-back images (left) and read-back waveforms (right) for magnetic tracks written by a drag tester, from Leong *et al.* (2011).⁵³ Top has a bit length of 0.4 μm , middle is 0.2 μm and bottom is 0.1 μm . The largest bits recorded by the drag tester (400 nm bit length) give a very clear, strong signal to the reader, so the integrity of the recorded information is good. The narrower 100 nm bits have very closely spaced readout, so the recorded information is more difficult to read.

The larger a bit of information, the more stable the magnetic orientation of the particles should be within that bit, so the signal should be strong and clear when read back. A high signal to noise ratio shows clear and accurate recording of information, so is highly desirable.^{28,29,53} The signal to noise ratio is used to assess the smallest size of a bit of information that can be reliably recorded. This smallest accurate bit size can then be used to work out an estimate of the potential storage density of the material being tested. If it can be demonstrated that biotemplated magnetic materials can be used for data storage, this will be a great advance towards the development of bioinspired products and devices. By using static drag testing, the recording ability and stability of the biotemplated magnetic surface can

be directly compared to the latest materials synthesised using the expensive conventional thin-film deposition techniques.

7.5.4 Multi-material Biotemplated Devices

The specificity of peptide sequences to their target material may also allow the fabrication of multi-material biotemplated devices under ambient conditions. For example, Kim *et al.* (2010)⁴⁰ demonstrated that biotemplated gold nanocables biotemplated by a peptide at 37°C could then be further functionalised with a silica templating peptide. This second peptide biotemplated a silica coating onto the gold nanocable, which formed biotemplated nanowires that should be externally insulated, but still able to conduct electricity. This sequential approach allowed Kim *et al.* (2010)⁴⁰ to produce multi-material biotemplated components that could be useful for fabricating electronic devices under mild reaction conditions.

The concept of multi-material biotemplated devices has also been explored by Nochomovitz *et al.* (2010).⁵⁴ They used two different dual affinity materials binding peptides to pattern gold nanoparticles and carbon nanotubes onto the same surface. They formed a pattern by stamping a DFP that binds to silicon oxide and gold nanoparticles onto a silicon oxide surface. Then, carbon nanotubes functionalised with a second DFP (one end binding to nanotubes, the other to silicon oxide) were stamped in a different pattern over the top of the first peptide pattern.⁵⁴ When exposed to Au nanoparticles, the surface was selectively functionalised with the gold particles onto the areas patterned with the first DFP. Although the application for such an assemblage of nanoparticles on a surface is unclear, this work demonstrates how useful the specificity of materials binding peptides is when controlling the positioning and assembling different materials onto the same surface.

The ability to control the location or formation of different types of materials patterned onto a surface using biologically derived peptides would allow the development of cheaper, more environmentally friendly devices. This work with Mms6 biotemplating MNPs onto a patterned surface has developed an adaptable methodology towards the optimisation and characterisation of patterned surfaces of biotemplated magnetic materials. The advantages of biotemplating materials on surfaces to form devices are many, as conventional device fabrication is often equipment, resource and energy intensive. For example, the patterning of the proteins and peptides does not require the ultra-clean conditions of conventional hard lithographic processes for device fabrication, as micro and nano-contact printing can be used. The formation of the materials by the immobilised peptides *in situ* is often done using aqueous 'green' chemicals rather than high temperature, high vacuum processes, such as sputtering. When combined, these factors mean

that, once optimised, bioinspired device fabrication will be cheaper, easier and less energy and resource intensive than many of the current industrial methods for device synthesis. This work using the Mms6 protein to biotemplate magnetic particles onto arrays is a big step towards realising such bioinspired devices in the future.

7.6 References

1. Wang, L., Prozorov, T., Palo, P.E., Liu, X., Vaknin, D., Prozorov, R., Mallapragada, S. & Nilsen-Hamilton, M. (2012). Self-assembly and biphasic iron-binding characteristics of Mms6, a bacterial protein that promotes the formation of superparamagnetic magnetite nanoparticles of uniform size and shape. *Biomacromolecules*. **13**, pp 98-105.
2. (2012). *ExpASY ProtParam tool by the Swiss Institute of Bioinformatics*. <http://web.expasy.org/protparam/> 16/01/2012.
3. Wang, W., Bu, W., Wang, L., Palo, P.E., Mallapragada, S., Nilsen-Hamilton, M. & Vaknin, D. (2012). Interfacial properties and iron binding to bacterial proteins that promote the growth of magnetite nanocrystals: X-ray reflectivity and surface spectroscopy studies. *Langmuir*. **28**, pp 4274-4282.
4. Arakaki, A., Webb, J. & Matsunaga, T. (2003). A novel protein tightly bound to bacterial magnetic particles in *Magnetospirillum magneticum* strain AMB-1. *J. Biol. Chem.* **278**, pp 8745-8750.
5. Xu, D. & Zhang, Y. (2012). Ab initio protein structure assembly using continuous structure fragments and optimized knowledge-based force field. *Proteins*. **80**, pp 1715-1735.
6. Schrödinger, LLC. (2012). *The PyMOL Molecular Graphics System, Version 1.5.0.1*.
7. Faivre, D. & Schüler, D. (2008). Magnetotactic bacteria and magnetosomes. *Chem. Rev.* **108**, pp 4875-4898.
8. Arakaki, A., Masuda, F., Amemiya, Y., Tanaka, T. & Matsunaga, T. (2010). Control of the morphology and size of magnetite particles with peptides mimicking the Mms6 protein from magnetotactic bacteria. *J. Colloid Interface Sci.* **343**, pp 65-70.
9. Naumann, R., Jonczyk, A., Kopp, R., van Esch, J., Ringsdorf, H., Knoll, W. & Gräber, P. (1995). Incorporation of membrane proteins in solid-supported lipid layers. *Angew. Chem. Int. Ed.* **34**, pp 2056-2058.
10. Loh, D., Ross, A.H., Hale, A.H., Baltimore, D. & Eisen, H.N. (1979). Synthetic phospholipid vesicles containing a purified viral antigen and cell membrane proteins stimulate the development of cytotoxic T lymphocytes. *J. Exp. Med.* **150**, pp 1067-1074.
11. Brown, S. (1992). Engineered iron oxide-adhesion mutants of the *Escherichia coli* phage lambda receptor. *Proc. Natl. Acad. Sci.* **89**, pp 8651-8655.
12. Barbas, C.F., Rosenblum, J.S. & Lerner, R.A. (1993). Direct selection of antibodies that coordinate metals from semisynthetic combinatorial libraries. *Proc. Natl. Acad. Sci.* **90**, pp 6385-6389.

13. Korndörfer, I.P. & Skerra, A. (2002). Improved affinity of engineered streptavidin for the Strep-tag II peptide is due to a fixed open conformation of the lid-like loop at the binding site. *Protein Sci.* **11**, pp 883-893.
14. Wedemeyer, W.J., Welker, E., Narayan, M. & Scheraga, H.A. (2000). Disulfide bonds and protein folding. *Biochemistry.* **39**, pp 4207-4216.
15. Amemiya, Y., Arakaki, A., Staniland, S.S., Tanaka, T. & Matsunaga, T. (2007). Controlled formation of magnetite crystal by partial oxidation of ferrous hydroxide in the presence of recombinant magnetotactic bacterial protein Mms6. *Biomaterials.* **28**, pp 5381-5389.
16. Sugimoto, T. & Matijevic, E. (1980). Formation of uniform spherical magnetite particles by crystallization from ferrous hydroxide gels. *J. Colloid Interface Sci.* **74**, pp 227-243.
17. Berry, C.C. & Curtis, A.S.G. (2003). Functionalisation of magnetic nanoparticles for applications in biomedicine. *J. Phys. D: Appl. Phys.* **36**, pp R198-R206.
18. Weissleder, R., Bogdanov, A., Neuwelt, E.A. & Papisov, M. (1995). Long-circulating iron oxides for MR imaging. *Adv. Drug Delivery Rev.* **16**, pp 321-334.
19. Alphandéry, E., Guyot, F. & Chebbi, I. (2012). Preparation of chains of magnetosomes, isolated from *Magnetospirillum magneticum* strain AMB-1 magnetotactic bacteria, yielding efficient treatment of tumors using magnetic hyperthermia. *Int. J. Pharm.* **434**, pp 444-452.
20. Ross, S.M. (1995). Overview of the hydrochemistry and solute processes in British wetlands, pp 133-181. in *Hydrology and Hydrochemistry of British Wetlands* (eds. Hughes, J.M.R. & Heathwaite, A.L.). (J. Wiley & Sons, Chichester, UK).
21. Kolber, Z.S., Barber, R.T., Coale, K.H., Fitzwater, S.E., Greene, R.M., Johnson, K.S., Lindley, S. & Falkowski, P.G. (1994). Iron limitation of phytoplankton photosynthesis in the equatorial Pacific Ocean. *Nature.* **371**, pp 145-149.
22. Winter, M. (2012). *Web Elements*. <http://www.webelements.com/> 14/08/2012.
23. Kim, D., Lee, N., Park, M., Kim, B.H., An, K. & Hyeon, T. (2009). Synthesis of uniform ferrimagnetic magnetite nanocubes. *J. Am. Chem. Soc.* **131**, pp 454-455.
24. Nagendran, R., Thirumurugan, N., Chinnasamy, N., Janawadkar, M.P. & Sundar, C.S. (2011). Development of high field SQUID magnetometer for magnetization studies up to 7 T and temperatures in the range from 4.2 to 300 K. *Rev. Sci. Instrum.* **82**, pp 015109.
25. Yamamoto, K., Hogg, C.R., Yamamuro, S., Hirayama, T. & Majetich, S.A. (2011). Dipolar ferromagnetic phase transition in Fe₃O₄ nanoparticle arrays observed by Lorentz microscopy and electron holography. *Appl. Phys. Lett.* **98**, pp 072509.
26. Piramanayagam, S.N. (2007). Perpendicular recording media for hard disk drives. *J. Appl. Phys.* **102**, pp 011301.
27. Chinnasamy, C.N., Senoue, M., Jeyadevan, B., Perales-Perez, O., Shinoda, K. & Tohji, K. (2003). Synthesis of size-controlled cobalt ferrite particles with high coercivity and squareness ratio. *J. Colloid Interface Sci.* **263**, pp 80-83.
28. Zhang, L., Takahashi, Y.K., Hono, K., Stipe, B.C., Juang, J.-Y. & Grobis, M. (2011). L1₀-ordered FePtAg--C granular thin film for thermally assisted magnetic recording media (invited). *J. Appl. Phys.* **109**, pp 07B703.

29. Mosendz, O., Pisana, S., Reiner, J.W., Stipe, B. & Weller, D. (2012). Ultra-high coercivity small-grain FePt media for thermally assisted recording (invited). *J. Appl. Phys.* **111**, pp 07B729.
30. Hellwig, O., Berger, A., Thomson, T., Dobisz, E., Bandic, Z.Z., Yang, H., Kercher, D.S. & Fullerton, E.E. (2007). Separating dipolar broadening from the intrinsic switching field distribution in perpendicular patterned media. *Appl. Phys. Lett.* **90**, pp 162516.
31. Metzler, R.A., Kim, I.W., Delak, K., Evans, J.S., Zhou, D., Beniash, E., Wilt, F., Abrecht, M., Chiou, J.-W., Guo, J., Coppersmith, S.N. & Gilbert, P.U.P.A. (2008). Probing the organic–mineral interface at the molecular level in model biominerals. *Langmuir*. **24**, pp 2680-2687.
32. Galloway, J.M., Arakaki, A., Masuda, F., Tanaka, T., Matsunaga, T. & Staniland, S.S. (2011). Magnetic bacterial protein Mms6 controls morphology, crystallinity and magnetism of cobalt-doped magnetite nanoparticles in vitro. *J. Mater. Chem.* **21**, pp 15244-15254.
33. Currie, H.A., Deschaume, O., Naik, R.R., Perry, C.C. & Kaplan, D.L. (2011). Genetically engineered chimeric silk–silver binding proteins. *Adv. Funct. Mater.* **21**, pp 2889-2895.
34. Wang, Y., Cao, L., Guan, S., Shi, G., Luo, Q., Miao, L., Thistlethwaite, I., Huang, Z., Xu, J. & Liu, J. (2012). Silver mineralization on self-assembled peptide nanofibers for long term antimicrobial effect. *J. Mater. Chem.* **22**, pp 2575-2581.
35. Górzny, M.Ł., Walton, A.S. & Evans, S.D. (2010). Synthesis of high-surface-area platinum nanotubes using a viral template. *Adv. Funct. Mater.* **20**, pp 1295-1300.
36. Chiu, C.-Y., Li, Y., Ruan, L., Ye, X., Murray, C.B. & Huang, Y. (2011). Platinum nanocrystals selectively shaped using facet-specific peptide sequences. *Nat. Chem.* **3**, pp 393-399.
37. Chiu, C.-Y., Li, Y. & Huang, Y. (2010). Size-controlled synthesis of Pd nanocrystals using a specific multifunctional peptide. *Nanoscale*. **2**, pp 927-930.
38. Pacardo, D.B., Slocik, J.M., Kirk, K.C., Naik, R.R. & Knecht, M.R. (2011). Interrogating the catalytic mechanism of nanoparticle mediated Stille coupling reactions employing bio-inspired Pd nanocatalysts. *Nanoscale*. **3**, pp 2194-2201.
39. Kim, J., Rheem, Y., Yoo, B., Chong, Y., Bozhilov, K.N., Kim, D., Sadowsky, M.J., Hur, H.-G. & Myung, N.V. (2010). Peptide-mediated shape- and size-tunable synthesis of gold nanostructures. *Acta Biomater.* **6**, pp 2681-2689.
40. Kim, J., Myung, N.V. & Hur, H.-G. (2010). Peptide directed synthesis of silica coated gold nanocables. *Chem. Commun.* **46**, pp 4366-4368.
41. Matmor, M. & Ashkenasy, N. (2011). Peptide directed growth of gold films. *J. Mater. Chem.* **21**, pp 968-974.
42. Naik, R.R., Jones, S.E., Murray, C.J., McAuliffe, J.C., Vaia, R.A. & Stone, M.O. (2004). Peptide templates for nanoparticle synthesis derived from polymerase chain reaction-driven phage display. *Adv. Funct. Mater.* **14**, pp 25-30.
43. Reiss, B.D., Mao, C., Solis, D.J., Ryan, K.S., Thomson, T. & Belcher, A.M. (2004). Biological routes to metal alloy ferromagnetic nanostructures. *Nano Lett.* **4**, pp 1127-1132.

44. Klem, M.T., Willits, D., Solis, D.J., Belcher, A.M., Young, M. & Douglas, T. (2005). Bio-inspired synthesis of protein-encapsulated CoPt nanoparticles. *Adv. Funct. Mater.* **15**, pp 1489-1494.
45. Brott, L.L., Naik, R.R., Pikas, D.J., Kirkpatrick, S.M., Tomlin, D.W., Whitlock, P.W., Clarson, S.J. & Stone, M.O. (2001). Ultrafast holographic nanopatterning of biocatalytically formed silica. *Nature*. **413**, pp 291-293.
46. Naik, R.R., Stringer, S.J., Agarwal, G., Jones, S.E. & Stone, M.O. (2002). Biomimetic synthesis and patterning of silver nanoparticles. *Nat. Mater.* **1**, pp 169-172.
47. Brun, N.E.L., Crow, A., Murphy, M.E.P., Mauk, A.G. & Moore, G.R. (2010). Iron core mineralisation in prokaryotic ferritins. *Biochim. Biophys. Acta.* **1800**, pp 732-744.
48. Uchida, M., Kang, S., Reichhardt, C., Harlen, K. & Douglas, T. (2010). The ferritin superfamily: Supramolecular templates for materials synthesis. *Biochim. Biophys. Acta.* **1800**, pp 834-845.
49. Martinez, R.V., Chiesa, M. & Garcia, R. (2011). Nanopatterning of ferritin molecules and the controlled size reduction of their magnetic cores. *Small*. **7**, pp 2914-2920.
50. Mao, C., Solis, D.J., Reiss, B.D., Kottmann, S.T., Sweeney, R.Y., Hayhurst, A., Georgiou, G., Iverson, B. & Belcher, A.M. (2004). Virus-based toolkit for the directed synthesis of magnetic and semiconducting nanowires. *Science*. **303**, pp 213-217.
51. Eteshola, E., Brillson, L.J. & Lee, S.C. (2005). Selection and characteristics of peptides that bind thermally grown silicon dioxide films. *Biomol. Eng.* **22**, pp 201-204.
52. Brown, S. (1997). Metal-recognition by repeating polypeptides. *Nat. Biotech.* **15**, pp 269-272.
53. Leong, S.H., Lim, M.J.B., Santoso, B., Ong, C.L., Yuan, Z.M., Chen, Y.J., Huang, T.L. & Hu, S.B. (2011). Patterned media and energy assisted recording study by drag tester. *IEEE Trans. Mag.* **47**, pp 1981-1987.
54. Nochomovitz, R., Amit, M., Matmor, M. & Ashkenasy, N. (2010). Bioassisted multi-nanoparticle patterning using single-layer peptide templates. *Nanotechnology*. **21**, pp 145305-145312.

Commonly Used Abbreviations

SAMs		self-assembled monolayers		subscripts - bulk solution	
PEG-OH		resists protein binding		Fe	magnetite
PE-COOH		protein attachment molecule		Co	6% cobalt doped magnetite or
mixed SAM		for protein attachment - 10% PE-COOH/90%PEG-OH		no protein	mineralised with no protein
μ CP		micro-contact printing		His ₆ -Mms6	mineralised with His ₆ -Mms6
				Mms6	mineralised with Mms6

Mms6		magnetite biomineralisation protein		subscripts - surfaces	
His _x		multi-histidine affinity tag		Fe	magnetite
SUMO		solubility enhancing tag - small		6%Co	6% cobalt doped magnetite
MBP		solubility enhancing tag - large		33%Co	cobalt ferrite
EDC/NHS		chemicals for binding proteins to mixed SAM		no protein	mineralised with no protein
pl		isoelectric point - protein has no net charge		Mms6	mineralised with Mms6
				bulk	from a bulk solution
				surface	on a surface

MNPs		magnetic nanoparticles		iron valency	
RTCP		room temperature co-precipitation		Fe ²⁺	ferrous - reduced
POFH		partial oxidation of ferrous hydroxide		Fe ³⁺	ferric - oxidised
POFHK		POFH with potassium hydroxide			
POFHN		POFH with ammonia and hydrazine			

magnetism		materials	
SP	superparamagnetic	α -Fe ₃ O ₄	magnetite
SD	single domain	CoFe ₂ O ₄	cobalt ferrite
MD	multi-domain	α -FeOOH	goethite
M _s	saturation magnetisation	γ -Fe ₂ O ₃	maghemite
H _c	coercivity	γ -FeOOH	lepidocrocite

example - bulk solution		example - surface	
CoHis₆-Mms6		POFHK_{33%Co}_Mms6_surface	
6% Co doped His ₆ -Mms6 templated MNPs		cobalt ferrite MNPs biotemplated by Mms6 onto a patterned surface	